



# PACIFIC EARTHQUAKE ENGINEERING RESEARCH CENTER

## **Detailing Requirements for Column Plastic Hinges subjected to Combined Flexural, Axial, and Torsional Seismic Loading**

**Gabriel Hurtado**

**Jack P. Moehle**

Department of Civil and Environmental Engineering  
University of California, Berkeley

PEER Report No. 2016/09  
Pacific Earthquake Engineering Research Center  
Headquarters at the University of California, Berkeley

December 2016

#### Disclaimer

The opinions, findings, and conclusions or recommendations expressed in this publication are those of the author(s) and do not necessarily reflect the views of the study sponsor(s), the Pacific Earthquake Engineering Research Center, or the Regents of the University of California.

# **Detailing Requirements for Column Plastic Hinges subjected to Combined Flexural, Axial, and Torsional Seismic Loading**

**Gabriel Hurtado**

**Jack P. Moehle**

Department of Civil and Environmental Engineering  
University of California, Berkeley

PEER Report 2016/09  
Pacific Earthquake Engineering Research Center  
Headquarters at the University of California, Berkeley

December 2016



## ABSTRACT

Under earthquake loading, bridge superstructures will in general experience both translational and rotational motions. The rotational motions arise from a number of effects, including shaking response of asymmetrical structures, wave passage effects, and ground failure including fault rupture at the bridge site. As a consequence, supporting columns may be subjected to torsion, which is often ignored in typical design practice. The degree to which torsion reduces bridge safety because of reduced lateral strength and, more importantly, because of reduced deformation capacity, is unclear.

A research program was designed to investigate whether torsional response of reinforced concrete (RC) bridge construction has an important effect on the strength and deformability of the supporting bridge columns. Five one-third scale RC bridge columns were tested in the laboratory under simulated seismic loading. Three circular columns and one oblong column were subjected to a compressive axial load and varying degrees of lateral and torsional loading, characterized by the imposed twist-to-drift ratio. Results are compared with results from tests of another column, reported previously, that was subjected to lateral displacement cycles without twist. It is observed that increasing the twist-to-drift ratio results in appreciable reductions in the lateral deformation capacity.

Analytical models are developed to understand the effect of twist on column response. In addition, the degree of anticipated twist occurring in actual bridge structures is investigated using analytical models of simplified bridge systems under a variety of loadings, including near-fault ground motions and ground motions across fault-rupture zones.

Design implications are addressed and a design procedure is proposed for enabling columns to achieve their intended deformation capacity under simultaneous lateral displacement and twisting deformations.



## **ACKNOWLEDGMENTS**

This report is based on the doctoral dissertation of the first author carried out under the supervision of the second author. The first author expresses his thanks to Professors Anil K. Chopra, Douglas S. Dreger, Gregory L. Fenves, Shaofan Li, and Stephen A. Mahin for their additional guidance during the course of this study.

The laboratory testing program would not have been possible without the dedication and expertise of the laboratory personnel at Davis Hall, namely, Bill MacCracken, Jeff Higginbotham, Dick Parsons, and Lev Stepanov. Additional assistance by graduate student Tran Ng; laboratory assistants Jesse Horn, Karly Ho, and Andrew Snyder; and summer interns Nick Trombetta and Dan Lombardi is also greatly appreciated. Special thanks to Webcor Builders for generously providing materials and labor for construction of the test specimens.

The research was financially supported by funds from the California Department of Transportation, Project 04-EQ091. Caltrans engineers Craig Whitten and Fadel Alameddine provided expert advice on the design and conduct of the laboratory experiments and the development of this report.

The opinions, findings, and conclusions or recommendations expressed in this publication are those of the author(s) and do not necessarily reflect the views of the Regents of the University of California or the Pacific Earthquake Engineering Research Center.



# Contents

<b>List of Figures</b>	<b>v</b>
<b>List of Tables</b>	<b>xiii</b>
<b>1 Introduction</b>	<b>1</b>
1.1 Motivation . . . . .	1
1.2 Objective and Scope . . . . .	3
1.3 Organization . . . . .	3
<b>2 Literature Review</b>	<b>5</b>
2.1 Performance of Columns Subjected to Lateral Loading . . . . .	5
2.1.1 Member Behavior . . . . .	5
2.1.2 Bar Slip Models . . . . .	7
2.2 Seismically Induced Torsion of Bridge Structures . . . . .	12
2.3 Torsional Strength and Stiffness of Reinforced Concrete Members . . . . .	14
2.4 Effects of Cyclic Torsional Loading on Reinforced Concrete Members . . . . .	21
2.5 Effects of Simulated Seismic Torsion on Reinforced Concrete Columns . . . . .	23
2.6 Design Provisions for Reinforced Concrete Members Subjected to Torsion . . . . .	30
<b>3 Specimen Design and Construction</b>	<b>32</b>
3.1 Prototype Columns . . . . .	32
3.2 Test Specimen Design . . . . .	33
3.2.1 Longitudinal Reinforcement . . . . .	35
3.2.2 Lateral Reinforcement . . . . .	37
3.2.3 Footing Reinforcement . . . . .	43
3.3 Measured Material Properties . . . . .	49
3.3.1 Concrete Properties . . . . .	50
3.3.2 Reinforcing Steel Properties . . . . .	55
3.4 Construction . . . . .	58
<b>4 Experimental Program</b>	<b>68</b>
4.1 Test Program . . . . .	68
4.2 Test Setup . . . . .	69
4.3 Loading Protocol . . . . .	73

4.4	Instrumentation . . . . .	75
<b>5</b>	<b>Experimental Results</b>	<b>84</b>
5.1	Overview . . . . .	84
5.2	Column 415 . . . . .	85
5.3	Column C1 . . . . .	86
	5.3.1 Observed Response . . . . .	86
	5.3.2 Global Response . . . . .	87
5.4	Column C2 . . . . .	88
	5.4.1 Observed Response . . . . .	88
	5.4.2 Global Response . . . . .	89
5.5	Column C3 . . . . .	89
	5.5.1 Observed Response . . . . .	90
	5.5.2 Global Response . . . . .	91
5.6	Column C4 . . . . .	91
	5.6.1 Observed Response . . . . .	91
	5.6.2 Global Response . . . . .	92
5.7	Bar Slip . . . . .	103
5.8	Comparative Summary . . . . .	104
	5.8.1 Circular Columns . . . . .	104
	5.8.2 Circular vs. Oblong Column . . . . .	109
<b>6</b>	<b>Evaluation of Analytical Models</b>	<b>142</b>
6.1	Material Modeling . . . . .	142
	6.1.1 Concrete . . . . .	142
	6.1.2 Reinforcing Steel . . . . .	144
6.2	Bar Slip Modeling . . . . .	146
6.3	Plastic Hinge Length Modeling . . . . .	147
6.4	Softened Truss Modeling . . . . .	148
	6.4.1 Governing Equations . . . . .	149
	6.4.2 Constitutive Laws of Materials . . . . .	151
	6.4.3 Additional Equations . . . . .	152
	6.4.4 Selected Constitutive Relationships . . . . .	154
	6.4.5 Solution Procedure . . . . .	156
	6.4.6 Effects of Axial Load and Steel Model . . . . .	158
6.5	Three-Dimensional Truss Modeling . . . . .	162
	6.5.1 Modeling of Truss Elements . . . . .	162
	6.5.2 Implementation . . . . .	168
6.6	Comparison of Analytical and Experimental Results . . . . .	170
	6.6.1 Torsional Loading . . . . .	170
	6.6.2 Lateral Loading . . . . .	172
	6.6.3 Combined Lateral and Torsional Loading . . . . .	173

<b>7</b>	<b>Investigation to Estimate Seismic Twist Demand</b>	<b>178</b>
7.1	Bridge Description . . . . .	178
7.1.1	Superstructure . . . . .	179
7.1.2	Substructure . . . . .	181
7.1.3	Abutments . . . . .	182
7.2	Structural Modeling of Bridge . . . . .	182
7.2.1	Materials Models . . . . .	183
7.2.2	Superstructure . . . . .	184
7.2.3	Substructure . . . . .	185
7.2.4	Abutments . . . . .	186
7.3	Ground Motions . . . . .	187
7.3.1	Near-Fault Ground Motions . . . . .	187
7.3.2	Ground Motions Across Fault-Rupture Zones . . . . .	193
7.4	Seismic Analysis . . . . .	197
7.5	Results . . . . .	202
7.6	Findings . . . . .	223
<b>8</b>	<b>Design Implications and Tentative Design Procedure</b>	<b>225</b>
8.1	Effect of Torsion on Flexural Ductility Capacity . . . . .	225
8.2	Theoretical Relation between Quantity of Hoop Reinforcement and Yield Twist	227
8.3	Proposed Design Procedure . . . . .	235
<b>9</b>	<b>Summary, Conclusions, and Future Research</b>	<b>241</b>
9.1	Summary . . . . .	241
9.1.1	Literature Review . . . . .	242
9.1.2	Laboratory Testing Phase . . . . .	242
9.1.3	Analytical Phase . . . . .	244
9.2	Conclusions . . . . .	246
9.2.1	Laboratory Testing Phase . . . . .	246
9.2.2	Analytical Phase . . . . .	247
9.2.3	Design Implications . . . . .	248
9.2.4	Proposed Design Procedure . . . . .	249
9.3	Future Research . . . . .	250
	<b>References</b>	<b>251</b>
<b>A</b>	<b>Test Setup</b>	<b>260</b>
A.1	Specimen Positioning . . . . .	260
A.2	Specimen Post-tensioning . . . . .	261
A.3	Axial Load Setup . . . . .	262
A.4	Lateral Load Setup . . . . .	263
<b>B</b>	<b>Data Reduction</b>	<b>267</b>
B.1	Displacements and Forces . . . . .	267
B.1.1	Lateral Displacement and Twist . . . . .	267
B.1.2	Lateral Force and Torque . . . . .	268
B.2	Column Deformations . . . . .	269

B.2.1	Average Vertical Strain . . . . .	269
B.2.2	Average Horizontal Strain . . . . .	269
B.2.3	Average Curvature . . . . .	271
B.2.4	Average Longitudinal Strain . . . . .	271
B.2.5	Shear Strain . . . . .	271
B.3	Displacement Components . . . . .	272
B.3.1	Column Bending . . . . .	272
B.3.2	Anchorage Slip . . . . .	275
B.3.3	Shear Deformation . . . . .	275
<b>C</b>	<b>Experimental Data</b>	<b>277</b>
C.1	Global Response . . . . .	277
C.2	Column Region . . . . .	278
C.2.1	Horizontal Expansion . . . . .	278
C.2.2	Average Curvature . . . . .	278
C.2.3	Average Longitudinal Strain . . . . .	279
C.2.4	Shear Strain . . . . .	279
C.2.5	Longitudinal Strains . . . . .	280
C.2.6	Hoop Strains . . . . .	280
C.3	Joint Region . . . . .	280
<b>D</b>	<b>Damage Progression</b>	<b>358</b>
D.1	Crack Patterns . . . . .	358
D.2	Measured Crack Widths . . . . .	364
D.3	Location of Fractured and Buckled Bars . . . . .	364
D.4	Photographs . . . . .	374

# List of Figures

2.1	Elastic and Plastic Deformation Components for the Plastic Hinge Model . . . . .	7
2.2	Illustration of Bar Slip . . . . .	8
2.3	Illustration of Bar Segment in Equilibrium . . . . .	9
2.4	Bond Stress versus Slip Model . . . . .	10
2.5	Reinforcement Slip Model . . . . .	11
2.6	Bar Stress versus Slip Models . . . . .	11
2.7	Determination of Slip at Yield . . . . .	12
2.8	Failure Mechanism of Members Subjected to Pure Torsion . . . . .	16
2.9	Thin-Walled Tube and Space Truss Analogies . . . . .	16
2.10	Vertical Side of Space Truss . . . . .	17
2.11	Resolution of Force in Side 2 of Space Truss . . . . .	17
3.1	Prototype Columns . . . . .	34
3.2	Test Columns . . . . .	35
3.3	Expected Material Properties for Moment-Curvature Analysis . . . . .	39
3.4	Fiber Discretized Circular and Oblong Cross Section . . . . .	39
3.5	Moment-Curvature Relationship for Circular Cross Section . . . . .	40
3.6	Moment-Curvature Relationship for Oblong Cross Section . . . . .	40
3.7	Columns C1 and C2 Footing Details . . . . .	44
3.8	Column C3 Footing Details . . . . .	45
3.9	Column C4 Footing Details . . . . .	46
3.10	Concrete Compressive Strength Increase With Age . . . . .	52
3.11	Column C1 Unconfined Concrete Stress-Strain Response . . . . .	53
3.12	Column C2 Unconfined Concrete Stress-Strain Response . . . . .	53
3.13	Column C3 Unconfined Concrete Stress-Strain Response . . . . .	54
3.14	Column C4 Unconfined Concrete Stress-Strain Response . . . . .	54
3.15	Tension Test Setup . . . . .	56
3.16	Main Longitudinal Reinforcement (No. 5 Bar) Stress-Strain Response . . . . .	56
3.17	Interlocking Longitudinal Reinforcement (No. 3 Bar) Stress-Strain Response . . . . .	57
3.18	Hoop Reinforcement (No. 3 Bar) Stress-Strain Response . . . . .	57
3.19	Spiral Reinforcement Stress-Strain Response . . . . .	58
3.20	Typical Footing Reinforcement Cage . . . . .	61
3.21	Column C4 Footing Reinforcement Cage . . . . .	61
3.22	Typical Circular Column Reinforcement Cage . . . . .	62

3.23	Oblong Column Reinforcement Cage . . . . .	63
3.24	Strain Gauges on Longitudinal and Hoop Reinforcement . . . . .	64
3.25	Concrete Placement and Vibration of Footing . . . . .	64
3.26	Concrete Placement and Vibration of Column . . . . .	65
3.27	Specimens Inside Laboratory Before Testing . . . . .	66
3.28	Column C4 Inside Laboratory Before Testing . . . . .	67
4.1	Test Matrix . . . . .	70
4.2	Test Setup . . . . .	71
4.3	Column C2 Ready for Testing . . . . .	72
4.4	Target Displacement and Twist Histories . . . . .	74
4.5	Arrangement of Linear Potentiometers for Measurement of Global Displacement and Twist . . . . .	78
4.6	Typical Displacement Transducer Setup for Measurement of Local Deformations . . . . .	79
4.7	Arrangement of Displacement Transducers for Measurement of Local Deformations . . . . .	80
4.8	Plan View of Displacement Transducers for Measurement of Local Deformations . . . . .	81
4.9	Typical Displacement Transducer Setup for Measurement of Bar Slip . . . . .	81
4.10	Arrangement of Displacement Transducers for Measurement of Bar Slip . . . . .	82
4.11	Arrangement of Strain Gauges . . . . .	83
5.1	Column 415 Force-Displacement Response . . . . .	94
5.2	Column C1 Force-Displacement Response . . . . .	95
5.3	Column C1 Torque-Twist Response . . . . .	95
5.4	Column C1 Force-Displacement Envelopes . . . . .	96
5.5	Column C1 Torque-Twist Envelopes . . . . .	96
5.6	Column C2 Force-Displacement Response . . . . .	97
5.7	Column C2 Torque-Twist Response . . . . .	97
5.8	Column C2 Force-Displacement Envelopes . . . . .	98
5.9	Column C2 Torque-Twist Envelopes . . . . .	98
5.10	Column C3 Force-Displacement Response . . . . .	99
5.11	Column C3 Torque-Twist Response . . . . .	99
5.12	Column C3 Force-Displacement Envelopes . . . . .	100
5.13	Column C3 Torque-Twist Envelopes . . . . .	100
5.14	Spreader Beam and Column Cap Not Twisting in Unison During First 5 deg Twist Amplitude Cycle . . . . .	101
5.15	Column C4 Torque-Twist Response . . . . .	102
5.16	Column C4 Torque-Twist Envelopes . . . . .	102
5.17	Calculated Bond Stress at Yield Level . . . . .	104
5.18	Columns C1 and C2 Crack Patterns after 1 in. Displacement Amplitude Cycle . . . . .	114
5.19	Columns C1 and C2 Crack Patterns after 3 in. Displacement Amplitude Cycle . . . . .	114
5.20	Columns C1 and C2 Crack Patterns after 5 in. Displacement Amplitude Cycle . . . . .	115
5.21	Columns C1 and C2 Crack Patterns after 7 in. Displacement Amplitude Cycle . . . . .	115
5.22	Circular Column Force-Displacement Envelopes . . . . .	116
5.23	Circular Column Torque-Twist Envelopes . . . . .	117
5.24	Columns C1 and C2 Longitudinal Strain History – West Gauges . . . . .	118

5.25	Columns C1 and C2 Longitudinal Strain History – East Gauges . . . . .	119
5.26	Circular Column Longitudinal Strain Profile – West and East Gauges . . .	120
5.27	Columns C1 and C2 Hoop Strain History – North Gauges . . . . .	121
5.28	Columns C1 and C2 Hoop Strain History – South Gauges . . . . .	122
5.29	Columns C1 and C2 Hoop Strain History – West Gauges . . . . .	123
5.30	Columns C1 and C2 Hoop Strain History – East Gauges . . . . .	124
5.31	Circular Column Hoop Strain Profile – North and South Gauges . . . . .	125
5.32	Circular Column Hoop Strain Profile – West and East Gauges . . . . .	126
5.33	Columns C1 and C3 Crack Patterns after 1 in. Displacement Amplitude Cycle	127
5.34	Columns C1 and C3 Crack Patterns after 3 in. Displacement Amplitude Cycle	127
5.35	Columns C1 and C3 Crack Patterns after 5 in. Displacement Amplitude Cycle	128
5.36	Columns C1 and C3 Crack Patterns after 7 in. Displacement Amplitude Cycle	128
5.37	Circular vs. Oblong Column Force-Displacement Envelopes . . . . .	129
5.38	Circular vs. Oblong Column Normalized Force-Displacement Envelopes . .	130
5.39	Circular vs. Oblong Column Torque-Twist Envelopes . . . . .	131
5.40	Circular vs. Oblong Column Normalized Torque-Twist Envelopes . . . . .	132
5.41	Columns C1 and C3 Longitudinal Strain History – West Gauges . . . . .	133
5.42	Columns C1 and C3 Longitudinal Strain History – East Gauges . . . . .	134
5.43	Columns C1 and C3 Longitudinal Strain Profile – West and East Gauges .	135
5.44	Columns C1 and C3 Hoop Strain History – North Gauges . . . . .	136
5.45	Columns C1 and C3 Hoop Strain History – South Gauges . . . . .	137
5.46	Columns C1 and C3 Hoop Strain History – West Gauges . . . . .	138
5.47	Columns C1 and C3 Hoop Strain History – East Gauges . . . . .	139
5.48	Columns C1 and C3 Hoop Strain Profile – North and South Gauges . . . .	140
5.49	Columns C1 an C3 Hoop Strain Profile – West and East Gauges . . . . .	141
6.1	Comparison of Measured Response with Analytical Model for Unconfined Concrete . . . . .	143
6.2	Unconfined and Confined Concrete Constitutive Relationships . . . . .	144
6.3	Comparison of Measured Response with Analytical Model for Main Longi- tudinal Reinforcing Steel . . . . .	145
6.4	Comparison of Measured Response with Analytical Model for Interlocking Longitudinal Reinforcing Steel . . . . .	145
6.5	Comparison of Measured Response with Analytical Model for Hoop Rein- forcing Steel . . . . .	146
6.6	Comparison of Estimated Response with Analytical Model for Bar Slip . . .	147
6.7	Illustration of Lumped-Plasticity Force-Based Element . . . . .	148
6.8	Illustration of Softened Truss Model for Torsion . . . . .	150
6.9	Calculation of $A_o$ and $p_o$ . . . . .	154
6.10	Stress-Strain Curve for Softened Concrete . . . . .	155
6.11	Effect of Axial Load on the Circular Column Torque-Twist Response Using Softened Truss Model for Torsion . . . . .	159
6.12	Effect of Axial Load on the Oblong Column Torque-Twist Response Using Softened Truss Model for Torsion . . . . .	160
6.13	Effect of Steel Model on the Circular Column Torque-Twist Response Using Softened Truss Model for Torsion . . . . .	163

6.14	Effect of Steel Model on the Oblong Column Torque-Twist Response Using Softened Truss Model for Torsion . . . . .	164
6.15	Modeling of Concrete and Reinforcing Bar Elements . . . . .	165
6.16	Comparison of Moment-Curvature Response of Fiberized and Lumped Sections	167
6.17	Illustration of 3D Nonlinear Truss Model . . . . .	169
6.18	Circular Column Measured and Calculated Torque-Twist Response . . . . .	175
6.19	Oblong Column Measured and Calculated Torque-Twist Response . . . . .	175
6.20	Circular Column Measured and Calculated Force-Displacement Response .	176
6.21	Oblong Column Measured and Calculated Force-Displacement Response . .	176
6.22	Illustration of Element Forces on the Compression Face at the Base of the 3D Truss Model Under Flexure . . . . .	177
7.1	Bridge Considered . . . . .	179
7.2	Box Girder Cross Section . . . . .	181
7.3	Column Cross Section . . . . .	181
7.4	Discretized Bridge Model . . . . .	182
7.5	Longitudinal Reinforcing Steel Model . . . . .	183
7.6	Unconfined and Confined Concrete Model . . . . .	184
7.7	Moment-Curvature Relationship for Column Section . . . . .	186
7.8	Torque-Unit Twist Relationship for Column Section . . . . .	187
7.9	Elastic Response Spectra for Magnitude Bin $M_w = 7.0 \pm 0.25$ . . . . .	191
7.10	Elastic Response Spectra for Magnitude Bin $M_w = 7.5 \pm 0.25$ . . . . .	192
7.11	Location of Stations Across Fault . . . . .	194
7.12	Fault-Parallel and Fault-Normal Ground Displacements at Stations Across a Strike-Slip Fault . . . . .	195
7.13	Elastic Response Spectra for Fault-Normal, Fault-Parallel, and Total Ground Motions . . . . .	196
7.14	Effects of Earthquake Magnitude on Fault-Parallel Ground Motions . . . . .	198
7.15	Effects of Earthquake Magnitude on Elastic Response Spectra for Fault-Parallel Ground Motions . . . . .	199
7.16	Vibration Periods and Mode Shapes of Benchmark Bridge . . . . .	200
7.17	Rayleigh Damping of Benchmark Bridge . . . . .	201
7.18	Dynamic Response of Benchmark Bridge Subjected to Loma Prieta 1989 Earthquake, Station LGPC . . . . .	204
7.19	Dynamic Response of Benchmark Bridge Subjected to a Simulated Magnitude 6.5 Event . . . . .	205
7.20	Twist Demand of Bridges Subjected to Magnitude Bin $M_w = 7.0 \pm 0.25$ Ground Motions . . . . .	206
7.21	Twist Demand of Bridges Subjected to Magnitude Bin $M_w = 7.5 \pm 0.25$ Ground Motions . . . . .	206
7.22	Twist Ductility of Bridges Subjected to Magnitude Bin $M_w = 7.0 \pm 0.25$ Ground Motions . . . . .	207
7.23	Twist Ductility of Bridges Subjected to Magnitude Bin $M_w = 7.5 \pm 0.25$ Ground Motions . . . . .	207
7.24	Twist Ductility vs. Displacement Ductility of Bridges Subjected to Magnitude Bin $M_w = 7.0 \pm 0.25$ Ground Motions . . . . .	208

7.25	Twist Ductility vs. Displacement Ductility of Bridges Subjected to Magnitude Bin $M_w = 7.5 \pm 0.25$ Ground Motions . . . . .	208
7.26	Twist History of Bridge Nos. 1 to 4 Subjected to Simulated Ground Motions Crossing Fault . . . . .	209
7.27	Twist History of Bridge Nos. 5 to 8 Subjected to Simulated Ground Motions Crossing Fault . . . . .	210
7.28	Twist History of Bridge Nos. 9 to 12 Subjected to Simulated Ground Motions Crossing Fault . . . . .	211
7.29	Twist History of Bridge Nos. 13 to 16 Subjected to Simulated Ground Motions Crossing Fault . . . . .	212
7.30	Twist Demand of Bridges Subjected to Simulated Ground Motions Crossing Fault . . . . .	213
7.31	Twist Ductility of Bridges Subjected to Simulated Ground Motions Crossing Fault . . . . .	213
7.32	Twist Ductility vs. Displacement Ductility of Bridges Subjected to Simulated Ground Motions Crossing Fault . . . . .	214
7.33	Longitudinal and Transverse Column Displacements of Bridge No. 1 . . . .	215
7.34	Longitudinal and Transverse Column Displacements of Bridge No. 16 . . . .	215
7.35	Twist History of Bridge Nos. 1 to 4 Subjected to Scaled FP Ground Motions	216
7.36	Twist History of Bridge Nos. 5 to 8 Subjected to Scaled FP Ground Motions	217
7.37	Twist History of Bridge Nos. 9 to 12 Subjected to Scaled FP Ground Motions	218
7.38	Twist History of Bridge Nos. 13 to 16 Subjected to Scaled FP Ground Motions	219
7.39	Twist Demand of Bridges Subjected to Scaled FP Ground Motions . . . . .	220
7.40	Twist Ductility of Bridges Subjected to Scaled FP Ground Motions . . . . .	221
7.41	Twist Ductility vs. Displacement Ductility of Bridges Subjected to Scaled FP Ground Motions . . . . .	222
8.1	Relation Between Twist and Drift Capacity . . . . .	226
8.2	Effect of Hoop Spacing on the Predicted Torque-Twist Response of Column C4 Using the Softened Truss Model . . . . .	229
8.3	Effect of $\rho_s$ on the Torque-Twist Response of 4 ft Diameter Columns . . . .	230
8.4	Effect of $\rho_s$ on the Torque-Twist Response of 5 ft Diameter Columns . . . .	231
8.5	Effect of $\rho_s$ on the Torque-Twist Response of 6 ft Diameter Columns . . . .	232
8.6	Effect of $\rho_s$ on the Torque-Twist Response of 8 ft Diameter Columns . . . .	233
8.7	Effect of $\rho_s$ on the Torque-Twist Response of 10 ft Diameter Columns . . .	234
8.8	Effect of $\rho_s$ and $f'_c$ on the Yield Twist of 4, 5, and 6 ft Diameter Columns .	236
8.9	Effect of $\rho_s$ and $f'_c$ on the Yield Twist of 8 and 10 ft Diameter Columns . .	237
8.10	Illustration of Maximum Expected Twist Demand . . . . .	239
A.1	Positioning of Specimen on Laboratory Floor . . . . .	261
A.2	Specimen Equilibrium Under Axial and Lateral Loading . . . . .	263
A.3	Axial Load Setup . . . . .	264
B.1	Force Components of Vertical Jack Under Lateral Displacement . . . . .	270
B.2	Column Segment Deformation Modes . . . . .	273
B.3	Actual and Measured Average Curvature Distribution for a Cantilever Column	274
B.4	Calculated Slip Rotation for Displacement due to Anchorage Slip . . . . .	275

B.5	Actual and Calculated Shear Strain Distribution for a Cantilever Column . . . . .	276
C.1	Column C1 Level Displacement History . . . . .	281
C.2	Column C1 Displacement Profile . . . . .	282
C.3	Column C1 Displacement Components . . . . .	282
C.4	Column C2 Level Displacement History . . . . .	283
C.5	Column C2 Displacement Profile . . . . .	284
C.6	Column C2 Displacement Components . . . . .	284
C.7	Column C3 Level Displacement History . . . . .	285
C.8	Column C3 Displacement Profile . . . . .	286
C.9	Column C3 Displacement Components . . . . .	286
C.10	Column C1 Level Twist History . . . . .	287
C.11	Column C1 Twist Profile . . . . .	288
C.12	Column C2 Level Twist History . . . . .	289
C.13	Column C2 Twist Profile . . . . .	290
C.14	Column C3 Level Twist History . . . . .	291
C.15	Column C3 Twist Profile . . . . .	292
C.16	Column C4 Level Twist History . . . . .	293
C.17	Column C4 Twist Profile . . . . .	294
C.18	Column C1 Horizontal Expansion History . . . . .	295
C.19	Column C1 Average Horizontal Expansion Profile . . . . .	296
C.20	Column C2 Horizontal Expansion History . . . . .	297
C.21	Column C2 Average Horizontal Expansion Profile . . . . .	298
C.22	Column C3 Horizontal Expansion History . . . . .	299
C.23	Column C3 Average Horizontal Expansion Profile . . . . .	300
C.24	Column C4 Horizontal Expansion History . . . . .	301
C.25	Column C4 Average Horizontal Expansion Profile . . . . .	302
C.26	Column C1 Average Curvature History . . . . .	303
C.27	Column C1 Average Curvature Profile . . . . .	304
C.28	Column C2 Average Curvature History . . . . .	305
C.29	Column C2 Average Curvature Profile . . . . .	306
C.30	Column C3 Average Curvature History . . . . .	307
C.31	Column C3 Average Curvature Profile . . . . .	308
C.32	Column C1 Average Longitudinal Strain History . . . . .	309
C.33	Column C1 Average Longitudinal Strain Profile . . . . .	310
C.34	Column C2 Average Longitudinal Strain History . . . . .	311
C.35	Column C2 Average Longitudinal Strain Profile . . . . .	312
C.36	Column C3 Average Longitudinal Strain History . . . . .	313
C.37	Column C3 Average Longitudinal Strain Profile . . . . .	314
C.38	Column C1 Shear Strain History . . . . .	315
C.39	Column C1 Shear Strain Profile . . . . .	316
C.40	Column C2 Shear Strain History . . . . .	317
C.41	Column C2 Shear Strain Profile . . . . .	318
C.42	Column C3 Shear Strain History . . . . .	319
C.43	Column C3 Shear Strain Profile . . . . .	320
C.44	Column C4 Shear Strain History . . . . .	321

C.45	Column C4 Shear Strain Profile . . . . .	322
C.46	Column C1 Longitudinal Strain History – North and South Gauges . . . . .	323
C.47	Column C1 Longitudinal Strain Profile – North and South Gauges . . . . .	324
C.48	Column C1 Longitudinal Strain History – West and East Gauges . . . . .	325
C.49	Column C1 Longitudinal Strain Profile – West and East Gauges . . . . .	326
C.50	Column C2 Longitudinal Strain History – North and South Gauges . . . . .	327
C.51	Column C2 Longitudinal Strain Profile – North and South Gauges . . . . .	328
C.52	Column C2 Longitudinal Strain History – West and East Gauges . . . . .	329
C.53	Column C2 Longitudinal Strain Profile – West and East Gauges . . . . .	330
C.54	Column C3 Longitudinal Strain History – North and South Gauges . . . . .	331
C.55	Column C3 Longitudinal Strain Profile – North and South Gauges . . . . .	332
C.56	Column C3 Longitudinal Strain History – West and East Gauges . . . . .	333
C.57	Column C3 Longitudinal Strain Profile – West and East Gauges . . . . .	334
C.58	Column C4 Longitudinal Strain History . . . . .	335
C.59	Column C4 Longitudinal Strain Profile . . . . .	336
C.60	Column C1 Hoop Strain History – North and South Gauges . . . . .	337
C.61	Column C1 Hoop Strain Profile – North and South Gauges . . . . .	338
C.62	Column C1 Hoop Strain History – West and East Gauges . . . . .	339
C.63	Column C1 Hoop Strain Profile – West and East Gauges . . . . .	340
C.64	Column C2 Hoop Strain History – North and South Gauges . . . . .	341
C.65	Column C2 Hoop Strain Profile – North and South Gauges . . . . .	342
C.66	Column C2 Hoop Strain History – West and East Gauges . . . . .	343
C.67	Column C2 Hoop Strain Profile – West and East Gauges . . . . .	344
C.68	Column C3 Hoop Strain History – North and South Gauges . . . . .	345
C.69	Column C3 Hoop Strain Profile – North and South Gauges . . . . .	346
C.70	Column C3 Hoop Strain History – West and East Gauges . . . . .	347
C.71	Column C3 Hoop Strain Profile – West and East Gauges . . . . .	348
C.72	Column C4 Hoop Strain History . . . . .	349
C.73	Column C4 Hoop Strain Profile . . . . .	350
C.74	Column C1 Bar Slip History . . . . .	351
C.75	Column C2 Bar Slip History . . . . .	351
C.76	Column C3 Bar Slip History . . . . .	351
C.77	Column C1 Joint Strain History – West Gauges . . . . .	352
C.78	Column C1 Joint Strain History – East Gauges . . . . .	352
C.79	Column C1 Joint Strain Profile . . . . .	353
C.80	Column C2 Joint Strain History – West Gauges . . . . .	354
C.81	Column C2 Joint Strain History – East Gauges . . . . .	354
C.82	Column C2 Joint Strain Profile . . . . .	355
C.83	Column C3 Joint Strain History – West Gauges . . . . .	356
C.84	Column C3 Joint Strain History – East Gauges . . . . .	356
C.85	Column C3 Joint Strain Profile . . . . .	357
D.1	Illustration of Convention . . . . .	359
D.2	Column C1 Crack Patterns . . . . .	360
D.3	Column C2 Crack Patterns . . . . .	361
D.4	Column C3 Crack Patterns . . . . .	362

D.5	Column C4 Crack Patterns . . . . .	363
D.6	Column C1 Location of Buckled and Fractured Bars . . . . .	364
D.7	Column C2 Location of Buckled and Fractured Bars . . . . .	371
D.8	Column C3 Location of Buckled and Fractured Bars . . . . .	373
D.9	Column C1 after 0.75 in. Displacement Amplitude Cycle . . . . .	375
D.10	Column C1 after 1 in. Displacement Amplitude Cycle . . . . .	376
D.11	Column C1 after 1.5 in. Displacement Amplitude Cycle . . . . .	377
D.12	Column C1 after 2 in. Displacement Amplitude Cycle . . . . .	378
D.13	Column C1 after 3 in. Displacement Amplitude Cycle . . . . .	379
D.14	Column C1 after 5 in. Displacement Amplitude Cycle . . . . .	380
D.15	Column C1 Final Damage State . . . . .	381
D.16	Column C2 after 0.75 in. Displacement Amplitude Cycle . . . . .	382
D.17	Column C2 after 1 in. Displacement Amplitude Cycle . . . . .	383
D.18	Column C2 after 1.5 in. Displacement Amplitude Cycle . . . . .	384
D.19	Column C2 after 2 in. Displacement Amplitude Cycle . . . . .	385
D.20	Column C2 after 3.0 in. Displacement Amplitude Cycle . . . . .	386
D.21	Column C2 after 5 in. Displacement Amplitude Cycle . . . . .	387
D.22	Column C2 Final Damage State . . . . .	388
D.23	Column C3 after 0.75 in. Displacement Amplitude Cycle . . . . .	389
D.24	Column C3 after 1 in. Displacement Amplitude Cycle . . . . .	390
D.25	Column C3 after 1.5 in. Displacement Amplitude Cycle . . . . .	391
D.26	Column C3 after 2 in. Displacement Amplitude Cycle . . . . .	392
D.27	Column C3 after 3 in. Displacement Amplitude Cycle . . . . .	393
D.28	Column C3 after 5 in. Displacement Amplitude Cycle . . . . .	394
D.29	Column C3 Final Damage State . . . . .	395
D.30	Column C4 after 0.5 deg Twist Amplitude Cycle . . . . .	396
D.31	Column C4 after 0.7 deg Twist Amplitude Cycle . . . . .	397
D.32	Column C4 after 1.1 deg Twist Amplitude Cycle . . . . .	398
D.33	Column C4 after 1.4 deg Twist Amplitude Cycle . . . . .	399
D.34	Column C4 after 2.1 deg Twist Amplitude Cycle . . . . .	400
D.35	Column C4 after 3.6 deg Twist Amplitude Cycle . . . . .	401
D.36	Column C4 after 5 deg Twist Amplitude Cycle . . . . .	402

# List of Tables

3.1	Longitudinal Reinforcement Ratio . . . . .	36
3.2	Volume Ratio of Lateral Reinforcement . . . . .	38
3.3	Maximum Allowable Contribution of Shear Reinforcement . . . . .	42
3.4	Required Minimum Amount of Shear Reinforcement . . . . .	42
3.5	Column Shear Demand and Capacity . . . . .	42
3.6	Footing Flexural Demand and Capacity . . . . .	48
3.7	Footing Shear Demand and Capacity . . . . .	48
3.8	Joint Stress Demand and Capacity . . . . .	49
3.9	Concrete Mix Design . . . . .	51
3.10	Test Day and Concrete Testing . . . . .	51
3.11	Mean Concrete Compressive Strength . . . . .	52
3.12	Reinforcement Properties . . . . .	55
4.1	Test Matrix . . . . .	69
4.2	Displacement Levels and Associated Twist . . . . .	75
4.3	Instrumentation . . . . .	76
4.4	Data Collection . . . . .	77
5.1	Measured Bar Slip at Yield Level . . . . .	104
5.2	Qualitative Damage Description of Circular Columns . . . . .	106
5.3	Qualitative Damage Description for Twist/Drift Ratio = 0.6 . . . . .	111
7.1	Column Aspect Ratios . . . . .	180
7.2	Superstructure Elastic Properties . . . . .	184
7.3	Selected Ground Motions for Magnitude Bin $M_w = 7.0 \pm 0.25$ . . . . .	189
7.4	Selected Ground Motions for Magnitude Bin $M_w = 7.5 \pm 0.25$ . . . . .	190
8.1	Column Parameters . . . . .	228
A.1	Specimen Rotation/Sliding Demand and Capacity . . . . .	262
A.2	Horizontal Acuator Demands . . . . .	266
D.1	Column C1 Peak Crack Widths . . . . .	365
D.2	Column C1 Residual Crack Widths . . . . .	366
D.3	Column C2 Peak Crack Widths . . . . .	367

D.4	Column C2 Residual Crack Widths . . . . .	368
D.5	Column C3 Peak Crack Widths . . . . .	369
D.6	Column C3 Residual Crack Widths . . . . .	370
D.7	Column C4 Peak Crack Widths . . . . .	371
D.8	Column C4 Residual Crack Widths . . . . .	372

# Chapter 1

## Introduction

### 1.1 Motivation

Bridge superstructures subjected to earthquake loading will in general experience both translational and rotational motions. The rotational motions arise from a number of effects, including shaking response of asymmetrical structures, wave passage effects, and ground failure including fault-rupture at the bridge site. As a consequence, the supporting columns may be subjected to torsion under earthquake loading. In typical design practice this torsion often is ignored. The degree to which torsion reduces bridge safety because of reduced lateral load strength or more importantly because of reduced deformation capacity, is unclear.

Current practice for the design of reinforced concrete (RC) columns is based on extensive experience gained from past earthquakes and laboratory tests. The design approach aims to achieve ductile response through flexural yielding in pre-selected flexural plastic hinges. These plastic hinges are provided with closely spaced transverse reinforcement that imparts considerable flexural ductility capacity, whereas the rest of the column is designed

to remain essentially elastic. Design procedures to reliably achieve the required ductility are verified by numerous static and dynamic tests of columns. These design procedures have proved effective in several earthquakes since they were introduced into design practice in the 1970s.

For a bridge frame that develops torsional dynamic response under earthquake ground shaking, two conditions need to be considered, depending on the bridge geometry:

**Condition 1 — Bridge frames having multiple columns or abutments that resist transverse loading.** In this case, alternate load paths exist for resisting bridge frame torsion. Torsion on the bridge column may result in torsional cracking, but significant reduction in torsional stiffness following cracking likely results in redistribution of the frame torsional action to adjacent lateral force resisting elements, thereby relieving to some degree the torsion in the column. In this case, the main question is not whether the column can resist the torsional moment but whether the resulting twist will affect the flexural and shear response of the column.

**Condition 2 — Bridge frames not having multiple columns or abutments that resist transverse loading.** In this case, there is no alternate load path for resisting bridge frame torsion. This condition can be more problematic for column torsion, as any torsional moment acting on the system must be resisted by direct torsion in the column.

Single column bridge frames are not uncommon in typical RC bridge construction, however, single column bridge frames without abutments (Condition 2) are uncommon. Condition 1 is the most common and will be the focus of this work.

## 1.2 Objective and Scope

The objective of this research was to investigate whether torsional response of RC bridge construction would have a significant effect on the strength and deformability of the supporting bridge columns. This objective was pursued through literature review, laboratory testing, analytical model development to understand the effect of twist on column response, and analyses of simplified bridge systems under a variety of loadings to investigate the degree of twist anticipated.

The scope is conventional RC bridge construction having columns reinforced with circular hoops, and loading conditions in which an alternate load path was available so the column did not need to resist superstructure torsion through column torsional moment.

## 1.3 Organization

Chapter 2 provides an overview of previous research on columns subjected to lateral loading, concrete members subjected to torsion, the effects of seismic torsion on concrete columns, and design provisions of concrete members subjected to torsion.

Chapter 3 introduces a series of RC bridge column test specimens that were constructed and tested as part of this research. The purpose of the tests was to provide data on the seismic behavior of bridge columns subjected to simultaneous flexure, shear, and torsion. This chapter presents test specimen design, reinforcement details, and materials properties. It also documents construction of the test specimens.

Chapter 4 describes the experimental program used for this investigation, including the test setup, loading protocol, and instrumentation.

Chapter 5 presents the observed and measured experimental results.

Chapter 6 describes the analytical models developed to model flexural and torsional response and compares the analytical and experimental results.

Chapter 7 investigates the seismic twist demand of bridge columns using simplified bridge systems under a variety of loadings.

Chapter 8 addresses the design implications of seismic torsion and proposes a design procedure for enabling columns to reach their estimated displacement capacity in the presence of seismic torsion.

Chapter 9 summarizes the findings, presents conclusions, and gives guidance on the direction of future research to be performed.

## Chapter 2

# Literature Review

### 2.1 Performance of Columns Subjected to Lateral Loading

There is extensive literature on the simulated seismic testing of bridge columns. Focus has been on unidirectional lateral loading, including quasi-static, dynamic and shaking table testing, with a smaller number of tests on bidirectional loading. An overview of the behavior of RC columns subjected to unidirectional and bidirectional lateral loading can be found in Lehman and Moehle (2000) and Hachem et al. (2003), respectively.

#### 2.1.1 Member Behavior

According to the method outlined by Aschheim et al. (1997), the total tip displacement of a cantilever column subjected to a lateral load at the tip can be idealized as the sum of the components due to column bending ( $\Delta_{bending}$ ), shear deformation ( $\Delta_{shear}$ ), and anchorage slip ( $\Delta_{slip}$ ), as shown in Eq. 2.1.

$$\Delta = \Delta_{bending} + \Delta_{slip} + \Delta_{shear} \quad (2.1)$$

$$\Delta_{bending} = \Delta_y + \Delta_p \quad (2.2)$$

$$\Delta_{slip} \cong \theta_{slip}L \quad (2.3)$$

$$\Delta_{shear} \cong \frac{V}{A_{eff}G_{eff}}L \quad (2.4)$$

where  $L$  = column length,  $\Delta_y$  = elastic bending component,  $\Delta_p$  = plastic bending component,  $\theta_{slip}$  = slip rotation,  $V$  = shear demand,  $A_{eff}$  = effective shear area, and  $G_{eff}$  = effective shear modulus. Assessment of the inelastic behavior due to bending can be simplified by using the plastic hinge method. The elastic and plastic deformation components due to bending are illustrated in Figure 2.1 and presented in Eqs. 2.5 to 2.6, respectively.

$$\Delta_y = \frac{\phi_{ye}L^2}{3} \quad (2.5)$$

$$\Delta_p = \phi_p L_p \left( L - \frac{L_p}{2} \right) \quad (2.6)$$

where  $L_p$  = plastic hinge length,  $\phi_p$  = plastic curvature =  $\phi - \phi_{ye}$ ,  $\phi_{ye}$  = effective yield curvature, and  $\phi$  = curvature corresponding to attaining  $\Delta_p$ .

Researchers have empirically developed expressions for the plastic hinge length,  $L_p$ . An overview of these models is presented in Lehman and Moehle (2000). Of these plastic hinge length expressions, a widely used expression proposed by Priestley et al. (1996) has been adopted by Caltrans (2004b) for estimating plastic rotations of columns, given by

$$L_p = 0.08L + 0.15f_{yl}d_{bl} \geq 0.3f_{yl}d_{bl} \quad (\text{in., ksi}) \quad (2.7)$$

where  $f_{yl}$  = yield strength of longitudinal reinforcing bars, and  $d_{bl}$  = diameter of longitudinal reinforcing bars.

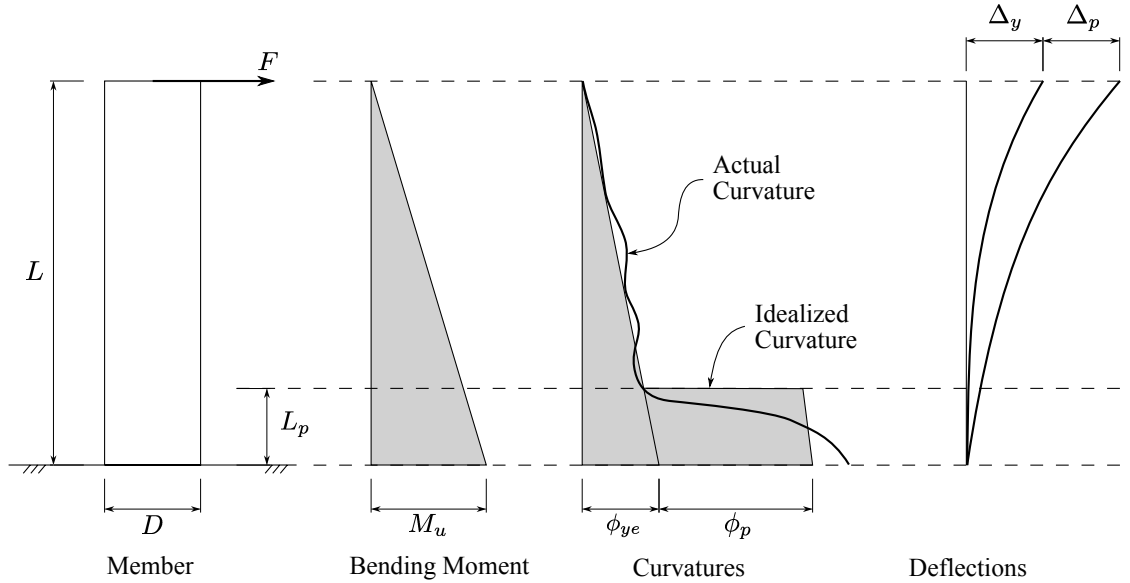


Figure 2.1: Elastic and Plastic Deformation Components for the Plastic Hinge Model

### 2.1.2 Bar Slip Models

Modern construction practice requires that the longitudinal reinforcement of RC columns be well anchored into the joint region so that anchorage failure is avoided. When an anchored bar is subjected to tension at the joint face, a finite distance is required for the bar to transfer tension force into the joint concrete. Therefore, the bar remains in tension along this length, resulting in bar elongation and slippage within the joint. Figure 2.2 illustrates this so-called bar slip. Bar slip causes rigid-body rotations at the ends of RC columns, which contributes to lateral deformations. Lehman and Moehle (2000) reported rotations to account for approximately 30% and 20% of lateral deformations at yield for columns with aspect ratios of four and greater than four, respectively.

Figure 2.3 illustrates equilibrium of an infinitesimal length of bar embedded in

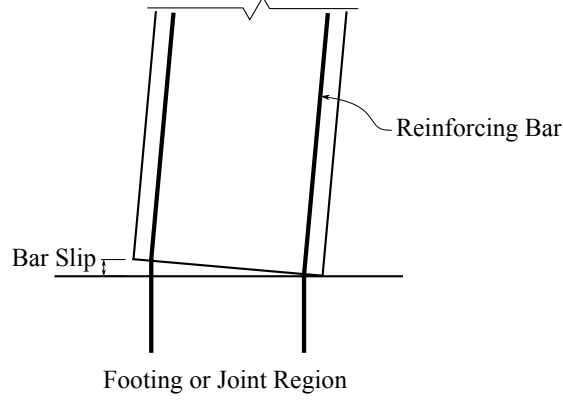


Figure 2.2: Illustration of Bar Slip

concrete. The governing differential equation is given by

$$\frac{d\sigma(x)}{dx} - \alpha\tau(x) = 0 \quad (2.8)$$

where the axial stress and bond stress distribution over the length of the bar are represented by the variables  $\sigma(x)$  and  $\tau(x)$ , respectively. The ratio of the bar circumference to the bar area  $\alpha = (\pi d_b) / (\pi d_b^2/4) = 4/d_b$ , where  $d_b =$  bar diameter. For a fully-anchored bar, assuming linear elastic behavior and a uniform bond stress,  $\mu$ , over the development length,  $l_d$ , the force in the bar,  $F$ , is

$$F = f_s A_b = \mu \pi d_b l_d \quad (2.9)$$

where  $f_s =$  steel stress and  $A_b =$  cross-sectional area of the bar. Substituting for the area of the bar ( $A_b = \pi d_b^2/4$ ), the length over which the bar will be in tension given these assumptions is

$$l_d = \frac{f_s d_b}{4\mu} \quad (2.10)$$

Given the assumption of uniform bond stress, the bar stress decreases linearly from  $f_s$  at the loaded end to zero at distance  $l_d$  from the loaded end. Hence, the bar slip can be

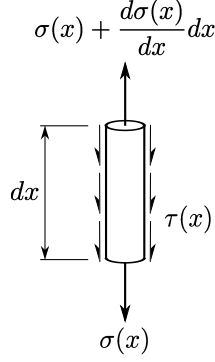


Figure 2.3: Illustration of Bar Segment in Equilibrium

determined from integrating the strains over the development length

$$\text{slip} = \frac{\epsilon_s l_d}{2} = \frac{f_s l_d}{2E_s} = \frac{f_s^2 d_b}{8E_s \mu} \quad (2.11)$$

At yield ( $f_s = f_y$ ), Eq. 2.11 can be rearranged to determine the uniform elastic bond stress at yield, given by

$$\mu_e = \frac{f_y^2 d_b}{8E_s (\text{slip at yield})} \quad (2.12)$$

Based on experiments, Lehman and Moehle (2000) proposed a stepped bond stress versus slip model, as shown in Figure 2.4. In this stepped bond stress model, the uniform bond stress is assumed constant prior to yielding ( $12\sqrt{f'_c}$  (psi)) and constant past yielding ( $6\sqrt{f'_c}$  (psi)). Using this bond stress to steel stress relation, Sezen (2002) obtained a monotonic relation for bar slip versus bar stress at a column base (Figure 2.5). The bar slip can be determined by integrating the strains over the development length

$$\text{slip} = \int_0^{l_d+l'_d} \epsilon(x) dx \quad (2.13)$$

where  $l_d$  = development length for the elastic region and  $l'_d$  = development length for the

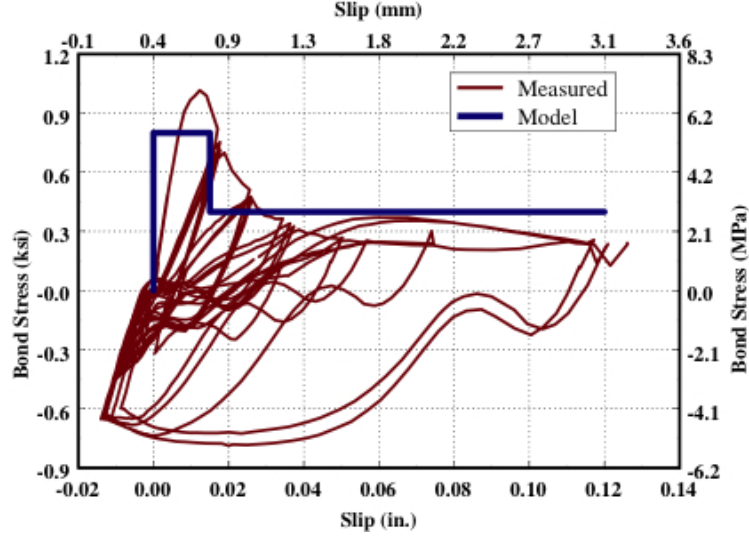


Figure 2.4: Bond Stress versus Slip Model (from Lehman and Moehle, 2000)

inelastic region. Carrying out the integration gives

$$\text{slip} = \frac{\epsilon_s f_s d_b}{8\mu_e}, \quad \epsilon_s \leq \epsilon_y \quad (2.14)$$

$$\text{slip} = \frac{\epsilon_y f_y d_b}{8\mu_e} + \frac{(\epsilon_s + \epsilon_y)(f_s - f_y) d_b}{8\mu_p}, \quad \epsilon_s > \epsilon_y \quad (2.15)$$

where  $d_b$  = reinforcing bar diameter,  $\mu_e$  = elastic bond stress =  $12\sqrt{f'_c}$  (psi), and  $\mu_p$  = plastic bond stress =  $6\sqrt{f'_c}$  (psi). For a bilinear steel stress-strain relationship, the bar stress versus slip relation is parabolic. Figure 2.6(a) shows this parabolic relation and a linearized version proposed by Berry (2006).

Instead of estimating the relation between bond and steel stresses to determine the bar slip, Zhao and Sritharan (2007) derived a bar slip versus bar stress relation based on experimental data. The proposed constitutive model for a bar subjected to monotonic loading consists of a straight line for the elastic region and a curvilinear portion for the post-yield region, as shown in Figure 2.6(b). Hysteretic rules were established for this bar stress

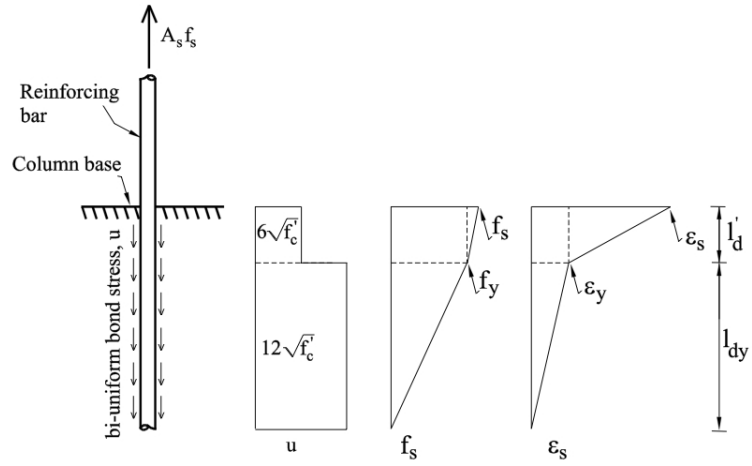
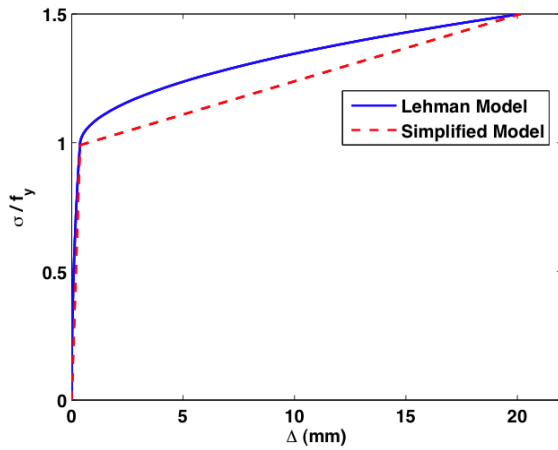
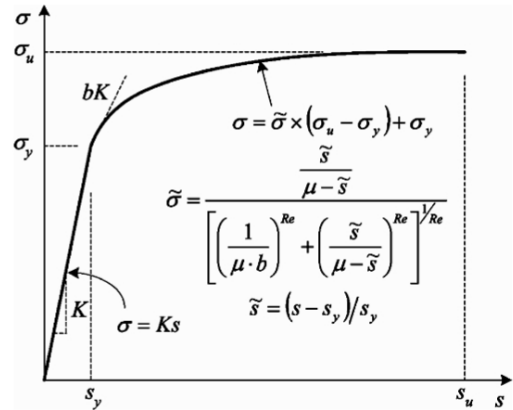


Figure 2.5: Reinforcement Slip Model (from Sezen, 2002)



(a) Lehman and Berry Models (from Berry, 2006)



(b) Zhao Model (from Zhao and Sritharan, 2007)

Figure 2.6: Bar Stress versus Slip Models

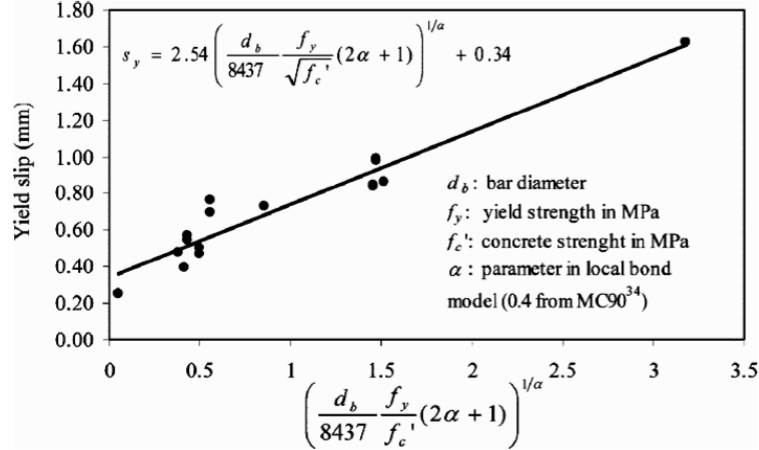


Figure 2.7: Determination of Slip at Yield (from Zhao and Sritharan, 2007)

versus slip relationship to model strain penetration effects for bars subjected to reversed cyclic loading.

Zhao and Sritharan also used results from pull-out test data to perform linear regression analysis (Figure 2.7) to establish an expression for the bar slip at yield strength, given by

$$s_y(\text{mm}) = 2.54 \left[ \frac{d_b(\text{mm})}{8437} \frac{f_y(\text{MPa})}{\sqrt{f'_c(\text{MPa})}} (2\alpha + 1) \right]^{1/\alpha} + 0.34 \quad (2.16)$$

where  $d_b$  = bar diameter,  $f_y$  = yield strength,  $f'_c$  = concrete strength, and the parameter used in the local bond-slip relation  $\alpha = 0.4$ .

## 2.2 Seismically Induced Torsion of Bridge Structures

Seismic torsion in bridges in past earthquakes has been documented (e.g. Goel and Chopra, 1994), analytically investigated (e.g.; Isakovic et al., 1998; Meng and Lui, 2000; Tirasit and Kawashima, 2005), and measured during laboratory testing (e.g.; Johnson et al., 2006; Nelson et al., 2007). Publications in this area emphasize the occurrence of torsional

rotation in bridge structures during strong ground-shaking and that torsion should be taken into consideration when designing the supporting bridge columns.

Goel and Chopra (1994) determined the stiffness values of the abutment-soil systems from the earthquake motions recorded at the US 101/Painter Street Overpass without finite-element modeling of the structure or abutment-soil systems. The road deck of the US 101/Painter Street Overpass experienced significant torsional motions about its vertical axis during the main shock of the 1992 Cape Mendocino/Petrolia earthquake; peak acceleration at the west end of the road deck was more than one-and-a-half times the value at the east end during this earthquake. The eccentricity between the centers of mass and rigidity contributed to the torsional motion of the deck.

Isakovic et al. (1998) performed a parametric study on the viaduct torsional sensitivity of idealized four-span, single-column bent structures. Isakovic et al. found that response was strongly influenced by the type of constraint at the abutments. Analyses showed that viaducts with rollers at the abutments were more torsionally sensitive than structures with pinned abutments. From the response plot presented for an asymmetric bridge with rollers at the abutments, the maximum deck rotation was approximately 0.06 deg.

Meng and Lui (2000) analytically investigated the torsional effect on symmetric and asymmetric short-span highway bridges subjected to seismically induced torque. Rotation of the bridge deck was assumed to be caused by the differential friction force at the deck ends, analogous to an impulsive torque. Furthermore, the maximum deck rotation was related to the impulse and the rotational frequency of the deck. For the nominally symmetric bridge considered, Meng and Lui presented an example value for deck rotation

equal to 0.038 deg.

Tirasit and Kawashima (2005) studied the seismic torsion response of a four-span continuous skewed bridge using the finite element method. Various conditions, including skewed angle, pounding gap, and the locking of steel bearing after failure, were taken into consideration. The in-plane deck rotation occurred due to the pounding between the skewed bridge deck and the abutments, resulting in torsion in the piers. Tirasit and Kawashima reported that the seismic torsions in skewed bridge piers was larger than those of straight bridge piers and that skewed bridge piers have higher ductility demands. Moreover, the effect of pounding was more pronounced in piers located at the center of a skewed bridge. The maximum deck rotation presented was approximately 0.29 deg.

The University of Nevada, Reno conducted large-scale experimental shaking table tests of a two-span (Johnson et al., 2006) and four-span (Nelson et al., 2007) reinforced concrete bridges. Both the two-span and four-span bridges were quarter-scale with symmetric span lengths, supported by two-column bents. Asymmetry of the bridge specimens was due to the different heights of the bents: aspect ratios of 6, 8, and 5 for the two-span test; and aspect ratios of 5, 7, and 6 for the four-span test. An array of instruments were set up to measure the response of the bridge during testing, including the longitudinal and transverse displacement of the deck. For the two-span tests, the maximum differential displacement at the exterior columns was 4.7 in., which resulted in 0.37 deg of twist. The in-plane rotation for the four-span test was explicitly reported to have a maximum twist during testing equal to 0.43 deg.

## 2.3 Torsional Strength and Stiffness of Reinforced Concrete Members

From mechanics of materials, equilibrium of a prismatic thin-tube member of arbitrary cross section subjected to torsion is given by Bredt's thin-tube theory (Ugural and Fenster, 1995)

$$T = q(2A_o) \quad (2.17)$$

where  $q$  = the shear flow and  $A_o$  = the area enclosed by the centerline of shear flow.

Analogously, in 1929 Rausch derived the torsional strength of a reinforced concrete member after cracking based on the shear flow around the perimeter of an idealized space truss. This concept came from the observation that torsion causes inclined cracks which tend to spiral around the member (Figure 2.8). After cracking, a rectangular beam subjected to pure torsion can be idealized as shown in Figure 2.9. A portion of one of the vertical sides is shown in Figure 2.10. Figure 2.11 shows the shear force in Side 2 can be resolved into a diagonal compression force parallel to the inclined compression struts and an axial tensile force. The torsional moment capacity using the space truss model is given by

$$T_n = \frac{A_t f_y \cot \theta}{s} (2A_o) \quad (2.18)$$

where  $A_t$  = cross-sectional area of hoop bar,  $f_y$  = yield strength of hoops,  $\theta$  = inclination angle of cracking relative to the longitudinal axis of the member,  $s$  = hoop spacing, and  $A_o$  = area enclosed by the hoops. This equation is based on the key assumption that the transverse reinforcement yields and the longitudinal steel and diagonals are not overloaded.

The implications of Eq. 2.18 on the placement of reinforcement for rectangular beams are as follows:



Figure 2.8: Failure Mechanism of Members Subjected to Pure Torsion (from Hsu and Liang, 2002)

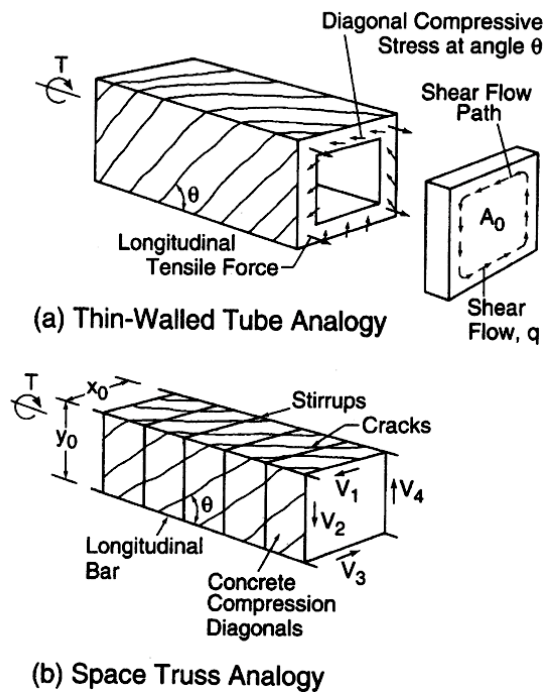


Figure 2.9: Thin-Walled Tube and Space Truss Analogies (from MacGregor and Ghoneim, 1995)

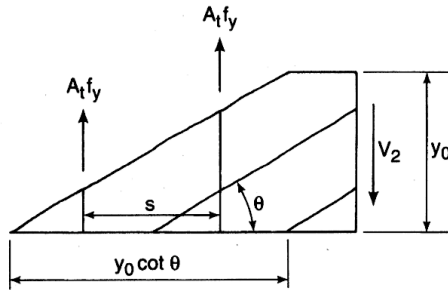


Figure 2.10: Vertical Side of Space Truss (from MacGregor and Ghoneim, 1995)

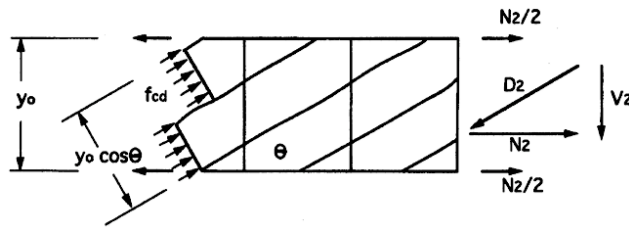


Figure 2.11: Resolution of Force in Side 2 of Space Truss (from MacGregor and Ghoneim, 1995)

1. Beams shall be reinforced with both longitudinal and transverse reinforcement.
2. Transverse reinforcement must consist of closed hoops with a significant component perpendicular to the axis of the member, at spacing no greater than the smallest beam dimension.
3. Longitudinal reinforcement must be distributed symmetrically around the section, with at least one longitudinal bar in each corner of the hoop.

Detailing consequences of longitudinal and transverse reinforcement were observed by Mitchell and Collins (1976) as follows:

**Holding the beam together longitudinally** — the primary function of the longitudinal steel is to hold the beam together along its axis. As the longitudinal steel is in tension, it is essential to provide adequate end anchorage.

**Holding the beam together laterally** — the primary function of the hoops is to hold the beam together in the lateral directions. Spalling of the concrete cover means that considerable care must be taken to achieve proper end anchorage of the hoops.

Mitchell and Collins also showed by laboratory tests that, in general, as the hoop spacing and longitudinal bar spacing were increased, the crack spacing and width increased.

Hsu (1968a) investigated the behavior of rectangular beams under pure torsion by conducting tests on nine series of beams (53 beams total). The eight major variables were (a) amount of reinforcement, (b) solid beams versus hollow beams, (c) ratio of volume of longitudinal bars to volume of hoops, (d) concrete strength, (e) scale effects, (f) depth-to-width ratio of cross section, (g) spacing of longitudinal bars, and (h) spacing of hoops. Some of the more significant findings by Hsu are:

- Before cracking, the behavior of a reinforced concrete beam was identical to its corresponding plain concrete beam with no effect from reinforcement. After cracking, the behavior was completely different from that predicted by Saint-Venant's theory.
- Reinforced concrete beams can be divided into under-reinforced beams, in which the reinforcement yields before compressive crushing of the concrete, and over-reinforced beams, in which the concrete fails before yielding of the steel.
- The concrete core of a reinforced concrete beam did not contribute to the ultimate resistance of the solid beam (also shown by: Hsu, 1990; MacGregor and Ghoneim, 1995).
- The effect of hoop spacing had a minimal effect on the ultimate strength of beams with identical volume ratio of hoops.

Lampert and Collins (1972) showed through laboratory tests and analyses that for under-reinforced and properly detailed beams the torsional strength could be accurately and simply predicted by the space truss model. However, the space truss model became increasingly unconservative with an increasing amount of steel. This was due to the thickness of the shear flow zone, which could become very large, on the order of 1/4 of the outer cross section dimension due to softening of the concrete, which in turn would over-estimate the area enclosed by the shear flow (Hsu, 1990).

Mitchell and Collins (1974) dealt with this unconservatism by presenting a general rational theory for members in pure torsion, called the "diagonal compression field theory." Based on the plastic truss model, they were able to relate steel strains to compressive concrete strains and thus able to model under-reinforced, partially over-reinforced, and

over-reinforced beams. They concluded that their model was capable of predicting the complete post-cracking torsional behavior of symmetrically reinforced concrete members. They further refined their model to be an iterative procedure to achieve better agreement with experimental data (Collins and Mitchell, 1980). Hsu also addressed the unconservatism by presenting a “softened” truss model (Hsu and Moy, 1985; Hsu, 1990), showing excellent agreement between the experimental and theoretical torsional strengths and ultimate twists of reinforced concrete beams. Although both iterative methods were based on slightly different assumptions about concrete properties and thickness of the shear flow zone, they were more accurate than the simple space truss model, but much more complicated to implement.

Most research has focused on the ultimate torsional strength of reinforced concrete beams with the torque-twist relationship being a side product. Hsu (1968a) observed that before cracking, the behavior of a reinforced concrete beam was identical to its corresponding plain concrete beam with no effect from reinforcement. Thus, the torsional stiffness of the reinforced beam would be identical to its corresponding plain concrete beam. However, the amount of reinforcement did affect the cracking torque (Hsu, 1968b), generally increasing with increasing reinforcement (Hsu, 1968a).

After cracking, the torque-twist relationship exhibits a short plateau followed by an increase in resistance at a tangential stiffness equal to a small fraction of the initial stiffness (e.g.; Hsu, 1968a; Collins et al., 1968; Lampert, 1973; Mitchell and Collins, 1974, 1978; Rabbat and Collins, 1978; Hsu and Moy, 1985). Lampert (1973) derived theoretical expressions for the post-cracking secant stiffness of concrete beams in pure torsion based on the space truss model. However, unlike Mitchell and Collins’ diagonal compression field

theory and Hsu's softened truss model, Lampert's expression cannot follow the complete torque-twist curve of a reinforced concrete beam subjected to pure torsion. In contrast, the diagonal compression field theory and the softened truss model have the capability of following the torque-twist curve and providing insight into the torsional stiffness of the beam as it is subjected to monotonically increasing torsion. Other more sophisticated models capable of producing the torque-twist relationship include those by Leung and Schnobrich (1987), Rahal and Collins (1996), and Cocchi and Volpi (1996).

Relatively few publications directly address the application of truss models to members with circular cross sections. Hsu (1968b) defines the cracking torque of a circular section as

$$T_{cr} = \frac{\pi D^3}{16} (0.85 f_r) \quad (2.19)$$

where  $D$  = diameter of the cross section and  $f_r$  = modulus of rupture of concrete. Collins and Mitchell (1980) illustrate the shear flow area of a circular section.

## 2.4 Effects of Cyclic Torsional Loading on Reinforced Concrete Members

Researchers (e.g.; Jakobsen et al., 1984; Venkappa and Pandit, 1987) have shown that, in general, reversed cyclic torsion reduces the torsional strength and stiffness of reinforced concrete members. The degree of reduction is sensitive to the prescribed twist history, peak twist, peak torque, and frequency. Tests have also shown axial compression reduces and delays the stiffness decrease (Jakobsen et al., 1984). These observations are relevant to behavior and response of bridge columns under seismic torsion.

Jakobsen et al. (1984) conducted tests on six one-tenth scale reinforced concrete box columns. Four specimens were subjected to pure torsion and the remaining two were subjected to a constant axial force and torsion. Torque was applied to the specimens by varying the angle of twist through a pre-selected deformation path. Some of the more significant findings by Jakobsen et al. are:

- Failure started as spalling of concrete in the corners outside the reinforcement. Further load cycling degraded the remaining concrete in the corner, which eventually lost shear transfer capacity.
- The secant stiffness decreased anywhere from 8 to 30 before final corner failure. The greatest part of the decrease took place at cracking.
- Load cycling at the current maximum twist level caused stiffness reduction proceeding at a decreasing rate, i.e., a stabilization was observed.
- Load repetitions below the current maximum twist level did not affect the stiffness perceptibly. It seems that the maximum twist level had greater effect on the stiffness than did the number of load repetitions.
- Axial compression reduced and delayed the decrease in stiffness. Increased reinforcement also reduced the stiffness decrease.

Venkappa and Pandit (1987) conducted cyclic torsion tests on 16 reinforced concrete beams and two companion monotonic tests to investigate the degradation of the torsional stiffness and strength of rectangular reinforced concrete beams under the action of reversed cyclic loading. In the monotonic tests, the torque was continuously increased until failure occurred. The cyclic tests were divided into four categories to study: (1) the

influence of the total number of cycles on the peak torque at failure, (2) the influence of prior application of a certain number of cycles of repetitive torsion on the monotonic behavior, (3) the behavior under cyclic torsion with successively increasing levels of the peak torque to examine whether a peak torque lower than the monotonic cracking torque could cause cracking if repeated a sufficiently large number of times, and (4) the nonlinearity of response and residuals with the peak torque increasing continuously. Some of the more significant findings by Venkappa and Pandit are:

- In the pre-cracking range, with a peak torque lower than the static cracking torque, the response was practically linear and was marked by the absence of residual strains and twists.
- The post-cracking range was marked by a considerable nonlinearity of strains and a progressive degradation of torsional stiffness with each successive cycle. The stiffness degradation was higher for higher peak torque and faster loading rate.
- The number of cycles causing failure declined sharply with increasing peak torque. Although a higher range and a faster loading rate also resulted in a decrease in the number of cycles, their effect was not as great as that of the peak torque.
- Torsional cracking could occur if a peak torque lower than the monotonic cracking torque was repeated a sufficiently large number of times.
- The torsional stiffness of a beam preloaded under cyclic torsion was significantly lower than that of a companion beam under virgin loading.

## 2.5 Effects of Simulated Seismic Torsion on Reinforced Concrete Columns

Effects of simulated seismic loading including torsion on bridge columns have been recently studied. The majority of research done in this area has focused on the experimental investigation of the seismic behavior of square bridge columns under flexural and torsional loading. Several researchers from Asia (e.g.; Ogata et al., 2000; Hsu and Wang, 2000; Hsu and Liang, 2003; Nagata et al., 2004; Otsuka et al., 2004; Tirasit et al., 2005) have looked at various types of square column sections (hollow, composite, and plain reinforced) subjected to cyclic and hybrid torsional loading. In the United States, McLean and Buckingham (1994) investigated the response of an oblong spirally reinforced column subjected to cyclic torsion and Belarbi et al. (2007) investigated the performance of circular columns under cyclic bending and torsion.

McLean and Buckingham (1994) investigated the seismic behavior of columns incorporating interlocking spirals under flexure, shear, and torsional loadings. The main tests were performed on eight approximately 1/5 scale column specimens subjected to reversed cyclic lateral displacements under constant axial load. A spiral cracking pattern was exhibited in the specimen under combined shear and torsion (Column 8) and was typical of cracking in reinforced concrete members under combined shear and torsional load. Additional cycles resulted in winding and unwinding of the spiral reinforcement around the longitudinal bars. For positive values of twist, the degradation in peak torque-carrying capacity for Column 8 was approximately 47%. In contrast, the deterioration in the capacity of the specimen for negative values of twist was only 12%. A possible explanation for this phenomena is that the spiral reinforcement tends to tighten around the concrete core when

twisted in one direction and separate from the core when twisted the opposite direction. Strain gauge readings on the spiral reinforcement and visual observation of separation of the spiral reinforcement from the concrete during counter-clockwise loading supports this hypothesis of an winding/unwinding mechanism. McLean and Buckingham concluded that further research into the behavior of interlocking spiral columns subjected to torsional load needed to be conducted, particularly in regard to twist-direction bias resulting in unwinding of the spirals.

Ogata et al. (2000) conducted cyclic loading tests using one-tenth scale models of tall piers having square hollow cross sections. The effects of transverse reinforcement arrangement on ultimate displacement and equivalent viscous damping due to hysteretic response were observed. Cyclic horizontal load and constant axial load was applied to the specimens, except for No. 14. For specimen No. 14, cyclic horizontal and torsional loads were applied. The column was loaded with a ratio of torsional to bending moment equal to 0.15 until cracking occurred. After cracking, loads were controlled to maintain the same ratio between the torsional and bending deformations as was observed when cracking occurred. The experimental data were used to develop indices for evaluating effects of arrangement of intermediate ties on ductility.

Hsu and Wang (2000) experimentally investigated the inelastic behavior of steel reinforced concrete members under cyclically applied bending and torsional loading. Test loadings included pure bending, pure torsion, and combined cyclic bending and torsion. To investigate the effect of torsion on the reduction of bending capacity, a series of combined loading tests using different levels of applied torsion were conducted. Some of the more significant findings by Hsu and Wang are:

- Major reductions in bending strength (approximately 27%) were exhibited when moderate degrees of torsion were applied (approximately 45% of the member torsional strength).
- The effect of torsion must be taken into account when calculating the strength of steel reinforced concrete members that may be subjected to earthquake-induced loading.
- Test data also demonstrated that the effect of torsion on reducing bending strength was more significant for members with larger aspect ratios.

Hsu and Liang (2002) tested twelve hollow composite members under eccentric lateral loading. The composite specimens were divided them into three test series: bending, pure torsion, and combined loading. Monotonically increasing displacement tests were used to obtain the flexural and torsional strengths. For the combined loading tests, a constant axial load was applied throughout the test and the actuator at one end of the loading beam was driven by a prescribed set of increasing cyclic displacement commands. Some of the more significant findings by Hsu and Liang are:

- Members with large concrete thickness possessed higher flexural stiffnesses; however, the loss in stiffness was also higher than in members with smaller concrete thicknesses.
- Major loss of member ductility was exhibited when the twist existed, which suggests the necessity of consideration of twist for members designed for earthquake-resistant purposes.

Nagata et al. (2004) conducted hybrid loading tests of six columns with the horizontal and vertical force eccentricities of one-half and one times the width of the columns.

Equal mass in the longitudinal and transverse direction was lumped at the top of the specimen. The columns were subjected to a unilateral excitation in the longitudinal direction (direction perpendicular to the eccentricity) and a bilateral excitation under a constant vertical load. The ground acceleration recorded at JMA Kobe Observatory during the 1995 Kobe earthquake was used as an input motion by scaling its intensity to 30% of the original. Some of the more significant findings by Nagata et al. are:

- Extensive failure occurred at the plastic hinge in the eccentric compression side under both the unilateral excitation and the bilateral excitation. This resulted in a large residual displacement in the eccentric compression side.
- The failure and the residual displacement under the bilateral excitation was more extensive than those under the unilateral excitation.
- The eccentricity resulted in twist of the columns around their axis under both the unilateral excitation and the bilateral excitation. The twist increased as the eccentricity increased.
- The cyclic load test with the rectangular orbit resulted in more extensive deterioration of the flexural strength than that under the hybrid loading test.

Otsuka et al. (2004) tested nine model columns with two different hoop spacings subjected to different ratios of bending and torsional moments. Types of loading were bending/shear, pure torsion, and combined moment and torsion. Bending loads and torsional loads were cyclic loadings, but axial forces (10% of target compressive strength of concrete) were maintained to be constant during the test. Torsional load surpass type loading was defined as when the target loading ratio is greater than unity (torsion/moment  $> 1$ ).

Bending load surpass type was defined as when the target loading ratio is less than unity (torsion/moment  $< 1$ ). Neutral load type was defined as when the target loading ratio is equal to unity (torsion/moment = 1). Some of the more significant findings by Otsuka et al. are:

- The spacing of hoops appreciably affected the hysteresis loop for torsion, but not for bending.
- Tensile strain in the column hoops uniformly increased due to expansion of the cross section in torsion surpass type, but does not increase in bending surpass type.
- In bending load surpass type, the unit angle of twist at the base was larger than at the center, because of the development of a plastic hinge by the bending moment.

Tirasit et al. (2005) conducted cyclic loading tests of seven reinforced concrete columns to investigate the effect of combined cyclic bending and torsion on the column behavior. Test loading included cyclic torsion, cyclic unilateral bending, and cyclic combined bending and torsion. A constant axial compression was applied to the specimens. The tests were conducted under lateral displacement and twist control. The loading sequence consisted of a series of reversed cycles at increasing displacement amplitudes with simultaneous twist. Levels of combined bending and torsion were set by the twist to drift ratio. The twist to drift ratios tested were 0 (bending only), 0.5, 1.0, 2.0, 4.0, and  $\infty$  (torsion only). Some of the more significant findings by Tirasit et al. are:

- Axial compression increased the torsional strength and the inclination angle of cracks relative to the longitudinal axis of the column. However, the effect of the axial compression became less significant as the twist increased.

- Damage of the column tended to shift upward from the plastic hinge zone as the twist to drift ratio increases. The length of the plastic hinge region tended to increase as the twist to drift ratio increases.
- The flexural strength and the ultimate displacement of the column was reduced as the torsion increased. On the other hand, an increase in bending moment resulted in the deterioration of the torsional strength and the ultimate twist. This interaction should be considered in design of columns subjected to combined flexure and torsion.

Based on the experimental results, Tirasit and Kawashima (2007) proposed a hysteretic model for torsional and flexural hysteresees of square RC columns subjected to combined cyclic bending and torsion. The proposed hysteretic model consists of a tri-linear backbone to idealize the flexural and torsional envelopes, along with unloading and reloading rules for torsion. They found that the hysteretic model provided a good approximation to the experimental result within a twist to drift ratio range of 0.5-4.0.

Belarbi et al. (2007) investigated the performance of circular columns under cyclic combined loading. Three half-scale specimens were designed to be representative of typical existing bridge columns. The specimens were 2 ft in diameter by 12 ft in length, i.e., aspect ratio of 6. Longitudinal reinforcement consisted of twelve No. 8 bars evenly spaced around the circumference. Lateral reinforcement consisted of a No. 3 spiral, spaced at 2.75 in., placed continuously throughout the column height and joint depth. The longitudinal reinforcement ratio and volume ratio of lateral reinforcement were 2.1% and 0.73%, respectively. Types of loading were reversed cyclic unilateral bending, reversed cyclic torsion, and reversed cyclic combined bending and torsion. A constant axial load (7% of target compressive strength of concrete) was applied by prestressing steel strands running through

a duct in the center of the column. The bending tests were conducted under load control until first yield of the longitudinal reinforcing bars and torsion tests were conducted under load control until first yield of the spiral. After the first yield, tests were continued under displacement control. Some of the more significant findings by Belarbi et al. are:

- Failure of the column subjected to bending was by formation of a flexural plastic hinge at the base of the column and subsequent buckling of the longitudinal reinforcing bars.
- Failure of the column subjected to torsion was by diagonal cracking leading to formation of a torsional plastic hinge near the mid-height of the column.
- The location and the length of the plastic hinge changed due to the specific combination of bending and torsion.
- The torsional stiffness degraded more rapidly than the bending stiffness of the column subjected to combined bending and torsion.

The investigations on cyclic torsional loading presented thus far have primarily focused on experimental observation and have not presented analytical models to explain their findings. Nagata et al. (2005) presented a hysteretic model for torsion to predict the experimental results from his previous work (Nagata et al., 2004); however, it is uncoupled from the flexural response and offered no insight into the behavior of flexure-torsion interaction within the plastic hinge region.

## 2.6 Design Provisions for Reinforced Concrete Members Subjected to Torsion

The ACI (2008) and AASHTO (2004) specifications address the torsion and torsion-shear design of RC members. Both codes state that it is permitted to neglect torsion effects when the factored torsional moment,  $T_u$ , is less than the threshold torsion (approximately 25% of the cracking torque).

For normal weight concrete, this threshold torsion is specified in AASHTO (2004) as

$$0.25\phi \left[ 0.125\sqrt{f'_c} \left( \frac{A_{cp}^2}{p_{cp}} \right) \sqrt{1 + \frac{f_{pc}}{0.125\sqrt{f'_c}}} \right] \quad (2.20)$$

where  $A_{cp}$  = total area enclosed by the outside perimeter of the concrete section,  $p_{cp}$  = length of the outside perimeter of the concrete section,  $f_{pc}$  = compressive stress in concrete after prestress losses have occurred, and  $\phi$  = resistance factor.

For nonprestressed members subjected to an axial tensile or compressive force, the threshold torsion is specified in ACI (2008) as

$$\phi\lambda\sqrt{f'_c} \left( \frac{A_{cp}^2}{p_{cp}} \right) \sqrt{1 + \frac{N_u}{4A_g\lambda\sqrt{f'_c}}} \quad (2.21)$$

where  $\lambda$  = modification factor for lightweight concrete,  $N_u$  = axial force, and  $A_g$  = gross area of the concrete section. If torsional effects are considered, the design torsion strength shall not be less than the factored torsion demand ( $\phi T_n \geq T_u$ ). The nominal torsion strength of RC member is given in ACI (2008) as

$$T_n = \frac{2A_oA_t f_{yt}}{s} \cot \theta \quad (2.22)$$

where  $A_o$  = gross area enclosed by the shear path, as determined by analysis or equal to  $0.85A_{oh}$ , where  $A_{oh}$  = area enclosed by the centerline of the outermost closed hoop;

$A_t$  = cross-sectional area of hoop bar;  $f_{yt}$  = specified yield strength of transverse reinforcement;  $s$  = spacing of hoops; and  $\theta$  = angle of compression diagonals, not to be taken smaller than 30 deg nor larger than 60 deg. Moreover, the member shall satisfy minimum hoop spacing requirements and an increase in the longitudinal reinforcement is required, evenly distributed around the perimeter of the hoops.

## Chapter 3

# Specimen Design and Construction

Four one-third scale reinforced concrete test columns were constructed in the laboratory. This chapter presents the specimen design, construction details, and measured materials properties.

### 3.1 Prototype Columns

The prototype column (Figure 3.1) had a circular cross section with a diameter of 6 ft, similar in many regards to columns tested previously at the University of California, Berkeley (e.g.; Lehman and Moehle, 2000; Hachem et al., 2003). However, unlike the previous research, this study used closed-circular hoops instead of a continuous spiral for the lateral reinforcement. This change was meant to more accurately represent current Caltrans practice; circular columns with a diameter of 3 ft or less are built with a continuous spiral, whereas columns with a diameter greater than 3 ft are built with closed-circular hoops (Caltrans Engineers, 2006). Closed-circular hoops were also chosen to avoid the phenomena of winding and unwinding of spiral reinforcement under twisting motions observed by McLean

and Buckingham (1994) and Belarbi et al. (2007).

To test the limits of current construction practice, the spacing of the hoops was set equal to the maximum allowable spacing according to Caltrans (2004b), and the diameter of the hoop reinforcement was increased to the maximum commonly in use to arrive at a volumetric ratio of hoop reinforcement similar to that used in previous research. Additionally, the longitudinal reinforcement and aspect ratio were selected considering past tests of columns subjected to lateral loading and discussions with Caltrans Engineers (2006).

In addition to the circular cross section columns, one oblong column with interlocking hoops was constructed. The prototype oblong column (Figure 3.1) had a cross-sectional dimension of 6 ft by 10 ft, resulting in the maximum permitted center-to-center spacing of hoops (Caltrans, 2004a). The longitudinal reinforcing bars in the interlocking portion of the column were chosen corresponding to current Caltrans practices. Also consistent with current practices, the interlocking bars were not anchored in the footing because they were not necessary for the flexural capacity of the column.

## **3.2 Test Specimen Design**

The circular and oblong prototype columns (Figure 3.1) were designed according to the current Caltrans practice (Caltrans, 2004a, 2004b), then all dimensions were linearly scaled by the factor 1/3. Resulting dimensions were then adjusted to accommodate available materials. Figure 3.2 shows the test column geometry and reinforcement.

Main longitudinal reinforcement of the columns consisted of No. 5 bars evenly spaced around the circumference of the circular and oblong columns. Longitudinal reinforcing bars in the interlocking portion of the oblong column consisted of No. 3 bars not

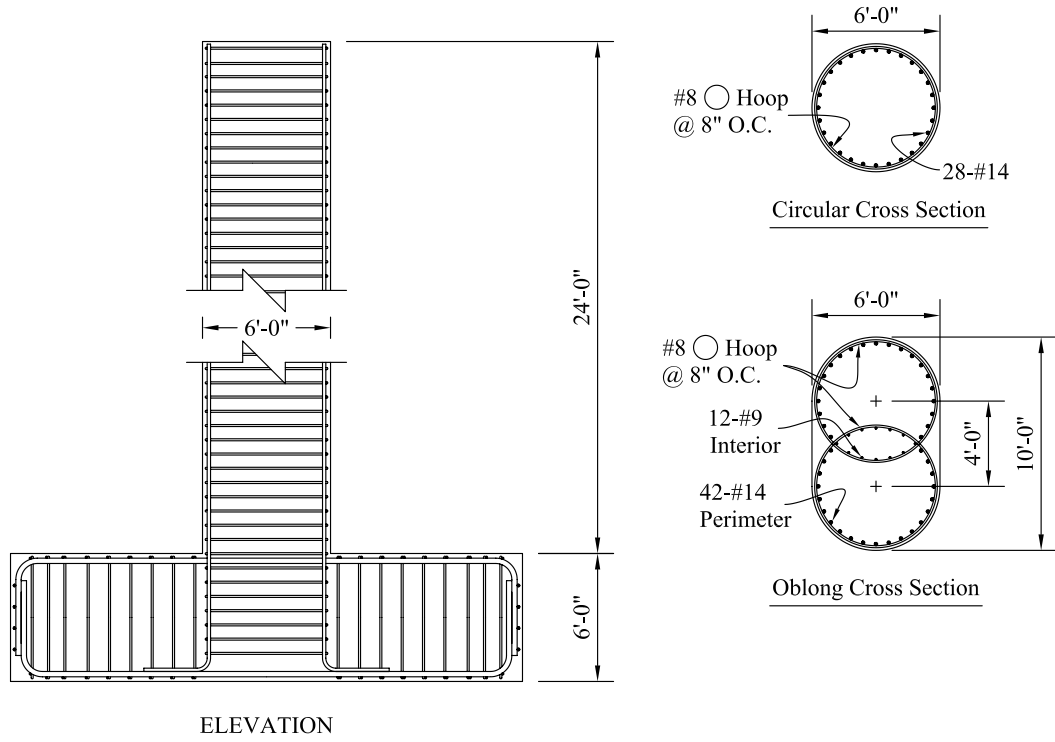


Figure 3.1: Prototype Columns

anchored in the footing. The lateral reinforcement consisted of No. 3 closed-circular hoops, spaced at 2.67 in., placed continuous throughout the column height and joint depth.

Due to construction tolerances, the nominal 24 in. diameter column forms were oversized in diameter by 0.75 in. Therefore, the intended concrete cover of 1/2 in. became 5/8 in. in all the test specimens.

The following sections (Sections 3.2.1 and 3.2.2) outline the column design requirements. All four test columns (Columns C1, C2, C3, and C4) were designed according to these requirements. Section 3.2.3 outlines the footing design requirements. These footing design requirements were not followed for Column C4 and are reflected in the footing reinforcing details.

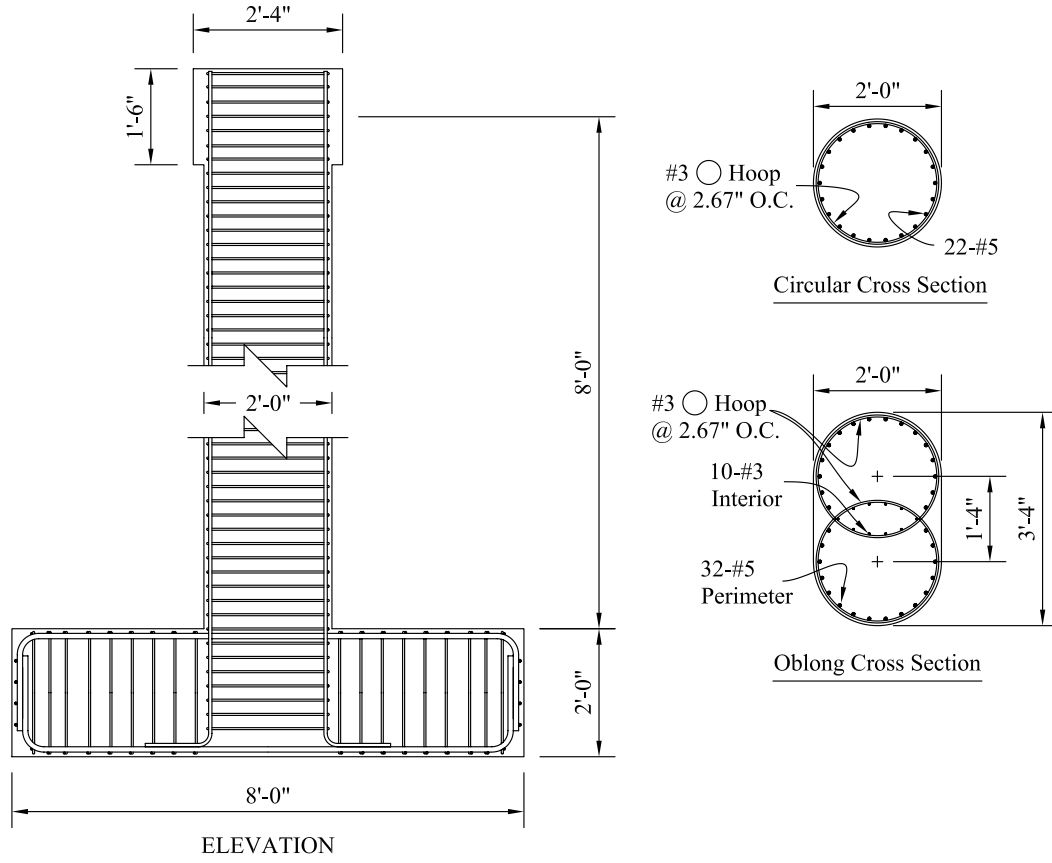


Figure 3.2: Test Columns

### 3.2.1 Longitudinal Reinforcement

#### Area of Reinforcement

The longitudinal reinforcement ratio is defined by

$$\rho_l = \frac{A_s}{A_g} \quad (3.1)$$

where  $A_s$  = area of longitudinal reinforcement and  $A_g$  = gross cross-sectional area. The maximum and minimum longitudinal reinforcement ratios are 0.04 and 0.01 (Caltrans, 2004b, Sec. 3.7), respectively. The longitudinal reinforcement ratio for each cross sec-

Table 3.1: Longitudinal Reinforcement Ratio

Cross Section	Provided	Maximum	Minimum
Circular	0.015		
Oblong	0.012	0.04	0.01

tion is summarized in Table 3.1. Note that this ratio does not include the discontinuous longitudinal reinforcement in the interlocking portion of the oblong column.

### Spacing

The spacing of column longitudinal reinforcement, provided around the perimeter of the hoops and inside the interlocking portion of the hoops, was equal to approximately 3 in.

The required minimum clear distance is defined by (Caltrans, 2004a, Sec. 8.22.1)

$$s_{min} = \text{largest of } \begin{cases} \text{one and one-half bar diameters, } 1.5d_{bl} \\ \text{one and one-half times the maximum size coarse aggregate} \\ 1.5 \text{ in.} \end{cases} \quad (3.2)$$

The provided spacing exceeded  $s_{min} = 1.5$  in. (No. 5 bar and 3/8 in. maximum size coarse aggregate).

The maximum allowable spacing of column longitudinal reinforcement is 8 in. (Caltrans, 2004a, Sec. 8.22.1.1), which when scaled by the factor of 1/3 equals 2.67 in. The provided column longitudinal reinforcement spacing exceeded the maximum allowable spacing by approximately 2/3 in. This was deemed acceptable to maintain similar longitudinal reinforcement ratios and details used in previous research by Lehman and Moehle (2000).

## Development of Reinforcement

The anchorage of the column longitudinal reinforcement in the footing met the specified minimum development length, defined by  $l_{ac,min} = 24d_{bl}$  (Caltrans, 2004b, Sec. 8.2). The minimum development length for a No. 5 column longitudinal bar, 15 in., was exceeded by extending the bar to the opposite face of the footing, approximately 22 in.

### 3.2.2 Lateral Reinforcement

The lateral reinforcement required inside the plastic hinge region met the confinement, shear, and spacing requirements.

#### Confinement

The volume ratio of lateral reinforcement provided inside the plastic hinge length for columns with circular or interlocking core sections is defined by (Caltrans, 2004b, Sec. 3.8.1)

$$\rho_s = \frac{4A_b}{D's} \quad (3.3)$$

where  $A_b$  = cross-sectional area of spiral or hoop,  $D'$  = diameter of the core measured between the centerline of the hoop, and  $s$  = spiral or hoop spacing.

The required minimum ratio of spiral or hoop reinforcement is defined by (Caltrans, 2004a, Sec. 8.18.2.2)

$$\rho_{s,min} = 0.45 \left( \frac{A_g}{A_c} - 1 \right) \frac{f'_c}{f_{yh}} \quad (3.4)$$

$$\geq 0.45 \left( \frac{A_g}{A_c} - 1 \right) \frac{f'_c}{f_{yh}} \left( 0.5 + \frac{1.25P_e}{f'_c A_g} \right), \quad D \leq 3 \text{ ft} \quad (3.5)$$

$$\geq 0.12 \frac{f'_c}{f_y} \left( 0.5 + \frac{1.25P_e}{f'_c A_g} \right), \quad D > 3 \text{ ft} \quad (3.6)$$

Table 3.2: Volume Ratio of Lateral Reinforcement

Provided	Minimum		
	Eq. 3.4	Eq. 3.5	Eq. 3.6
0.0073	0.0033	0.0021	0.0063

where  $A_c$  = area of core measured to the outside of the hoop,  $f'_c$  = specified compressive strength of concrete,  $f_{yh}$  = specified yield strength of spiral or hoop reinforcement but not more than 60 ksi, and  $P_e$  = design axial load. The provided and required volume ratios of lateral reinforcement are summarized in Table 3.2 for  $f_{yh} = 60$  ksi,  $f'_c = 5$  ksi, and  $P_e = 0.1f'_cA_g$ . Note that this provided volume ratio was computed for the nominal column diameter (24 in.) and the intended cover concrete (0.5 in.).

### Shear

The seismic shear demand was based on the plastic shear, defined by

$$V_o = \frac{M_o}{L} = \frac{1.2M_p}{L} \quad (3.7)$$

where  $M_p$  = plastic moment strength of the column and  $L$  = length of the column. The plastic moment capacity was calculated by moment-curvature analysis using expected material properties (Caltrans, 2004b, Sec. 3.3). The stress-strain models for concrete and reinforcing steel are shown in Figure 3.3 (Caltrans, 2004b, Sec. 3.2). The stress-strain model for confined concrete was computed using the relations by Mander et al. (1988). The moment-curvature analysis was performed in *OpenSees* (McKenna et al., 2000) using a fiber discretized circular and oblong cross section (Figure 3.4). The moment-curvature relationship for circular and oblong cross sections, including axial load ( $0.1f'_cA_g$ ), is shown

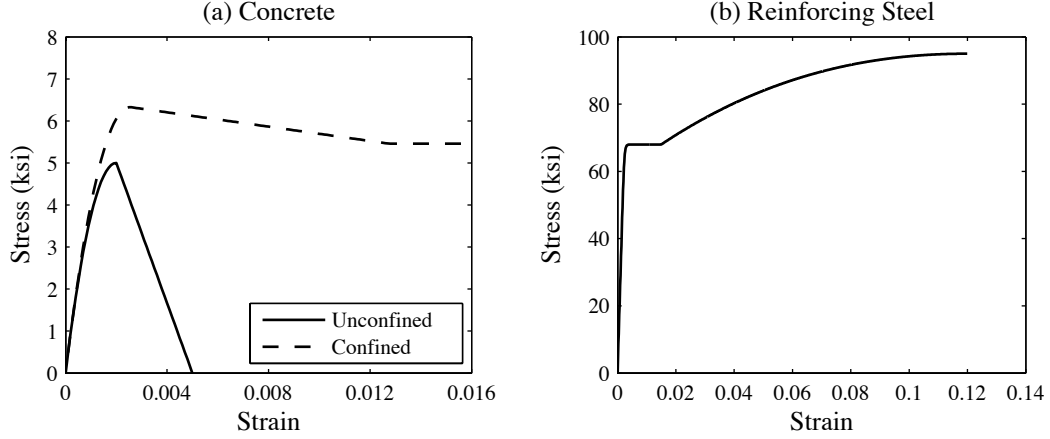


Figure 3.3: Expected Material Properties for Moment-Curvature Analysis

in Figures 3.5 and 3.6, respectively.

The shear strength for ductile concrete members is based on the nominal material strengths, defined by (Caltrans, 2004b, Sec. 3.6)

$$\phi_v V_n \geq V_p, \quad \phi_v = 0.85 \quad (3.8)$$

$$V_n = V_c + V_s \quad (3.9)$$

where  $V_c$  = concrete shear contribution and  $V_s$  = shear reinforcement contribution.

The concrete shear strength inside the plastic hinge zone is defined by (Caltrans, 2004b, Sec. 3.6.2)

$$V_c = v_c A_e \quad (3.10)$$

$$v_c = (\text{Factor1})(\text{Factor2})\sqrt{f'_c} \leq 4\sqrt{f'_c} \text{ (psi)} \quad (3.11)$$

where  $A_e$  = effective shear area =  $0.8A_g$ , and Factor1 and Factor2 can be taken conservatively to be 0.3 and 1.0, respectively, assuming the lower bound values (Caltrans, 2004b, Fig. 3.8).

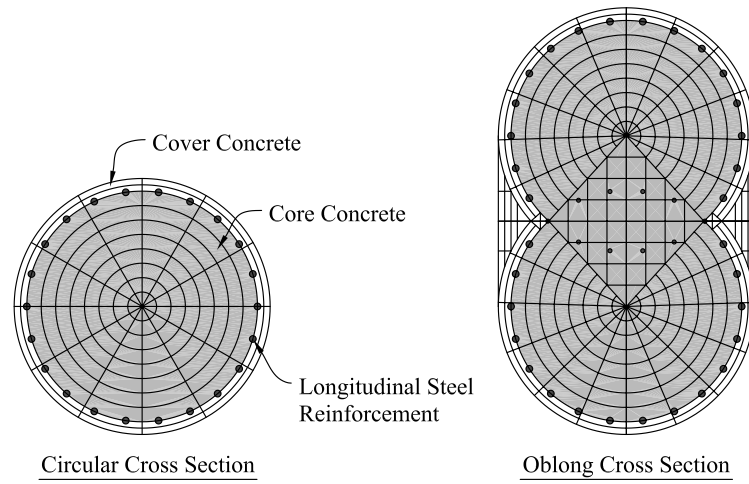


Figure 3.4: Fiber Discretized Circular and Oblong Cross Section

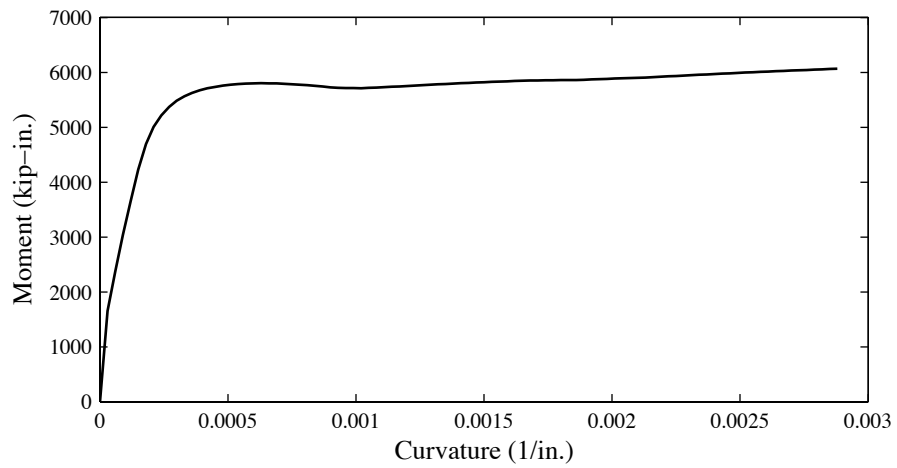


Figure 3.5: Moment-Curvature Relationship for Circular Cross Section

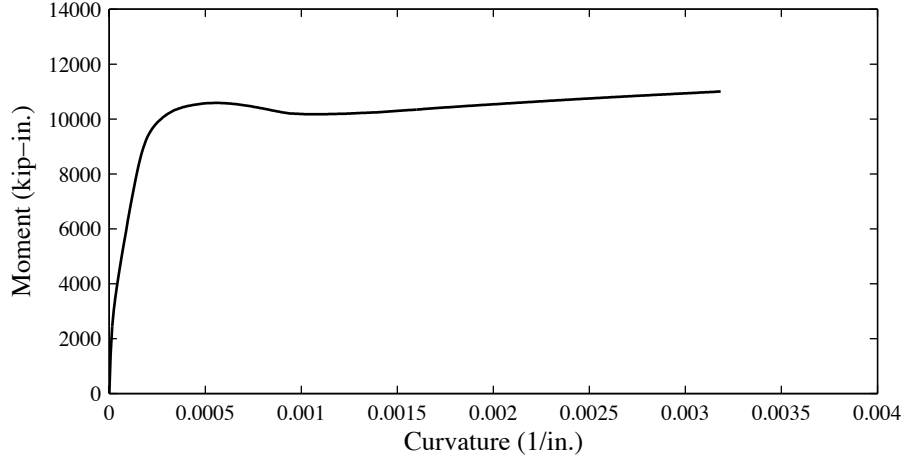


Figure 3.6: Moment-Curvature Relationship for Oblong Cross Section

For confined circular or interlocking core sections the shear reinforcement contribution is defined by (Caltrans, 2004b, Sec. 3.6.3)

$$V_s = \left( \frac{A_v f_{yh} D'}{s} \right) \leq 8 \sqrt{f'_c} A_e \text{ (psi)} \quad (3.12)$$

$$A_v = n \left( \frac{\pi}{2} \right) A_b \leq 0.025 \frac{D' s}{f_{yh}} \text{ (in.}^2\text{)} \quad (3.13)$$

where  $n$  = number of individual interlocking spiral or hoop core sections and  $A_b$  = cross-sectional area of spiral or hoop. The maximum allowable contribution of shear reinforcement and the required minimum amount of reinforcement for shear is summarized in Tables 3.3 and 3.4, respectively. The column shear demand and capacity for each cross section are summarized in Table 3.5.

Table 3.3: Maximum Allowable Contribution of Shear Reinforcement (kips)

Cross Section	Provided	Maximum
Circular	88	205
Oblong	176	379

Table 3.4: Required Minimum Amount of Shear Reinforcement (in.<sup>2</sup>)

Cross Section	Provided	Minimum*
Circular	0.17	0.025
Oblong	0.17	

\* For each individual column core

Table 3.5: Column Shear Demand and Capacity

Cross Section	$V_o$ (kips)	$V_s$ (kips)	$V_c$ (kips)	$\phi_v V_n$ (kips)	$V_o/\phi_v V_n$
Circular	76	88	8	82	0.93
Oblong	138	176	18	165	0.84

## Spacing

The maximum spacing for lateral reinforcement in the plastic end regions is defined by (Caltrans, 2004b, Sec. 8.2.5)

$$s_{max} = \text{smallest of } \begin{cases} \text{one-fifth of the least dimension of the cross section, } D/5 \\ \text{six times the diameter of the longitudinal reinforcement, } 6d_{bl} \\ \text{prototype, 8 in.; one-third scale model, } 8/3 = 2.67 \text{ in.} \end{cases} \quad (3.14)$$

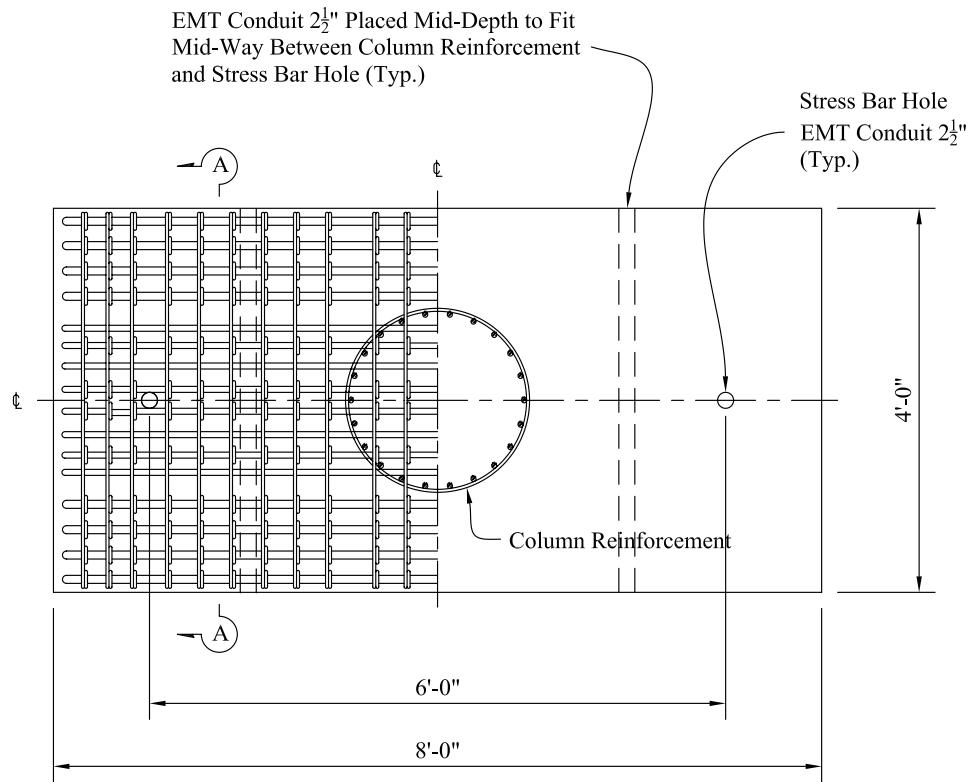
The center-to-center spacing of the interlocking hoops in the oblong column was set to the maximum allowable spacing, 0.75 times the diameter of the cage (Caltrans, 2004a, Sec. 8.18.1.4), equal to 16 in.

### 3.2.3 Footing Reinforcement

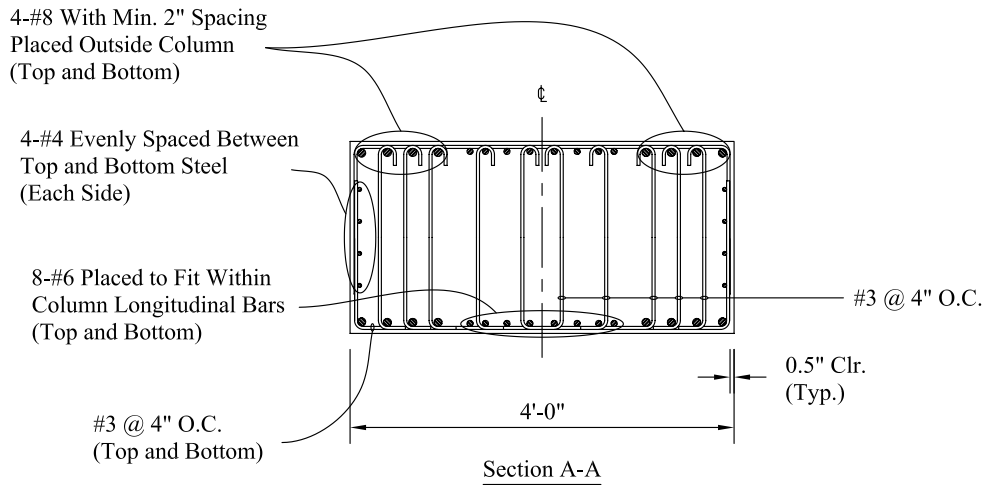
Footing reinforcement details for Columns C1 and C2, Column C3, and Column C4 are shown in Figures 3.7, 3.8, and 3.9, respectively. The footing of Column C4 was not designed for flexural strength, shear strength, or joint shear; Column C4 was to be tested under torsional loading only, thus the footing was detailed to prevent rotation under twisting of the column. The design for torsional loading only allowed for significant cost savings in the plan dimensions of the footing and the amount of reinforcement.

### Flexural Strength

The footing was not intended to model an actual footing in the field and thus was not designed using industry standards. The cross section of the footing was proportioned, based on the nominal material strengths of steel and concrete, to exceed the plastic moment

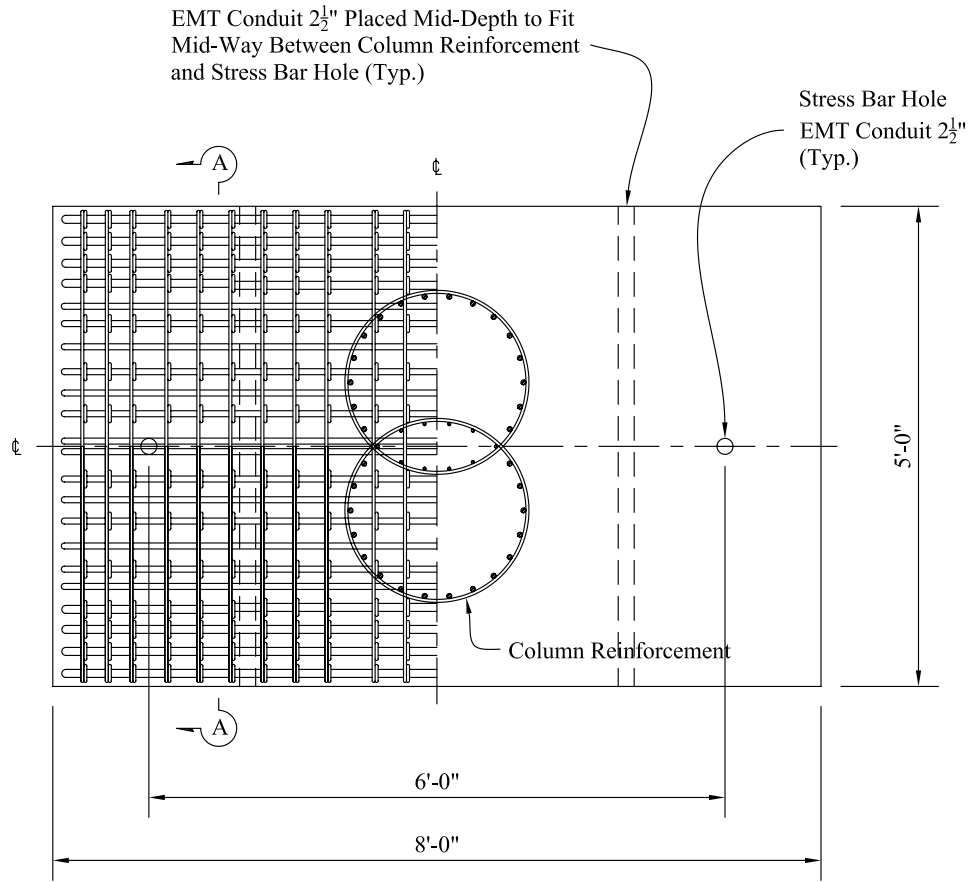


(a) Top and Bottom Mat of Reinforcement

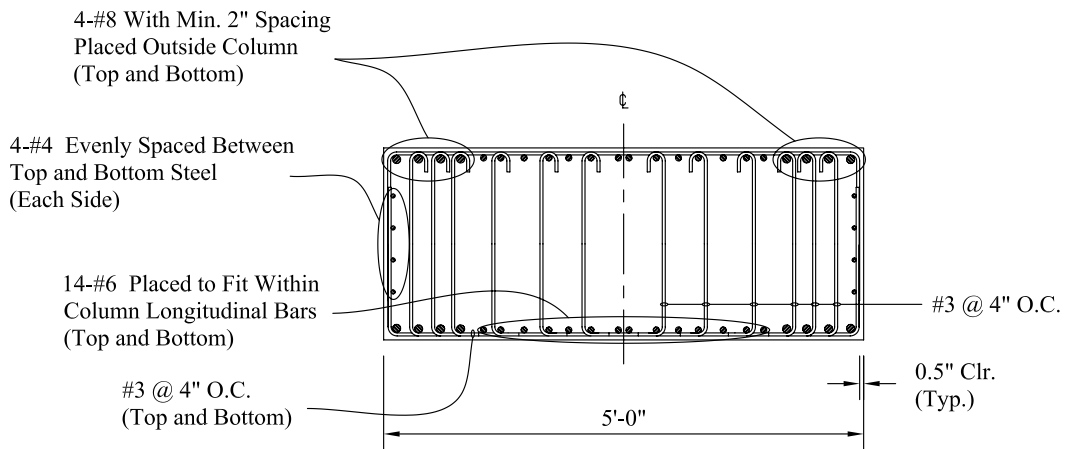


(b) Cross Section of Footing

Figure 3.7: Columns C1 and C2 Footing Details

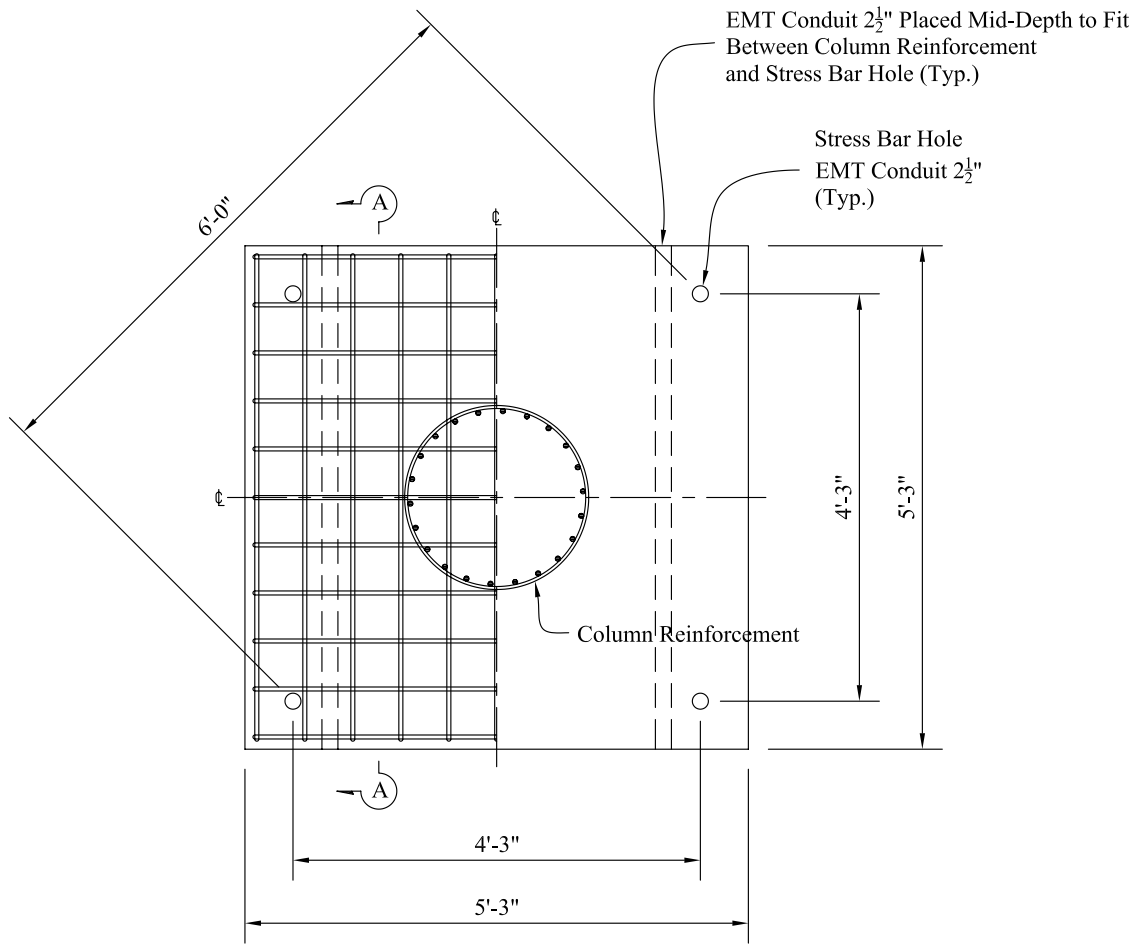


(a) Top and Bottom Mat of Reinforcement

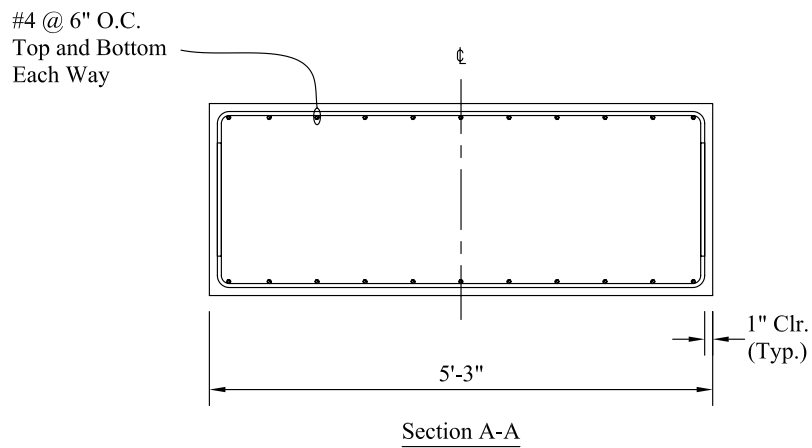


(b) Cross Section of Footing

Figure 3.8: Column C3 Footing Details



(a) Top and Bottom Mat of Reinforcement



(b) Cross Section of Footing

Figure 3.9: Column C4 Footing Details

strength of the column,  $M_{p,col}$ .

$$\phi_b M_{n,ftg} \geq M_{p,col}, \quad \phi_b = 0.9 \quad (3.15)$$

$$M_{n,ftg} \simeq 0.9 A_s f_y (j d_{ftg}) \quad (3.16)$$

where  $A_s$  = area of tension steel,  $f_y$  = nominal yield strength of steel reinforcement, and  $j d_{ftg} \simeq 0.9 \times$  (distance from extreme compression fiber to centroid of tension reinforcement).

The footing flexural demand and capacity for each cross section are summarized in Table 3.6.

### Shear Strength

The corresponding design shear for the footing was equal to the plastic moment strength of the column,  $M_{p,col}$ , divided by the distance from the joint region to strong floor tie-down location,  $L_{ftg}$ .

$$\phi_v V_{n,ftg} \geq V_{u,ftg}, \quad \phi_v = 0.85 \quad (3.17)$$

$$V_{u,ftg} = M_{p,col} / L_{ftg} \quad (3.18)$$

$$V_{n,ftg} = V_c + V_s \quad (3.19)$$

$$V_c = 2\sqrt{f'_c} b_{ftg} d_{ftg} \text{ (psi)} \quad (3.20)$$

$$V_s = \frac{A_v f_y d_{ftg}}{s} \quad (3.21)$$

where  $b_{ftg}$  = width of footing and  $A_v$  = area of shear reinforcement. This overly-conservative design, given that the footing would be post-tensioned to the laboratory floor and thus unlikely be subjected to the design forces, was to ensure that inelastic response of the footing would not affect the test results. The footing shear demand and capacity for each cross section are summarized in Table 3.7.

Table 3.6: Footing Flexural Demand and Capacity

Cross Section	$M_{p,col}$ (kip-in.)	$\phi_b M_{n,ftg}$ (kip-in.)	$M_{p,col}/\phi_b M_{n,ftg}$
Circular*	6050	10820	0.56
Oblong	11050	13720	0.81

\* Columns C1 and C2

Table 3.7: Footing Shear Demand and Capacity

Cross Section	$V_{u,ftg}$ (kips)	$\phi_v V_{n,ftg}$ (kips)	$V_{p,ftg}/\phi_v V_{n,ftg}$
Circular*	250	510	0.49
Oblong	460	608	0.76

\* Columns C1 and C2

### Joint Shear

The footing joint region was designed not to exceed the maximum allowable principal stresses, defined by (Caltrans, 2004b, Sec. 7.7.1.4)

$$\text{Principal Compression: } p_c \leq 0.25 f'_c \quad (3.22)$$

$$\text{Principal Tension: } p_t \leq 12\sqrt{f'_c} \text{ (psi)} \quad (3.23)$$

where

$$p_{t,max} = \frac{f_v}{2} - \sqrt{\left(\frac{f_v}{2}\right)^2 + v_j^2} \quad (3.24)$$

$$p_{c,max} = \frac{f_v}{2} + \sqrt{\left(\frac{f_v}{2}\right)^2 + v_j^2} \quad (3.25)$$

$$v_{jv} = \frac{T_{jv}}{B_{eff}^{ftg} D_{ftg}} \quad (3.26)$$

Table 3.8: Joint Stress Demand and Capacity

Cross Section	$p_t$ (ksi)	$p_c$ (ksi)	$p_{t,max}$ (ksi)	$p_{c,min}$ (ksi)	$p_t/p_{t,max}$	$p_c/p_{c,max}$
Circular*	-0.07	0.41	-0.85	1.25	0.08	0.33
Oblong	-0.11	0.44			0.13	0.35

\* Columns C1 and C2

$$B_{eff}^{ftg} = \begin{cases} \sqrt{2}D_c & \text{Circular Cross Section} \\ B_c + D_c & \text{Oblong Cross Section} \end{cases} \quad (3.27)$$

$$f_v = \frac{P_e}{A_{jh}^{ftg}} \quad (3.28)$$

$$A_{jh}^{ftg} = \begin{cases} \left(D_c + \frac{D_{ftg}}{2}\right)^2 & \text{Circular Cross Section} \\ \left(D_c + \frac{D_{ftg}}{2}\right) \left(B_c + \frac{D_{ftg}}{2}\right) & \text{Oblong Cross Section} \end{cases} \quad (3.29)$$

where  $T_c$  = column tensile force  $\simeq M_{p,col}/0.9D$ ,  $D_c$  = cross-sectional dimension of column in the direction of bending,  $B_c$  = cross-sectional dimension of column perpendicular to the direction of bending, and  $D_{ftg}$  = depth of footing. The joint stress demand and capacity for each cross section are shown in Tables 3.8.

### 3.3 Measured Material Properties

The specified, expected, and measured properties of the reinforcing steel and concrete are summarized and described in this section.

### 3.3.1 Concrete Properties

The scaled concrete mix, summarized in Table 3.9, was designed to model a full-scale mix, with a target 28-day compressive strength equal to 5 ksi. Two batches of concrete were used: one for the specimen footings and the other for the specimen columns. At the time of casting, a slump test was performed to ensure that the concrete slump was between 3 and 5 in. Standard 6 in. by 12 in. cylinders were cast for both batches according to ASTM C31 requirements. The test cylinders were kept in the same location as the test specimens and were subjected to a similar environment. The forms were removed and the cylinders were stripped on the same day.

Concrete coupons were capped with high-strength mortar and tested in compression according to ASTM C39. Compressive strength tests were performed at 7, 14, 21, 28 days after casting and near the day of column testing. Table 3.10 summarizes the age of the concrete at the time of column testing and at time of concrete coupon testing. In each case, three 6 in. by 12 in. concrete cylinders were tested (Table 3.11). Figure 3.10 shows the increase of compressive strength with age (columns batch only), along with a curve passing through the data to approximate the strength increase with age (ACI, 1982). The split-cylinder test was performed according to ASTM C496 on three 6 in. by 12 in. concrete cylinders. The measured tensile strength of concrete near the day of Column C2 testing was found to be 0.43 ksi and 0.47 ksi for the footing and column concrete batches, respectively.

Several months after the initial column testing (Columns C1, C2, and C3), another test specimen with a circular cross section (Column C4) was constructed with the same scaled concrete mix. Instead of two batches of concrete, only one batch was used for both

Table 3.9: Concrete Mix Design

28-day strength = 5 ksi, w/c ratio = 0.426, slump = 6 ± 1 in.		
Material	Volume (ft <sup>3</sup> )	Weight (lb)
Coarse Aggregate (3/8 in. max.)	5.98	1000
Fine Aggregate	11.82	1955
Cement	2.51	494
Flyash	1.47	211
Water	4.81	300
Type A Admixture	0.11	21.2 fl.oz.
Type F Admixture	0.30	56.4 fl.oz.
Total	27.00	3960

the specimen footing and specimen column. The concrete coupons were constructed, cured, and prepared for testing in a similar manner as described previously. One day prior to column testing, compressive strength and tensile strength tests were performed. For each test, three 6 in. by 12 in. concrete cylinders were tested. The mean measured compressive and tensile strengths were 6.89 ksi and 0.49 ksi, respectively.

The stress-strain response (columns batch only) for the unconfined concrete under compression was measured for Columns C1, C2, and C3 near the day of test, shown in Figures 3.11, 3.12, and 3.13, respectively. The stress-strain response for unconfined concrete under compression was measured for Column C4 one day prior to testing, shown in Figure 3.14. In each case, three 6 in. by 12 in. concrete cylinders were tested.

### 3.3.2 Reinforcing Steel Properties

The longitudinal and hoop reinforcement was specified as ASTM A706 Grade 60 steel. The reinforcing bars were tested as-is in tension according to ASTM A370. Coupons of the longitudinal reinforcement were readily available; preparation involved cutting each

Table 3.10: Test Day and Concrete Testing (Days after Casting)

Column	Day of Test	Concrete Testing
C1	88 and 97*	90
C2	126	127
C3	161	162

\* 5 and 7 in. Displacement Cycles Completed

Table 3.11: Mean Concrete Compressive Strength (ksi)

Day	Footings	Columns
7	3.46	3.54
14	4.24	4.49
21	4.83	5.01
28	5.20	5.43
90	6.11	6.04
127	5.92	6.17
162	5.77	5.87

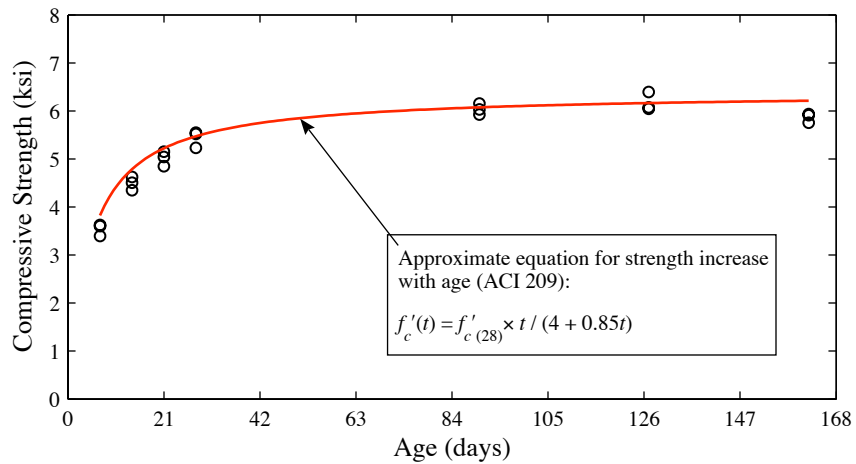


Figure 3.10: Concrete Compressive Strength Increase With Age (Columns Batch Only)

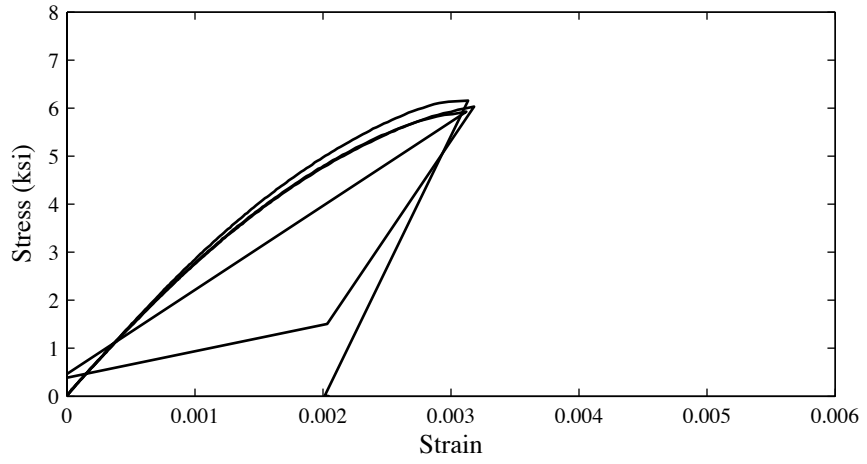


Figure 3.11: Column C1 Unconfined Concrete Stress-Strain Response

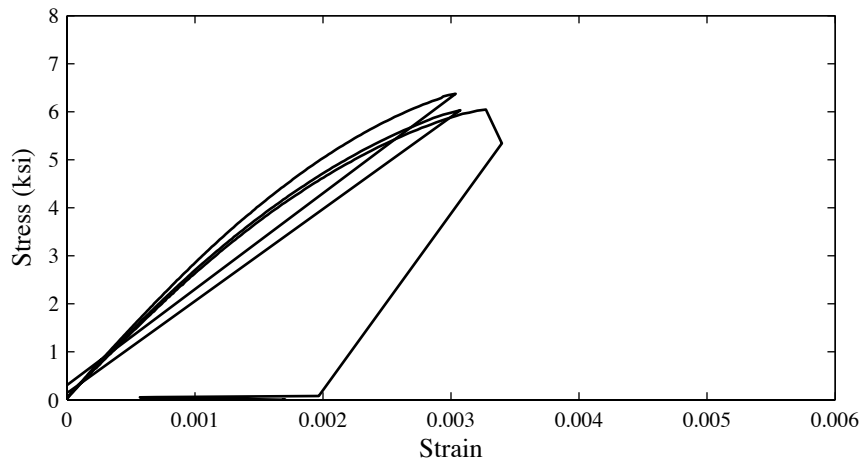


Figure 3.12: Column C2 Unconfined Concrete Stress-Strain Response

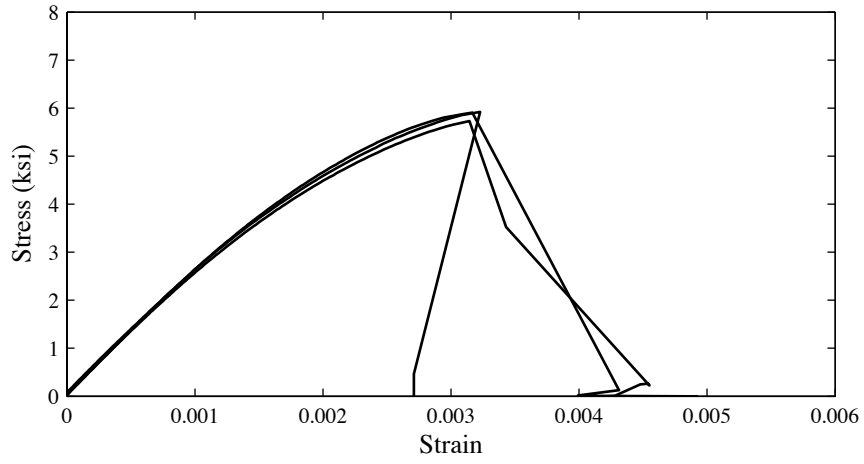


Figure 3.13: Column C3 Unconfined Concrete Stress-Strain Response

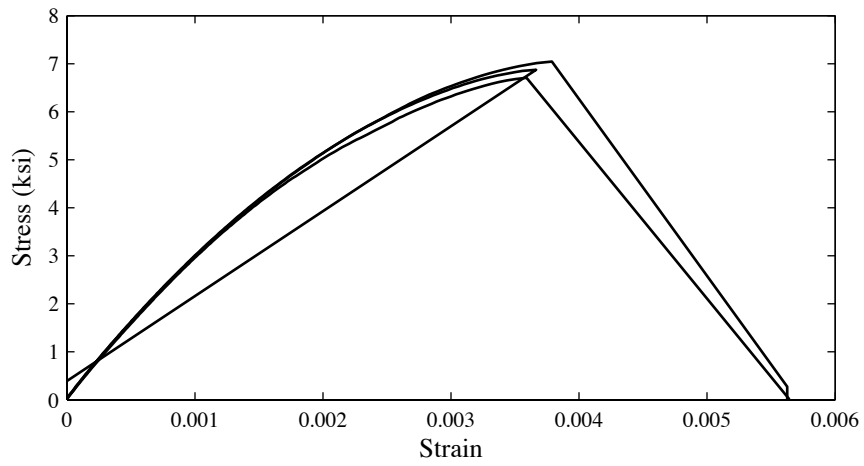


Figure 3.14: Column C4 Unconfined Concrete Stress-Strain Response

Table 3.12: Reinforcement Properties

Type	Size	Specified (ksi)		Expected (ksi)		Measured (ksi)	
		Yield	Ultimate	Yield	Ultimate	Yield	Ultimate
Longitudinal	No. 5	60	80			73	100
	No. 3	60	80	68	95	55	74
Hoop	No. 3	60	80			60	95

bar size to approximately 2 ft in length. Coupons of the hoop reinforcement were not as readily available; preparation involved cutting a 2 ft segment of the hoop and straightening the curved bar. The welded splice of the hoops was also tested for tensile strength. Ten welded splice specimens, approximately 3 ft in length, were tested in tension until fracture at a loading rate of approximate 4 kips per minute. No specimens fractured near the weld and were thus adequate to develop the tension strength of the hoop bars. The tension test setups for the reinforcing bar and welded splice specimens are shown in Figure 3.15.

The measured relations between tension stress and strain for the main longitudinal, interlocking longitudinal, and hoop reinforcement are shown in Figures 3.16, 3.17, and 3.18, respectively. Note, the area used for calculation of bar stresses were taken as the nominal bar area for each bar size. The specified, expected, and measured strengths of the reinforcing steel are summarized in Table 3.12.

As mentioned previously, this study used closed-circular hoops instead of a continuous spiral for the lateral reinforcement. The spiral reinforcement used in previous studies (e.g.; Lehman and Moehle, 2000; Hachem et al., 2003) was specified as ASTM A82 Grade 80 steel. Figure 3.19 shows the measured stress-strain relation for the spiral reinforcement used in the study by Lehman and Moehle (2000). As compared with the hoop reinforcement (Fig-



(a) Reinforcing Bar



(b) Welded Splice

Figure 3.15: Tension Test Setup

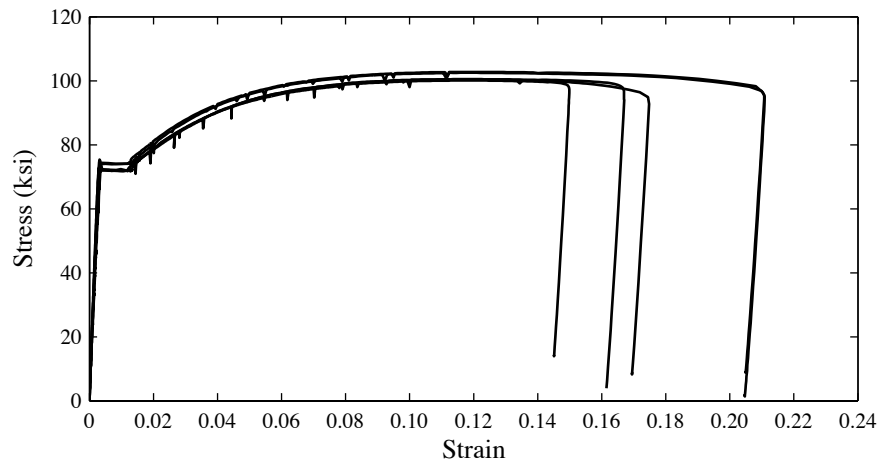


Figure 3.16: Main Longitudinal Reinforcement (No. 5 Bar) Stress-Strain Response

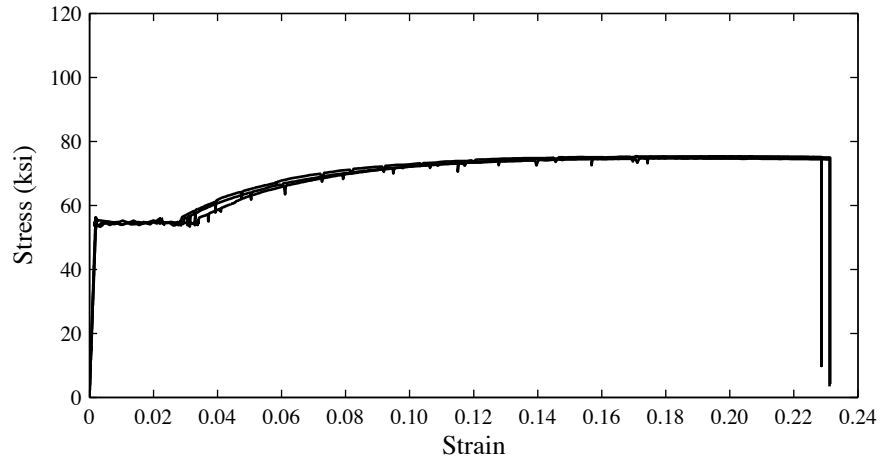


Figure 3.17: Interlocking Longitudinal Reinforcement (No. 3 Bar) Stress-Strain Response

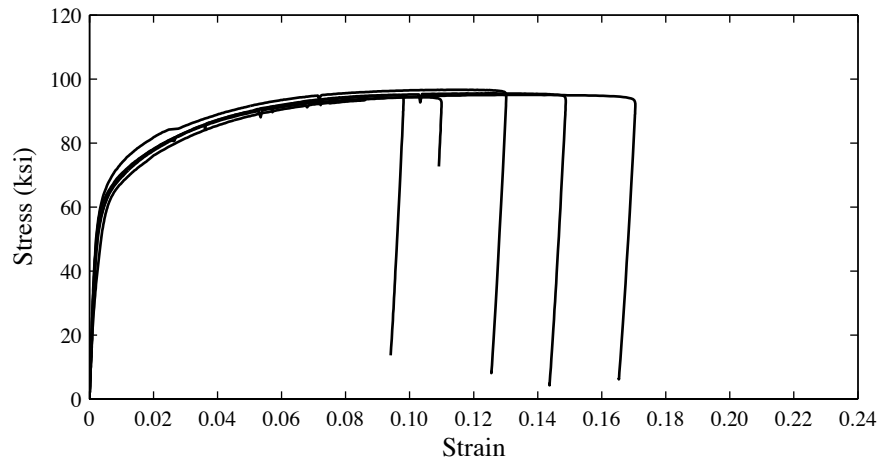


Figure 3.18: Hoop Reinforcement (No. 3 Bar) Stress-Strain Response

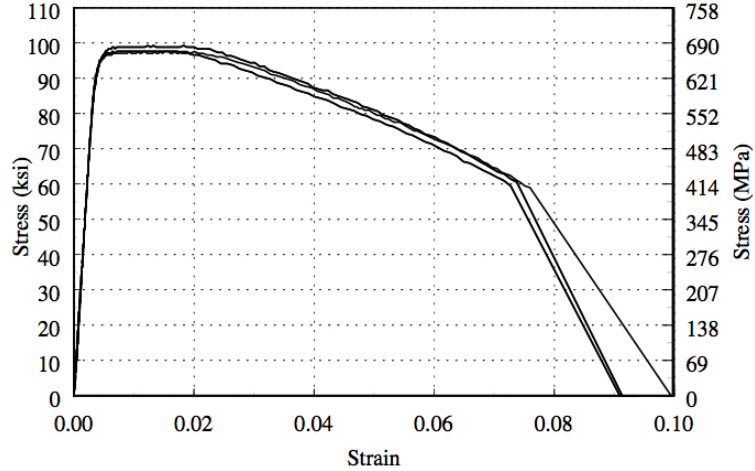


Figure 3.19: Spiral Reinforcement Stress-Strain Response (from Lehman and Moehle, 2000)

ure 3.18), the spiral reinforcement (Figure 3.19) has a higher yield stress and yield strain, lower strain capacity, and lower ductility. In the elastic range up to the yield strain of the hoop reinforcement, the stress-strain relation of the hoop and spiral reinforcement are similar.

### 3.4 Construction

Construction of the all the test specimens (Columns C1, C2, C3, and C4) consisted of three major phases: installation of strain gauges on the reinforcement, assembly of reinforcement cages, and concrete placement.

The columns were constructed inside the Structures Laboratory at Davis Hall on the University of California, Berkeley campus. Steel reinforcement was fabricated by off-site contractors. The longitudinal reinforcement was delivered bent and cut to size, ready to be assembled into the reinforcement cages. Similarly, the hoops were delivered bent and welded, ready to place. The concrete formwork for the footing and column cap was constructed off-

site and erected on-site by the contractor. Additional formwork and bracing were erected on-site by the contractor. The concrete was provided by a nearby concrete contractor.

Prior to construction of the reinforcement cages, strain gauges were installed on the column longitudinal and hoop reinforcement. The reinforcement cages were constructed prior to the column cages. For ease of construction, the footing cage was tied outside the formwork and then lowered into the formwork using the laboratory crane. Figure 3.20 shows a typical reinforcement cage inside the footing of Columns C1, C2, and C3. The reinforcement cage inside the footing of Column C4 is shown in Figure 3.21. Once the footing cage was properly positioned in the formwork, the column cage was erected from bottom to top. First, the column longitudinal reinforcement was placed into the footing cage. Next, the hoops were lowered one-by-one from the top of the column longitudinal reinforcement to the top of the footing. Figures 3.22 and 3.23 show the finished column cages for the circular and oblong columns, respectively. Figure 3.24 shows the strain gauges on the longitudinal and hoop reinforcement of the column cage.

After the footing and column reinforcement cages were completed, the column form was placed over the column cage with the help of a fork-lift. The column form was then braced and plumbed. Next, over-sized holes were drilled into the column form for the instrumentation rods. The holes were sealed with ethafoam to isolate the rods from the concrete cover and prevent leakage during casting.

The specimens were cast monolithically using two concrete batches, except Column C4, which was cast using one batch. The first batch was used to cast the footings followed by the second batch, delivered approximately two and one-half hours later, to cast the columns. Due to access restrictions into the Structures Laboratory, a pump was used to

convey both batches of concrete into the laboratory. Concrete was shot atop the footings and was vibrated with stick- and form-vibrators, as shown in Figure 3.25. The columns were continuously cast; concrete was shot into the top of the column form at a constant rate and was meanwhile vibrated with a stick-vibrator, as shown in Figure 3.26.

A week after casting, the formwork was removed. Figures 3.27 and 3.28 show the finished specimens prior to testing.



Figure 3.20: Typical Footing Reinforcement Cage



Figure 3.21: Column C4 Footing Reinforcement Cage



Figure 3.22: Typical Circular Column Reinforcement Cage

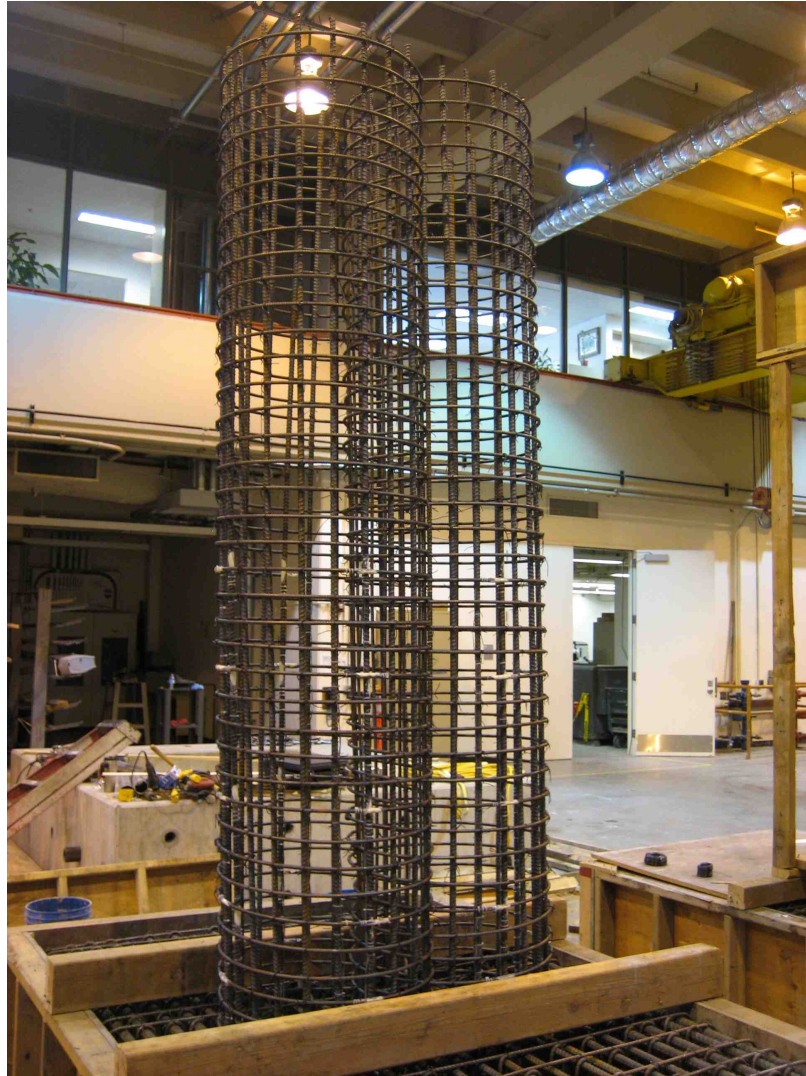


Figure 3.23: Oblong Column Reinforcement Cage

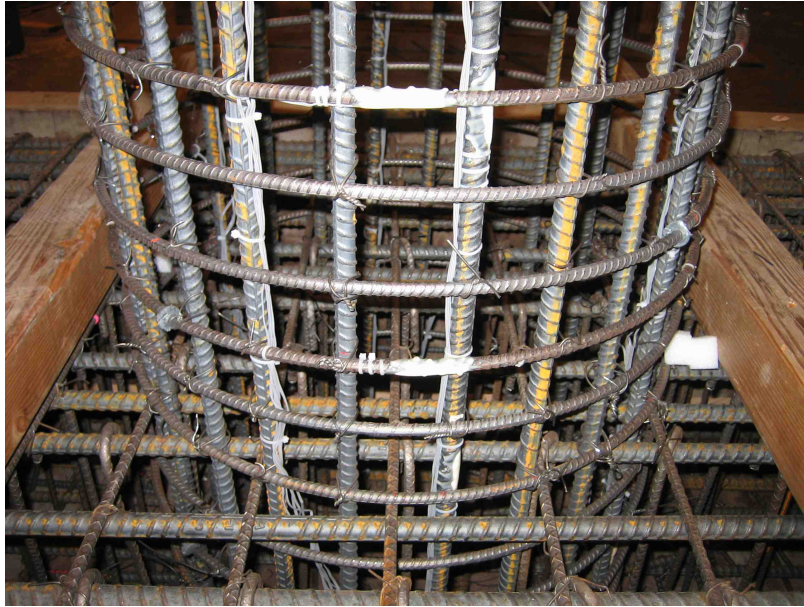


Figure 3.24: Strain Gauges on Longitudinal and Hoop Reinforcement



Figure 3.25: Concrete Placement and Vibration of Footing

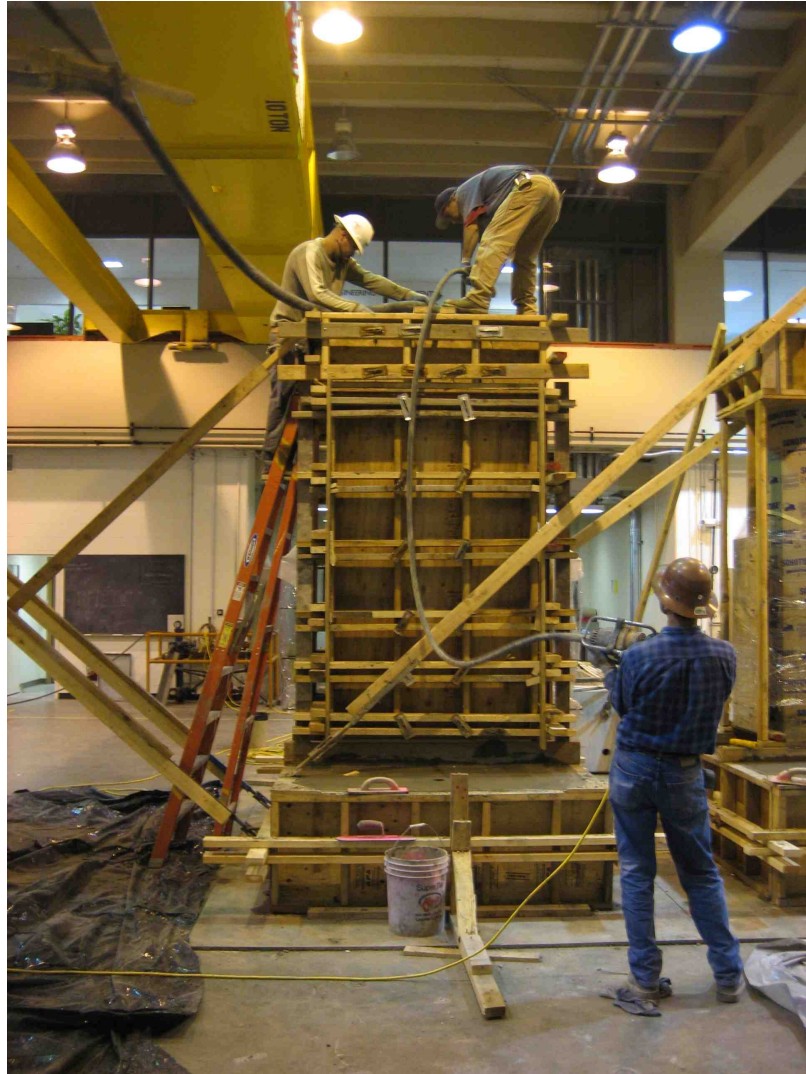


Figure 3.26: Concrete Placement and Vibration of Column



Figure 3.27: Specimens Inside Laboratory Before Testing



Figure 3.28: Column C4 Inside Laboratory Before Testing

## Chapter 4

# Experimental Program

This chapter presents the experimental program, which was designed to investigate the influence of twist on the inelastic behavior of reinforced concrete bridge columns.

Development of the experimental investigation emphasized:

- Studying the effect of simultaneous lateral and twisting deformations on the stiffness, strength, and deformation capacity of bridge columns;
- Comparing results with previous research;
- Modeling bond distribution and bar slip.

### 4.1 Test Program

The test program included a comparative study of the behavior of five large-scale columns, as shown in Figure 4.1 and outlined in Table 4.1. The test program varied cross-sectional geometry and type of loading; the aspect ratio of each column was 4:1. Column 415 was tested in a previous study reported by Lehman and Moehle (2000) and

Table 4.1: Test Matrix

Column ID	Cross Section	$\rho_l$ (%)	$\rho_s$ (%)	Loading	Twist/Drift Ratio
415	Circular	1.5	0.7	$M+P$	0
C1	Circular	1.5	0.73	$T+M+P$	0.6
C2	Circular	1.5	0.73	$T+M+P$	1.2
C3	Oblong	1.2	0.73	$T+M+P$	0.6
C4	Circular	1.5	0.73	$T+P$	$\infty$

Column C4 was tested by, and in collaboration with, Le (2008).

## 4.2 Test Setup

The test setup, shown in Figure 4.2, consisted of a reaction frame, various steel sections, manually-controlled hydraulic jacks, and servo-controlled hydraulic actuators. The steel sections were used as follows: tie-down beams to anchor the specimen to the strong-floor of the laboratory; spreader beam to distribute the axial load applied by the two manually-controlled hydraulic jacks; lateral loading beam to apply the imposed lateral displacement and twist prescribed by the two 120 kip capacity, 36 in. stroke servo-controlled hydraulic actuators. The actuators were attached to the reaction frame and loading beam with 3D clevises at either end of the actuator. The actuator-clevis connection at the reaction frame was oriented to provide 180 degrees of rotation about the horizontal axis, whereas the actuator-clevis connection at the loading beam was oriented perpendicularly to provide 180 degree of rotation about the vertical axis. This orientation allowed the clevis to accommodate the prescribed lateral displacement and rotation at the tip of the column without being damaged. The axial load setup also consisted of 3D clevises to accommodate the lateral displacement and twist. Figure 4.3 shows Column C2 ready for testing.

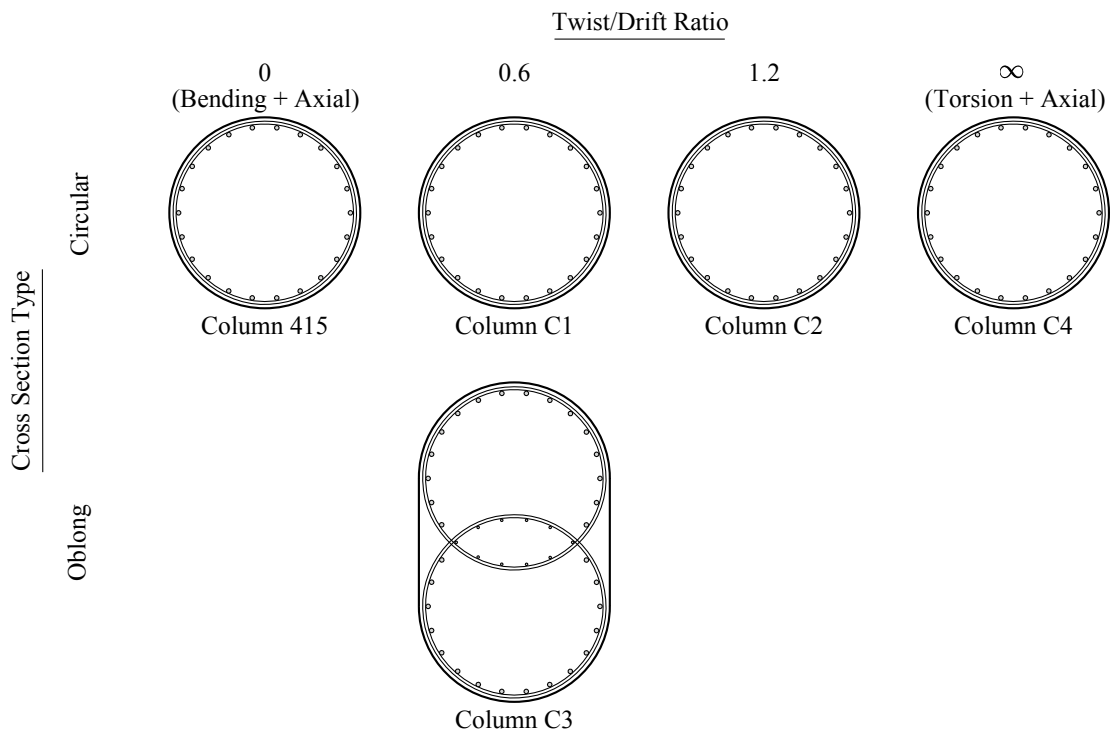


Figure 4.1: Test Matrix

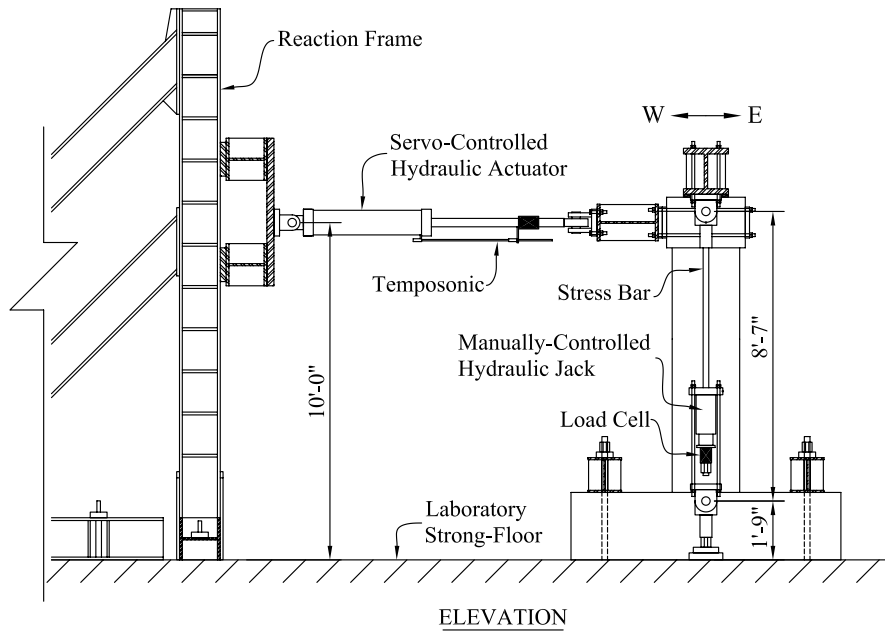
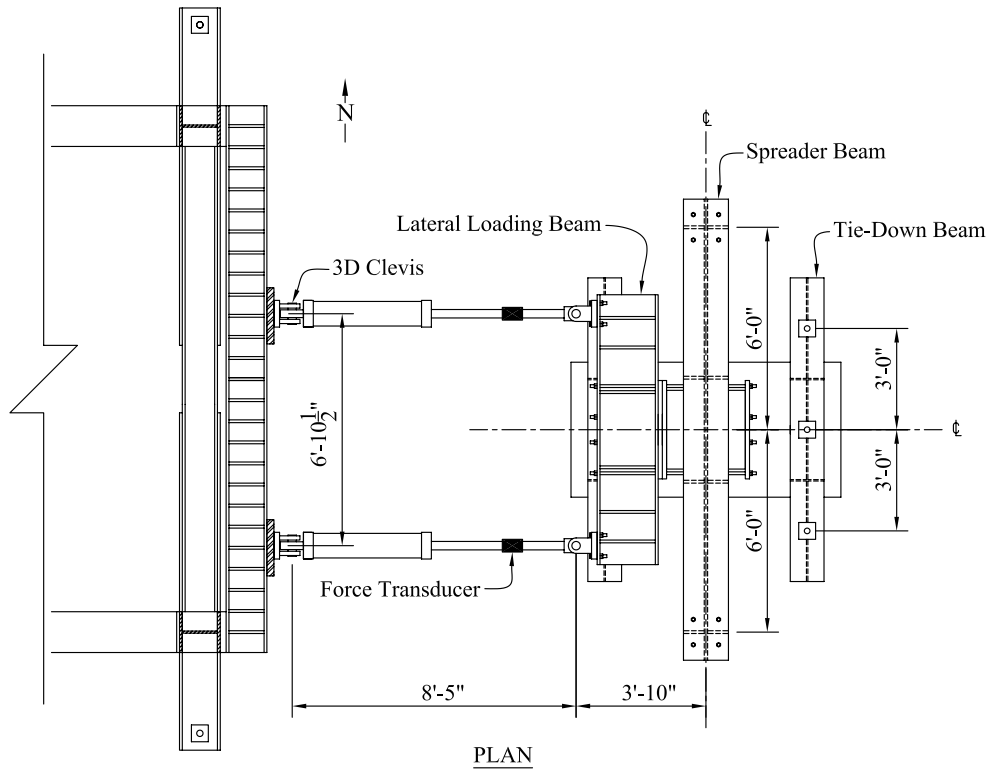


Figure 4.2: Test Setup

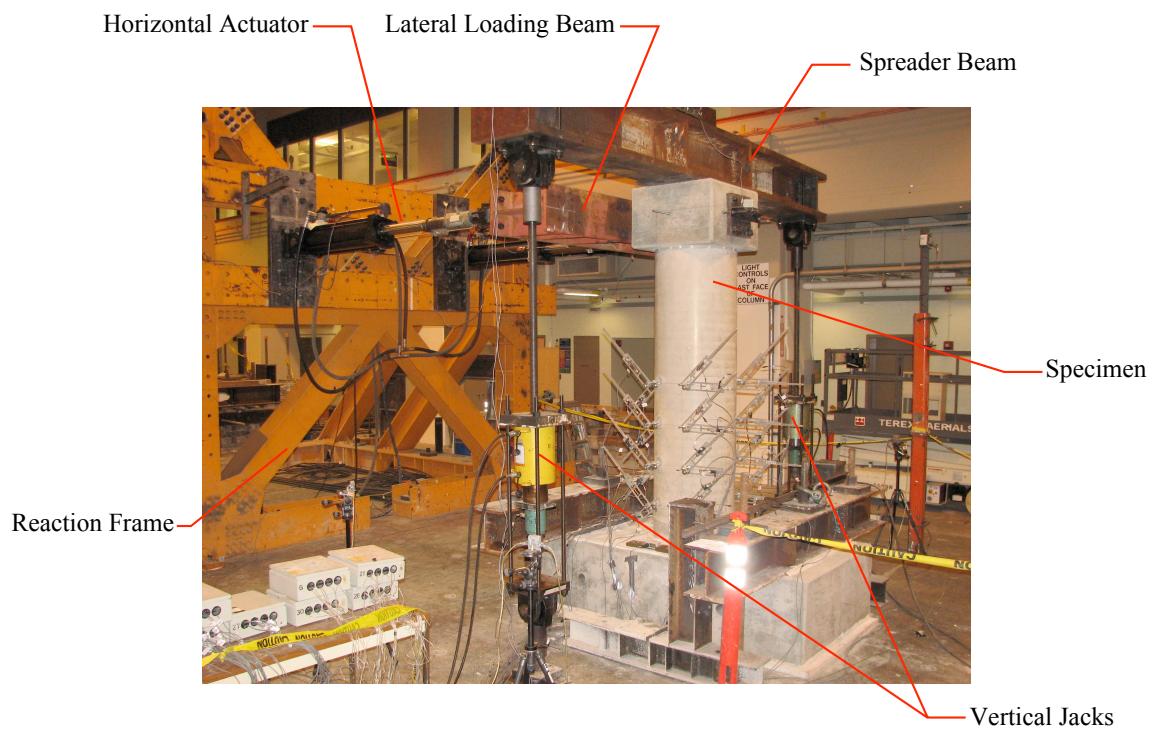


Figure 4.3: Column C2 Ready for Testing

### 4.3 Loading Protocol

Experimental testing was conducted in the Structures Laboratory at Davis Hall on the University of California, Berkeley campus. A constant axial load was applied followed by reversed cyclic lateral loading. The applied axial load was 225 kips ( $\sim 0.1f'_cA_g$ ) and 380 kips ( $\sim 0.09f'_cA_g$ ) for the circular and oblong columns, respectively, where  $f'_c$  = target concrete compressive strength (5.0 ksi) and  $A_g$  = nominal cross-sectional area.

Reversed cyclic combined lateral and torsional loading was imposed on Columns C1, C2, and C3 by two horizontal actuators under displacement control. The imposed displacement history (Lehman and Moehle, 2000), shown in Figure 4.4, consisted of a series of reversed cycles at increasing displacement amplitudes with simultaneous twist. The displacement levels and associated twist are summarized in Table 4.2. The first four series consisted of three reversed cycles. These pre-yield displacement levels of subsequently increasing displacement corresponded to: pre-cracking, two levels between cracking and yielding, and approximately first yield of the longitudinal reinforcement. The remaining six displacement series consisted of three reversed cycles followed by a smaller cycle equal to one-third of the previous cycle. These post-yield displacement levels of subsequently increasing displacement corresponded to 1, 1.5, 2, 3, 5, and 7 times the  $\Delta_y$ , where  $\Delta_y = 1$  in. = first post-yield displacement level.

Reversed cyclic torsional loading was imposed on Column C4 by two horizontal actuators under displacement-control. The prescribed twist pattern consisted of a series of reversed cycles at increasing twist amplitudes, similar in shape and amplitude to the associated twist history for Column C2 (Table 4.2).

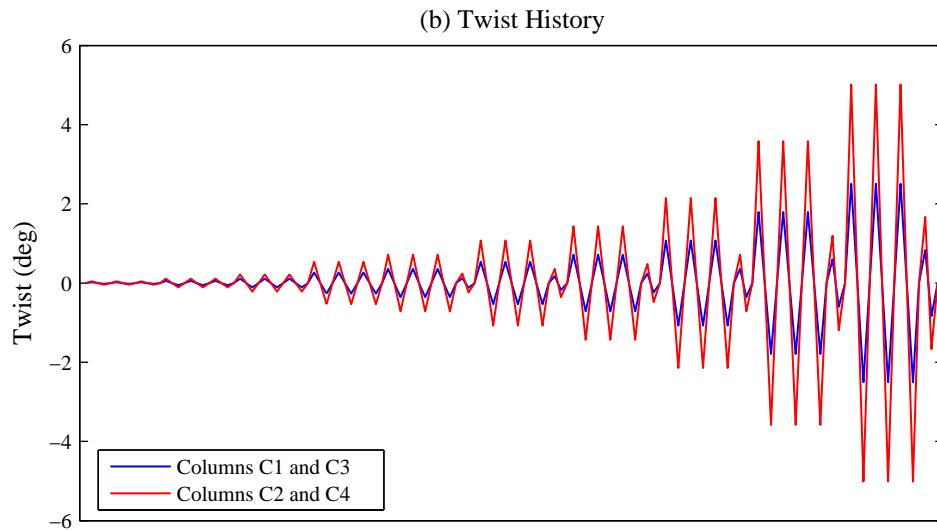
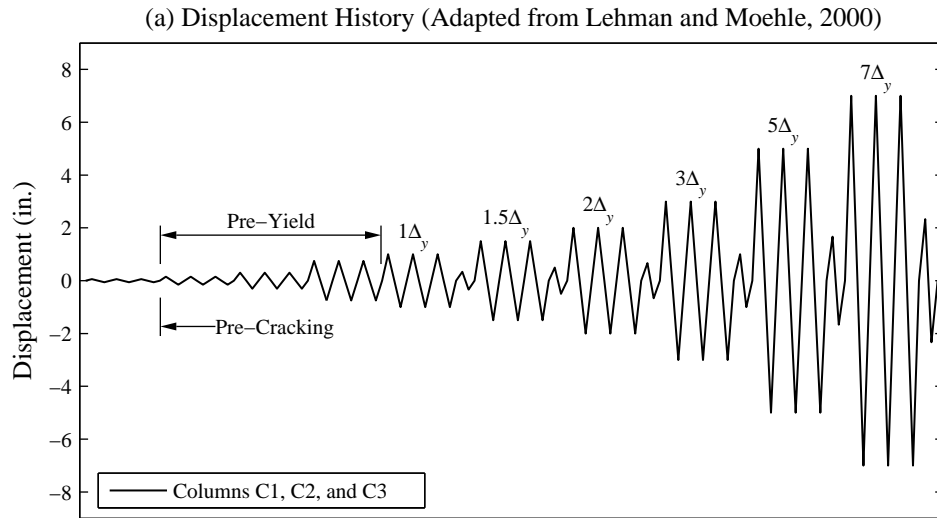


Figure 4.4: Target Displacement and Twist Histories

Table 4.2: Displacement Levels and Associated Twist

Level	Displacement Amplitude (in.)	Associated Twist (deg)	
		Columns C1 and C3	Column C2
Pre-Cracking	0.06	0.02	0.04
	0.15	0.05	0.1
	0.30	0.1	0.2
First Yield	0.75	0.25	0.5
$\Delta_y$	1	0.35	0.7
$1.5\Delta_y$	1.5	0.55	1.1
$2\Delta_y$	2	0.7	1.4
$3\Delta_y$	3	1.1	2.1
$5\Delta_y$	5	1.8	3.6
$7\Delta_y$	7	2.5	5.0

#### 4.4 Instrumentation

External and internal instrumentation was arranged to monitor both global and local response. A total of 95, 127, and 47 data channels were used in testing Columns C1 and C2, Column C3, and Column C4, respectively. These channels corresponded to several types of instruments, including force transducers (FT), load cells (LC), temposonics, linear potentiometers (LP), displacement transducers (DT), and strain gauges (SG). The types of quantities of instruments used are summarized in Table 4.3.

Data were collected by a standalone NEFF 470 data acquisition system. Command signals for the hydraulic controllers were provided by a Keithley DAS1601. Software for data collection and the production of control signals was provided by Autonet. It runs under QNX which is a true real time, multi-tasking operating system. QNX is UNIX-like in nature and well known for its reliability and stable operation and thus is well suited for the testing lab environment.

Table 4.3: Instrumentation

Instrument Type	No. of Channels		
	Columns C1 and C2	Column C3	Column C4
Force Transducer	2	2	2
Load Cell	2	2	2
Temposonic	2	2	2
Linear Potentiometer	13	13	9
Displacement Transducer	34	36	18
Strain Gauge	46	72	16
Total	95	127	47

Prior to testing, each SG, LP, and DT was calibrated. The SGs were calibrated by shunting a resistor across the terminals inside the instrumentation box. SGs that did not measure the proper resistance were removed and not used during testing. The LPs and DTs were calibrated using measurements of three calibration blocks. These measurements were input to the NEFF data acquisition system software where a corresponding calibration factor for each LP and DT was calculated.

Data were collected at various displacement intervals with increasing increment at larger displacement amplitude cycles. Table 4.4 shows the number of data collection points per ramp (zero displacement to peak displacement) for each displacement level.

The forces in the servo-controlled horizontal actuators were measured by built-in FTs. The forces in the manually-controlled vertical jacks were measured by external load cells. The stroke of horizontal actuators was measured with temposonic sensors mounted on the actuator. The stroke of the vertical jacks was monitored visually during testing.

The global displacement and twist at the tip of the column was measured with a pair of LPs, one to the North and one to the South, equally spaced from the column

Table 4.4: Data Collection

Level	Data Points Per Ramp
Prior to Cracking	10
First Yield	20
$\Delta_y$	20
$1.5\Delta_y$	30
$2\Delta_y$	40
$3\Delta_y$	50
$5\Delta_y$	50
$7\Delta_y$	50

centerline, mounted on the instrumentation frame, as shown in Figure 4.5. The North and South LP wires were attached to a threaded rod extending from the North and South face of the column cap, respectively. Similarly, the lateral displacement and twist along the height of the column was measured with a pair LPs at the top of each column segment. The lateral displacement and twist were measured at elevations of 12, 24, 36, and 48 in. along the height of the Columns C1, C2, and C3, and at elevations 24 and 48 in. along the height of Column C4.

The local column deformations were measured with DTs, located on either face of the column in the loading direction, along the height of the column. The setup consisted of several DTs mounted on aluminum brackets attached to 1/2 in. diameter threaded rods placed through the column cross section, as shown in Figure 4.6. The arrangement of DTs and plan view of the DTs for the circular and oblong cross sections are shown in Figures 4.7 and 4.8, respectively.

The bar slip deformation was also measured with DTs, located on either face of the column in the loading direction. The setup consisted of a DT mounted on an aluminum

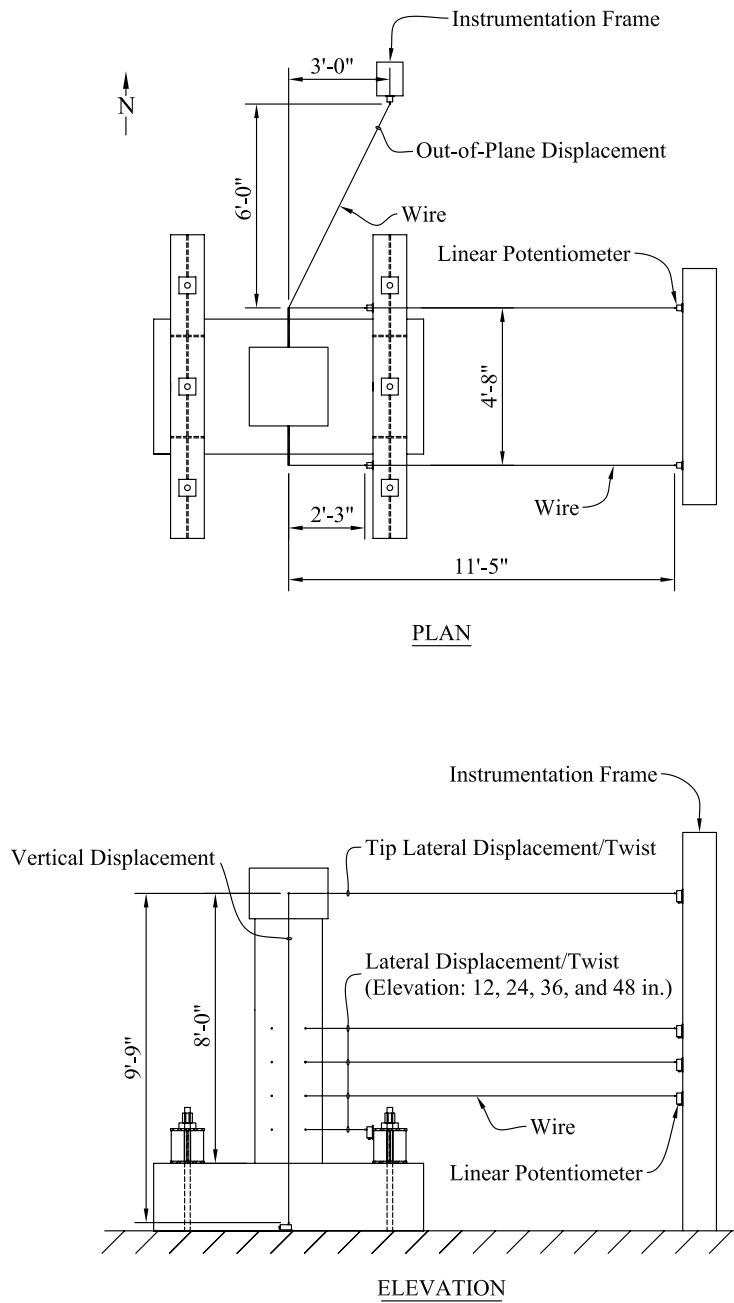


Figure 4.5: Arrangement of Linear Potentiometers for Measurement of Global Displacement and Twist

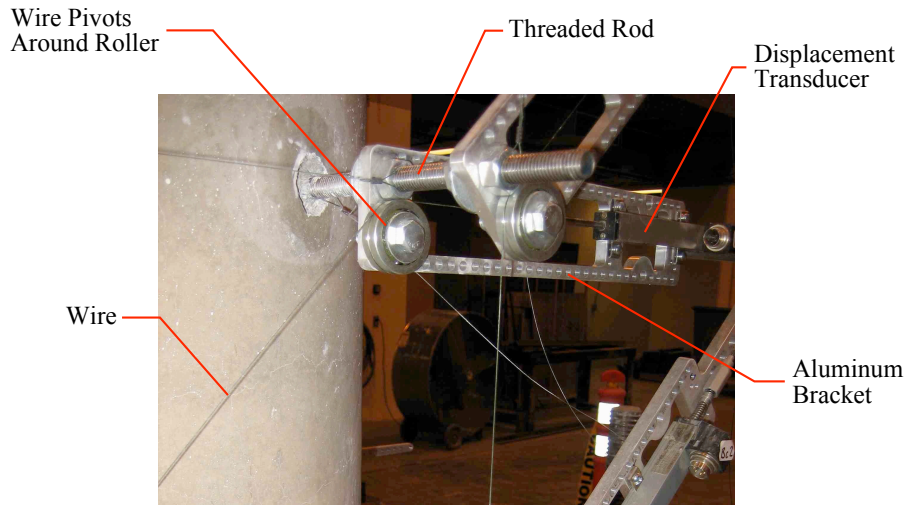


Figure 4.6: Typical Displacement Transducer Setup for Measurement of Local Deformations angle attached to a 1/2 in. diameter threaded rod that was anchored into the footing. This setup provided a stable base to measure the bar slip at the interface of the column and footing, as shown in Figure 4.9. Figure 4.10 shows the arrangement of DTs for the measurement of bar slip for the circular and oblong columns. Bar slip was not measured for Column C4.

The specimens were instrumented with SGs to measure the internal strains. The strain gauges were installed on the longitudinal and hoop reinforcement along the height of the column. Additional SGs were located on the longitudinal reinforcement within the footing to measure the bond stress distribution. The locations of the SGs are shown in Figure 4.11. Note that the Column C4 has strain gauges (4 longitudinal and 4 hoop) at the 24 and 48 in. elevations only.

Refer to Appendices A and B for more details on the test apparatus and the data reduction procedures.

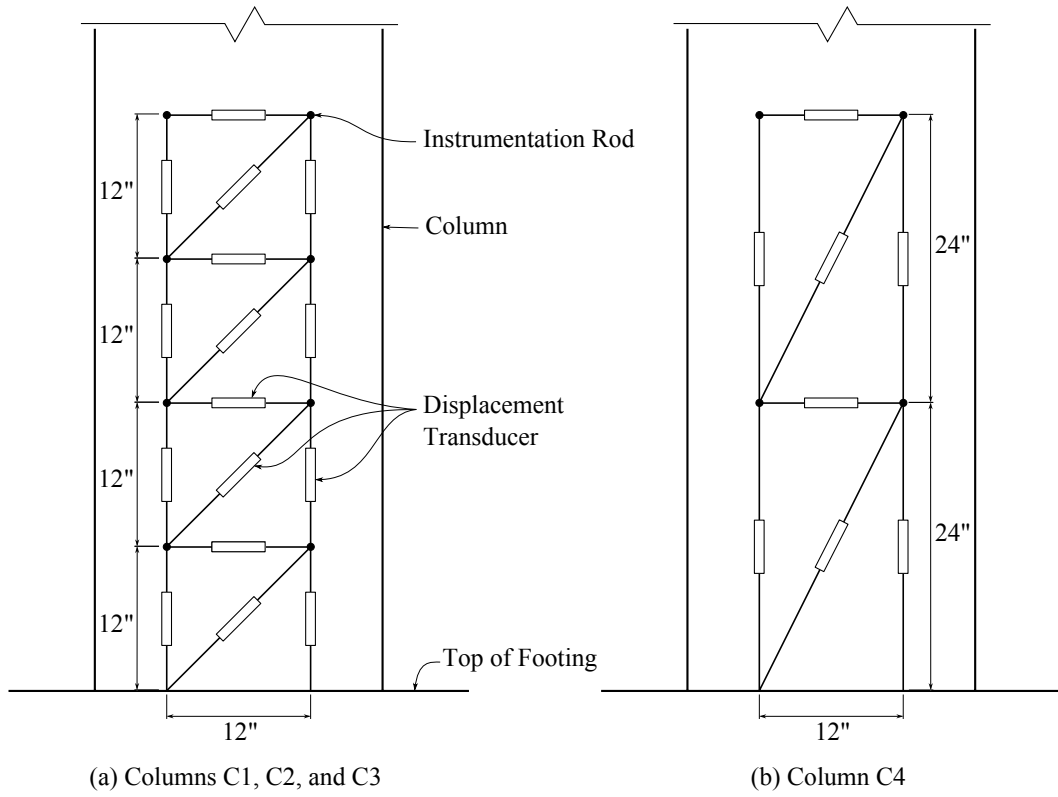


Figure 4.7: Arrangement of Displacement Transducers for Measurement of Local Deformations

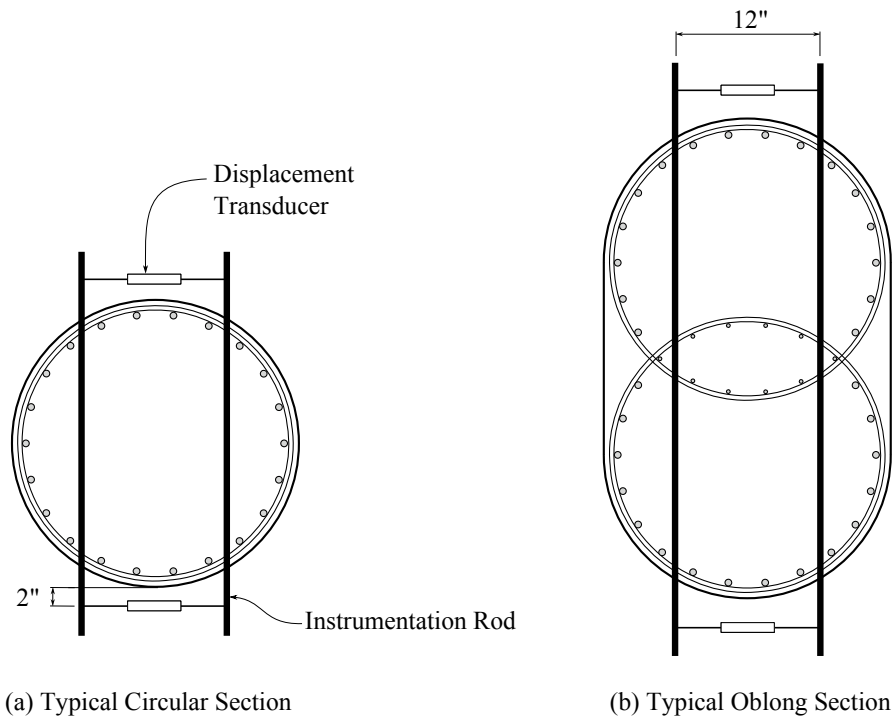


Figure 4.8: Plan View of Displacement Transducers for Measurement of Local Deformations

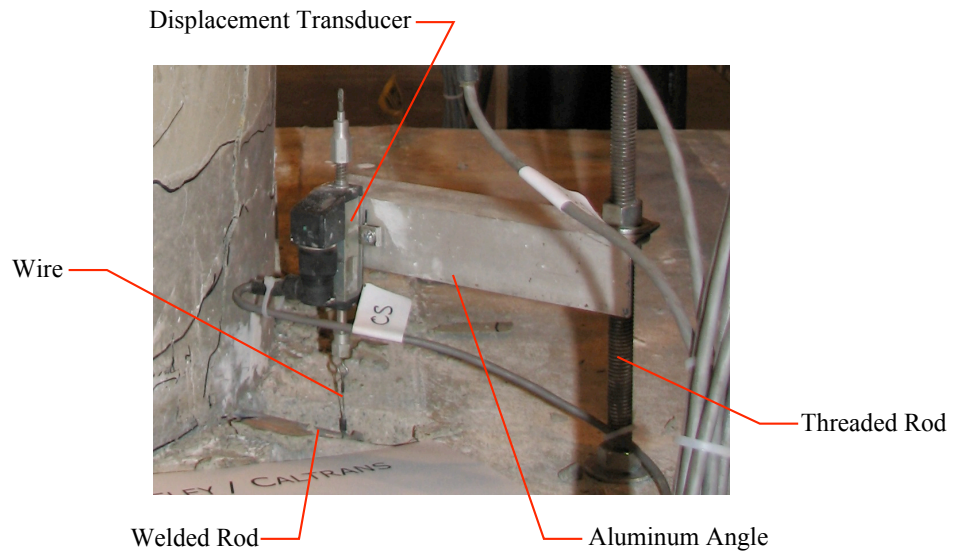


Figure 4.9: Typical Displacement Transducer Setup for Measurement of Bar Slip

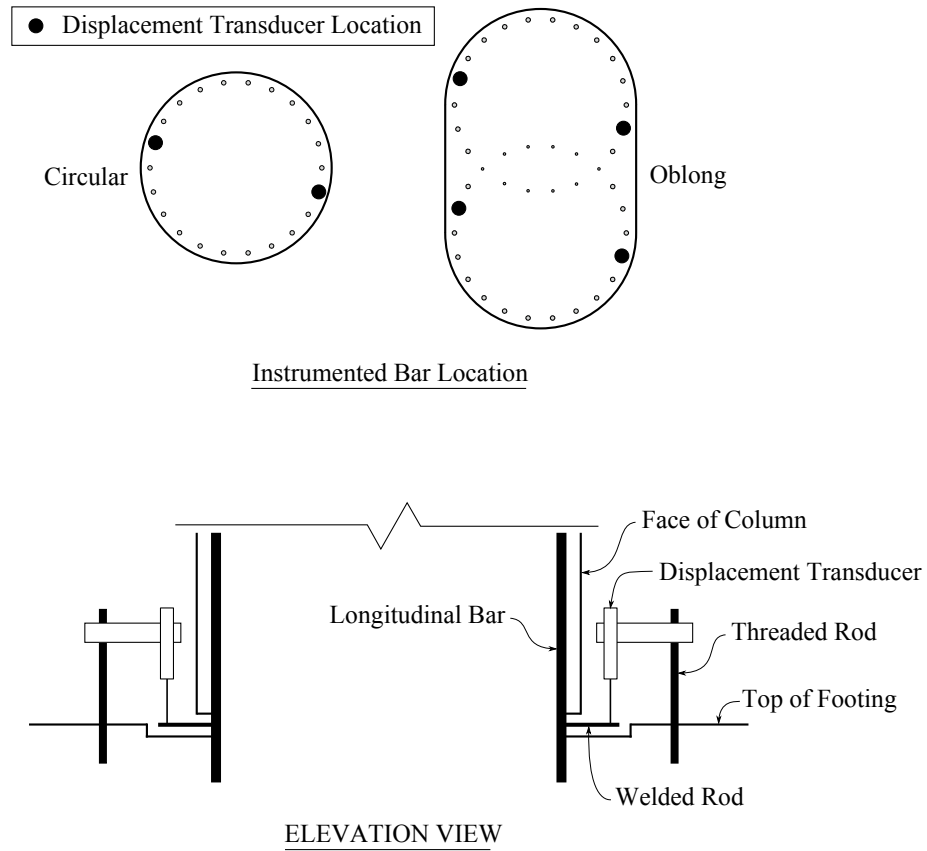


Figure 4.10: Arrangement of Displacement Transducers for Measurement of Bar Slip

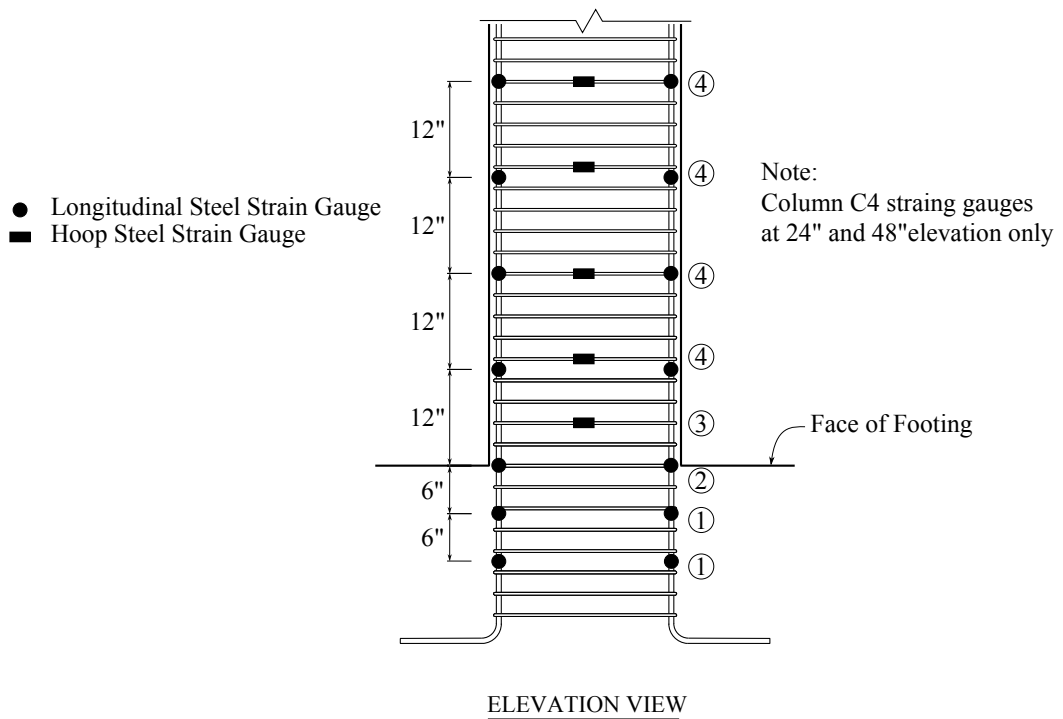
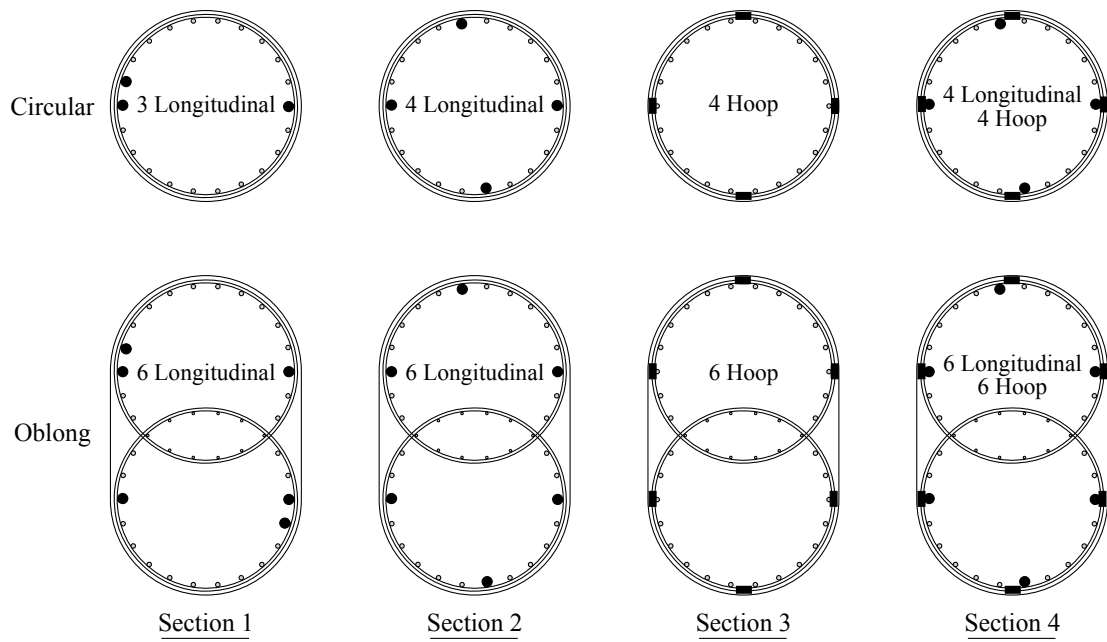


Figure 4.11: Arrangement of Strain Gauges

## Chapter 5

# Experimental Results

This chapter presents the observed and measured response of each column tested, including select data of Lehman 415 (Lehman and Moehle, 2000). A comparative summary of circular columns and columns with similar twist/drift ratio is also presented. For this comparative summary, force-displacement and torque-twist envelope curves are compared, along with key longitudinal and hoop strain gauge data. Additional experimental data can be found in Appendix C.

### 5.1 Overview

The progression of damage was similar for columns subjected to simultaneous reversed cyclic lateral and torsional loading. The chronological progression of damage was:

1. **Cracking**, typically observed during the first-yield displacement level, with increased crack width and length for subsequently increased displacement;
2. **Yielding of longitudinal reinforcing bars**, detected using strain gauges installed

on longitudinal reinforcing bars prior to construction and apparent in the force-displacement response;

3. **Spalling**, typically initiated above the column-footing interface during the 2 in. displacement amplitude cycle, spreading vertically and laterally for subsequently increasing displacement;
4. **Exposure of hoops**, typically observed during the 3 in. displacement amplitude cycle;
5. **Buckling and exposure of longitudinal reinforcing bars**, typically observed during the 5 in. displacement amplitude cycle, indicative of complete loss of cover concrete;
6. **Visible Extension of hoops**, typically observed during the 5 in. displacement amplitude cycle, concurrent with buckling of longitudinal reinforcing bars;
7. **Fracture of longitudinal reinforcing bars**, typically initiated during the 5 in. or 7 in. displacement amplitude cycle and continued during the 7 in. displacement amplitude cycle, resulting in significant strength loss of the column;

## 5.2 Column 415

Column 415 was tested under reversed cyclic lateral loading without twist. The applied axial load of 147 kips was approximately  $0.1f'_cA_g$ , where  $f'_c$  = the target concrete compressive strength (3.25 ksi). The force-displacement plot is shown in Figure 5.1.

## 5.3 Column C1

Column C1 was tested under reversed cyclic combined lateral displacement and twist loading with a twist/drift ratio = 0.6. The applied constant axial load of 225 kips was approximately  $0.1f'_cA_g$ , where  $f'_c$  = target concrete compressive strength (5.0 ksi).

### 5.3.1 Observed Response

Initial cracking was observed on the East and West faces during the 0.75 in. displacement amplitude cycle. The widest crack was at the column-footing interface, and crack widths decreased with increased elevation. Note the lateral displacements were in the East and West directions. Cracks on the East and West face were horizontal and spanned the entire East and West faces. Subsequently increasing displacement cycles widened and lengthened existing cracks and developed inclined cracks on the South face. Inclined cracks were not observed on the North face during testing. The peak crack widths (largest of the crack width measurements at the first peak East or first peak West) for Column C1 are summarized in Table D.1. The residual crack widths (crack width measurements at the end of each displacement amplitude cycle) for Column C1 are summarized in Table D.2.

The onset of concrete spalling was observed at the interface on the East and West faces during the 2 in. displacement amplitude cycle. Subsequently increasing displacement amplitudes caused the spalled regions to spread vertically and laterally, eventually spanning the entire East and West faces. Exposure of the hoops on the East and West faces was observed during the 3 in. displacement amplitude cycle. Concrete spalling was observed on the South face during the first 7 in. displacement amplitude cycle and continued to spread, eventually spanning the entire South face. The North face showed no signs of concrete

spalling until the third 7 in. displacement amplitude cycle, which coincided with exposure of the hoops around the entire circumference of the column. Upon completion of testing, spalled elevation around the circumference of the column were as follows: 13 in. height on the North face, 20 in. on the West face, 16 in. on the South face, and 21 in. on the East face. Figure D.2 illustrates the progression of cracking and spalling of Column C1.

Significant column damage in the form of bar buckling and bar fracture was observed during the final two displacement amplitude cycles. Longitudinal reinforcing bars located on the extreme East and West faces buckled and subsequently fractured during the 5 in. and 7 in. displacement amplitude cycles, respectively; longitudinal reinforcing bars located on the North and South faces buckled during the 7 in. displacement amplitude cycle. In total, 17 longitudinal reinforcing bars had fractured and the remaining 5 longitudinal reinforcing bars had buckled upon completion of testing. Additionally, a single hoop, located 6 in. above the interface, fractured on the West face during the 7 in. displacement amplitude cycle. Figure D.6 shows the location of buckled and fractured longitudinal reinforcing bars of Column C1.

### **5.3.2 Global Response**

The force-displacement response of Column C1 is shown in Figure 5.2. The torque-twist response of Column C1 is shown in Figure 5.3. The force-displacement envelopes and torque-twist envelopes of Column C1 are shown in Figures 5.4 and 5.5, respectively.

## 5.4 Column C2

Column C2 was tested under reversed cyclic combined lateral displacement and twist loading with a twist/drift ratio = 1.2. The applied constant axial load of 225 kips was approximately  $0.1f'_cA_g$ , where  $f'_c$  = target concrete compressive strength (5.0 ksi).

### 5.4.1 Observed Response

Similar to Column C1, initial cracking was observed on the East and West faces during the 0.75 in. displacement amplitude cycle, with the widest crack at the column-footing interface and decreased crack widths with increase in elevation. Unlike Column C1, cracking on the East and West faces of Column C2 were inclined, and inclined cracks were observed on all faces. Subsequently increasing displacement cycles widened and lengthened existing cracks, eventually spanning the entire East and West faces. The measured peak and residual crack widths of Column C2 are summarized in Tables D.3 and D.4, respectively.

The onset of concrete spalling was observed at the interface on the East and West faces during the 2 in. displacement amplitude cycle, similar to Column C1. Subsequently increasing displacement amplitudes caused the spalled regions to spread vertically and laterally, eventually spanning the entire East and West faces. Exposure of the hoops on the East and West faces was also observed during the 3 in. displacement amplitude cycle. Concrete spalling was observed on the North and South faces during the third 5 in. displacement amplitude cycle. Spalling on the North face started at an elevation of 12 in. to 19 in., and continued to spread down to the interface during the 7 in. amplitude displacement cycle, eventually spanning from the interface to approximately the 19 in. elevation. By the end of the 5 in. displacement amplitude cycle, spalling on the South face spanned from the in-

terface to approximately 14 in. elevation. Upon completion of testing, hoops were exposed around the entire circumference of the column and spalling had spread as follows: 18 in. height on the North face, 33 in. height on the West face, 19 in. height on the South face, and 28 in. height on the East face. Figure D.3 illustrates the progression of cracking and spalling of Column C2.

Significant column damage in the form of bar buckling and bar fracture was observed during the 5 in. displacement amplitude cycle. Longitudinal reinforcing bars located on the extreme East and West faces buckled during the first 5 in. displacement amplitude cycles and fractured during the third cycle. Adjacent longitudinal reinforcing bars located on the East and West faces fractured and bars located on the North and South faces buckled during the 7 in. displacement amplitude cycle. In total, 13 longitudinal reinforcing bars had fractured and the remaining 9 longitudinal reinforcing bars had buckled upon completion of testing. Figure D.7 shows the location of buckled and fractured longitudinal reinforcing bars of Column C2.

#### **5.4.2 Global Response**

The force-displacement response of Column C2 is shown in Figure 5.6. The torque-twist response of Column C2 is shown in Figure 5.7. The force-displacement envelopes and torque-twist envelopes of Column C2 are shown in Figures 5.8 and 5.9, respectively.

### **5.5 Column C3**

Column C3 was tested under reversed cyclic combined lateral displacement and twist loading with a twist/drift ratio = 0.6. The applied axial load of 380 kips was approx-

imately  $0.09f'_cA_g$ , where  $f'_c$  = target concrete compressive strength (5.0 ksi).

### 5.5.1 Observed Response

Initial cracking was observed on the East and West faces during the 0.75 in. displacement amplitude cycle. The widest crack was at the column-footing interface, and crack widths decreased with increased elevation. Cracks on the East and West faces were horizontal at the base of the column and more inclined with increased elevation. Subsequently increasing displacement cycles widened and lengthened existing cracks and developed inclined cracks on the entire South face and on the upper half of the East and West faces. Cracks on the North face were predominately horizontal during testing. The measured peak and residual crack widths of Column C3 are summarized in Tables D.5 and D.6, respectively

The onset of concrete spalling was observed at the interface on the East and West faces during the 2 in. displacement amplitude cycle. Subsequently increasing displacement amplitudes caused the spalled regions to spread vertically and laterally, eventually spanning the entire East and West faces. Concrete spalling was observed on the South face during the first 5 in. displacement amplitude cycle, which coincided with exposure of the hoops on the East and West faces. The North face showed no signs of concrete spalling until the third 5 in. displacement amplitude cycle. Upon completion of testing, spalled elevation around the circumference of the column were as follows: 14 in. height on the North face, 21 in. on the West face, 10 in. on the South face, and 23 in. on the East face. Figure D.4 illustrates the progression of cracking and spalling of Column C3.

Significant column damage in the form of bar buckling and bar fracture was observed during the final two displacement amplitude cycles. Main longitudinal reinforcing bars (No. 5) located on the extreme East and West faces buckled during the first 5 in.

displacement amplitude cycle and fractured during the third cycle. The remaining main longitudinal reinforcing bars on the East and West faces fractured and the bars located on the North and South faces buckled during the 7 in. displacement amplitude cycle. In total, 24 main longitudinal reinforcing bars had fractured and 8 main longitudinal reinforcing bars had buckled upon completion of testing. Additionally, buckling of the interlocking longitudinal reinforcing bars (No. 3) at the overlapping of hoops was also observed; no visual observations were possible for the interior interlocking bars. Figure D.8 shows the location of buckled and fractured longitudinal reinforcing bars of Column C3.

### 5.5.2 Global Response

The force-displacement response of Column C3 is shown in Figure 5.10. The torque-twist response of Column C3 is shown in Figure 5.11. The force-displacement envelopes and torque-twist envelopes of Column C3 are shown in Figures 5.12 and 5.13, respectively.

## 5.6 Column C4

Column C4 was tested under reversed cyclic torsional loading in collaboration with Le (2008), similar to the twist history of Column C2. The applied axial load of 225 kips was approximately  $0.1f'_cA_g$ , where  $f'_c$  = target concrete compressive strength (5.0 ksi).

### 5.6.1 Observed Response

Initial cracking was observed on all the faces during the 0.5 deg twist amplitude cycle. Subsequently increasing twist amplitudes widened and lengthened existing cracks

and caused more inclined cracking on all faces. Crack widths were similar on all the faces along the height of the column. The measured peak and residual crack widths of Column C4 are summarized in Tables D.7 and D.8, respectively

The onset of concrete spalling was observed approximately mid-height of the column on all the faces during the 3.6 deg twist amplitude cycle. The height of spalling increased from approximately 24 in. on all the faces during the first 3.6 deg twist amplitude cycle to 24, 41, 45, and 30 in. on the North, West, East, and South faces, respectively, by the end of the 3.6 deg amplitude cycle. The spalled regions spread vertically during the 5 deg amplitude cycle, eventually spanning about 85% of the column height on all the faces. Figure D.5 illustrates the progression of cracking and spalling of Column C4.

During the 5 deg twist amplitude cycle it was observed that the spreader beam, used to distribute the axial load applied by the two hydraulic jacks, was not twisting in unison with the top of the column (Figure 5.14). Inspection of the column cap-spreader beam connection confirmed that the anchor bolts were damaged. As a result, the spreader beam was no longer “fixed” to the top of the column. This partially-fixed condition caused the spreader beam to twist less than the column.

### **5.6.2 Global Response**

The torque-twist response and torque-twist envelopes of Column C4 are shown in Figures 5.15 and 5.16, respectively. The dotted line represents the 5 deg twist amplitude cycle, during which the anchor bolts that attach the spreader beam to the top of the column were damaged.

Because the spreader beam was not twisting as much as the column due to the damaged anchor bolts, the calculated torque due to the horizontal force component of

the vertical jacks is overestimated following the data reduction procedure presented in Appendix B. Accordingly, overestimation of the torque due to the horizontal component of the vertical jacks underestimates the actual torque. Therefore, the torque for the 5 deg twist amplitude cycle should be larger than that shown in Figures 5.15 and 5.16. Unfortunately, a reasonable estimation of the twist of the spreader beam cannot be made. For future research, additional vertical and lateral measurements of the vertical jacks will provide data for calculation of a more accurate torque-twist relationship.

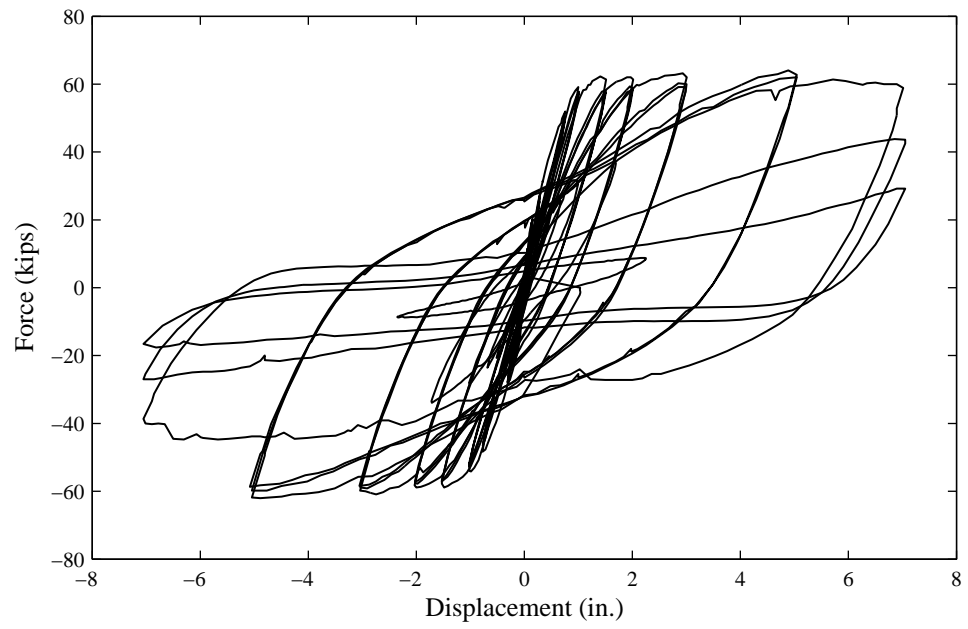


Figure 5.1: Column 415 Force-Displacement Response (Adapted from Lehman and Moehle, 2000)

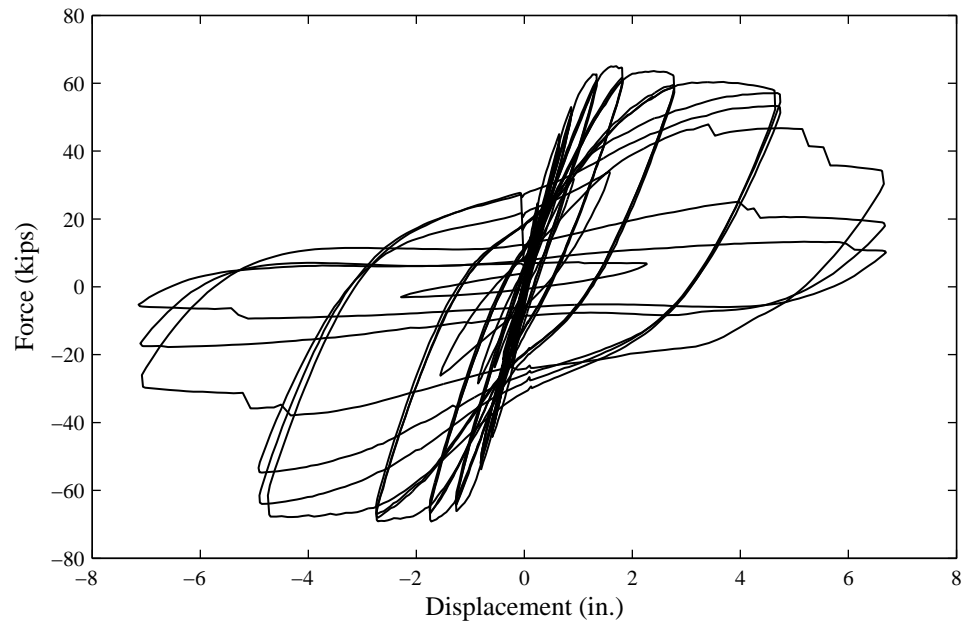


Figure 5.2: Column C1 Force-Displacement Response

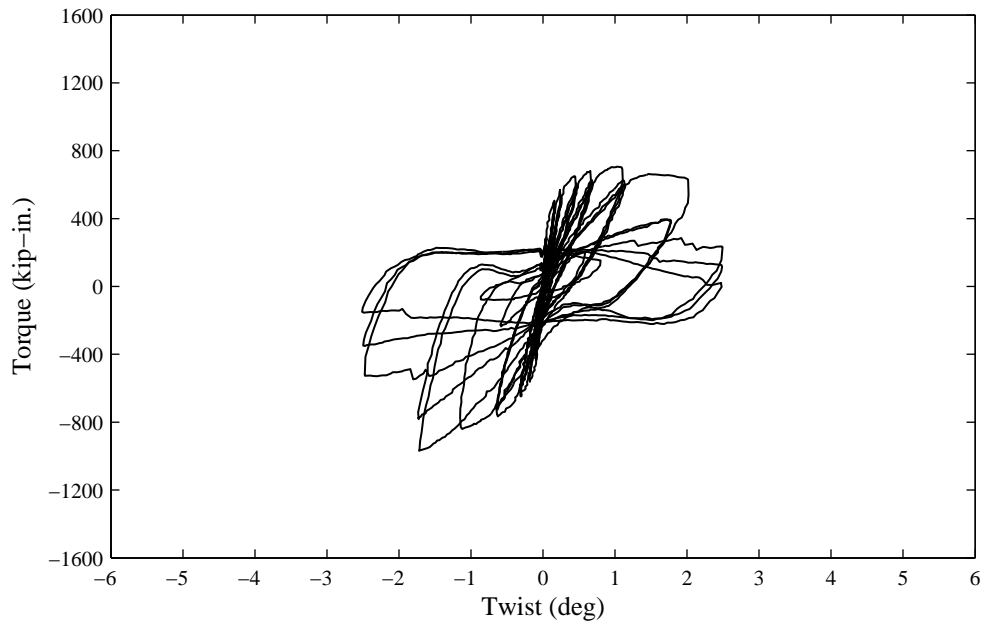


Figure 5.3: Column C1 Torque-Twist Response

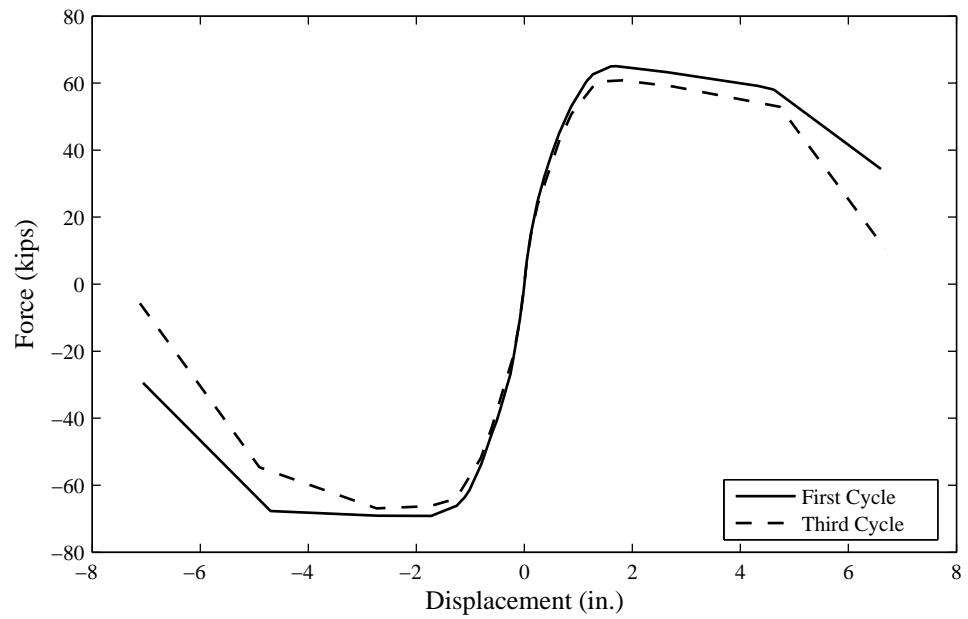


Figure 5.4: Column C1 Force-Displacement Envelopes

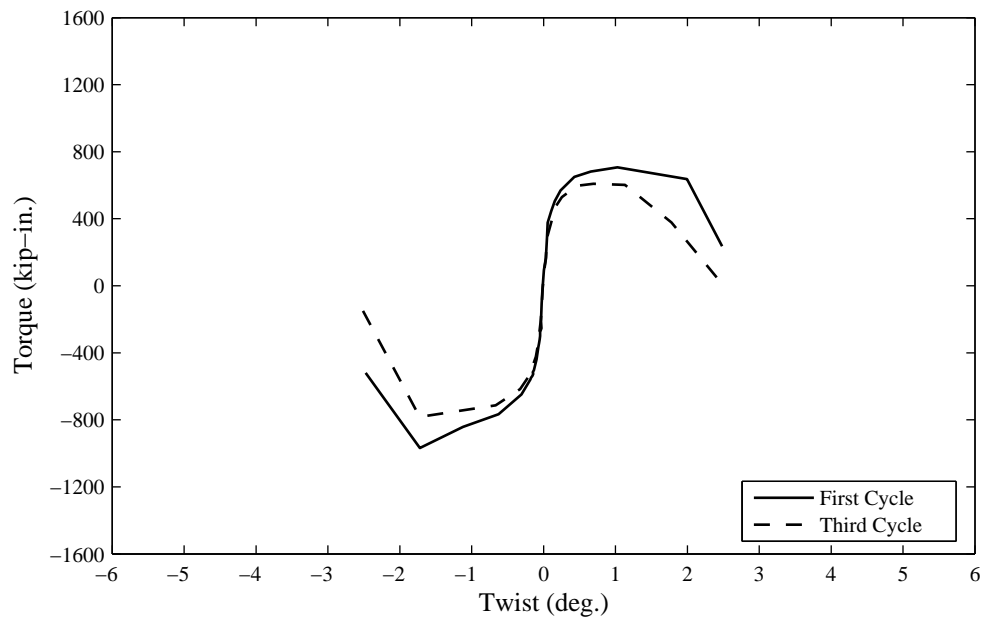


Figure 5.5: Column C1 Torque-Twist Envelopes

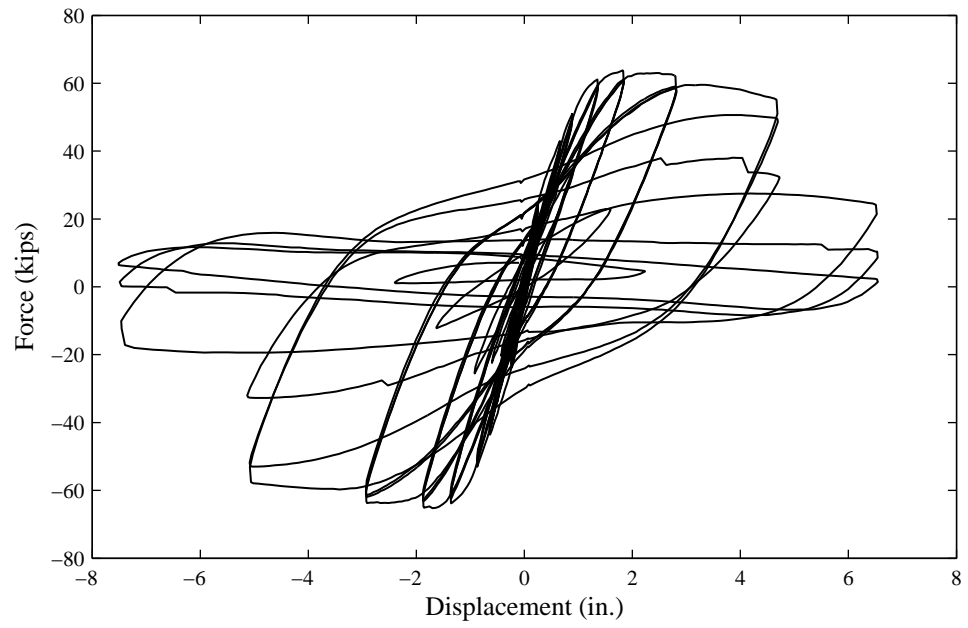


Figure 5.6: Column C2 Force-Displacement Response

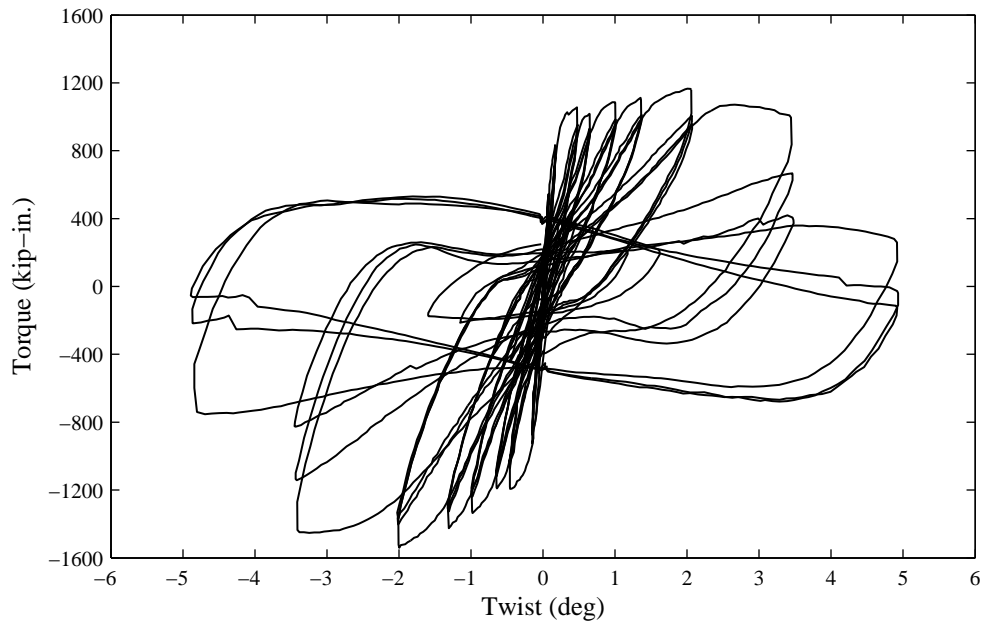


Figure 5.7: Column C2 Torque-Twist Response

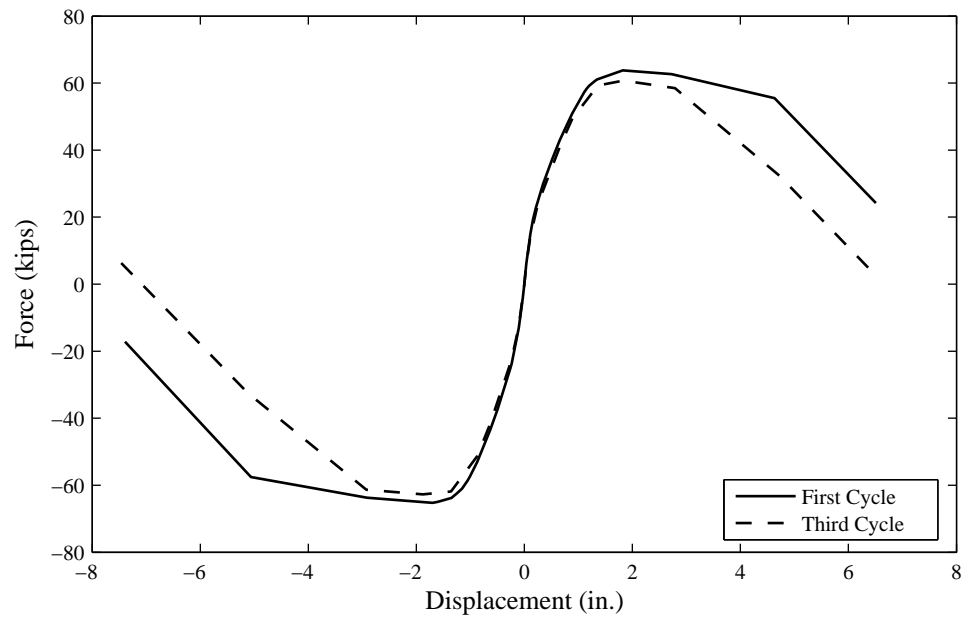


Figure 5.8: Column C2 Force-Displacement Envelopes

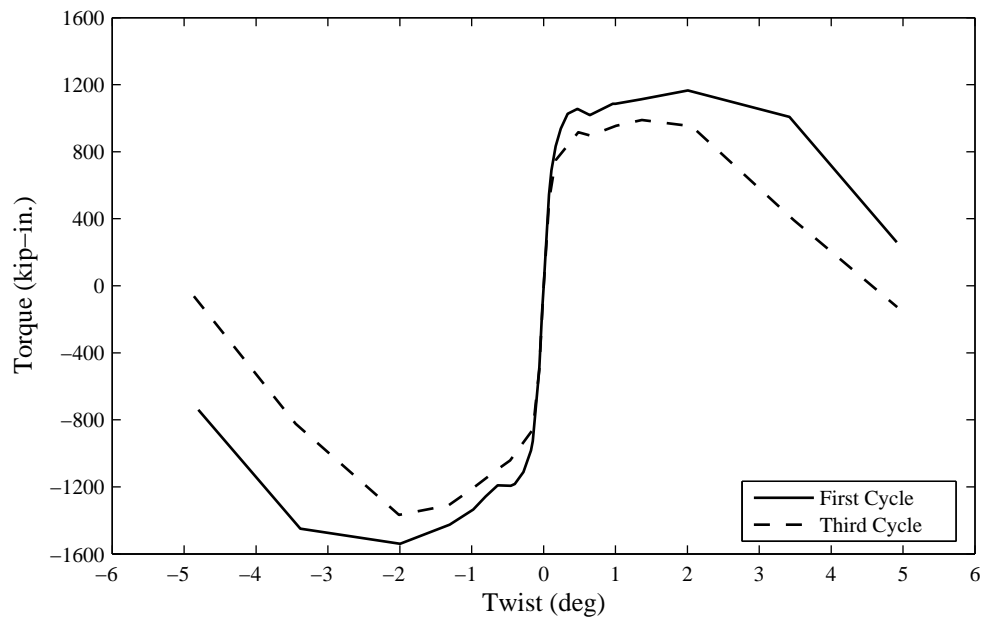


Figure 5.9: Column C2 Torque-Twist Envelopes

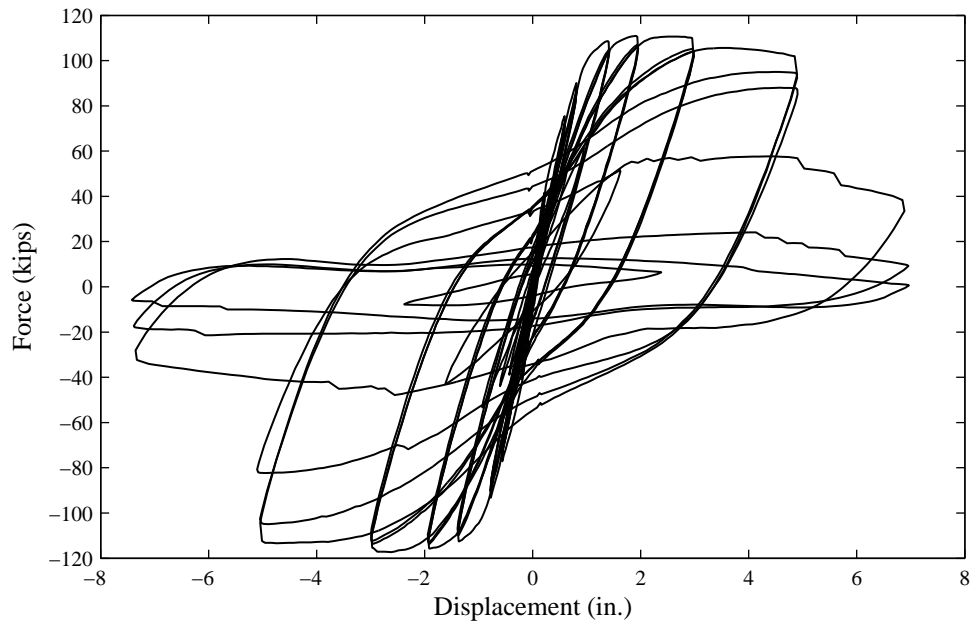


Figure 5.10: Column C3 Force-Displacement Response

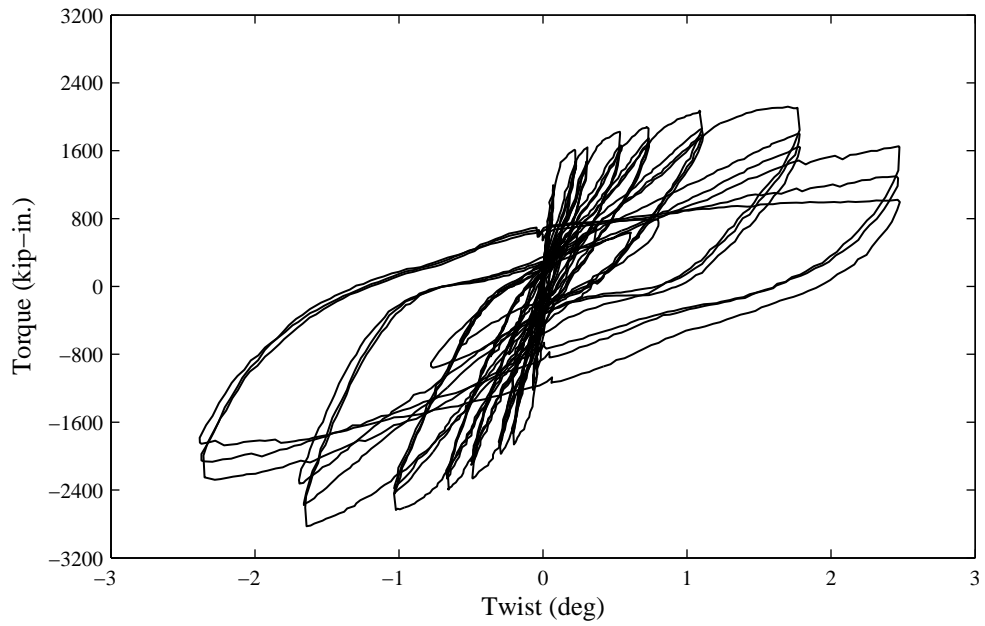


Figure 5.11: Column C3 Torque-Twist Response

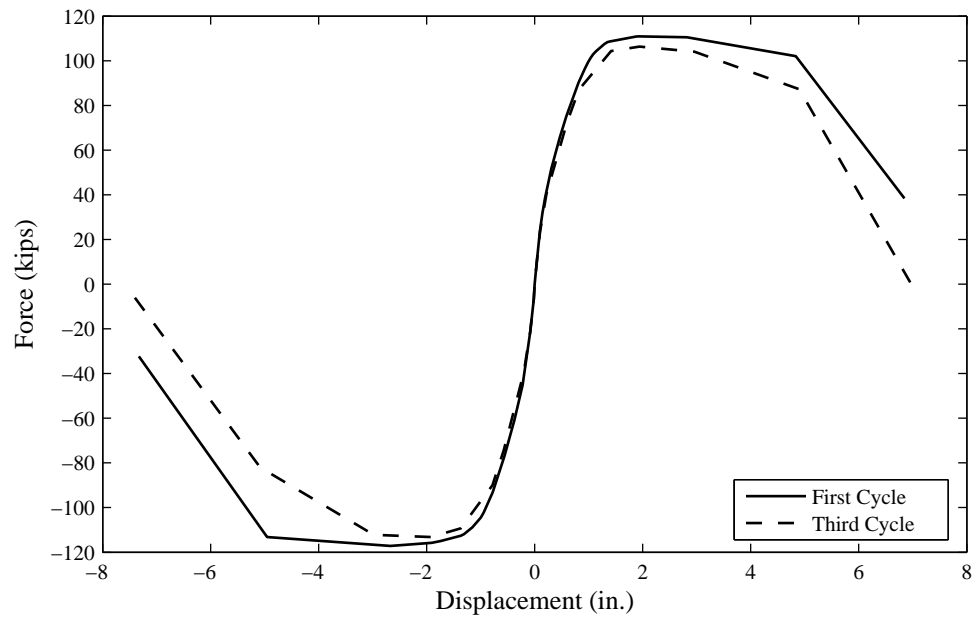


Figure 5.12: Column C3 Force-Displacement Envelopes

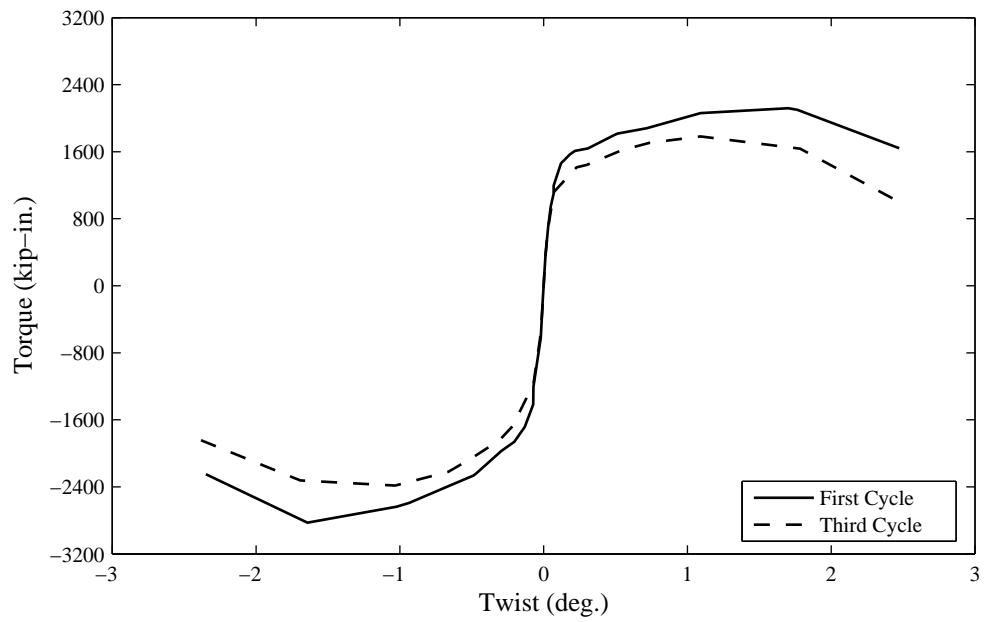


Figure 5.13: Column C3 Torque-Twist Envelopes



Figure 5.14: Spreader Beam and Column Cap Not Twisting in Unison During First 5 deg Twist Amplitude Cycle (Le, 2008)

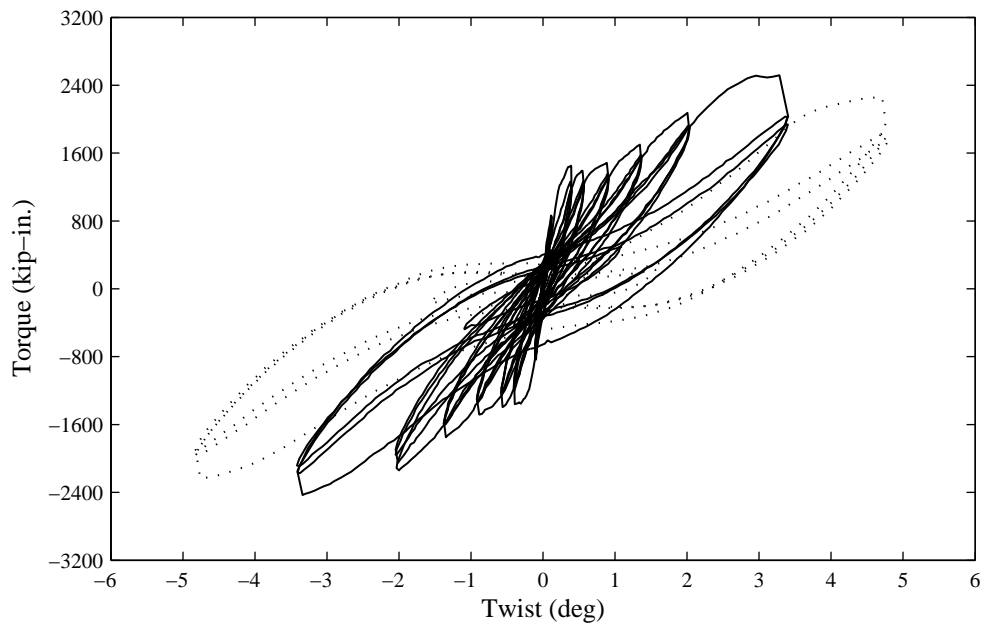


Figure 5.15: Column C4 Torque-Twist Response

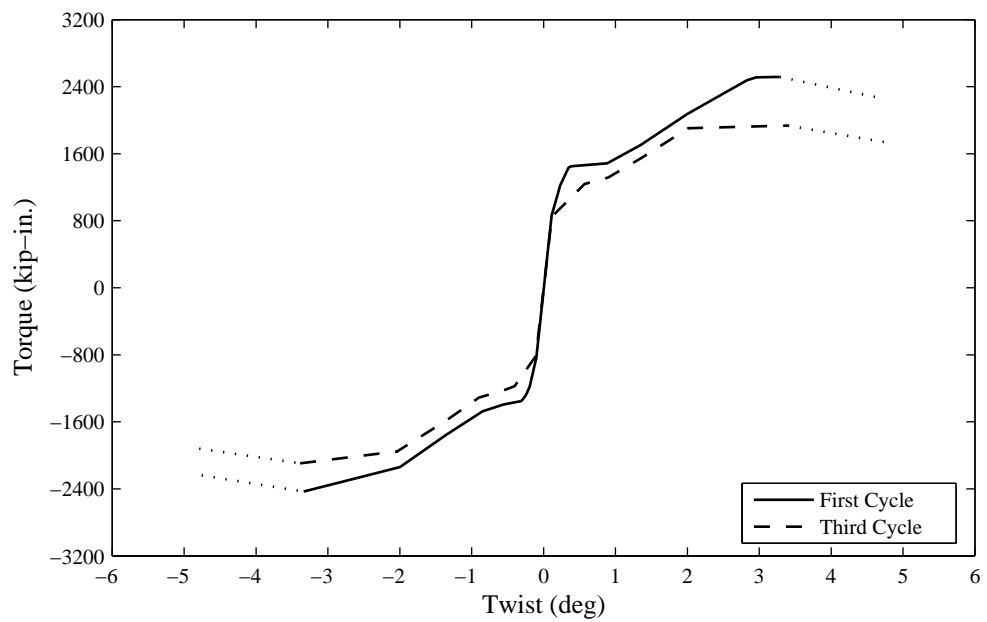


Figure 5.16: Column C4 Torque-Twist Envelopes

## 5.7 Bar Slip

Direct measurement of bar slip at the column-footing interface and strains along the length of the bar inside the footing provide data for an accurate estimate of the bond stress distribution. Bar slip data for the tested columns can be found in Appendix C, including slip history, joint strain history, and joint strain profiles.

The measured bar slip at yield for the column specimens is summarized in Table 5.1. Based on the measured yield strength of the longitudinal reinforcing bars and the target concrete compressive strength ( $f'_c = 5000$  psi), the slip at yield according to Eq. 2.16 (Zhao and Sritharan, 2007) is equal to 0.018 in. This calculated bar slip is approximately 70% of the measured value of 0.025 in.

Using the measured bar slip at yield (Table 5.1), the average bond stress at yield is determined using Eq. 2.12. The calculated bond stresses are divided by the square root of the target and measured concrete compressive strengths, shown in Figure 5.17 for Columns C1, C2, and C3. Using the target compressive strength (5000 psi), the calculated average bond stress is equal to  $7.89\sqrt{f'_c}$  (psi). Using the measured compressive strength, which varies from specimen to specimen, the calculated average bond stress is equal to  $7.25\sqrt{f'_c}$  (psi).

The calculated average bond stresses are within the range of average bond stress values reported. Lehman and Moehle (2000) computed an average bond stress equal to  $12\sqrt{f'_c}$  (psi) using the experimental results of Column 415. Sezen (2002) computed a mean average bond stress equal to  $11.4\sqrt{f'_c}$  (psi) using 12 column specimens. The range of average bond stress of the 12 columns was from approximately  $6\sqrt{f'_c}$  (psi) to  $16\sqrt{f'_c}$  (psi). Ranf (2007) developed a bond stress versus slip model, based on the stepped model by Lehman

Table 5.1: Measured Bar Slip (in.) at Yield Level

Location	Column C1	Column C2	Column C3
West Face	0.028	0.024	0.025*, 0.029 <sup>†</sup>
East Face	0.025	0.025	0.025 <sup>‡</sup>

\* NorthWest, <sup>†</sup> SouthWest, <sup>‡</sup> NorthEast  
 Note: Column C3 SouthEast not measured

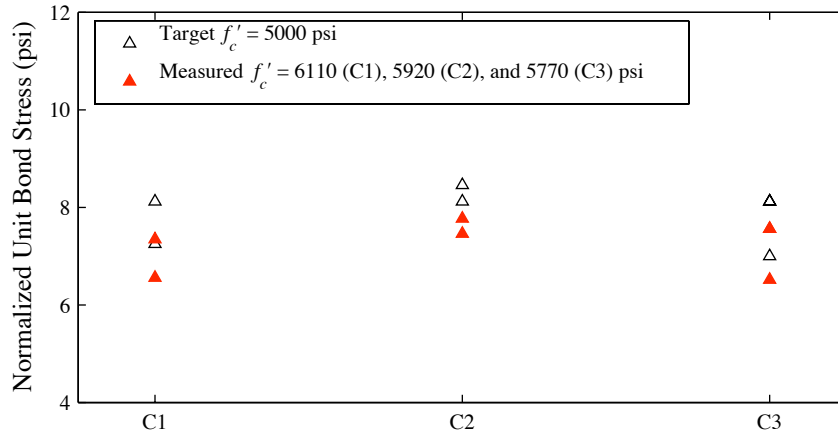


Figure 5.17: Calculated Bond Stress at Yield Level

and Moehle, using the shaking table test results of a two-span reinforced concrete bridge (Johnson et al., 2006). Ranf proposed a best-fit average bond stress equal to  $8\sqrt{f'_c}$  (psi).

## 5.8 Comparative Summary

### 5.8.1 Circular Columns

#### Observed Response

Table 5.2 qualitatively describes the damage for the  $0.75\Delta_y$  to  $7\Delta_y$  displacement amplitude cycles of the circular columns (Columns 415, C1 and C2). Figures 5.18, 5.19,

5.20, and 5.21 compare the crack patterns for Columns C1 and C2 after the 1, 3, 5, and 7 in. displacement amplitude cycles, respectively. As summarized in Table 5.2 and seen in Figures 5.18 to 5.21, inclined cracking was more pronounced for Column C2 than Column C1, i.e., more pronounced for higher twist/drift ratio. Moreover, the extent of the spalled height and circumference was increased by the associated twist and more pronounced for higher twist/drift ratio. The associated twist also affected the initiation of bar buckling and subsequently bar fracture due to buckling and straightening of the longitudinal reinforcing bars upon cyclic load reversal.

### **Force-Displacement Response**

The force-displacement envelopes for the first and third cycles of the circular columns (Columns 415, C1, and C2) are shown in Figure 5.22. As seen in Figure 5.22, the flexural strength was not strongly affected by the associated twist. Deformation capacity, however, was reduced by the associated twist. The reduction of deformation capacity was more evident in the third cycle response as compared with the first cycle response. In conjunction, the strength degradation, also more evident in the third cycle response as compared with the first cycle response, was increased with associated twist. Overall, reduction of deformation capacity and increase of strength degradation was more pronounced for Column C2 than Column C1, i.e., more pronounced for higher twist/drift ratio.

### **Torque-Twist Response**

The torque-twist envelopes for the first and third cycles of the circular columns (Columns C1, C2, and C4) are shown in Figure 5.23. As seen in Figure 5.23, the initial torsional stiffness was similar for all twist/drift ratios, however, the torque demand varied

Table 5.2: Qualitative Damage Description of Circular Columns

Cycle	Column 415*	Column C1	Column C2
$0.75\Delta_y$	horizontal cracking just over half of column height	horizontal cracking on the East and West faces	inclined cracking on all faces
$\Delta_y$	increased horizontal cracking	increased horizontal cracking; initial inclined cracking on the South face	increased inclined cracking
$1.5\Delta_y$	onset of concrete spalling located 4 in. above the interface	increased horizontal and inclined cracking	increased inclined cracking
$2\Delta_y$	spalled region increased to 6 in. height x 5 in. circumference	onset of concrete spalling on the East and West faces at the interface; inclined cracking on all faces	onset of concrete spalling on the East and West faces at the interface; inclined cracking on all faces
$3\Delta_y$	spalled region increased to 10 in. x 7 in.	spalled region increased to 21 in. x 19 in. on the East face; hoops on the East and West faces exposed	spalled region increased to 20 in. x 18 in. on the East face; hoops on the East and West faces exposed
$5\Delta_y$	spalled region increased to 12 in. x 16 in.; spirals on the compression/tension face exposed	bar buckling on the East and West faces;	bar buckling on the East and West faces; bar fracture on the East and West faces during the third cycle; spalled region extended to North and South faces
$7\Delta_y$	bar buckling and fracture on the compression/tension face; spiral fracture on the compression/tension face	bar buckling on all faces; bar fracture on the East and West faces; hoop fracture located 6 in. above interface; spalled region extended to entire circumference; hoops on all faces exposed	bar buckling on all faces; bar fracture on the East and West faces; spalled region extended to entire circumference; hoops on all faces exposed

\* Adapted from Lehman and Moehle (2000)

depending on twist/drift ratio. Reduction of the torque demand was more pronounced for Column C1 than Column C2, i.e., more pronounced for lower twist/drift ratios. Moreover, the onset of deteriorating torsional stiffness occurred at smaller twist demands for Column C1 than Column C2, i.e., occurred at lower twist/drift ratio.

### **Strain Gauge Measurements**

The longitudinal strain history of the West and East gauges of Columns C1 and C2 are shown in Figures 5.24 and 5.25, respectively. As seen in Figure 5.24, the longitudinal strains on the West face of Columns C1 and C2 were similar along the height of the column. However, differences exist; for example, at the interface the strains for Column C2 were slightly larger than those for Column C1. Likewise, the longitudinal strains on the East face of Columns C1 and C2 were also similar along the height of the column, particularly at the 36 in. and 48 in. elevations, as seen in Figure 5.25. Similar to the West face, the longitudinal strains at the interface of the East face were also slightly larger for Column C2 compared with Column C1.

Figure 5.26 compares the longitudinal strain profiles of the West (compression) and East (tension) faces of the circular columns (Columns 415, C1, and C2) at the first peak of displacement amplitude cycles 0.75, 1, 2, 3, and 5 in. Data for Column 415 were only available up to the 2 in. cycle. Note, the yield strain shown is for the longitudinal reinforcement of Columns C1 and C2, which is approximately equal to the yield strain for the longitudinal reinforcement of Column 415 reported by Lehman and Moehle (2000). The longitudinal reinforcement stress-strain relations of Columns 415, C1, and C2 are also similar.

As seen in Figure 5.31(a)-(d), strain measurements on the tension face were larger

at the lower elevations (ratio of column height  $< 0.2$ ) for Column 415 compared with Columns C1 and C2, however, larger strains were measured for Columns C1 and C2 compared with Column 415 at the higher elevations (ratio of column height  $> 0.2$ ).

The hoop strain histories of the North, South, West, and East gauges for Columns C1 and C2 are shown in Figures 5.27 to 5.30. As expected, the strain measurements were larger on the South face (Figure 5.28) compared with the North face (Figure 5.27) due to the larger deformation demand from combined lateral and torsional loading on the South face than the North face. Additionally, hoop strains were larger for Column C2 compared with Column C1 along the height of the column, particularly evident on the South faces. Although several gauges failed at the lower elevations (12 in. and 24 in.), the hoop yield strain was reached on the West and East faces at smaller displacement amplitude cycles for Column C2 compared with Column C1.

Figures 5.31 and 5.32 compare the hoop strain profiles of the circular columns (Columns 415, C1, and C2) on the North/South and West/East (compression/tension) faces, respectively, at the first peak of displacement amplitude cycles 0.75, 1, 2, 3, and 5 in. Data from Column 415 were available for all cycles except the 0.75 in. displacement amplitude for Figure 5.31 and were available for the 1, 2, and 5 in. cycles only for Figure 5.32. Note, the yield strain shown is for the hoop reinforcement of Columns C1 and C2, which is less than the yield strain for the spiral reinforcement of Column 415 reported by Lehman and Moehle (2000). The stress-strain relations of the hoop reinforcement (Figure 3.18) and spiral reinforcement (Figure 3.19) are also dissimilar.

As seen in Figure 5.31, strain measurements were very similar along the height of the columns up to the 2 in. cycle. After the 2 in. cycle, hoop strains were larger at the

lower elevations for Column 415 compared with Columns C1 and C2. Variation of the strain measurements for Column 415 compared with Columns C1 and C2 can be attributed to both the effect of the twist and the use of different materials for the lateral reinforcement. In particular, at strains exceeding the hoop yield strain, the stress-strain relation could have a significant effect on the hoop strains. Keeping this in mind, the hoop strains were larger for Column 415 near the base, however, hoop yielding extended to higher elevations and was more pronounced for Column C2 compared with Column C1, i.e., more pronounced for higher twist/drift ratio.

As seen in Figure 5.32, strain measurements on the West and East faces were at or below the yield strain along the height of the columns up to the 2 in. cycle. After the 2 in. cycle, hoop strains exceeded the yield strain at the lower elevations for Columns C1 and C2. The hoop yielding extended to higher elevations and was more pronounced for high twist/drift ratio at larger displacement amplitudes. The strain measurements up to the 5 in. cycle for Column 415 did not exceed the hoop yield strain. Thus, the influence of different materials for lateral reinforcement was not apparent, and the variation of hoop strains for Columns C1 and C2 compared with Column 415 was due to the effect of the twist.

## 5.8.2 Circular vs. Oblong Column

### Observed Response

Table 5.3 qualitatively describes the damage for the  $0.75\Delta_y$  to  $7\Delta_y$  displacement amplitude cycles of the columns with twist/drift ratio = 0.6 (Columns C1 and C3). Figures 5.33, 5.34, 5.35, and 5.36 show the crack patterns for Columns C1 and C3 after the 1,

3, 5, and 7 in. displacement amplitude cycles, respectively.

As summarized in Table 5.3 and seen in Figures 5.33, 5.34, inclined cracking on the West and East faces was more pronounced for Column C3 compared with Column C1, particularly with increase in elevation along the height of the column. For both Columns C1 and C3, predominantly horizontal cracking was observed on the North face. Also observed was the difference in the height of spalling, which was slightly less for Column C3 compared with Column C1. Extensive damage in the form of bar fracture occurred earlier for Column C3 compared with Column C1, i.e., during the third 5 in. cycle for Column C3 compared with the first 7 in. cycle for Column C1.

### **Force-Displacement Response**

The force-displacement envelopes for the first and third cycles of columns with twist/drift ratio = 0.6 (Columns C1 and C3) are shown in Figure 5.37. The force-displacement envelope curves from Figure 5.37 are normalized to their maximum respective force and presented in Figure 5.38.

As seen in Figure 5.37, the initial lateral stiffness was larger for Column C3 compared with Column C1. And as expected, the lateral strength of Column C3 was almost twice the strength of Column C1. As seen in the normalized force-displacement envelope curves (Figure 5.38), strength degradation occurred at a similar displacement demand for Columns C1 and C3. Moreover, the deformation/ductility capacity was also similar for Columns C1 and C3.

Table 5.3: Qualitative Damage Description for Twist/Drift Ratio = 0.6

Cycle	Column C1	Column C3
$0.75\Delta_y$	horizontal cracking on the East and West faces	horizontal cracking at the base and more inclined with increase in elevation on the East and West faces; inclined cracking on South face
$\Delta_y$	increased horizontal cracking; initial inclined cracking on the South face	increased horizontal and inclined cracking
$1.5\Delta_y$	increased horizontal and inclined cracking	increased horizontal and inclined cracking
$2\Delta_y$	onset of concrete spalling on the East and West faces at the interface; inclined cracking on all faces	onset of concrete spalling on the East and West faces at the interface; inclined cracking on all faces
$3\Delta_y$	spalled region increased to 21 in. x 19 in. on the East face; hoops on the East and West faces exposed	spalled region increased to 14 in. x 32 in. on the East face; spalled region extended to South face
$5\Delta_y$	bar buckling on the East and West faces;	hoops on the East and West faces exposed; spalled region extended to North face; bar buckling on the East and West faces; bar fracture on the East and West faces during the third cycle;
$7\Delta_y$	bar buckling on all faces; bar fracture on the East and West faces; hoop fracture located 6 in. above interface; spalled region extended to entire circumference; hoops on all faces exposed	bar buckling on all faces; bar fracture on the East and West faces; spalled region extended to entire circumference; hoops on all faces exposed

## Torque-Twist Response

The torque-twist envelopes for the first and third cycles of columns with twist/drift ratio = 0.6 (Columns C1 and C3) are shown in Figure 5.39. The torque-twist envelope curves from Figure 5.39 are normalized to their maximum respective torque and presented in Figure 5.40.

As expected, the initial torsional stiffness and torque demand was larger for Column C3 compared with Column C1, seen in Figure 5.39. As seen in the normalized torque-twist envelope curves (Figure 5.40), the onset of deteriorating torsional stiffness occurred at smaller twist demand for Column C1 compared with Column C3. This was more apparent when comparing the third cycle of torque-twist envelopes (Figure 5.40(b)).

## Strain Gauge Measurements

The longitudinal strain histories of the West and East gauges for Column C1 and C3 are shown in Figures 5.41 and 5.42, respectively. As seen in Figure 5.41, longitudinal strain measurements on the West face tend to be larger for Column C3 compared with Column C1, especially at the interface. A similar trend was also observed on the East face (Figure 5.42).

Figure 5.43 compares the longitudinal strain profiles of the West (compression) and East (tension) faces of Columns C1 and C3 at the first peak of displacement amplitude cycles 0.75, 1, 2, 3, and 5 in. For clarity, only the northern West and East strain measurements are presented for Column C3. Although longitudinal strains were larger for Column C3 compared with Column C1 at the interface, similar strains were observed along the height of the columns (Figure 5.43(e))

The hoop strain histories of the North, South, West, and East gauges for Columns C1 and C3 are shown in Figures 5.44 to 5.47. As expected, the strain measurements were larger on the South face (Figure 5.45) compared with the North face (Figure 5.44). As seen in Figures 5.46 and 5.47, strain measurements exceeded the yield strain along the height of the columns, with largest strains at the lower elevations (6 and 12 in.). Overall, there was no clear trend to differentiate the hoop strains of Columns C1 and C3.

Figures 5.48 and 5.49 compare the hoop strain profiles of Columns C1 and C3 on the North/South and West/East (compression/tension) faces, respectively, at the first peak of displacement amplitude cycles 0.75, 1, 2, 3, and 5 in. For clarity, only the northern West and East strain measurements of Column C3 are presented in Figure 5.49. The hoop strains were larger on the South face compared with the North face of Columns C1 and C3, as seen in Figure 5.48, and exceeded the yield strain along the height of the column for the 3 in. cycle and greater. Likewise for the West and East faces (Figure 5.49), hoop strains also exceeded the yield strain at the first peak of the 3 in. cycle, with the largest strains at the lower elevations.

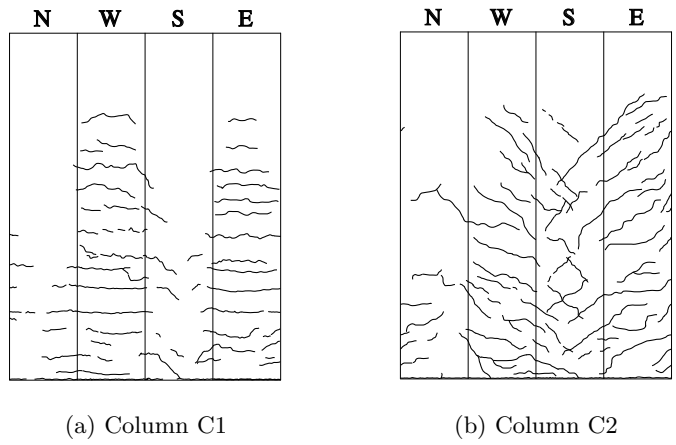


Figure 5.18: Columns C1 and C2 Crack Patterns after 1 in. Displacement Amplitude Cycle

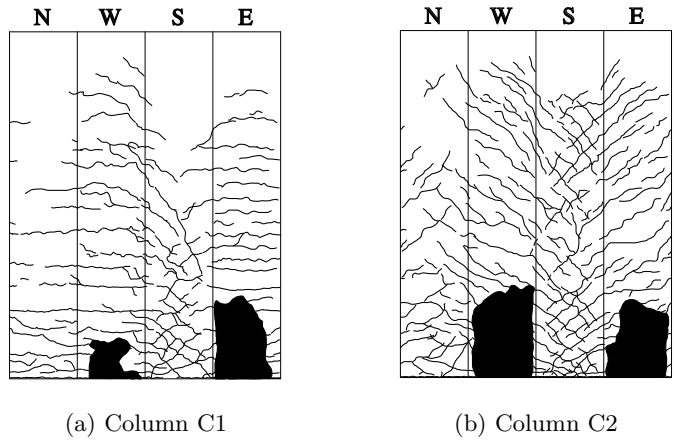


Figure 5.19: Columns C1 and C2 Crack Patterns after 3 in. Displacement Amplitude Cycle

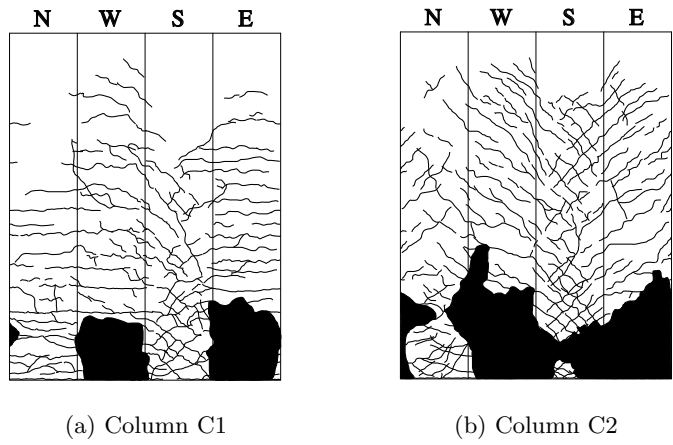


Figure 5.20: Columns C1 and C2 Crack Patterns after 5 in. Displacement Amplitude Cycle

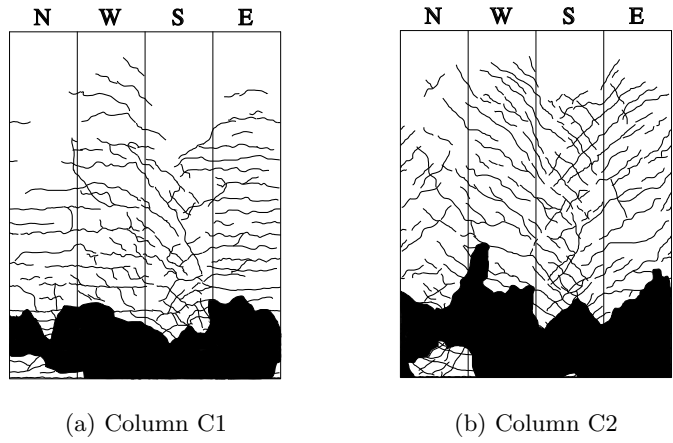


Figure 5.21: Columns C1 and C2 Crack Patterns after 7 in. Displacement Amplitude Cycle

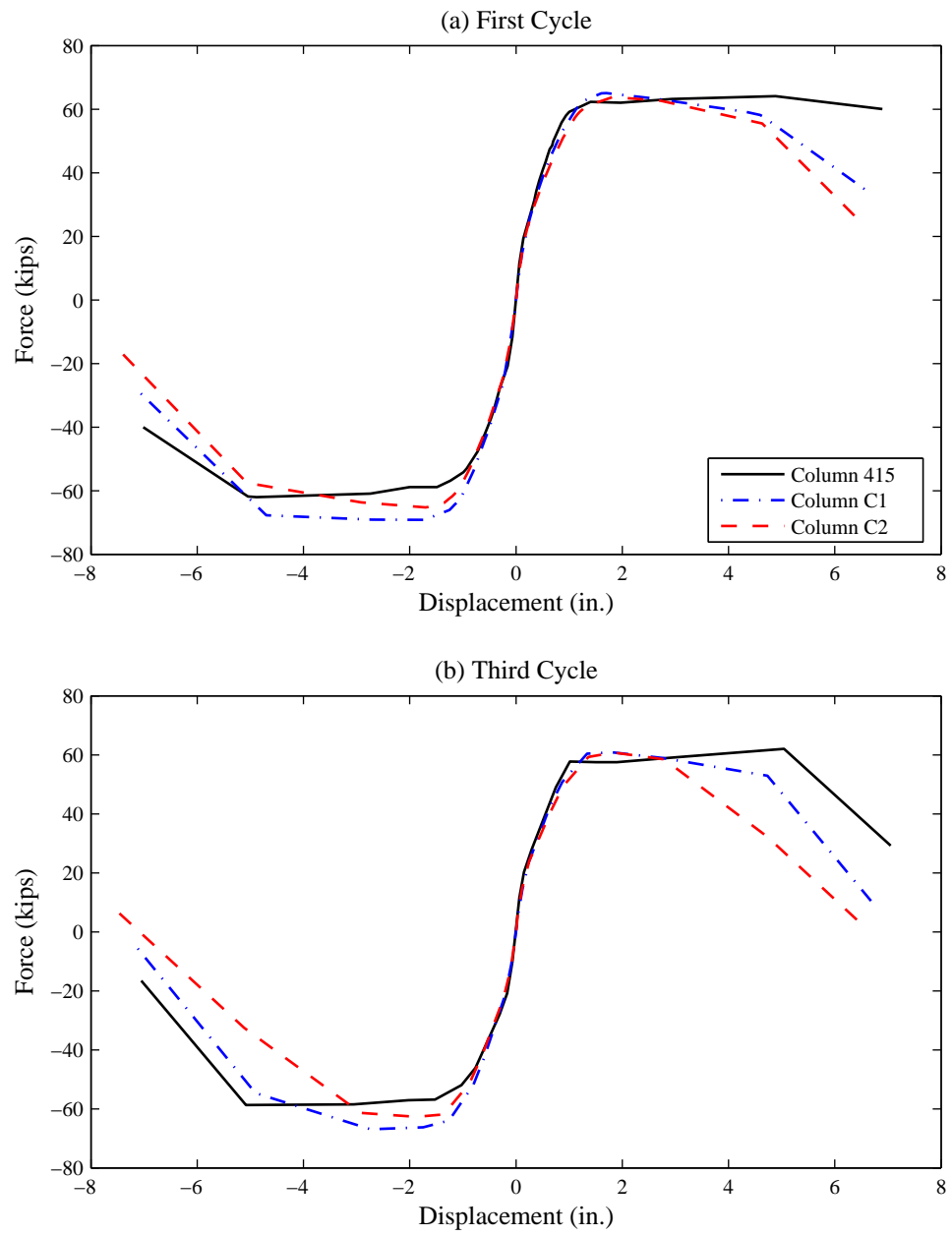


Figure 5.22: Circular Column Force-Displacement Envelopes

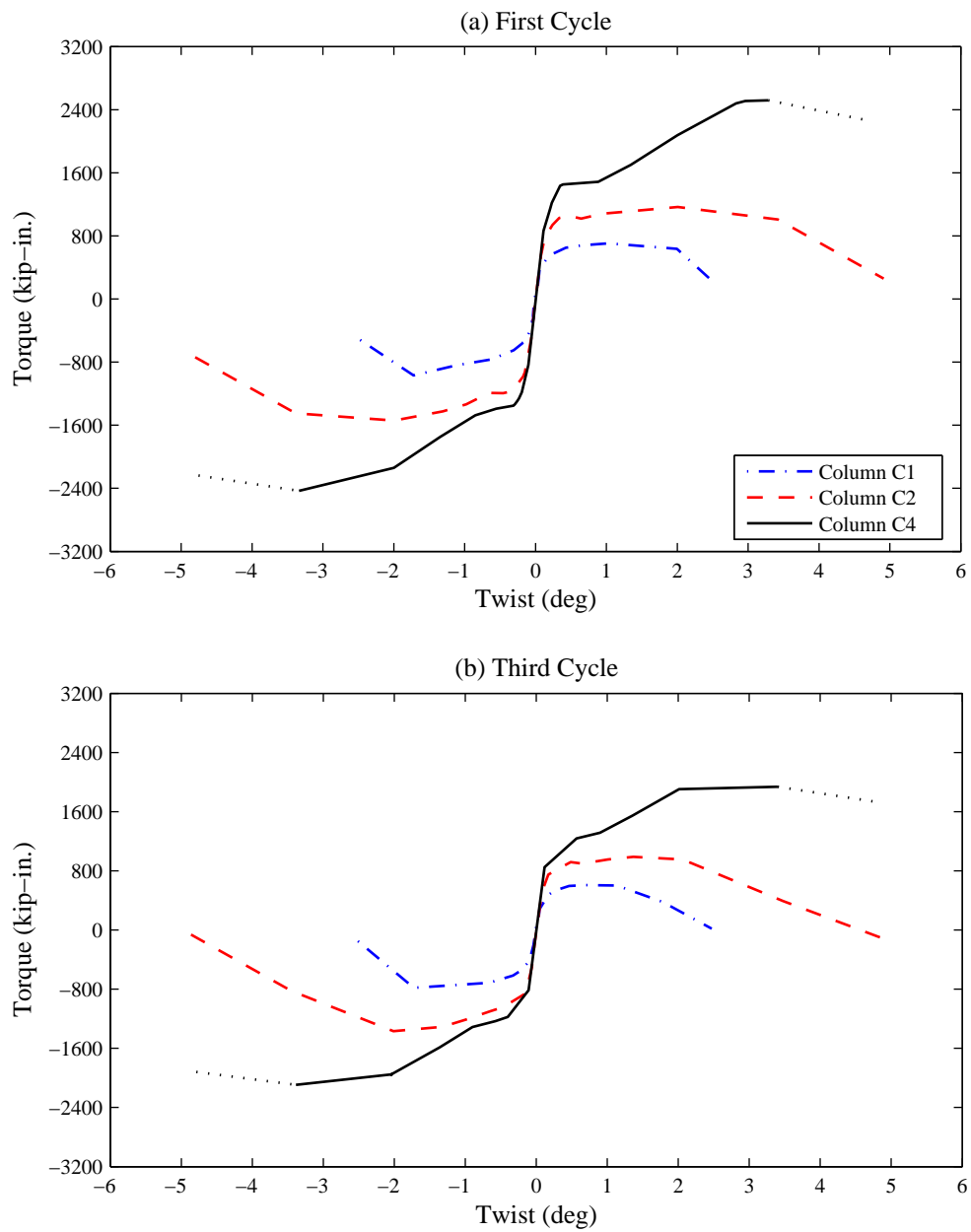


Figure 5.23: Circular Column Torque-Twist Envelopes

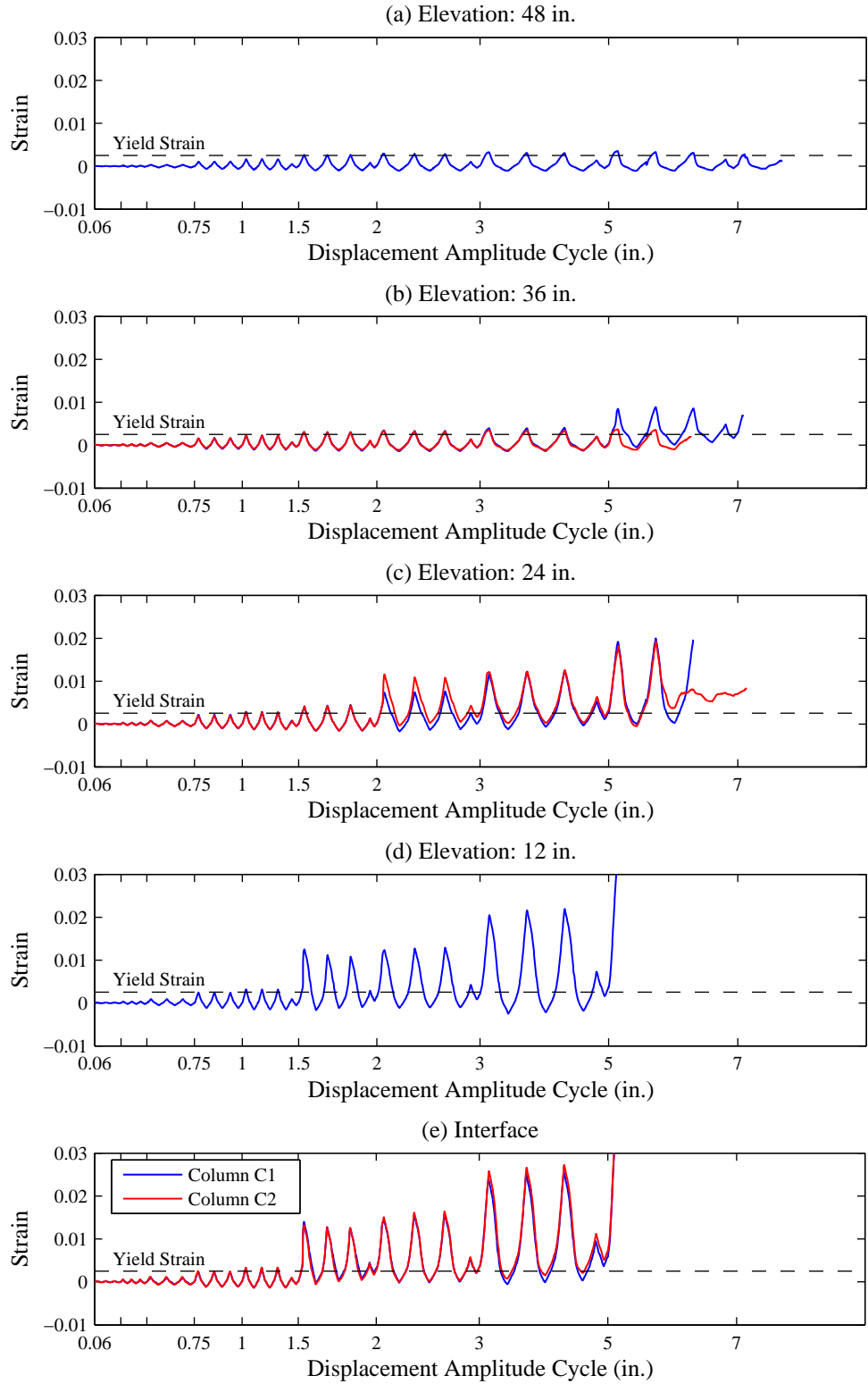


Figure 5.24: Columns C1 and C2 Longitudinal Strain History – West Gauges

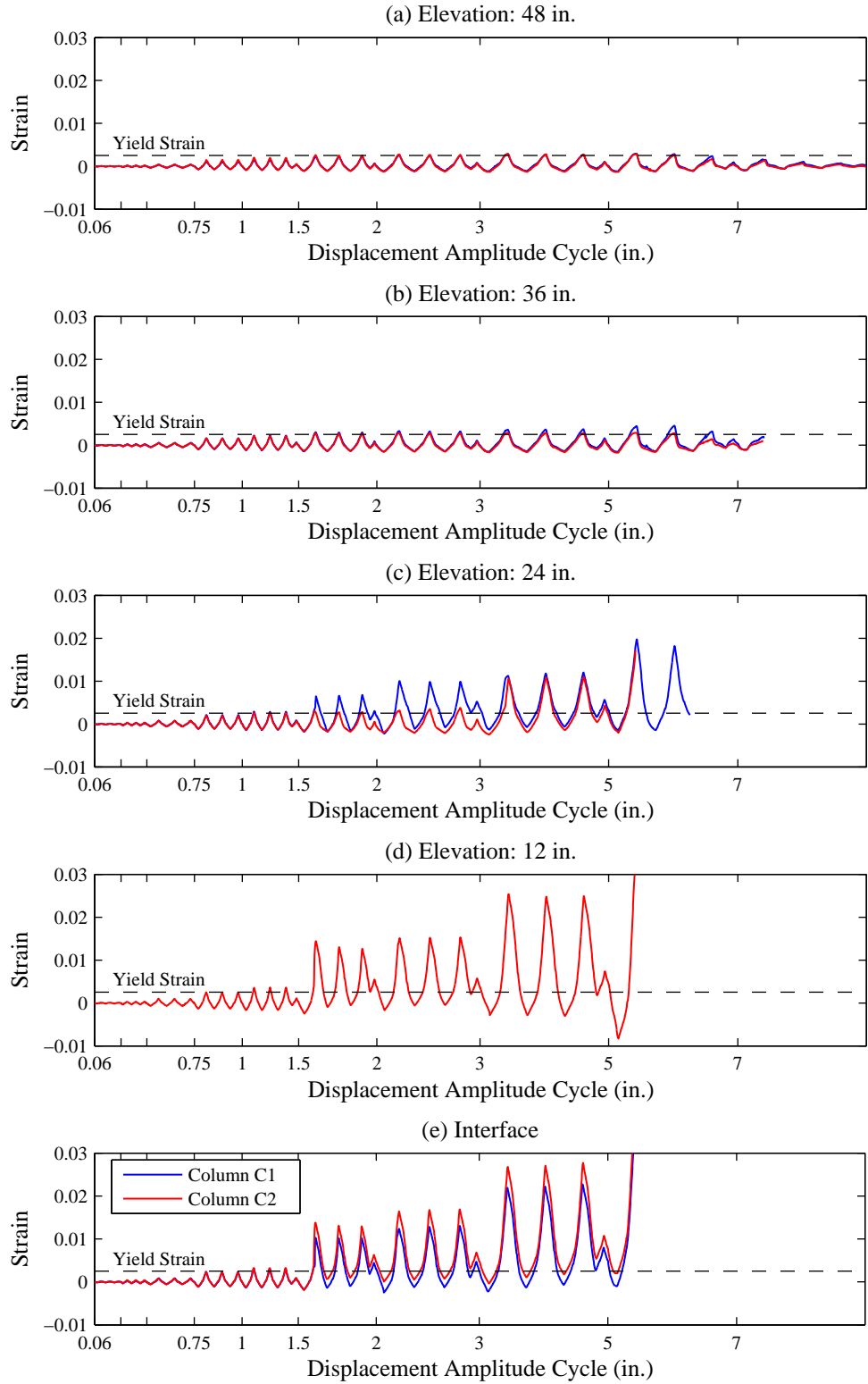


Figure 5.25: Columns C1 and C2 Longitudinal Strain History – East Gauges

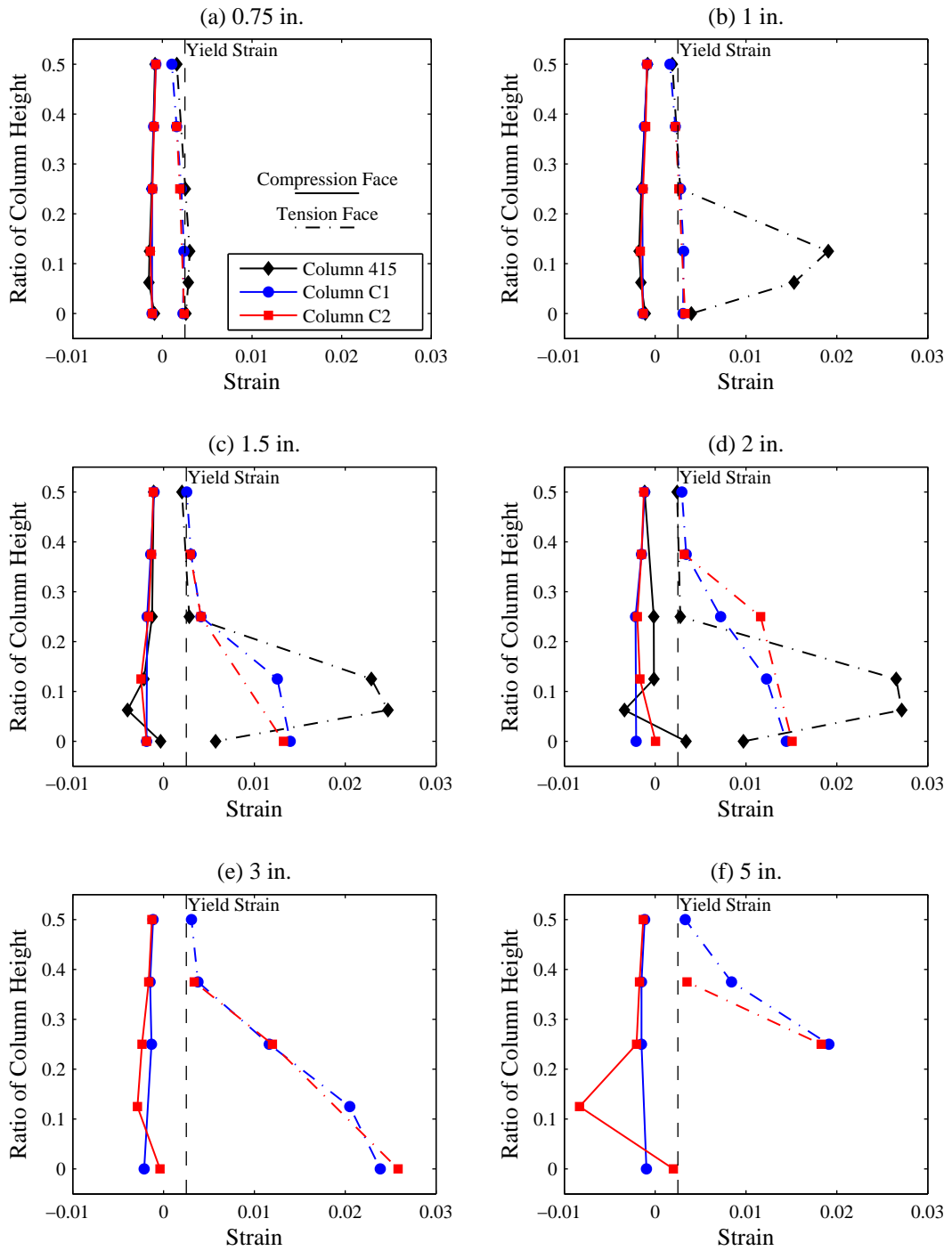


Figure 5.26: Circular Column Longitudinal Strain Profile – West and East Gauges

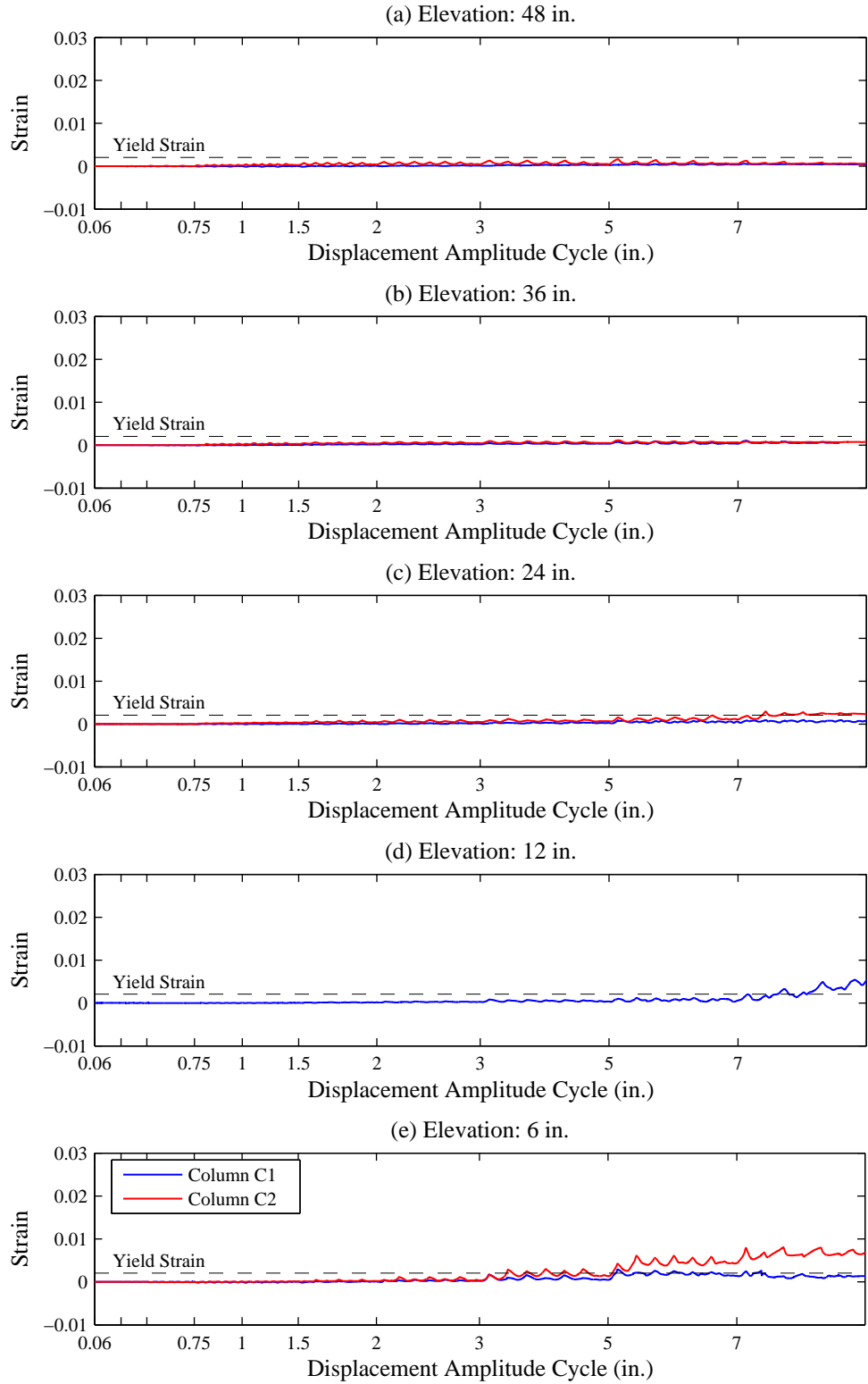


Figure 5.27: Columns C1 and C2 Hoop Strain History – North Gauges

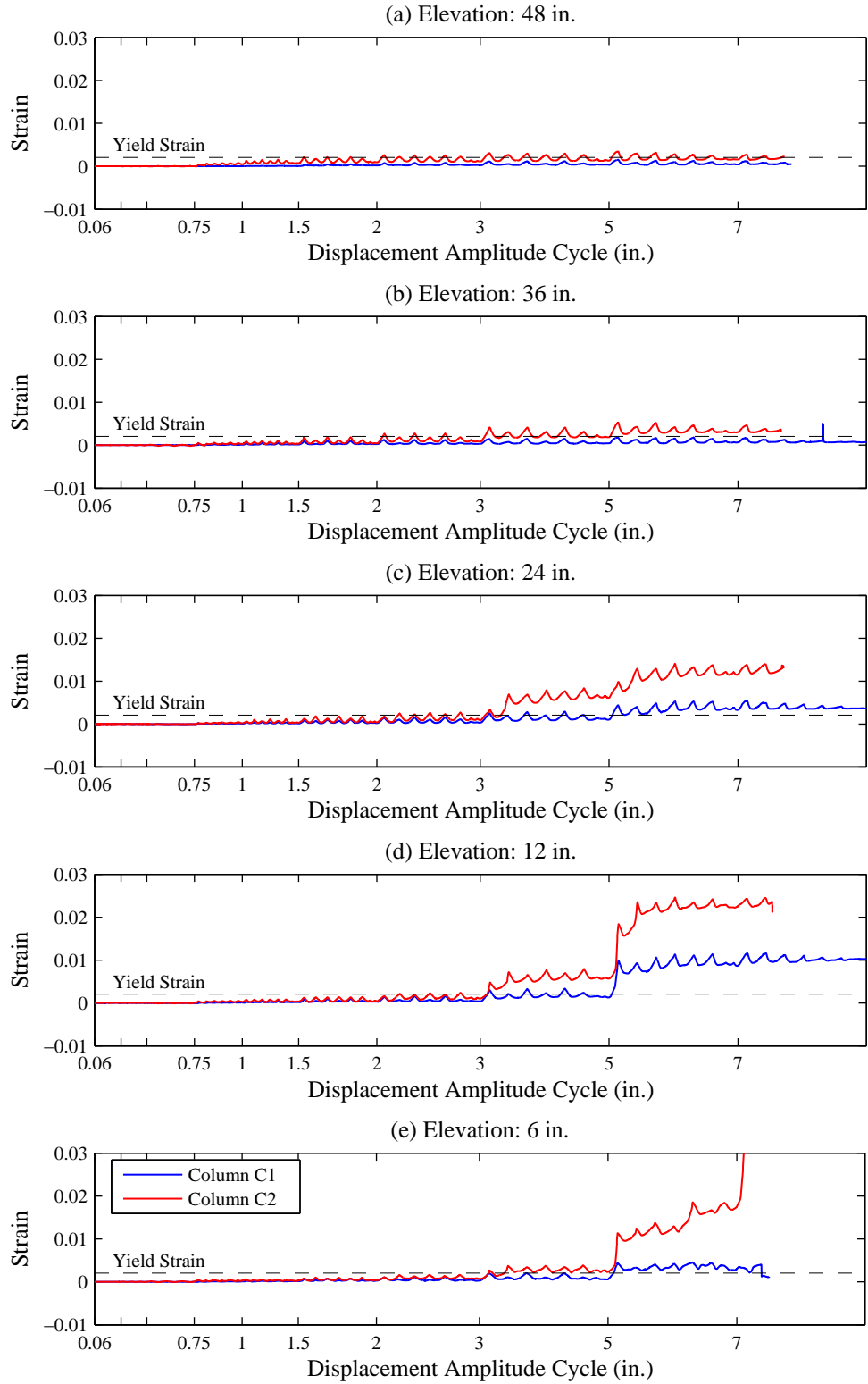


Figure 5.28: Columns C1 and C2 Hoop Strain History – South Gauges

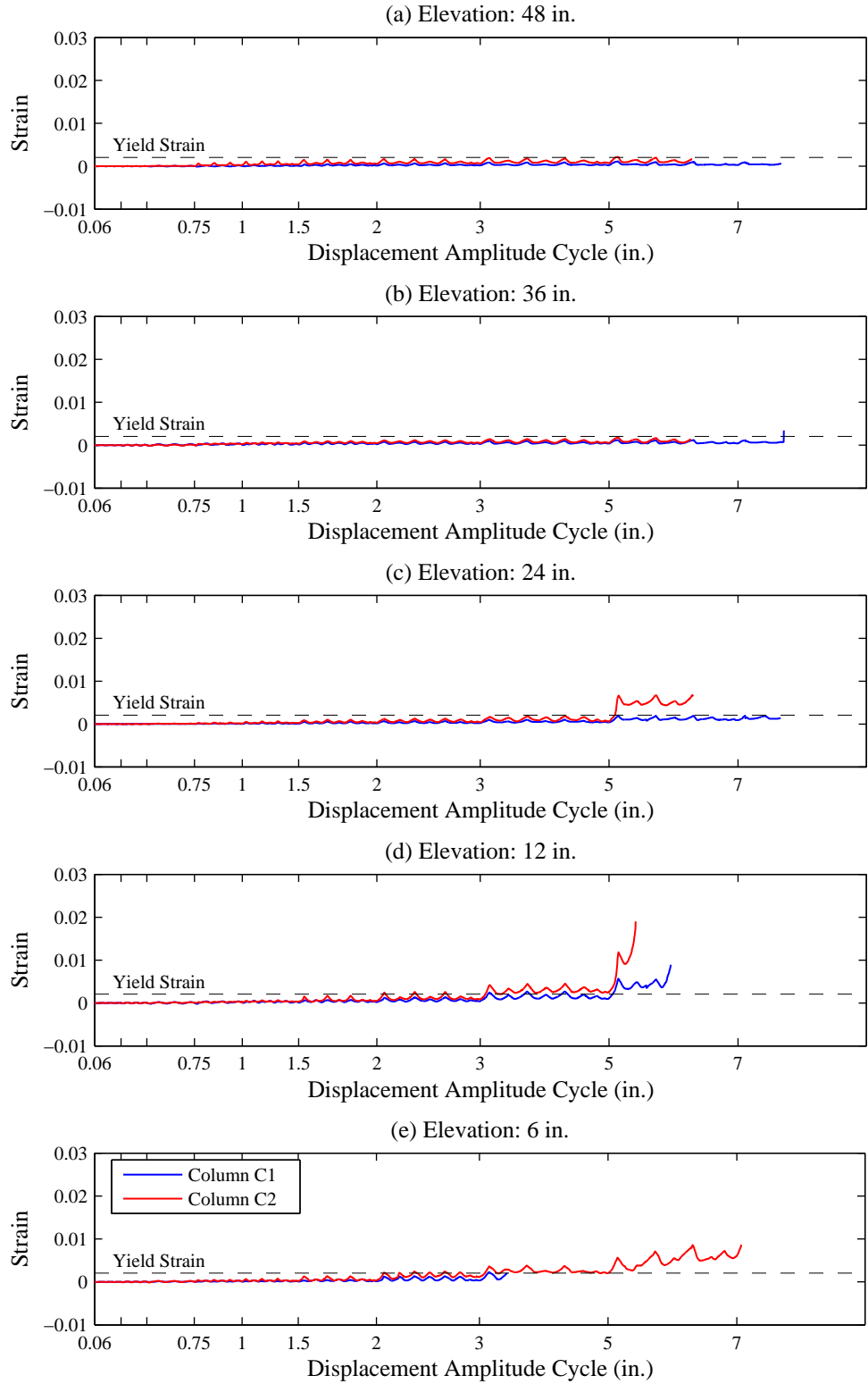


Figure 5.29: Columns C1 and C2 Hoop Strain History – West Gauges

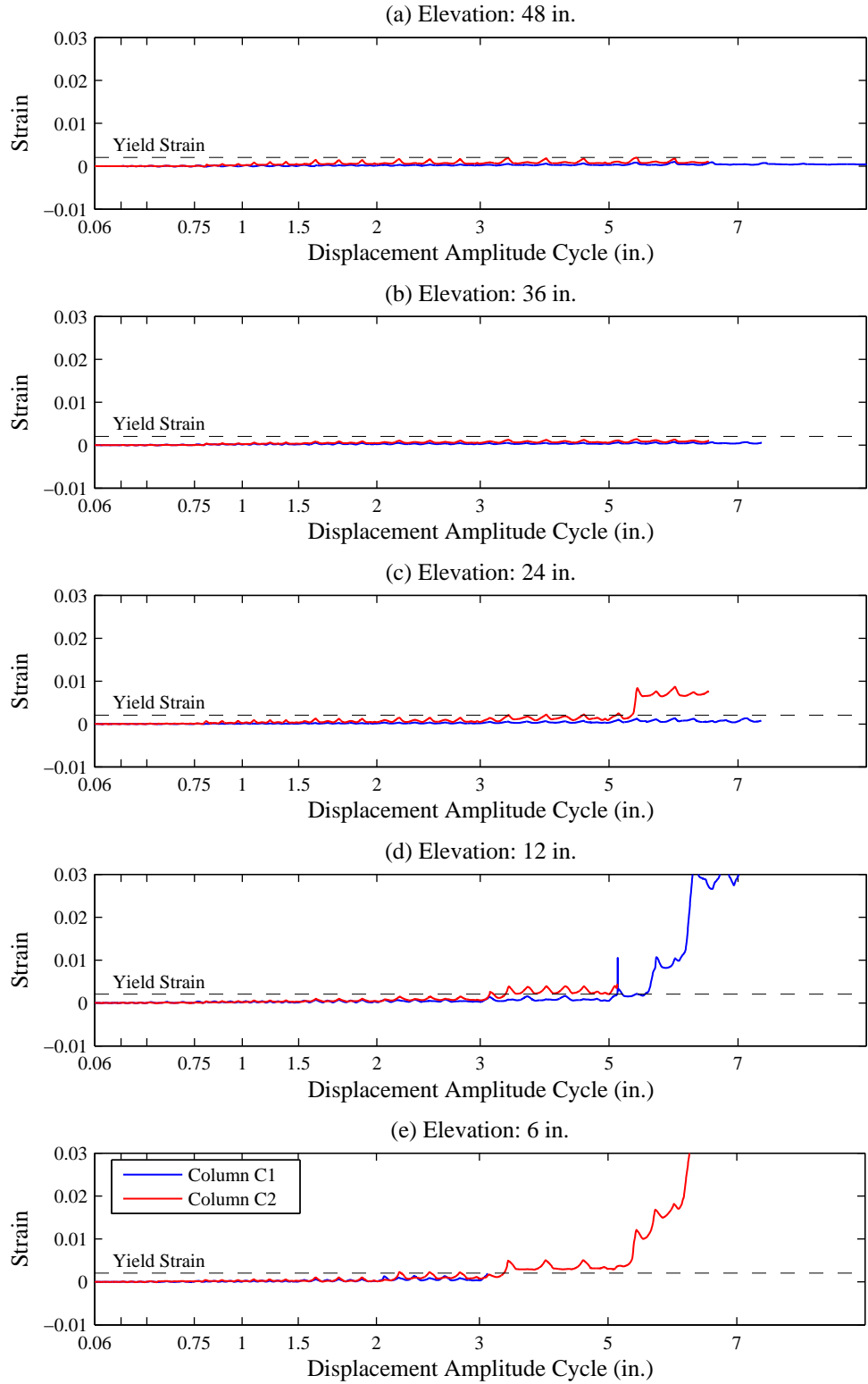


Figure 5.30: Columns C1 and C2 Hoop Strain History – East Gauges

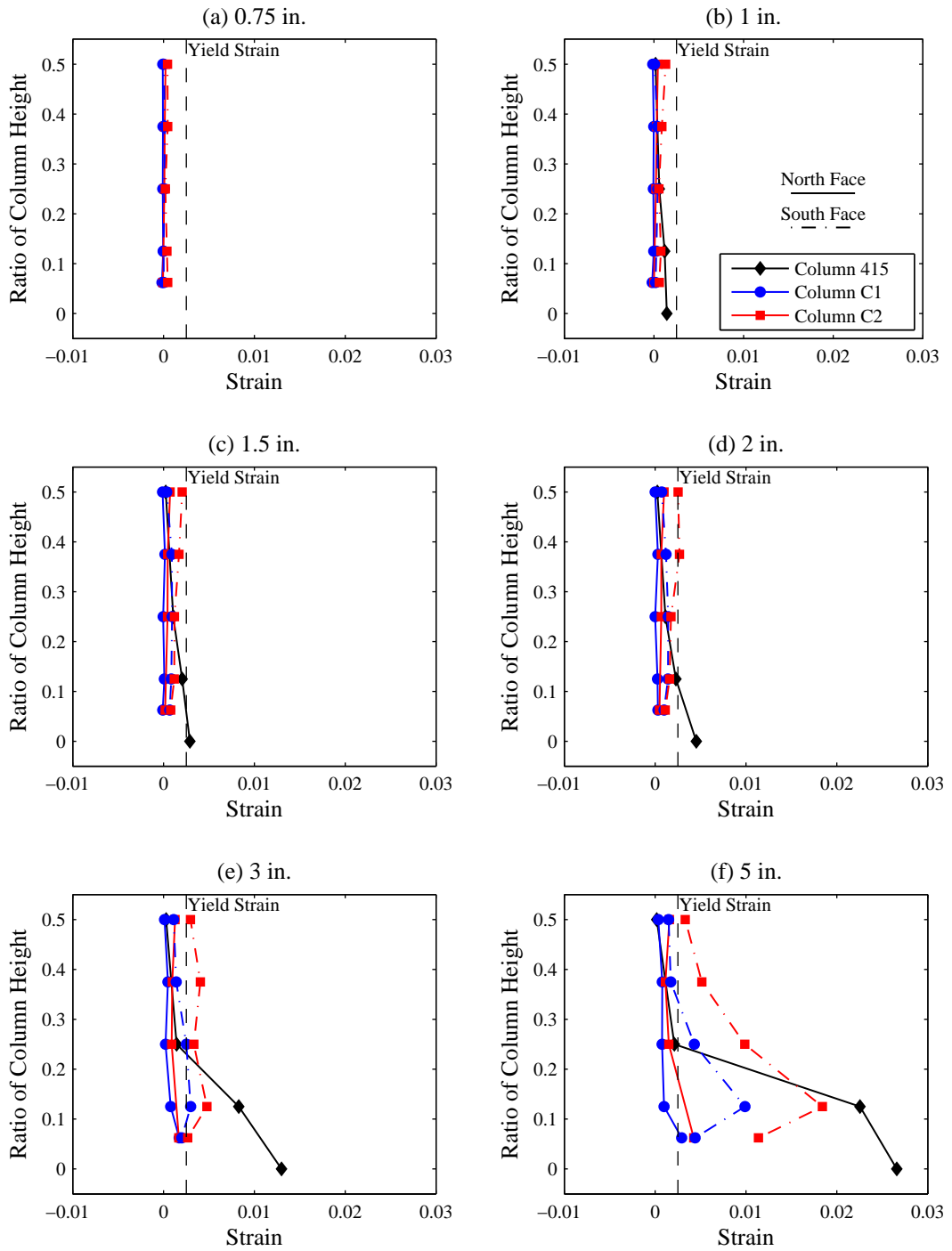


Figure 5.31: Circular Column Hoop Strain Profile – North and South Gauges

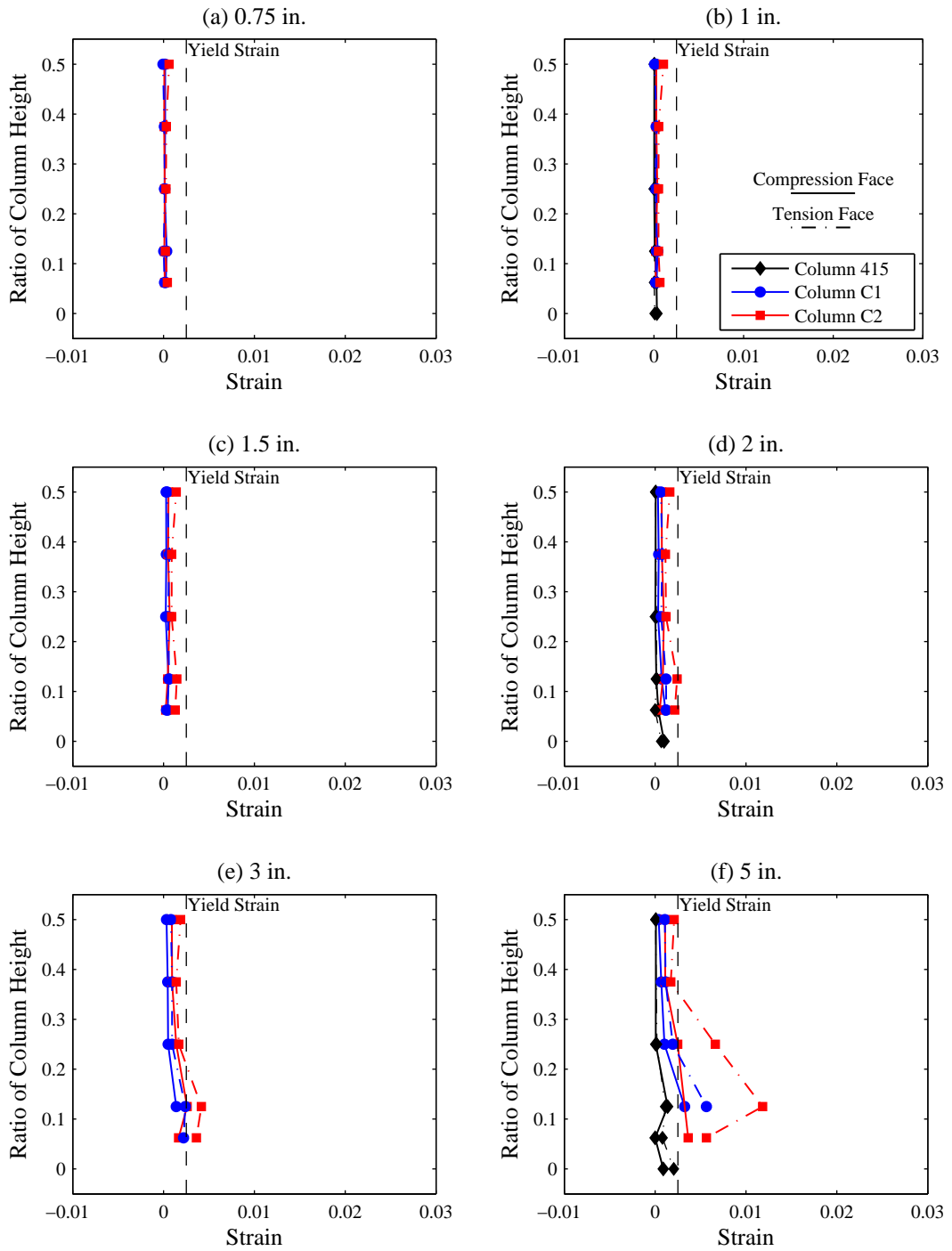


Figure 5.32: Circular Column Hoop Strain Profile – West and East Gauges

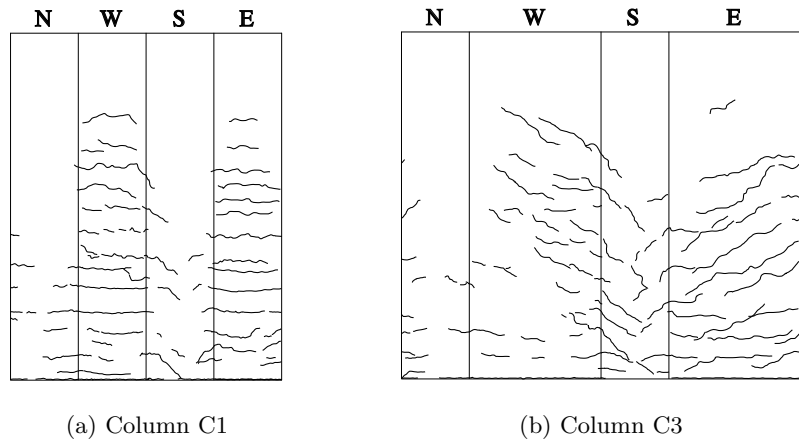


Figure 5.33: Columns C1 and C3 Crack Patterns after 1 in. Displacement Amplitude Cycle

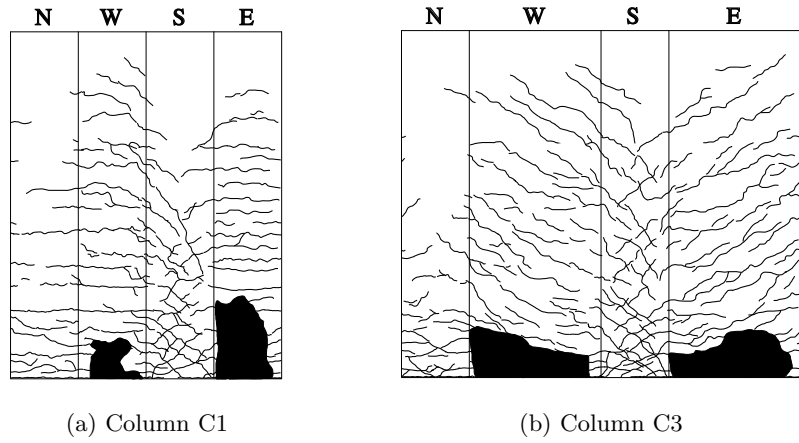
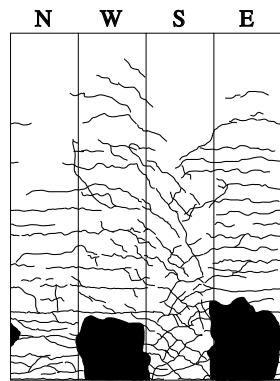
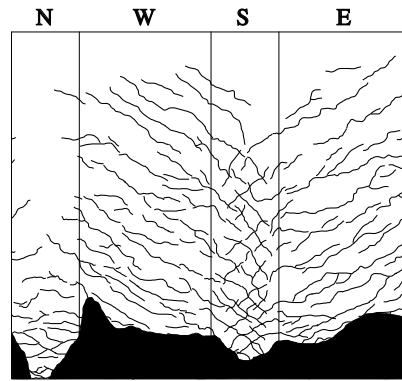


Figure 5.34: Columns C1 and C3 Crack Patterns after 3 in. Displacement Amplitude Cycle

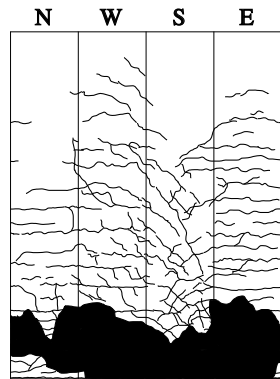


(a) Column C1

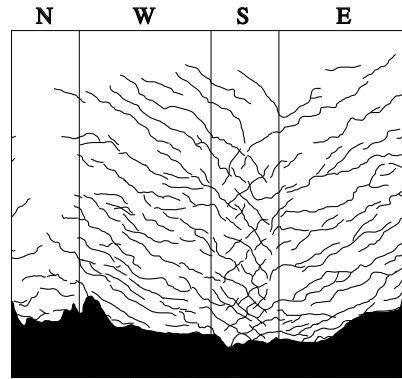


(b) Column C3

Figure 5.35: Columns C1 and C3 Crack Patterns after 5 in. Displacement Amplitude Cycle



(a) Column C1



(b) Column C3

Figure 5.36: Columns C1 and C3 Crack Patterns after 7 in. Displacement Amplitude Cycle

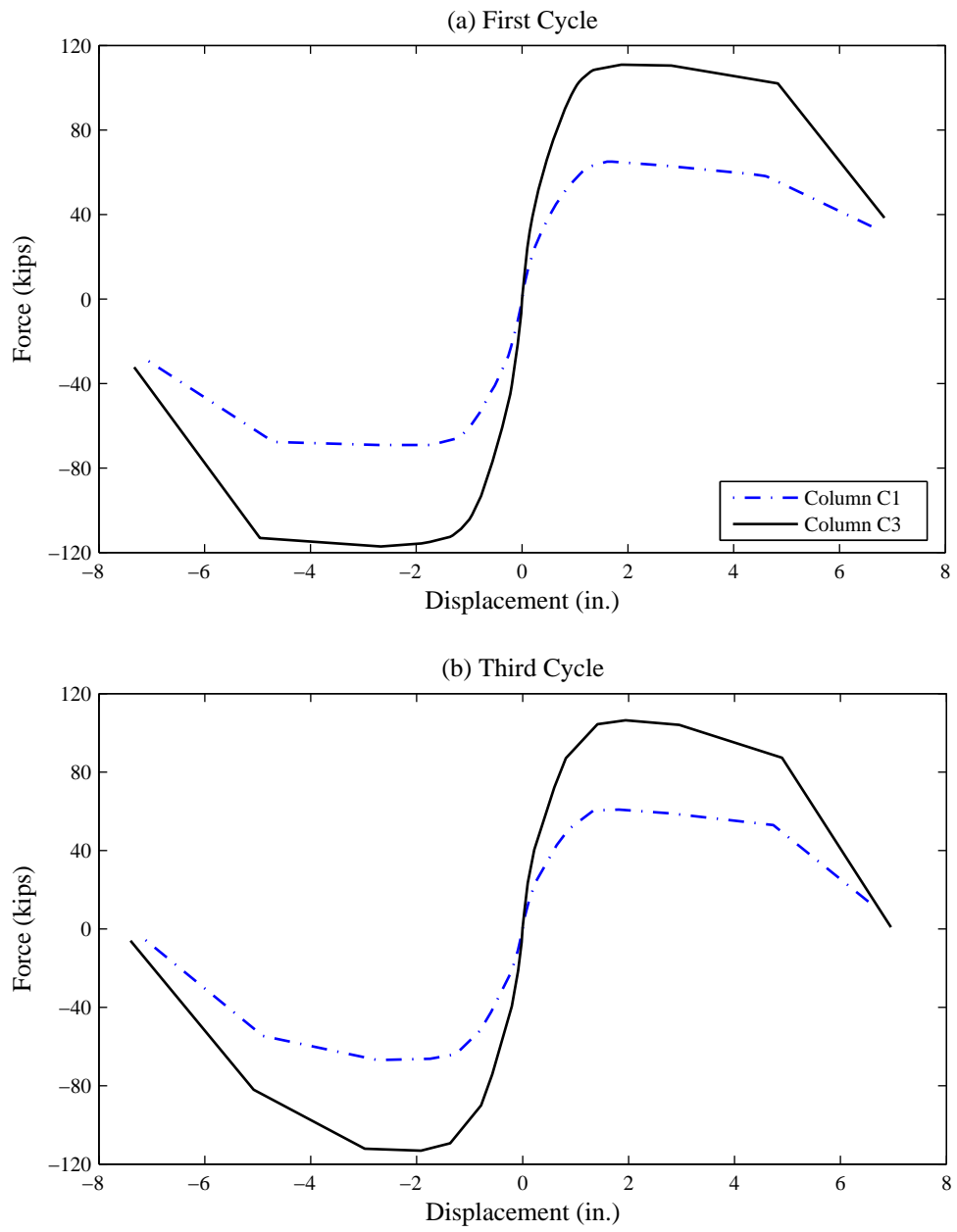


Figure 5.37: Circular vs. Oblong Column Force-Displacement Envelopes

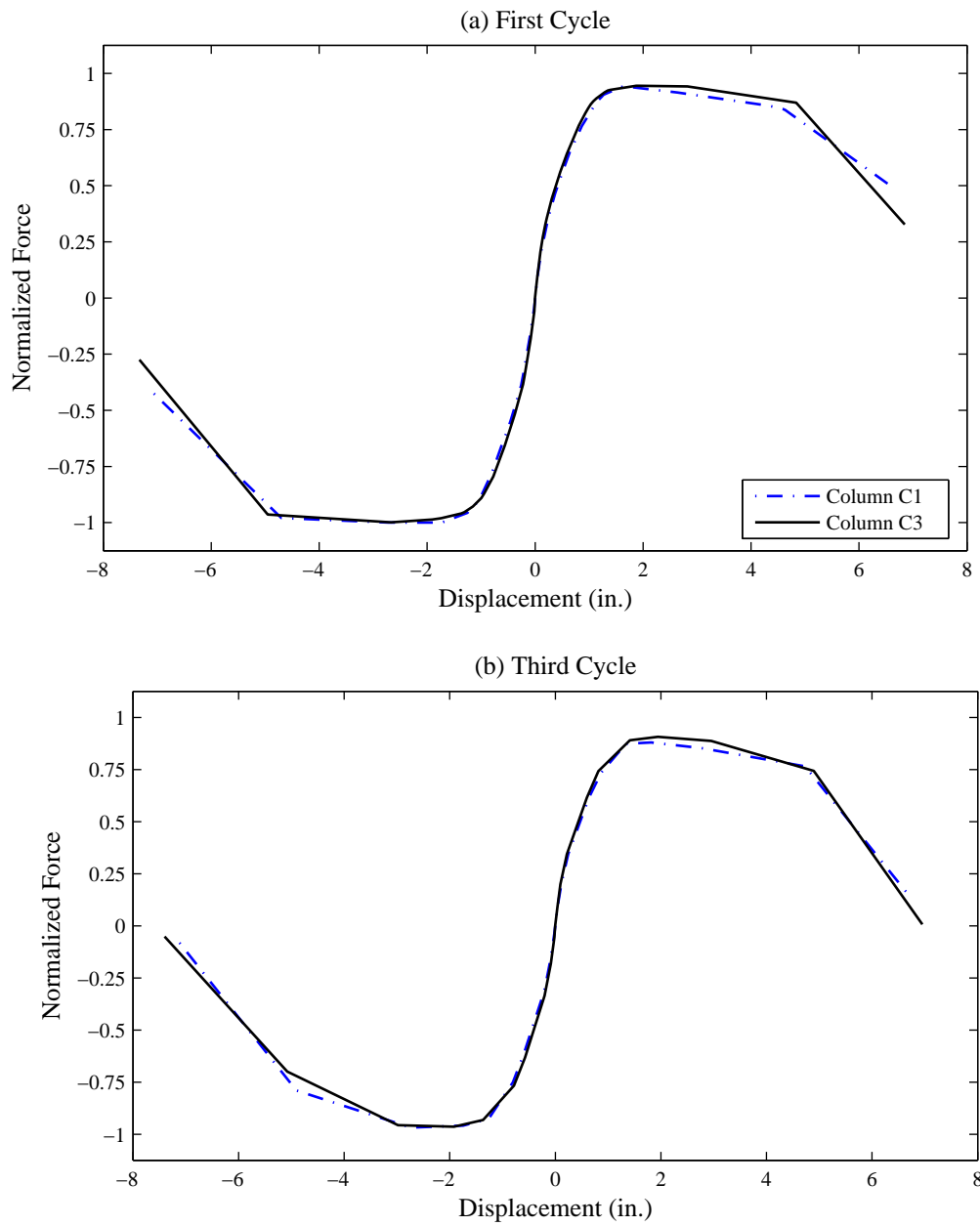


Figure 5.38: Circular vs. Oblong Column Normalized Force-Displacement Envelopes

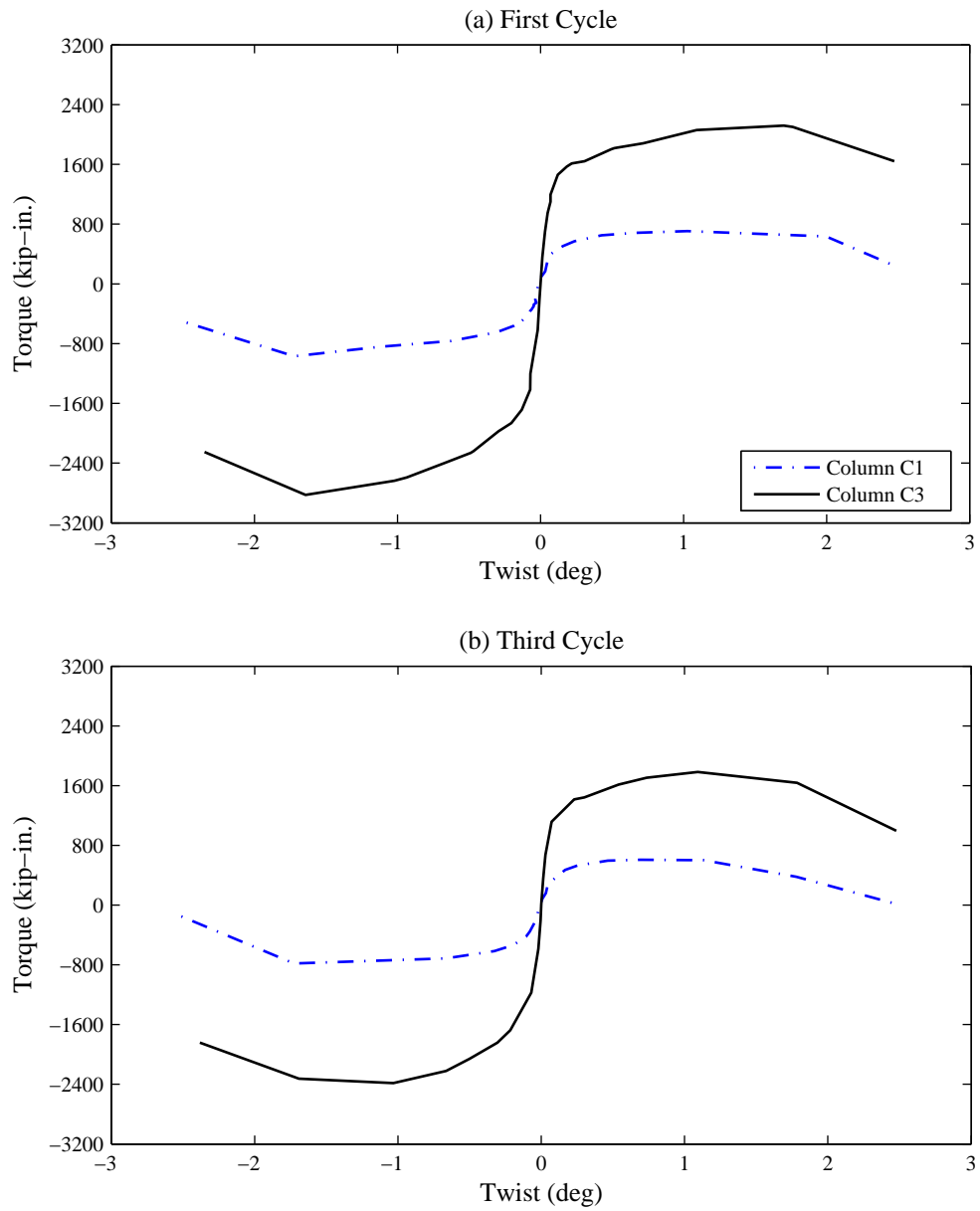


Figure 5.39: Circular vs. Oblong Column Torque-Twist Envelopes

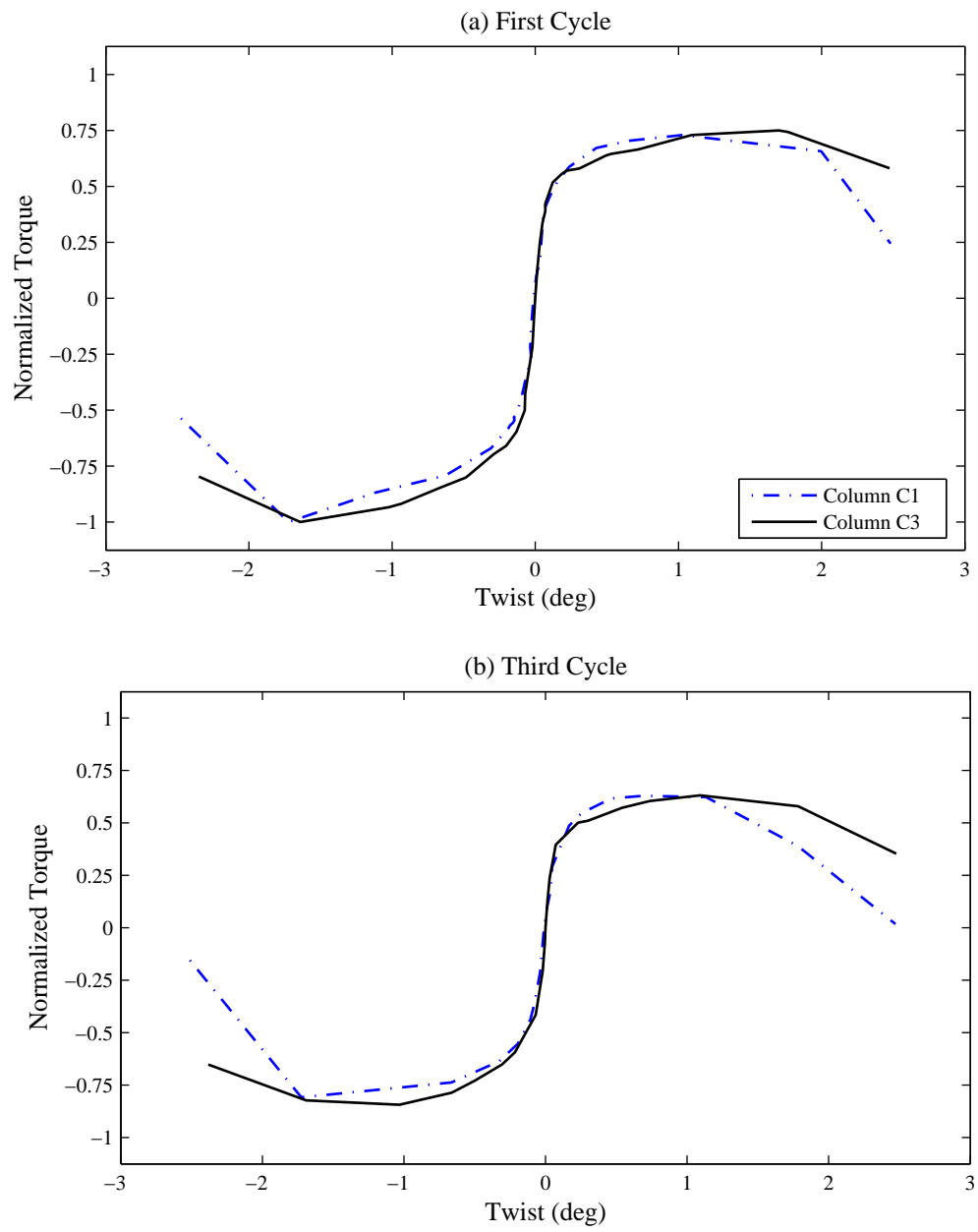


Figure 5.40: Circular vs. Oblong Column Normalized Torque-Twist Envelopes

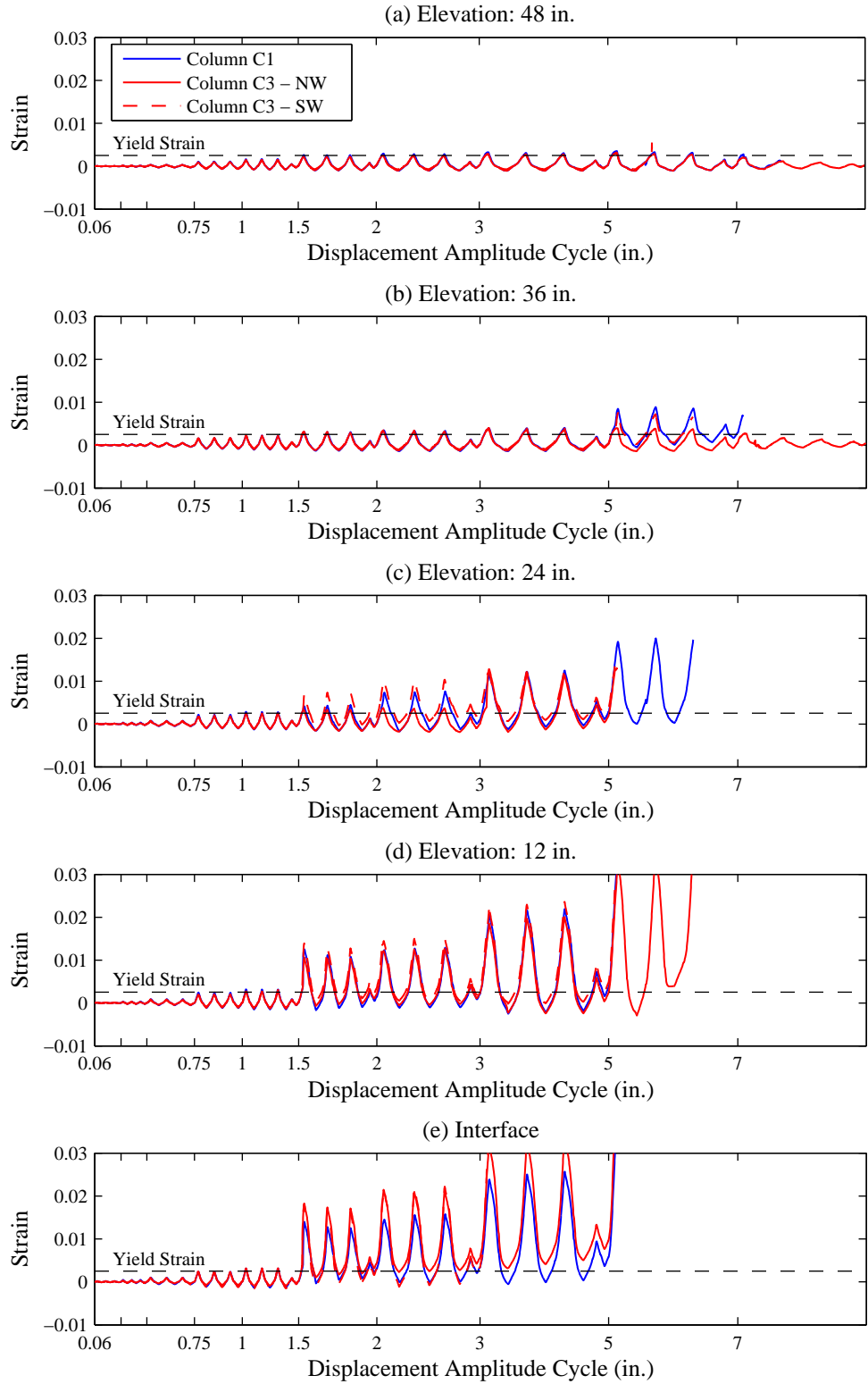


Figure 5.41: Columns C1 and C3 Longitudinal Strain History – West Gauges

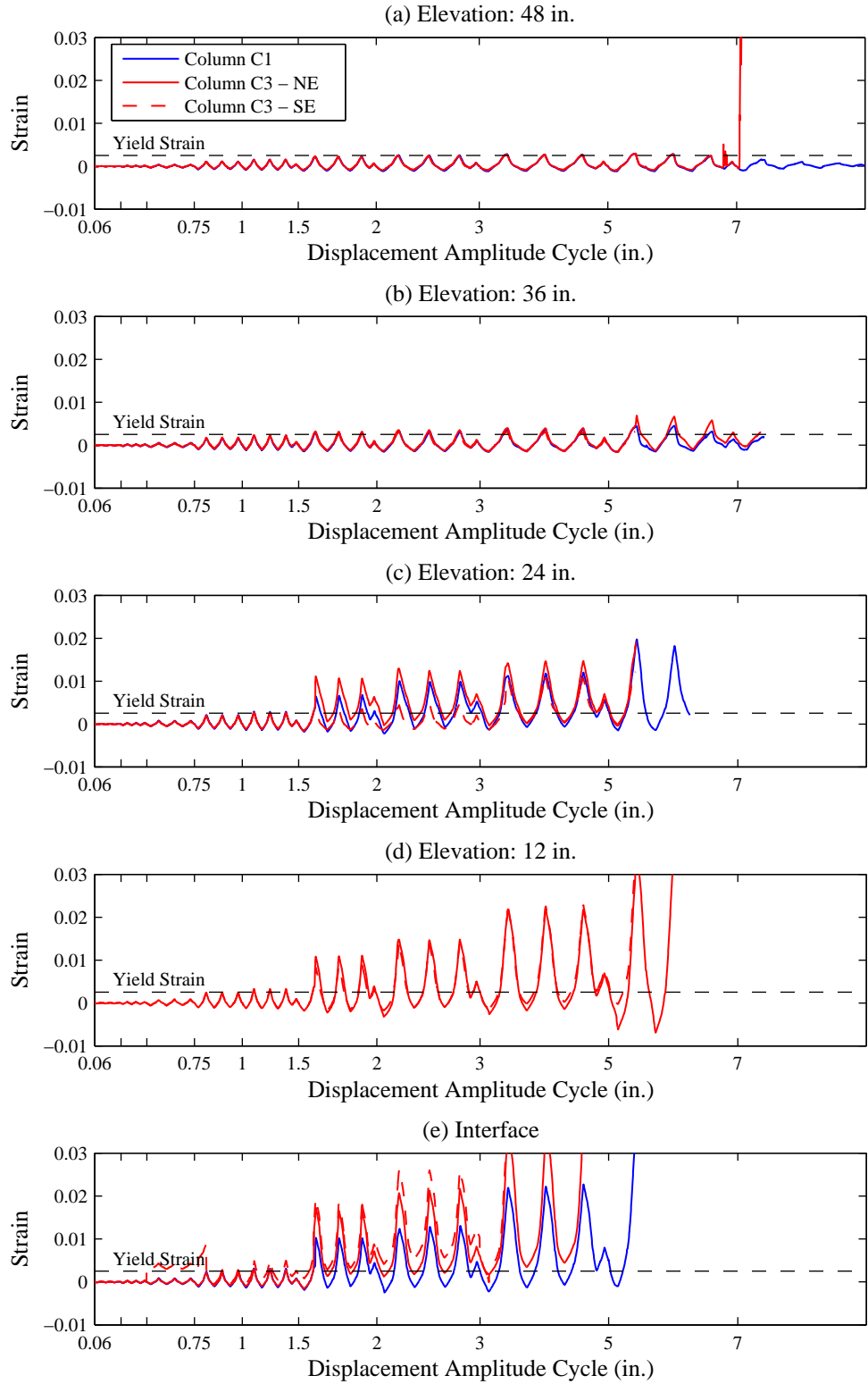


Figure 5.42: Columns C1 and C3 Longitudinal Strain History – East Gauges

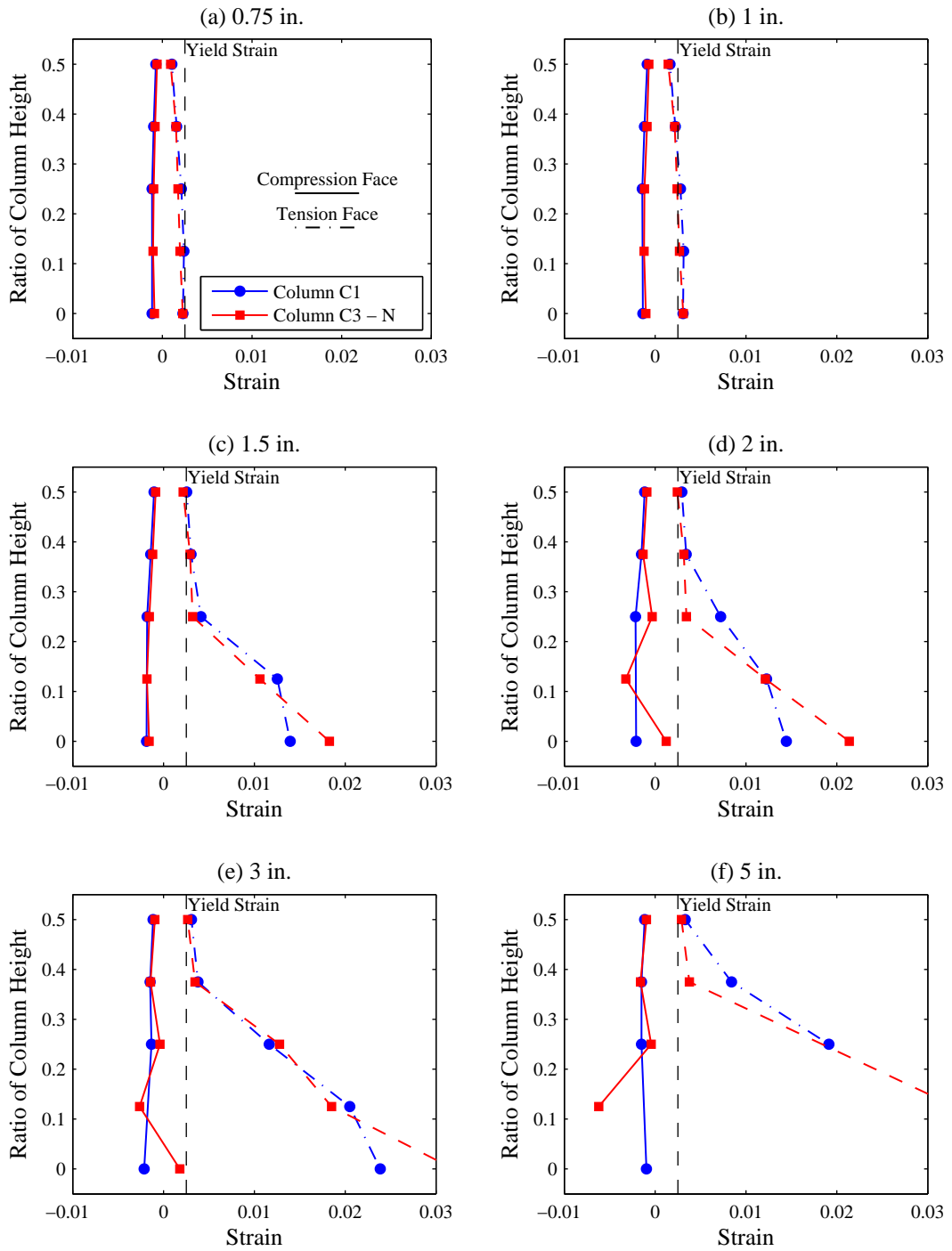


Figure 5.43: Columns C1 and C3 Longitudinal Strain Profile – West and East Gauges

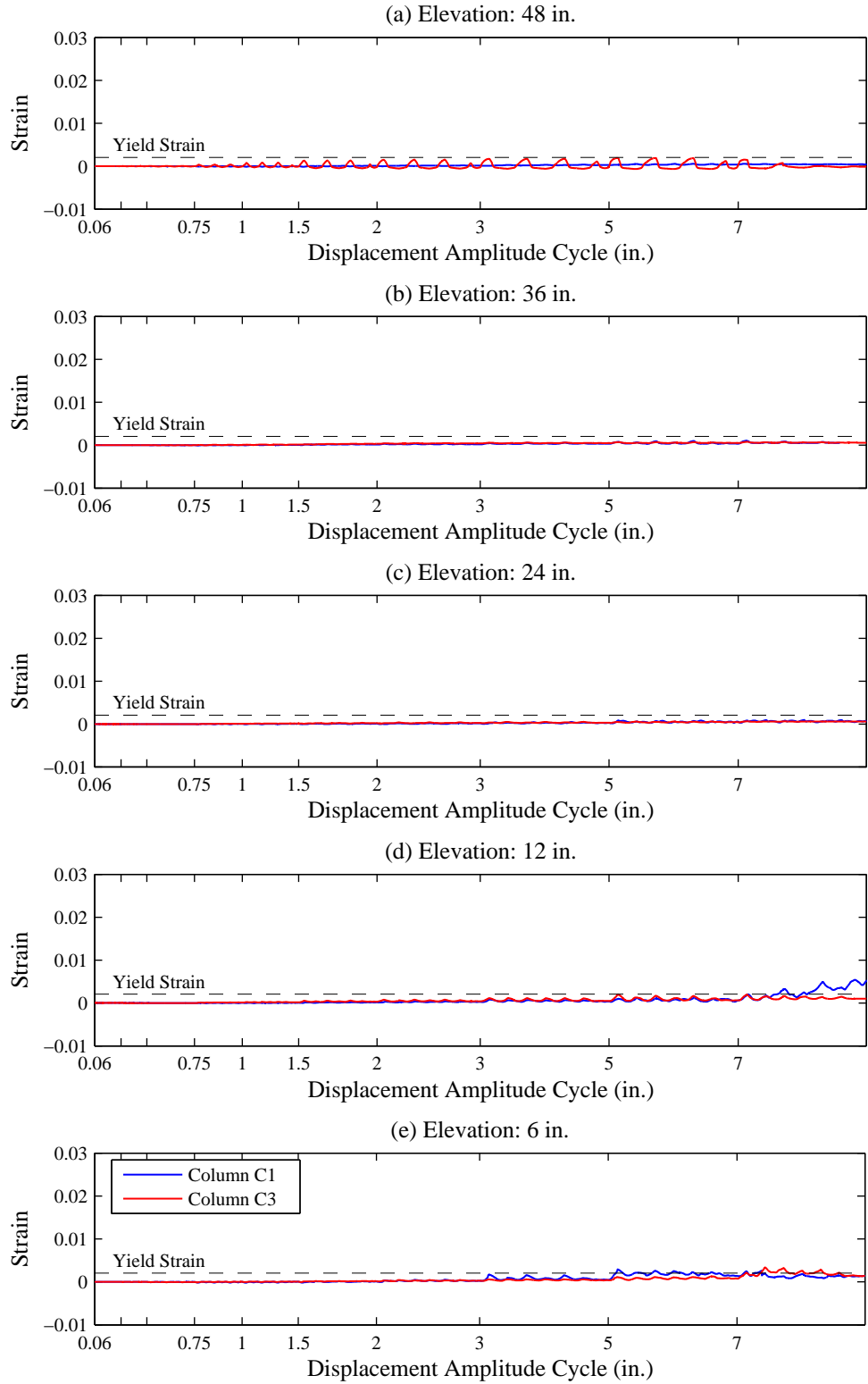


Figure 5.44: Columns C1 and C3 Hoop Strain History – North Gauges

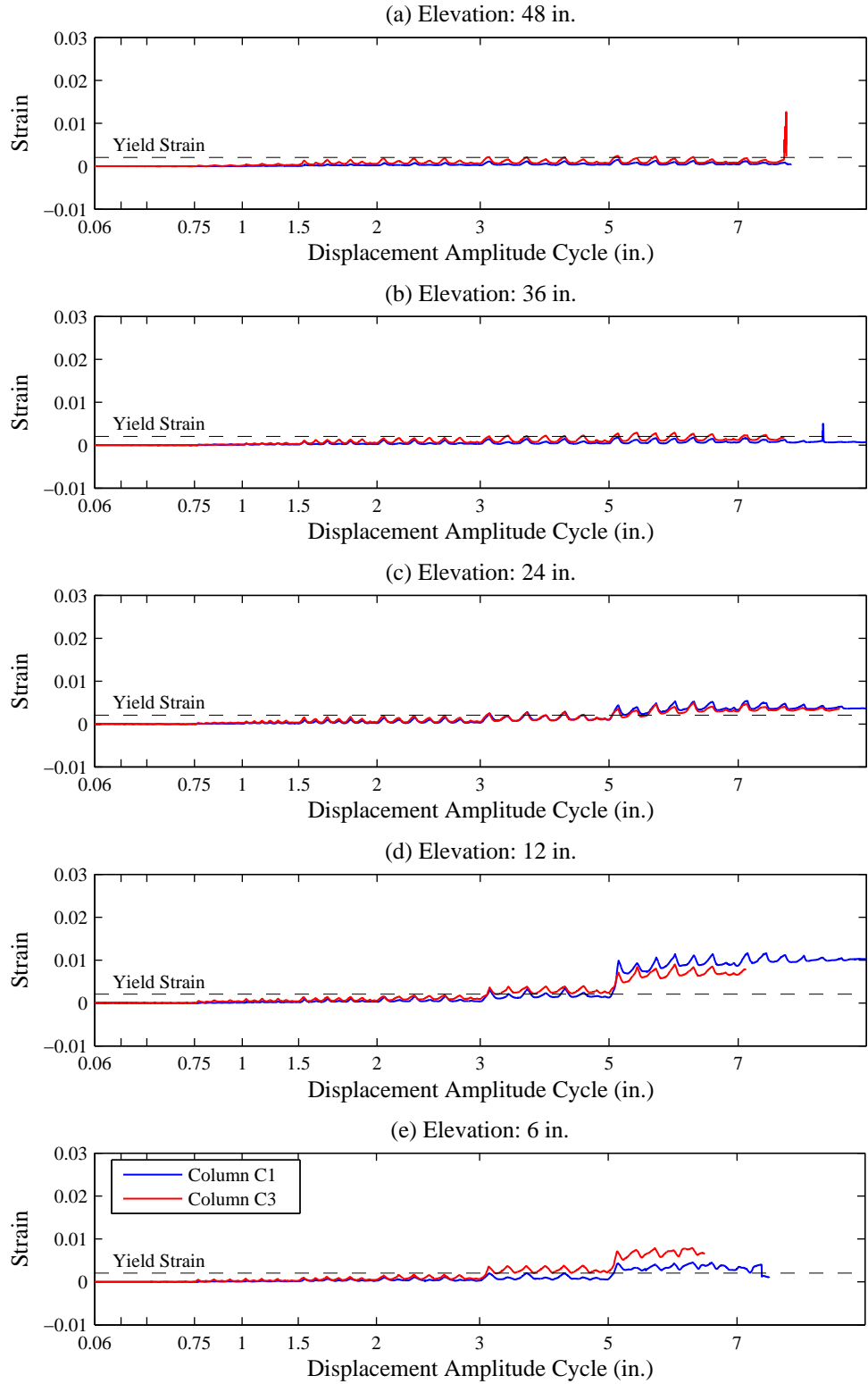


Figure 5.45: Columns C1 and C3 Hoop Strain History – South Gauges

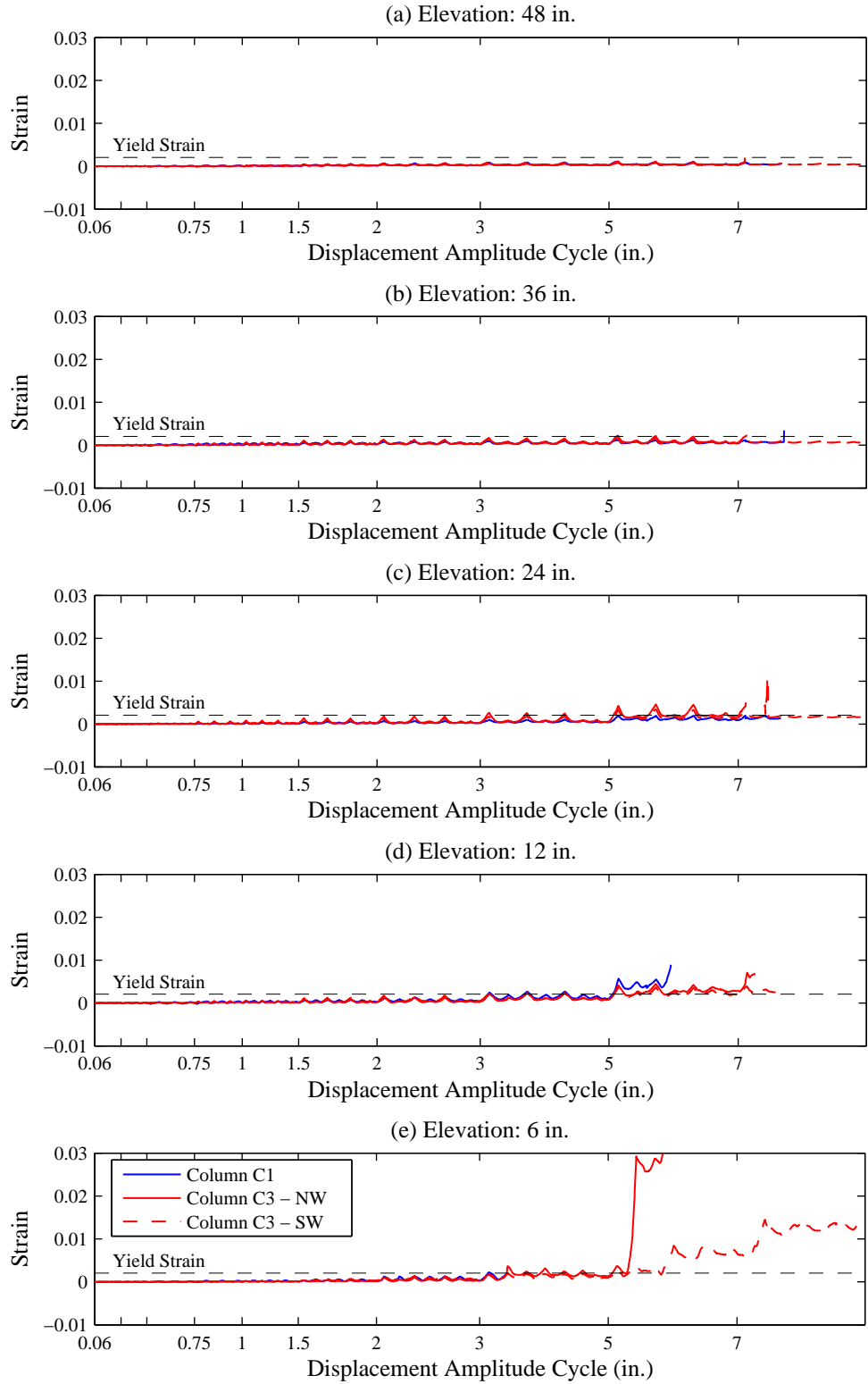


Figure 5.46: Columns C1 and C3 Hoop Strain History – West Gauges

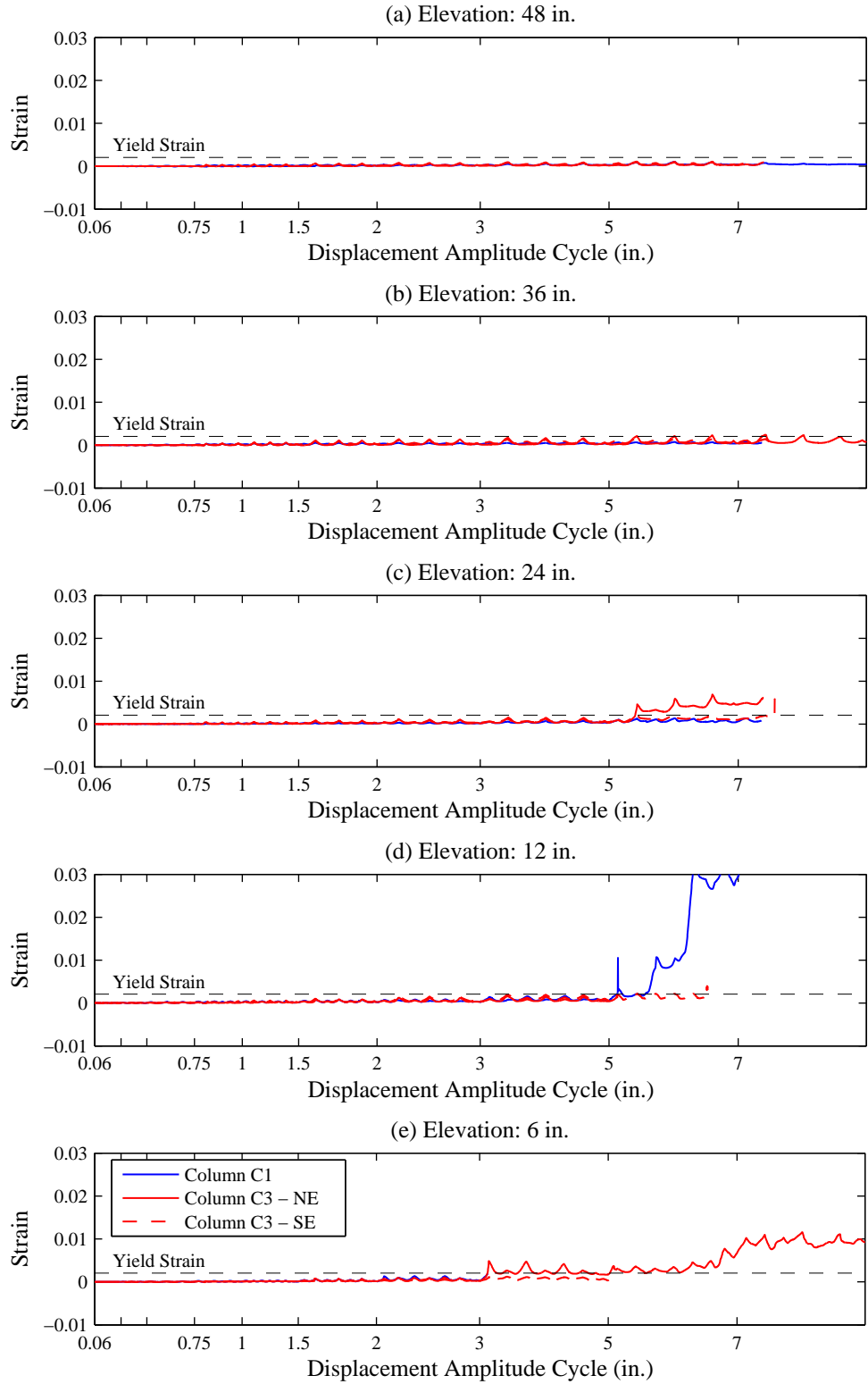


Figure 5.47: Columns C1 and C3 Hoop Strain History – East Gauges

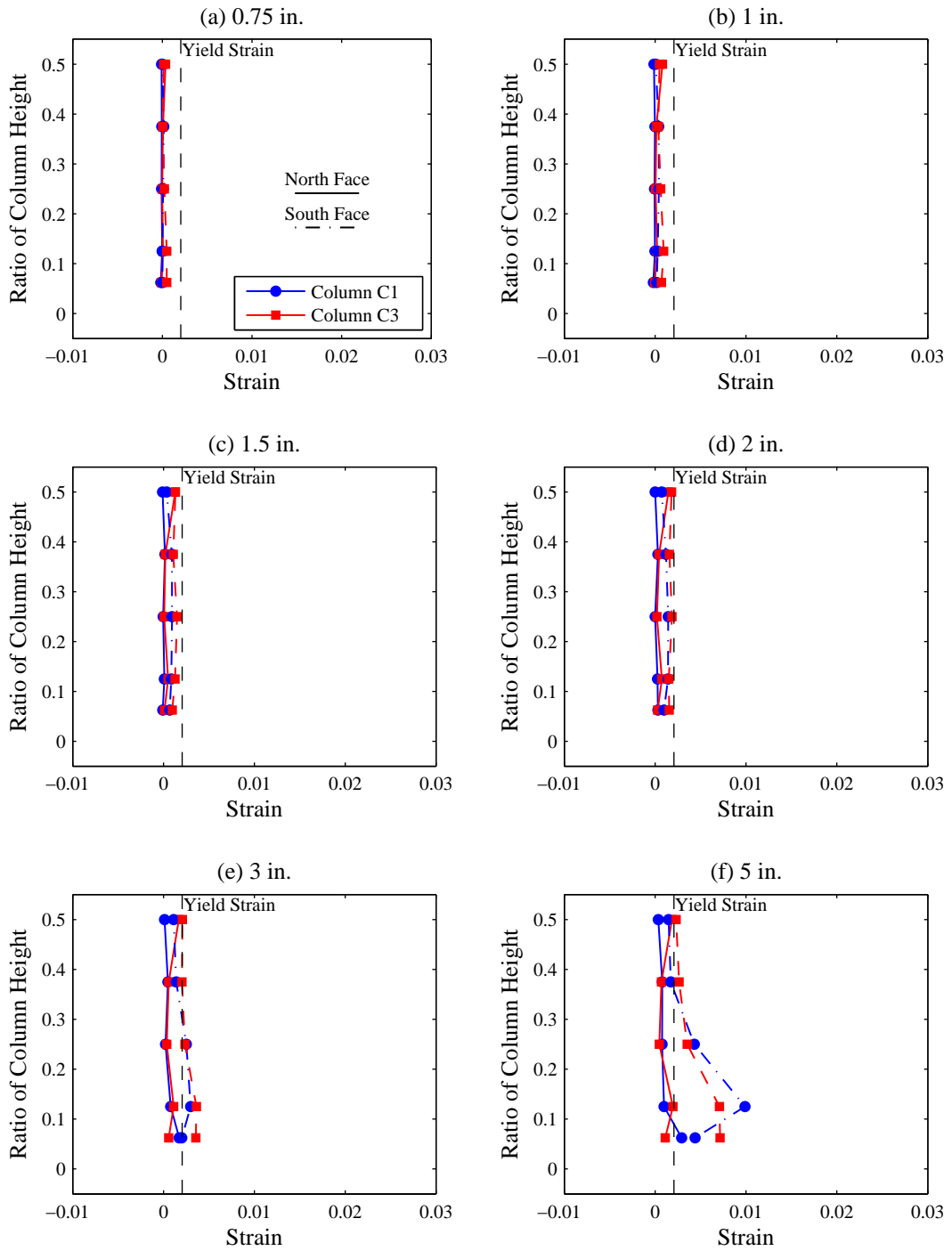


Figure 5.48: Columns C1 and C3 Hoop Strain Profile – North and South Gauges

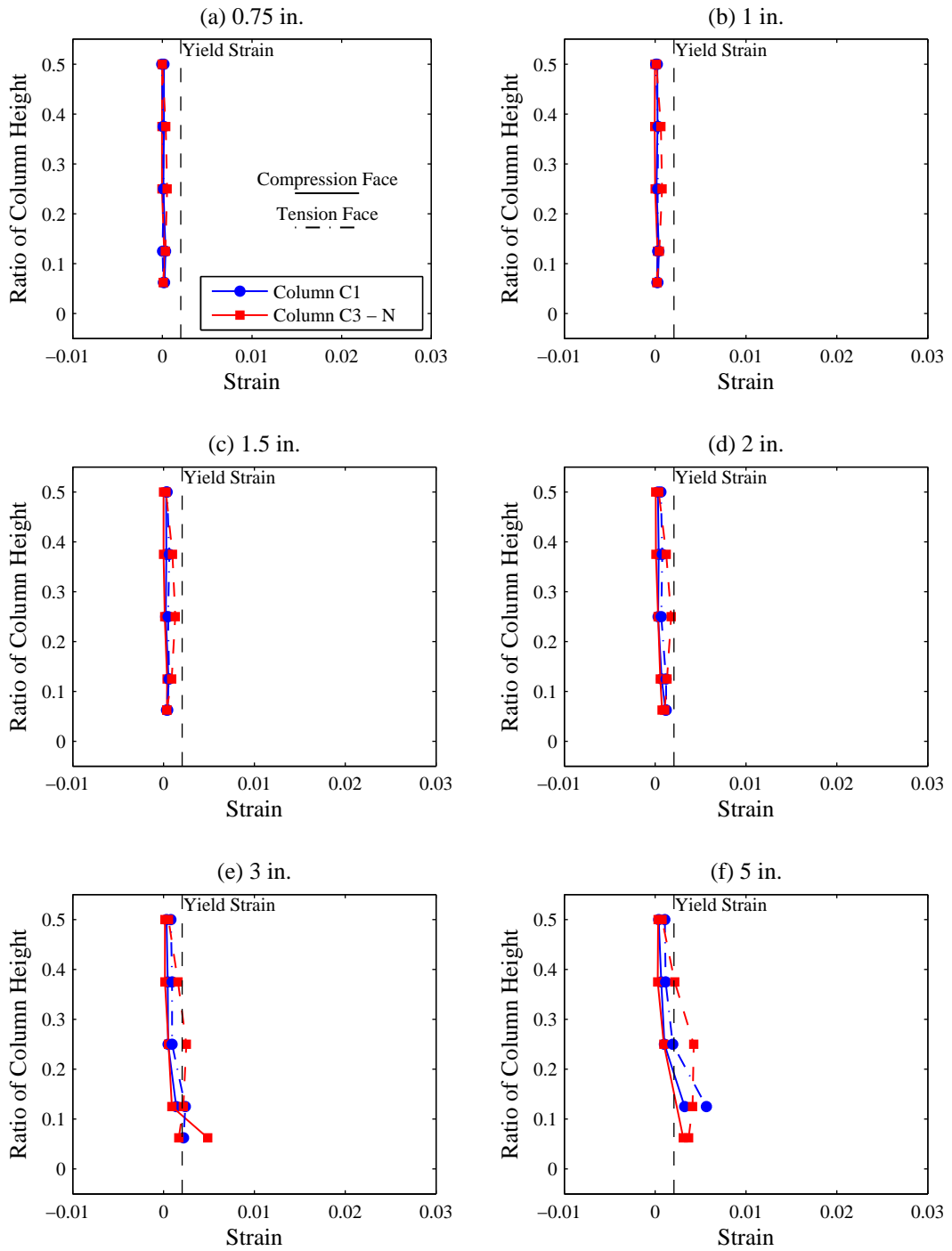


Figure 5.49: Columns C1 and C3 Hoop Strain Profile – West and East Gauges

## Chapter 6

# Evaluation of Analytical Models

This chapter describes the analytical models used for modeling the response of the test specimens. The analytical modeling includes material modeling, plastic hinge length modeling, softened truss modeling for torsion, and three-dimensional truss modeling. A comparison between the analytical and experimental results is also presented.

### 6.1 Material Modeling

Accurate modeling of materials contributes to accurate modeling of test specimen behavior. This section describes the constitutive relationships used for modeling the stress-strain response of concrete and reinforcing steel.

#### 6.1.1 Concrete

The constitutive model for unconfined concrete is based on the Kent-Scott-Park model (Kent and Park, 1971). The model is parabolic with an initial slope equal to  $2f'_c/\epsilon_{co}$ . Upon reaching the concrete strain at the maximum compressive strength, the model de-

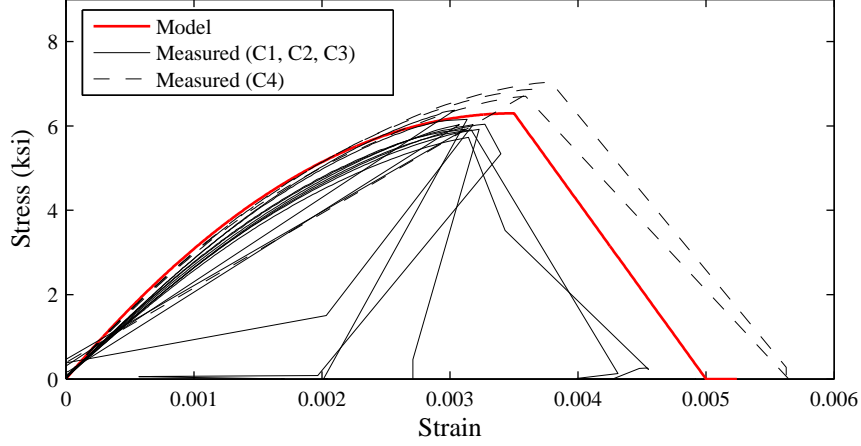


Figure 6.1: Comparison of Measured Response with Analytical Model for Unconfined Concrete

grades linearly to the specified crushing strain corresponding to the crushing strength. Figure 6.1 compares the measured response from uniaxial compression tests with the analytical model for unconfined concrete.

The enhanced strength and strain capacity for confined concrete is computed using the relations by Mander et al. (1988). The confined concrete compressive strength  $f'_{cc}$  is defined by

$$f'_{cc} = f'_{co} \left( -1.254 + 2.254 \sqrt{1 + \frac{7.94 f'_l}{f'_{co}}} - 2 \frac{f'_l}{f'_{co}} \right) \leq 2.23 f'_{co} \quad (6.1)$$

where the effective lateral confining stress  $f'_l$  is determined for hoop confinement as

$$f'_l = \frac{1}{2} \rho_s f_{yh} \left( \frac{1 - \frac{s'}{2d_s}}{1 - \rho_{cc}} \right) \quad (6.2)$$

where  $s'$  = clear spacing between hoops,  $d_s$  = centerline diameter of the hoops,  $\rho_{cc}$  = ratio of area of longitudinal reinforcement to area of core section, and the yield strength of hoop reinforcement  $f_{yh} = 60$  ksi. A simple approach, in lieu of the energy balance approach by Mander et al., is used for defining the ultimate compressive strain for confined concrete  $\epsilon_{cu}$ ,

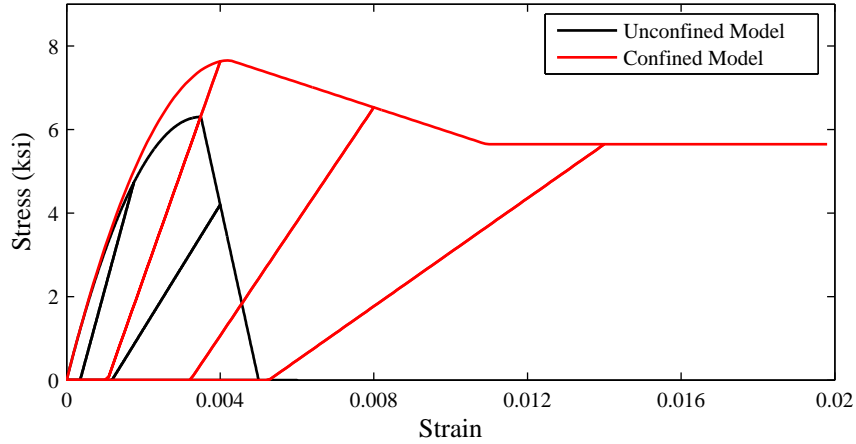


Figure 6.2: Unconfined and Confined Concrete Constitutive Relationships

given by

$$\epsilon_{cu} = 0.004 + 0.1\rho_s \frac{f_{yh}}{f'_{co}} \leq 0.02 \quad (6.3)$$

Figure 6.2 presents the stress-strain response for both the unconfined and confined concrete models.

### 6.1.2 Reinforcing Steel

The constitutive model for the longitudinal reinforcing steel is based on the Chang-Mander model (Chang and Mander, 1994). This model has an initial elastic slope followed by a yield plateau. The strain at the end of the yield plateau corresponds to initial strain hardening, at which point the backbone curve is parabolic. The peak of the parabolic curve is defined by the strain corresponding to the ultimate stress in tension. Figures 6.3 and 6.4 compare the measured response from pull tests with the analytical model for the main longitudinal reinforcement (No. 5 bar) and the interlocking longitudinal reinforcement (No 3 bar), respectively.

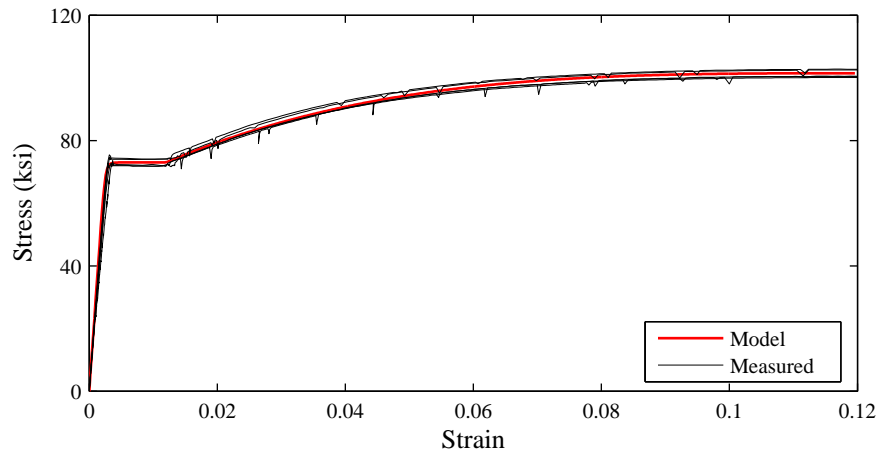


Figure 6.3: Comparison of Measured Response with Analytical Model for Main Longitudinal Reinforcing Steel (No. 5 Bar)

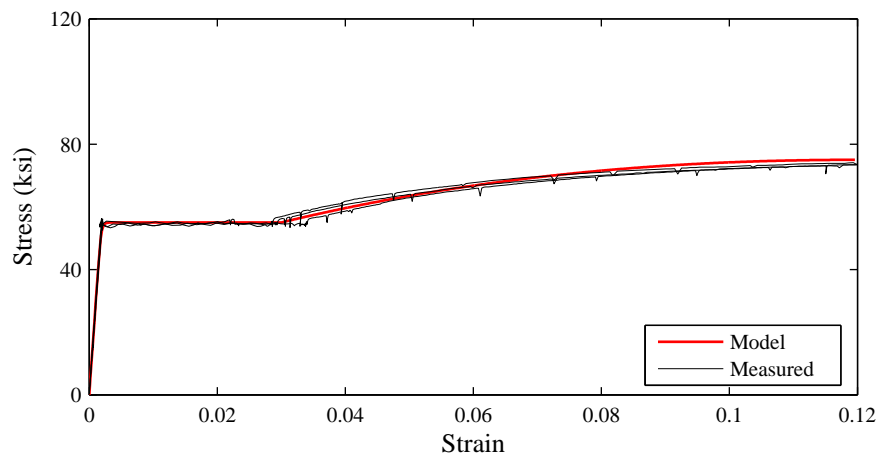


Figure 6.4: Comparison of Measured Response to Analytical Model for Interlocking Longitudinal Reinforcing Steel (No. 3 Bar)

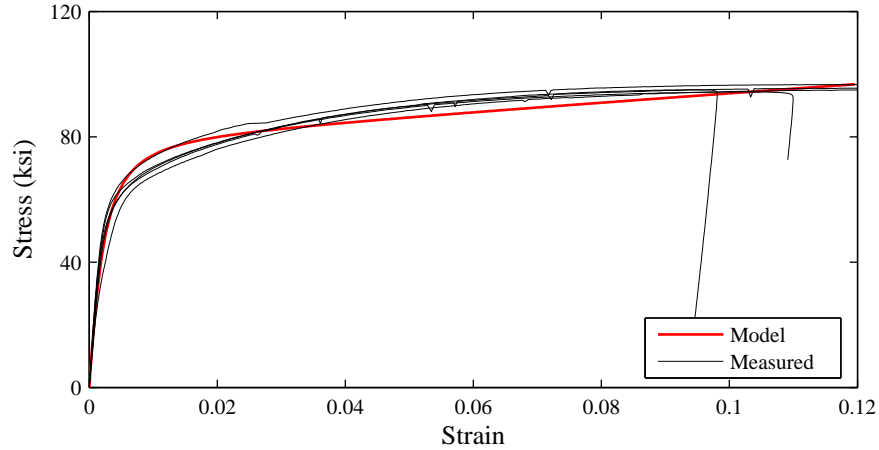


Figure 6.5: Comparison of Measured Response with Analytical Model for Hoop Reinforcing Steel

The constitutive model for the hoop reinforcing steel is based on the Giuffre-Menegotto-Pinto model (Taucer et al., 1991). The backbone of the model is defined by an initial (elastic) slope, a parameter controlling the transition from elastic to plastic branches, and a post-yield (plastic) slope. Figure 6.5 compares the measured response from pull tests with the analytical model for the hoop reinforcement (No. 3 bar).

## 6.2 Bar Slip Modeling

Direct measurement of the bar slip and the longitudinal reinforcement strain at the column-footing interface provided data for the development of a bar stress versus slip model. For the measured longitudinal strain history, the stress history can be estimated using a reinforcing steel constitutive model. Since the longitudinal reinforcing bars are subjected to reversed cyclic loading, this reinforcing steel constitutive model requires rules for loading and unloading to track the cyclic stress-strain response. The reinforcing steel

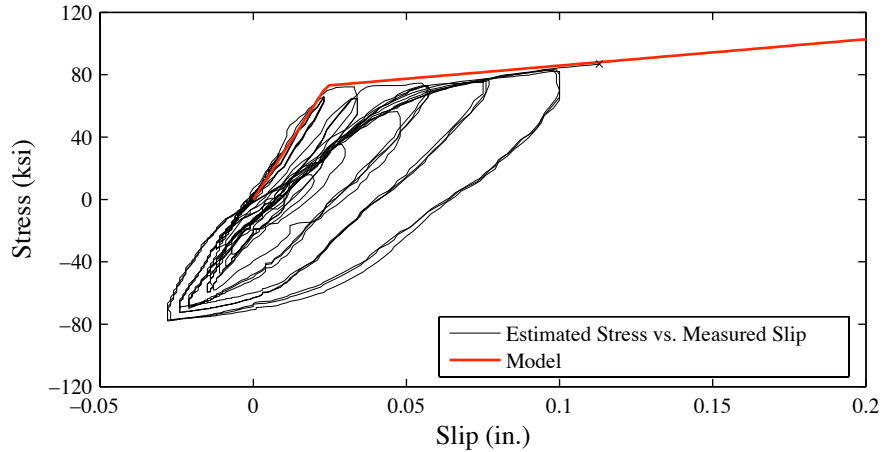


Figure 6.6: Comparison of Estimated Response with Analytical Model for Bar Slip

constitutive model selected is identical to the Chang-Mander model (Chang and Mander, 1994) for the main longitudinal reinforcing bars (Figure 6.3) with the additional rules for modeling the cyclic behavior.

Lehman and Moehle (2000), Berry (2006), and Zhao and Sritharan (2007) (Figure 2.6) proposed models for modeling the bar stress versus slip relationship. For simplicity, the bilinear model is adopted. The bilinear model is calibrated such that the longitudinal bar slip at yield is equal to the measured bar slip at yield. The post-yield stiffness is set equal to 5% of the elastic stiffness. Figure 6.6 compares the proposed bar stress versus slip model with the estimated stress versus measured slip response of the West longitudinal bar of Column C1. Note, the proposed envelope curve for the bar stress versus slip relationship is limited to modeling the monotonic behavior of a longitudinal bar under tension only.

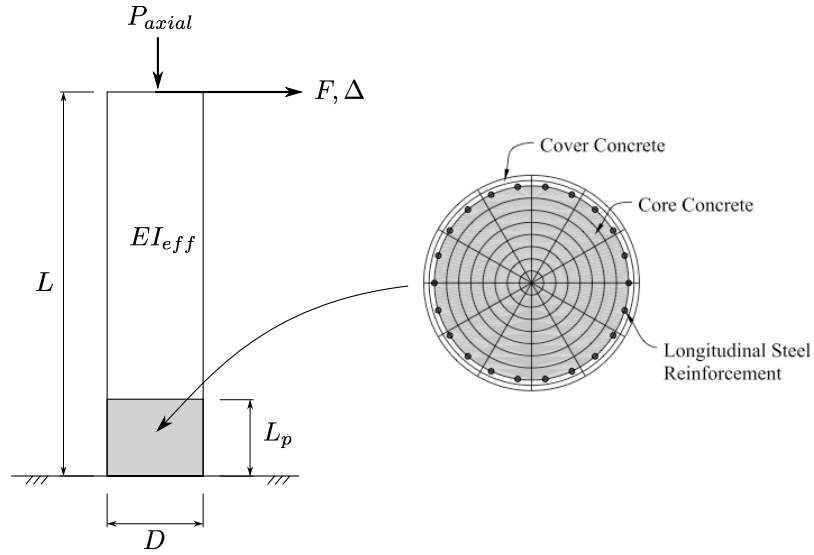


Figure 6.7: Illustration of Lumped-Plasticity Force-Based Element

### 6.3 Plastic Hinge Length Modeling

Because of expected flexural yielding at the base of reinforced concrete columns, a lumped-plasticity force-based element (Scott and Fenves, 2006) can be used to model the force-displacement response. As shown in Figure 6.7, the element is divided into a linear-elastic region and a plastic hinge region of a specified length ( $L_p$ ). The nonlinear behavior of the element is confined to the plastic hinge region, represented by a fiber section. The analytical plastic hinge length is determined according to Caltrans (2004b), given in Eq. 2.7. For the circular and oblong columns, this results in a plastic hinge length  $L_p = 14.5$  in. ( $0.15L$ ). The lumped-plasticity model is available in *OpenSees* (McKenna et al., 2000) under the `beamWithHinges` element. Together with the  $P$ - $\Delta$  geometric transformation (Filippou and Fenves, 2004), nonlinear geometry effects can be accounted for.

## 6.4 Softened Truss Modeling

The torque-twist response after cracking of a reinforced concrete section can be modeled using the softened truss model for torsion, illustrated in Figure 6.8 (from Leu and Lee, 2000). Figure 6.8(a) shows diagonal cracks around a beam under torsion, idealized as a space truss; (b) shows in-plane stresses of Element A, where the  $L$ -axis is along the longitudinal direction and the  $t$ -axis is along the transverse direction; and (c) shows the deformations and actions on the diagonal concrete struts. This model requires a solution of 18 equations, which contain 21 unknown variables. Assuming 3 unknowns, a trial-and-error method can be used to solve these 18 equations. The calculated torque-twist relationship depends on many variables, in particular: section shape and dimensions, longitudinal reinforcing ratio, unconfined concrete compressive strength and compressive strain at the maximum compressive stress, yield strength of hoops, and axial load.

Details of the equilibrium conditions, compatibility conditions, and constitutive relationships for concrete can be found in Hsu (1993). Presented here is an overview of the equations necessary to model the torque-twist curve for members subjected to pure torsion.

### 6.4.1 Governing Equations

#### Equilibrium Conditions

The two necessary equilibrium equations give the following expressions for the shear stress in the  $L$ - $t$  coordinate system  $\tau_{Lt}$  (Eq. 6.4) and torque  $T$  (Eq. 6.5)

$$\tau_{Lt} = (-\sigma_d + \sigma_r) \sin \alpha \cos \alpha \quad (6.4)$$

$$T = \tau_{Lt} (2A_o t_d) \quad (6.5)$$

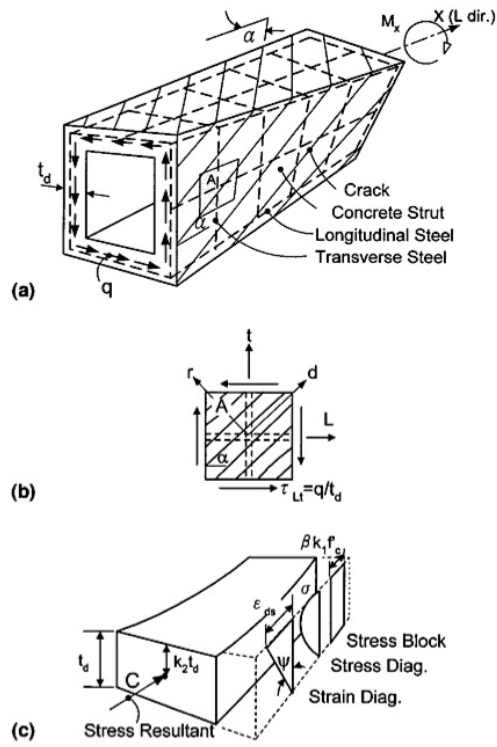


Figure 6.8: Illustration of Softened Truss Model for Torsion: (a) Space Truss; (b) In-Plane Behavior; (c) Out-of-Plane Behavior (from Leu and Lee, 2000)

where  $\sigma_d$  = stress in the concrete struts,  $\sigma_r$  = stress in the  $r$  direction,  $\alpha$  = angle of inclination of the concrete struts,  $A_o$  = area bounded by the centerline of the shear flow, and  $t_d$  = thickness of the shear flow zone.

### Compatibility Conditions

The three necessary compatibility equations give the following expressions for the shear strain in the  $L-t$  coordinate system  $\gamma_{Lt}$  (Eq. 6.6 ), angle of twist  $\theta$  (Eq. 6.7), and curvature of the concrete struts  $\psi$  (Eq. 6.8)

$$\frac{\gamma_{Lt}}{2} = (-\epsilon_d + \epsilon_r) \sin \alpha \cos \alpha \quad (6.6)$$

$$\theta = \frac{p_o}{2A_o} \gamma_{Lt} \quad (6.7)$$

$$\psi = \theta \sin 2\alpha \quad (6.8)$$

where  $\epsilon_d$  = average concrete strain,  $\epsilon_r$  = strain in the  $r$  direction,  $p_o$  = perimeter of the centerline of the shear flow zone. The average concrete strain can be simply related to the maximum strain by

$$\epsilon_d = \epsilon_{ds}/2 \quad (6.9)$$

where  $\epsilon_{ds}$  = concrete strain at the surface of the diagonal concrete strut.

## 6.4.2 Constitutive Laws of Materials

### Concrete Struts

The average stress capacity of the diagonal strut  $\sigma_d$ , compression stress block coefficient  $k_1$ , and softening coefficient  $\zeta$  are defined by Eqs. 6.10, 6.11, and 6.12, respectively.

The tensile stress of concrete is assumed to be zero (Eq. 6.12).

$$\sigma_d = k_1 \zeta f'_c \quad (6.10)$$

$$k_1 = f_k(\epsilon_{ds}, \zeta) \quad (6.11)$$

$$\zeta = f_2(\epsilon_d, \epsilon_r) \quad (6.12)$$

$$\sigma_r = 0 \quad (6.13)$$

### Mild Steel

The longitudinal steel stress  $f_L$  (Eq. 6.14) and transverse steel stress  $f_t$  (Eq. 6.15) are functions of strain,  $\epsilon_L$  and  $\epsilon_t$ , respectively

$$f_L = f_4(\epsilon_L) \quad (6.14)$$

$$f_t = f_5(\epsilon_t) \quad (6.15)$$

### 6.4.3 Additional Equations

#### Thickness $t_d$ as a Function of Strains

The following expression gives the thickness of the shear flow zone  $t_d$  in terms of strains in the  $d$ ,  $r$ ,  $L$ , and  $t$  directions

$$t_d = \frac{A_o}{p_o} \left[ \frac{(-\epsilon_d)(\epsilon_r - \epsilon_d)}{(\epsilon_L - \epsilon_d)(\epsilon_t - \epsilon_d)} \right] \quad (6.16)$$

#### $\epsilon_L$ as a Function of $f_L$

For pure torsion ( $\sigma_L = 0$ ) the following expression gives the strain in the  $L$  direction  $\epsilon_L$  in terms of the longitudinal steel stress  $f_L$

$$\epsilon_L = \epsilon_d + \frac{A_o(-\epsilon_d)(-\sigma_d)}{A_L f_L} \quad (6.17)$$

In Eq. 6.17,  $\epsilon_L$  and  $f_L$  must be solved simultaneously with the stress-strain relationships defined in Eq. 6.14.

### $\epsilon_t$ as a Function of $f_t$

The following expression gives the strain in the  $t$  direction in terms of the transverse steel stress  $f_t$

$$\epsilon_t = \epsilon_d + \frac{A_o s (-\epsilon_d) (-\sigma_d)}{p_o (A_t f_t)} \quad (6.18)$$

In Eq. 6.18,  $\epsilon_t$  and  $f_t$  must be solved simultaneously with the stress-strain relationship defined in Eq. 6.15.

### Formulas for $A_o$ and $p_o$

According to Hsu (1993), formulas for the area bounded by the centerline of the shear flow  $A_o$  and the perimeter of the centerline of the shear flow  $p_o$  can be derived, assuming that the centerline of the shear flow coincides with the centerline of the shear flow zone. For a circular and oblong cross-section (Figure 6.9),  $A_o$  and  $p_o$  are defined in Eqs. 6.19 and 6.20, respectively

$$A_o = A_c - \frac{1}{2} p_c t_d + \frac{\pi}{4} t_d^2 \quad (6.19)$$

$$p_o = p_c - \pi t_d \quad (6.20)$$

where  $A_c$  = cross-sectional area and  $p_c$  = perimeter of the section.

For a circular cross-section (Figure 6.9a) of diameter  $D$ ,  $A_c$  and  $p_c$  are defined in Eqs. 6.21 and 6.22, respectively

$$A_c = \frac{\pi}{4} D^2 \quad (6.21)$$

$$p_c = \pi D \quad (6.22)$$

For an oblong cross-section (Figure 6.9b),  $A_c$  and  $p_c$  are defined in Eqs. 6.23

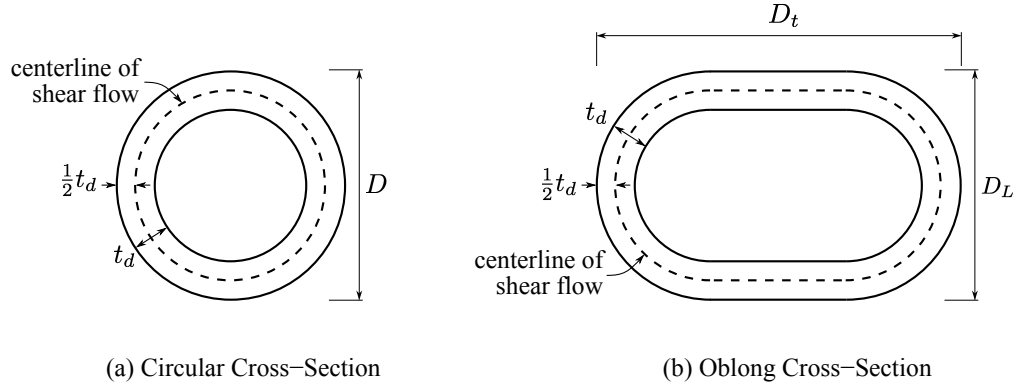


Figure 6.9: Calculation of  $A_o$  and  $p_o$

and 6.24, respectively

$$A_c = \frac{\pi}{4} D_L^2 + (D_t - D_L) D_L \quad (6.23)$$

$$p_c = \pi D_L + 2(D_t - D_L) \quad (6.24)$$

where  $D_t$  = transverse column diameter and  $D_L$  = longitudinal column diameter.

### $\epsilon_r$ and $\alpha$ as a Function of Strains

The following expression gives the strain in the  $r$  direction,  $\epsilon_r$  (Eq. 6.25), and the angle of inclination of the concrete struts,  $\alpha$  (Eq. 6.26), in terms of strains in the  $d$ ,  $L$ , and  $t$  directions

$$\epsilon_r = \epsilon_L + \epsilon_t - \epsilon_d \quad (6.25)$$

$$\tan^2 \alpha = \frac{\epsilon_L - \epsilon_d}{\epsilon_t - \epsilon_d} \quad (6.26)$$

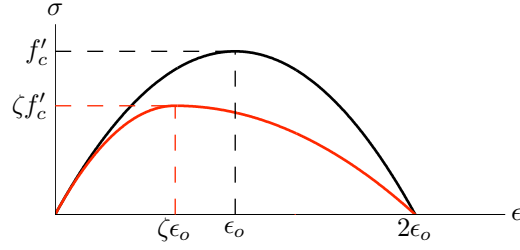


Figure 6.10: Stress-Strain Curve for Softened Concrete

#### 6.4.4 Selected Constitutive Relationships

##### Concrete Struts

The ascending and descending branches of the softened stress-strain curve (Figure 6.10) are defined by Eqs. 6.27a and 6.27b, respectively

$$\sigma = \zeta f'_c \left[ 2 \left( \frac{\epsilon}{\zeta \epsilon_o} \right) - \left( \frac{\epsilon}{\zeta \epsilon_o} \right)^2 \right], \quad \frac{\epsilon}{\zeta \epsilon_o} \leq 1 \quad (6.27a)$$

$$\sigma = \zeta f'_c \left[ 1 - \left( \frac{\epsilon - \zeta \epsilon_o}{2\epsilon_o - \zeta \epsilon_o} \right)^2 \right], \quad \frac{\epsilon}{\zeta \epsilon_o} > 1 \quad (6.27b)$$

When the strain distribution in the concrete struts is assumed to be linear, the coefficient  $k_1$  (Eq. 6.10) can be obtained from integrating the compression stress block and using Eqs. 6.27a and 6.27b. The following gives the two expressions for the coefficient  $k_1$

$$k_1 = \frac{\epsilon_{ds}}{\zeta \epsilon_o} \left( 1 - \frac{1}{3} \frac{\epsilon_{ds}}{\zeta \epsilon_o} \right), \quad \frac{\epsilon_{ds}}{\zeta \epsilon_o} \leq 1 \quad (6.28a)$$

$$k_1 = \left[ 1 - \frac{\zeta^2}{(2 - \zeta)^2} \right] \left( 1 - \frac{1}{3} \frac{\zeta \epsilon_o}{\epsilon_{ds}} \right) + \frac{\zeta^2}{(2 - \zeta)^2} \frac{\epsilon_{ds}}{\zeta \epsilon_o} \left( 1 - \frac{1}{3} \frac{\epsilon_{ds}}{\zeta \epsilon_o} \right), \quad \frac{\epsilon_{ds}}{\zeta \epsilon_o} > 1 \quad (6.28b)$$

Hsu and Moy (1985), Vecchio and Collins (1986), and Zhang and Hsu (1998) have proposed expressions for modeling the softening of the stiffness and strength of the concrete struts due to the effect of transverse tensile cracking. The expression for the softening

coefficient,  $\zeta$ , given in Hsu (1993) is adopted, which takes the form

$$\zeta = \frac{0.9}{\sqrt{1 + 600\epsilon_r}} \quad (6.29)$$

### Reinforcing Steel

The longitudinal steel (Eq. 6.14) and transverse steel (Eq. 6.15) constitutive relationships are based on the measured response from pull tests of the main longitudinal reinforcement (Figure 3.16) and hoop reinforcement (Figure 3.18), respectively. The stress-strain relationship for the longitudinal steel and transverse steel are presented in Figures 6.3 and 6.5, respectively.

#### 6.4.5 Solution Procedure

The steps necessary to compute the torque-twist ( $T$  versus  $\theta$ ) curve are:

1. Select a value of  $\epsilon_d$ .
2. Assume values of  $\epsilon_r$  and  $t_d$ .
3. Calculate  $\zeta$ ,  $k_1$ , and  $\sigma_d$  from Eqs. 6.12, 6.11, and 6.10, respectively.
4. Calculate  $A_o$  and  $p_o$  by Eqs. 6.19 and 6.20, respectively.
5. Solve the strains and stresses in the longitudinal steel ( $\epsilon_L$  and  $f_L$ ) from Eqs. 6.17 and 6.14, respectively, and in the transverse steel ( $\epsilon_t$  and  $f_t$ ) from Eqs. 6.18 and 6.15, respectively.
6. Calculate  $\epsilon_r$  from Eq. 6.25 and  $t_d$  from Eq. 6.16. If  $\epsilon_r$  and  $t_d$  are the same as assumed, proceed to Step 7. If  $\epsilon_r$  and  $t_d$  are not the same as assumed, then assume other values and repeat Steps 3-5.

7. Calculate  $\alpha$ ,  $\tau_{Lt}$ ,  $T$ ,  $\gamma_{Lt}$ , and  $\theta$  from Eqs. 6.26, 6.4, 6.5, 6.6, 6.7, and 6.8, respectively.

This produces one point on the  $T$  versus  $\theta$  curve.

8. To calculate additional points on the torque-twist curve, select another value of  $\epsilon_d$  and repeat Steps 2 to 7.

Instead of arbitrarily selecting values for  $\epsilon_r$  and  $t_d$  (Step 2), Leung (1982) used a more efficient procedure for obtaining good initial guesses for solving the space truss model. This improved procedure was the secant method for nonlinear simultaneous equations (Burden and Faires, 2001). Similar to Leung, the secant method is implemented for finding two roots (case of  $n = 2$ ), the values of  $\epsilon_r$  and  $t_d$  for a selected value of  $\epsilon_d$ .

The iteration scheme starts with three, i.e.  $(n + 1)$ , trial solutions

$$\mathbf{x} = \begin{bmatrix} \mathbf{x}^1 & \mathbf{x}^2 & \mathbf{x}^3 \end{bmatrix} = \begin{bmatrix} \epsilon_r^1 & \epsilon_r^2 & \epsilon_d^3 \\ t_d^1 & t_d^2 & t_d^3 \end{bmatrix} \quad (6.30)$$

Multipliers of the trial solution sets are determined by solving the system of equations below

$$\begin{bmatrix} f_1(\mathbf{x}^1) & f_1(\mathbf{x}^2) & f_1(\mathbf{x}^3) \\ f_2(\mathbf{x}^1) & f_2(\mathbf{x}^2) & f_2(\mathbf{x}^3) \\ 1 & 1 & 1 \end{bmatrix} \begin{pmatrix} \Pi_1 \\ \Pi_2 \\ \Pi_3 \end{pmatrix} = \begin{pmatrix} 0 \\ 0 \\ 1 \end{pmatrix} \quad (6.31)$$

where the functions  $f_1$  and  $f_2$  are specific for the softened truss model of the form

$$f_1(\mathbf{x}) = \epsilon_r - (\epsilon_L + \epsilon_t - \epsilon_d) = 0 \quad (6.32)$$

$$f_2(\mathbf{x}) = t_d - \left( \frac{A_o}{p_o} \left[ \frac{(-\epsilon_d)(\epsilon_r - \epsilon_d)}{(\epsilon_L - \epsilon_d)(\epsilon_t - \epsilon_d)} \right] \right) = 0 \quad (6.33)$$

and the derivatives of the functions are assumed to exist. The solution produces a new set of trial solutions

$$\bar{\mathbf{x}} = \Pi_1 \mathbf{x}^1 + \Pi_2 \mathbf{x}^2 + \Pi_3 \mathbf{x}^3 \quad (6.34)$$

A new pool of trial solutions is obtained by replacing one of the previous trial solutions with the new set of trial solutions. The  $j$ th column of the previous solutions which produces the largest norm  $\|\mathbf{x}^j\|_2$  is replaced by  $\bar{\mathbf{x}}$ . The iteration scheme starts again from Eq. 6.30 with the new pool of trial solutions, and terminates when the calculated and assumed values of  $\epsilon_r$  and  $t_d$  (Step 6) are the same.

This iteration scheme requires initial trial solutions to start. Leung (1982) found that for the case of pure torsion, convergence is almost always achieved, even for bad initial guesses. This was found to be the case in the present study using initial trial solutions of  $\epsilon_r^1$ ,  $\epsilon_r^2$ , and  $\epsilon_r^3$  equal to 0,  $1.0 \times 10^{-3}$ , and  $2.0 \times 10^{-3}$ , respectively, and initial trial solutions of  $t_d^1$ ,  $t_d^2$ , and  $t_d^3$  equal to  $D/10$ ,  $D/7$ , and  $D/4$ , respectively. For subsequent values of  $\epsilon_d$ , the previous step is used as a good initial guess as long as the  $\epsilon_d$  increment is sufficiently small.

#### 6.4.6 Effects of Axial Load and Steel Model

##### Axial Load

The calculated torque-twist curves without axial load and with axial load ( $0.1 f'_c A_g$ ), are shown for the circular and oblong column specimens in Figures 6.11 and 6.12, respectively. In addition to the torque versus twist relationship (a), each figure also shows the hoop strain (b), thickness of shear flow zone (c), longitudinal strain (d), angle of inclination relative to the longitudinal axis (e), and softening coefficient (f) versus twist. As seen in Figures 6.11 and 6.12, the calculated torque capacity increases while the twist capacity decreases with axial load compared to zero axial load for both the circular and oblong columns. As a result of the peak torque occurring at a smaller twist for columns with axial load, the twist necessary to yield the hoops decreases with axial load. Inclusion of axial

load also decreases the longitudinal steel strains, increases the thickness of the shear flow zone, and decreases the angle of inclination of the concrete struts.

## Steel Modeling

Solution of the softened truss model requires significant computational effort not only to obtain values for  $\epsilon_r$  and  $t_d$ , but also to solve for the strains of the reinforcing steel. The longitudinal strain ( $\epsilon_L$ ) and transverse strain ( $\epsilon_t$ ) must be solved simultaneously for a given stress-strain relationship, as given in Eqs. 6.17 and 6.17, respectively. Using an elastic perfectly-plastic (EPP) model for both the longitudinal and transverse reinforcing steel reduces the number of iterations necessary to satisfy Eqs. 6.17 and 6.17 because of the simple stress-strain relationship. Figures 6.13 and 6.14 compares the torque-twist curves, including axial load ( $0.1f'_cA_g$ ), using the calibrated steel models (Figures 6.11 and 6.12) and the EPP model ( $f_{yt} = 73$  ksi and  $f_{yt} = 60$  ksi), for the circular and oblong column specimens, respectively.

As seen in Figures 6.13 and 6.14, the calibrated model is not as stiff as the EPP prior to reaching the peak torque, due to the gradual transition from elastic to plastic branches of the calibrated hoop steel model. This difference in initial elastic stiffness of the steel causes the EPP model to underestimate the twist at the peak torque. However, there is reasonable agreement of torque capacity for the columns with the calibrated and EPP models. Reasonable agreement of hoop strains for the two models is also found, particularly for the twist necessary to yield the hoops. As expected, there is excellent agreement of longitudinal strains for the calibrated and EPP models, since the longitudinal strains do not reach the yield strain and thus the post-yield differences of the calibrated and EPP longitudinal steel models are not engaged.

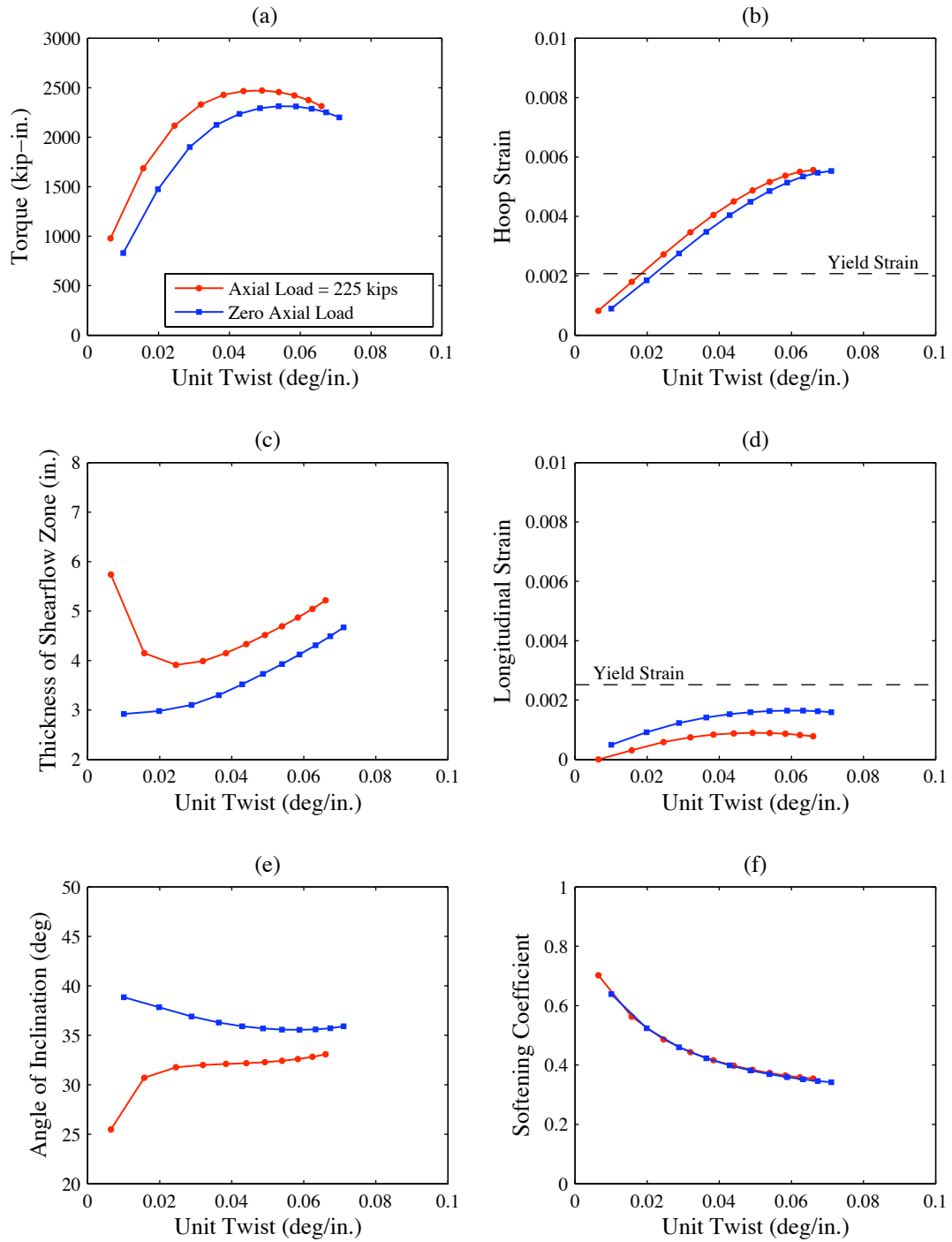


Figure 6.11: Effect of Axial Load on the Circular Column Torque-Twist Response Using Softened Truss Model for Torsion

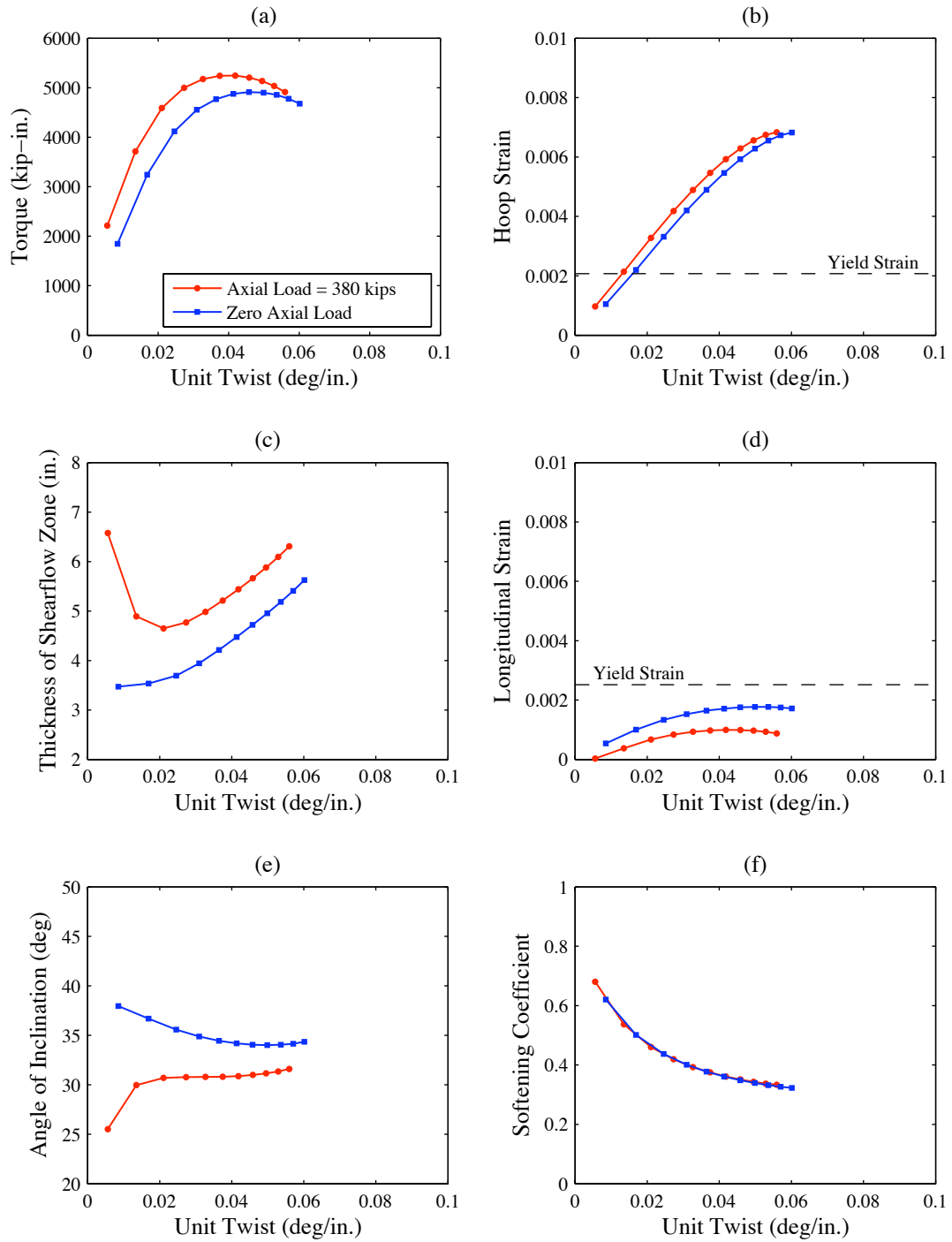


Figure 6.12: Effect of Axial Load on the Oblong Column Torque-Twist Response Using Softened Truss Model for Torsion

Overall, calculation of the torque-twist response for the circular and oblong column specimens using the EPP models for both longitudinal and transverse reinforcing steels gives good results compared to results using the calibrated steel models.

## 6.5 Three-Dimensional Truss Modeling

Truss models (also known as strut and tie models) provide a simplified analytical method for evaluating the nonlinear behavior of reinforced concrete members. Park and Eom (2007) showed reasonable agreement when comparing the nonlinear truss model to existing test specimens with various reinforcing details under cyclic loading. The nonlinear truss models developed by Park and Eom and other truss models developed by previous researchers have been limited to 2D geometry and loading. This section proposes a method for constructing a 3D truss model of a RC column, which can be used to model the response to lateral, torsional, and combined lateral and torsional loading.

### 6.5.1 Modeling of Truss Elements

Figure 6.15 illustrates the proposed method for constructing the 3D truss model. The concrete and reinforcing bar cross-sectional areas are denoted as  $A_c$  and  $A_r$ , respectively.

#### Longitudinal Element

The longitudinal elements **L**, located at the corners of the idealized octagon cross section, are modeled with confined concrete and steel reinforcing bars in parallel.

The area of confined concrete corresponding to each longitudinal element is determined using the following steps. First, the column cross section is divided into eight wedges

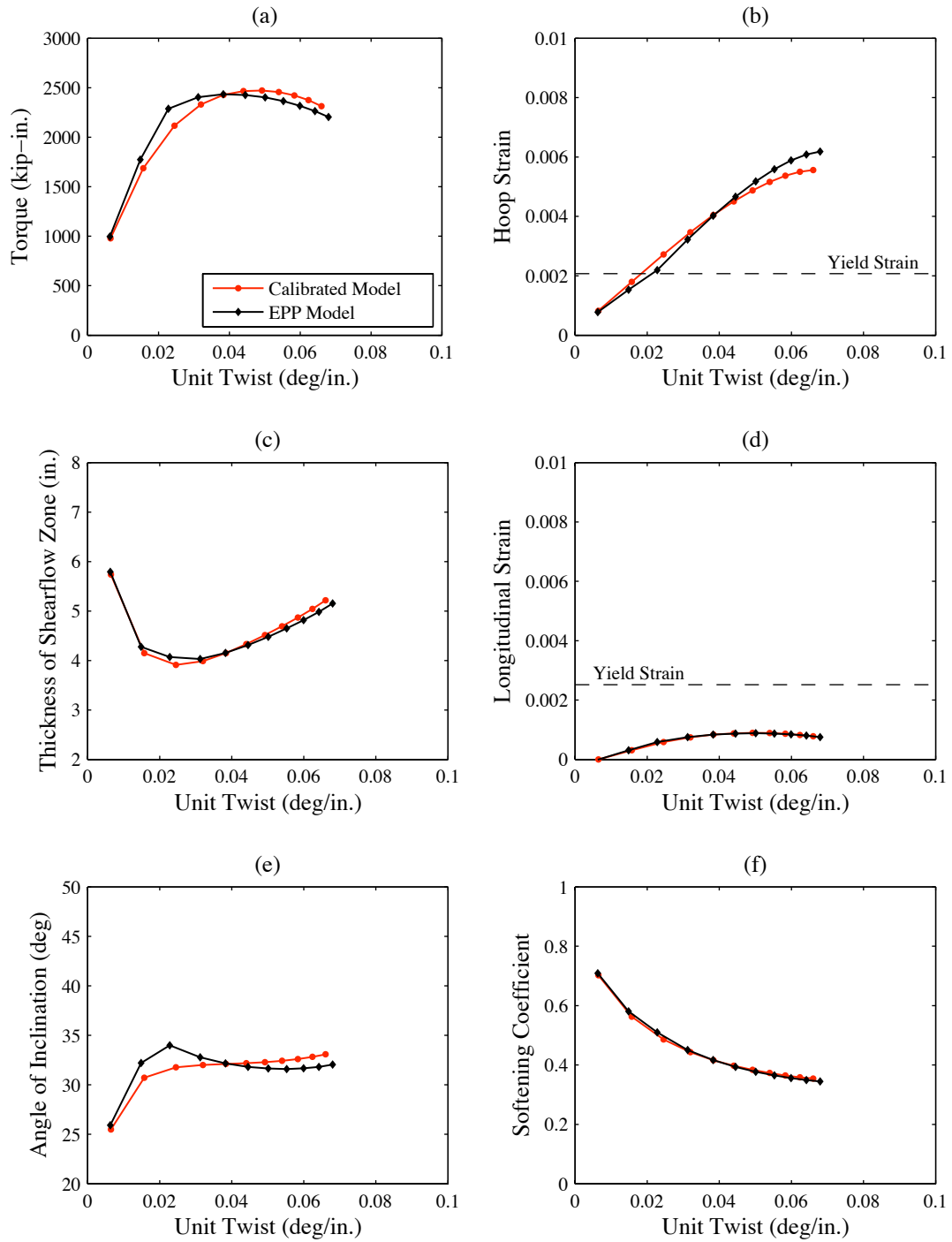


Figure 6.13: Effect of Steel Model on the Circular Column Torque-Twist Response Using Softened Truss Model for Torsion

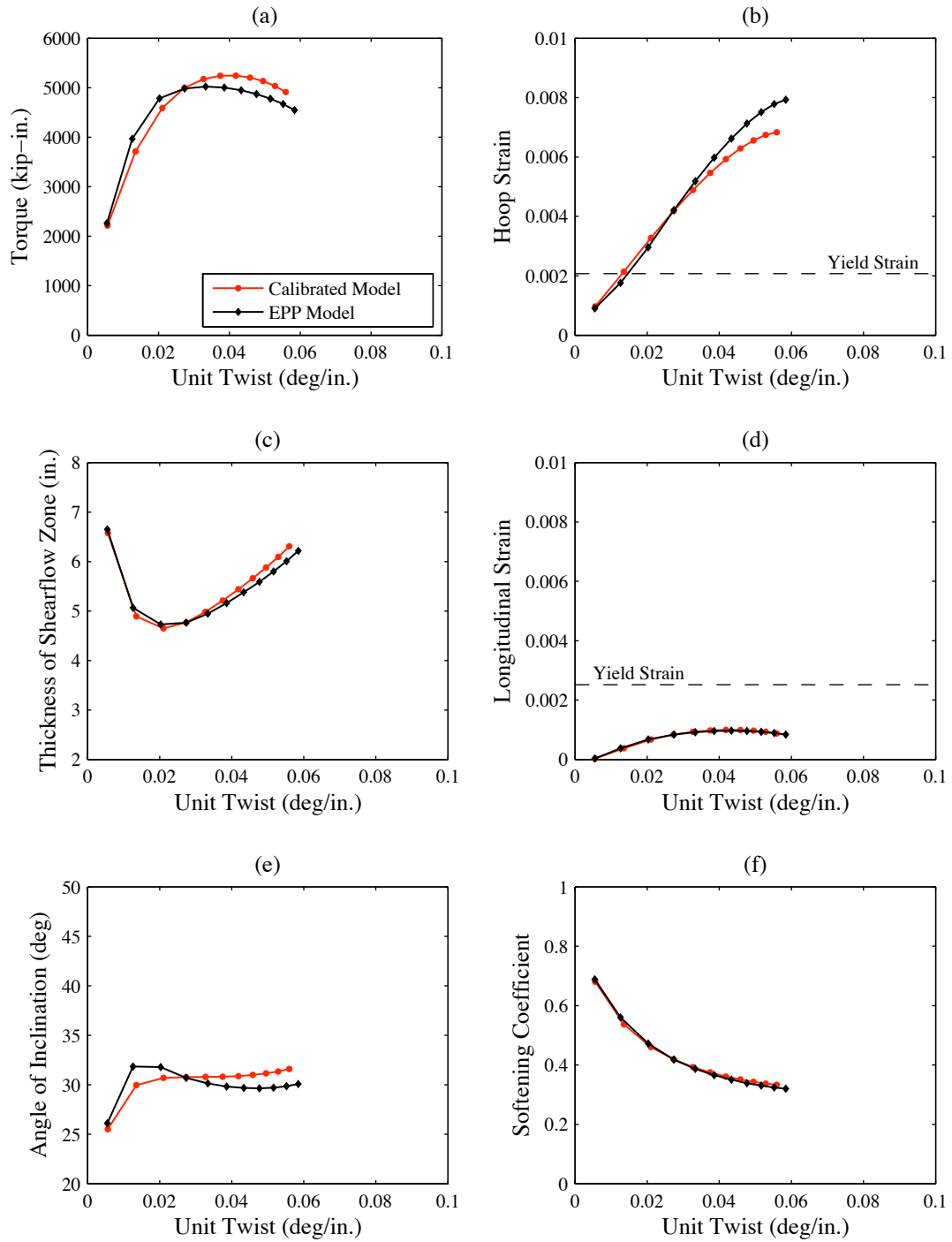


Figure 6.14: Effect of Steel Model on the Oblong Column Torque-Twist Response Using Softened Truss Model for Torsion

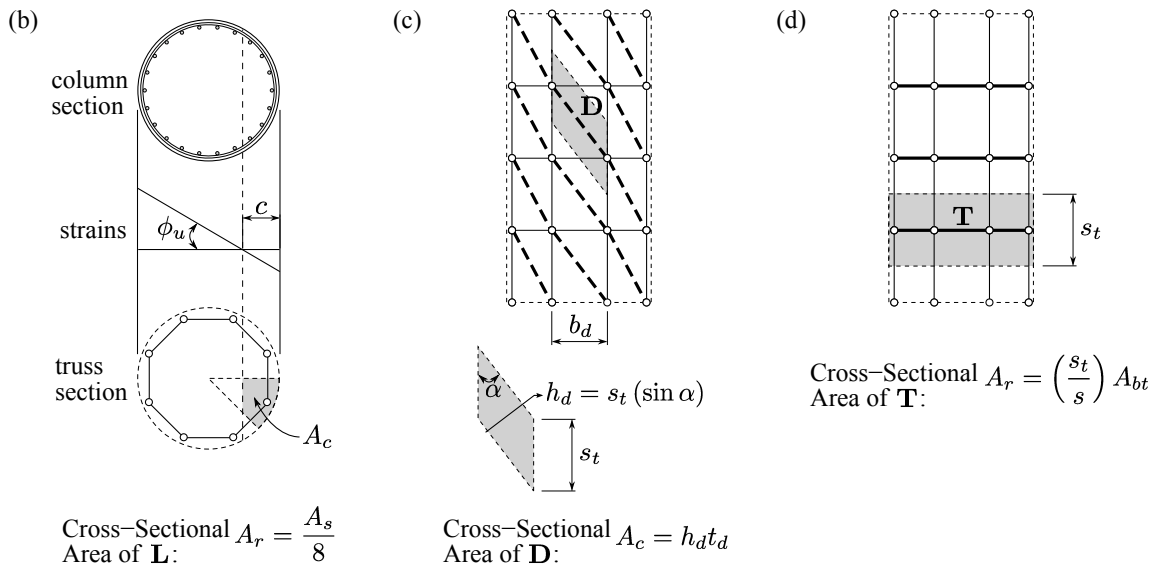
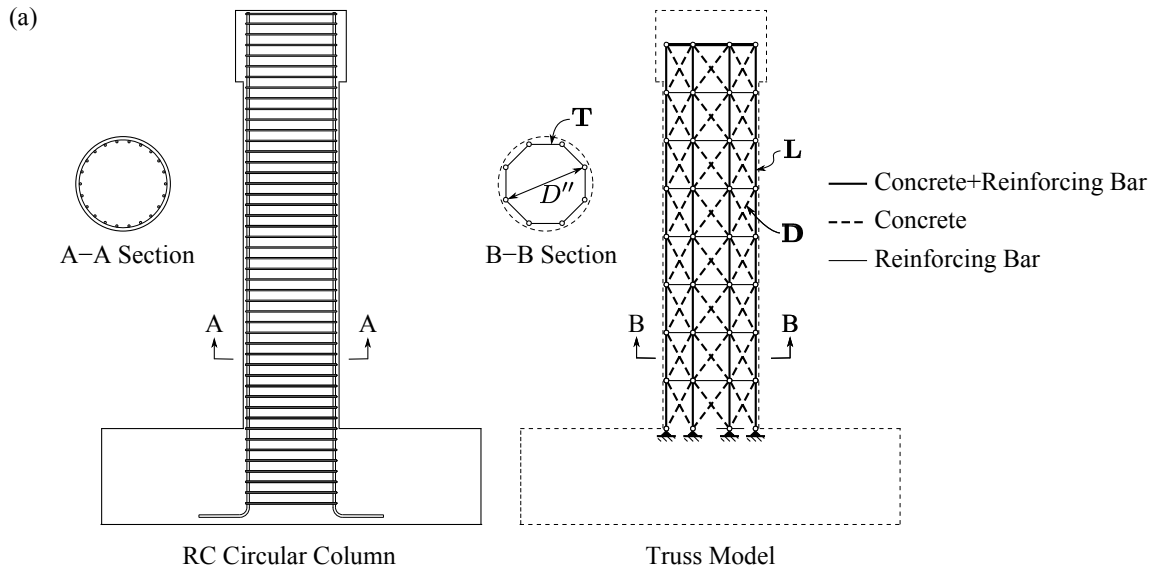


Figure 6.15: Modeling of Concrete and Reinforcing Bar Elements

of equal size, as shown by the dashed lines in Figure 6.15(b). Next, moment-curvature analysis under flexural and axial loads (zero torsion) is performed to determine the neutral axis depth of the section,  $c$ , at the ultimate curvature capacity,  $\phi_u$ . Then, the area of the wedge in compression is calculated, shown by the shaded portion in Figure 6.15(b). The area of this sector corresponds to the area of confined concrete lumped at the corner of the idealized octagon cross section. The steel reinforcing bar area corresponding to each longitudinal element, also lumped at the corner of the idealized octagon cross section, is defined as

$$A_r = \frac{A_s}{8} \quad (6.35)$$

where  $A_s$  = area of longitudinal reinforcement.

Lumping of the steel reinforcement and concrete introduces error in the moment-curvature response of the column cross section. Figure 6.16 compares the moment-curvature response of a fully-fiberized section (solid black line) with a fiber section with lumped steel (dashed black line) and with a section with lumped steel and concrete (solid red line). As seen in Figure 6.16, the moment-curvature response is similar for the fully-fiberized section and fiber section with lumped steel. This is not surprising because condensing the area of longitudinal reinforcement from 22 evenly spaced locations to the 8 corners of the idealized octagon does not significantly affect the strain profile of the cross section. The section with lumped steel and concrete shows good agreement of initial stiffness and post-yield tangent stiffness with the fully-fiberized section. However, the section with lumped steel and concrete over-estimates the moment capacity. This over-prediction of moment-capacity is due to lumping of the confined concrete at the corners of the idealized octagon.

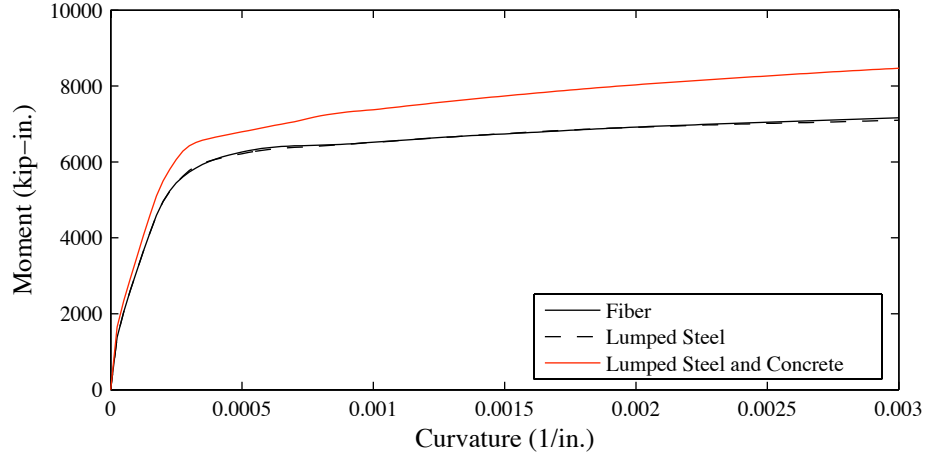


Figure 6.16: Comparison of Moment-Curvature Response of Fiberized and Lumped Sections

### Diagonal Element

The diagonal elements  $\mathbf{D}$  are idealized as an unconfined concrete element. As shown in Figure 6.15(c), the angle of inclination of the diagonal elements is

$$\alpha = \arctan\left(\frac{b_d}{s_t}\right) \quad (6.36)$$

where  $b_d$  = side length of octagon and  $s_t$  = spacing of transverse elements. This angle  $\alpha$  can vary depending on the defined spacing  $s_t$ , which ranges from 30 to 60 deg adopting ACI (2008) provisions on limitations of angles for compression diagonals. The cross-sectional area of the diagonal element is defined as

$$A_c = h_d t_d \quad (6.37)$$

where the depth of the diagonal element  $h_d = s_t (\sin \alpha)$  and  $t_d$  = thickness of the equivalent thin-walled tube from sectional analysis using the softened truss model for torsion. The diagonal concrete elements are symmetrically arranged, similar to the work of Park and

Eom (2007), to model the reversed cyclic behavior of RC members and to model the change of stiffness due to cracking of members.

### Transverse Element

The transverse elements **T** are modeled with transverse steel reinforcing bars only. The shear resistance is assumed to be entirely due to shear reinforcement. As shown in Figure 6.15(d), the cross-sectional area of the transverse element is defined as

$$A_r = \left(\frac{s_t}{s}\right) A_{bt} \quad (6.38)$$

where  $s_t$  = spacing of the transverse elements,  $s$  = hoop spacing, and  $A_{bt}$  = cross-sectional area of hoop reinforcing bar.

### 6.5.2 Implementation

The 3D truss model for a circular column is modeled using *OpenSees* (McKenna et al., 2000), shown in Figure 6.17. Selection of the thickness and angle of inclination of the diagonal elements is based on sectional analysis of the column cross section using the softened truss model for torsion (Figure 6.11). The thickness and angle of inclination at the maximum computed torque from sectional analysis are used. To account for nonlinear geometry effects, the corotational truss formulation (`corotTruss`) is used for all the elements.

The stress-strain relationship for the confined concrete and reinforcing steel portion of the longitudinal elements are based on data from material testing and modeled using the uniaxial materials `Concrete01` (Figure 6.2) and `ReinforcingSteel` (Figure 6.3), respectively. The stress-strain relationship for the transverse elements is based on material

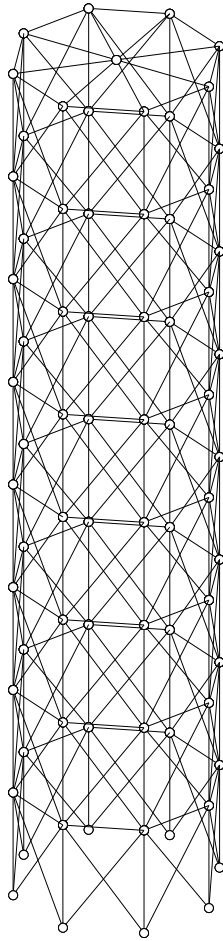


Figure 6.17: Illustration of 3D Nonlinear Truss Model

testing (Figure 6.5) and modeled using the uniaxial material `Steel02`.

To model the cracking of the diagonal elements, the unconfined concrete is modeled using the uniaxial material `Concrete02`, which models tensile strength and linear tension softening. The value for the tensile strength is based on the measured tensile strength during split-cylinder testing of unconfined concrete and the tension softening stiffness is assumed to equal 10% of the modulus of elasticity of concrete ( $0.1E_c$ ). Moreover, to include the effect of concrete softening due to transverse tensile strain, the compressive strength and strain at the maximum compressive stress are modified by a softening coefficient. Similar to selection of the thickness and angle of inclination of the diagonal elements, the softening coefficient at the maximum computed torque from sectional analysis is used.

## 6.6 Comparison of Analytical and Experimental Results

This section compares the analytical and experimental results for torsional loading only and lateral loading only. Limitations of the analytical models are discussed as they pertain to combined lateral and torsional loading.

### 6.6.1 Torsional Loading

Figures 6.18 and 6.19 show the measured and calculated torque-twist response for the circular and oblong column specimens, respectively, including the cracking torque and nominal torque capacity according to ACI (2008). The cracking torque was estimated as four times the threshold torsion (Eq. 2.21) and the nominal torque (Eq. 2.22) was determined using the angle of inclination at the peak torque using the softened truss model (Figures 6.11 and 6.12).

The torque-twist response of circular columns subjected to torsional loading only (Column C4) is compared with the 3D truss model and softened truss model in Figure 6.18. For completeness, the torque-twist response of circular columns subjected to combined lateral and torsional loading (Columns C1 and C2) is also included. There is excellent agreement of initial torsional stiffness between the 3D truss model and the torque-twist response of Column C4. There is also excellent agreement of cracking torque between the 3D truss model and that obtained using equations from ACI (2008) with the measured cracking torque of Column C4. No comparison for initial torsional stiffness or cracking torque can be made for the softened truss model because it is valid only after cracking.

After cracking, there is reasonable agreement of the post-cracking stiffness between the 3D truss model, the softened truss model, and Column C4. Moreover, both models also do a reasonable job of estimating the twist at which yielding of the hoop occurs, indicated by circles on the torque-twist curves. The 3D truss model overestimates the torque capacity of the column, whereas the softened truss model does a good job. There is also a good agreement between nominal torque capacity according to ACI (2008) and the maximum torque response of Column C4.

Figure 6.19 compares the torque-twist response of the oblong column subjected to combined lateral and torsional loading (Column C3) and the softened truss model. Obviously, this is not a one-to-one comparison because the softened truss model is limited to torsional loading only whereas the torque-twist response of Column C3 is for combined lateral and torsional loading (twist/drift ratio = 0.6). Thus, as expected there is poor agreement between the softened truss model and Column C3. An appropriate comparison would be between the softened truss model and test data for an oblong column subjected

to torsional loading only, which would allow for assessment of the accuracy of the softened truss model. The nominal torque capacity according to ACI (2008) and the maximum torque calculated using the softened truss model can be compared. The ACI (2008) model results in a torsion strength moderately less than that calculated using the softened truss model.

### 6.6.2 Lateral Loading

Figures 6.20 and 6.21 show the measured and calculated force-displacement response for the circular and oblong column specimens, respectively, including the expected first yield of the longitudinal reinforcement.

Figure 6.20 compares the measured force-displacement response of the circular columns subjected to lateral loading only (Column 415) and combined lateral and torsional loading (Columns C1 and C2) with the responses calculated using the 3D truss model and the plastic hinge length model. There is reasonable agreement of the force-displacement response (initial stiffness and lateral load capacity) and displacement at first yield of the longitudinal reinforcement between the plastic hinge model and Column 415. The plastic hinge model also models well the initial stiffness and lateral load capacity of Column C1 and C2, but it does not recognize the reduced stiffness and displacement capacity observed for these columns as a result of the combined lateral and torsional loading. As observed in Chapter 5, torsional loading results in the reduction of deformation capacity and increase of strength degradation, both of which are more pronounced for higher twist/drift ratios.

The 3D truss model does not do as well as the plastic hinge model of modeling the force-displacement response of Column 415. As seen in Figure 6.20, the 3D truss model over-estimates the initial stiffness and the peak lateral load. Moreover, the 3D truss

model estimates yielding of the hoops in the flexural compression zone prior to yielding of the longitudinal reinforcing bars, which does not model the real behavior of Column 415. The premature yielding is caused by the presence of the diagonal elements around the entire perimeter of the analytical model, as required for modeling torsional behavior. Such elements would not normally be used in the flexural compression zone of a flexure-only column without torsion. When diagonal elements are included, the flexural compression is resisted by both the longitudinal and diagonal elements, creating compressive forces in the diagonal elements. These compressive forces must be resisted by tension in the transverse elements modeling the hoops. Although hoops do participate in resisting the flexural compression force through dilation of the compressed concrete, the angles of the diagonal members, as required for torsion, overestimate the “dilation” effect under pure flexure. The result is that the hoops yield prematurely in the analytical model. This force distribution is illustrated in Figure 6.22 for the compression face at the base of the 3D truss model.

Figure 6.21 compares the force-displacement response of the oblong column subjected to combined lateral and torsional loading (Column C3) to the plastic hinge length model. There is good agreement of initial lateral stiffness and lateral load capacity between the plastic hinge model and Column C3; however, there is poor agreement of deformation capacity. Again, the poor agreement of deformation capacity is due to limitations of the plastic hinge model, which can not model the effect of torsional-flexural interaction on the hoops.

### 6.6.3 Combined Lateral and Torsional Loading

Unlike the softened truss model and plastic hinge model, the 3D truss model can be used to model combined loading but does not do a good job in modeling the real behavior. Under combined loading, similar to the case of lateral loading, the diagonal elements induce unrealistically large hoop strains in the flexural compression zone. Thus, the 3D truss model under combined loading does not model correctly the variation of hoop strain around the perimeter of the section, which is necessary to model the flexural-torsional interaction. Therefore, the 3D truss model should be used for modeling the torque-twist response only for the case of pure torsion with or without axial load.

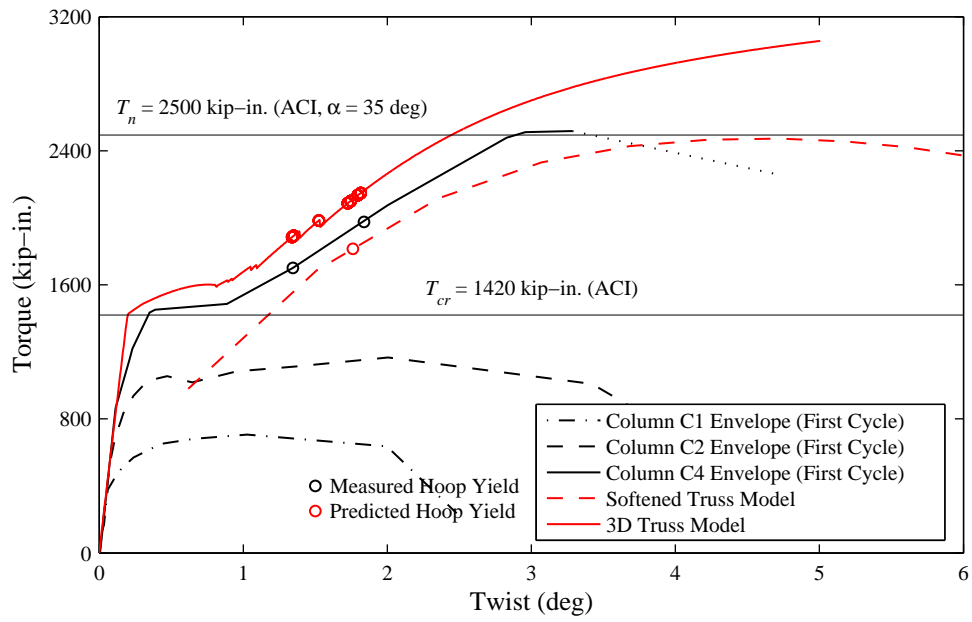


Figure 6.18: Circular Column Measured and Calculated Torque-Twist Response

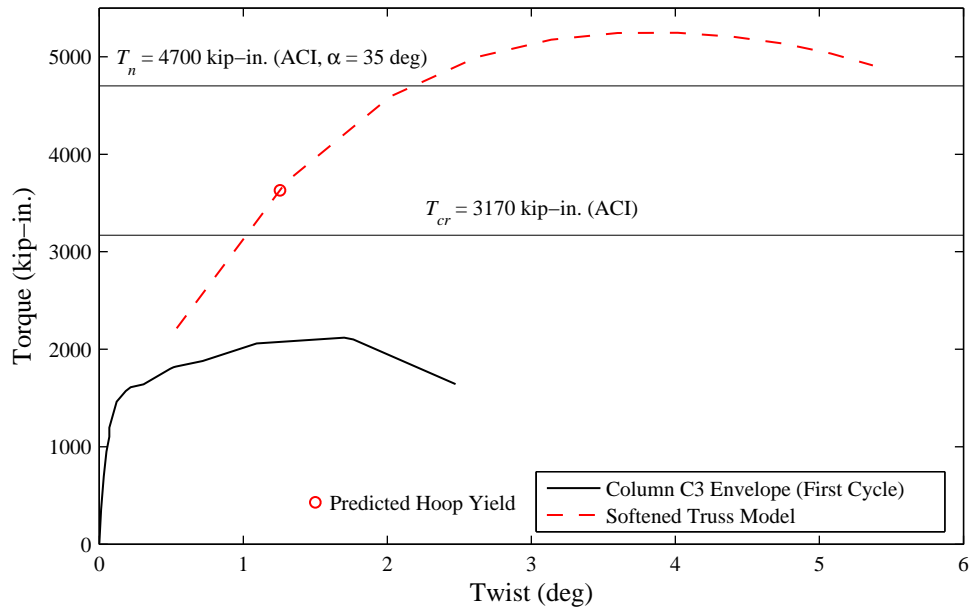


Figure 6.19: Oblong Column Measured and Calculated Torque-Twist Response

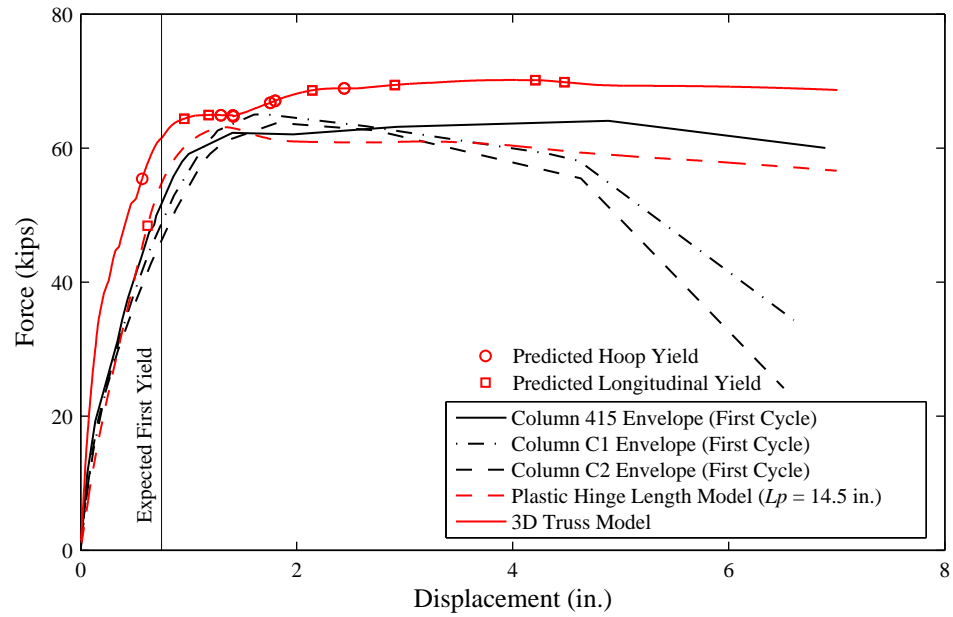


Figure 6.20: Circular Column Measured and Calculated Force-Displacement Response

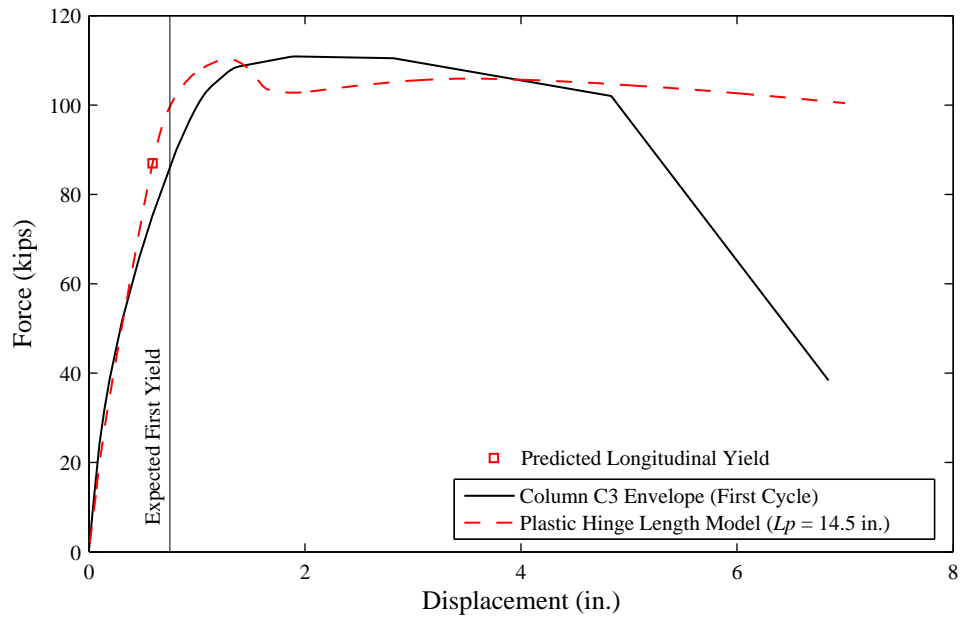


Figure 6.21: Oblong Column Measured and Calculated Force-Displacement Response

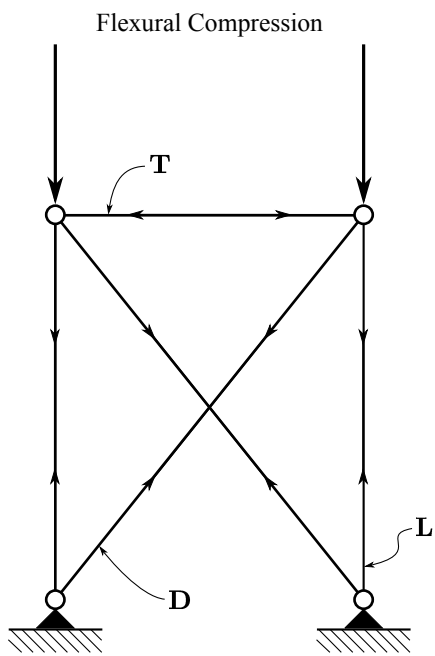


Figure 6.22: Illustration of Element Forces on the Compression Face at the Base of the 3D Truss Model Under Flexure

## Chapter 7

# Investigation to Estimate Seismic Twist Demand

Due to limited recorded data on the torsion response of bridge structures, the seismic twist demands on representative bridges is unclear. This chapter investigates the seismic twist that occurs in columns of “ordinary” bridges whose design is governed by Caltrans (2004a, 2004b). For this purpose, a bridge similar to the types presented in the PEER lifelines report by Ketchum et al. (2004) is modeled and subjected to strong ground-shaking representative of a highly seismic region.

### 7.1 Bridge Description

The bridge considered is a three-span, cast-in-place concrete box girder superstructure with a single-column bent substructure, as shown in Figure 7.1. The material properties are based on the expected properties according to Caltrans (2004b, Sec. 3.2). The expected concrete compressive strength for both the superstructure and substructure

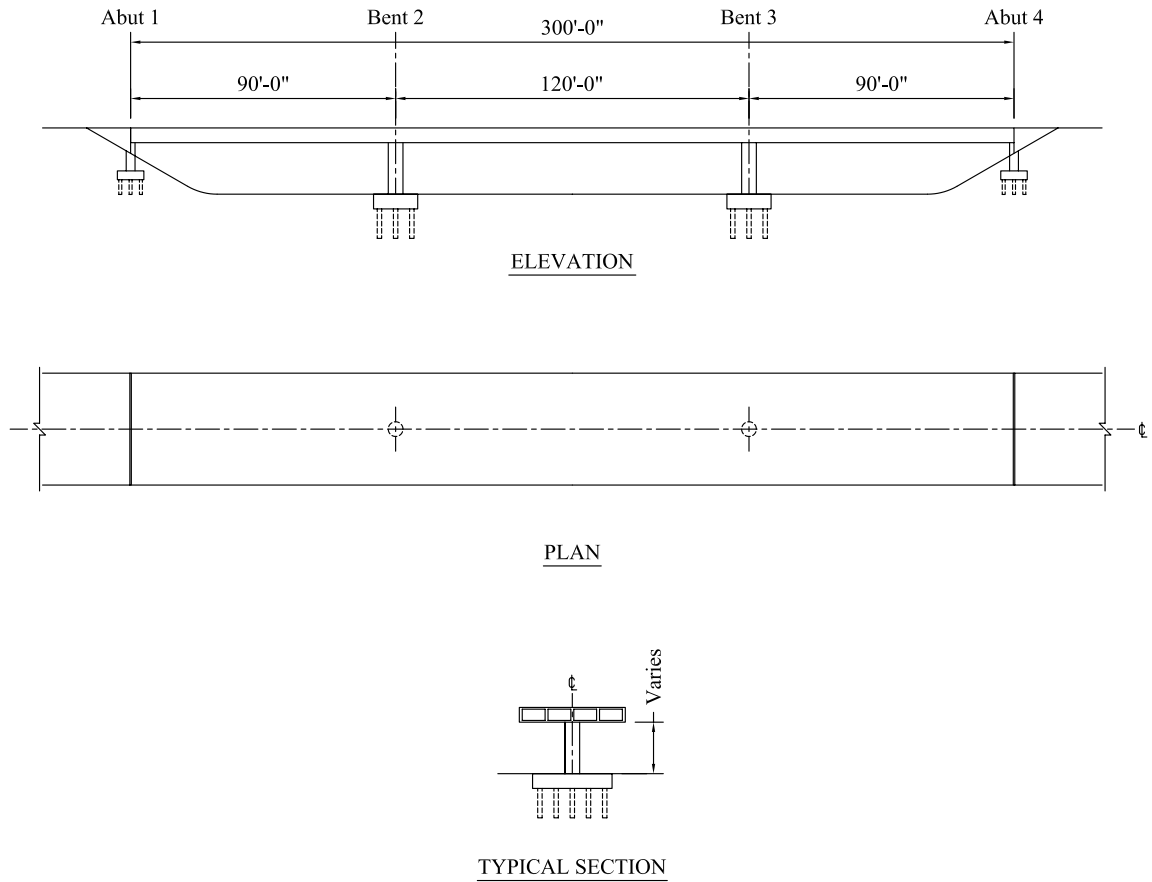


Figure 7.1: Bridge Considered

is 5 ksi. The expected yield strength for A706, Grade 60 reinforcing steel is 68 ksi.

A bridge with identical column aspect ratios equal to four was selected for the design of the “benchmark bridge”. A suite of bridges was created by varying the aspect ratios given this design. Table 7.1 summarizes the bridges.

### 7.1.1 Superstructure

The superstructure (Figure 7.2) is a typical 3-lane, 4-cell box girder section, with a width of 36 ft and a depth of 5 ft. The box girder has a top and bottom thickness of 7 in.

Table 7.1: Column Aspect Ratios

Bridge No.	Aspect Ratio	
	Bent 2	Bent 3
1*		4
2		6
3	4	8
4		10
5		4
6		6
7	6	8
8		10
9		4
10		6
11	8	8
12		10
13		4
14		6
15	10	8
16		10

\* Benchmark Bridge

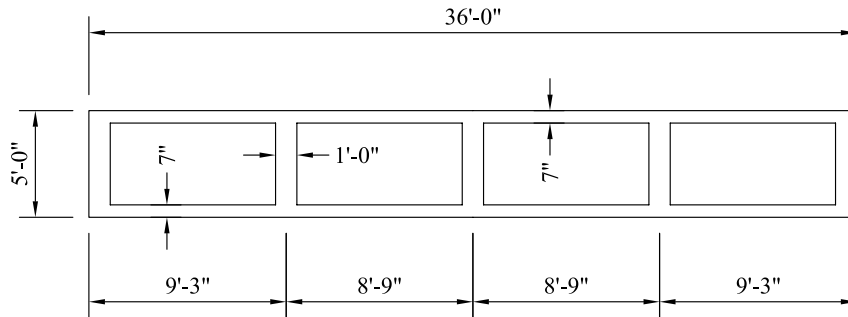


Figure 7.2: Box Girder Cross Section

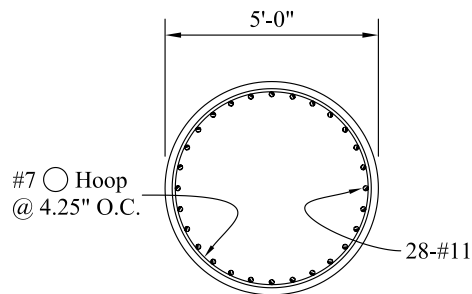


Figure 7.3: Column Cross Section

and a vertical web thickness of 12 in., similar for each cell.

### 7.1.2 Substructure

The superstructure is supported by two single-column bents, designed according to current Caltrans specifications (Caltrans, 2004a, 2004b). The column cross section is shown in Figure 7.3. The longitudinal reinforcement consists of 28 No. 11 bars and the transverse reinforcement consists of No. 7 hoops spaced at 4.25 in. The resulting longitudinal steel reinforcement ratio and transverse volumetric steel ratios are  $\rho_l = 1.5\%$  and  $\rho_s = 1.0\%$ , respectively.

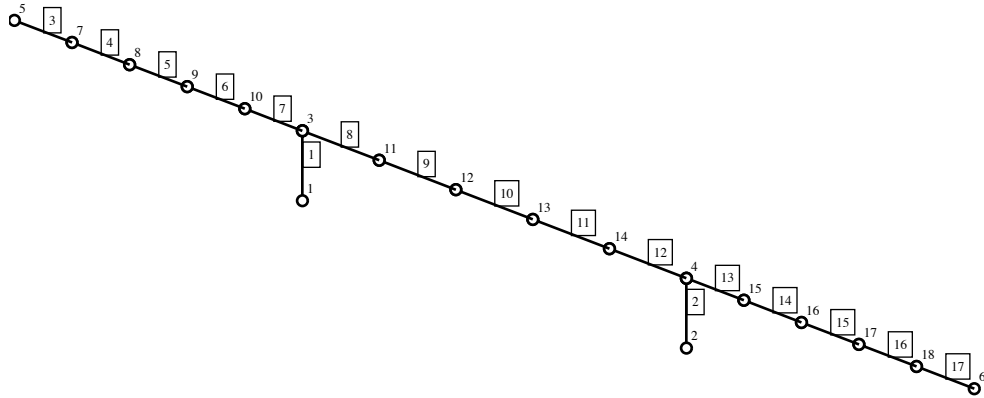


Figure 7.4: Discretized Bridge Model

### 7.1.3 Abutments

Seat-type abutments without shear keys, detailed with a knock-off backwall, provide bearing support for the end spans of the bridge. The top of the backwall contains a weak plane that fails under large longitudinal displacement, providing a large gap between the backwall and the superstructure. The large gap allows the longitudinal displacements to develop unimpeded in either direction (Priestley et al., 1996).

## 7.2 Structural Modeling of Bridge

The modeling objective is to estimate the seismic torsion demand on the bridge columns. The analytical model describes the geometry, seismic mass distribution, boundary conditions, and loading as closely as possible to model the structural response. The bridge is modeled in *OpenSees* (McKenna et al., 2000) and is shown in Figure 7.4.

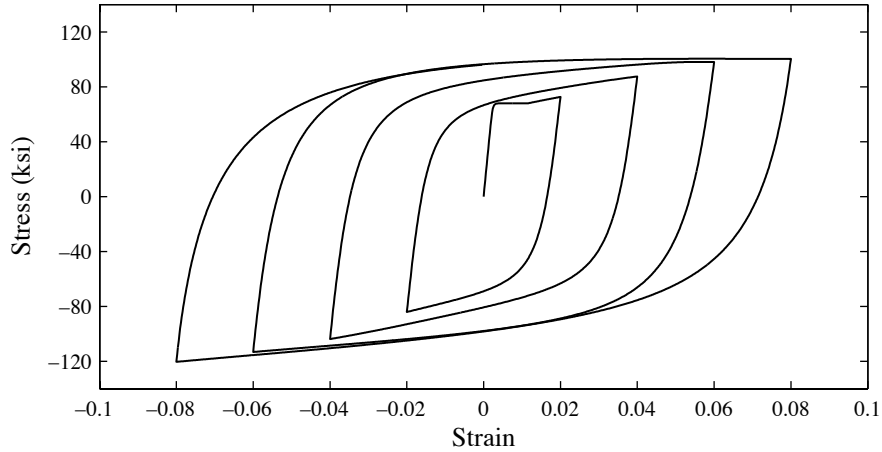


Figure 7.5: Longitudinal Reinforcing Steel Model

## 7.2.1 Materials Models

### Reinforcing Steel

The constitutive model for the longitudinal reinforcing steel is based on the Chang-Mander model (Chang and Mander, 1994), modeled by the `ReinforcingSteel` material in *OpenSees*. The elastic stiffness is  $E_s = 29000$  ksi with an expected yield strength  $f_{ye} = 68$  ksi and an expected tensile strength  $f_{ue} = 95$  ksi. The onset of strain hardening and the ultimate tensile strain are based on the expected material properties for reinforcing steel according to Caltrans (2004b). Figure 7.5 shows the stress-strain relationship for the longitudinal reinforcing steel model.

### Concrete

The constitutive model for unconfined and confined concrete is based on the Kent-Scott-Park model (Kent and Park, 1971), modeled by the `Concrete01` material in *OpenSees*. The expected unconfined concrete compressive strength is  $f'_{co} = 5$  ksi at a corresponding

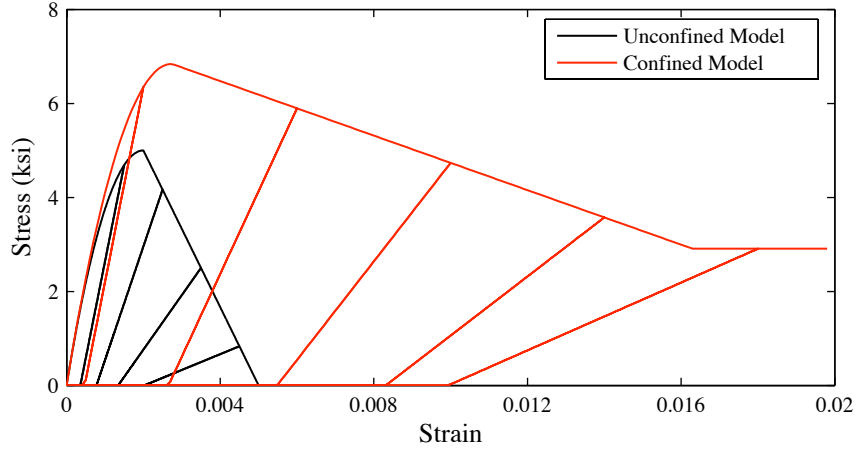


Figure 7.6: Unconfined and Confined Concrete Model

Table 7.2: Superstructure Elastic Properties

$A$ (in. <sup>2</sup> )	$I_z$ (in. <sup>4</sup> )	$I_y$ (in. <sup>4</sup> )	$I_x$ (in. <sup>4</sup> )	$J$ (in. <sup>4</sup> )
$8.81 \times 10^3$	$4.76 \times 10^6$	$1.56 \times 10^8$	$1.60 \times 10^8$	$2.01 \times 10^7$

compressive strain  $\epsilon_{co} = 0.002$ . The ultimate (spalling) strain,  $\epsilon_{sp}$ , is assumed to be 0.005. The enhanced strength and strain capacity for confined concrete is computed using the relations by Mander et al. (1988). Figure 7.6 shows the stress-strain relationship for the unconfined and confined concrete models.

### 7.2.2 Superstructure

The superstructure is modeled with a linear-elastic beam-column element placed at the geometric centroid of the box girder cross section, with the properties described in Table 7.2.

The flexural stiffness is modified to approximate the cracked stiffness  $I_{eff} = 0.75I_g$ ,

as recommend by Caltrans (2004b, Sec. 5.6.1). The torsional moment of inertia  $J$  is approximated assuming a thin-walled section of varying thickness consisting of the perimeter of the box girder (Ugural and Fenster, 1995), given by

$$J = \frac{2t_{web}t_{deck}W_s^2D_s^2}{W_s t_{web} + D_s t_{deck}} \quad (7.1)$$

where  $t_{web}$  = thickness of the vertical web,  $t_{deck}$  = top and bottom thickness,  $W_s$  = width of the box girder section, and  $D_s$  = depth of the box girder section. A reduction of torsional moment of inertia is not required because the bridge superstructure meet the requirements for an Ordinary Standard bridge (Caltrans, 2004b, Sec. 1.1).

Each span is discretized into five equal subspans to better approximate the mass distribution. Each node is assigned three translation mass terms and one rotational (mass moment of inertia about the centroid) term, determined from the self-weight properties.

### 7.2.3 Substructure

The columns are modeled in *OpenSees* using fully three-dimensional fiberized non-linear beam-column elements (Filippou and Neuenhofer, 1998) with five integration points per element. To account for nonlinear geometry effects, the  $P$ - $\Delta$  geometric transformation (Filippou and Fenves, 2004) is used for the columns.

The column cross section is discretized into 96 core concrete, 24 cover concrete, and 28 longitudinal steel reinforcement fibers, as shown in Figure 3.4. Each fiber has an assigned material model to represent the uniaxial stress-strain behavior. The computed and idealized moment-curvature relationships for the column section, including compressive axial load ( $0.1f'_cA_g$ ), are shown in Figure 7.7.

The torsional behavior is modeled elastically with the elastic stiffness modified to

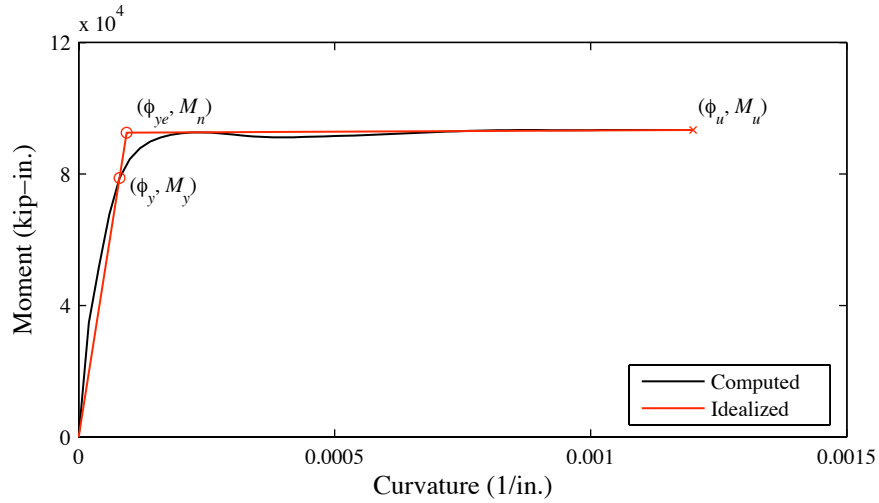


Figure 7.7: Moment-Curvature Relationship for Column Section

approximate the cracked stiffness  $J_{eff} = 0.2J_g$ , reduced for columns according to Caltrans (2004b, Sec. 5.6.2). The computed torque-unit twist relationship for the column section using the softened truss, including compressive axial load ( $0.1f'_cA_g$ ), is shown in Figure 7.8.

#### 7.2.4 Abutments

The abutments are modeled assuming the limiting case of providing bearing support only to the superstructure. The shear keys are assumed to have failed, providing no transverse resistance, and the longitudinal displacement is assumed to be accommodated by a sufficient gap between the superstructure and the abutment backwall. As reported by Isakovic et al. (1998) and Goel and Chopra (2008), bridge structures with rollers at the abutments are more torsionally sensitive, so this modeling assumption should produce a conservatively high estimate of twist response.

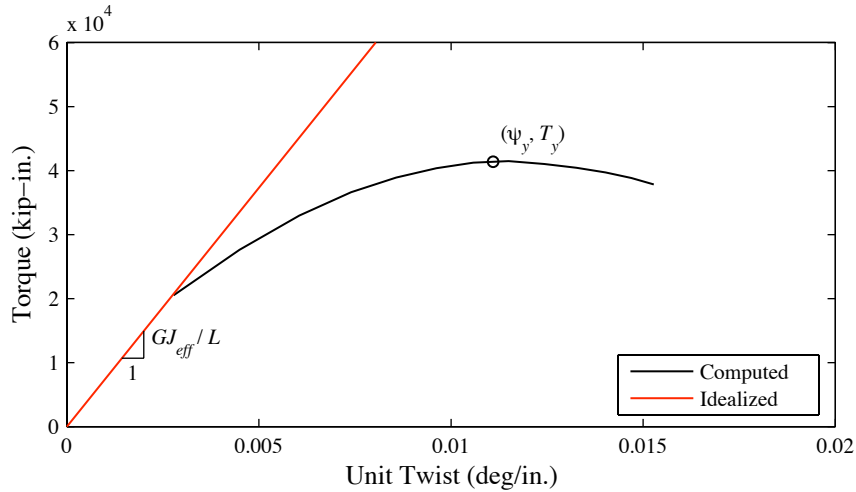


Figure 7.8: Torque-Unit Twist Relationship for Column Section

### 7.3 Ground Motions

For each bridge configuration listed in Table 7.1, two location scenarios are considered for determining representative ground motions. The first scenario considers a bridge located near a fault and the second scenario considers a bridge crossing a fault rupture zone.

#### 7.3.1 Near-Fault Ground Motions

Recorded near-fault ground motions are readily available from past earthquakes. These recorded ground motions are assumed to be spatially non-varying, i.e., similar excitation at all bridge supports. Thus, the spatial variability that may arise from the incoherence effect, the wave-passage effect, the attenuation effect, and the site-response effect is not considered. Der Kiureghian et al. (1997) analyzed a bridge with 120 ft spans and did not find a correlation between increased response and spatial variability effects, i.e., sometimes the response increased and other times the response decreased. The effect of spatial variability

on the response of bridges is beyond the scope of this investigation, hence, the recorded ground motions are treated as uniform excitation.

The PEER NGA database (PEER, 2008) was used to select a suite of ground motions at a distance 0 to 20 km for magnitude bins  $M_w = 7.0 \pm 0.25$  and  $7.5 \pm 0.25$ , listed in Tables 7.3 and 7.4, respectively. The selected ground motions are grouped by event and listed with the recording name in both horizontal components, the closest distance from the station to the fault rupture plane, the peak ground acceleration (PGA), and NEHRP site class (BSSC, 2000).

The elastic response spectra (5% damping) for magnitude bins  $M_w = 7.0 \pm 0.25$  and  $7.5 \pm 0.25$  ground motions are shown in Figures 7.9 and 7.10, respectively. The plots show the spectrum (thin solid black line) for each ground motion, the mean (thick solid black line) for all the ground motions, the mean minus one standard deviation (dashed-dotted black line), mean plus one standard deviation (dashed black line), and the closest magnitude group ARS curve for  $\text{PGA} = 0.6\text{g}$  and soil profile type D (Caltrans, 2004b, Appendix B). The acceleration value of 0.6g was chosen based on the PGA contour near the Hayward Fault on the current Caltrans Seismic Hazard Map (Caltrans, 1996).

As seen in Figure 7.9, there is poor agreement over the entire range of periods between the mean spectrum for magnitude bin  $M_w = 7.0 \pm 0.25$  and the ARS curves for  $M_w = 6.5 \pm 0.25$  and  $M_w = 7.25 \pm 0.25$ . However, the mean plus one standard deviation matches well with the ARS curve for  $M_w = 7.25 \pm 0.25$ . Poor agreement is also seen in Figure 7.10 between the mean spectrum for magnitude bin  $M_w = 7.5 \pm 0.25$  and the ARS curves for  $M_w = 7.25 \pm 0.25$  and  $M_w = 8.0 \pm 0.25$ . The mean spectrum is below the ARS curves for the entire range of periods.

Table 7.3: Selected Ground Motions for Magnitude Bin  $M_w = 7.0 \pm 0.25$

Event	Magnitude ( $M_w$ )	Station Name	Horizontal Component 1	Horizontal Component 2	Distance (km)	PGA (g)	NEHRP Site Class
Cape Mendocino 1992	7.01	Cape Mendocino	CPM000	CPM090	6.96	1.35	C
		Fortuna - Fortuna Blvd	FOR000	FOR090	19.95	0.18	C
		Petrolia	PET000	PET090	8.18	0.62	C
		Rio Dell Overpass	RIO270	RIO360	14.33	0.42	D
Duzce, Turkey 1999	7.14	Bolu	BOL000	BOL090	12.04	0.77	D
		Duzce	DZC180	DZC270	6.58	0.43	D
Gazli, USSR 1976	6.8	Karakyr	GAZ000	GAZ090	5.46	0.64	C
Hector Mine 1999	7.13	Hector	HEC000	HEC090	11.66	0.31	C
Kobe, Japan 1995	6.9	Amagasaki	AMA000	AMA090	11.34	–	D
		Fukushima	FKS000	FKS090	17.85	0.04	D
		KJMA	KJM000	KJM090	0.96	0.71	D
		Kobe	KBU000	KBU090	0.92	–	B
		Nishi-Akashi	NIS000	NIS090	7.08	0.49	C
		Port Island	PRI000	PRI090	3.31	–	D
		Shin-Osaka	SHI000	SHI090	19.15	0.23	D
Loma Prieta 1989	6.93	BRAN	BRN000	BRN090	10.72	0.53	C
		Gilroy Array #3	G03000	G03090	12.82	0.46	D
			LGPC	LGP000	LGP090	3.88	0.78
		Lexington Dam	LEX000	LEX090	5.02	0.44	B
		Santa Teresa Hills	SJTE225	SJTE315	14.69	0.28	C
		Saratoga - Aloha Ave	STG000	STG090	8.50	0.38	C
			W Valley College	WVC000	WVC270	9.31	0.31
		UCSC	UC2000	UC2090	18.51	0.34	C
		WAHO	WAH000	WAH090	17.47	0.52	C
		Nahanni, Canada 1985	6.76	Site 1	S1010	S1280	9.60
Site 2	S2240			S2330	4.93	0.38	C
Site 3	S3270			S3360	5.32	0.15	C

Table 7.4: Selected Ground Motions for Magnitude Bin  $M_w = 7.5 \pm 0.25$

Event	Magnitude ( $M_w$ )	Station Name	Horizontal Component 1	Horizontal Component 2	Distance (km)	PGA (g)	NEHRP Site Class		
Chi-Chi, Taiwan 1999	7.62	CHY010	CHY010-N	CHY010-W	19.96	0.21	C		
		CHY041	CHY041-E	CHY041-N	19.83	0.46	C		
		CHY101	CHY101-E	CHY101-N	9.96	0.38	D		
		TCU061	TCU061-E	TCU061-N	17.19	0.14	D		
		TCU065	TCU065-E	TCU065-N	0.59	0.66	D		
		TCU067	TCU067-E	TUC067-N	0.64	0.41	C		
		TCU068	TCU068-E	TCU068-N	0.32	0.54	C		
		TCU088	TCU088-E	TCU088-N	18.16	0.52	C		
		TCU101	TCU101-E	TCU101-N	2.13	0.23	D		
		Kocaeli, Turkey 1999	7.51	Arcelik	ARC000	ARC090	13.49	0.17	C
Duzce	DZC180			DZC270	15.37	0.33	D		
Gebze	GBZ000			GBZ270	10.92	0.18	B		
Izmit	IZT180			IZT090	7.21	0.20	B		
Yarimca	YPT060			YPT330	4.83	0.31	D		
Landers 1992	7.28			Coolwater	CLW-LN	CLW-TR	19.74	0.37	D
				Joshua Tree	JOS000	JOS090	11.03	0.25	C
				Lucerne	LCN260	LCN345	2.19	0.72	C
				Morongo Valley	MVH000	MVH090	17.32	0.16	D
				Abbar	ABBAR-L	ABBAR-T	12.56	0.51	C
Manjil, Iran 1990	7.37	Dayhook	DAY-LN	DAY-TR	13.94	0.35	C		
		Tabas	TAB-LN	TAB-TR	2.05	0.81	B		

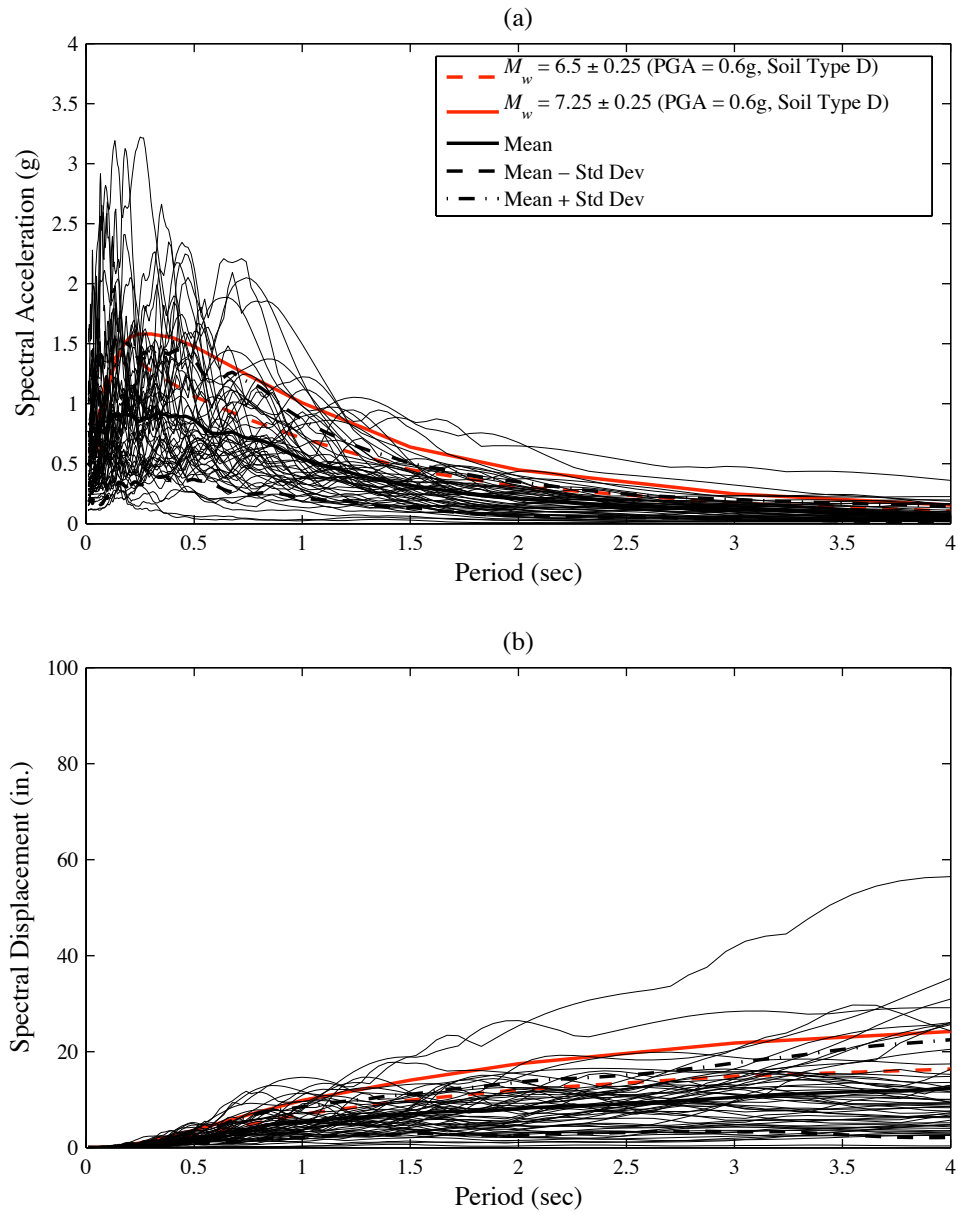


Figure 7.9: Elastic Response Spectra (5% Damping) for Magnitude Bin  $M_w = 7.0 \pm 0.25$ :  
 (a) Spectral Acceleration and (b) Spectral Displacement

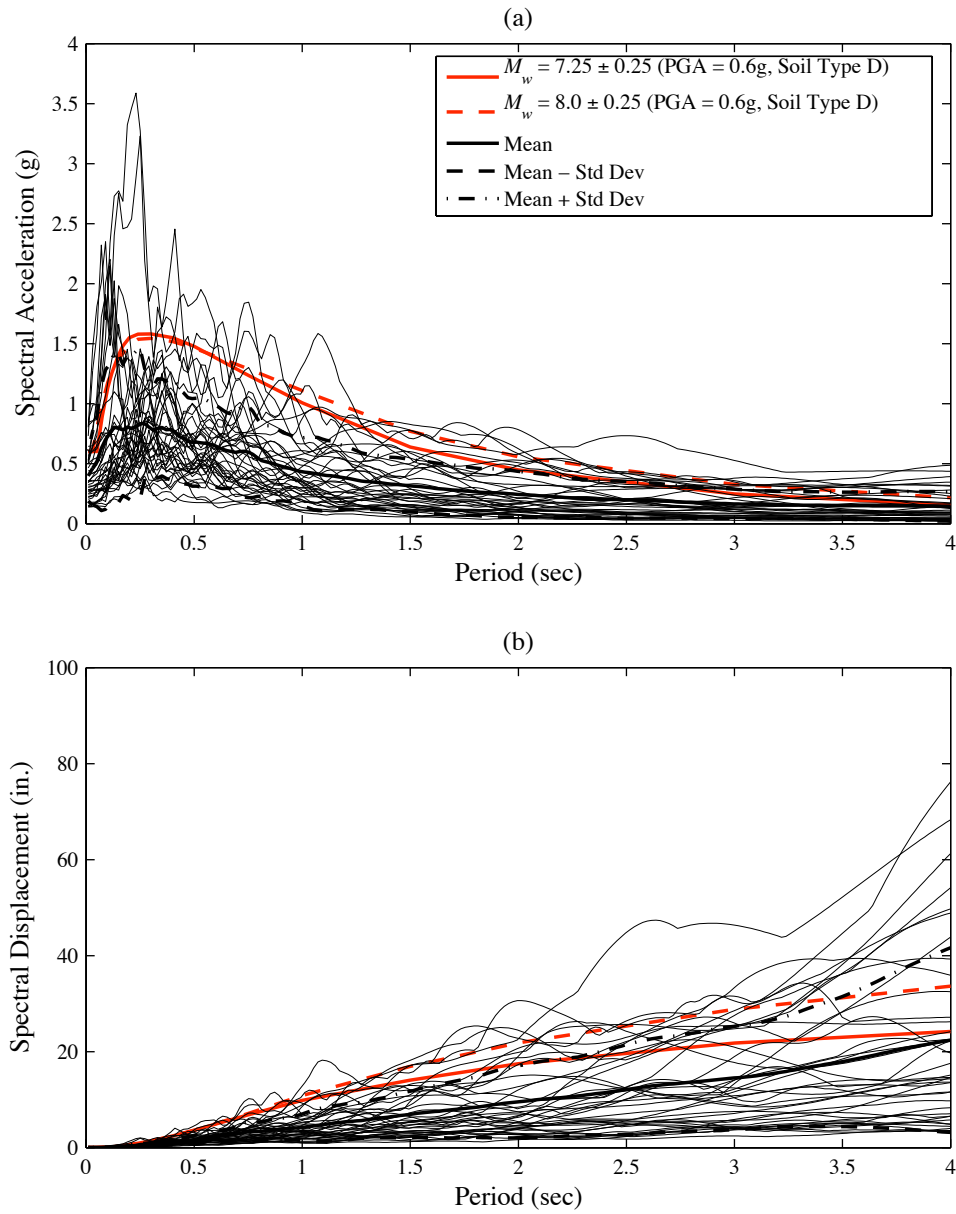


Figure 7.10: Elastic Response Spectra (5% Damping) for Magnitude Bin  $M_w = 7.5 \pm 0.25$ :

(a) Spectral Acceleration and (b) Spectral Displacement

### 7.3.2 Ground Motions Across Fault-Rupture Zones

Ground motions recorded very close to fault-rupture zones are essentially nonexistent, and therefore numerical simulations are necessary. Dreger et al. (2007) numerically simulated ground motions at stations spaced 15 m from the fault (Figure 7.11) for a magnitude 6.5 earthquake. Five fault geometry models systematically varying the dip and rake, while keeping the strike fixed, were performed. Ground motions from the vertical strike-slip (dip = 90 deg, rake = 180 deg) were selected because analyses by Goel and Chopra (2008) on bridges crossing fault-rupture zones found these motions caused the largest seismic demands in the transverse direction. The simulated fault-parallel (FP) and fault-normal (FN) ground displacements at stations across a vertical strike-slip fault are presented in Figure 7.12.

Goel and Chopra (2008) used the ground motions (Figure 7.12) to analyze a bridge with supports spaced at 30 m, i.e., stations 1, 3, 4, and 6. These essentially identical waveforms of fault-parallel ground motions on one side of the fault and fault-normal ground motions across the fault, lend themselves to be used as input for bridges with supports at similar spacings (e.g., 80-120 ft). In this light, the simulated ground motions are applied as follows: stations 1, 3, 4, and 6 are applied to abutment 1, bent 2, bent 3, and abutment 4, respectively.

Figure 7.13 presents the elastic response spectra (5% damping) for FP, FN, and total (FP+FN) ground motions at station 3, including the ARS curve for  $PGA = 0.6g$  and soil profile type D (Caltrans, 2004b, Appendix B). The total ground motion response quantities are calculated by taking the vector sum of the FP and FN response.

As seen in Figure 7.13, there is poor agreement between the spectrum of the total

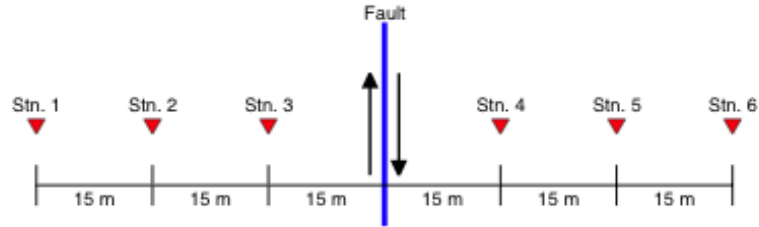


Figure 7.11: Location of Stations Across Fault (from Goel and Chopra, 2008)

ground motion (solid black line) and the ARS curve (red solid line) in the short period range ( $< 1$  sec). However, the spectrum of the total ground motion is larger for the period range 1-3 sec, within the range of periods of Caltrans “ordinary” bridge structures. Additionally, the spectrum of the total ground motion is more influenced by the FN ground motion (dashed-dotted black line) than the FP ground motion (dashed black line), as the spectrum of the total ground motion and the spectrum of the FN ground motion are very similar. The spectrum of the FP ground motion is below the spectrum of the FN and total ground motions, and below the ARS curve, for the entire range of periods.

As seen in the ground displacements (Figure 7.12) and in the response spectra (Figure 7.13), the simulated ground motions lack the high frequency content of recorded ground motions from actual seismic events. This is due to the elastic half space earth model and uniform slip distribution used to generate the ground motions. As discussed by Dreger et al. (2007) these simplifying assumptions affect the character of the ground motions as follows: nonlinear behavior is likely for the range of computed strains; a more complex velocity model with a low velocity zone would have substantial effect on the FN motions; and a variable slip distribution would affect both the directivity component and static offsets, yet the the general shape of the motions would be similar.

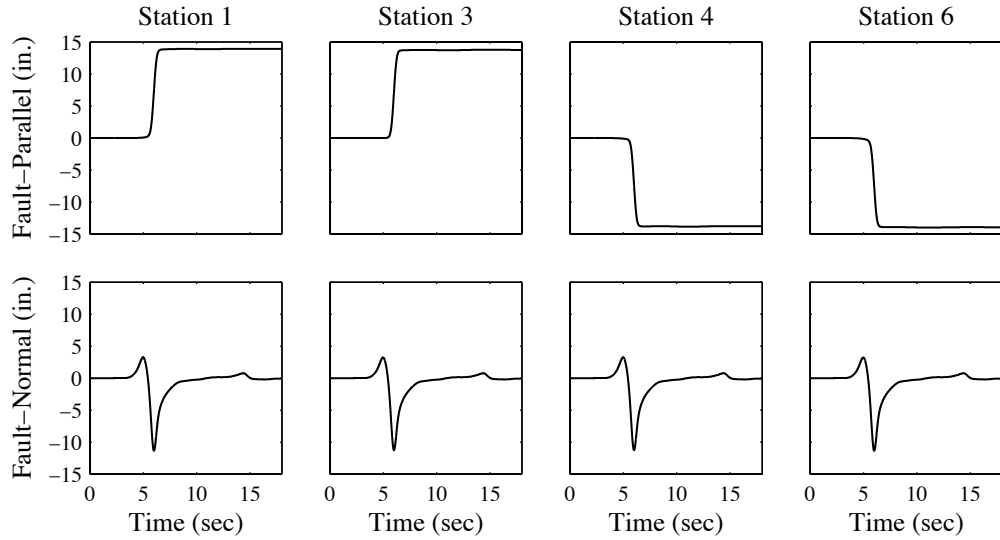


Figure 7.12: Fault-Parallel and Fault-Normal Ground Displacements at Stations Across a Strike-Slip Fault (Adapted from Dreger et al., 2007)

### Other Earthquake Magnitudes

Simulated FP ground motions for earthquakes with different magnitudes on a vertical strike-slip fault were generated according to Dreger et al. (2007), outlined in Goel and Chopra (2008, Appendix A). This simple approach utilizes the relationships for rise time  $T_R$  (Eq. 7.2) and total fault-offset  $u_{go}$  (Eq. 7.3) in terms of magnitude  $M_w$  for motion in the fault-parallel direction (Somerville et al., 1999)

$$T_R = 10^{0.5(M_w - 6.69)} \quad (\text{sec}) \quad (7.2)$$

$$u_{go} = 10^{0.5(M_w - 2.91)} \quad (\text{cm}) \quad (7.3)$$

The ground displacements for the other earthquake magnitudes are obtained by multiplying the time scale (Eq. 7.4) and the displacement scale (Eq. 7.5) of the numerically simulated

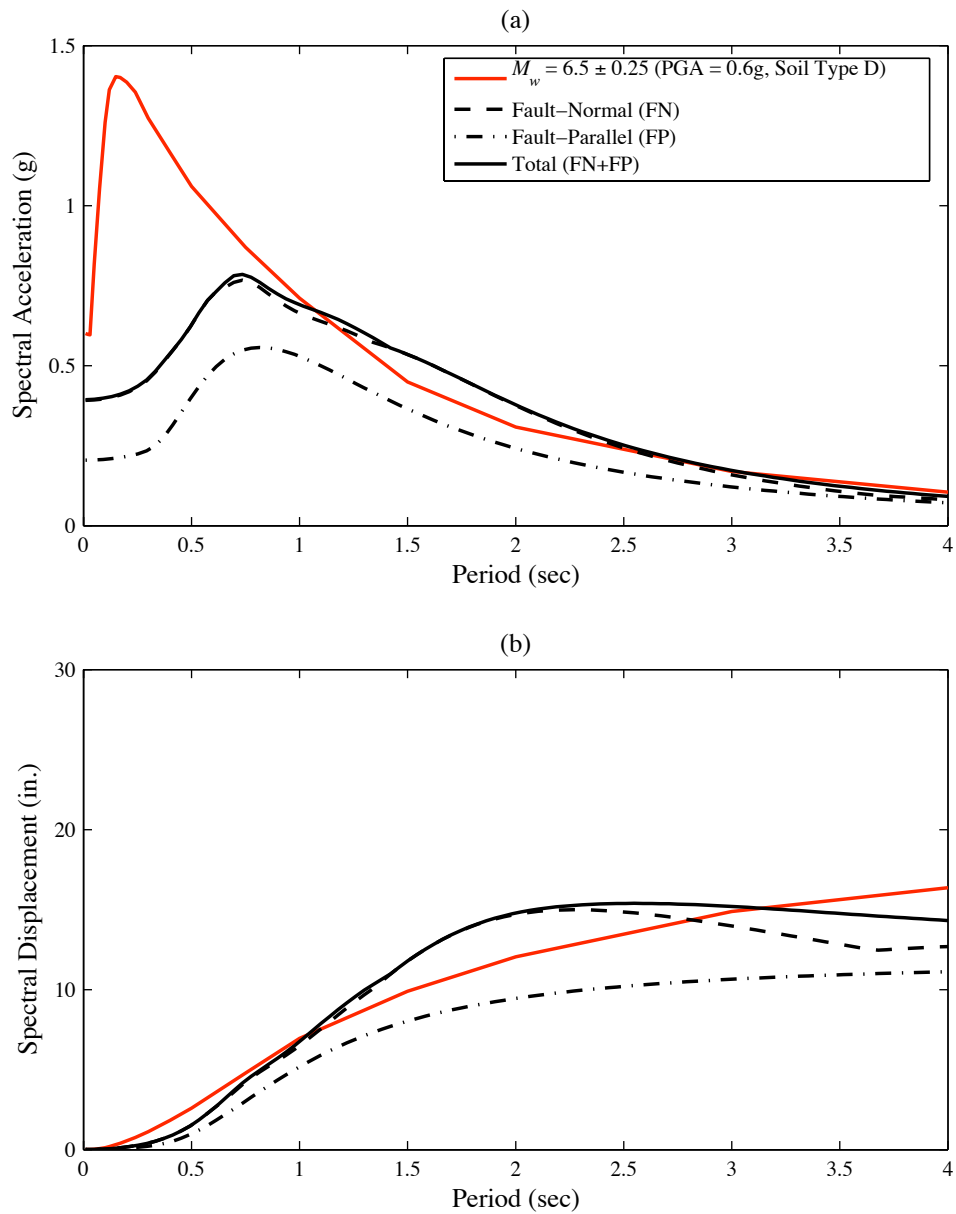


Figure 7.13: Elastic Response Spectra (5% Damping) for Fault-Normal, Fault-Parallel, and Total Ground Motions: (a) Spectral Acceleration and (b) Spectral Displacement

ground displacement for a magnitude 6.5 by the following ratios:

$$\frac{T_R(M_w)}{T_R(M_w = 6.5)} \quad (7.4)$$

$$\frac{u_{go}(M_w)}{u_{go}(M_w = 6.5)} \quad (7.5)$$

The effects of earthquake magnitude on the fault-parallel ground motion, for magnitudes 6.0, 6.5, 7.0, and 7.5, are shown in Figure 7.14. Figure 7.15 presents the elastic response spectra (5% damping) for the ground motions of Figure 7.14.

## 7.4 Seismic Analysis

Prior to seismic analysis, a linear-elastic model, based on the cracked section properties of the box girder and columns, is used to determine the vibration periods and mode shapes of the bridge. The first four vibration periods and mode shapes of the benchmark bridge are shown in Figure 7.16. The lowest vibration mode (1.02 sec) involves transverse vibration of the entire bridge. The second vibration mode (0.57 sec) involves torsional vibration of the bridge about the superstructure center of mass. The third vibration mode (0.35 sec) involves longitudinal vibration of the entire bridge. The fourth vibration mode (0.30 sec) involves vertical vibration of the three superstructure spans.

Damping for all bridges is provided by Rayleigh viscous damping (Chopra, 2001)

$$\mathbf{c} = a_o \mathbf{m} + a_1 \mathbf{k} \quad (7.6)$$

where  $\mathbf{m}$  = mass matrix of the system,  $\mathbf{k}$  = initial elastic stiffness matrix of the system; and  $a_o$  and  $a_1$  = mass- and stiffness-proportionality coefficients. Five percent damping is assumed in the first and third vibration modes. For the benchmark bridge, the mass proportional coefficient is  $0.46 \text{ sec}^{-1}$  and the stiffness proportional coefficient is  $0.0041 \text{ sec}$ .

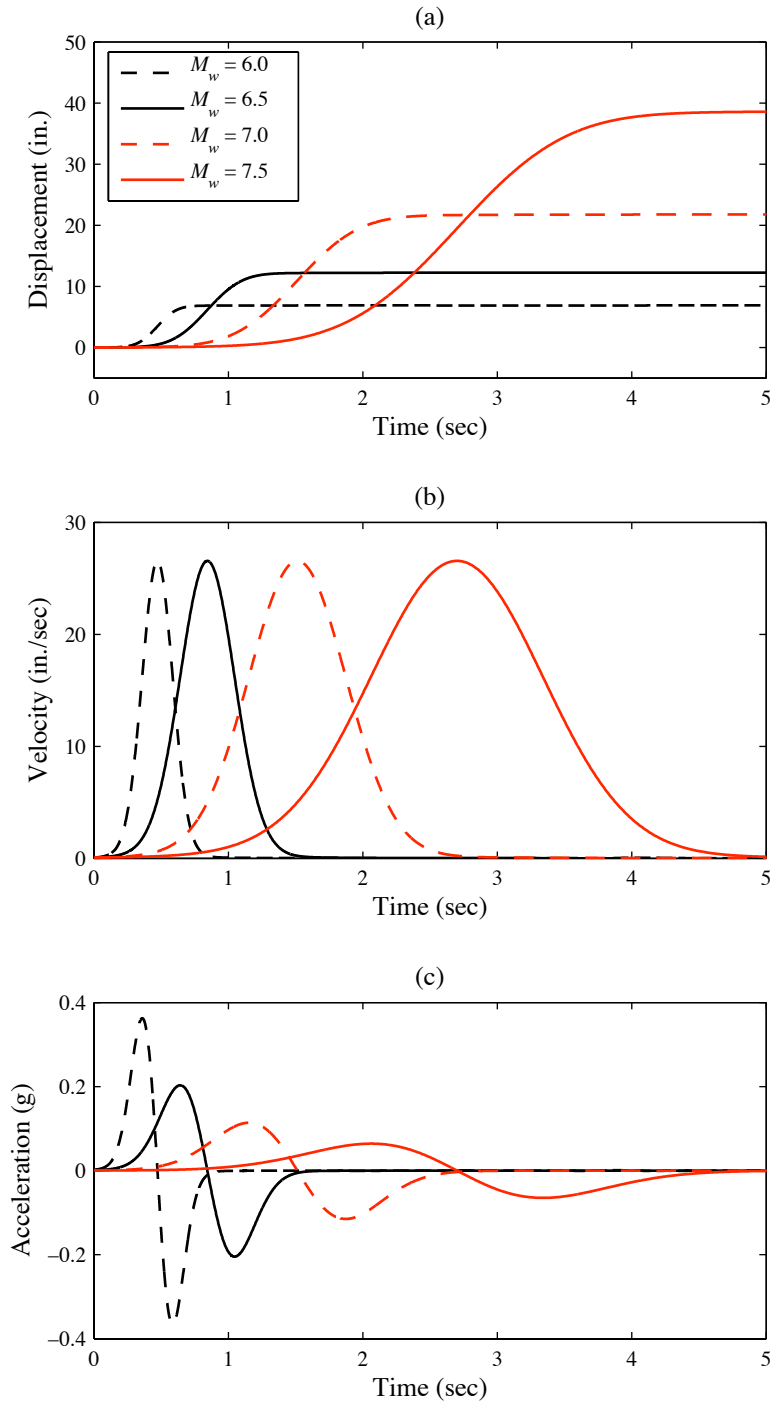


Figure 7.14: Effects of Earthquake Magnitude on Fault-Parallel Ground Motions: (a) Ground Displacement; (b) Ground Velocity; and (c) Ground Acceleration (Adapted from Goel and Chopra, 2008)

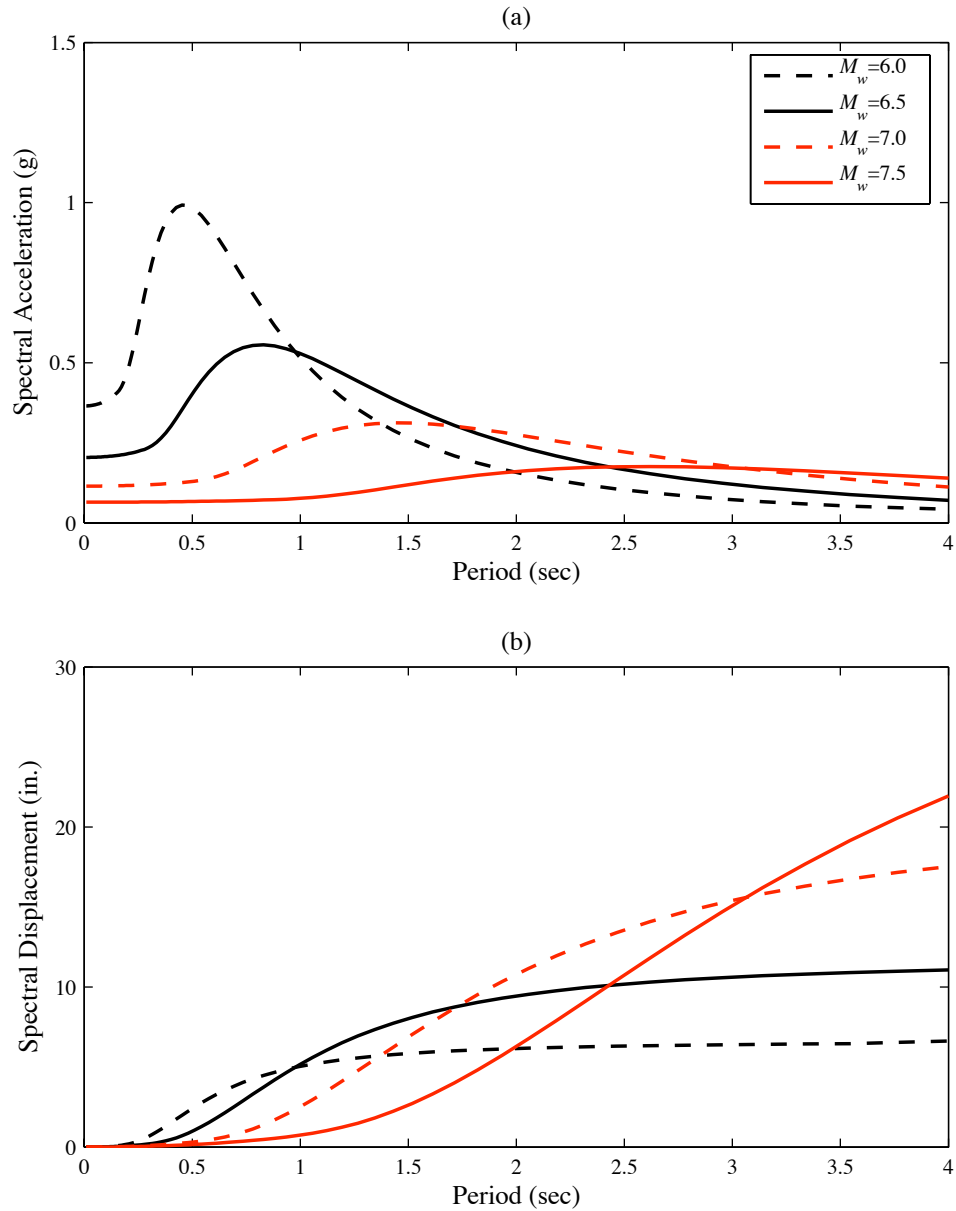


Figure 7.15: Effect of Earthquake Magnitudes on Elastic Response Spectra (5% Damping) for Fault-Parallel Ground Motions: (a) Spectral Acceleration and (b) Spectral Displacement (Adapted from Goel and Chopra, 2008)

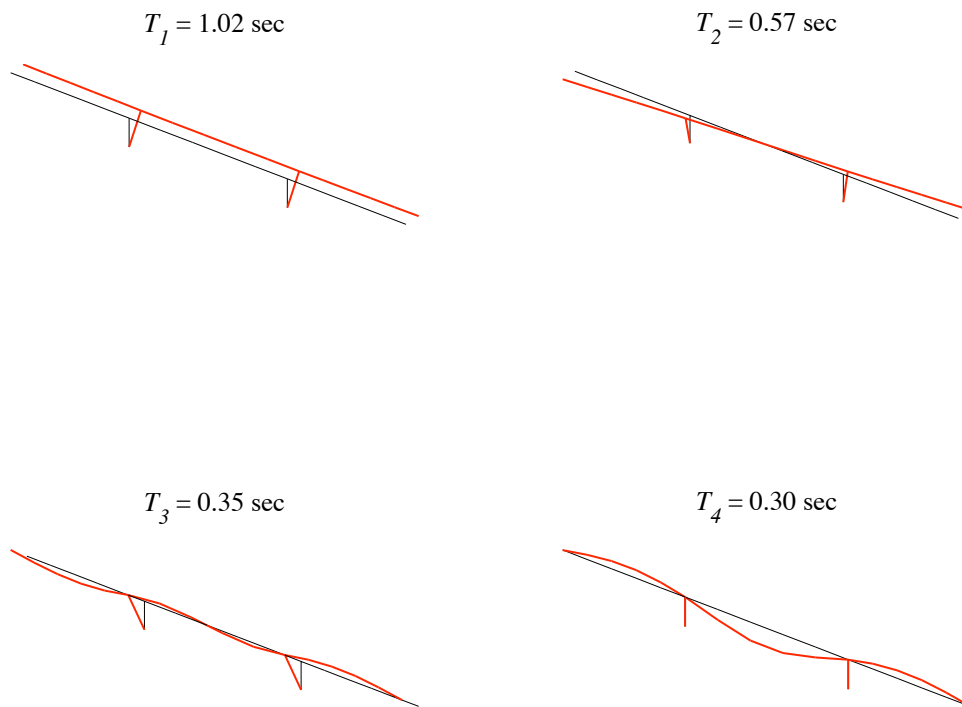


Figure 7.16: Vibration Periods and Mode Shapes of Benchmark Bridge

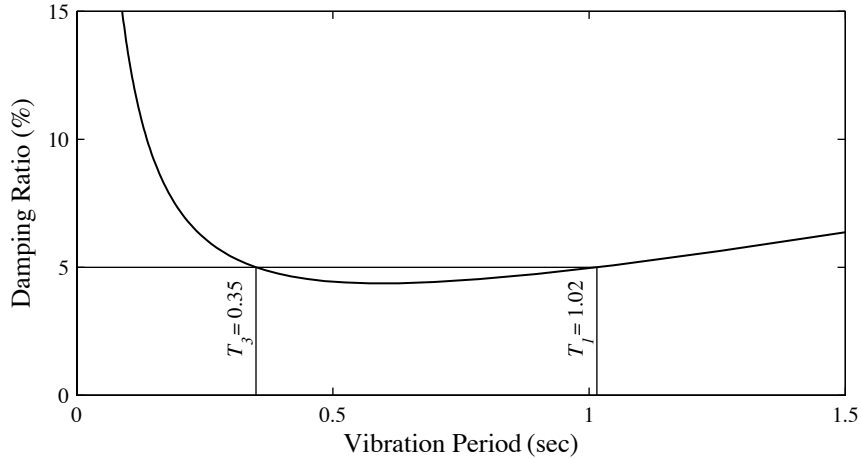


Figure 7.17: Rayleigh Damping of Benchmark Bridge

The variation of damping ratio versus vibration period of the benchmark bridge are shown in Figure 7.17. The damping ratio for modes 1, 2, 3, and 4 are 5%, 4.4%, 5%, and 5.5%, respectively.

A static analysis is first performed by applying the gravity loads. Next, the dynamic analysis is performed in *OpenSees* using Newmark's average acceleration time integrator with Newton-Raphson iteration to advance to the next time step (Filippou and Fenves, 2004). The norm of the displacement increment (`NormDispIncr`) test with a convergence tolerance of  $1 \times 10^{-9}$  is used to monitor convergence at each iteration step of the solution for all dynamic analyses.

For the near-fault records, each pair of records is run in two orthogonal directions using the uniform excitation (`UniformExcitation`) pattern. First, horizontal components 1 and 2 are input as the longitudinal and transverse excitations, respectively, and then the horizontal components are swapped, i.e., horizontal component 1 is the transverse excitation and horizontal component 2 is the longitudinal excitation. For the fault-ruputre ground

motions, the ground displacements are input as support excitations at the base nodes and the imposed nodal displacements and boundary constraints are enforced using the penalty method with a factor of  $1 \times 10^{12}$ .

## 7.5 Results

Figures 7.18 and 7.19 demonstrate that the benchmark bridge model is working properly; flexural response of the columns is expected without twist under near-fault ground motion and simultaneous flexural and torsional response of the columns is expected under ground motion crossing a fault. The dynamic response of the benchmark bridge subjected to a recorded near-fault ground motion (Loma Prieta 1989 earthquake, Station LGPC) and a simulated ground motion crossing a fault (magnitude 6.5 event) are presented in Figures 7.18 and 7.19, respectively. Both figures show (a) column longitudinal displacement history; (b) column transverse displacement history; (c) column twist history; (d) bent 2 Y moment vs. X displacement; (e) bent 2 X moment vs. Y displacement; (f) bent 2 torque vs. twist; (g) bent 3 Y moment vs. X displacement; (h) bent 3 X moment vs. Y displacement; and (i) bent 3 torque vs. twist.

The analysis results are focused on the seismic torsion demand of the columns (bents 2 and 3) in terms of the twist ductility. The twist ductility is defined as

$$\mu_t = \frac{\theta_{twist}}{\psi_y L} \quad (7.7)$$

where  $\theta_{twist}$  = maximum twist demand from seismic analysis,  $\psi_y$  = unit twist to yield the hoops (Figure 7.8), and  $L$  = column length (varies).

Figures 7.20 and 7.21 present the twist demand of the bridges subjected to ground motions from magnitude bins  $M_w = 7.0 \pm 0.25$  and  $M_w = 7.5 \pm 0.25$ , respectively. The twist

ductility demands for the same motions are shown in Figures 7.22 and 7.23, respectively. Figures 7.24 and 7.25 plot the twist ductility demand vs. displacement ductility demand for the same motions.

The twist history response of bridges crossing a fault, subjected to the simulated ground motions for a  $M_w = 6.5$  event, are shown in Figures 7.26 to 7.29. Each plot shows the twist history response due to the total ground motion (FN+FP) and the FP component only. The longitudinal versus transverse displacement of bents 2 and 3 of Bridge No. 1 and 16 are shown in Figures 7.33 and 7.34, respectively, for the total ground motion and FP component only. The twist demand of the bridges subjected to the total ground motion and FP component only are presented in Figure 7.30. Figures 7.31 and 7.32 show the twist ductility and twist ductility vs. displacement ductility, respectively, of bents 2 and 3 of each bridge due to the total ground motion.

Figures 7.35 to 7.38 present the twist history response of bridges subjected to scaled FP ground motions. Each plot shows the twist history response for FP ground motions corresponding to  $M_w = 6.0, 6.5, 7.0,$  and  $7.5$  events. The twist ductility and twist ductility vs. displacement ductility of bents 2 and 3 of each bridge, grouped by event magnitude, are shown in Figures 7.40 and 7.41, respectively.

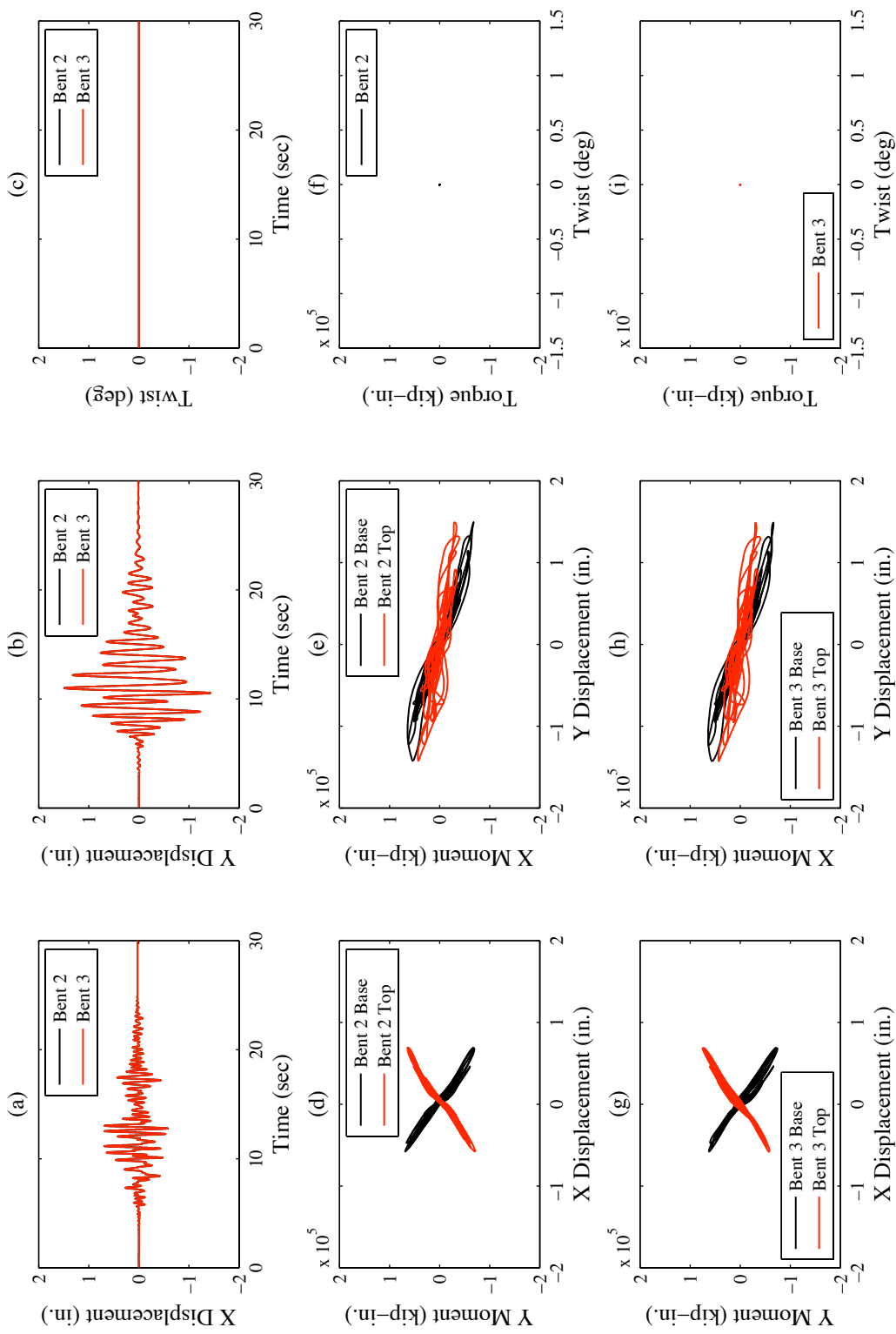


Figure 7.18: Dynamic Response of Benchmark Bridge Subjected to Loma Prieta 1989 Earthquake, Station LGPC

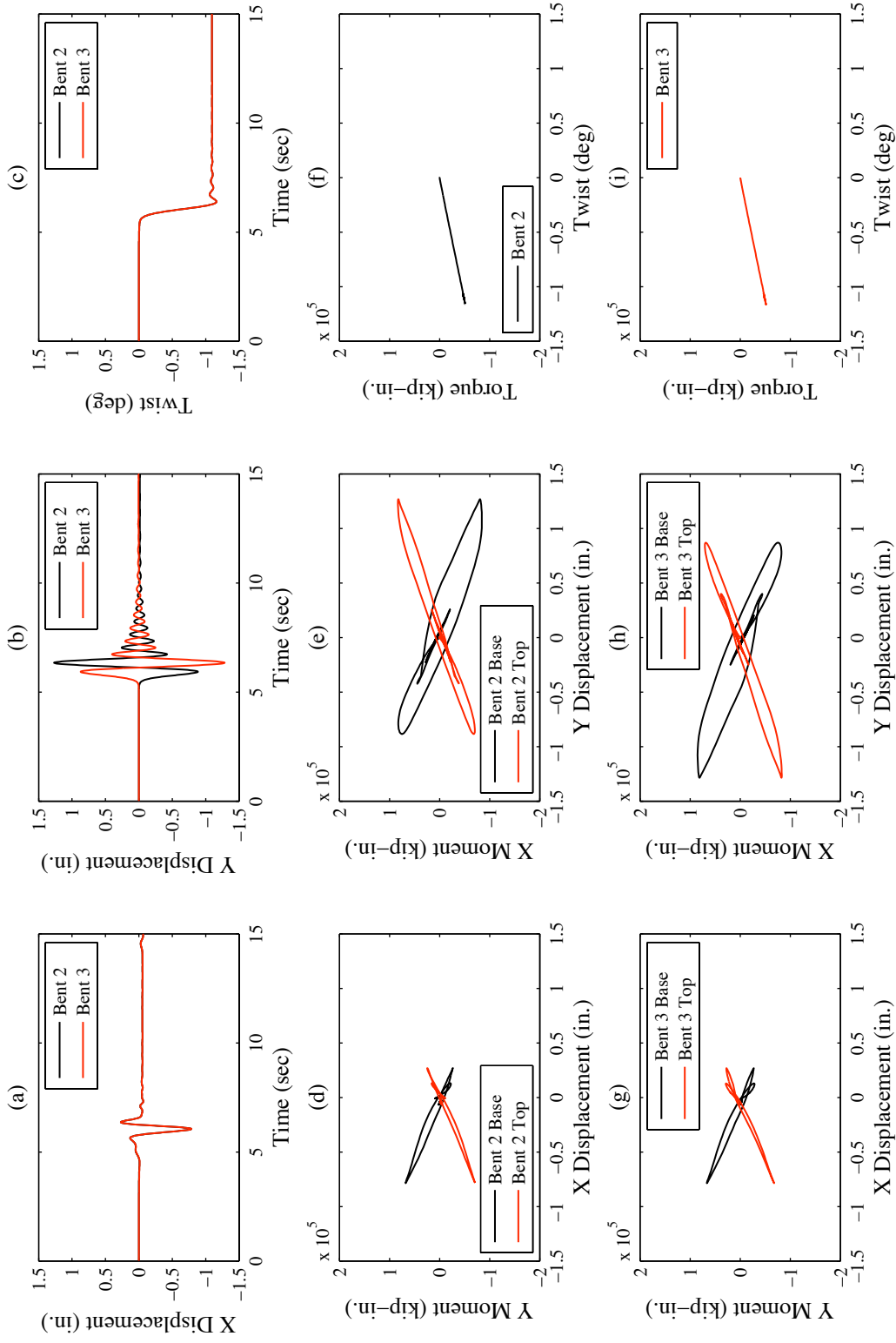


Figure 7.19: Dynamic Response of Benchmark Bridge Subjected to a Simulated Magnitude 6.5 Event

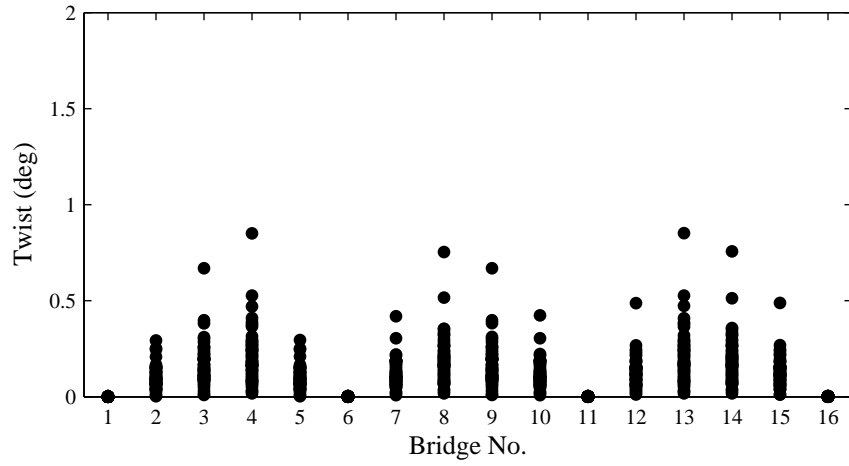


Figure 7.20: Twist Demand of Bridges Subjected to Magnitude Bin  $M_w = 7.0 \pm 0.25$  Ground Motions

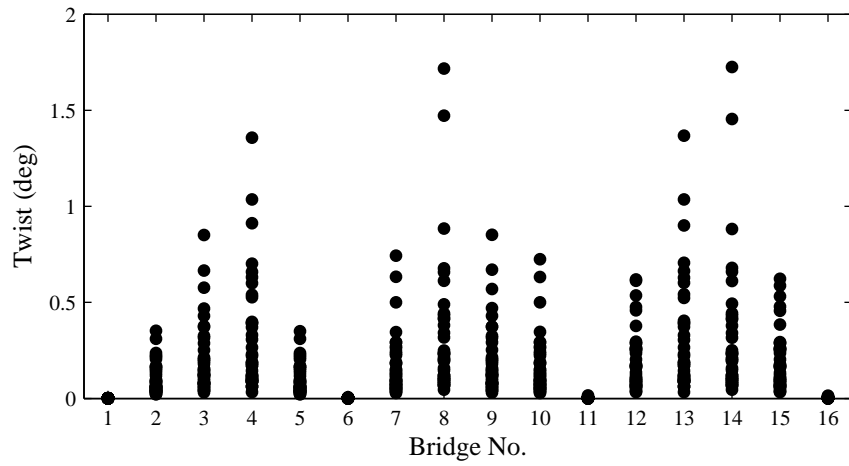


Figure 7.21: Twist Demand of Bridges Subjected to Magnitude Bin  $M_w = 7.5 \pm 0.25$  Ground Motions

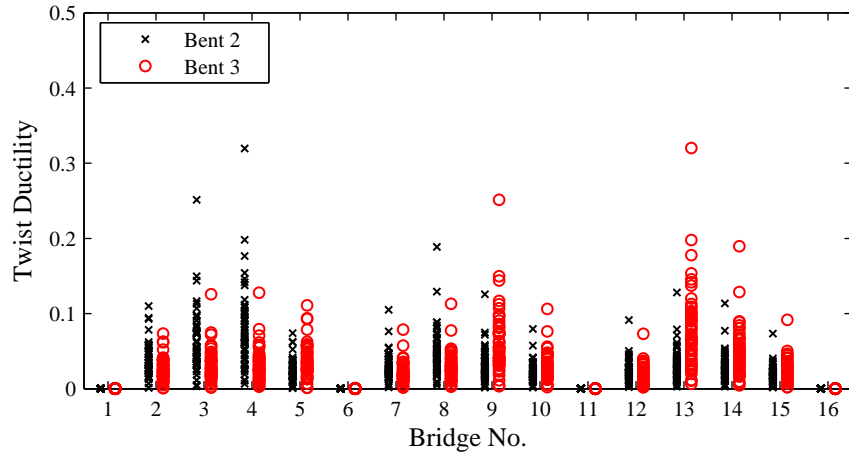


Figure 7.22: Twist Ductility of Bridges Subjected to Magnitude Bin  $M_w = 7.0 \pm 0.25$  Ground Motions

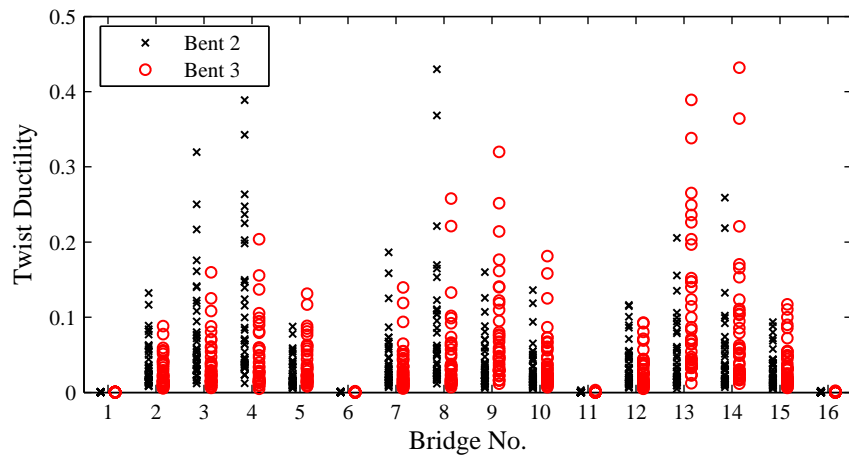


Figure 7.23: Twist Ductility of Bridges Subjected to Magnitude Bin  $M_w = 7.5 \pm 0.25$  Ground Motions

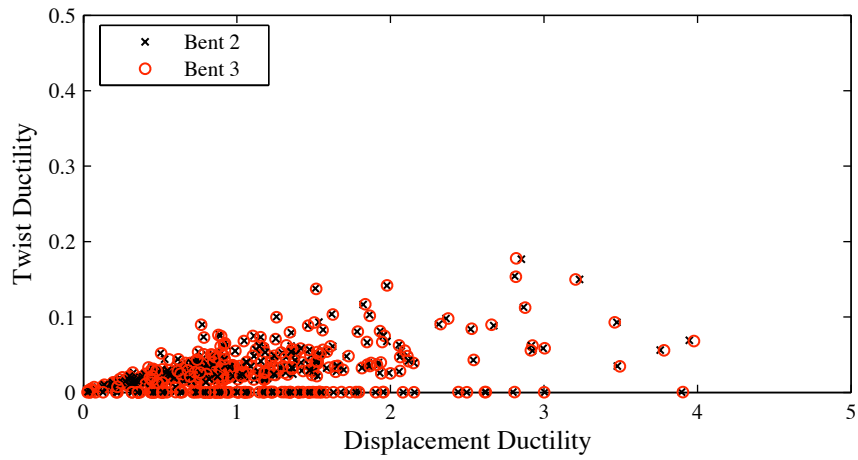


Figure 7.24: Twist Ductility vs. Displacement Ductility of Bridges Subjected to Magnitude Bin  $M_w = 7.0 \pm 0.25$  Ground Motions

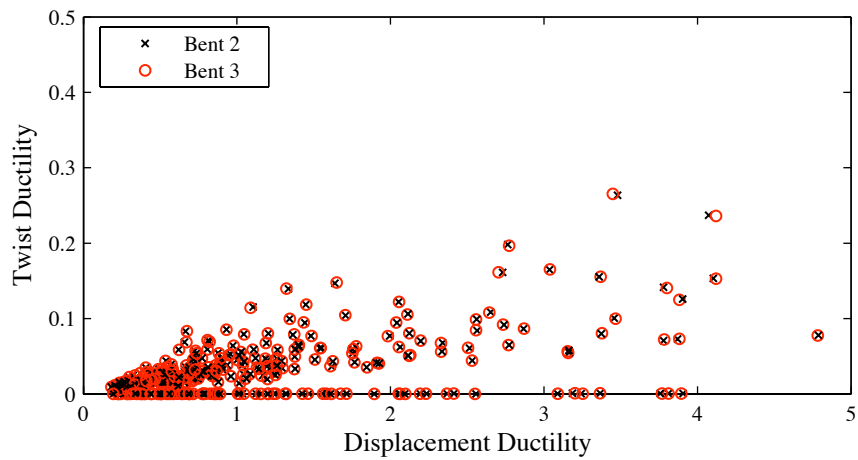


Figure 7.25: Twist Ductility vs. Displacement Ductility of Bridges Subjected to Magnitude Bin  $M_w = 7.5 \pm 0.25$  Ground Motions

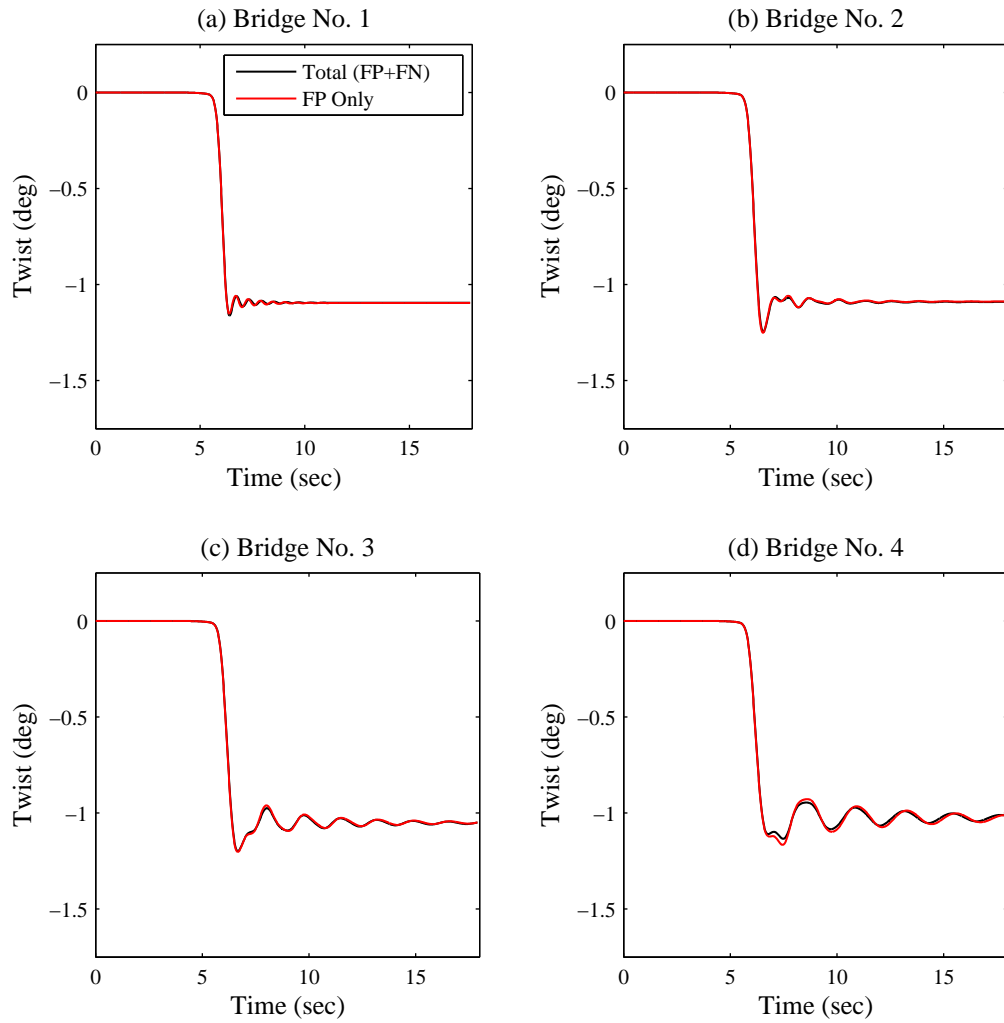


Figure 7.26: Twist History of Bridge Nos. 1 to 4 Subjected to Simulated Ground Motions Crossing Fault

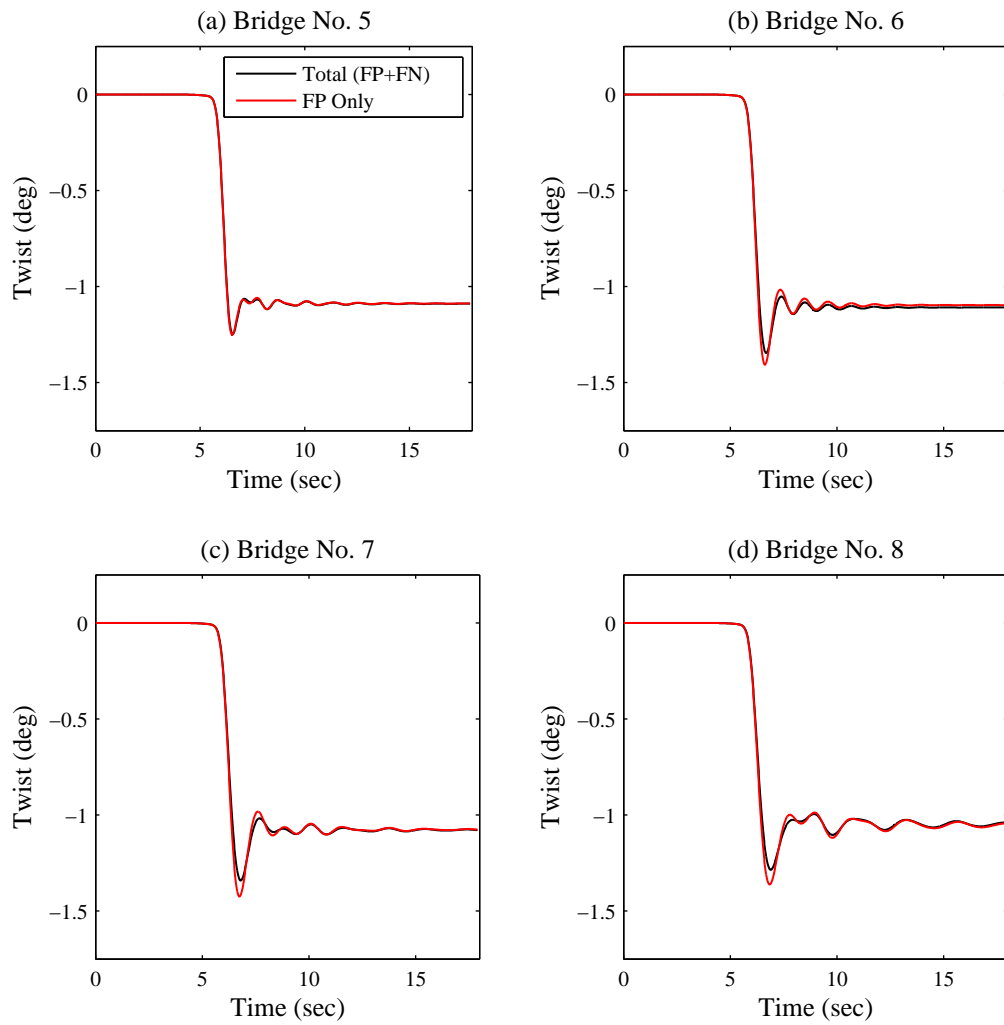


Figure 7.27: Twist History of Bridge Nos. 5 to 8 Subjected to Simulated Ground Motions Crossing Fault

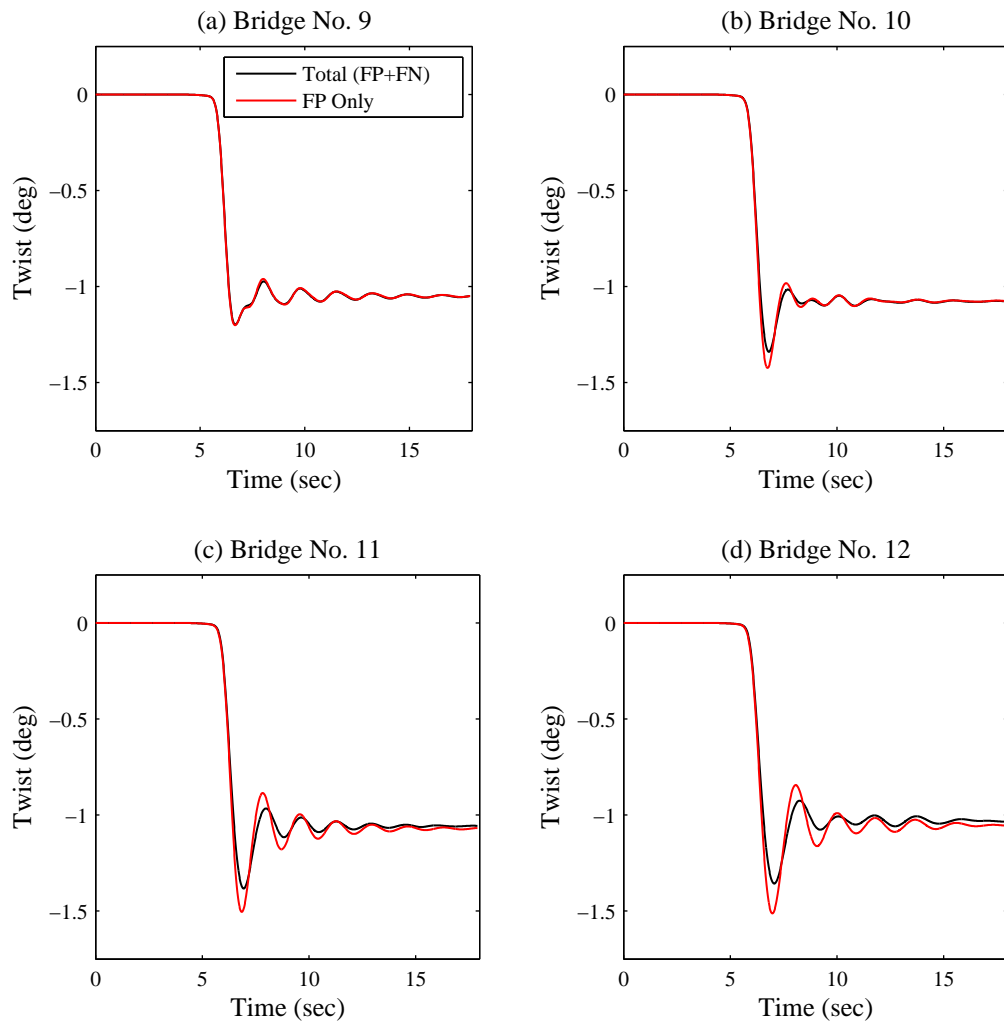


Figure 7.28: Twist History of Bridge Nos. 9 to 12 Subjected to Simulated Ground Motions Crossing Fault

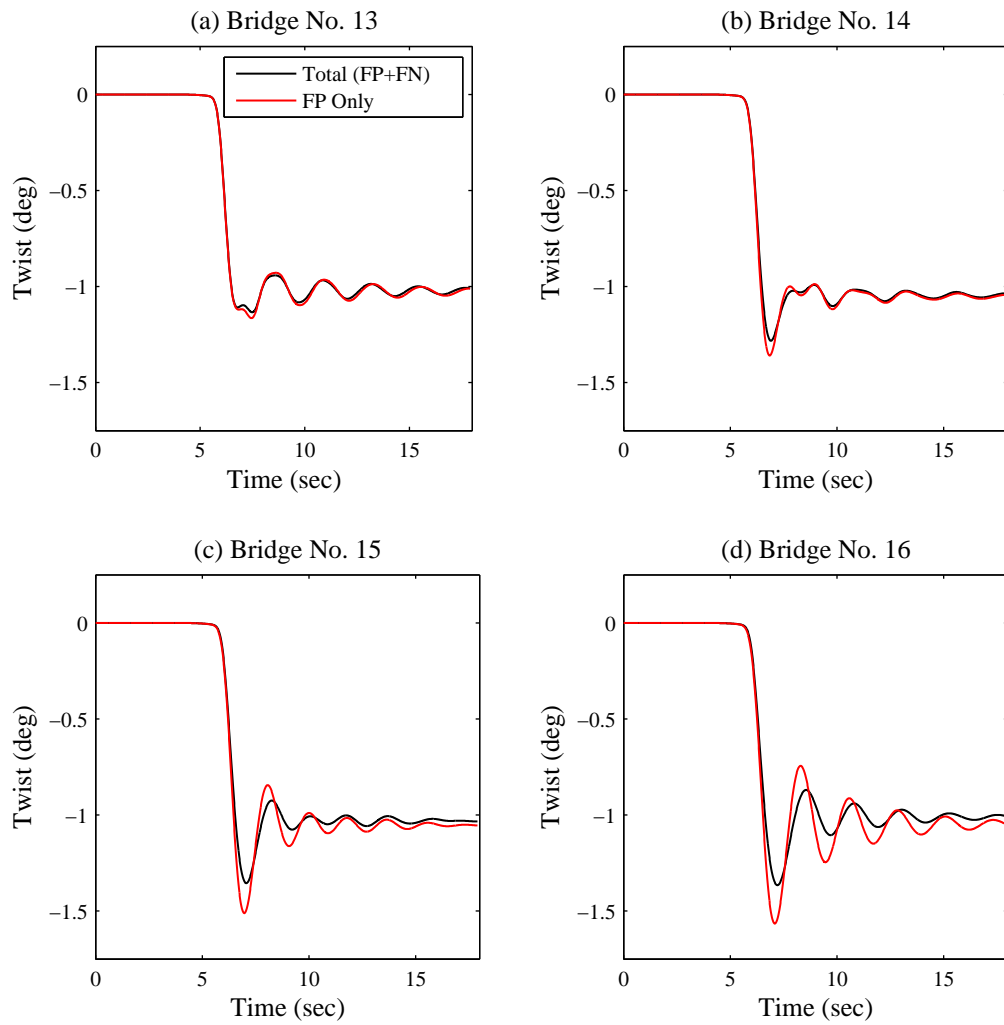


Figure 7.29: Twist History of Bridge Nos. 13 to 16 Subjected to Simulated Ground Motions Crossing Fault

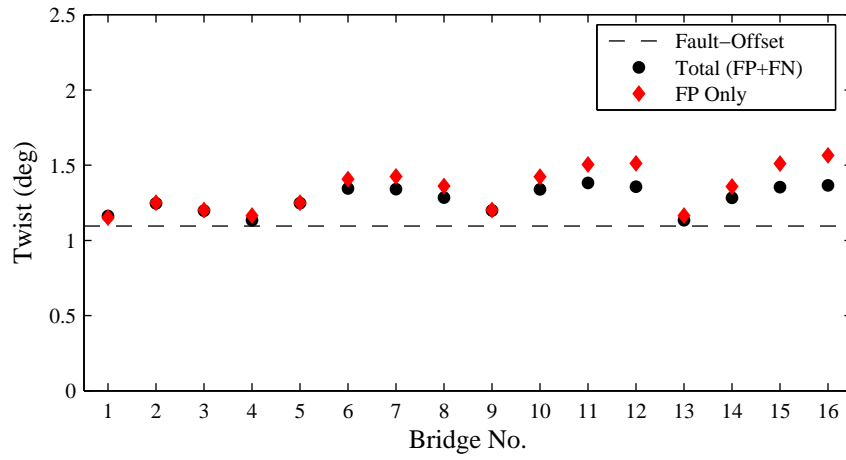


Figure 7.30: Twist Demand of Bridges Subjected to Simulated Ground Motions Crossing Fault

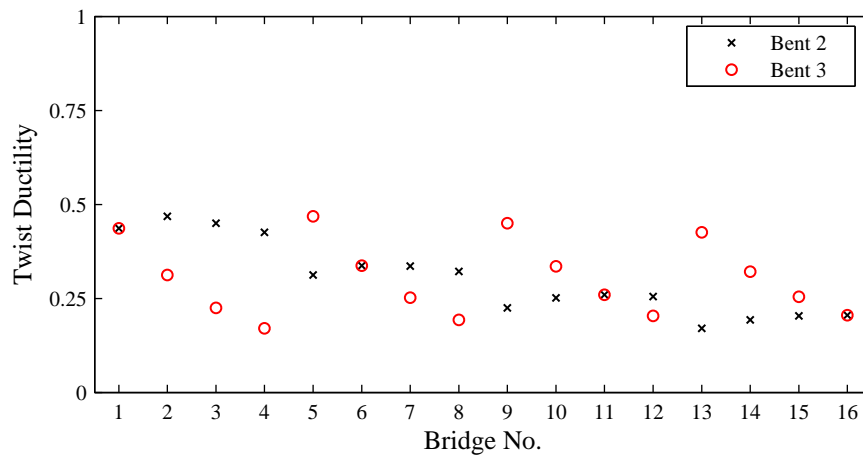


Figure 7.31: Twist Ductility of Bridges Subjected to Simulated Ground Motions Crossing Fault

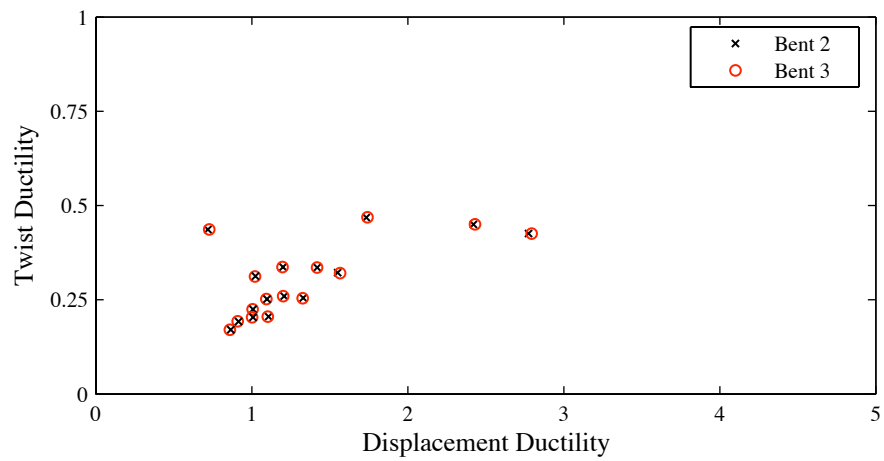


Figure 7.32: Twist Ductility vs. Displacement Ductility of Bridges Subjected to Simulated Ground Motions Crossing Fault

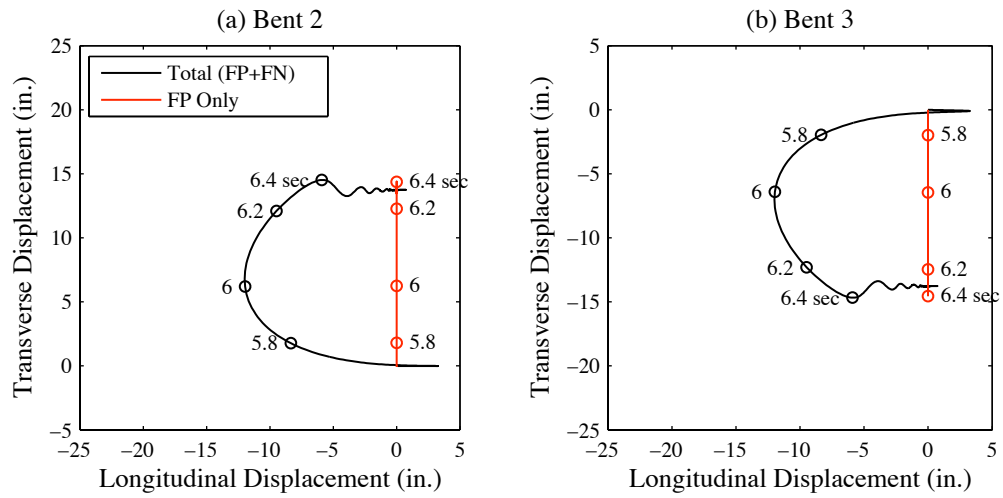


Figure 7.33: Longitudinal and Transverse Column Displacements of Bridge No. 1

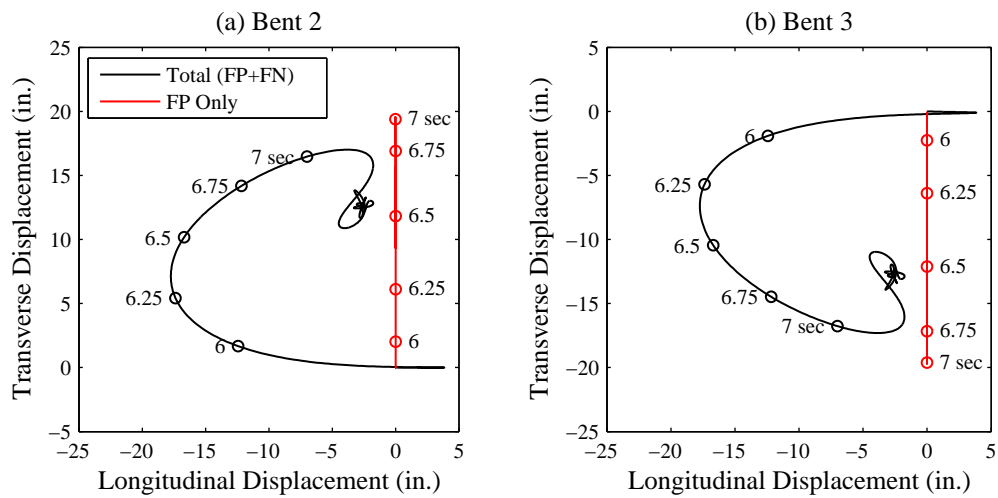


Figure 7.34: Longitudinal and Transverse Column Displacements of Bridge No. 16

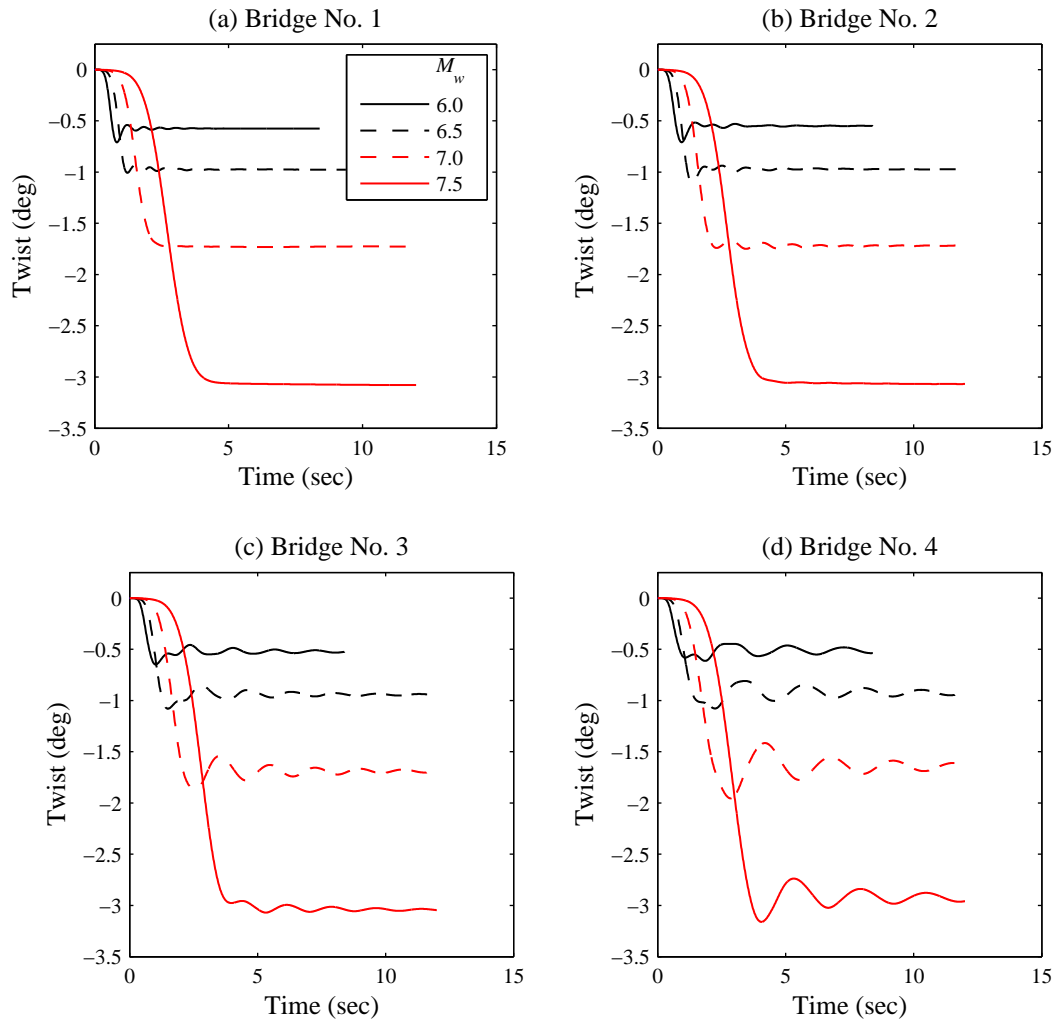


Figure 7.35: Twist History of Bridge Nos. 1 to 4 Subjected to Scaled FP Ground Motions

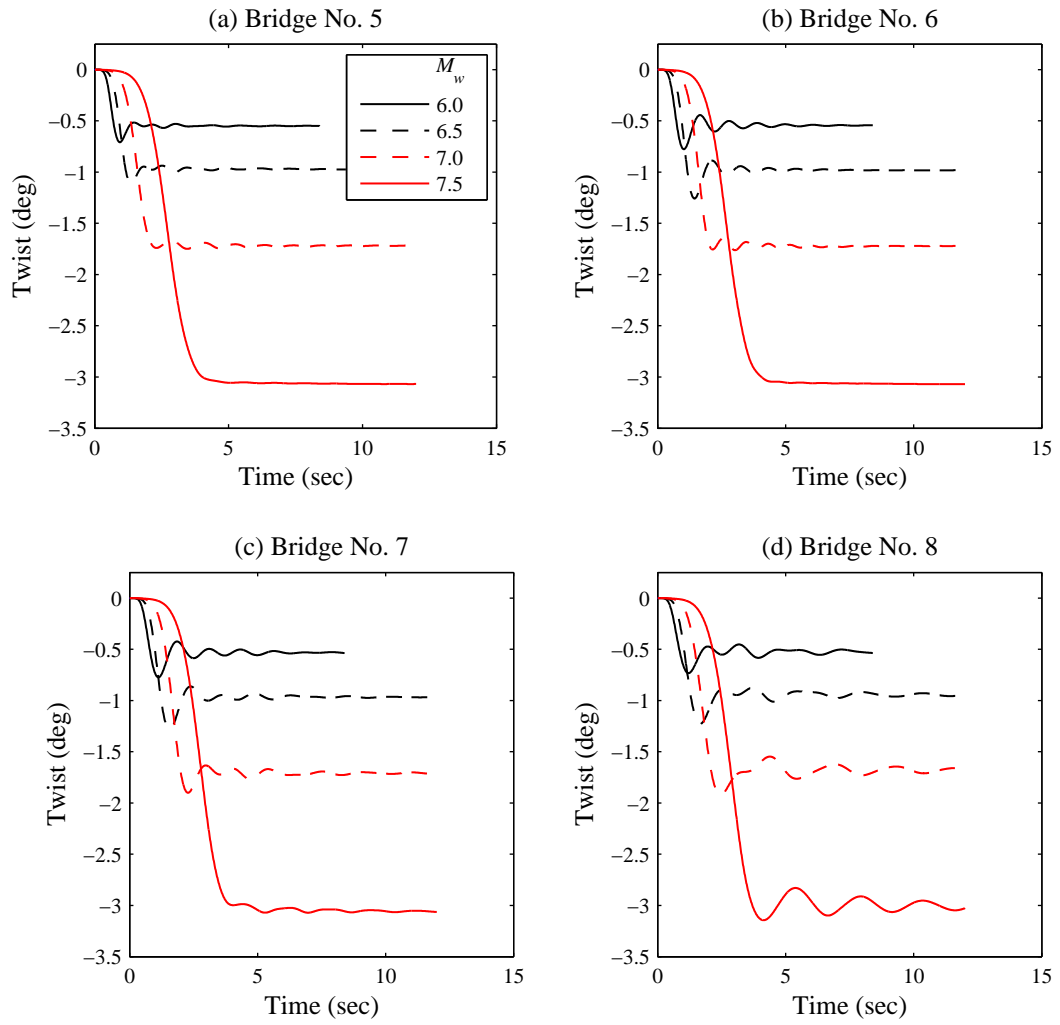


Figure 7.36: Twist History of Bridge Nos. 5 to 8 Subjected to Scaled FP Ground Motions

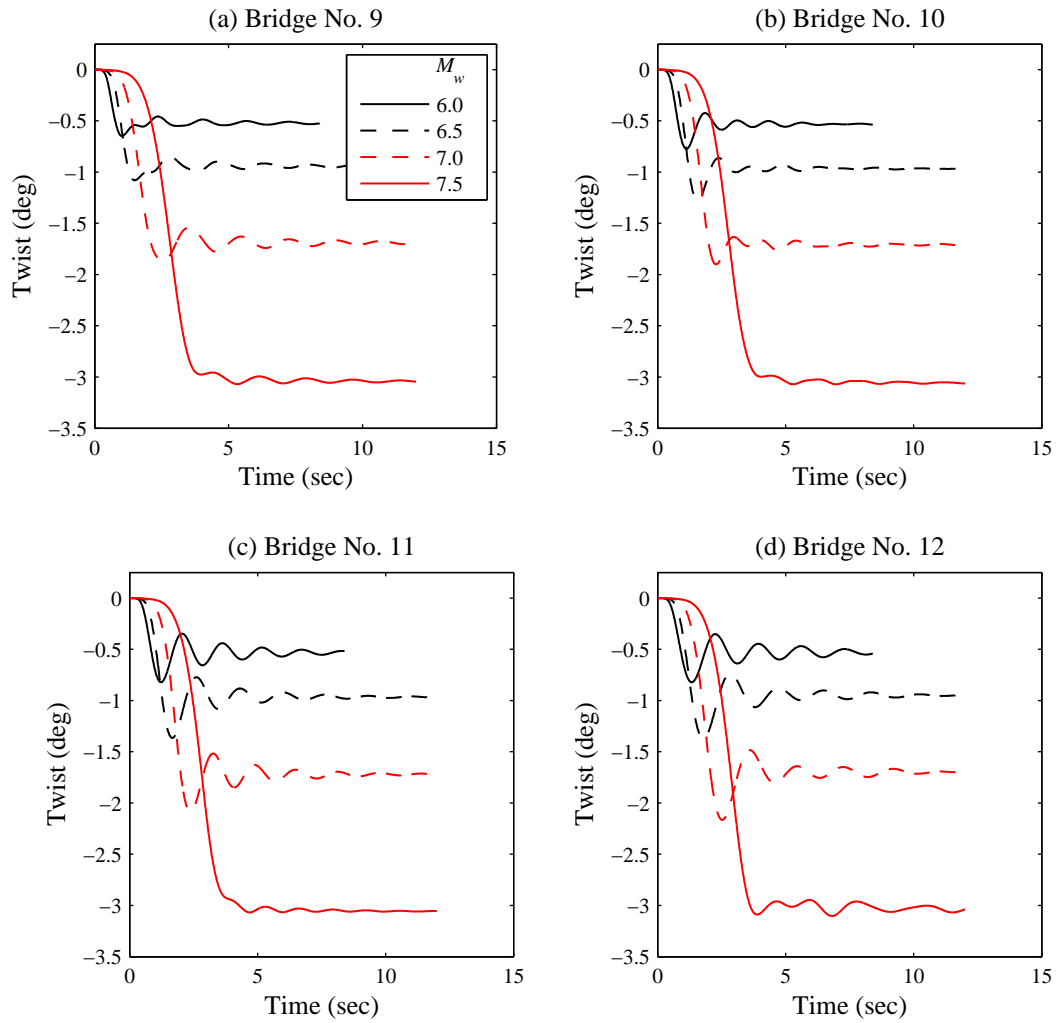


Figure 7.37: Twist History of Bridge Nos. 9 to 12 Subjected to Scaled FP Ground Motions

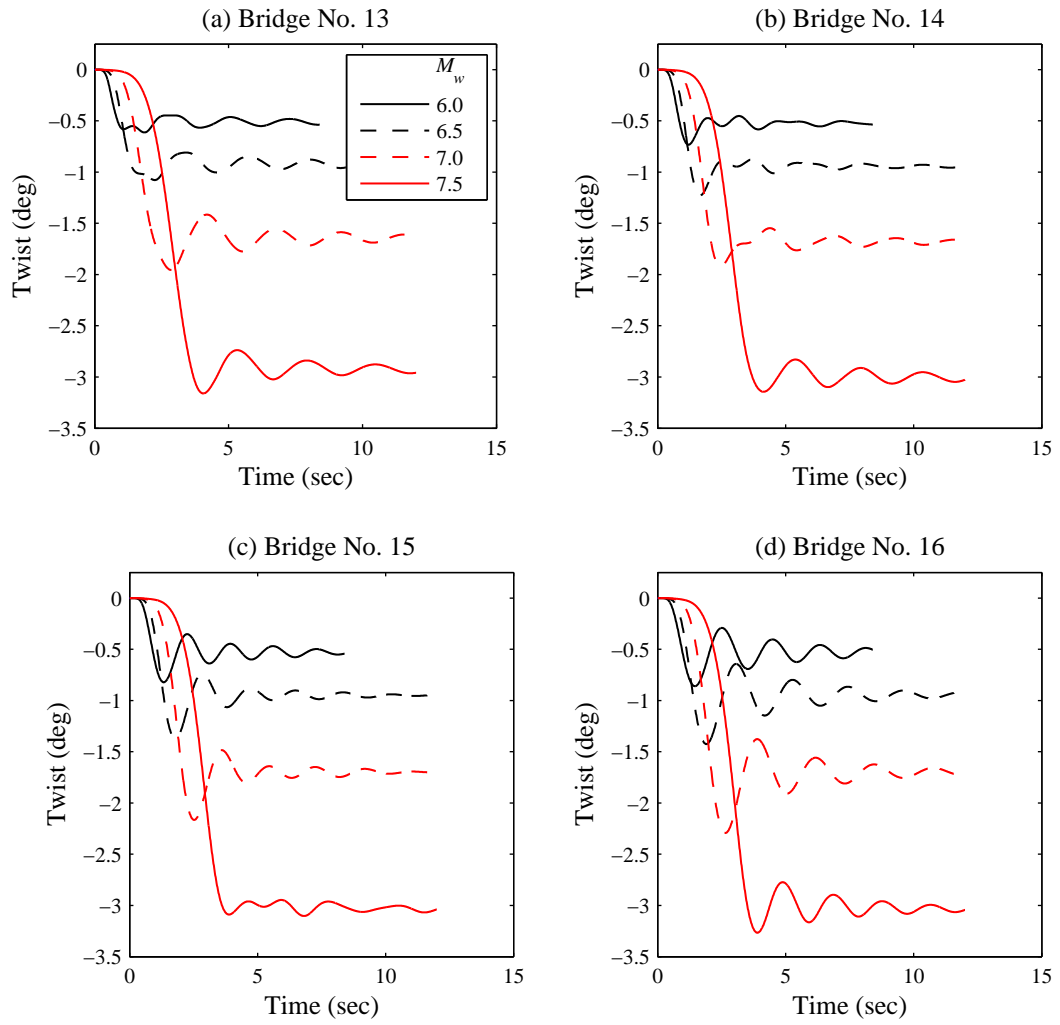


Figure 7.38: Twist History of Bridge Nos. 13 to 16 Subjected to Scaled FP Ground Motions

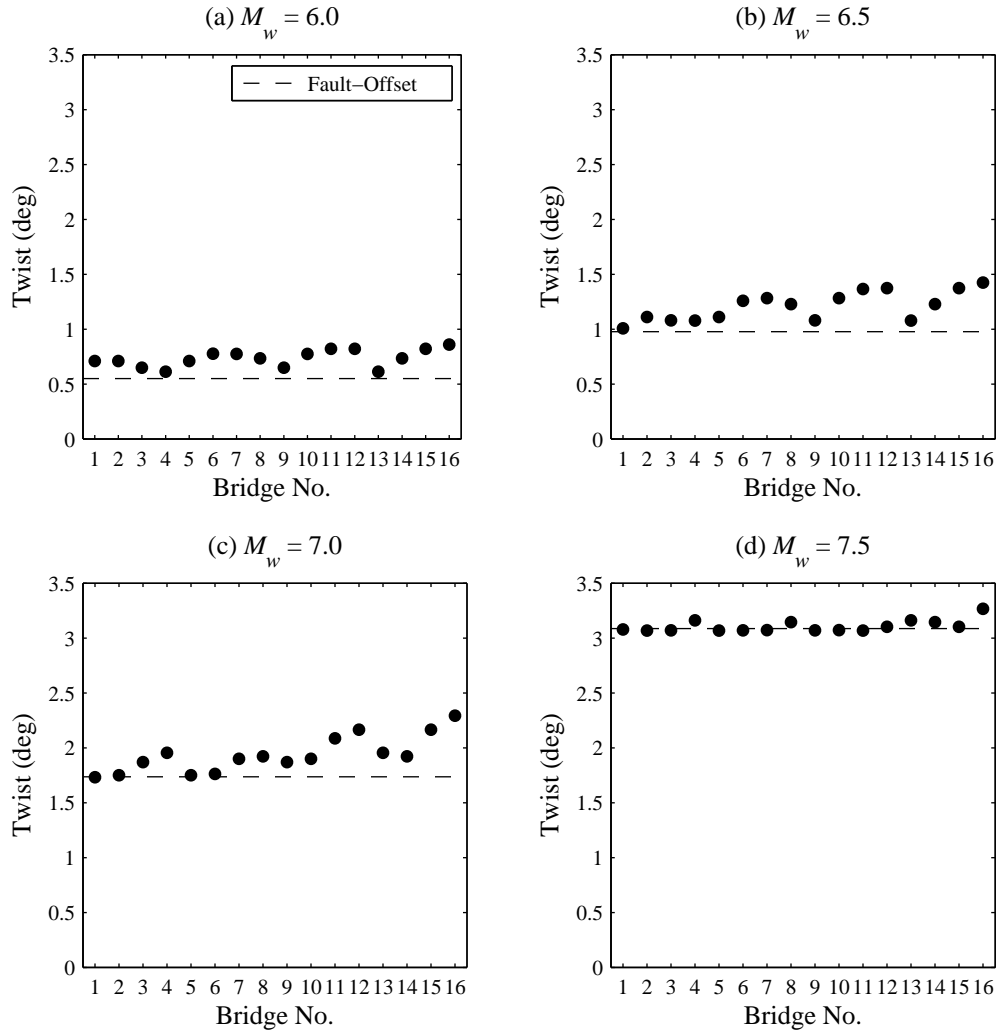


Figure 7.39: Twist Demand of Bridges Subjected to Scaled FP Ground Motions

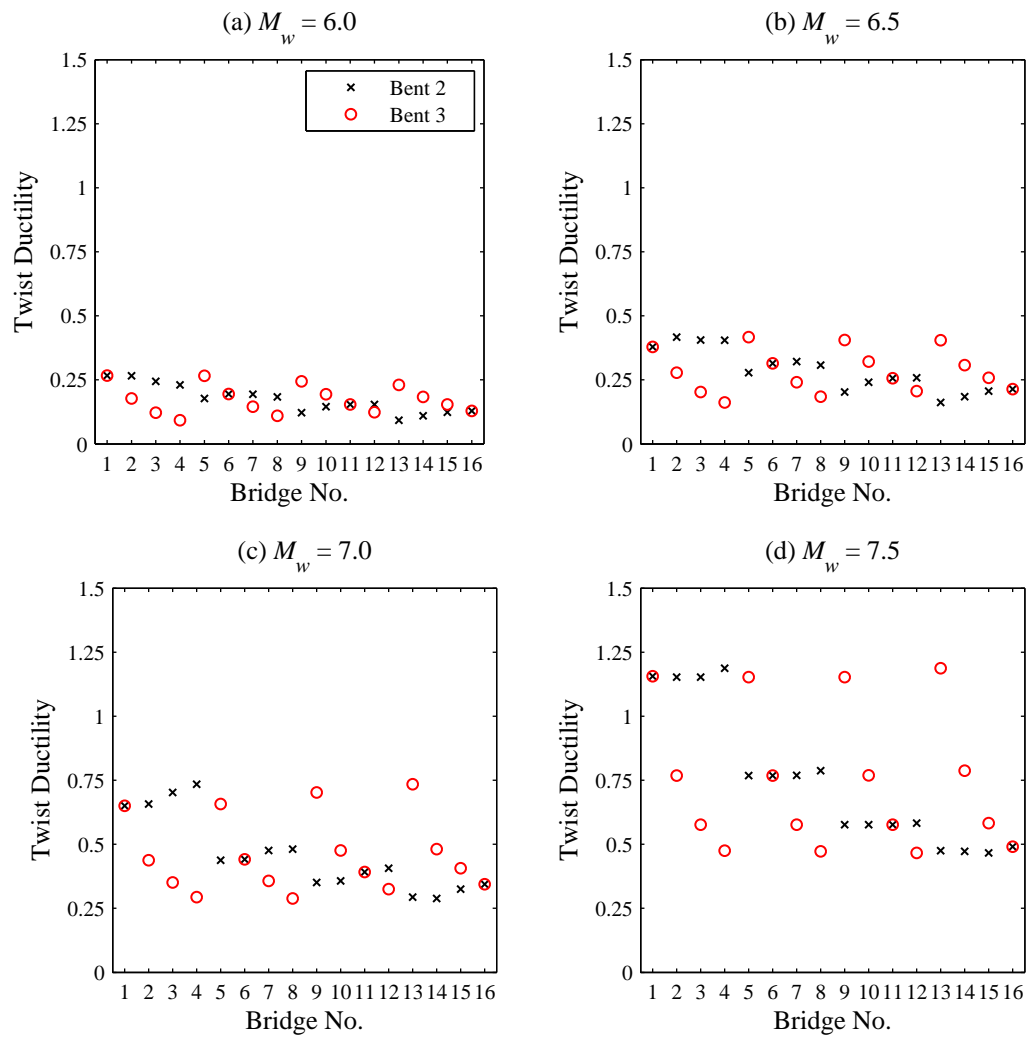


Figure 7.40: Twist Ductility of Bridges Subjected to Scaled FP Ground Motions

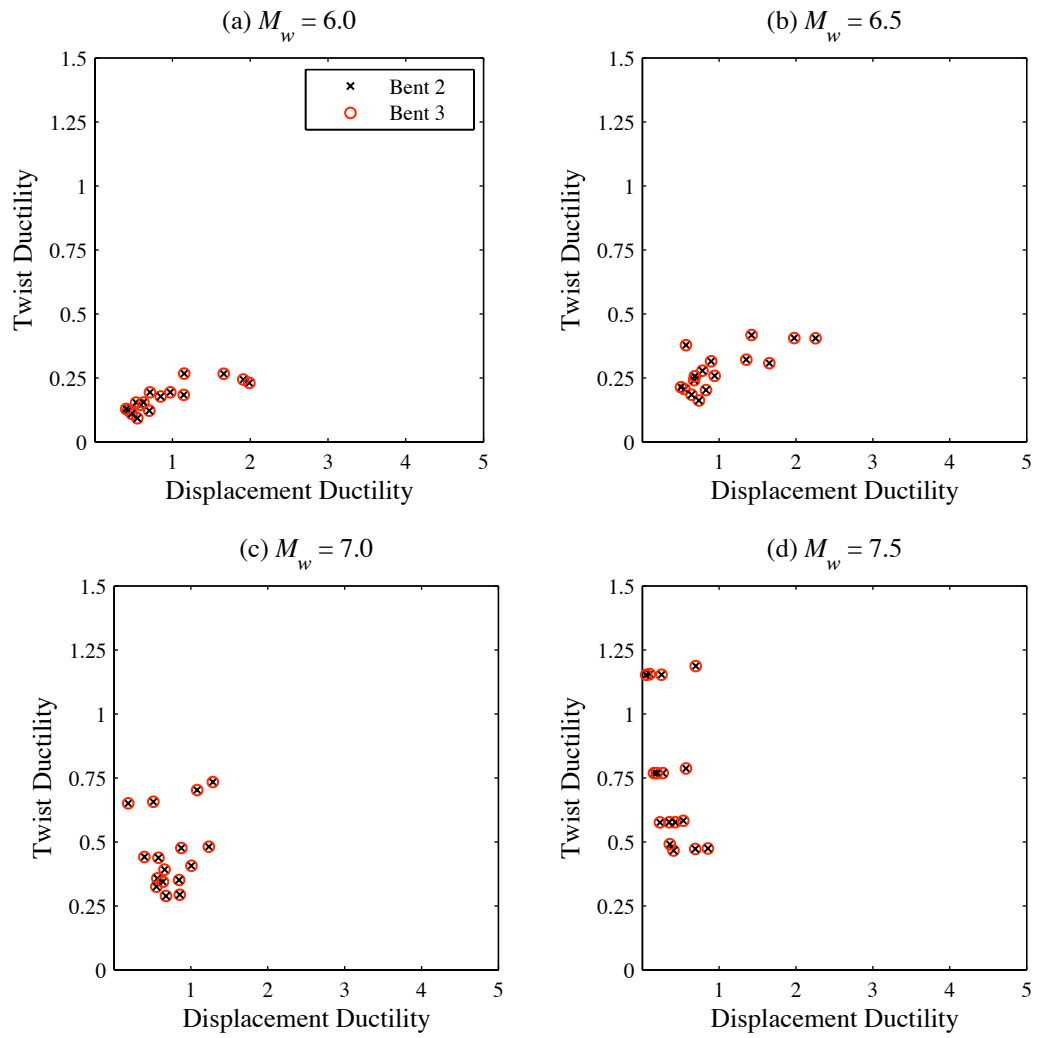


Figure 7.41: Twist Ductility vs. Displacement Ductility of Bridges Subjected to Scaled FP Ground Motions

## 7.6 Findings

The twist demand for magnitude bin  $M_w = 7.0 \pm 0.25$  (Figures 7.20) and  $M_w = 7.5 \pm 0.25$  (Figure 7.21) varies according to bridge configuration. As expected, for bridges with equal column heights (Bridge No. 1, 6, 11, and 16), there is essentially zero twist demand due to the symmetric stiffness and uniform ground motion applied. However, twist occurs for the bridges having asymmetric stiffness, i.e., unequal column heights (e.g., Bridge Nos. 4 and 13). The largest twist demands tend to occur for columns with larger aspect ratios, which also require more twist to yield the hoops. Thus, a better representation of the seismic torsion demand on the columns is the twist ductility. As seen in Figures 7.22 and 7.23, the twist ductility does not exceed 0.5 for any of the bridges subjected to the near-fault ground motions (Tables 7.3 and 7.4). The maximum displacement ductility at the maximum twist ductility is approximately 2.8 and 3.5 for magnitude bin  $M_w = 7.0 \pm 0.25$  (Figures 7.24) and  $M_w = 7.5 \pm 0.25$  (Figure 7.25), respectively.

Twist demand (Figure 7.30) occurs for both symmetric and asymmetric bridges crossing a fault (Figures 7.26 to 7.29). For the simulated ground motions for  $M_w = 6.5$  event, the twist ductility (Figure 7.31) for any of the bridges does not exceed 0.5 and the corresponding maximum displacement ductility (Figure 7.32) does not exceed 3.

Examining the twist history response of the bridges when subjected to the total (FP+FN) ground motion and to the FP component only reveals that more twist is generated when using the FP component only compared with the total ground motion. The complex interaction of the FP and FN components of the total ground motion on the bridge response (Figures 7.33 and 7.34) reduces the opposing transverse displacements, which reduces the amount of twist, as compared with the FP component only. This suggests that analysis of

bridges crossing faults using the FP component of ground motion only should give reasonable estimates of the twist demand for scaled FP ground motions (Figure 7.14). This conclusion is valid only for the case where the bridge is at 90 deg to the orientation of the fault rupture.

The twist history response of the bridges subjected to the scaled FP ground motions (Figures 7.26 to 7.29) varies according to event magnitude. As seen in Figure 7.30, the greater the fault-offset, i.e., larger event magnitude, the greater the twist demand for all the bridges. However, the twist demand is not only dependent on the fault-offset, but also dependent on the rise time of the FP ground motions, evident by twist demands that are greater from dynamic analysis as compared with those due to the fault-offset only. The twist demands range from approximately 1 deg ( $M_w = 6.0$ ) to 3 deg ( $M_w = 7.5$ ). The corresponding twist ductility (Figure 7.40) also increases with event magnitude. The maximum twist ductility is approximately 0.25, 0.4, 0.75, and 1.2 for  $M_w = 6.0$ , 6.5, 7.0, and 7.5, respectively. As the twist ductility increases, the displacement ductility decreases, as seen in Figure 7.41. The corresponding maximum displacement ductility at the maximum twist ductility is approximately 2, 2.3, 1.3, and 0.7, for  $M_w = 6.0$ , 6.5, 7.0, and 7.5, respectively.

Overall, for the limited number of bridge configurations and ground motions used in this study, the column hoop reinforcement is not expected to yield due to twist under most cases. Specifically, bridges subjected to bidirectional near-fault ground motions (magnitude bins  $M_w = 7.0 \pm 0.25$  and  $M_w = 7.5 \pm 0.25$ ), simulated ground motions across fault-rupture zones for magnitude 6.5 earthquake, and scaled FP ground motions ( $M_w = 6.0$ , 6.5, and 7.0) did not generate sufficient twist to exceed a twist ductility of one. The scaled FP ground motion  $M_w = 7.5$  did cause the twist ductility to exceed one for some bridges.

## Chapter 8

# Design Implications and Tentative Design Procedure

This chapter addresses design implications of the laboratory tests and analytical models reported in previous chapters. A tentative design procedure is proposed to increase the flexural ductility capacity of columns subjected to combined twist and lateral displacement histories. The tentative design procedure is based on observations from the laboratory and analytical program, but has not been demonstrated through laboratory testing of columns designed according to the design procedure.

### 8.1 Effect of Torsion on Flexural Ductility Capacity

Chapter 5 presented test data comparing the load-deformation responses of columns with and without imposed torsion. Figure 8.1 summarizes the observed relation between drift and twist at failure for circular cross section columns 415, C1, C2, and C4. To define failure, the envelope curves for first cycles and third cycles were constructed. For

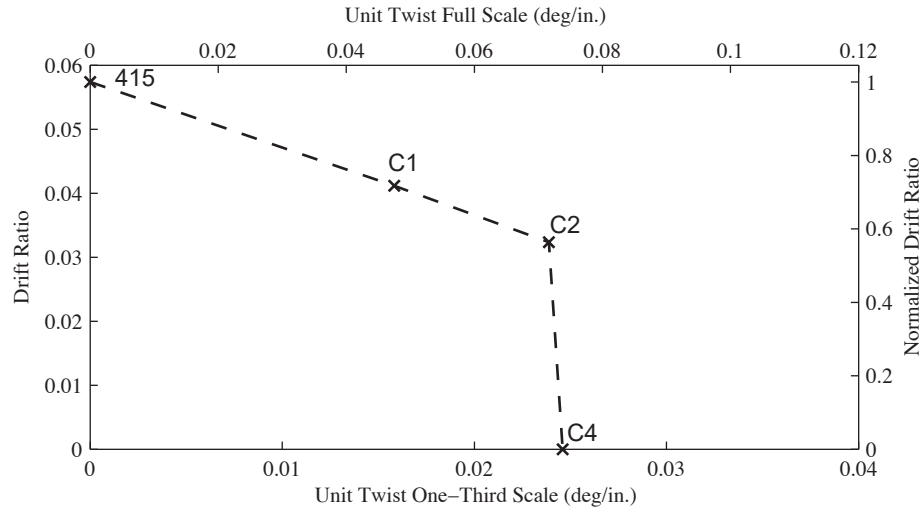


Figure 8.1: Relation Between Twist and Drift Capacity

Columns 415, C1, and C2, failure was defined as the drift and corresponding twist for which the third-cycle lateral force envelope dropped to 85% of the peak lateral force. For Column C4, failure was defined as the twist at which the third-cycle envelope torque dropped to 85% of the corresponding first-cycle torque. Twist is reported as the unit twist in units of degrees per inch, defined as the total twist in degrees divided by the column length in inches. Values are given as recorded for the one-third-scale test specimens as well as scaled to full scale.

As shown in Figure 8.1, the lateral drift capacity decreased with increasing twist-to-drift ratio. Furthermore, the unit twist corresponding to lateral drift capacity was approximately 0.016 deg/inch for Column C1, increasing moderately for Columns C2 and C4. It is concluded that imposed twist can reduce the flexural drift/ductility capacity of reinforced concrete bridge columns with circular hoop reinforcement.

For the columns studied in this research program, observed failure appeared to be

linked with yielding of the circular hoop reinforcement in the following way. For Column 415 (Lehman and Moehle, 2000) under lateral loading without twist, yielding of the hoops was not observed. Failure in that column (and other similar columns reported by Lehman and Moehle (2000); Hachem et al. (2003); Belarbi et al. (2007)) was associated with buckling of longitudinal reinforcement followed by tensile fracture of the reinforcement upon reversed loading. Transverse reinforcement apparently was more than sufficient to confine the core concrete, but insufficient to prevent local buckling of reinforcement. For Columns C1, C2, and C3 under combined lateral and torsional loading, yielding of hoop reinforcement occurred, leading to earlier buckling and fracture of the longitudinal reinforcement. In Column C4 under torsional loading without lateral deformation, hoop yielding also occurred, leading to general decay in the torque-twist response.

## **8.2 Theoretical Relation between Quantity of Hoop Reinforcement and Yield Twist**

The softened truss model was presented in Chapter 6. According to this model, the angle of diagonal cracks and diagonal compression struts in pure torsion depends on the relative quantities of longitudinal reinforcement (and axial load) and transverse reinforcement. Varying the quantities of reinforcement also can affect the twist at onset of yielding of the hoop reinforcement. Figure 8.2 shows the effect for a column having the same geometry and reinforcement as Column C4 but with differing amounts of transverse reinforcement. The continuous curve shows results for the hoop volume ratio used in Column C4, whereas the broken curves are for increased hoop reinforcement. As can be seen, increasing the volume ratio of hoop reinforcement (by decreasing hoop spacing) increases

Table 8.1: Column Parameters

Parameter	Value
$D$ (ft)	4, 5, 6, 8, 10
$\rho_l$ (%)	1.0, 1.5, 2.0, 3.0
$\rho_s$ (%)	0.5, 0.75, 1.0, 1.25, 1.5, 1.75, 2.0, 2.25, 2.5, 2.75, 3.0
$f'_c$ (ksi)	5 (target), 6, 7

the twist corresponding to hoop yielding. It will be shown subsequently that hoop yielding under pure torsion can be eliminated completely by further increasing the quantity of hoop reinforcement.

A parameter study was conducted to further investigate the torque-twist behavior of full-scale circular cross section columns. The parameters of the study were column diameter  $D$ , longitudinal steel ratio  $\rho_l$ , transverse reinforcement ratio  $\rho_s$ , and concrete compressive strength  $f'_c$ , as summarized in Table 8.1. For all columns, the hoop reinforcement was modeled using an elastic-perfectly plastic model with yield strength  $f_{yh} = 60$  ksi. Axial load was set equal to  $0.1f'_cA_g$  where  $f'_c$  is the target compressive strength (5 ksi).

Figures 8.3 to 8.7 show the effect of  $\rho_s$  on the torque-twist relation for  $f'_c = 5$  ksi for full-scale columns of different diameters. For clarity, only the curves for longitudinal steel ratio  $\rho_l = 1.5\%$  are presented. It can be seen that increasing  $\rho_s$  increases the twist at which hoop yielding occurs. Moreover, it is possible to preclude hoop yielding (for pure torsional loading) by increasing the hoop reinforcement sufficiently.

According to Figure 8.5, a full-scale column having properties similar to those reported here would experience yielding of hoop reinforcement for twist approximately equal to 0.007 deg/inch. This rotation is close to the rotation (scaled to full scale) at which

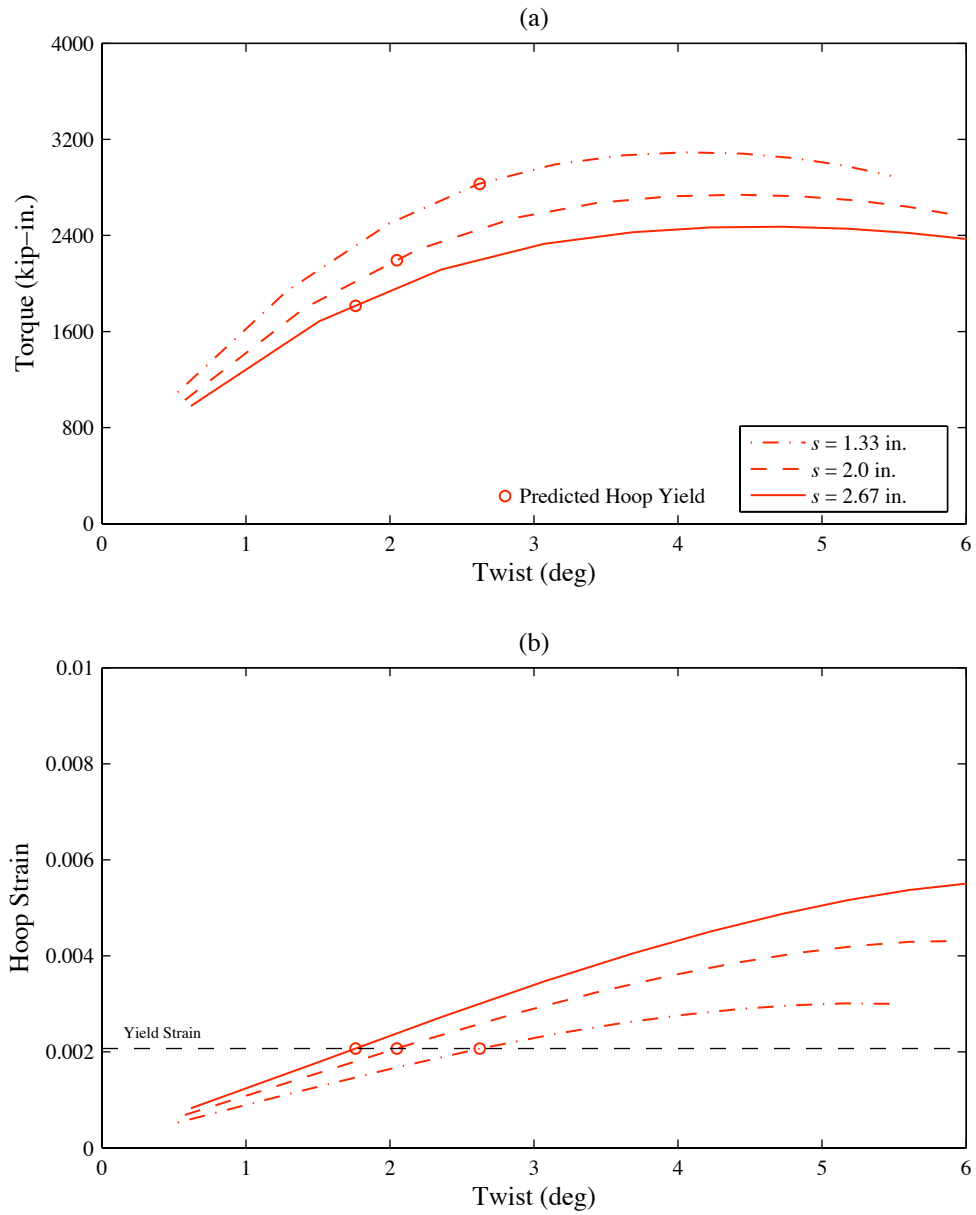


Figure 8.2: Effect of Hoop Spacing on the Predicted Torque-Twist Response of Column C4 Using the Softened Truss Model: (a) Torque-Twist Relationship and (b) Hoop Strain-Twist Relationship

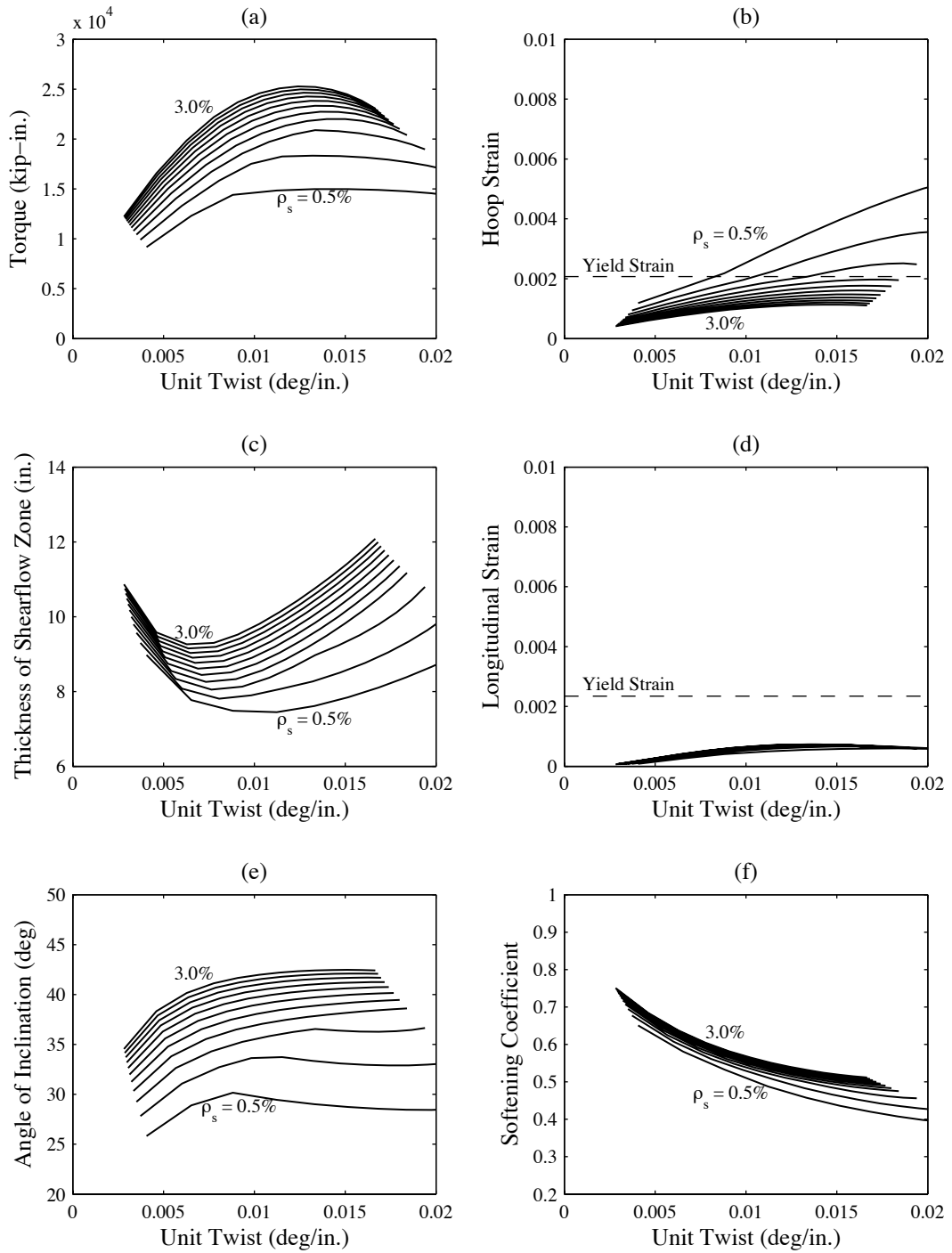


Figure 8.3: Effect of  $\rho_s$  on the Torque-Twist Response of 4 ft Diameter Columns

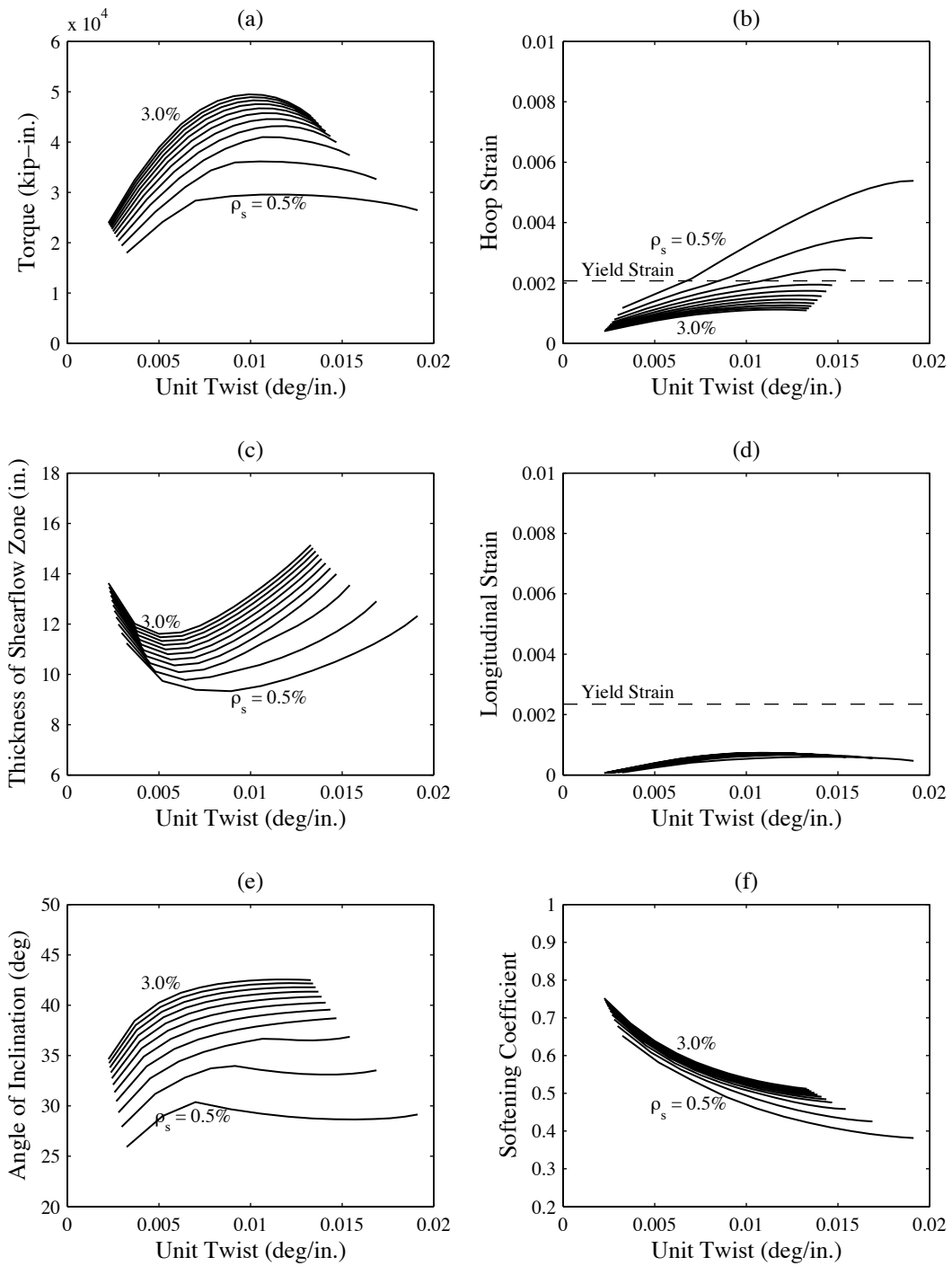


Figure 8.4: Effect of  $\rho_s$  on the Torque-Twist Response of 5 ft Diameter Columns

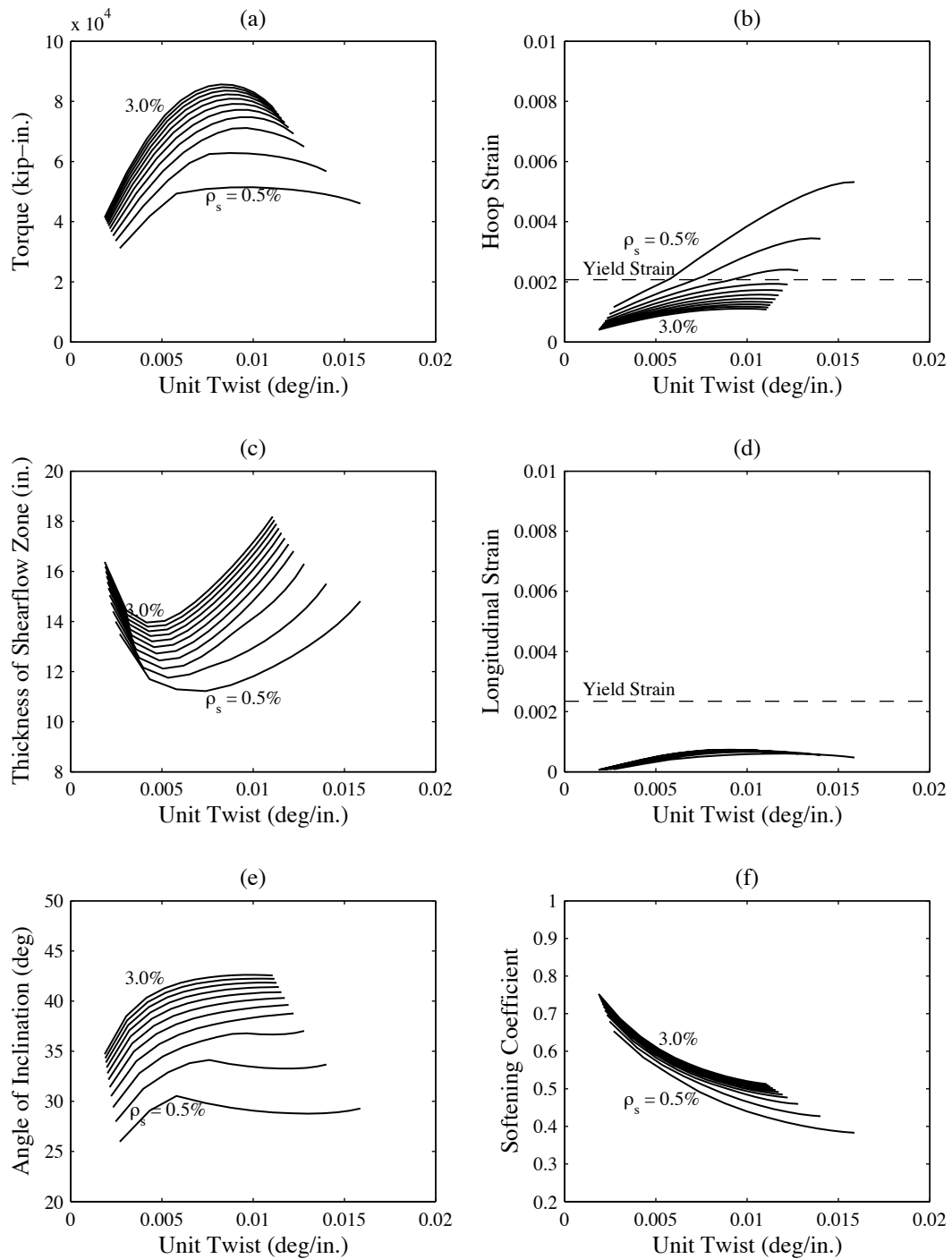


Figure 8.5: Effect of  $\rho_s$  on the Torque-Twist Response of 6 ft Diameter Columns

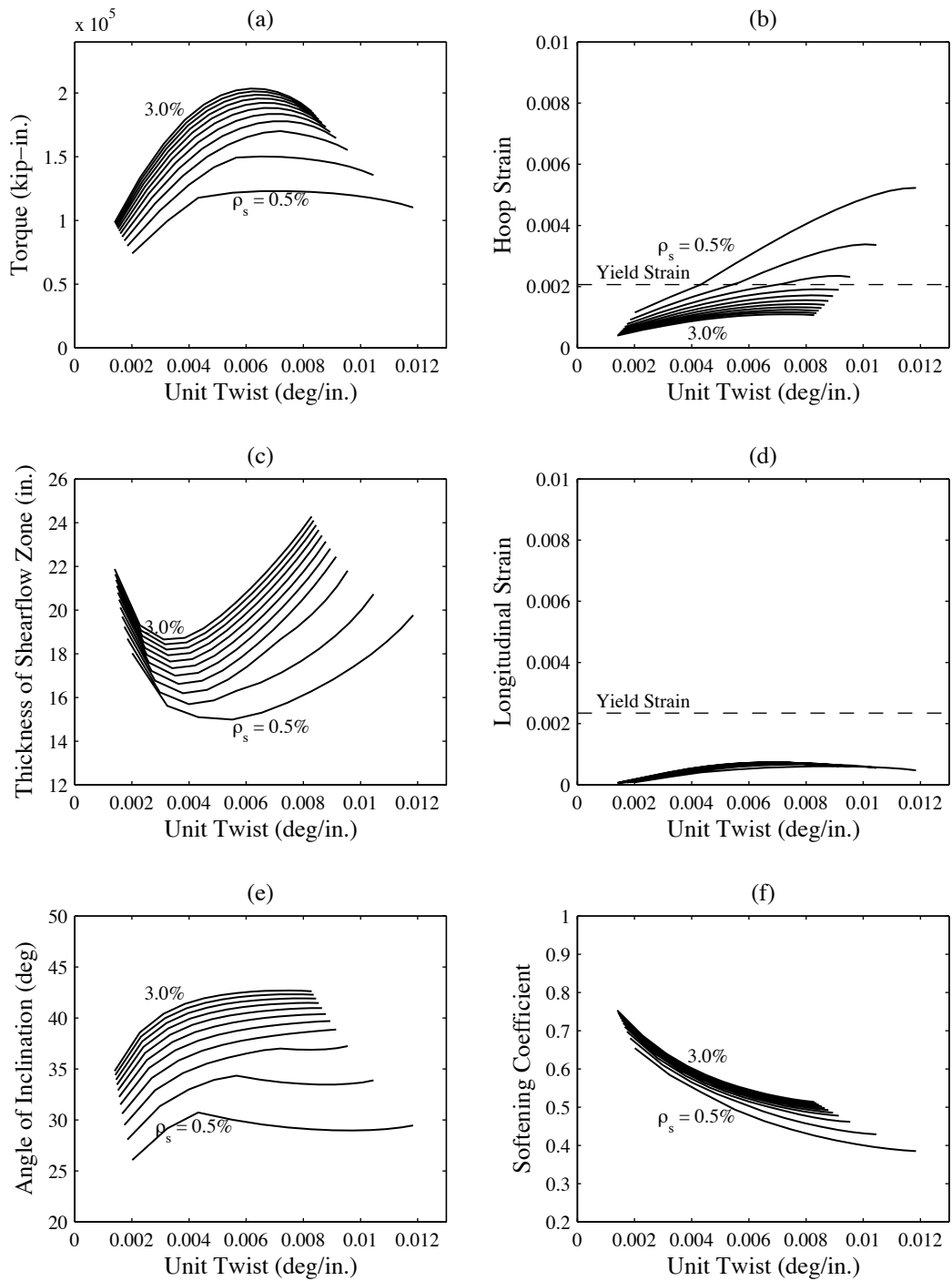


Figure 8.6: Effect of  $\rho_s$  on the Torque-Twist Response of 8 ft Diameter Columns

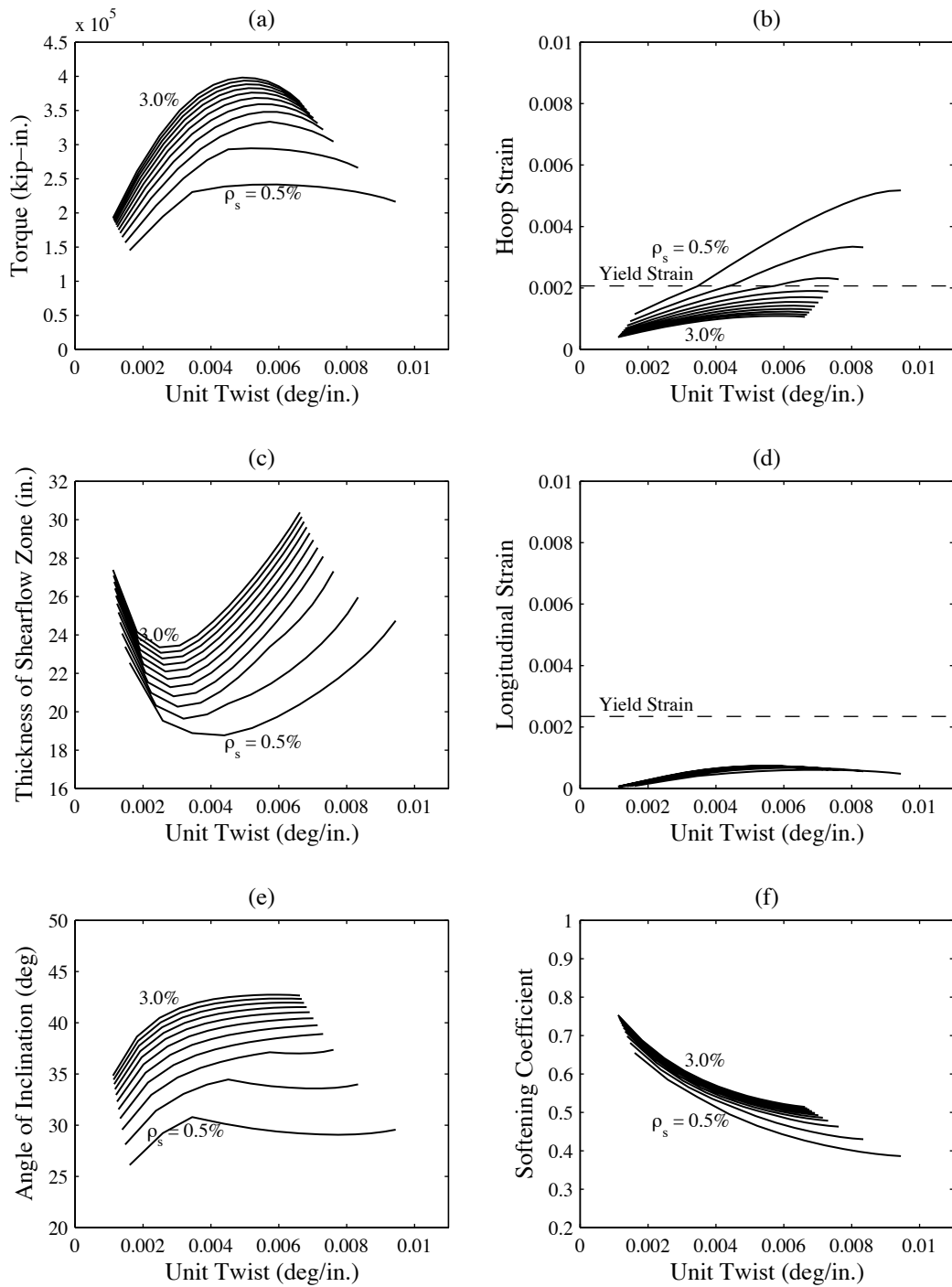


Figure 8.7: Effect of  $\rho_s$  on the Torque-Twist Response of 10 ft Diameter Columns

Columns C1 and C2 experienced failure (Figure 8.1). The broken curve in Figure 8.1, whose precise location admittedly is incompletely defined by the available data, indicates that the reduction in displacement capacity would be on the order of ten percent if the twist was approximately half the twist corresponding to yield in pure torsion. Assuming ten percent reduction to be within the acceptable range suggests a limit for the twist demand for use in design.

The results of Figures 8.3 through 8.7 were repeated for  $f'_c = 6$  ksi and 7 ksi, and for different reinforcement ratios  $\rho_l$ . The detailed results are not shown here for brevity. Rather, Figures 8.8 and 8.9 summarize the effects of concrete compressive strength and steel reinforcement ratio on the yield twist. The symbols correspond to calculated results, and the straight lines correspond to best fit lines determined by linear regression. It can be observed that the longitudinal steel ratio  $\rho_l$  does not have a significant effect on the torque-twist response within the range of longitudinal and transverse reinforcement considered and, likewise, does not significantly affect the yield twist. Concrete compressive strength  $f'_c$  has a more significant effect on yield twist, with higher compressive strength resulting in lower twist. (Therefore, in a design method that establishes transverse reinforcement to achieve a target yield twist, a high estimate of the concrete compressive strength should be used.) Also, yielding does not occur (lack of yield markers) for  $\rho_s > 1.5\%$ .

### 8.3 Proposed Design Procedure

The preceding results indicate that twisting a circular cross section bridge column reduces the lateral displacement capacity. The failure appears to be triggered by twist-induced yielding of the transverse reinforcement. Furthermore, at least for columns under

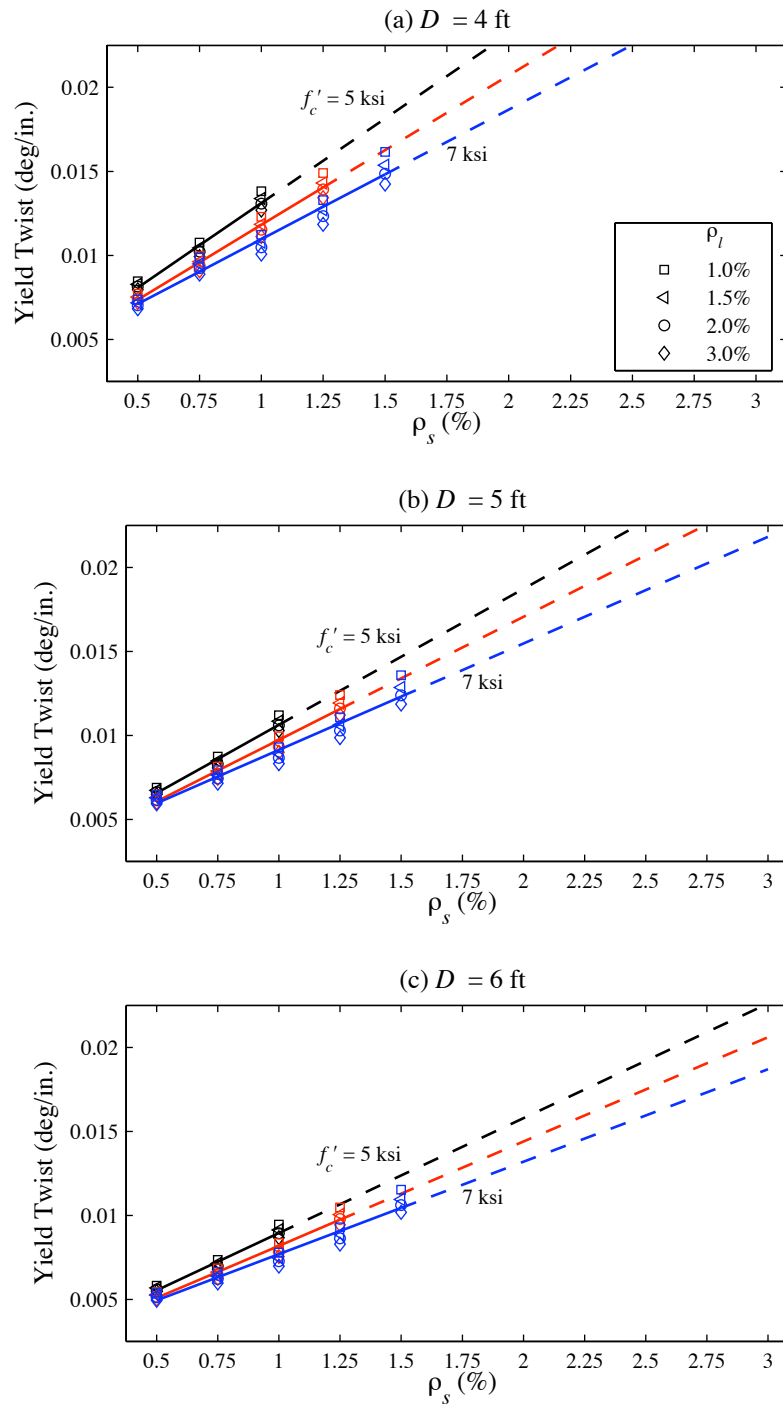


Figure 8.8: Effect of  $\rho_s$  and  $f'_c$  on the Yield Twist of 4, 5, and 6 ft Diameter Columns

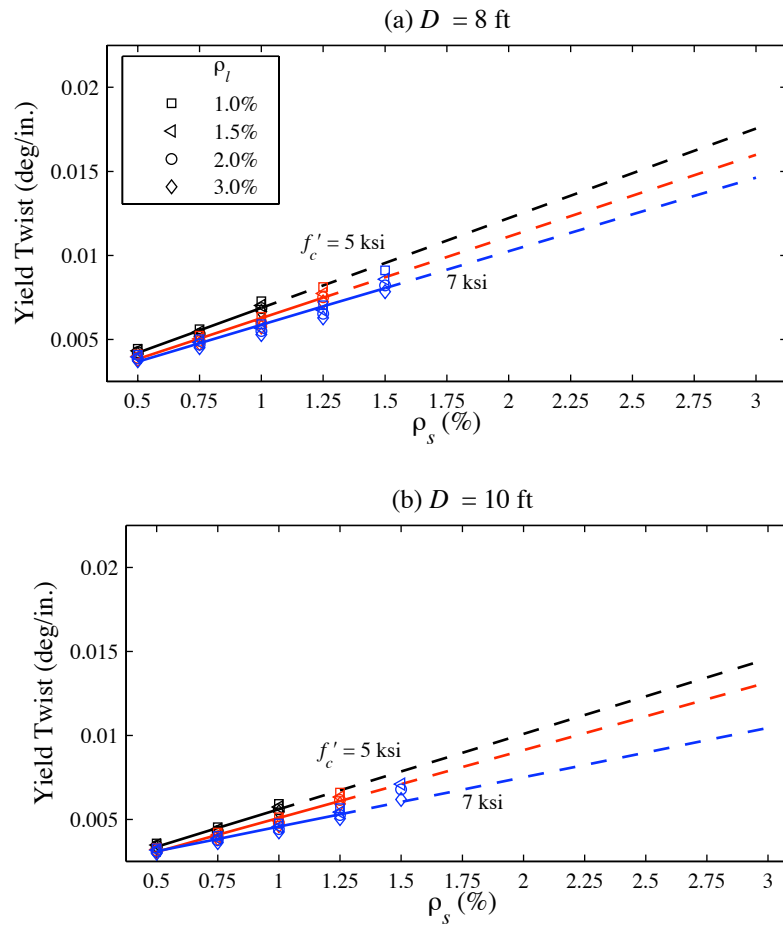


Figure 8.9: Effect of  $\rho_s$  and  $f'_c$  on the Yield Twist of 8 and 10 ft Diameter Columns

pure torsion, yielding of transverse reinforcement can be delayed by increasing the transverse reinforcement volume ratio. The available laboratory data are for a single transverse reinforcement ratio, and therefore cannot demonstrate how lateral displacement capacity can be increased by increasing the transverse reinforcement ratio. Lacking laboratory data to demonstrate effects in detail, a simple approach is proposed, as described in the following paragraph.

For bridge columns susceptible to twist under earthquake loading, the twist demand should be compared with the yield twist for columns under pure torsional loading. Charts similar to those in Figures 8.8 and 8.9 are suitable for determining the quantity of hoop reinforcement corresponding to yielding under pure twist. If the twist demand is less than half the yield twist, the effect on flexural displacement capacity is small, such that torsional effects can be ignored. Otherwise, the provided transverse reinforcement should not be less than  $\rho_s = \rho'_s + \rho''_s$ , where  $\rho'_s$  is the transverse reinforcement ratio required for lateral displacement in the absence of twist, and  $\rho''_s$  is the transverse reinforcement required to prevent hoop yielding under pure twist loading.

The twist demand can be determined using dynamic analysis considering ground shaking and/or fault offset demands, as appropriate. Chapter 7 presented procedures and results for dynamic analysis considering near-fault and cross-fault conditions, for a range of irregular bridge frames. For the near-fault condition, the torsion ductility demand was less than 0.5 for all cases considered, indicating torsion effects can be ignored for a broad range of irregular bridge structures. On the other hand, for cross-fault conditions, ductility demands exceeding 0.5 were observed, especially for larger magnitude earthquakes. In such cases, torsion effects on flexural ductility capacity should not be ignored.

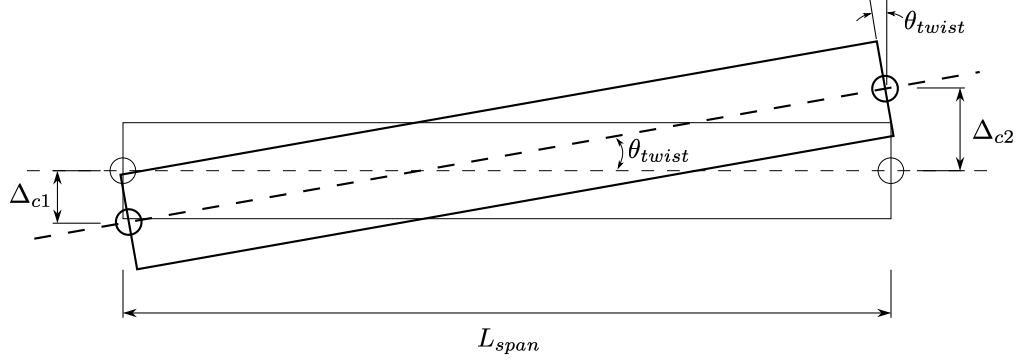


Figure 8.10: Illustration of Maximum Expected Twist Demand

The observed insensitivity to torsion effects for near-fault (not cross-fault) motions can be explained by the model in Figure 8.10. In this model, the maximum twist demand is defined by assuming the columns are deflected to their maximum flexural displacement capacity in opposite directions. In this case, the superstructure twist is equal to

$$\theta_{twist} = \frac{\Delta_{c1} + \Delta_{c2}}{L_{span}} \quad (8.1)$$

in which  $\Delta_{c1}$  and  $\Delta_{c2}$  are the displacement capacities of column bents 1 and 2 and  $L_{span}$  is the span between the column bents. For the case of equal column heights  $L_1 = L_2 = L$ , we can write the unit twist as

$$\frac{\theta_{twist}}{L} = \frac{\Delta_{c1}/L + \Delta_{c2}/L}{L_{span}} \quad (8.2)$$

As an example, for flexural drift capacity  $\Delta_{c1}/L$  and  $\Delta_{c2}/L = 0.05$  in the absence of twist, Eq. 8.2 gives  $\theta_{twist}/L = 0.1/L_{span}$ . From Figure 8.8, for  $\rho_s = 0.0075$ , the unit twist at yield for a 6-ft diameter column is approximately 0.0075 deg/in. = 0.0016 rad/ft. Thus according to Eq. 8.2, the column would be at half the yield twist (the critical value proposed above) only for  $L_{span} \leq 125$  ft. Note that this result is for the extreme and unlikely case of the two columns deflected to their ultimate flexural displacement capacity simultaneously

in opposite directions. For the case of one column being stationary and the other being displaced to its ultimate displacement capacity, the condition becomes  $L_{span} \leq 63$  ft.

The preceding examples demonstrate the extreme conditions required for torsion to be a controlling design parameter for a symmetric bridge structures. As a structure becomes less symmetric (e.g., different column diameters or heights), torsional sensitivity increases.

## Chapter 9

# Summary, Conclusions, and Future Research

### 9.1 Summary

Bridge superstructures subjected to earthquake loading will in general experience both translational and rotational motions. As a consequence, the supporting columns may be subjected to torsion under earthquake loading. The degree to which torsion reduces lateral load strength or deformation capacity is unclear. A research program was undertaken to characterize the effects of earthquake-induced torsion on the flexural ductility of reinforced concrete bridge columns. This objective was pursued through literature review, laboratory testing, analytical model development to understand the effects of twist on column response, and analyses of simplified bridge systems under a variety of loadings to investigate the degree of twist anticipated.

### 9.1.1 Literature Review

Previous research on the performance of reinforced concrete columns subjected to lateral loading was reviewed. The review included seismic torsion of bridge structures, torsional strength and stiffness of members, effects of cyclic torsional loading and simulated seismic loading on members, and design provisions for members subjected to torsion.

### 9.1.2 Laboratory Testing Phase

Four conventional one-third scale reinforced concrete bridge columns were tested under simulated seismic loading. The principal test variables were cross section type and twist to drift ratio. Three of the specimens were identical circular columns and one of the specimens was an oblong column; all four columns were reinforced with circular hoops. The response of the columns was observed visually and monitored through various force, displacement, and strain measuring devices. Experimental results were presented for each of the four columns tested.

Column C1 had a circular cross section and was tested under simultaneously reversed cyclic lateral and torsional loading with a twist/drift ratio = 0.6. The applied constant axial load of 225 kips was approximately  $0.1f'_cA_g$ , where  $f'_c$  = target concrete compressive strength (5.0 ksi). During testing, inclined cracks were observed on the South face; cracking on the East, West, and North faces consisted of predominantly horizontal cracks. Significant column damage in the form of bar buckling and bar fracture was observed during the final cycles, which resulted in reduction of lateral strength and stiffness. Longitudinal reinforcing bars located on the extreme East and West faces buckled during the 5 in. displacement amplitude cycles and subsequently fractured during the 7 in. dis-

placement amplitude cycles; longitudinal reinforcing bars located on the North and South faces buckled during the 7 in. displacement amplitude cycles. Additionally, a single hoop, located 6 in. above the interface, fractured on the West face during the 7 in. displacement amplitude cycles.

Column C2 was nominally identical to Column C1 except it was tested with a twist/drift ratio = 1.2. During testing, inclined cracks were observed on all faces. Significant column damage in the form of bar buckling and bar fracture, which resulted in reduction of lateral strength and stiffness, was observed during the 5 in. displacement amplitude cycle. Longitudinal reinforcing bars located on the extreme East and West faces buckled during the first 5 in. displacement amplitude cycles and subsequently fractured during the third cycle. Adjacent longitudinal reinforcing bars located on the East and West faces fractured and bars located on the North and South faces buckled during the 7 in. displacement amplitude cycle.

Column C3 had an oblong cross section and was tested under simultaneously reversed cyclic combined lateral and torsional loading with a twist/drift ratio = 0.6. The applied constant axial load was 380 kips ( $0.09f'_cA_g$ ). During testing, horizontal cracks were observed at the base of column on the East and West faces and cracks were more inclined with increase in elevation. Cracks on the South face were inclined, whereas cracks on the North face were predominately horizontal. Significant column damage in the form of bar buckling and bar fracture was observed during the final two displacement amplitude cycles, which resulted in reduction of lateral strength and stiffness. Main longitudinal reinforcing bars (No. 5) located on the extreme East and West faces buckled during the first 5 in. displacement amplitude cycle and subsequently fractured during the third cycle.

The remaining main longitudinal reinforcing bars on the East and West faces fractured and the bars located on the North and South faces buckled during the 7 in. displacement amplitude cycle. Additionally, buckling of the interlocking longitudinal reinforcing bars (No. 3) at the overlapping of hoops was also observed; no visual observations were possible for the interior interlocking bars.

Similar to Columns C1 and C2, Column C4 had a circular cross section with an applied constant axial load of 225 kips ( $0.1f'_cA_g$ ). However, unlike Columns C1 and C2, Column C4 was tested under reversed cyclic torsional loading, similar to the twist history of Column C2. During testing, inclined cracks spiralling around the member were observed. The onset of concrete spalling was observed approximately mid-height of the column on all the faces during the 3.6 deg twist amplitude cycle. Upon completion of the 5 deg twist amplitude cycle, the spalled region had spread, spanning about 85% of the column height on all the faces

### 9.1.3 Analytical Phase

The analytical phase of this investigation consisted of two components. First, analytical models were developed to understand the effects of twist on column response. Second, analyses of simplified bridge systems under a variety of loadings were performed to investigate the degree of twist anticipated.

To understand the effect of twist on column response, three analytical models were developed, namely, the plastic hinge length model, the softened truss model for torsion, and a 3D truss model. The force-displacement response of the columns was modeled with the plastic hinge model, using the lumped-plastic force-based element available in *OpenSees*. Nonlinear geometry effects were accounted for with the  $P$ - $\Delta$  geometric transformation. The

torque-twist response of the columns was modeled with the softened truss model, which can model the torque-twist curve after cracking of concrete. A 3D truss model was developed to model the response of the columns under lateral loading only, torsional loading only, and combined lateral and torsional loading. The analytical and experimental results were compared and evaluated.

Simplified bridge systems were analyzed under near-fault ground motions and ground motions across a fault-rupture zone to investigate the degree of twist anticipated. The bridge systems consisted of a three-span superstructure supported on two single-column bents. The aspect ratio of the columns was varied, equal to 4, 6, 8, and 10. For the near-fault ground motions, the PEER NGA database was used to select a suite of ground motions at a distance 0-20 km for magnitude bins  $7.0 \pm 0.25$  and  $7.5 \pm 0.25$ . Each pair of recorded ground motions was applied as uniform bidirectional excitation. First, horizontal components 1 and 2 were input as the longitudinal and transverse excitations, respectively, and then horizontal components were swapped. For the ground motions across fault-rupture zones, numerically simulated ground motions for a magnitude 6.5 event were used. Simulated FP ground motions for earthquakes with different magnitudes on a vertical strike-slip fault were also generated, according to scaling laws for rise time and total fault-offset. The simulated ground displacements were input as support excitations at the base nodes of the bridge.

## 9.2 Conclusions

### 9.2.1 Laboratory Testing Phase

The laboratory testing phase of this investigation provided observed and measured data for the characterization of the effect of seismic torsion on the flexural ductility of the test specimens. The following primary conclusions are restricted to the range of column geometries tested:

- Combined torsion and lateral loading changed concrete cracking from predominantly horizontal cracks associated with flexure to inclined cracks associated with torsion-induced shear. The degree of cracking was greater on the faces of the column where torsion and shear loading added to the local shear stresses and less on other faces.
- Combined torsion and lateral loading increased the strain demands on the hoop reinforcement, leading to earlier yielding of the hoops. The reduced restraint from the hoops appears to have contributed to earlier buckling and subsequent fracture of the longitudinal reinforcement.
- Combined torsion and lateral loading resulted in more rapid degradation of lateral resistance. For a given set of reinforcement details, increasing the twist demand reduced the lateral displacement capacity.
- The applied torsion did not appear to adversely affect the flexural strength of the columns. This observation likely is limited to columns for which torsional resistance is controlled by the hoop reinforcement, as in the case of the test columns.

### 9.2.2 Analytical Phase

The analytical phase of this investigation developed analytical models to understand the effects of twist on column response and to investigate the degree of twist anticipated for simplified bridge systems. The primary conclusions are:

- The plastic hinge model was able to model the force-displacement response of the columns tested under lateral loading only.
- The softened truss model was able to model the post-cracking torque-twist response of columns under torsional loading only. It is not intended to model behavior before cracking.
- The 3D truss model was suitable for modeling the initial torsional stiffness, post-cracking stiffness, and occurrence of yielding of the hoops. However, the 3D truss model over-predicted the torsional strength of columns under torsional loading only.
- The 3D truss model was able to model the force-displacement response. However, the strength was overestimated using this model. Other models such as the plastic-hinge model can produce equally accurate results with less modeling and computational effort.
- The 3D truss model has shortcomings for generalized loadings because the orientation of the truss members is fixed in the model whereas the effective truss mechanism in a column varies with loading. As a consequence, the 3D model was not able to model correctly the variation of hoop strain around the perimeter of the section, which is necessary to model the flexural-torsional interaction. Therefore, the 3D truss model is not recommended for generalized loading.

- Parameter studies identified the effect of configuration and material properties on torque-twist response of circular cross section bridge columns. Yielding of hoop reinforcement under twist loading can be avoided by increasing the quantity of hoop reinforcement as the twist increases. Charts are provided for determining required hoop reinforcement.
- For the range of simplified bridge systems studied, the degree of anticipated twist for near-fault ground motions is less than the twist corresponding to hoop yielding under pure torsion.
- In contrast, bridge systems subjected to simulated ground motions across fault-rupture zones may see twist deformations sufficient to exceed the yield twist under pure torsion. This is the result of the combination of static offset and transient motion. For the bridge systems and earthquake magnitudes tested, hoop yielding was anticipated for several configurations and ground motions associated with the magnitude 7.5 event.

### 9.2.3 Design Implications

Based on data from laboratory testing and analytical modeling of the effect of twist on column response, the primary design implications are:

- Twist results in earlier yielding of the hoops, which results in reduced flexural deformation capacity due to reduction of the ultimate compressive strain of the core concrete due to loss of confining effect of the hoops, buckling of the longitudinal reinforcing bars due to loss of lateral restraint by the hoops, and subsequent fracture of the longitudinal reinforcing bars due to buckling and straightening of the bars under reversed cyclic loading.

- Analysis suggests that increasing the hoops to delay yielding would enable the column to respond as intended.

#### **9.2.4 Proposed Design Procedure**

A design procedure was proposed for enabling the columns subjected to combined lateral and torsional loading to reach their estimated displacement capacity. The procedure is based on observations from the laboratory tests and analytical studies, as well as engineering judgment. The procedure has not been verified through laboratory tests, but is recommended as an interim approach pending further laboratory tests. The primary elements of the approach are:

- For reasonably symmetric bridge structures not crossing a fault generating the design ground motions, effects of torsion can be ignored.
- For bridges with significant torsional imbalance, analyses should be conducted to estimate the degree of twist anticipated for design-level earthquakes. For bridges with relatively long spans between movement joints, simple static analyses under arbitrary displacements may be sufficient to demonstrate that column twist is small relative to the yield twist, in which case twist can be ignored. For smaller spans, dynamic analyses may be required to identify the design twist.
- For bridges crossing active faults, detailed studies of the additive effects of static offset and transient response should be conducted to determine the design twist.
- Where the design twist is less than half the yield twist under pure torsion loading, effects of twist can be ignored. Otherwise, the quantity of hoops required to prevent

yielding in pure torsion should be determined, and that quantity should be added to the hoops required for lateral drift demands.

### 9.3 Future Research

Future investigations should address the following:

- Test additional circular columns with increased hoops in plastic hinge region under combined lateral and torsional loading to verify that delaying yielding of hoops due to twist will enable the column to perform as intended
- Test oblong column under torsional loading only
- Develop analytical models capable of accurately simulating response of bridge columns under combined lateral and torsional cyclic deformations.
- Conduct additional analytical studies to develop additional simplified methods to estimate twist demands under earthquake loading, including cases of bridges crossing fault rupture zones.

# References

- ACI Committee 209. (1982). Prediction of Creep, Shrinkage, and Temperature Effects in Concrete Structures. *Designing for Creep and Shrinkage in Concrete Structures*. SP-76, American Concrete Institute, Detroit, MI.
- ACI Committee 318. (2008). *Building Code Requirements for Structural Concrete (318-08) and Commentary*. American Concrete Institute, Farmington Hills, MI.
- American Association of State Highway and Transportation Officials. (2004). *AASHTO LRFD Bridge Design Specifications* (3rd ed.). Washington, DC.
- Aschheim, M. A., Moehle, J. P., and Mahin, S. A. (1997). Design and Evaluation of Reinforced Concrete Bridges for Seismic Resistance. UCB/EERC Report No. 97/04, Earthquake Engineering Research Center, University of California, Berkeley, CA.
- Belarbi, A., Ayoub, A., Greene, G., Shanmugam, S. P., Mullapudi, R., and Farley, C. (2007). Seismic Performance of RC Bridge Columns Subjected to Combined Loading including Torsion. *ASCE Structures Congress*. Long Beach, CA.
- Berry, M. P. (2006). *Performance Modeling Strategies for Modern Reinforced Concrete Bridge Columns*. Doctoral dissertation. University of Washington, Seattle, WA.
- Building Seismic Safety Council. (2000). *NEHRP Provisions*. Building Seismic Safety Council, Washington, DC.

- Burden, R. L., and Faires, J. D. (2001). *Numerical Analysis* (7th ed.). Wadsworth Group, Pacific Grove, CA.
- Caltrans. (1996). *Seismic Hazard Map*. California Department of Transportation, Sacramento, CA.
- Caltrans. (2004a). *Bridge Design Specifications*. California Department of Transportation, Sacramento, CA.
- Caltrans. (2004b). *Seismic Design Criteria version 1.3*. California Department of Transportation, Sacramento, CA.
- Caltrans Engineers. (2006, September). *Private Communication*.
- Chang, G., and Mander, J. (1994). Seismic Energy Based Fatigue Damage Analysis of Bridge Columns: Part I Evaluation of Seismic Capacity. NCEER Technical Report 94-0006, National Center for Earthquake Engineering Research, State University of New York, Buffalo, NY.
- Chopra, A. K. (2001). *Dynamics of Structures: Theory and Applications to Earthquake Engineering* (2nd ed.). Prentice Hall, Upper Saddle River, NJ.
- Cocchi, G. M., and Volpi, M. (1996). Inelastic Analysis of Reinforced Concrete Beams Subjected to Combined Torsion, Flexural and Axial loads. *Computers and Structures*, 61, 479-494.
- Collins, M. P., and Mitchell, D. (1980). Shear and Torsion Design of Prestressed and Non-Prestressed Concrete Beams. *Journal of the Prestressed Concrete Institute*, 25(5), 32-100.
- Collins, M. P., Walsh, P. F., Archer, F. E., and Hall, A. S. (1968). Ultimate Strength of Reinforced Concrete Beams Subjected to Combined Torsion and Bending. *Torsion of*

*Structural Concrete*. SP-18, American Concrete Institute, Detroit, MI.

- Der Kiureghian, A., Keshishian, P., and Hakobian, A. (1997). Multiple Support Response Spectrum Analysis of Bridges Including the Site-Response Effect and the MSRS Code. UCB/EERC Report No. 1997/02, Earthquake Engineering Research Center, University of California, Berkeley, CA.
- Dreger, D., Hurtado, G., Chopra, A. K., and Larsen, S. (2007). Near-Fault Seismic Ground Motions. UCB/EERC Report No. 2007/03, Earthquake Engineering Research Center, University of California, Berkeley, CA.
- Filippou, F. C., and Fenves, G. L. (2004). Methods of Analysis for Earthquake Resistant Structures. In Y. Bozorgnia and V. V. Bertero (Eds.), *Earthquake Engineering: From Engineering Seismology to Performance-Based Engineering* (chap. 6). CRC Press, Boca Raton, FL.
- Filippou, F. C., and Neuenhofer, A. (1998). Geometrically Nonlinear Flexibility-Based Frame Finite Element. *Journal of Structural Engineering, ASCE*, 124, 704-711.
- Goel, R. K., and Chopra, A. K. (1994). Seismic Response of the US 101/Painter Street Overpassing Using Strong Motion Records. *SMIP94 Seminar on Seismological and Engineering Implications of Recent Strong-Motion Data*. California Division of Mines and Geology, Sacramento, CA.
- Goel, R. K., and Chopra, A. K. (2008). Analysis of Bridge Structures Crossing Fault Rupture Zones. UCB/EERC Report No. 2008/01, Earthquake Engineering Research Center, University of California, Berkeley, CA.
- Hachem, M. M., Mahin, S. A., and Moehle, J. P. (2003). Performance of Circular Reinforced Concrete Columns under Bidirectional Earthquake Loading . PEER Report No.

- 2003/03, Pacific Earthquake Engineering Research Center, University of California, Berkeley, CA.
- Hsu, H. L., and Liang, L. L. (2002). Effect of Torsion on Seismic Performance of Composite Members. *Seventh U.S. National Conference on Earthquake Engineering (7NCEE)*.
- Hsu, H. L., and Liang, L. L. (2003). Performance of Hollow Composite Members Subjected to Cyclic Eccentric Loading. *Earthquake Engineering and Structural Dynamics*, 32, 443-461.
- Hsu, H. L., and Wang, C. L. (2000). Flexural-Torsional Behavior of Steel Reinforced Concrete Members Subjected to Repeated Loading. *Earthquake Engineering and Structural Dynamics*, 29, 667-682.
- Hsu, T. T. C. (1968a). Torsion of Structural Concrete - Behavior of Reinforced Concrete Rectangular Members. *Torsion of Structural Concrete*. SP-18, American Concrete Institute, Detroit, MI.
- Hsu, T. T. C. (1968b). Torsion of Structural Concrete - Plain Concrete Rectangular Sections. *Torsion of Structural Concrete*. SP-18, American Concrete Institute, Detroit, MI.
- Hsu, T. T. C. (1990). Shear Flow Zone in Torsion of Reinforced Concrete. *Journal of Structural Engineering, ASCE*, 116, 3206-3226.
- Hsu, T. T. C. (1993). *Unified Theory of Reinforced Concrete*. CRC Press, Boca Raton, FL.
- Hsu, T. T. C., and Moy, Y. L. (1985). Softening of Concrete Torsional Members Theory and Tests. *Journal of the American Concrete Institute*, 82, 290-303.
- Isakovic, T., Fischinger, M., and Fajfar, P. (1998). Torsional Behavior of Single Column Bent Viaducts. *Sixth U.S. National Conference on Earthquake Engineering (6NCEE)*.

- Jakobsen, B., Hjorth-Hansen, E., and Holand, I. (1984). Cyclic Torsion Tests of Concrete Box Columns. *Journal of Structural Engineering, ASCE*, 110, 803-822.
- Johnson, N. S., Saiidi, M., and Sanders, D. H. (2006). Large-Scale Experimental and Analytical Seismic Studies of a Two-Span Reinforced Concrete Bridge System. CCEER Report No. 06-02, Center for Civil Engineering Earthquake Research, University of Nevada, Reno, NV.
- Kent, D. C., and Park, R. (1971). Flexural members with confined concrete. *Journal of Structural Engineering, ASCE*, 97, 1969-1990.
- Ketchum, M., Chang, V., and Shantz, T. (2004). Influence of Design Ground Motion Level on Highway Bridge Costs. PEER Report No. Lifelines 6D01, Pacific Earthquake Engineering Research Center, University of California, Berkeley, CA.
- Lampert, P. (1973). Postcracking Stiffness of Reinforced Concrete Beams in Torsion and Bending. *Analysis of Structural Systems for Torsion*. SP-35, American Concrete Institute, Detroit, MI.
- Lampert, P., and Collins, M. P. (1972). Torsion, Bending, and Confusion An Attempt to Establish the Facts. *Journal of the American Concrete Institute*, 69, 501-504.
- Le, T. N. (2008). *Torsion Test of Circular RC Column*. Unpublished Master's thesis. University of California, Berkeley.
- Lehman, D. E., and Moehle, J. P. (2000). Seismic Performance of Well-Confined Concrete Bridge Columns. PEER Report No. 98/01, Pacific Earthquake Engineering Research Center, University of California, Berkeley, CA.
- Leu, L.-J., and Lee, Y.-S. (2000). Torsion Design Charts for Reinforced Concrete Rectangular Members. *Journal of Structural Engineering, ASCE*, 126, 210-218.

- Leung, M. B. (1982). *Inelastic Analysis of Reinforced Concrete Beams Subjected to Combined Axial Force, Bending and Torsion*. Doctoral dissertation. University of Illinois, Urbana-Champaign.
- Leung, M. B., and Schnobrich, W. C. (1987). Reinforced Concrete Beams Subjected to Bending and Torsion. *Journal of Structural Engineering, ASCE, 113*, 307-320.
- MacGregor, J. G., and Ghoneim, M. G. (1995). Design for Torsion. *ACI Structural Journal, 92*, 211-218.
- Mander, J. B., Priestly, M. J. N., and Park, R. (1988). Theoretical Stress-Strain Model for Confined Concrete. *Journal of Structural Engineering, ASCE, 114*, 1804-1826.
- McKenna, F., Fenves, G. L., Scott, M. H., and Jeremić, B. (2000). *Open System for Earthquake Engineering Simulation*. <http://opensees.berkeley.edu/>.
- McLean, D. I., and Buckingham, G. C. (1994). Seismic Performance of Bridge Columns with Interlocking Spiral Reinforcement. Report WA-RD 357.1, Washington State Department of Transportation, Olympia, WA.
- Meng, J. Y., and Lui, E. M. (2000). Torsional Effects on Short-Span Highway Bridges. *Computers and Structures, 75*, 619-629.
- Mitchell, D., and Collins, M. P. (1974). Diagonal Compression Field Theory A Rational Model for Structural Concrete in Pure Torsion. *Journal of the American Concrete Institute, 71*, 396-408.
- Mitchell, D., and Collins, M. P. (1976). Detailing for Torsion. *Journal of the American Concrete Institute, 73*, 507-511.
- Mitchell, D., and Collins, M. P. (1978). Pure Torsion in Rectangular Sections A Re-Examination. *Journal of the American Concrete Institute, 75*, 511-519.

- Nagata, S., Kawashima, K., and Watanabe, G. (2004). Seismic Performance of Reinforced Concrete C-Bent Columns Based on a Hybrid Loading Test. *First International Conference on Urban Earthquake Engineering*. Tokyo, Japan.
- Nagata, S., Kawashima, K., and Watanabe, G. (2005). Fiber Element Analysis of Reinforced Concrete C-Bent Columns. *Second International Conference on Urban Earthquake Engineering*. Tokyo, Japan.
- Nelson, R. B., Saiidi, M., and Zadeh, S. (2007). Experimental Evaluation of Performance of Conventional Bridge Systems. CCEER Report No. 07-04, Center for Civil Engineering Earthquake Research, University of Nevada, Reno, NV.
- Ogata, T., Suda, K., and Masukawa, J. (2000). Transverse Reinforcement and Ductility of Reinforced Concrete High Pier with Hollow Section. *12th World Conference on Earthquake Engineering (12WCEE)*.
- Otsuka, H., Takeshita, E., Yabuki, W., Wang, Y., Yoshimura, T., and Tsunomoto, M. (2004). Study on the Seismic Performance of Reinforced Concrete Columns Subjected to Torsional Moment, Bending Moment and Axial Force. *13th World Conference on Earthquake Engineering (13WCEE)*.
- Pacific Earthquake Engineering Research Center. (2008). *Next Generation Attenuation (NGA) Database*. <http://peer.berkeley.edu/nga/>.
- Park, H., and Eom, T. (2007). Truss Model for Nonlinear Analysis of RC Members Subject to Cyclic Loading. *Journal of Structural Engineering, ASCE*, 133(10), 1351-1363.
- Priestley, M. N. J., Seible, F., and Calvi, G. M. (1996). *Seismic Design and Retrofit of Bridges*. John Wiley & Sons, New York.
- Rabbat, B. G., and Collins, M. P. (1978). A Variable Angle Space Truss Model for Struc-

- tural Concrete Members Subjected to Complex Loading. *Douglas McHenry International Symposium on Concrete and Concrete Structures*. SP-55, American Concrete Institute, Detroit, MI.
- Rahal, K. N., and Collins, M. P. (1996). Simple Model for Predicting Torsional Strength of Reinforced and Prestressed Concrete Sections. *ACI Structural Journal*, 93, 658-666.
- Ranf, R. T. (2007). *Model Selection for Performance-Based Earthquake Engineering of Bridges*. Doctoral dissertation. University of Washington, Seattle, WA.
- Scott, M. H., and Fenves, G. L. (2006). Plastic Hinge Integration Methods for Force-Based Beam-Column Elements. *Journal of Structural Engineering, ASCE*, 132, 244-252.
- Sezen, H. (2002). *Seismic Behavior and Modeling of Reinforced Concrete Building Columns*. Doctoral dissertation. University of California, Berkeley.
- Somerville, P. G., Irikura, K., Graves, R., Sawada, S., Wald, D., Abrahamson, N., et al. (1999). Characterizing Crustal Earthquake Slip Models for the Prediction of Strong Ground Motion. *Seismological Research Letters*, 70, 59-80.
- Taucer, F., Spacone, E., and Filippou, F. C. (1991). A Fiber Beam-Column Element for Seismic Response Analysis of Reinforced Concrete Structures. UCB/EERC Report No. 91/17, Earthquake Engineering Research Center, University of California, Berkeley, CA.
- Tirasit, P., and Kawashima, K. (2005). Seismic Torsion Response of Skewed Bridge Piers. *Journal of Earthquake Engineering, JSCE*, 116. (CD-ROM).
- Tirasit, P., and Kawashima, K. (2007). Seismic Performance of Square Reinforced Concrete Columns under Combined Cyclic Flexural and Torsional Loadings. *Journal of Earthquake Engineering, JSCE*, 11, 425-452.

- Tirasit, P., Kawashima, K., and Watanabe, G. (2005). An Experimental Study on the Performance of RC Columns Subjected to Cyclic Flexural-Torsional Loading. *Second International Conference on Urban Earthquake Engineering*. Tokyo, Japan.
- Ugural, A. C., and Fenster, S. K. (1995). *Advanced Strength and Applied Elasticity* (3rd ed.). Prentice Hall, Upper Saddle River, NJ.
- Vecchio, F. J., and Collins, M. P. (1986). The Modified Compression-Field Theory for Reinforced Concrete Elements Subjected to Shear. *Journal of the American Concrete Institute*, 83, 219-231.
- Venkappa, V., and Pandit, G. S. (1987). Cyclic Torsion Tests on Reinforced Concrete Beams. *Journal of Structural Engineering, ASCE*, 113, 1329-1340.
- Zhang, L. X., and Hsu, T. T. C. (1998). Behavior and Analysis of 100 MPa Concrete Membrane Elements. *Journal of Structural Engineering, ASCE*, 124, 24-34.
- Zhao, J., and Sritharan, S. (2007). Modeling of Strain Penetration Effects in Fiber-Base Analysis of Reinforced Concrete Structures. *ACI Structural Journal*, 104, 133-141.

# Appendix A

## Test Setup

As discussed in Chapter 4, the test setup consisted of various components for the application of axial and lateral load. This appendix presents additional information on the assembly and configuration of the test setup, which consisted of four major phases: positioning the specimen, post-tensioning the specimen to the laboratory floor, axial load setup, and lateral load setup.

### A.1 Specimen Positioning

Each specimen was lifted by the crane and lowered into the test location, approximately 9 ft from the reaction frame. The specimen was aligned on the holes of the laboratory floor, which are spaced at 3 ft on center. The columns were then plumbed using shims between the specimen footing and the laboratory floor. Once plumbed, the specimen was lifted with the crane about 2 ft to allow sufficient room for placing of hydrostone, as shown in Figure A.1. Next, the specimen was gently lowered into the hydrostone. The hydrostone was allowed to cure for a minimum of 24 hours prior to post-tensioning the



Figure A.1: Positioning of Specimen on Laboratory Floor

specimen to the laboratory floor.

## A.2 Specimen Post-tensioning

Once the hydrostone had cured, the tie-down beams were placed on the specimen footing. The holes in the tie-down beams were aligned with the holes in the footing and the laboratory floor. Next, stress bars were inserted in the holes of the laboratory floor and thru the tie-down beams. A hydraulic jack was used to post-tension each stress bar.

Each specimen was post-tensioned to the laboratory floor with six stress bars to prevent sliding and rotation during testing. The stress bars running through the footing were post-tensioned to a force of 200 kips, whereas the stress bars outside of the footing were post-tensioned to 100 kips. Figure A.2 illustrates equilibrium of the specimen under lateral and axial loading. Assuming the specimen acts as a rigid member, the required

Table A.1: Specimen Rotation/Sliding Demand and Capacity

Cross Section	$V_o$ (kips)	$V_{max}$ (kips)		$V_o/V_{max}$	
		Rotation	Sliding	Rotation	Sliding
Circular	76	385	165	0.2	0.46
Oblong	138	445	240	0.31	0.58

lateral force to initiate rotation and sliding are

$$V_{max} = \begin{cases} [P_{bar}d_{bar} + P_{axial}(d_{bar}/2)]/L & \text{Rotation} \\ \mu(2P_{bar} + P_{axial}) & \text{Sliding} \end{cases} \quad (\text{A.1})$$

where  $P_{bar}$  = post-tensioning force for one side of the specimen footing,  $P_{axial}$  = column axial force,  $d_{bar}$  = distance between stress bars,  $L$  = column length, and  $\mu$  = coefficient of friction. The specimen rotation/sliding demand and capacity for each cross section is summarized in Table A.1, assuming  $\mu = 0.2$

### A.3 Axial Load Setup

The axial load was transferred to the column by stress bars, located on the North and South faces of the specimen, through a spreader beam. Each stress bar was attached to the spreader beam using a 3D clevis, which was attached to the underside of the spreader beam using four 1 in. diameter threaded rods, and a coupling nut between the stress bar and clevis. A manually-controlled hydraulic jack was used to load each stress bar, as shown in Figure A.3. A cage consisting of an upper steel plate, a lower 3D clevis, and four 1 in. diameter threaded rods was constructed around each jack. The lower clevis was attached to a stress bar, which was post-tensioned to the laboratory floor, using a coupling nut. Steel

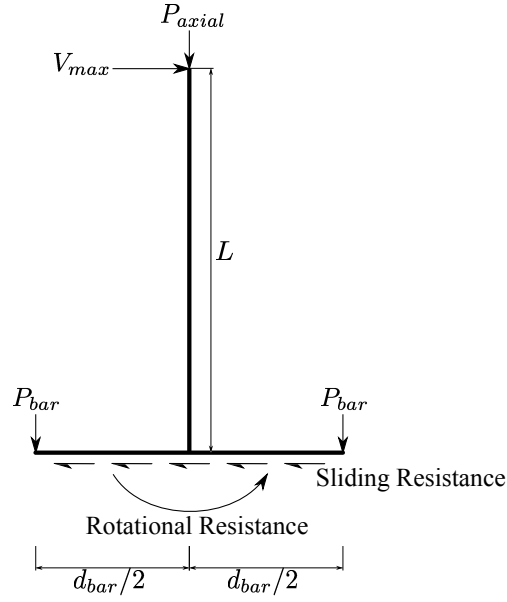


Figure A.2: Specimen Equilibrium Under Axial and Lateral Loading

plates, which were hydrostoned to the laboratory floor, were used as bearing supports for the stress bars.

#### A.4 Lateral Load Setup

The lateral load setup involved attaching the horizontal actuators to the reaction frame, attaching the lateral loading beam to the face of the column cap, and connecting the actuator clevises to the lateral loading beam. The horizontal actuators were attached to the reaction frame in the fully-retracted position. The lateral loading beam was post-tensioned to the face of the column cap using four stress bars passing through the column cap and four stress bars outside of the column cap. Due to interference of stiffeners, the lateral loading beam was post-tensioned to the face of the oblong column with four stress bars passing through the column cap. Additionally, four 1 in. diameter threaded rods tightened

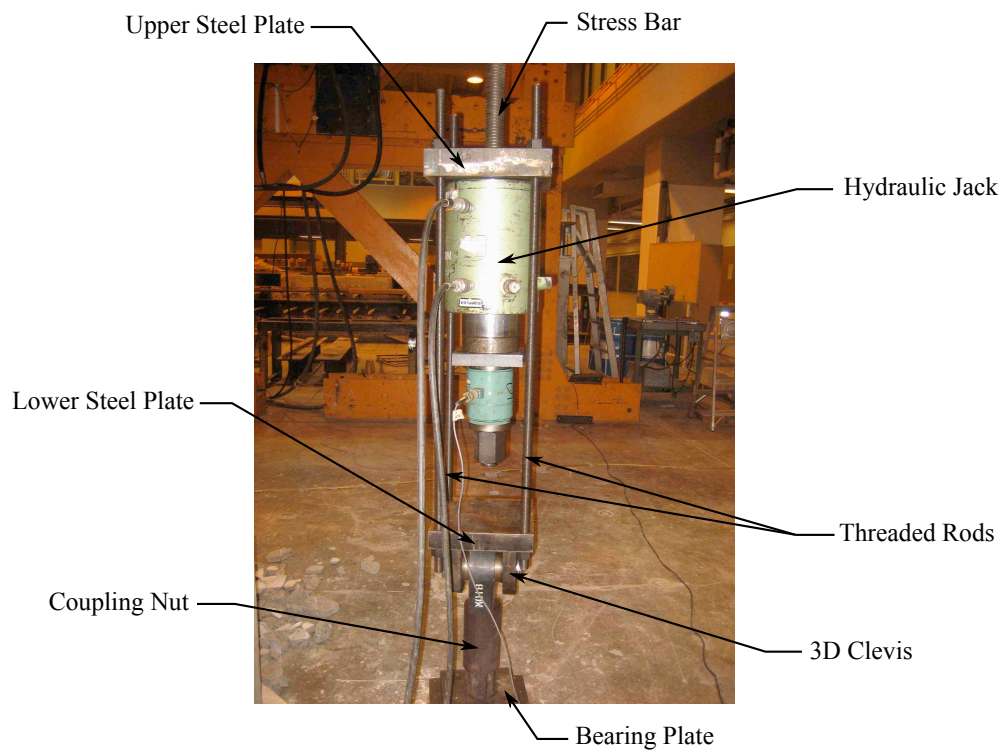


Figure A.3: Axial Load Setup

using the impact gun were used in lieu of stress bars. The actuator clevises were connected to the lateral loading beam by extending the horizontal actuators sufficiently to initiate contact between the clevis and beam. The clevis and beam holes were aligned and bolts were installed to complete installation.

The lateral load setup was designed to test the columns to failure. Failure required exceeding the displacement and twist capacity of the columns as well as imposing the necessary lateral force and torque to reach these displacements.

The design lateral displacement was 10 in. or approximately equal to a displacement ductility of 10, based on the measured force-displacement response of Lehman 415 (Lehman and Moehle, 2000). The minimum design lateral force, corresponding to the necessary lateral force to displace the column 10 in., was estimated equal to the plastic shear for the oblong cross section computed in Section 3.2. An upper-bound for twist/drift ratio = 2.0 was chosen.

The minimum design torque was estimated using the space truss analogy (ACI, 2008) for the oblong cross section, shown in Equation 2.18. The inclination of cracking was taken equal to  $\alpha = 45$  deg and the area enclosed by the shear flow path equal conservatively to the gross cross-sectional area  $A_o = A_g$ . The resulting minimum design lateral force and torque was 115 kips and 4130 kip-in., respectively.

The horizontal actuator demands, for a range of spacings, are summarized in Table A.2 for a design lateral displacement and twist equal to 10 in. and 2.0 radians, respectively, and for a design lateral force and torque equal to 150 kips and 5000 kip-in., respectively. The 84 in. spacing meets the allowable actuator extension and force if the actuators are positioned at mid-stroke to provide  $\pm 18$  in. stroke and 120 kips force. The

Table A.2: Horizontal Acuator Demands

Spacing (in.)	Extension (in.)		Force (kips)	
	North	South	North	South
48	4.8	14.4	164	-44
60	3.6	15.6	143	-23
72	2.4	16.8	129	-9
84	1.2	18.0	120	0
96	0	19.2	112	8

horizontal actuators were spaced at 82.5 in., centered about the column centerline, and positioned at mid-stroke when attached to the lateral loading beam.

# Appendix B

## Data Reduction

This appendix presents an overview of how the measured data was reduced to produce global response data and column region response data.

### B.1 Displacements and Forces

#### B.1.1 Lateral Displacement and Twist

The lateral displacement  $\delta$  was determined as the average of the LP measurements

$$\Delta = \frac{\Delta_N + \Delta_S}{2} \quad (\text{B.1})$$

The twist  $\theta$  was determined as the difference in LP measurements divided by the distance between LP's

$$\theta = \frac{\Delta_S - \Delta_N}{d_{lp}} \quad (\text{B.2})$$

where  $d_{lp}$  = distance between the LP's.

### B.1.2 Lateral Force and Torque

The horizontal component of the vertical jacks, caused by lateral displacement and twist of the column, further added to the forces measured by the built-in force transducers of the horizontal actuators. This is shown schematically in Figure B.1, where the vertical tip displacement of the column was assumed to be negligible and the measured lateral force and torque were larger than the actual lateral force and torque, being more pronounced at larger amplitude displacement cycles. Thus, the lateral force  $F$  was equal to the sum of the actuator forces minus the horizontal component of the vertical jacks  $F_h^{jack}$ , determined by

$$F = F_N + F_S - F_h^{jack} \quad (B.3)$$

$$F_h^{jack} = F_{Nh}^{jack} + F_{Sh}^{jack} \quad (B.4)$$

$$F_{Nh}^{jack} = F_N^{jack} \left[ \frac{\Delta_N^{jack}}{\sqrt{(L_{pin-pin})^2 + (\Delta_N^{jack})^2}} \right] \quad (B.5)$$

$$F_{Sh}^{jack} = F_S^{jack} \left[ \frac{\Delta_S^{jack}}{\sqrt{(L_{pin-pin})^2 + (\Delta_S^{jack})^2}} \right] \quad (B.6)$$

$$\Delta_N^{jack} = \Delta - \theta \left( \frac{d_{jack}}{2} \right) \quad (B.7)$$

$$\Delta_S^{jack} = \Delta + \theta \left( \frac{d_{jack}}{2} \right) \quad (B.8)$$

where  $d_{jack}$  = distance between vertical jacks and  $L_{pin-pin}$  = distance between clevis pins.

The torque  $T$  was determined as the difference in actuator forces multiplied by half to distance between actuators, which were equally spaced from the column centerline, minus the torque due to the horizontal component of the vertical jacks

$$T = (F_S - F_N) \left( \frac{d_{act}}{2} \right) - T_h^{jack} \quad (B.9)$$

$$T_h^{jack} = \left( F_{Sh}^{jack} - F_{Sh}^{jack} \right) \left( \frac{d_{jack}}{2} \right) \quad (\text{B.10})$$

where  $d_{act}$  = distance between the horizontal actuators.

## B.2 Column Deformations

The DTs along the height of the column (Figure 4.7) were used to calculate the horizontal, axial, rotational, and shear deformation. Figure B.2 shows a typical column segment in the original configuration and the four deformation modes. The segment height and width are  $h$  and  $b$ , respectively. The length of the diagonal was  $d = \sqrt{h^2 + b^2}$ .

### B.2.1 Average Vertical Strain

The average vertical strain  $\bar{\epsilon}_v$  was the average vertical displacement divided by the original segment height

$$\bar{\epsilon}_v = \frac{\Delta_v}{h} \quad (\text{B.11})$$

where  $\Delta_v$  = vertical extension. The vertical extension  $\Delta_v$  was the average of the two vertical displacements, defined by

$$\Delta_v = \frac{\Delta_W + \Delta_E}{2} \quad (\text{B.12})$$

### B.2.2 Average Horizontal Strain

The average horizontal strain  $\bar{\epsilon}_h$  was the average horizontal displacement divided by the original segment width

$$\bar{\epsilon}_h = \frac{\Delta_h}{b} \quad (\text{B.13})$$

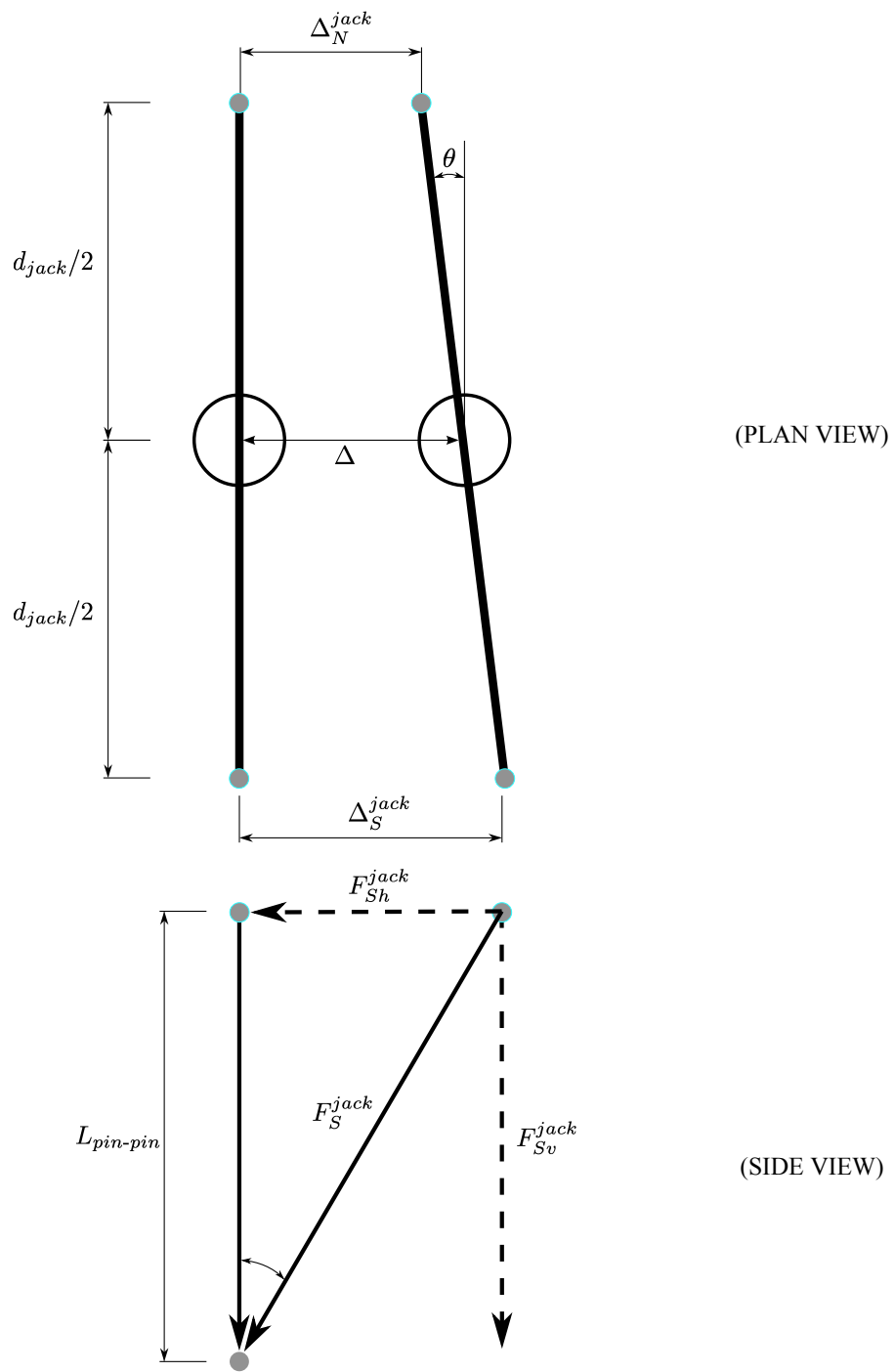


Figure B.1: Force Components of Vertical Jack Under Lateral Displacement

where  $\Delta_h$  = horizontal expansion. The horizontal expansion  $\Delta_h$  was the average of the two horizontal displacements, defined by

$$\Delta_h = \frac{\Delta_T + \Delta_B}{2} \quad (\text{B.14})$$

### B.2.3 Average Curvature

The average curvature was approximated as the segment rotation divided by the segment height

$$\bar{\phi} = \frac{\theta}{h} \quad (\text{B.15})$$

where  $\theta$  = segment rotation. The segment rotation  $\theta$  was the difference of the two vertical displacements divided by the original segment width, defined by

$$\theta = \frac{\Delta_W - \Delta_E}{b} \quad (\text{B.16})$$

### B.2.4 Average Longitudinal Strain

The average longitudinal strain at the column faces was approximated using the external DT by the following

$$\bar{\epsilon}_l = \frac{\Delta_v - e \tan \theta}{h} \quad (\text{B.17})$$

where  $e$  = distance from the center of the column to the desired location.

### B.2.5 Shear Strain

The shear strain due to shear was the average shear strain of a segment, defined by

$$\gamma_V = \frac{\gamma_N + \gamma_S}{2} \quad (\text{B.18})$$

where  $\gamma_N$  and  $\gamma_S$  was the shear strain measured on the North and South face, respectively. The shear strain due to torsion was the difference of the shear strain measured on the North and South face, defined by

$$\gamma_T = \gamma_N - \gamma_S \quad (\text{B.19})$$

The local shear strain  $\gamma$  was approximated as

$$\gamma = \frac{\sqrt{(d + \Delta D)^2 - (h + \Delta_v)^2} - (b + \Delta_h)}{h + \Delta_v} \quad (\text{B.20})$$

where  $\Delta D$  = extension of the diagonal instrument. Eq. B.20 was determined by removing the extension of the instrument due to horizontal and vertical extension.

### B.3 Displacement Components

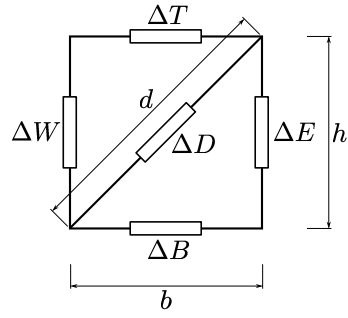
As explained in Section 2.1, the total tip displacement of a cantilever column subjected to a lateral load at the tip can be idealized as the summation of the components due to column bending, shear deformation, and anchorage slip (Eq. 2.1). Unfortunately, the displacement components cannot be measured precisely and thus are approximated using the column deformations along the height of the column (Section B.2).

#### B.3.1 Column Bending

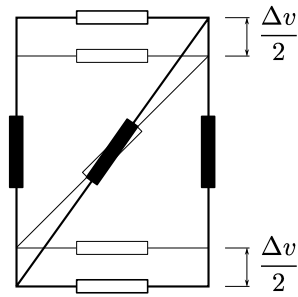
The lateral displacement of a column due to bending can be calculated by integrating the flexural curvature along the height of the column

$$\Delta_{bending} = \int_0^L \phi(x) x dx \quad (\text{B.21})$$

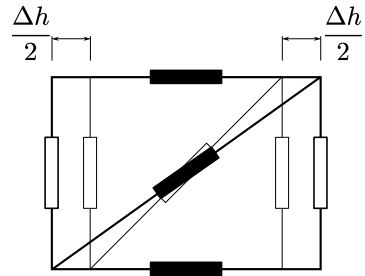
The flexural curvature  $\phi(x)$  cannot be continuously measured along the height of the column, but rather at segments along the height. For a discrete number of segments, the



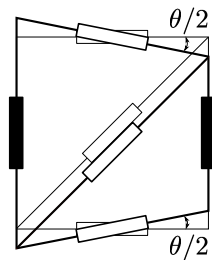
Original Configuration



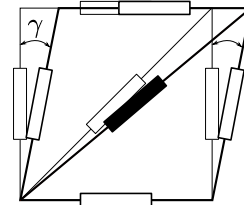
Vertical Extension



Horizontal Expansion



Segment Rotation



Shear Strain

Figure B.2: Column Segment Deformation Modes

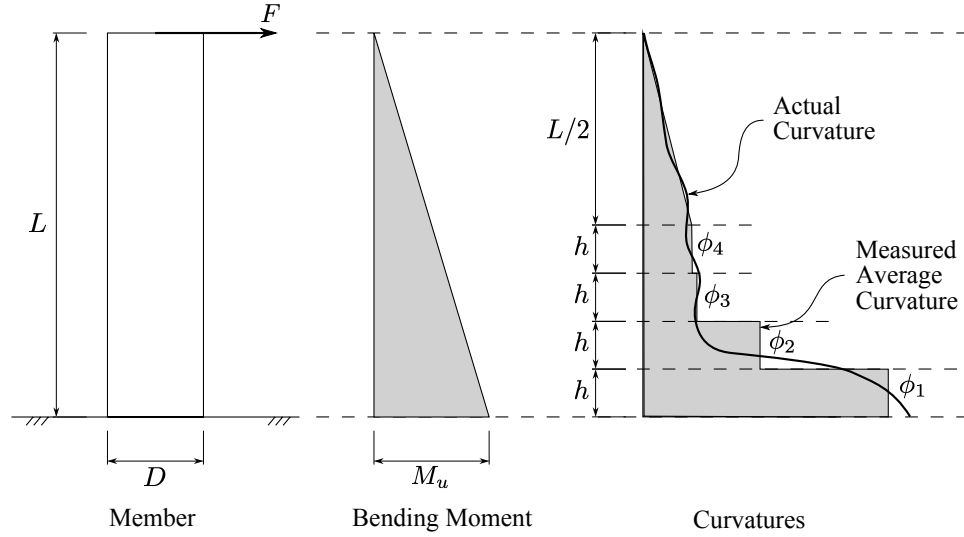


Figure B.3: Actual and Measured Average Curvature Distribution for a Cantilever Column

lateral displacement can be approximated as

$$\Delta_{bending} \simeq \sum_1^n (\text{area under curve})_i \times (\text{distance to centroid})_i \quad (\text{B.22})$$

where  $n$  = total number of segments. Figure B.3 shows the idealized and measured average curvature distributions for a cantilever column subjected to lateral load. The measured average curvatures can be used to calculate the displacement due to bending in the following manner

$$\begin{aligned} \Delta_{bending} \simeq & \left[ (\phi_1 h) \times \left( L - \frac{1}{2} h \right) \right] + \left[ (\phi_2 h) \times \left( L - \frac{3}{2} h \right) \right] \\ & + \left[ (\phi_3 h) \times \left( L - \frac{5}{2} h \right) \right] + \left[ (\phi_4 h) \times \left( L - \frac{7}{2} h \right) \right] \\ & + \left[ \left( \frac{1}{2} \phi_4 L \right) \left( \frac{2}{3} L \right) \right] \end{aligned} \quad (\text{B.23})$$

where  $\phi_1$  = average curvature for elevation 0-12 in.,  $\phi_2$  = average curvature for elevation 12-24 in.,  $\phi_3$  = average curvature for elevation 24-36 in., and  $\phi_4$  = average curvature for elevation 36-48 in.

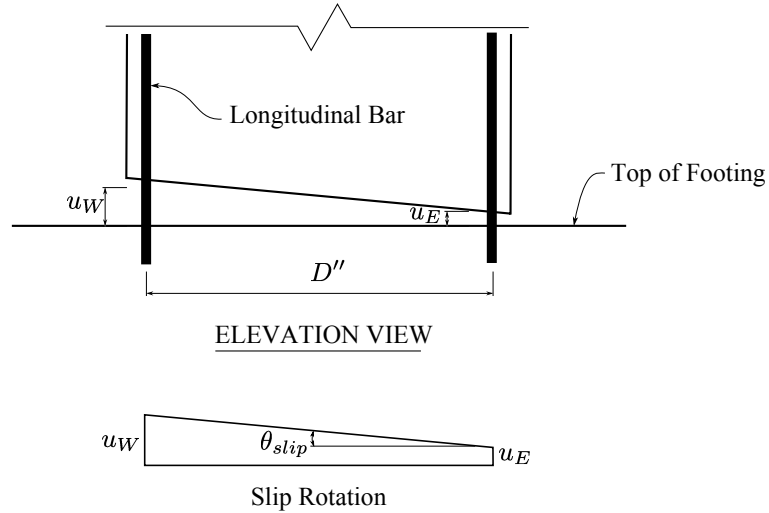


Figure B.4: Calculated Slip Rotation for Displacement due to Anchorage Slip

### B.3.2 Anchorage Slip

The displacement component due to anchorage slip can also be approximated using the slip extension instruments attached to the longitudinal reinforcing bars at the East and West faces of the column (Figure 4.10). The slip displacement and slip rotation, illustrated in Figure B.4, can be calculated with the following

$$\Delta_{slip} = \theta_{slip} L \simeq \left( \frac{u_W - u_E}{D''} \right) L \quad (\text{B.24})$$

where  $u_W$  = slip extension on the West face,  $u_E$  = slip extension on the East face, and  $D''$  = distance between the longitudinal reinforcing bars.

### B.3.3 Shear Deformation

The displacement component due to shear deformation can be approximated using the measured average shear strain due to shear force along the height of the column. Figure B.5 shows the idealized and measured average shear strain distributions for a cantilever

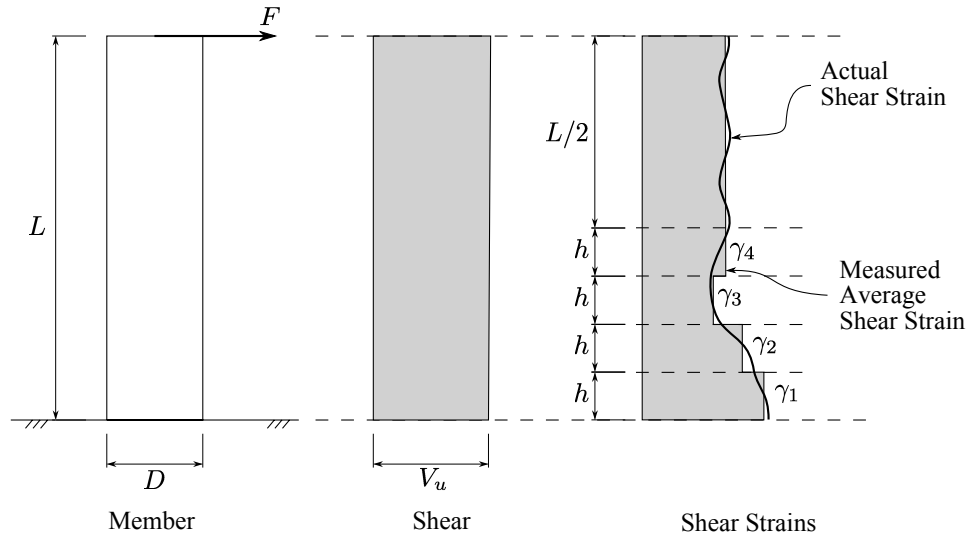


Figure B.5: Actual and Calculated Shear Strain Distribution for a Cantilever Column

column subjected to lateral load. The measured average shear strain due to shear force can be used to calculate the displacement due to shear deformation in the following manner

$$\Delta_{shear} \simeq \gamma_1 h + \gamma_2 h + \gamma_3 h + \gamma_4 \left( h + \frac{L}{2} \right) \quad (\text{B.25})$$

where  $\gamma_1$  = shear strain for elevation 0-12 in.,  $\gamma_2$  = shear strain for elevation 12-24 in.,  $\gamma_3$  = shear strain for elevation 24-36 in.,  $\gamma_4$  = shear strain for elevation 36-48 in.,

## Appendix C

# Experimental Data

This appendix presents the measured response of the four column specimens tested. The reduction of raw data was performed according to Appendix B.

### C.1 Global Response

The lateral displacement histories along the height of the columns are shown in Figures C.1, C.4, and C.7 for Columns C1, C2, and C3, respectively. Figures C.2, C.5, and C.8 show the lateral displacement profiles for Columns C1, C2, and C3, respectively. Measurements corresponding to the first peak of each displacement amplitude cycle are indicated by markers. The contributions of slip, shear, and bending to the lateral displacement are shown in Figures C.2, C.5, and C.8 for Columns C1, C2, and C3, respectively.

The twist histories along the height of the columns are shown in Figures C.10, C.12, C.14, and C.16 for Columns C1, C2, C3, and C4, respectively. The twist profiles corresponding to the first peak of each displacement amplitude cycle are shown in Figures C.11, C.13, and C.15 for Columns C1, C2, and C3, respectively. Figure C.17 shows the

twist profile for Column C4 corresponding to the first peak of each twist amplitude cycle. Measurements are indicated by markers.

## **C.2 Column Region**

The arrangement of DTs (Figure 4.7) and SGs (Figure 4.11) were used to measure the local deformations along the height of the columns.

### **C.2.1 Horizontal Expansion**

The horizontal expansion was measured on the North and South faces along the height of Columns C1, C2, C3, and C4, shown in Figures C.18, C.20, C.22, and C.24, respectively. The average horizontal expansion profiles corresponding to the first peak of each displacement amplitude cycle are shown in Figures C.19, C.21, and C.23 for Columns C1, C2, and C3, respectively. Figure C.25 shows the average horizontal profile for Column C4 corresponding to the first peak of each twist amplitude cycle. Measurements are indicated by markers.

### **C.2.2 Average Curvature**

The average curvature was approximated for each column segment of Columns C1, C2, and C3, shown in Figures C.26, C.28, and C.30, respectively. Two average curvatures are presented for the bottom-most segment: the solid line corresponds to the total segment rotation divided by the segment height and the dashed line corresponds to the total rotation minus the slip rotation divided by the segment height. The average curvature profiles are shown in Figures C.27, C.29, and C.31 for Columns C1, C2, and C3, respectively.

Measurements corresponding to the first peak of each displacement amplitude cycle are indicated by markers.

### **C.2.3 Average Longitudinal Strain**

The average longitudinal strain was approximated using the external DTs at the location of the extreme West and East longitudinal reinforcing bars for Columns C1, C2, and C3, shown in Figures C.32, C.34, and C.36, respectively. The total segment rotation from the arrangement of DTs was used in the calculation for the bottom-most segment. The average longitudinal strain profiles are shown in Figures C.33, C.35, and C.37 for Columns C1, C2, and C3, respectively. Measurements corresponding to the first peak of each displacement amplitude cycle are indicated by markers.

### **C.2.4 Shear Strain**

The segment shear strain was measured on the North and South faces of Columns C1, C2, C3, and C4, shown in Figures C.38, C.40, C.42, and C.44, respectively. The shear strain due to shear (average of North and South faces) and the shear strain due to torsion (difference of North and South faces) profiles corresponding to the first peak of each displacement amplitude cycle are shown in Figures C.39, C.43, and C.43 for Columns C1, C2, and C3, respectively. Figure C.45 shows the shear strain due to shear and shear strain due to torsion profiles for Column C4 corresponding to the first peak of each twist amplitude cycle. Measurements are indicated by markers.

### **C.2.5 Longitudinal Strains**

The longitudinal strain gauge histories and profiles of Columns C1, C2, and C3 are shown in Figures C.46 to C.49, Figures C.50 to C.53, and Figures C.54 to C.57, respectively. Measurements corresponding to the first peak of each displacement amplitude cycle are indicated by markers. Figures C.58 and C.59 show the longitudinal strain gauge history and profile corresponding to the first peak of each twist amplitude cycle, respectively, for Column C4.

### **C.2.6 Hoop Strains**

The hoop strain gauge histories and profiles of Columns C1, C2, and C3 are shown in Figures C.60 to C.63, Figures C.64 to C.67, and Figures C.68 to C.71, respectively. Measurements corresponding to the first peak of each displacement amplitude cycle are indicated by markers. Figures C.72 and C.73 show the hoop strain gauge history and profile corresponding to the first peak of each twist amplitude cycle, respectively, for Column C4.

## **C.3 Joint Region**

The arrangement of DTs (Figure 4.10) and strain gauges (Figure 4.11) were used to measure the joint region deformations.

The bar slip histories of Columns C1, C2, and C3 are shown in Figures C.74, C.75, and C.76, respectively. The joint strain histories and profiles of Columns C1, C2, and C3 are shown in Figures C.77 to C.79, Figures C.80 to C.82, and Figures C.83 to C.85, respectively. Measurements corresponding to the first peak of each displacement amplitude cycle are indicated by markers.

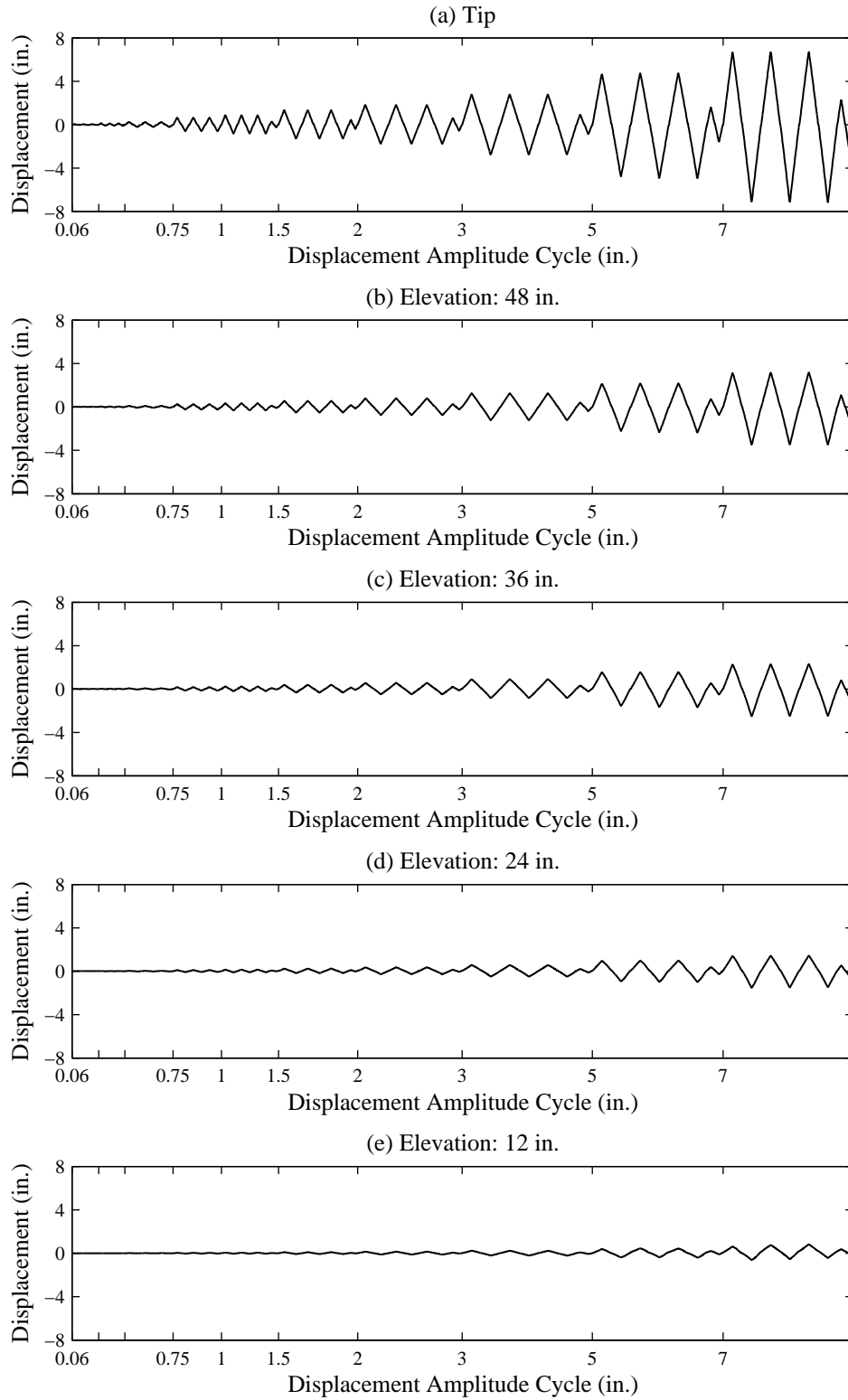


Figure C.1: Column C1 Level Displacement History

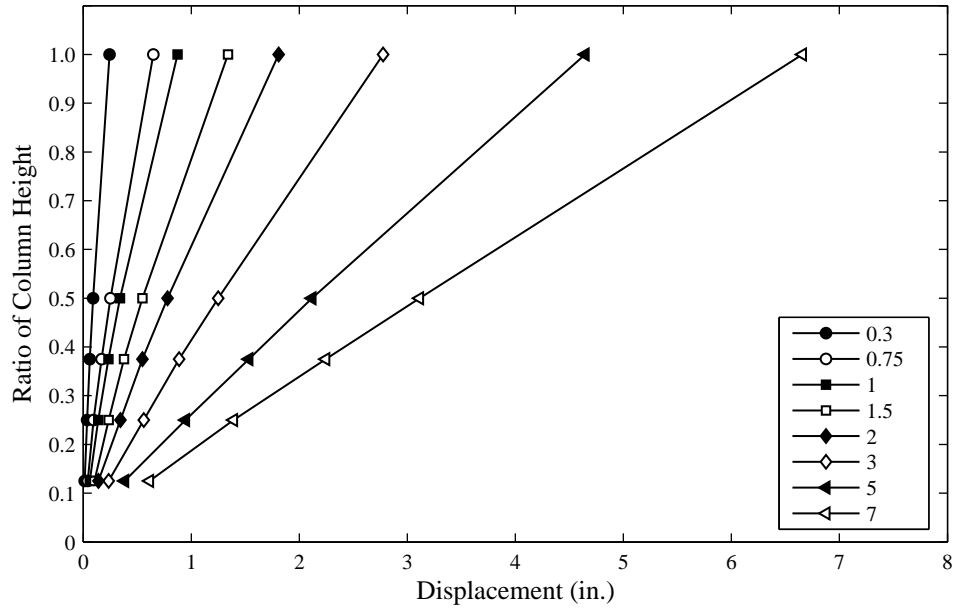


Figure C.2: Column C1 Displacement Profile

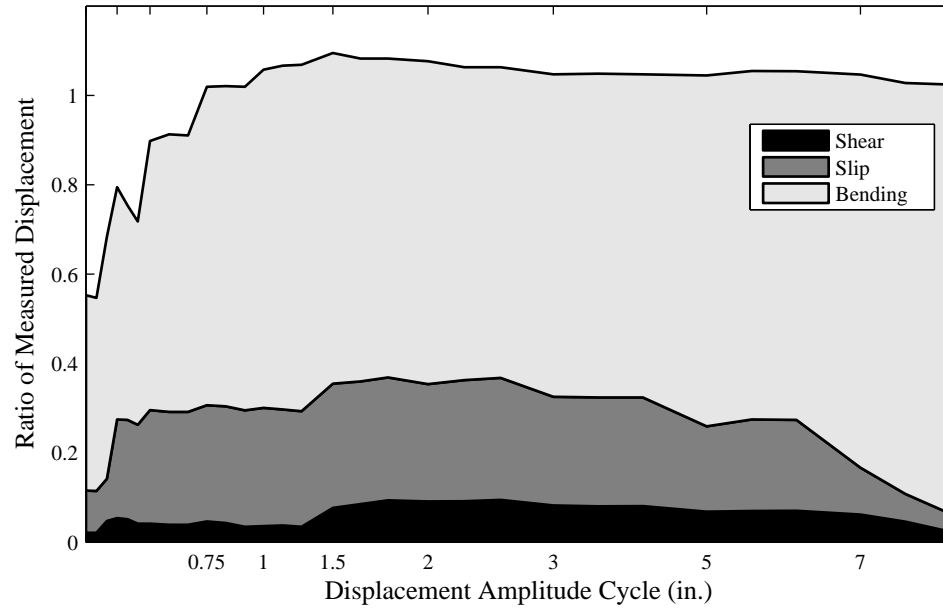


Figure C.3: Column C1 Displacement Components

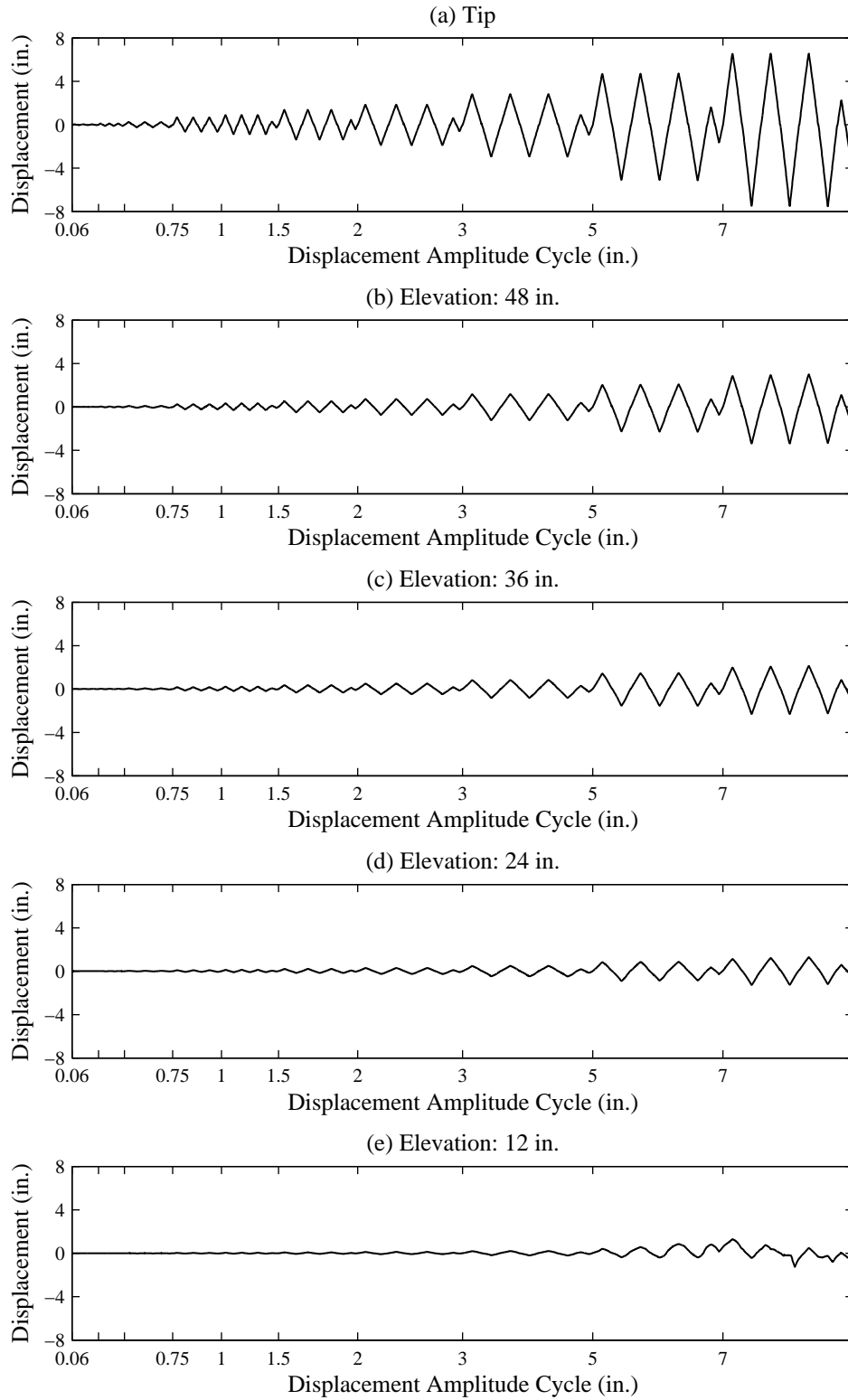


Figure C.4: Column C2 Level Displacement History

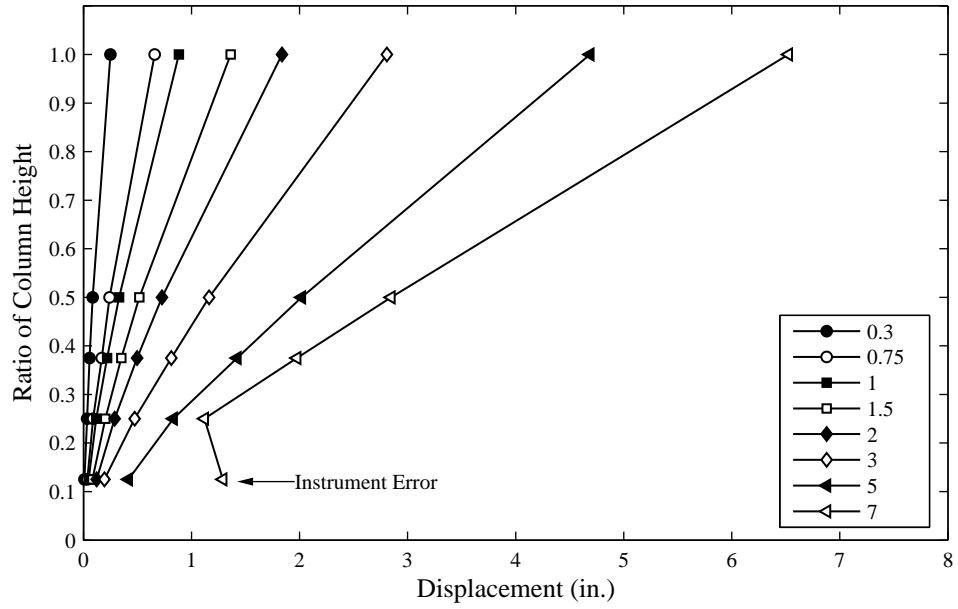


Figure C.5: Column C2 Displacement Profile

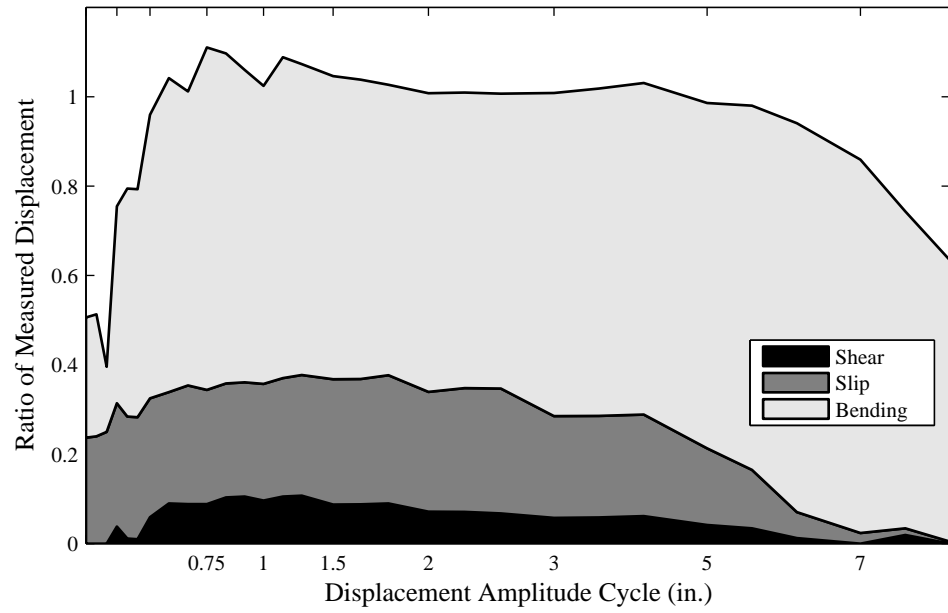


Figure C.6: Column C2 Displacement Components

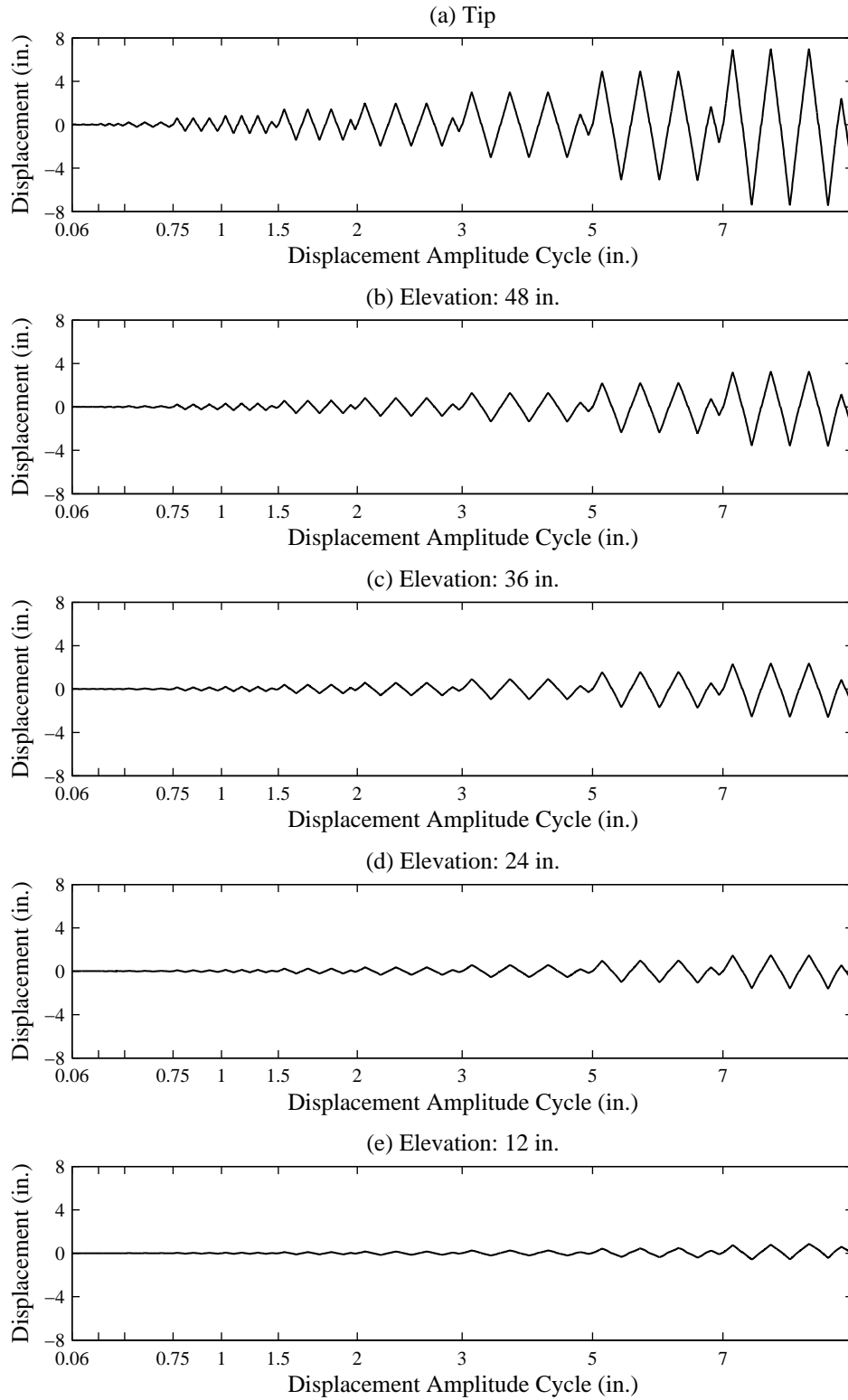


Figure C.7: Column C3 Level Displacement History

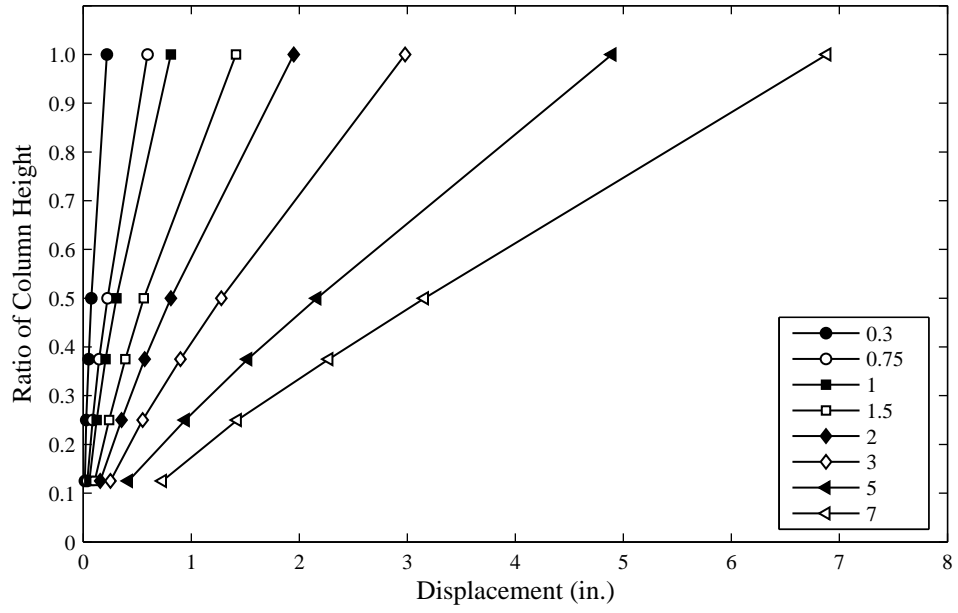


Figure C.8: Column C3 Displacement Profile

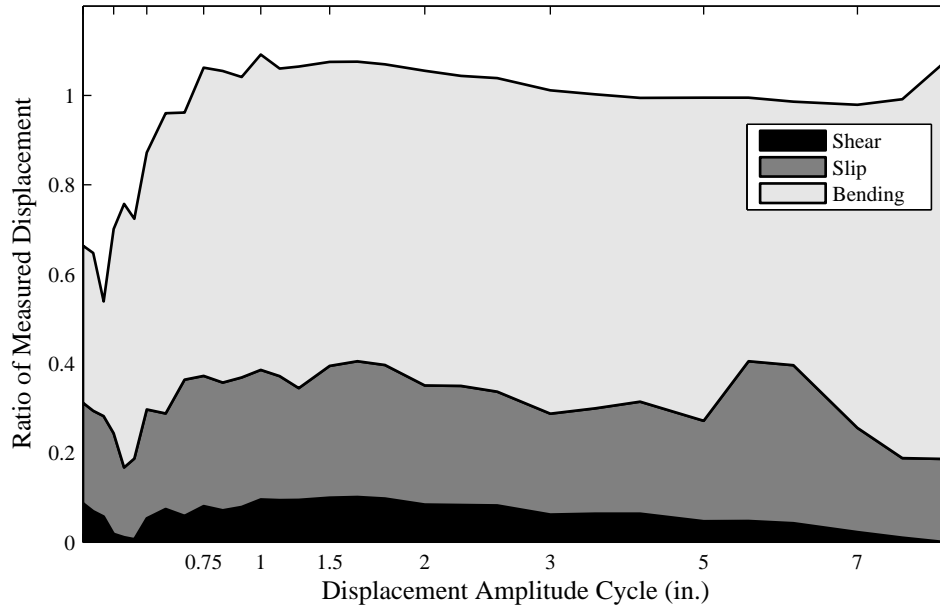


Figure C.9: Column C3 Displacement Components

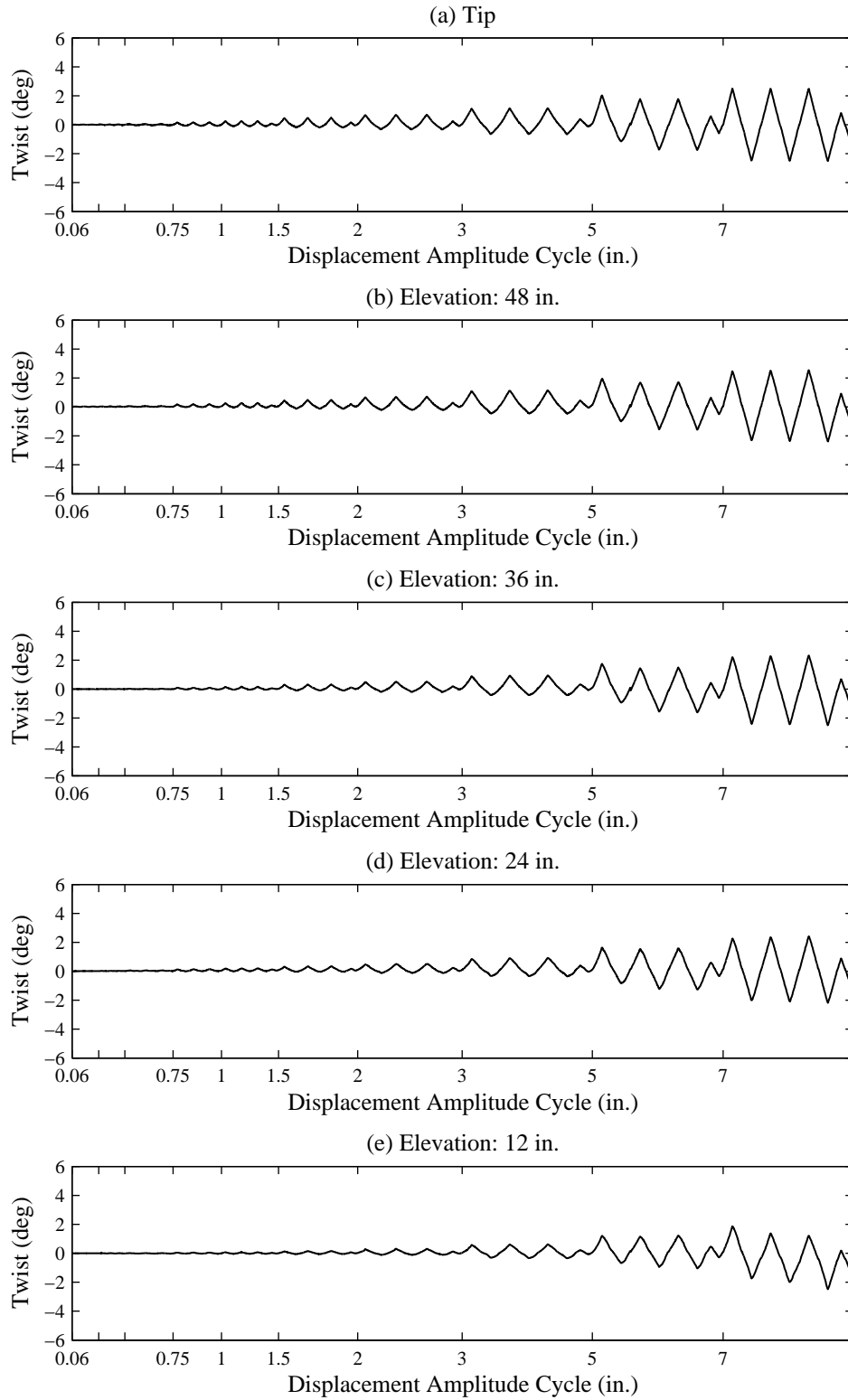


Figure C.10: Column C1 Level Twist History

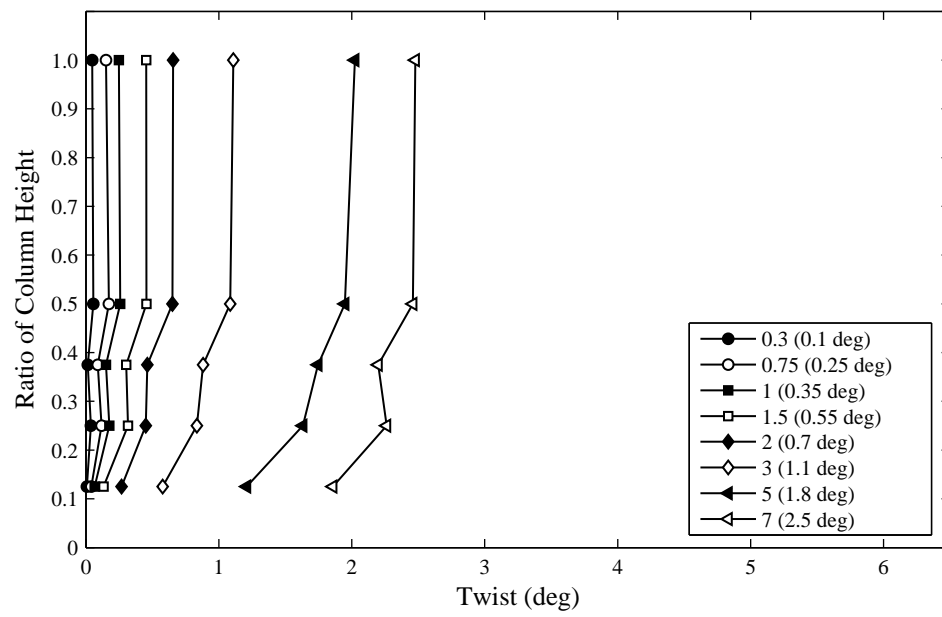


Figure C.11: Column C1 Twist Profile

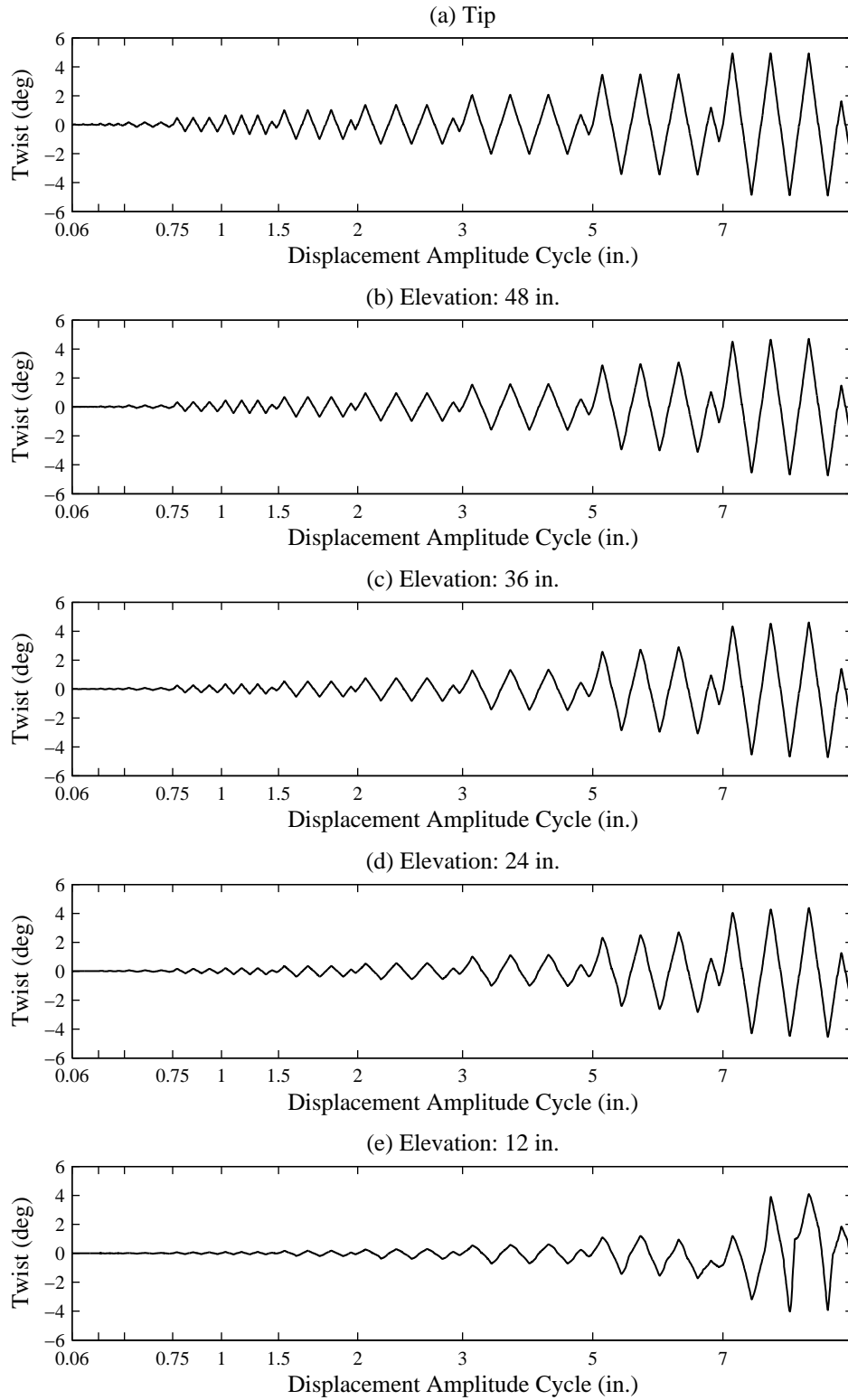


Figure C.12: Column C2 Level Twist History

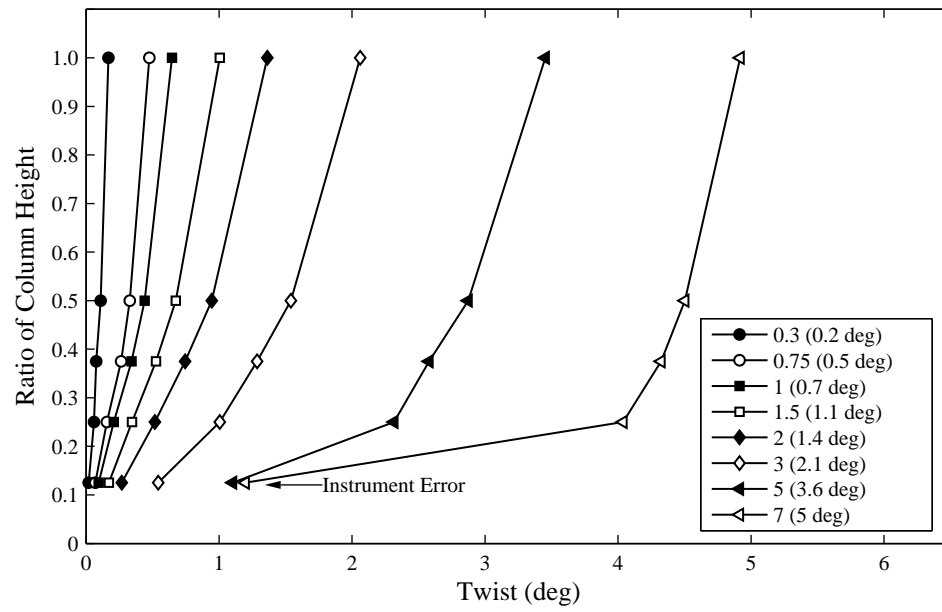


Figure C.13: Column C2 Twist Profile

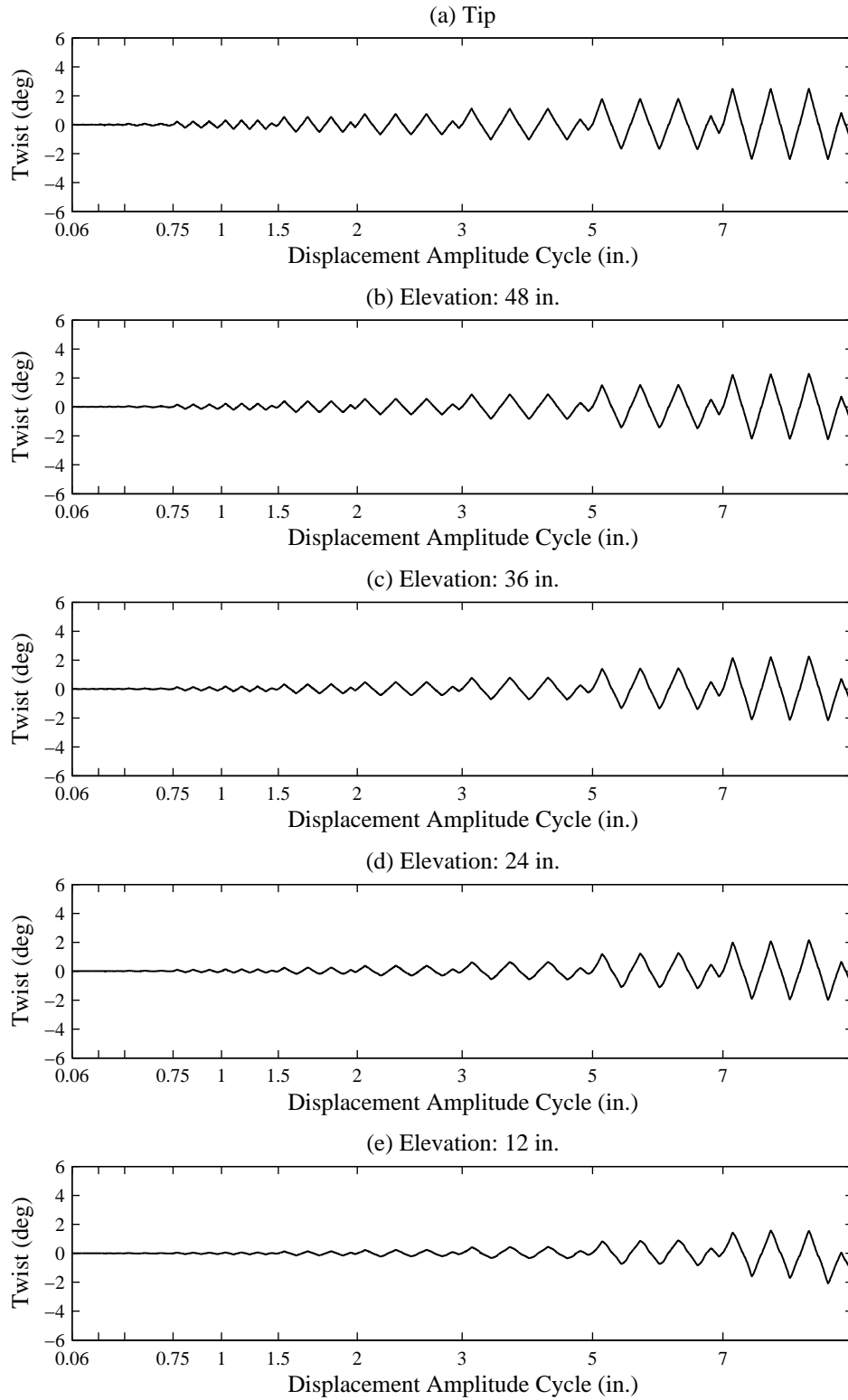


Figure C.14: Column C3 Level Twist History

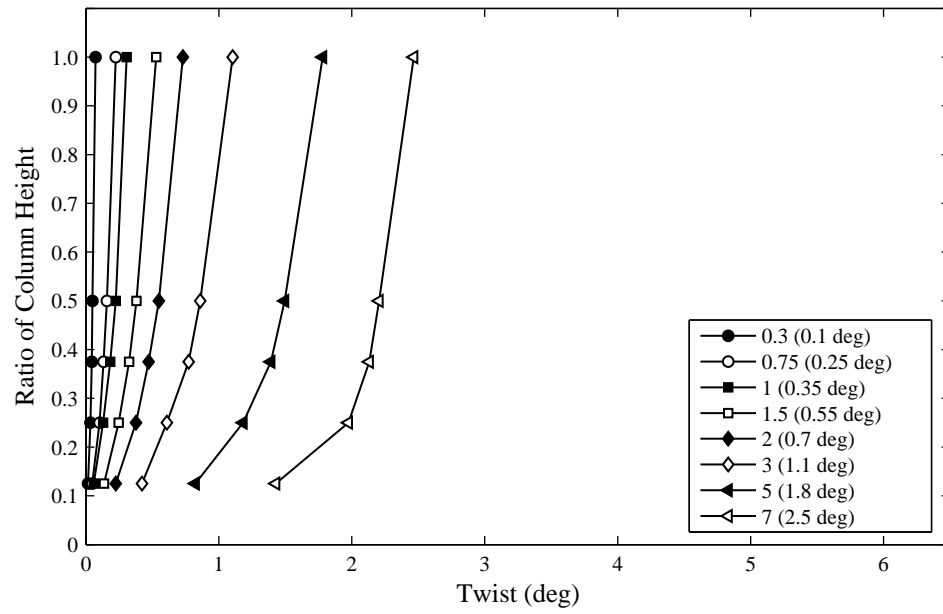


Figure C.15: Column C3 Twist Profile

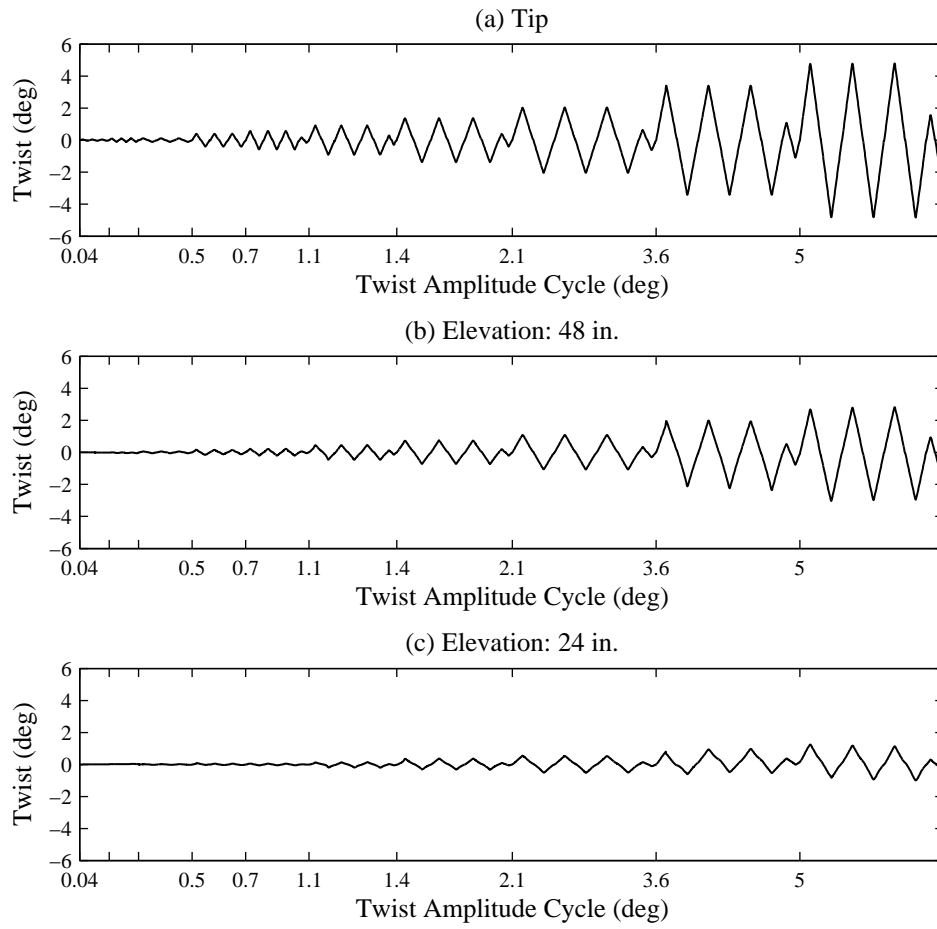


Figure C.16: Column C4 Level Twist History

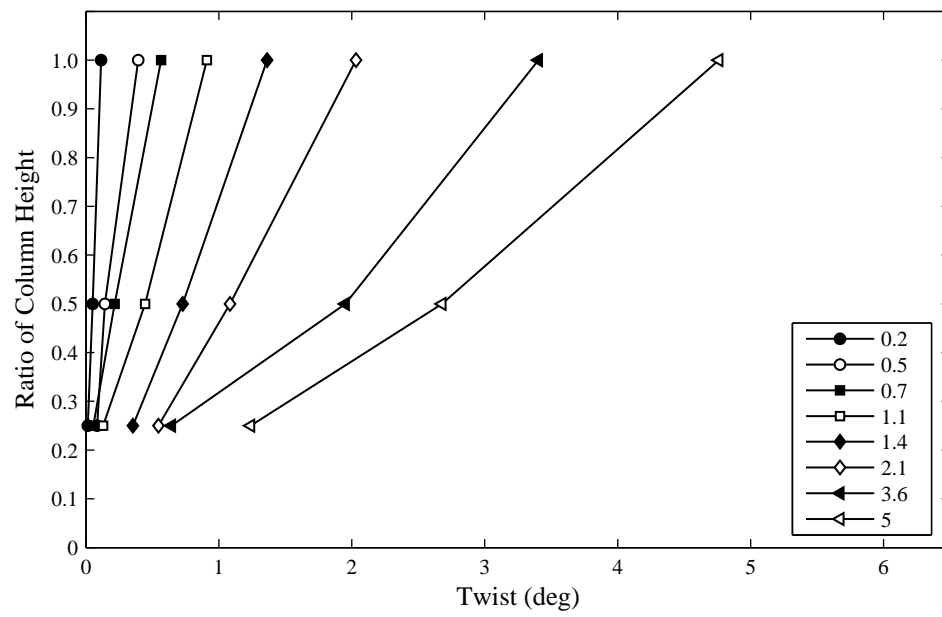


Figure C.17: Column C4 Twist Profile

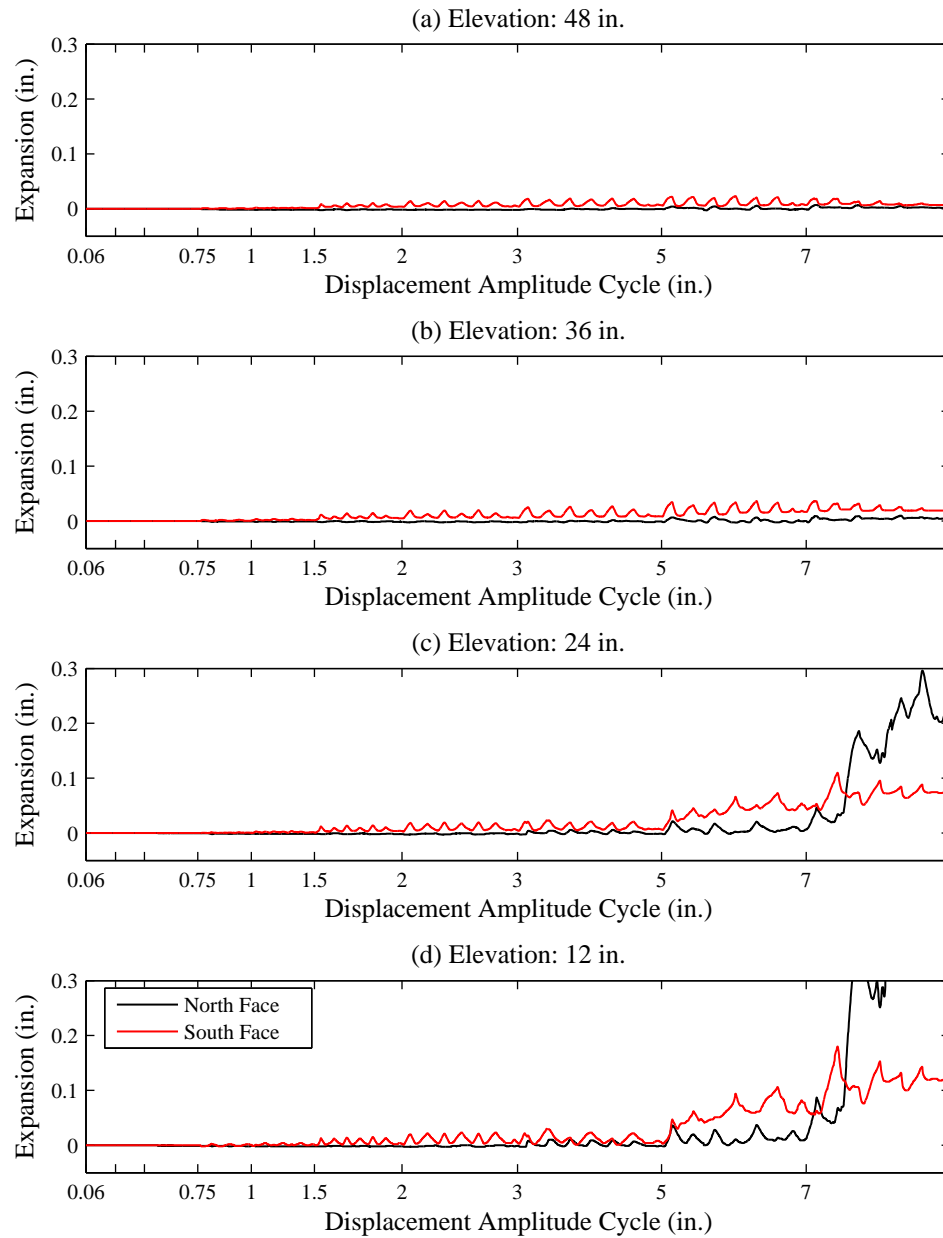


Figure C.18: Column C1 Horizontal Expansion History

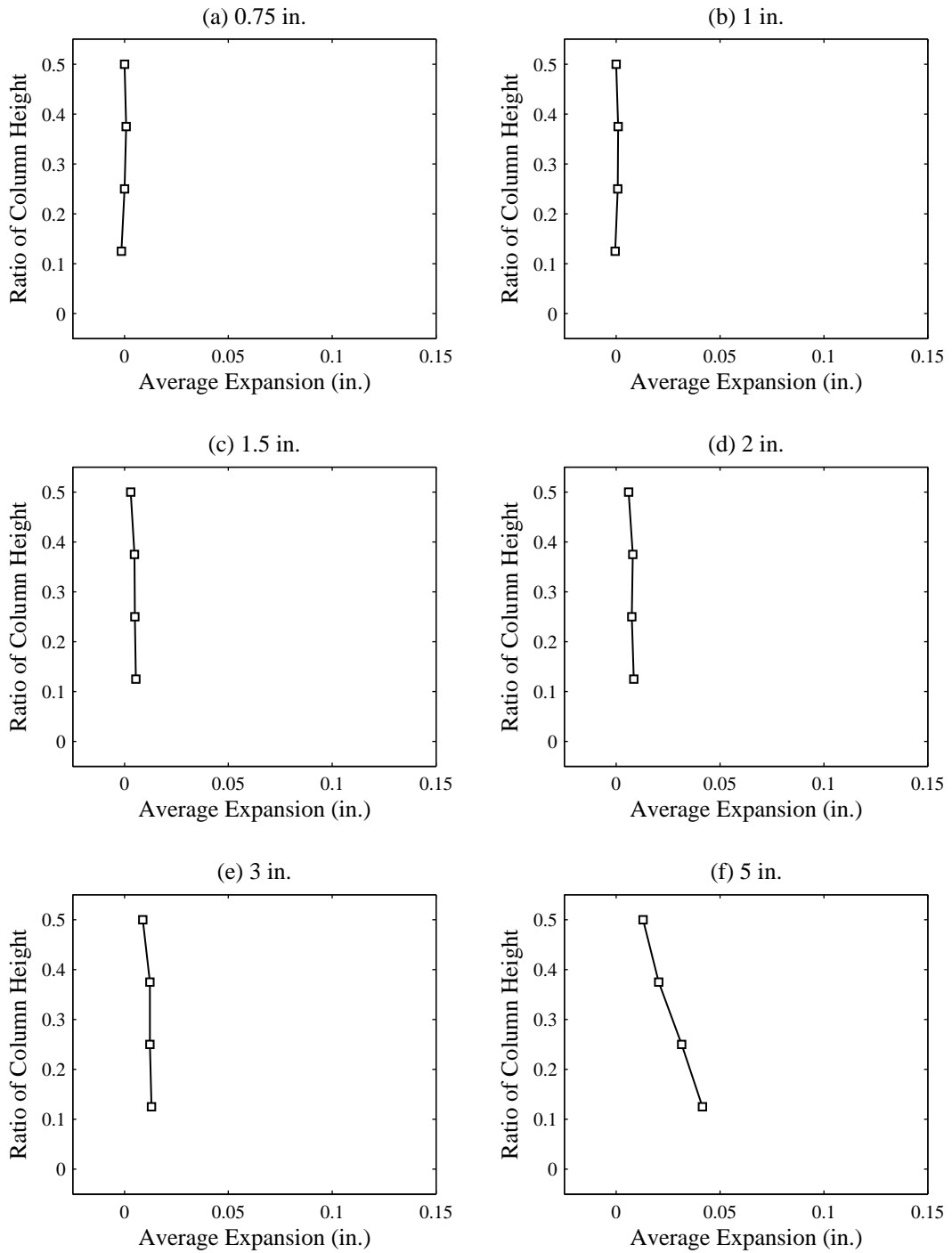


Figure C.19: Column C1 Average Horizontal Expansion Profile

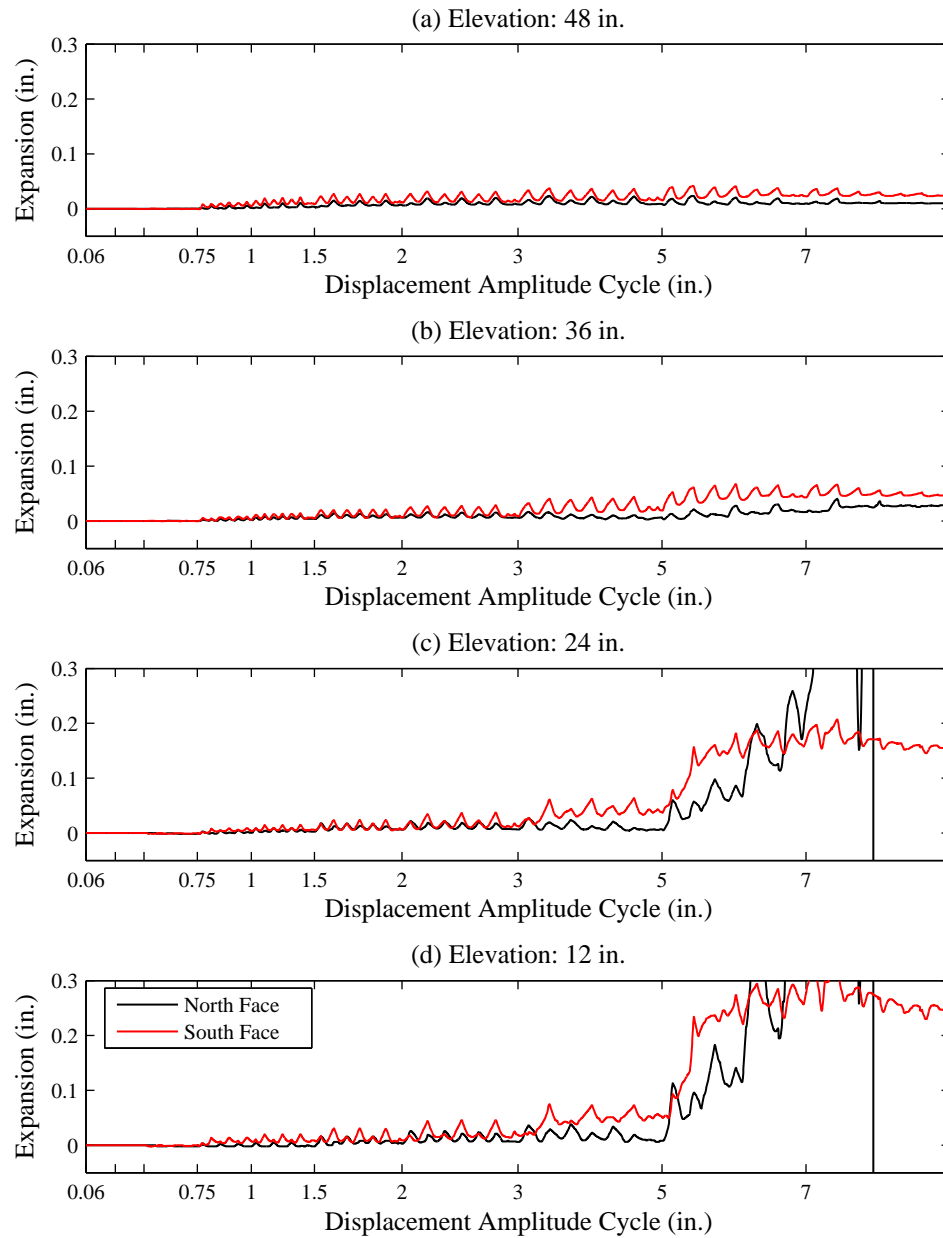


Figure C.20: Column C2 Horizontal Expansion History

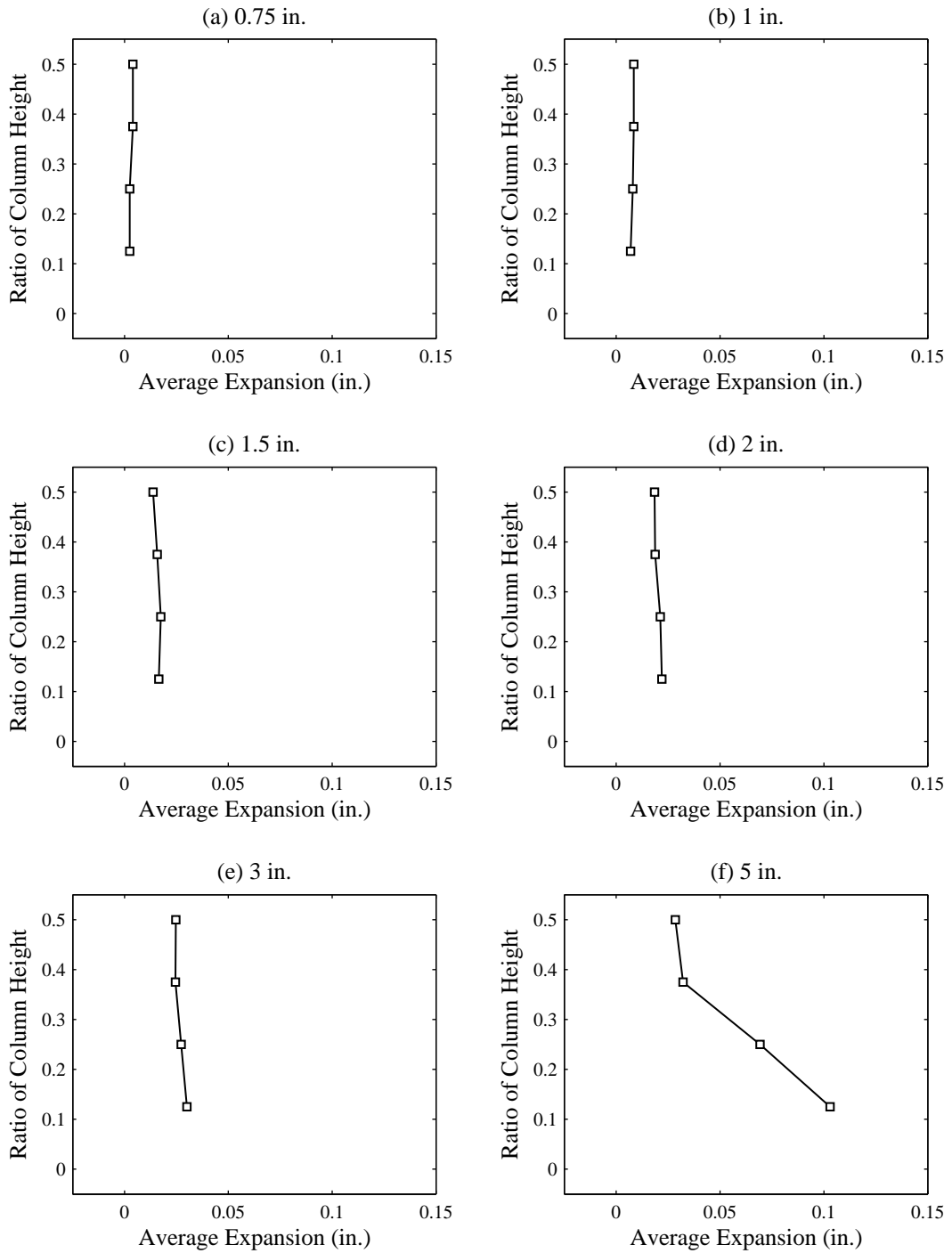


Figure C.21: Column C2 Average Horizontal Expansion Profile

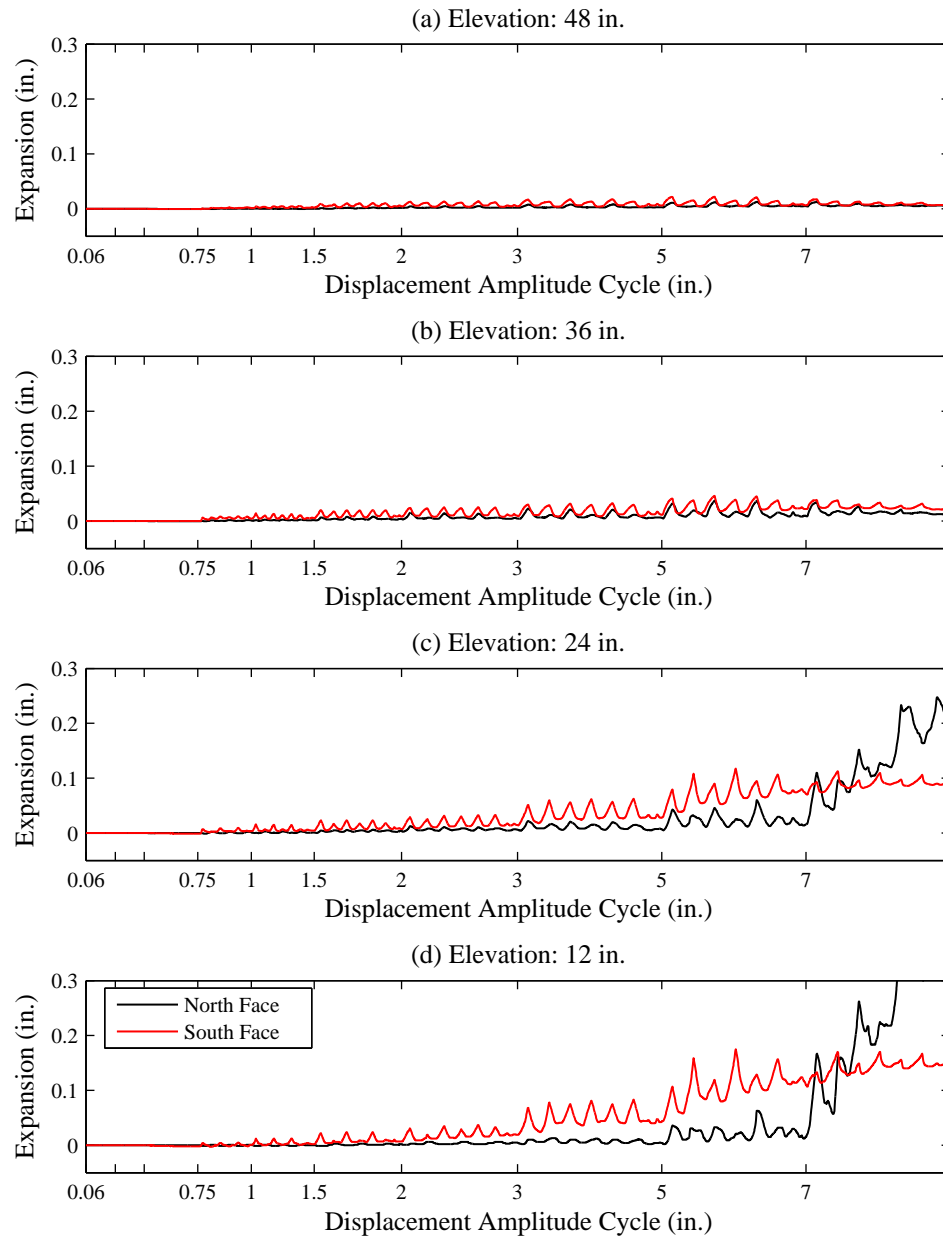


Figure C.22: Column C3 Horizontal Expansion History

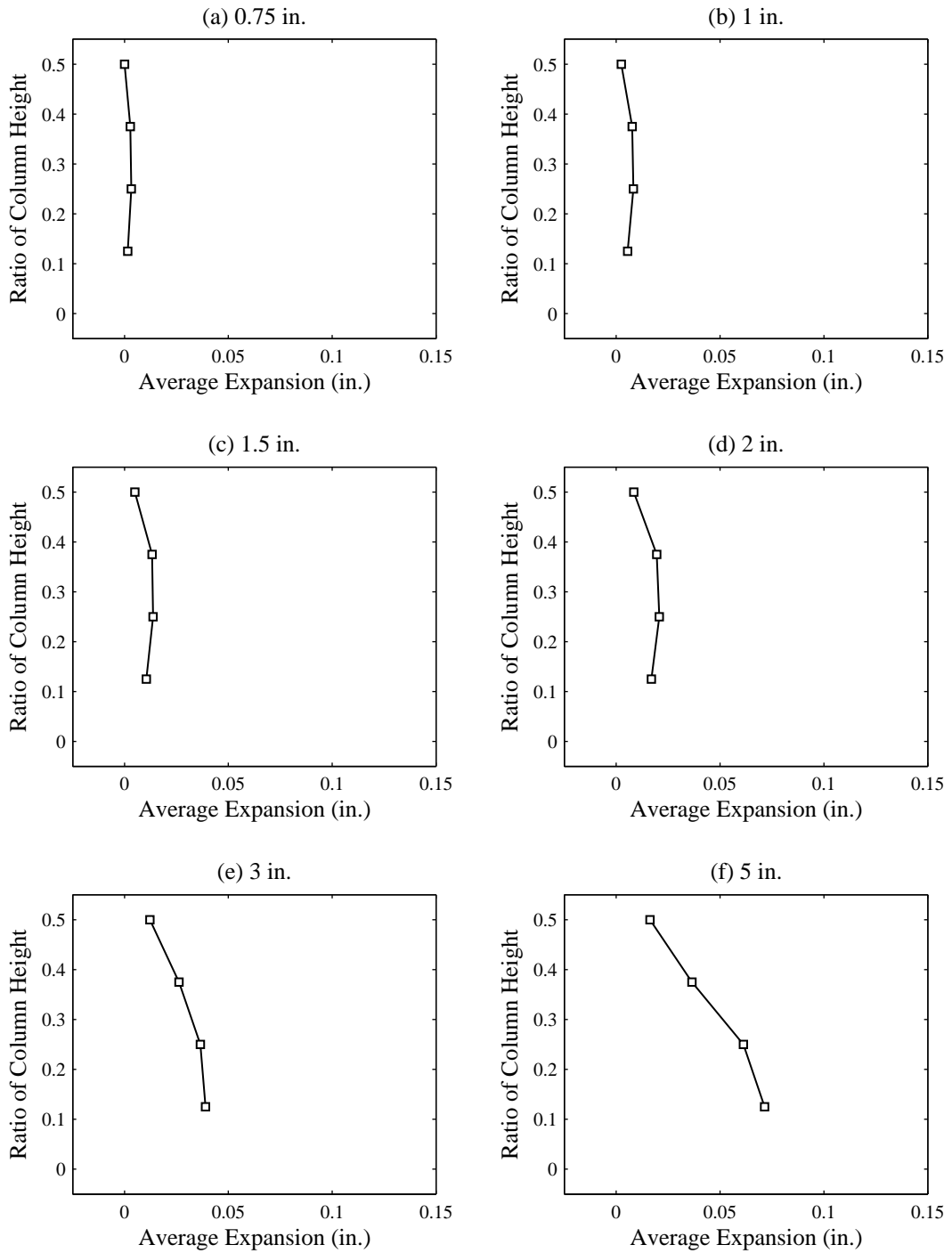


Figure C.23: Column C3 Average Horizontal Expansion Profile

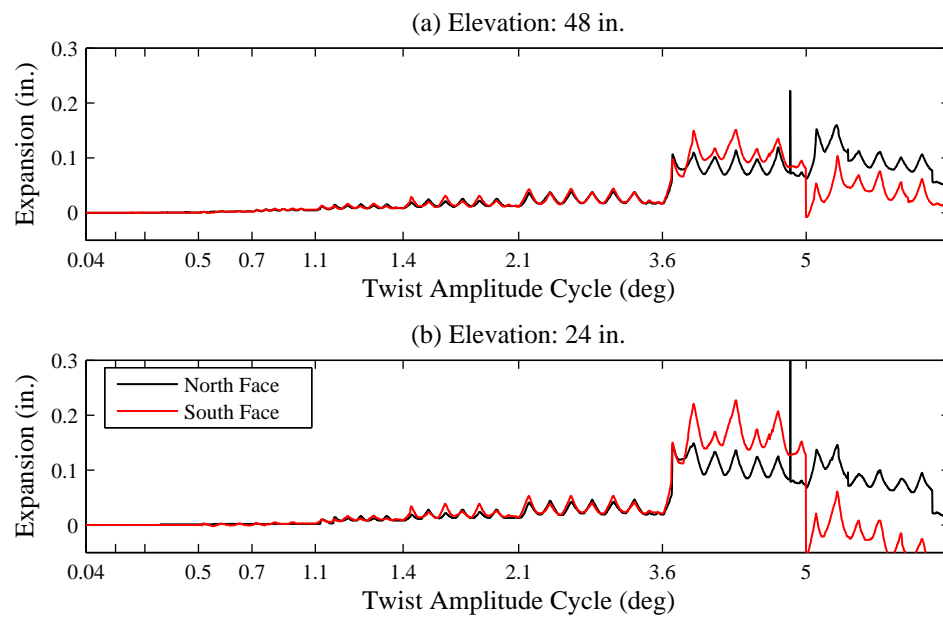


Figure C.24: Column C4 Horizontal Expansion History

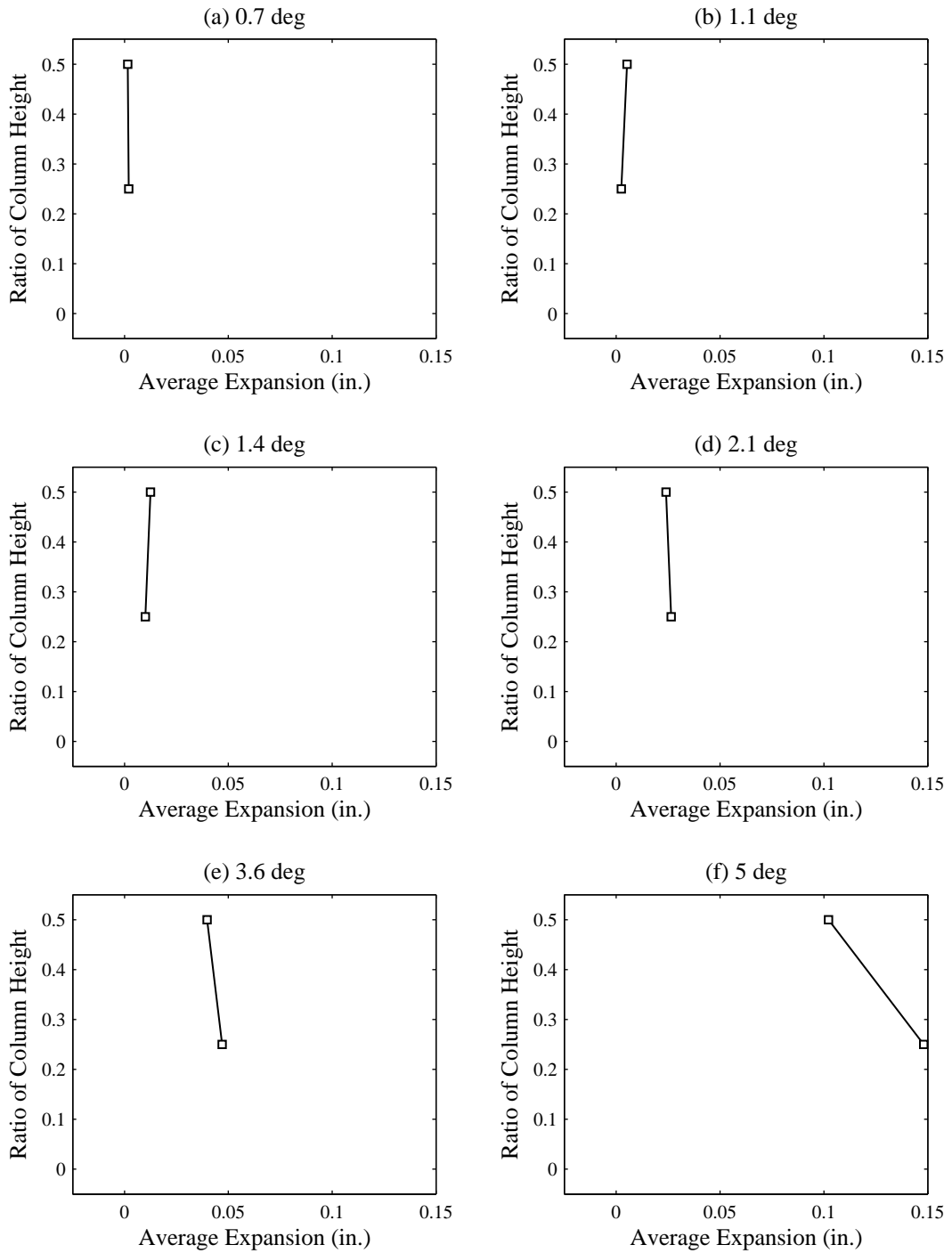


Figure C.25: Column C4 Average Horizontal Expansion Profile

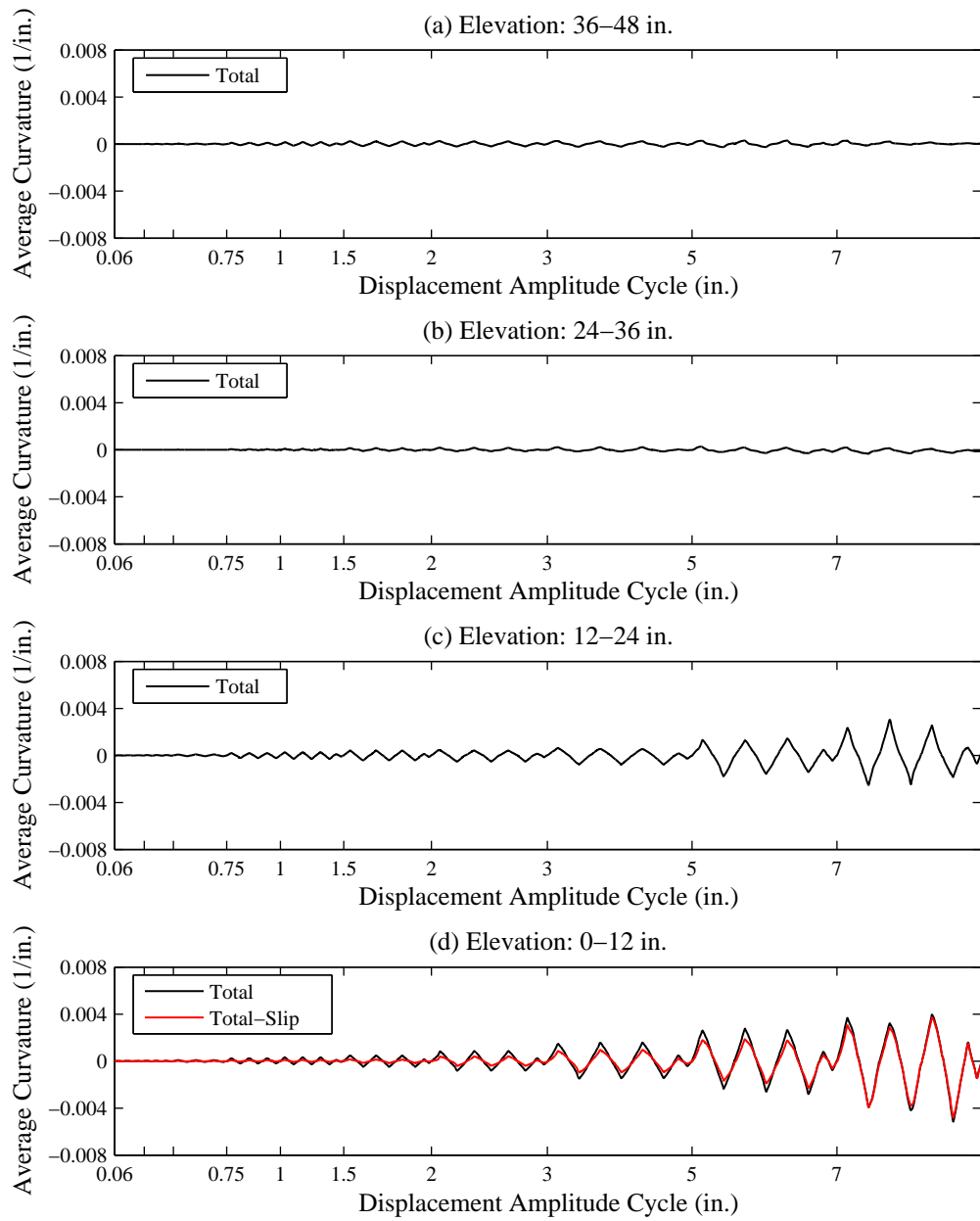


Figure C.26: Column C1 Average Curvature History

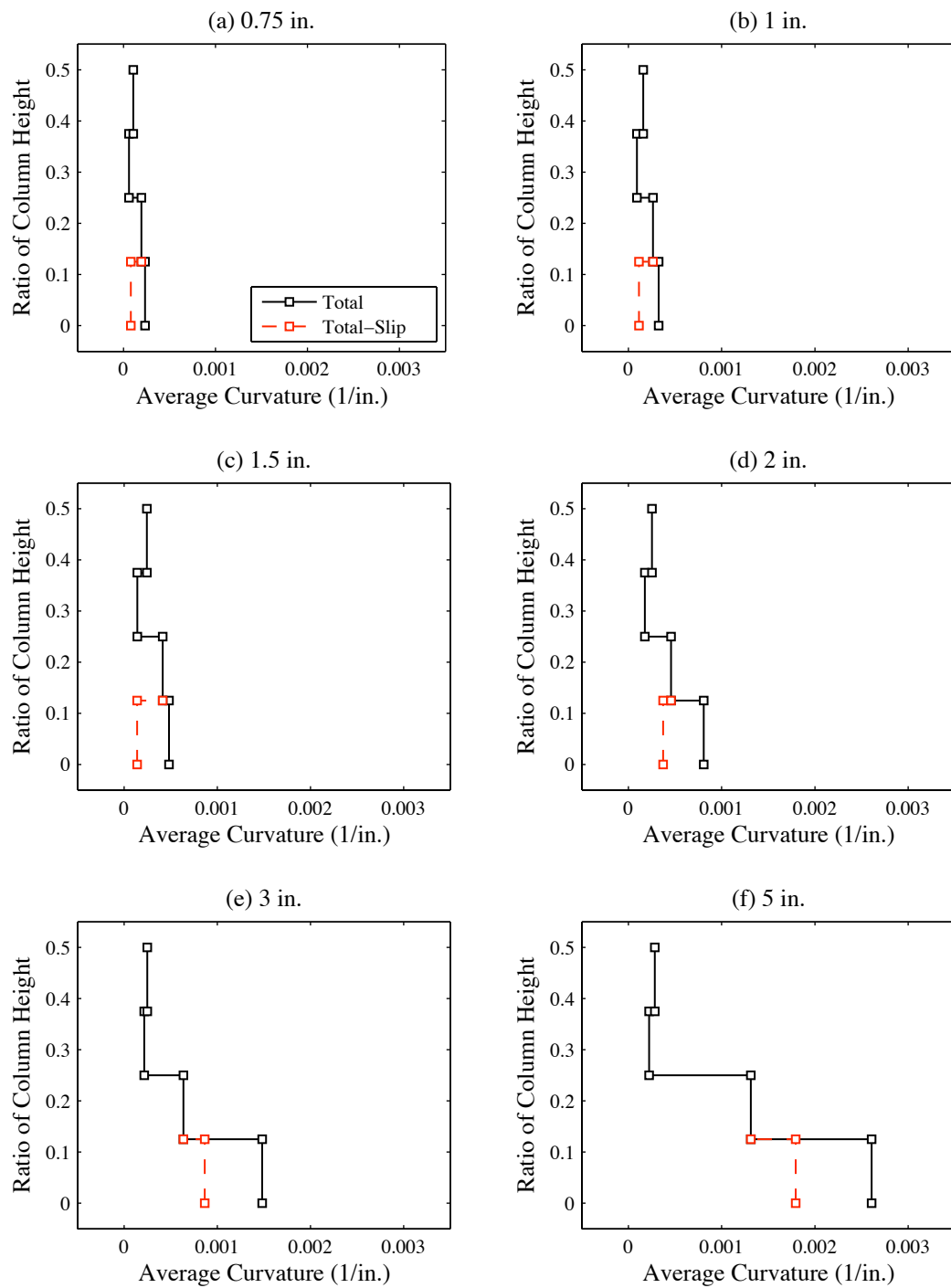


Figure C.27: Column C1 Average Curvature Profile

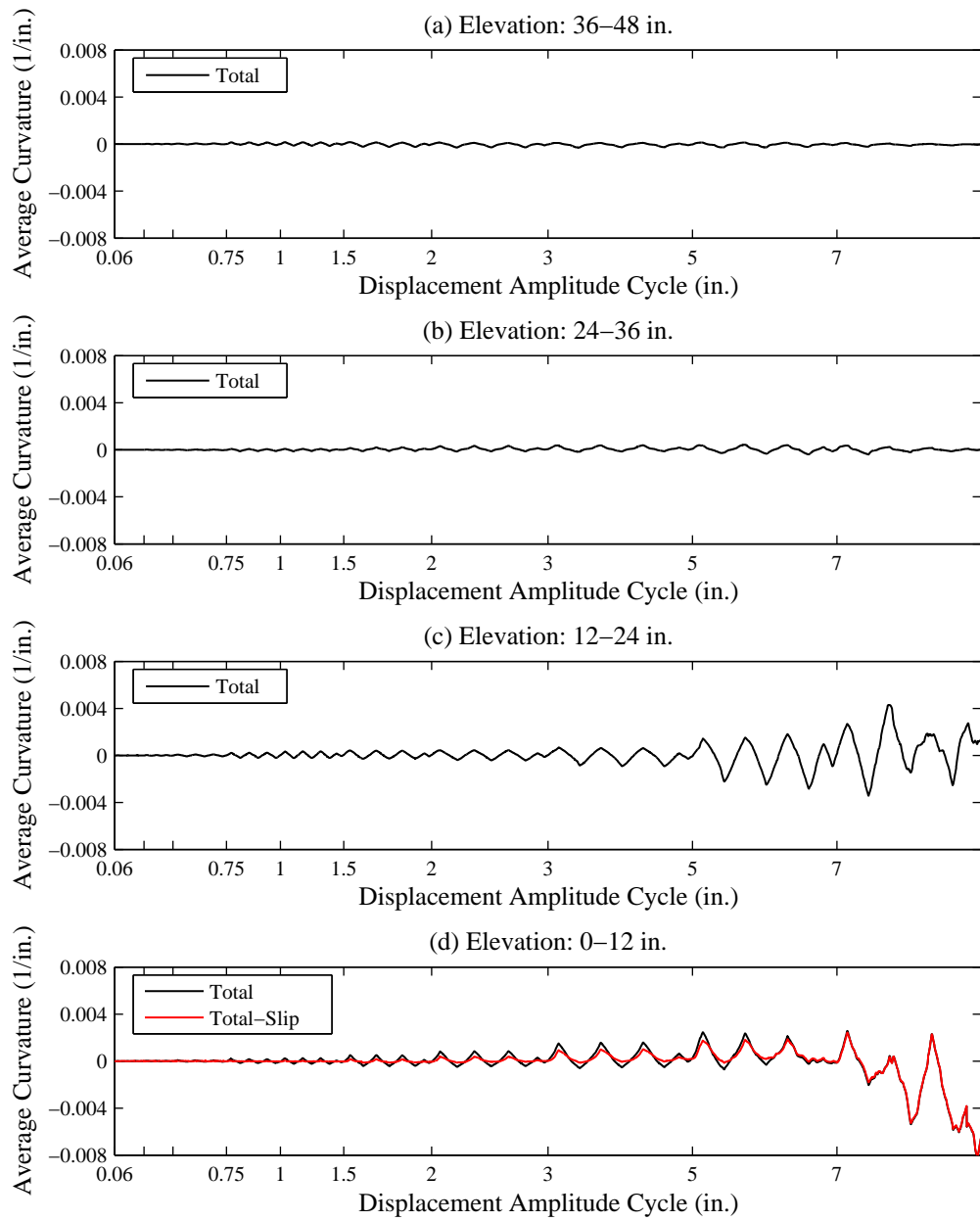


Figure C.28: Column C2 Average Curvature History

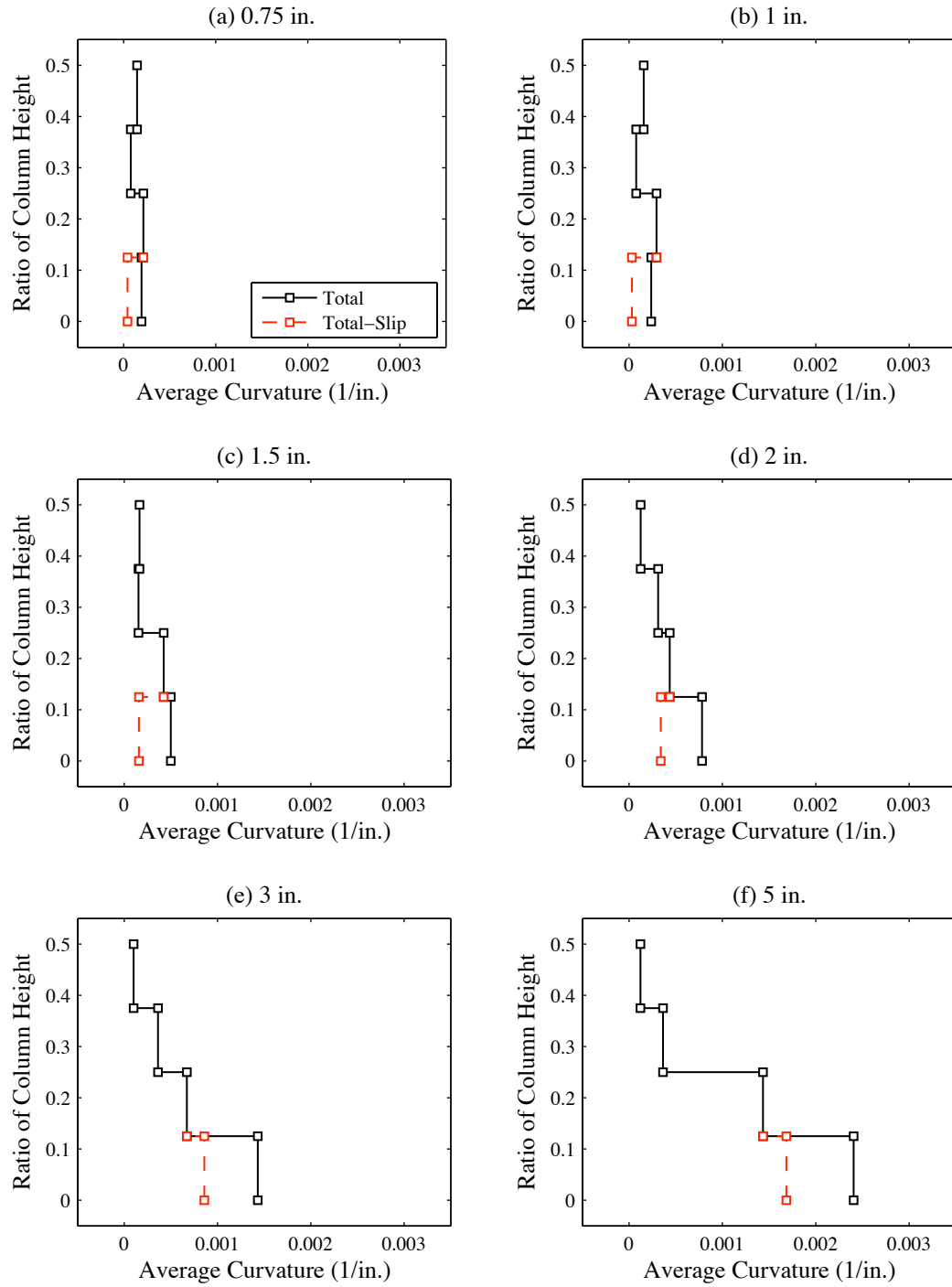


Figure C.29: Column C2 Average Curvature Profile

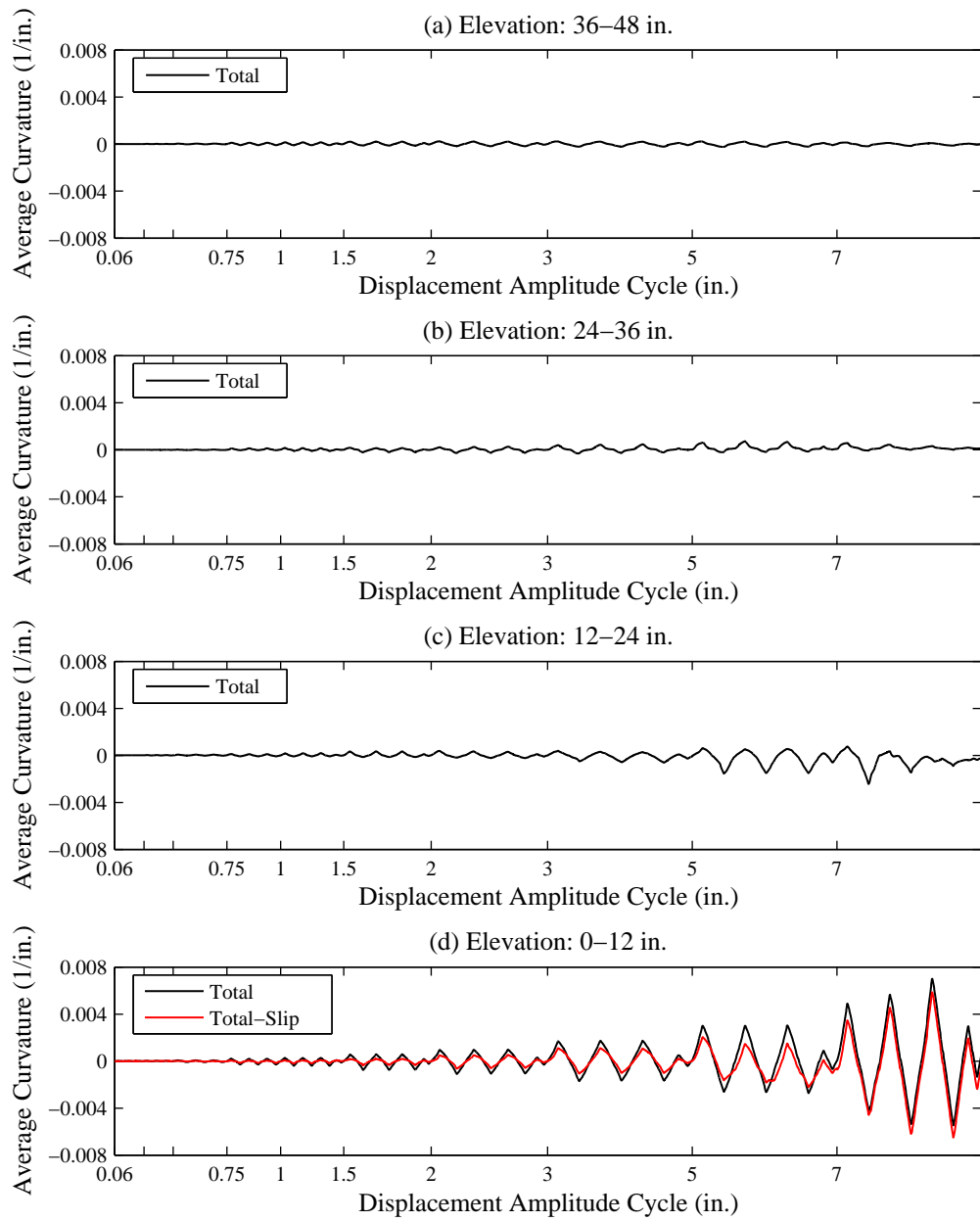


Figure C.30: Column C3 Average Curvature History

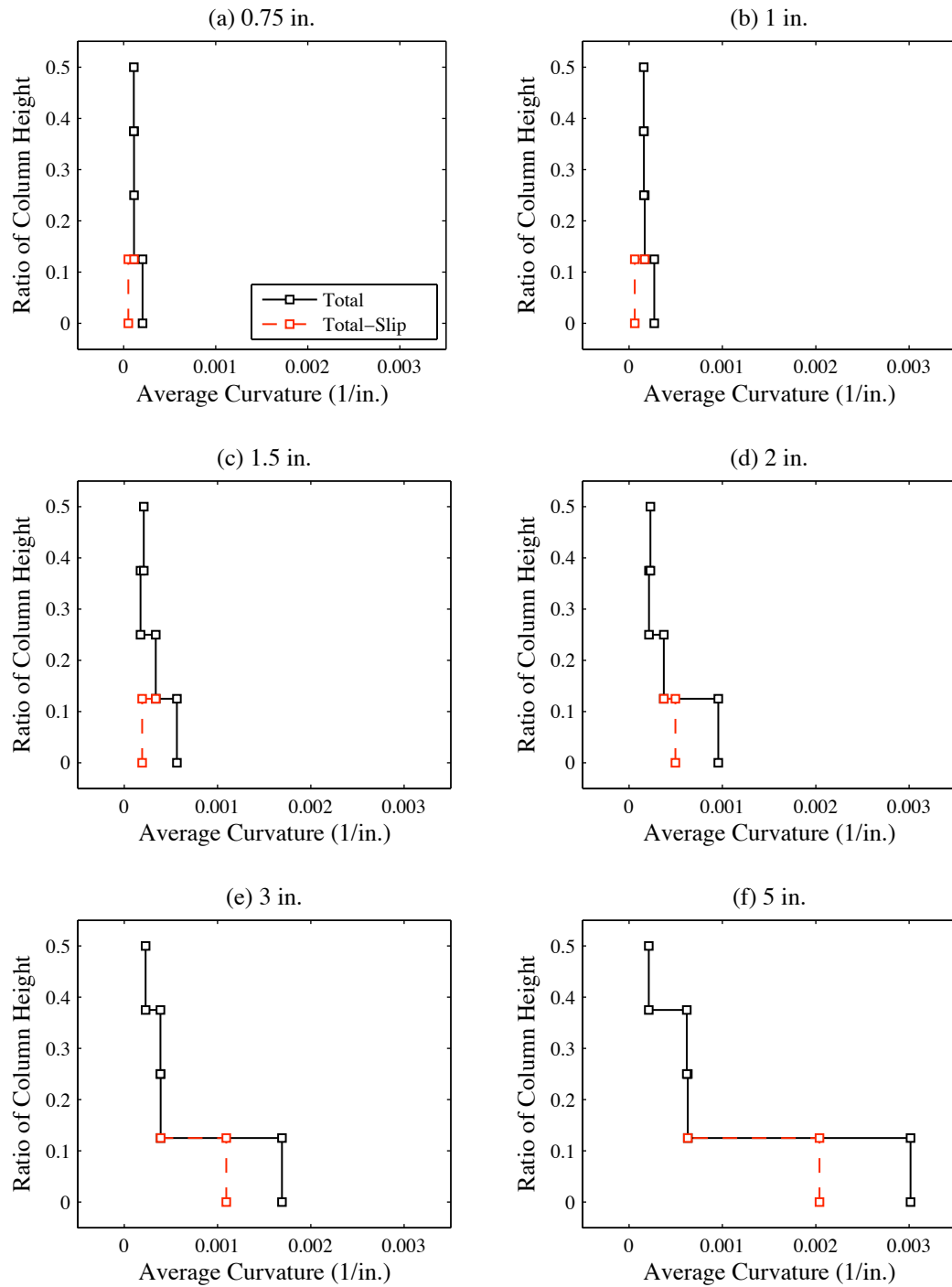


Figure C.31: Column C3 Average Curvature Profile

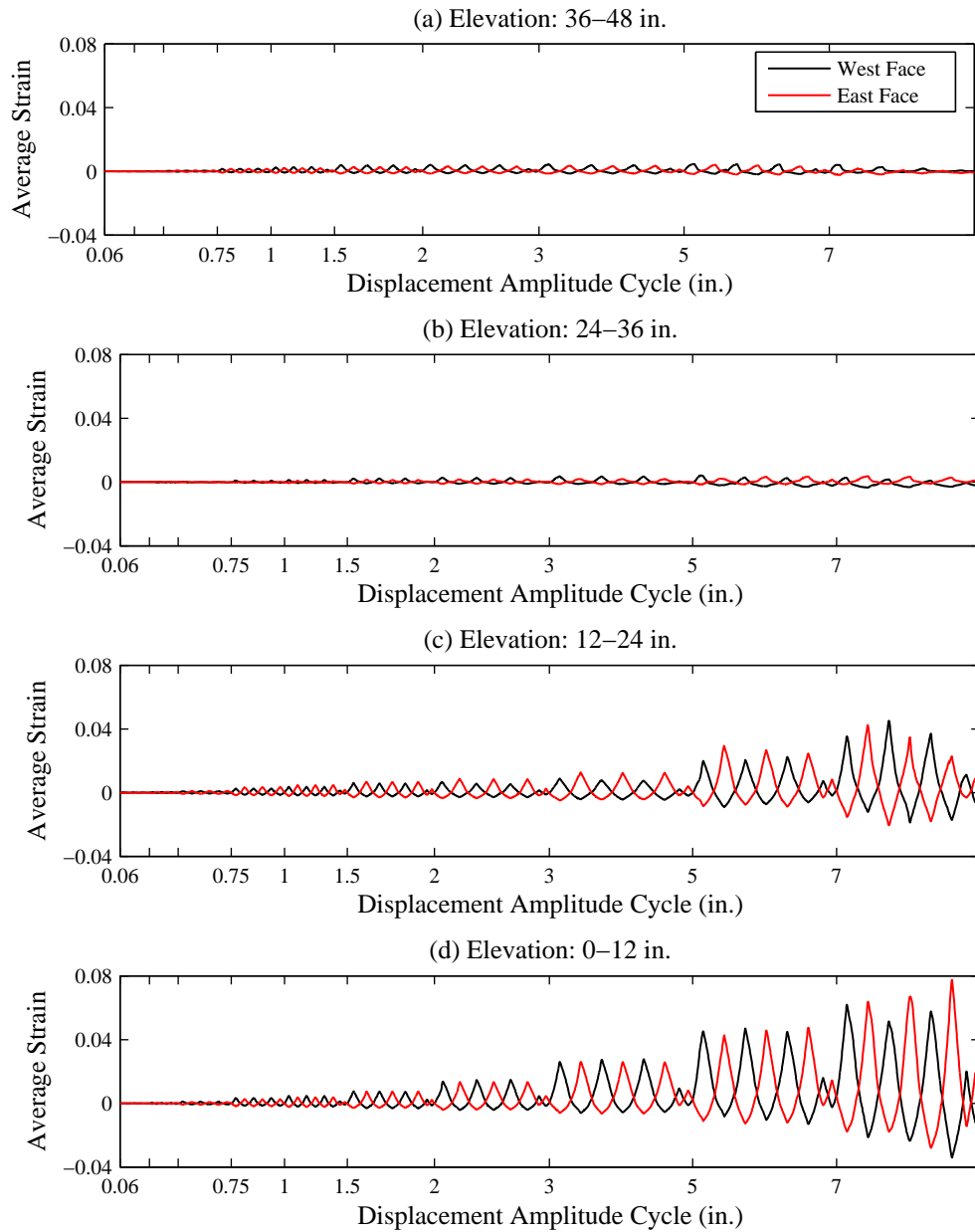


Figure C.32: Column C1 Average Longitudinal Strain History

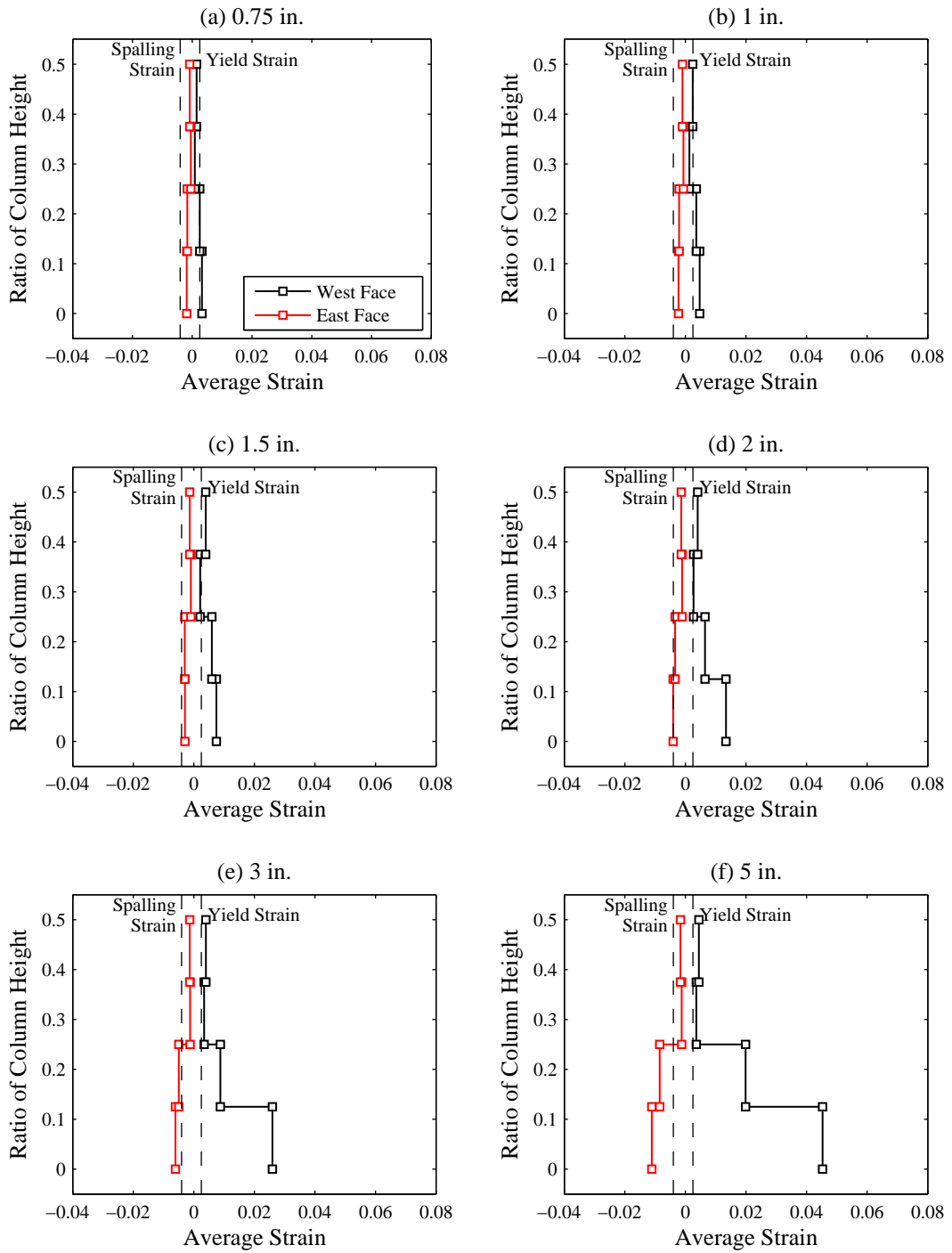


Figure C.33: Column C1 Average Longitudinal Strain Profile

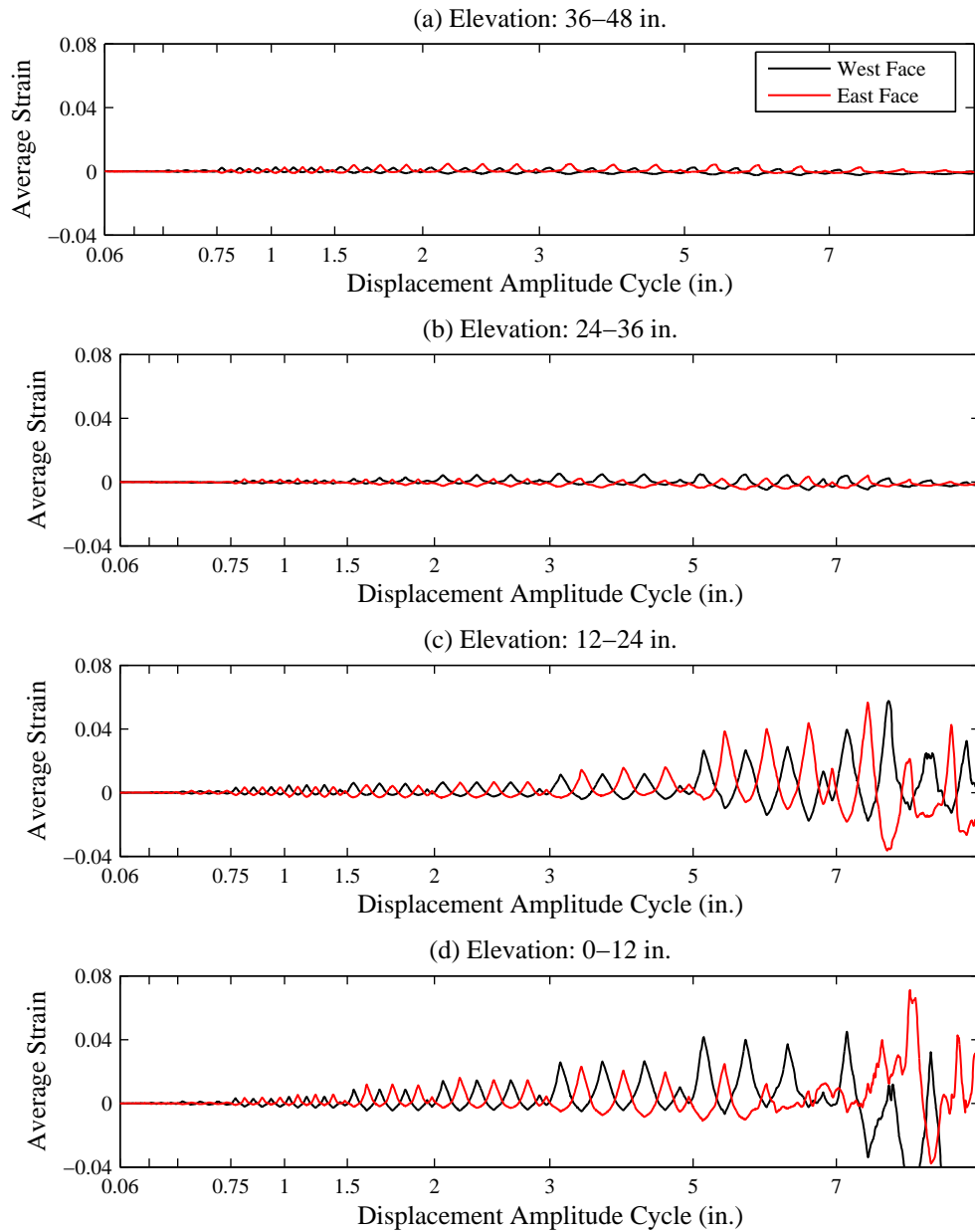


Figure C.34: Column C2 Average Longitudinal Strain History

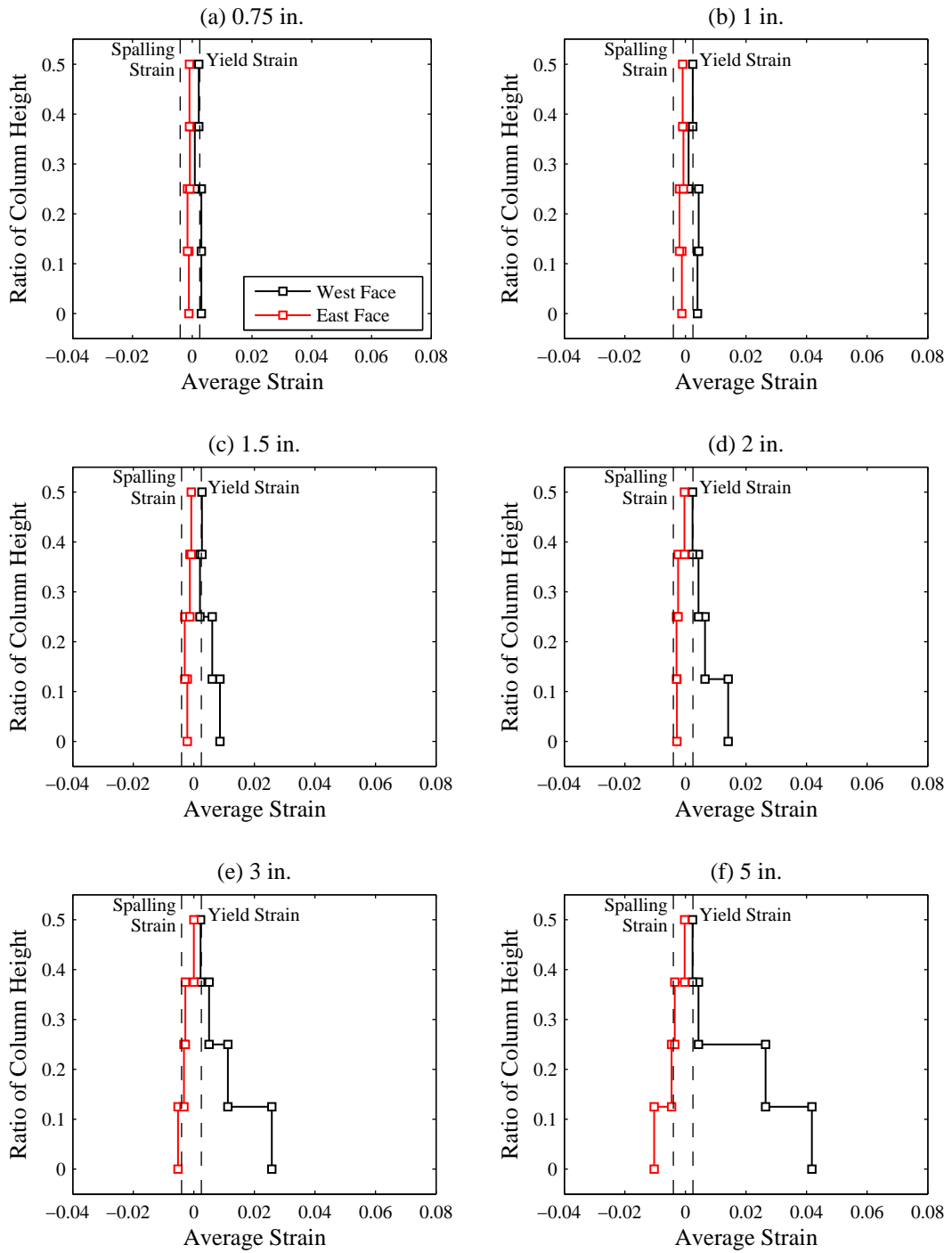


Figure C.35: Column C2 Average Longitudinal Strain Profile

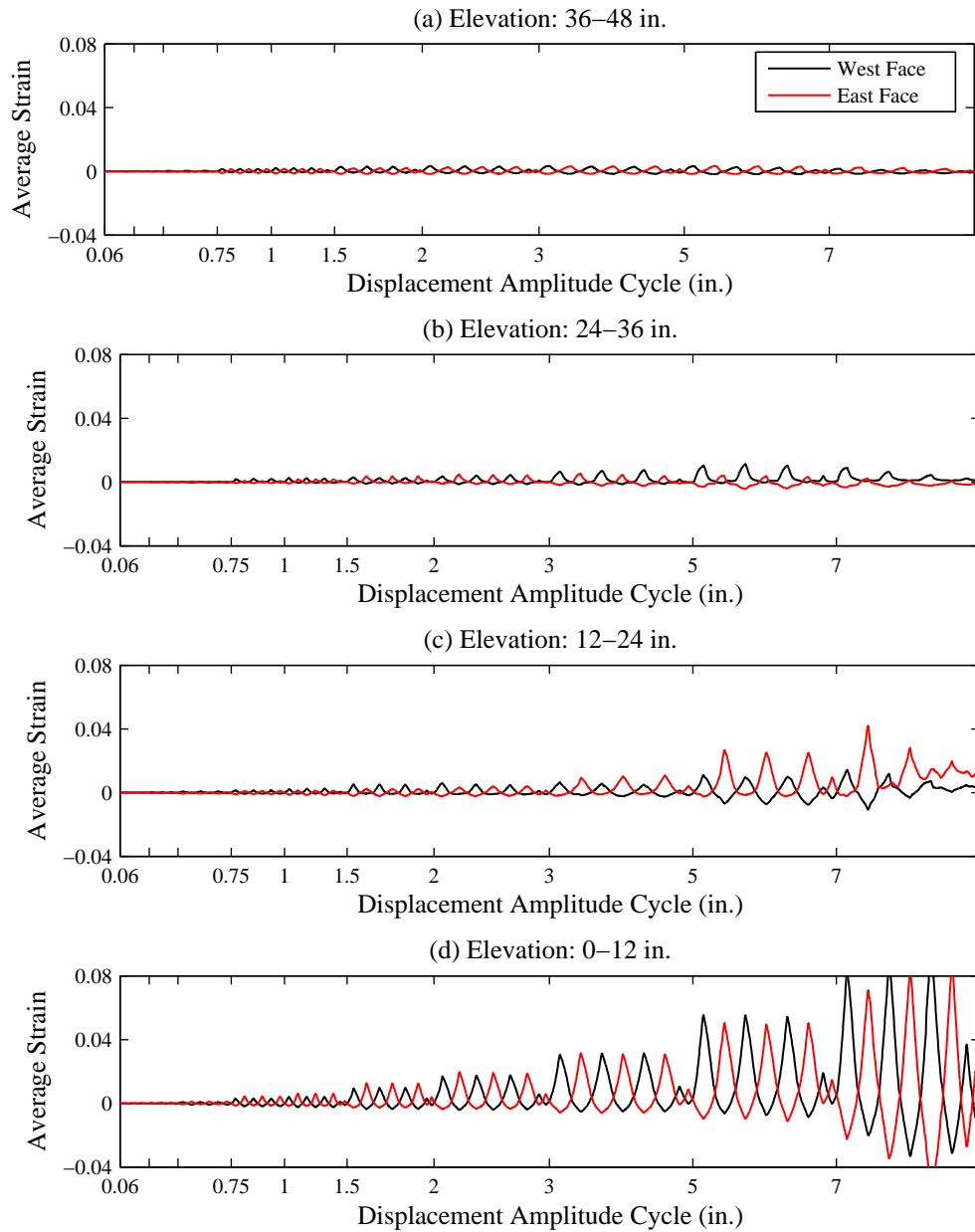


Figure C.36: Column C3 Average Longitudinal Strain History

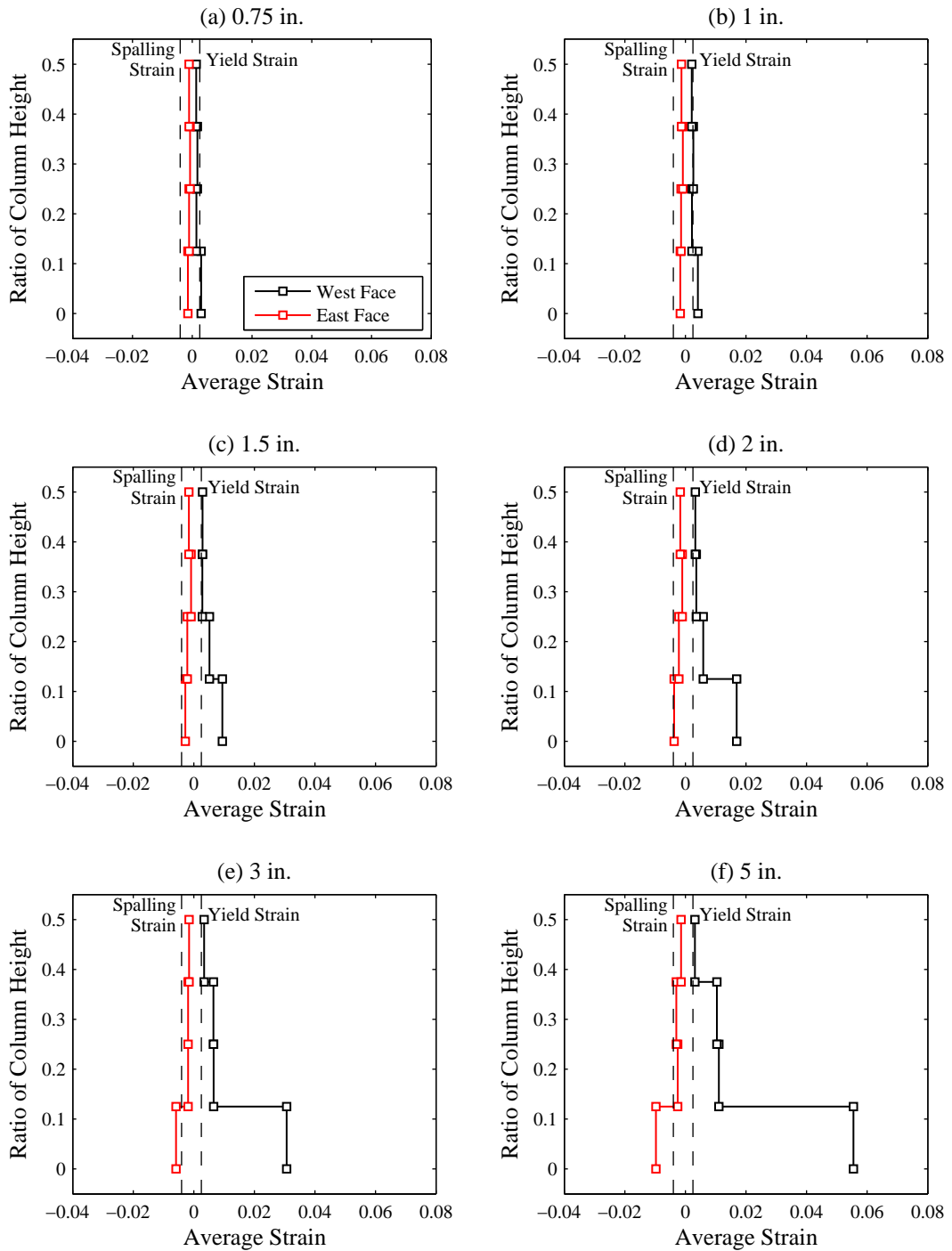


Figure C.37: Column C3 Average Longitudinal Strain Profile

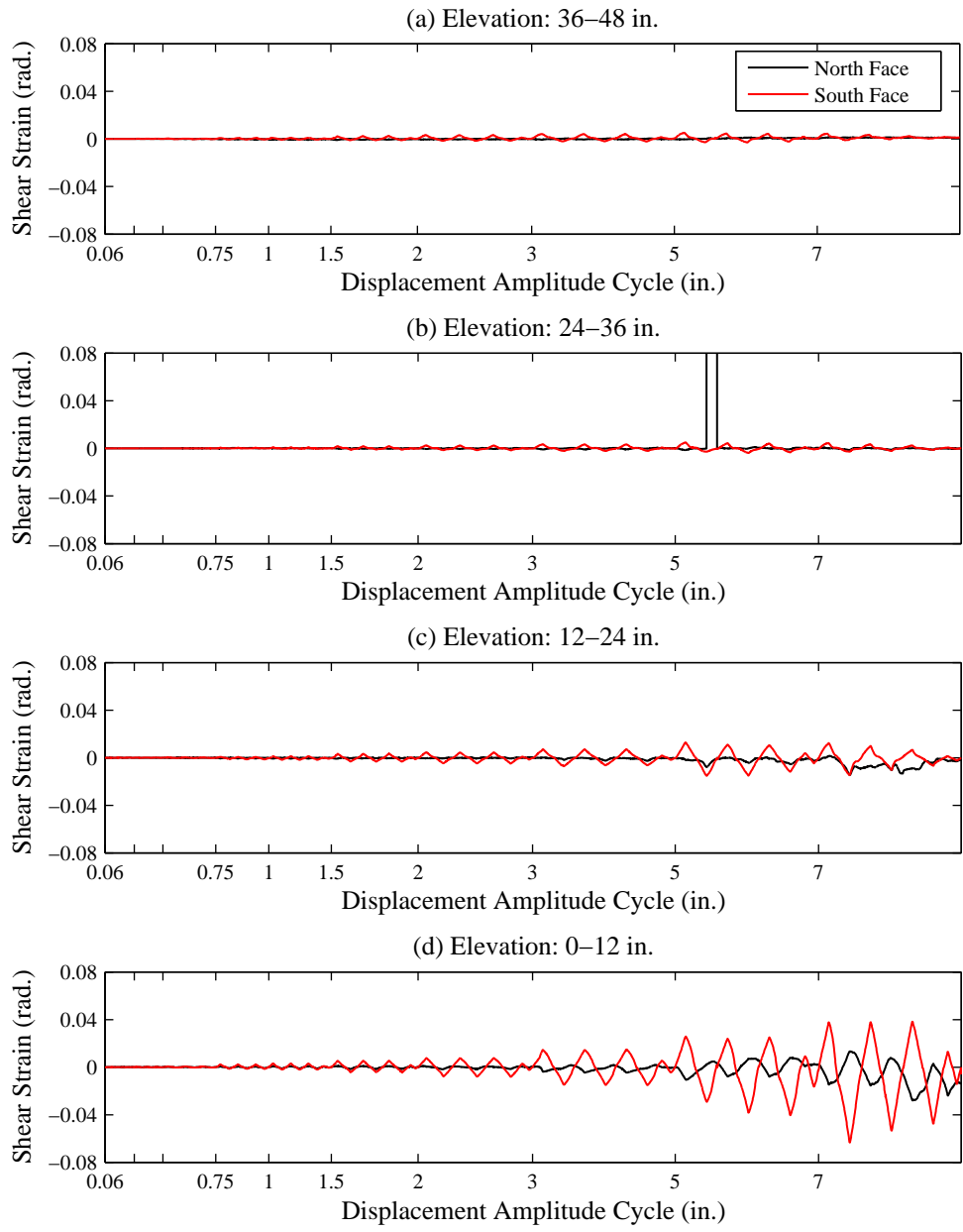


Figure C.38: Column C1 Shear Strain History

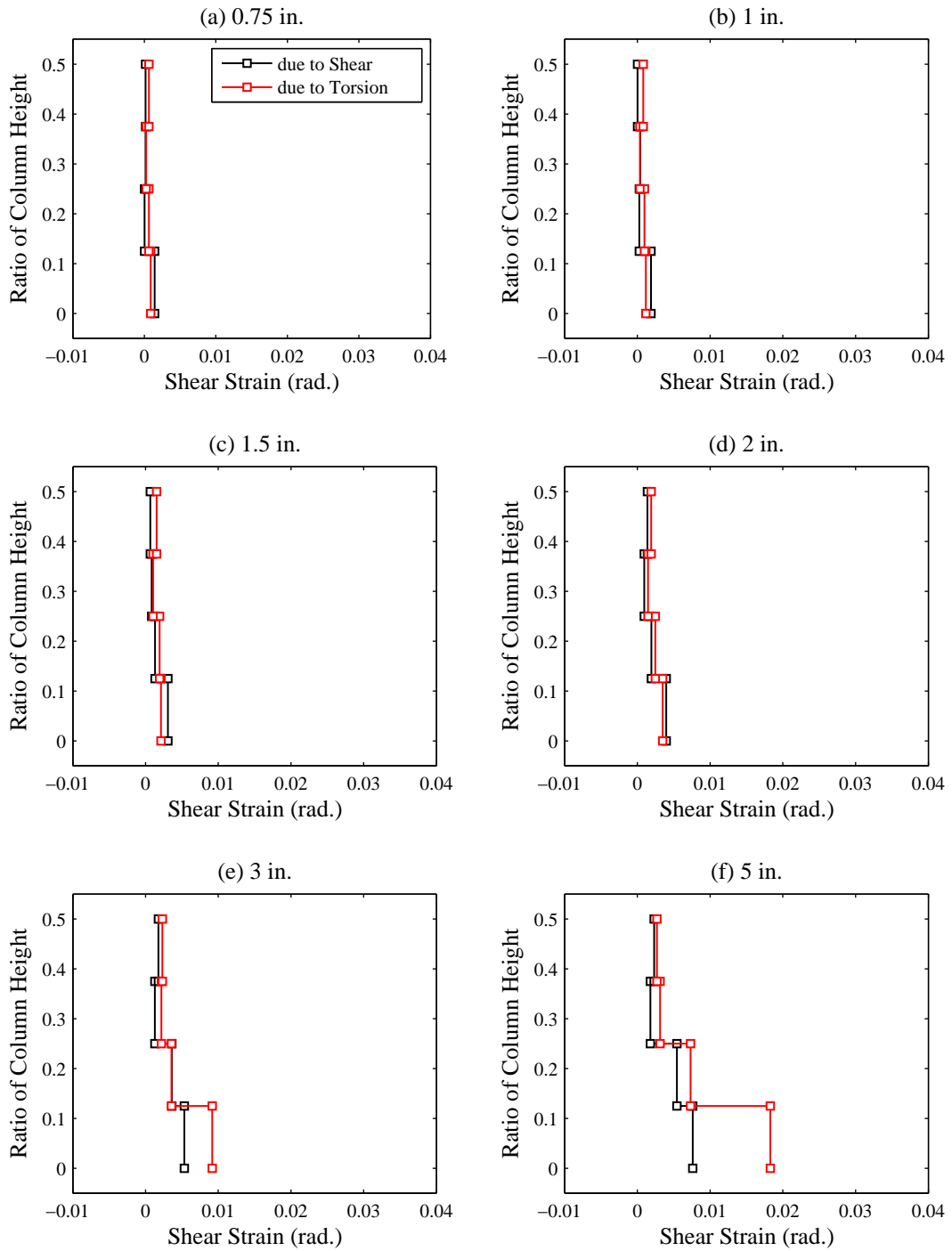


Figure C.39: Column C1 Shear Strain Profile

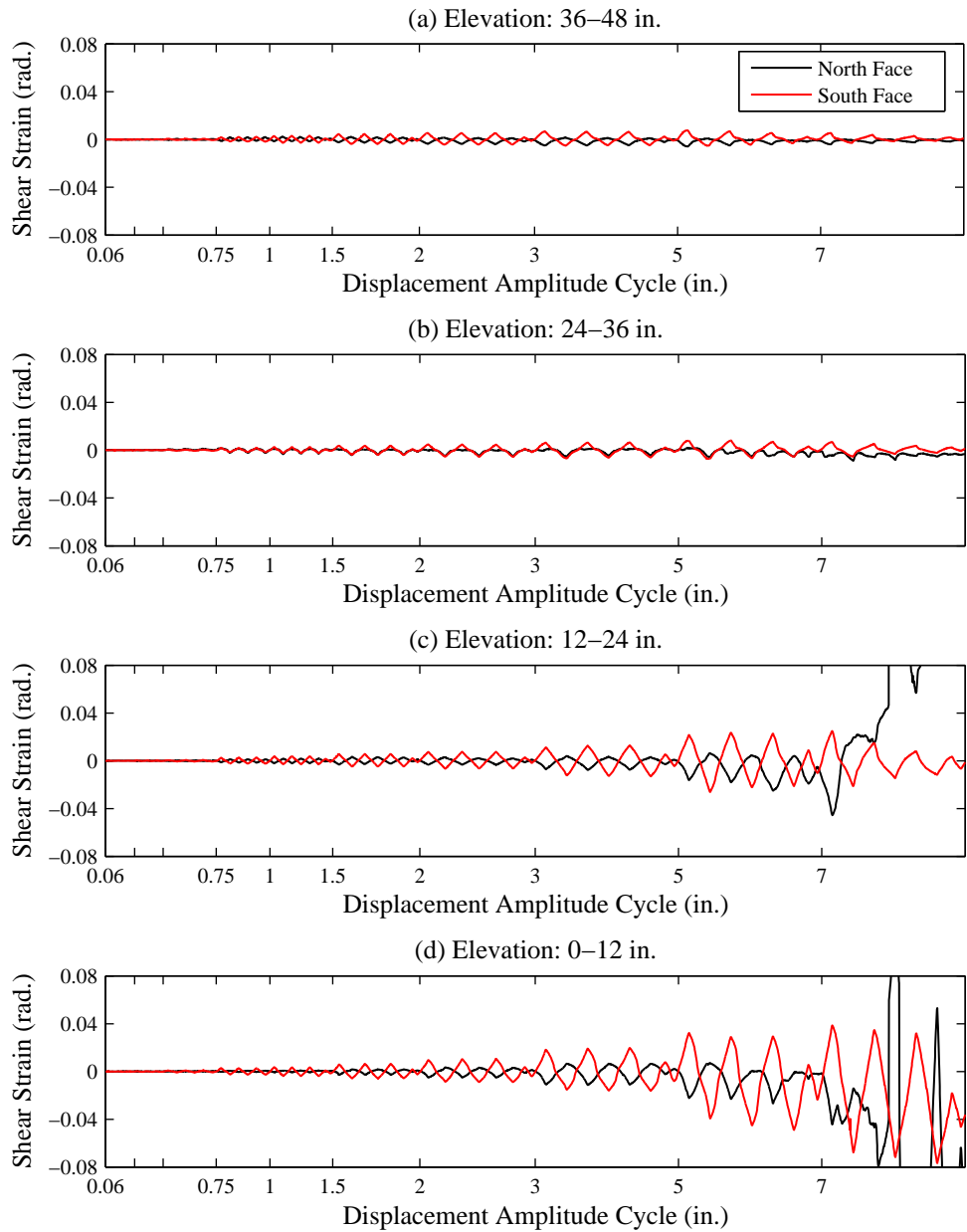


Figure C.40: Column C2 Shear Strain History

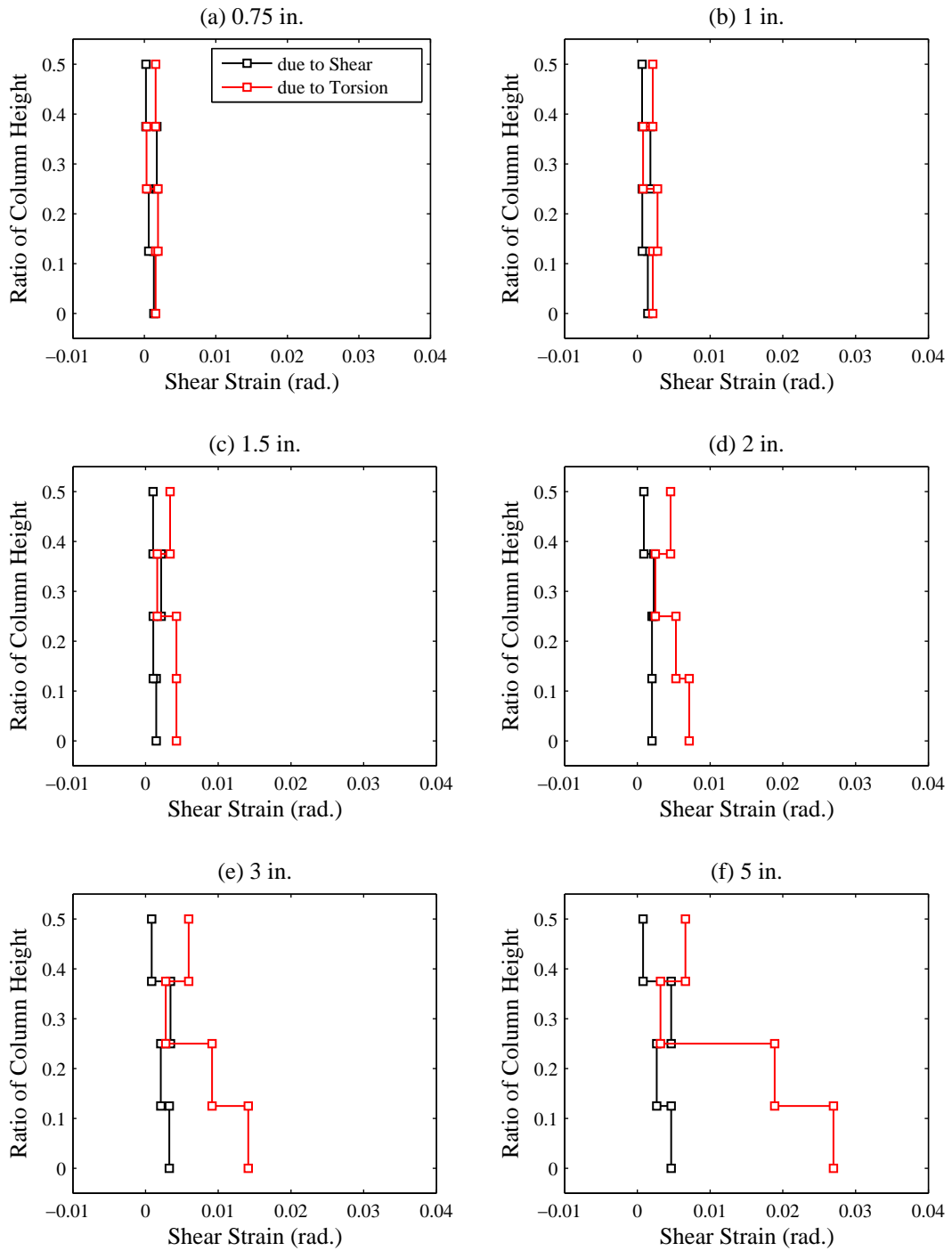


Figure C.41: Column C2 Shear Strain Profile

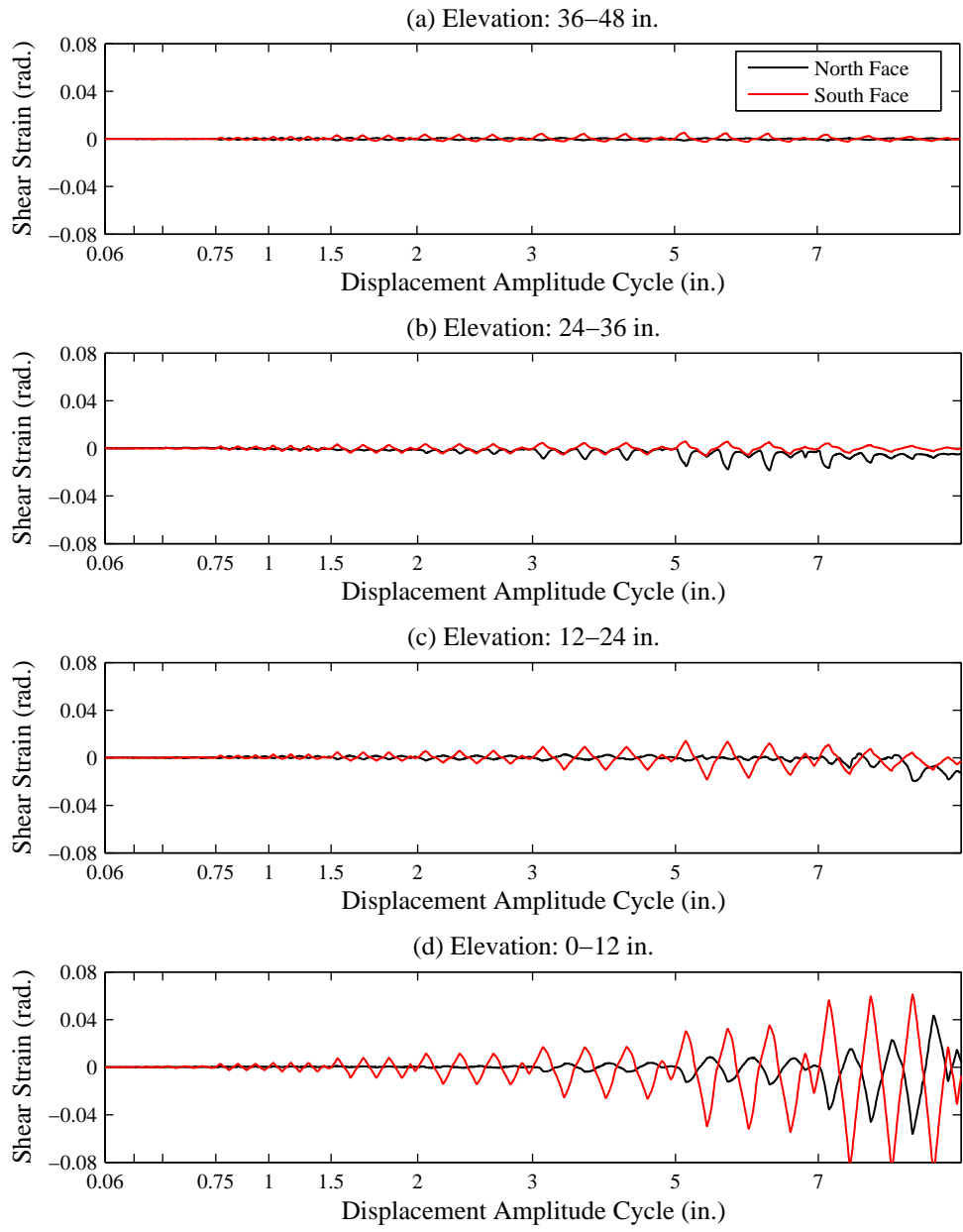


Figure C.42: Column C3 Shear Strain History

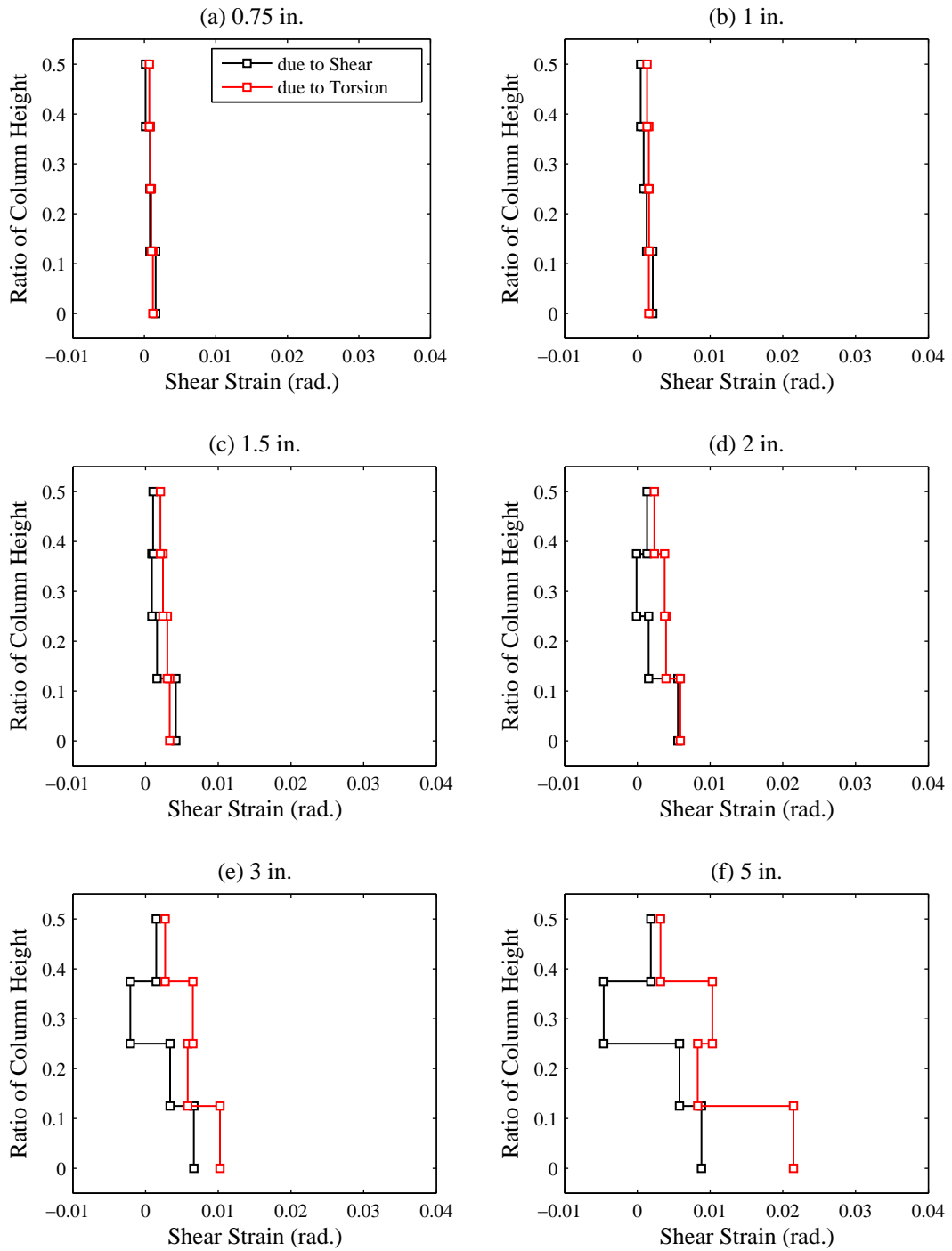


Figure C.43: Column C3 Shear Strain Profile

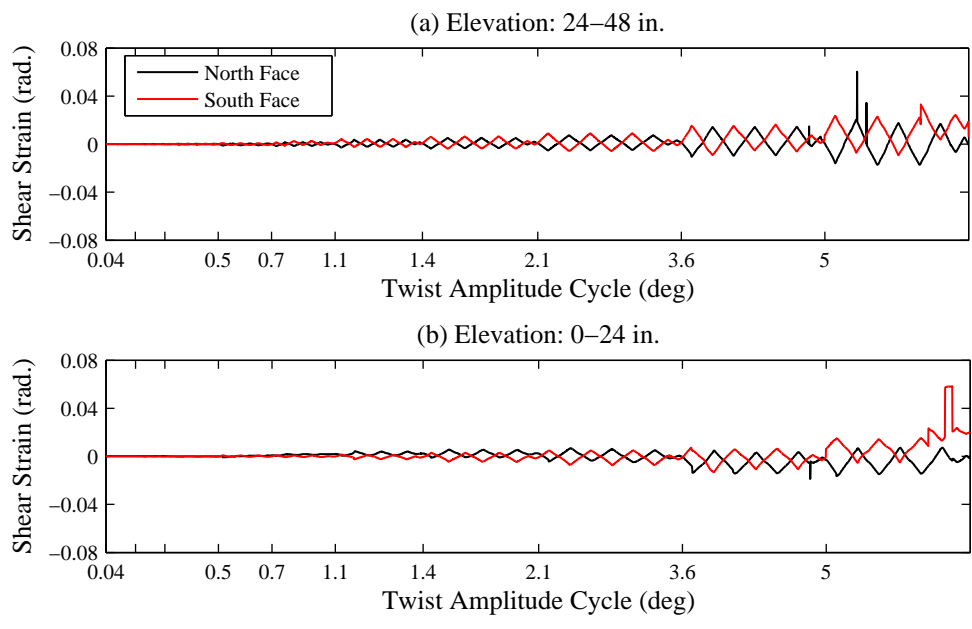


Figure C.44: Column C4 Shear Strain History

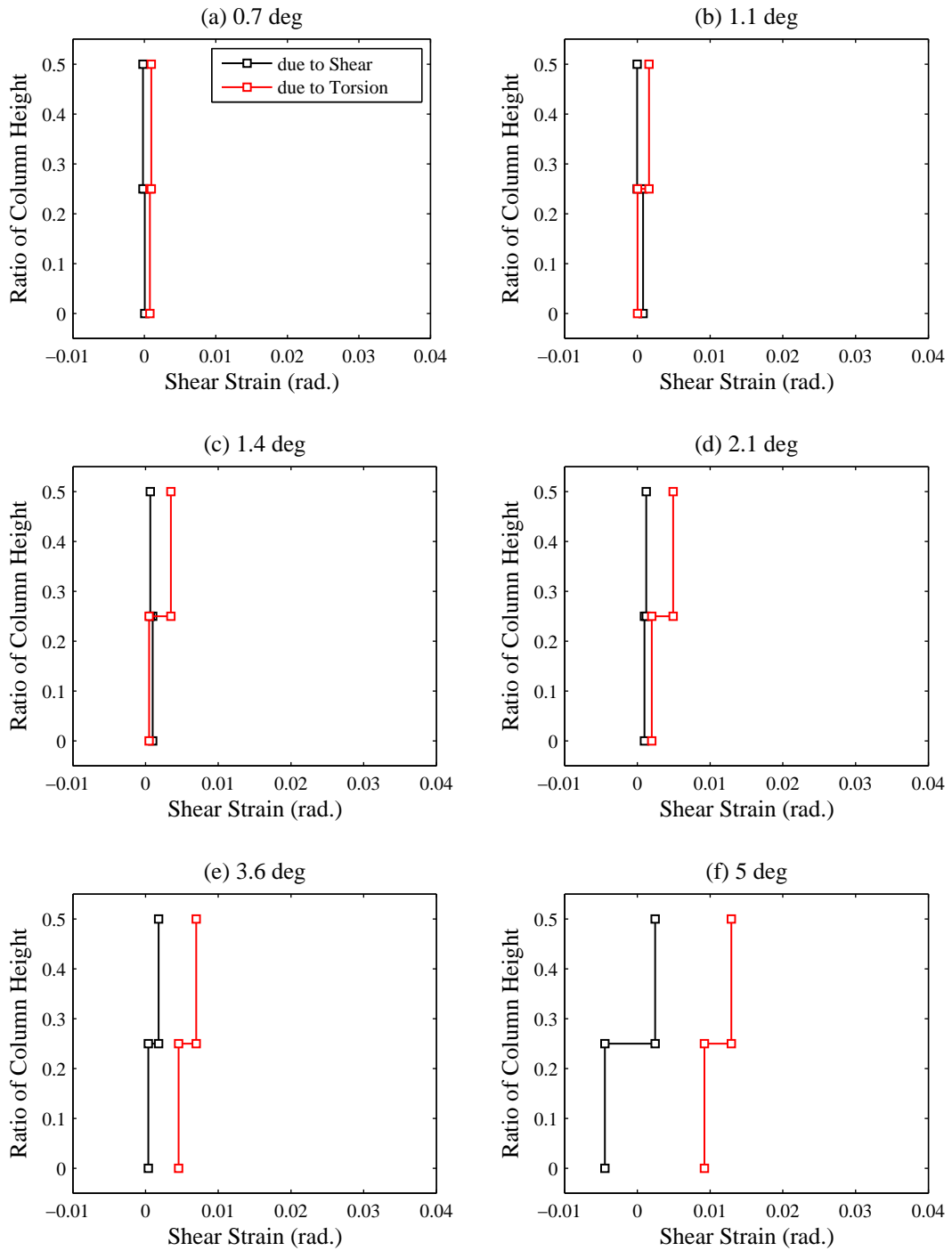


Figure C.45: Column C4 Shear Strain Profile

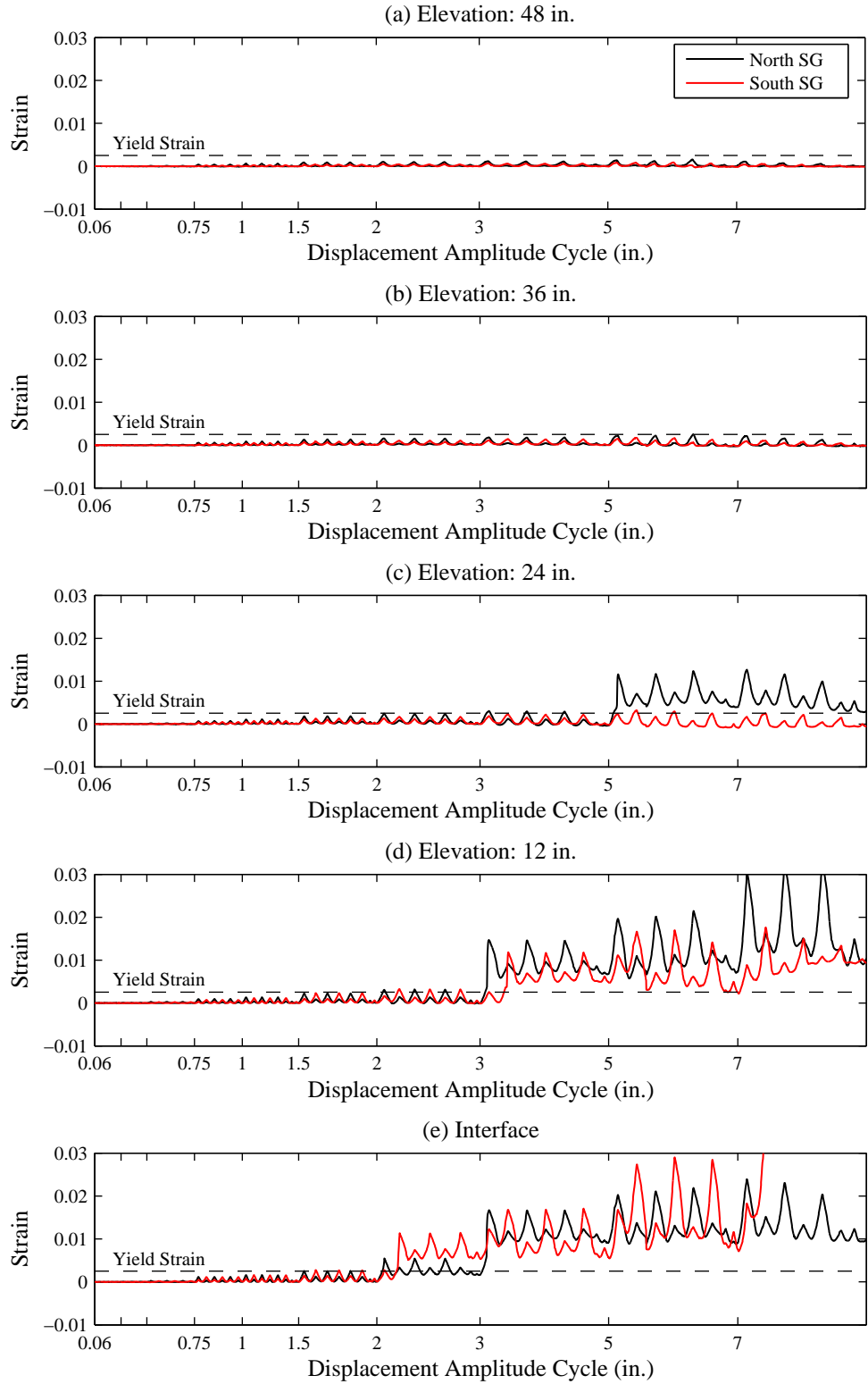


Figure C.46: Column C1 Longitudinal Strain History – North and South Gauges

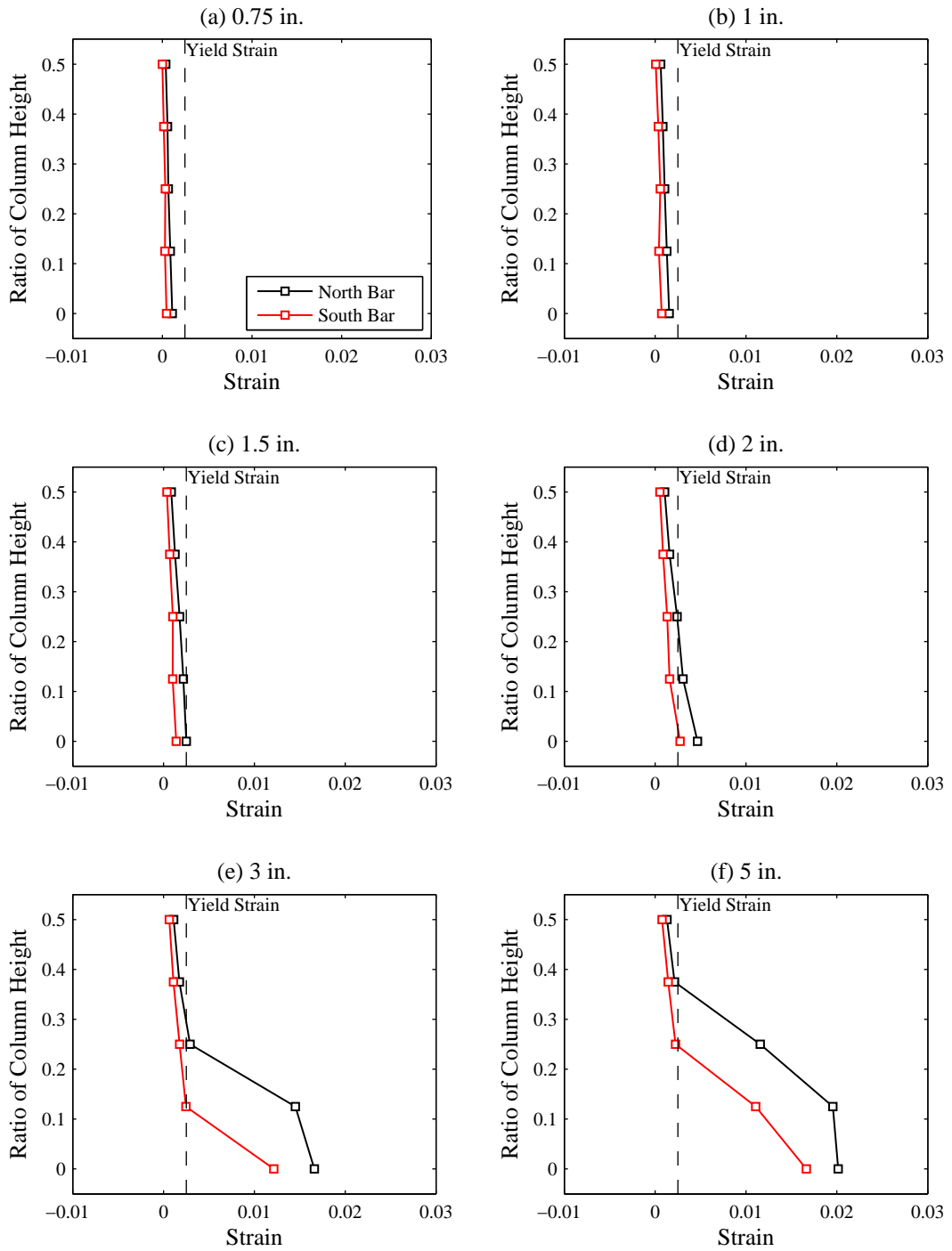


Figure C.47: Column C1 Longitudinal Strain Profile – North and South Gauges

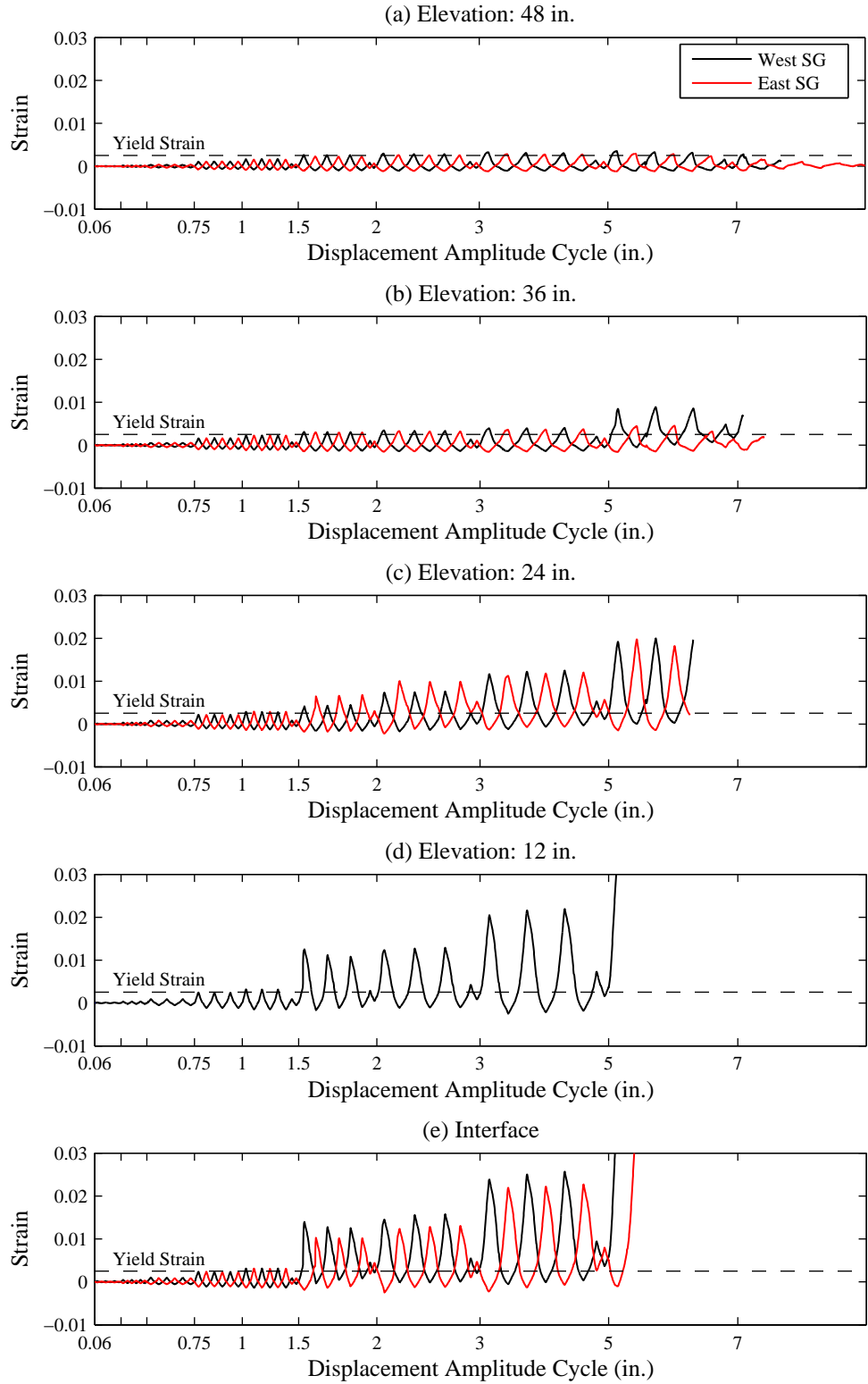


Figure C.48: Column C1 Longitudinal Strain History – West and East Gauges

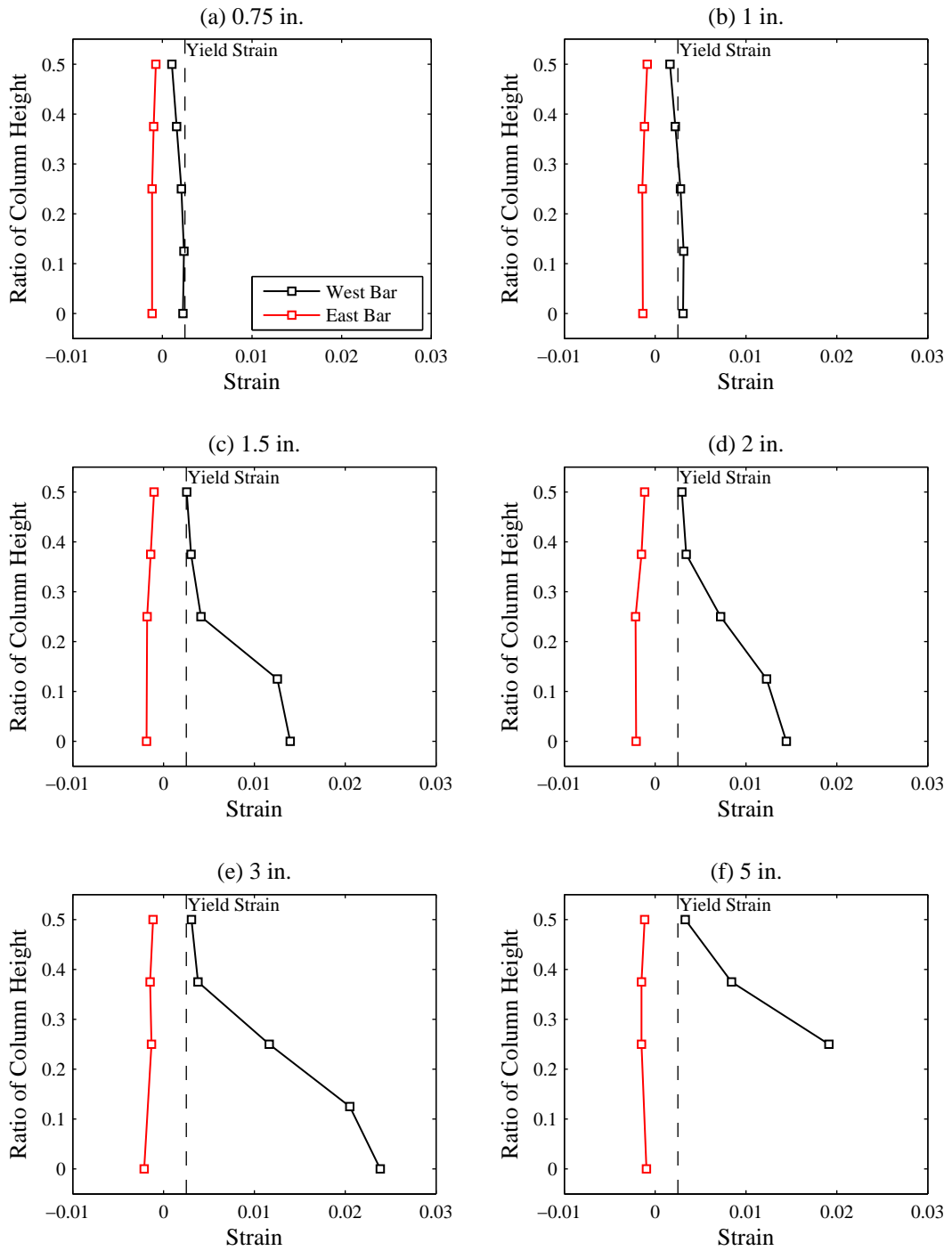


Figure C.49: Column C1 Longitudinal Strain Profile – West and East Gauges

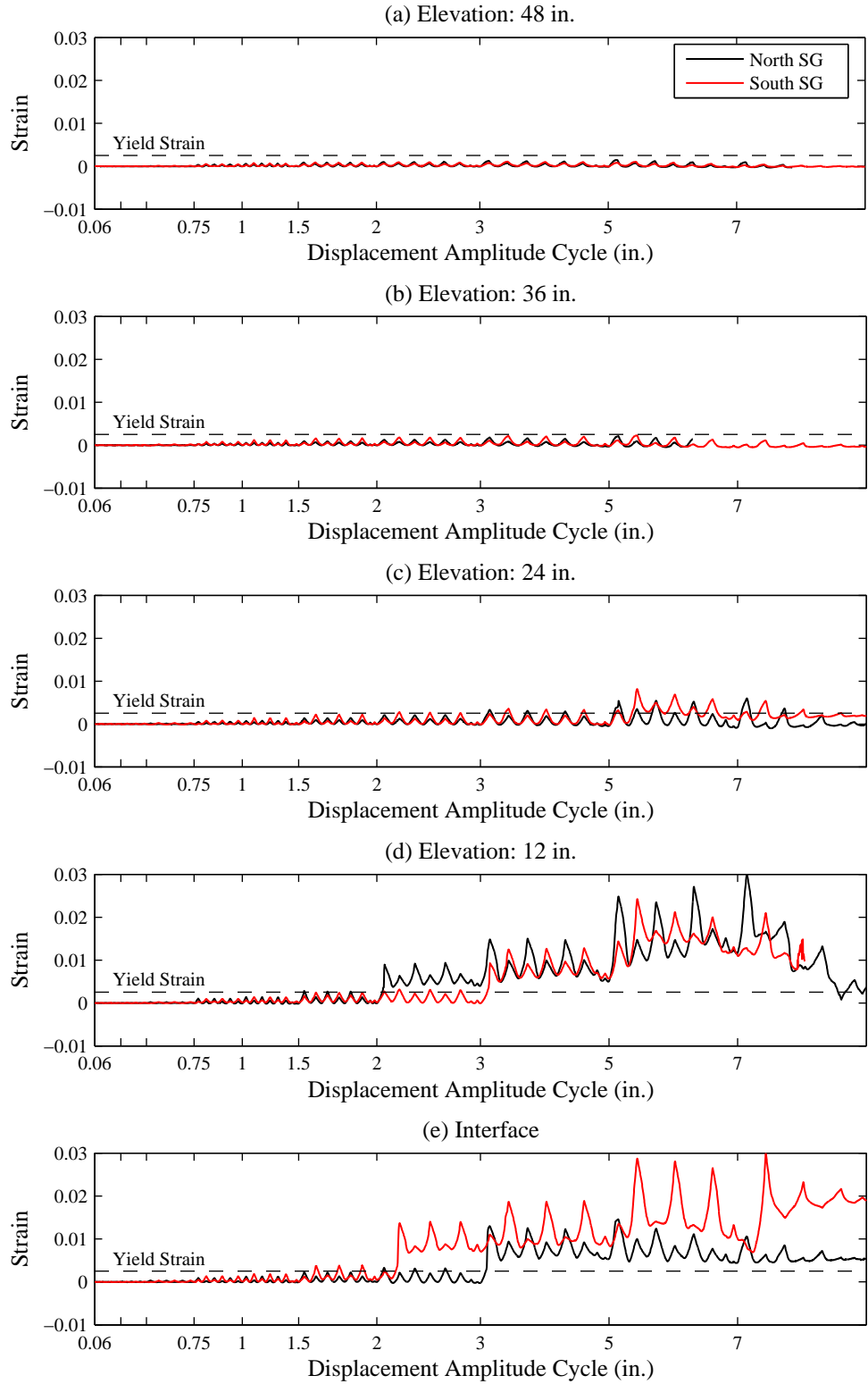


Figure C.50: Column C2 Longitudinal Strain History – North and South Gauges

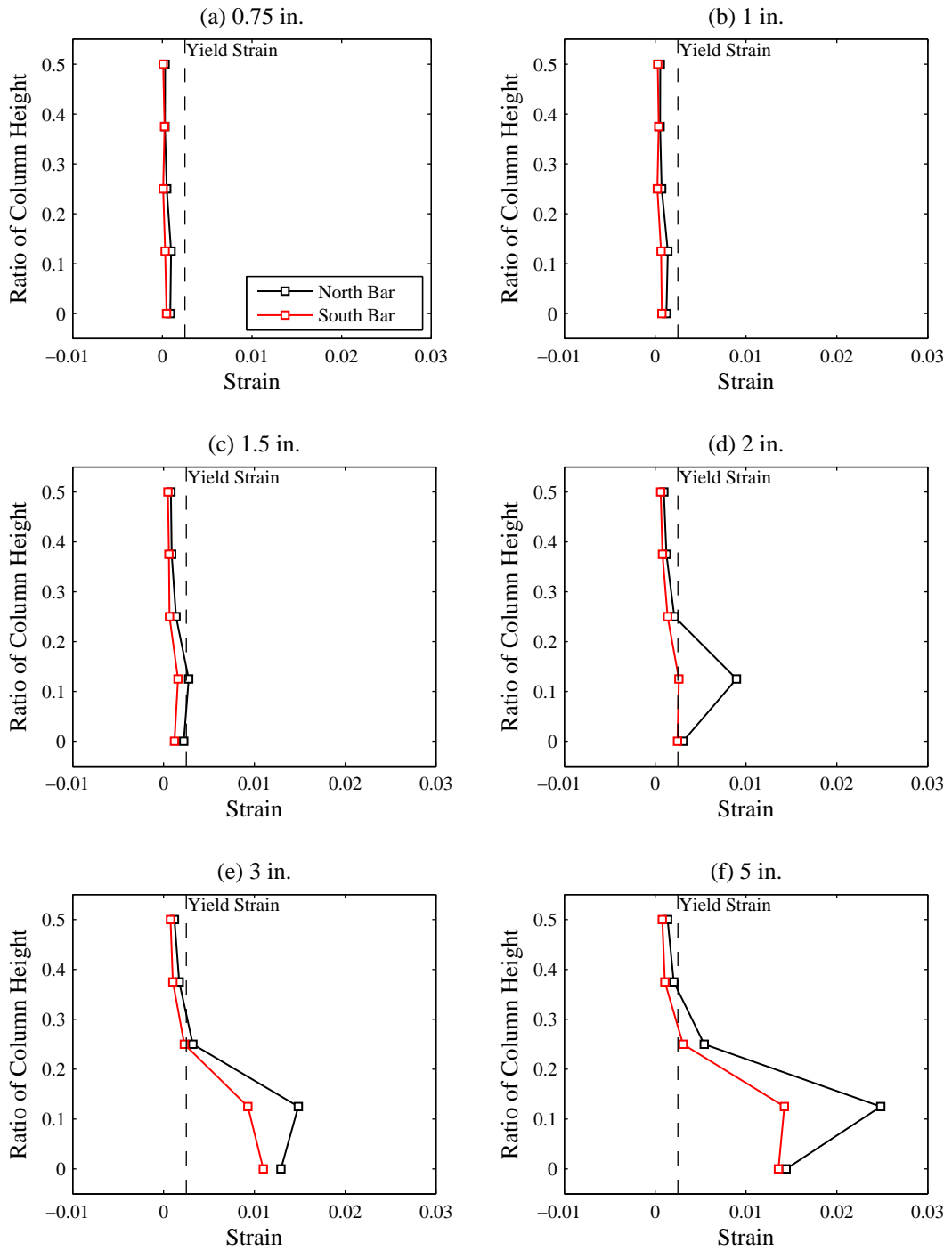


Figure C.51: Column C2 Longitudinal Strain Profile – North and South Gauges

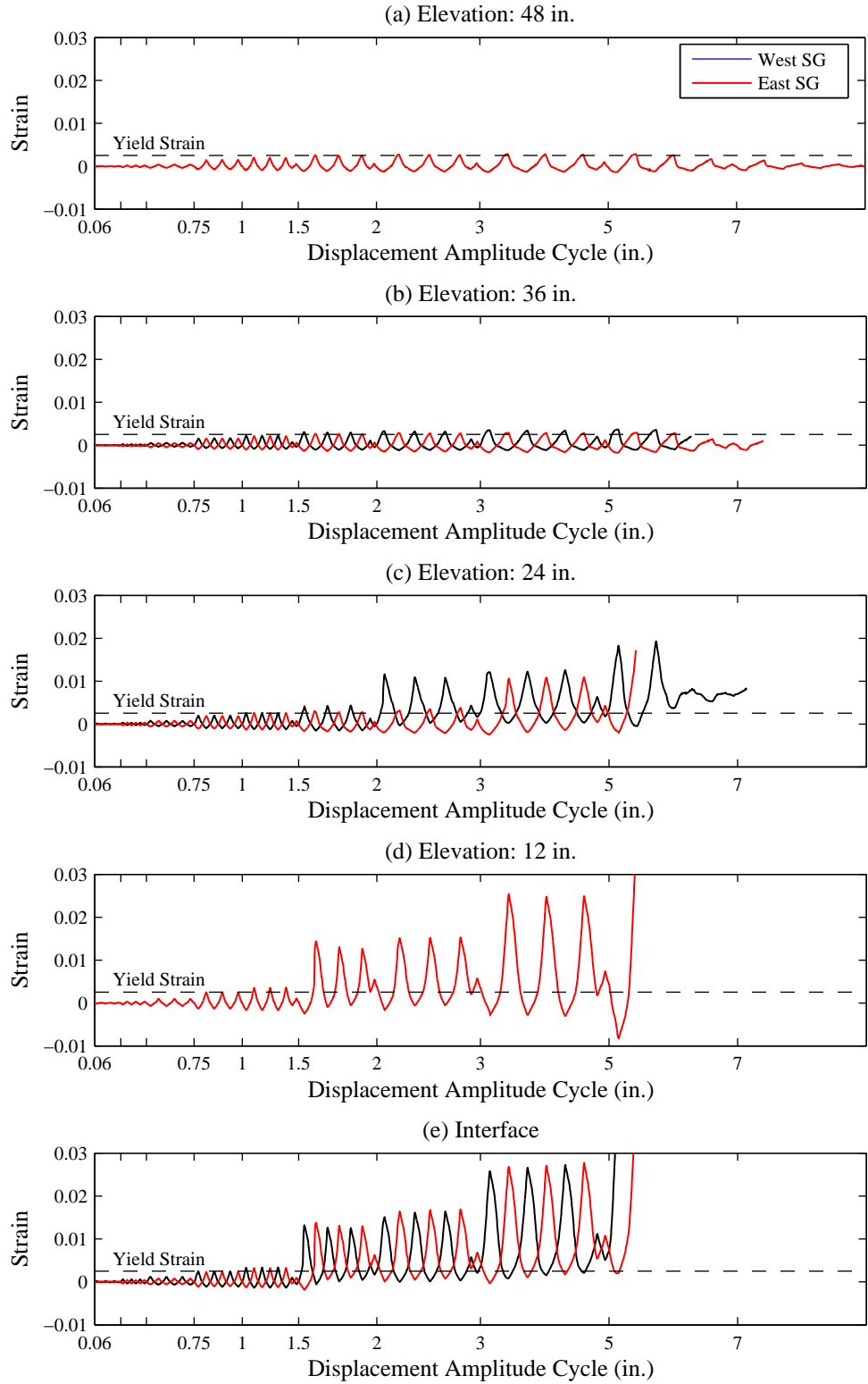


Figure C.52: Column C2 Longitudinal Strain History – West and East Gauges

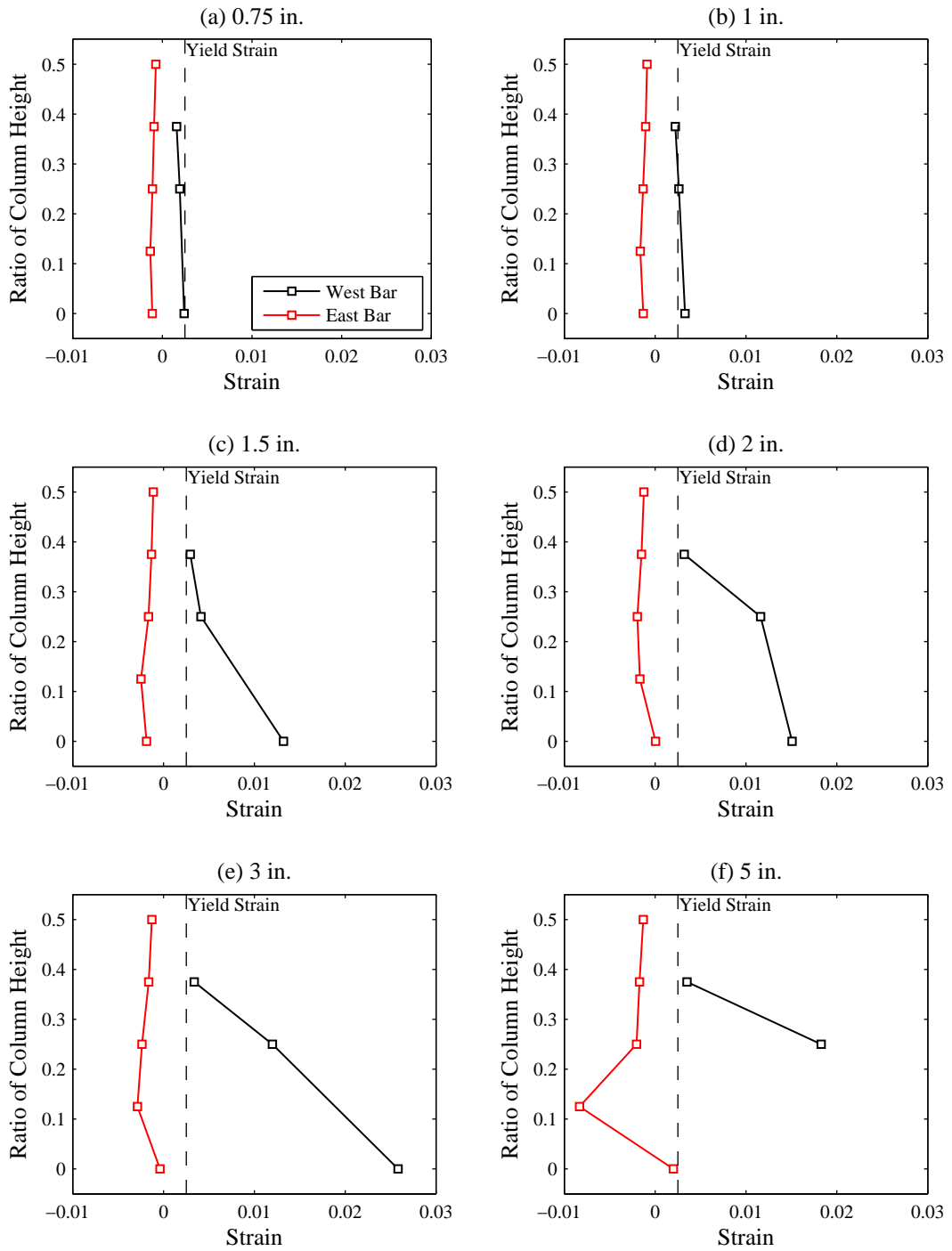


Figure C.53: Column C2 Longitudinal Strain Profile – West and East Gauges

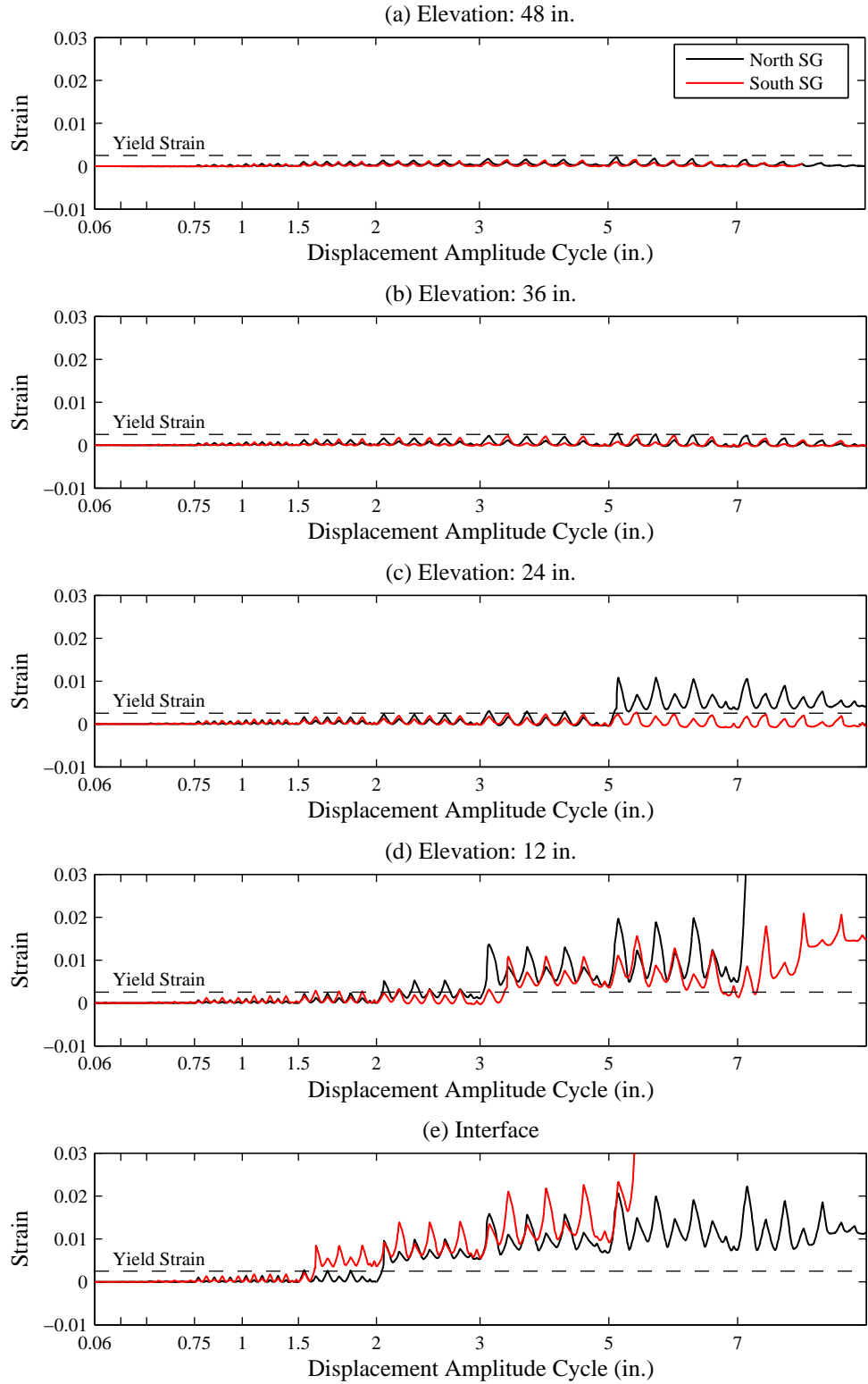


Figure C.54: Column C3 Longitudinal Strain History – North and South Gauges

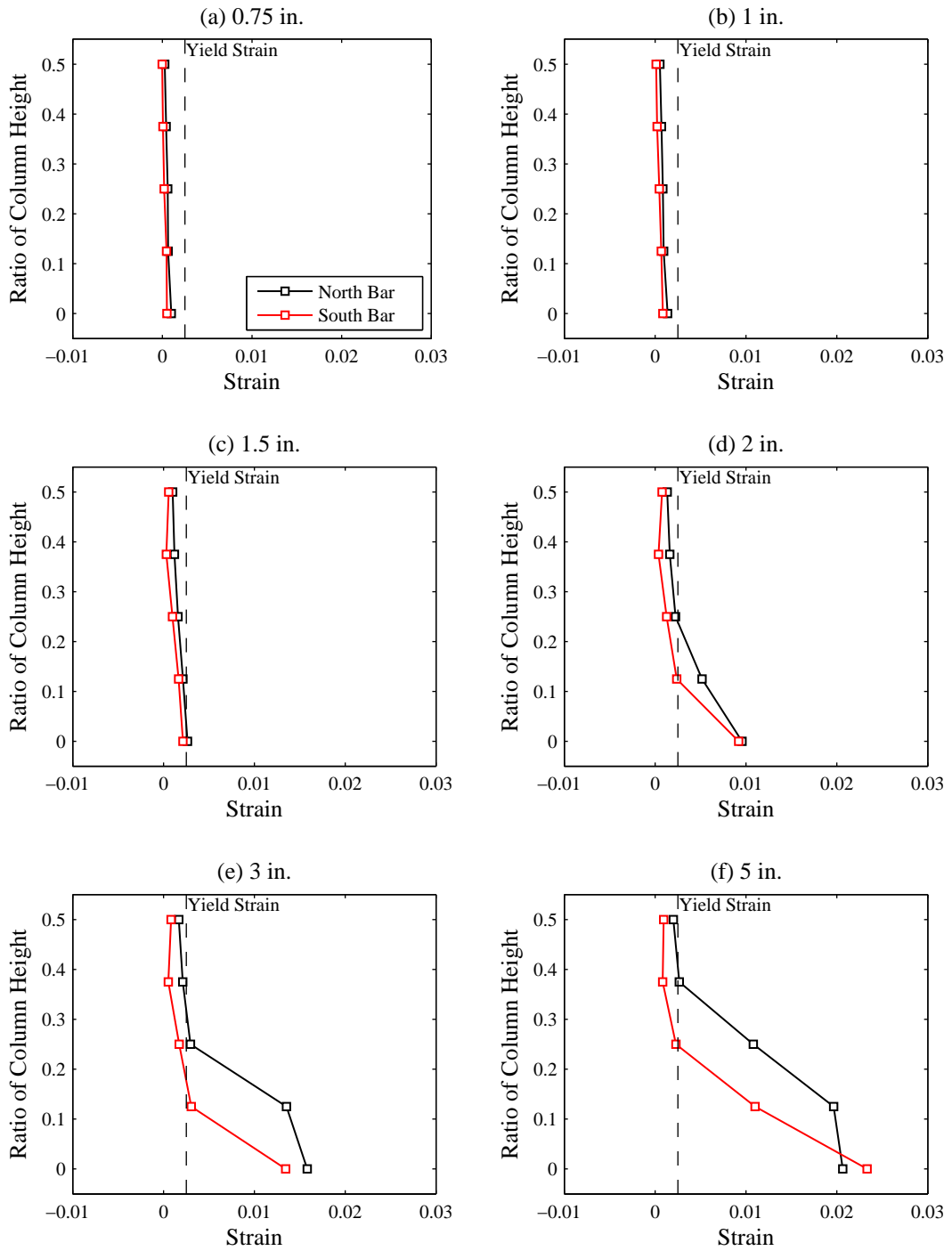


Figure C.55: Column C3 Longitudinal Strain Profile – North and South Gauges

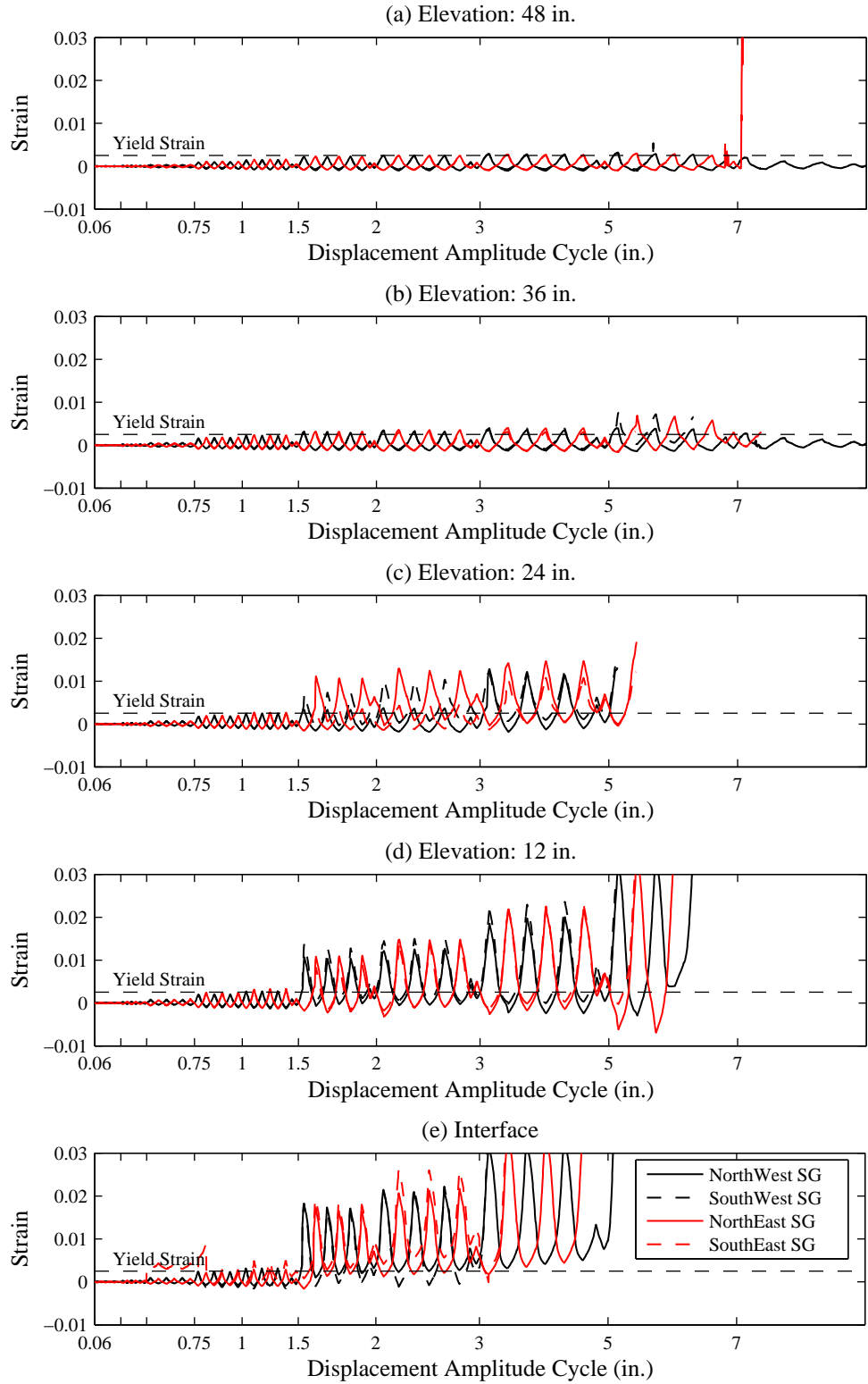


Figure C.56: Column C3 Longitudinal Strain History – West and East Gauges

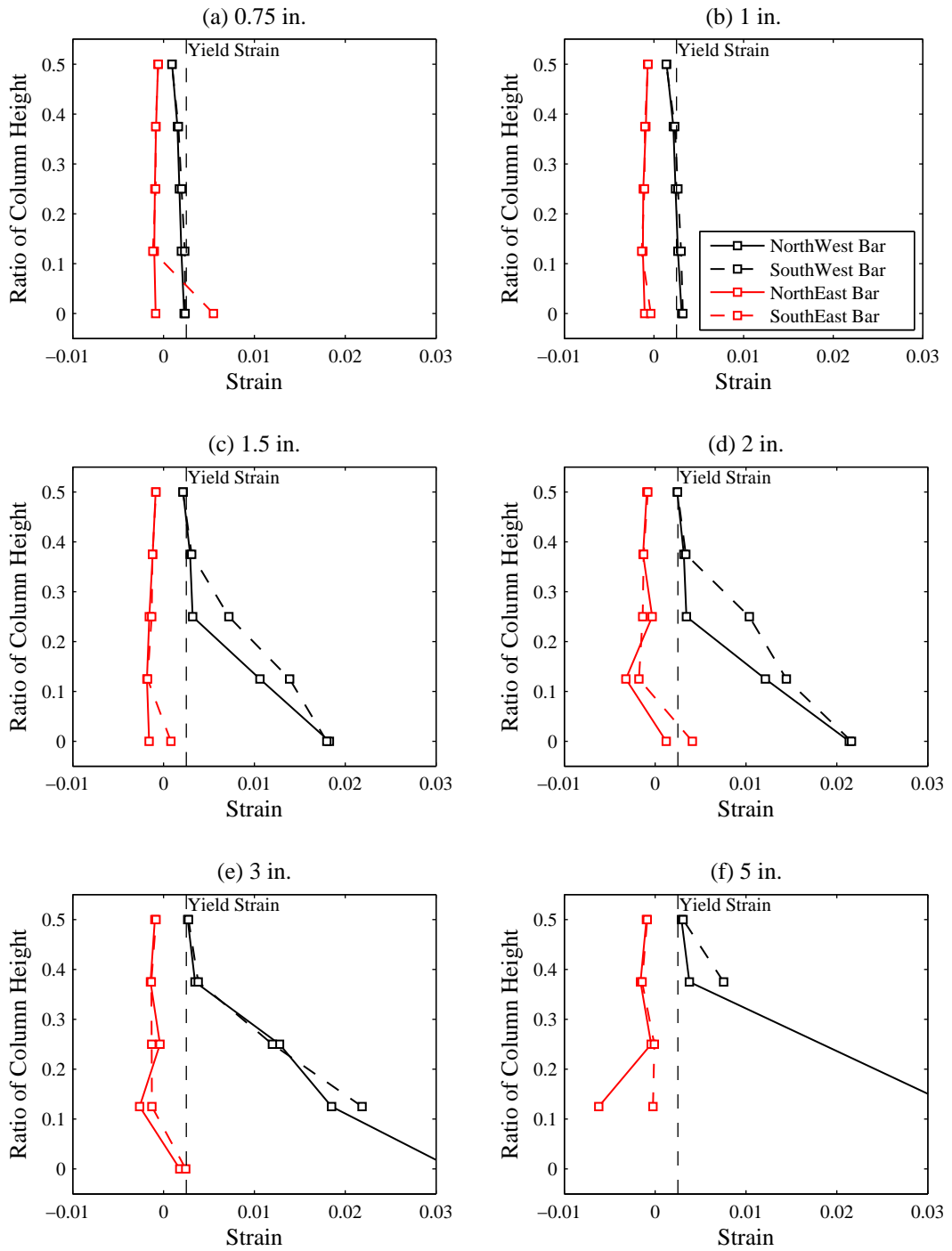


Figure C.57: Column C3 Longitudinal Strain Profile – West and East Gauges

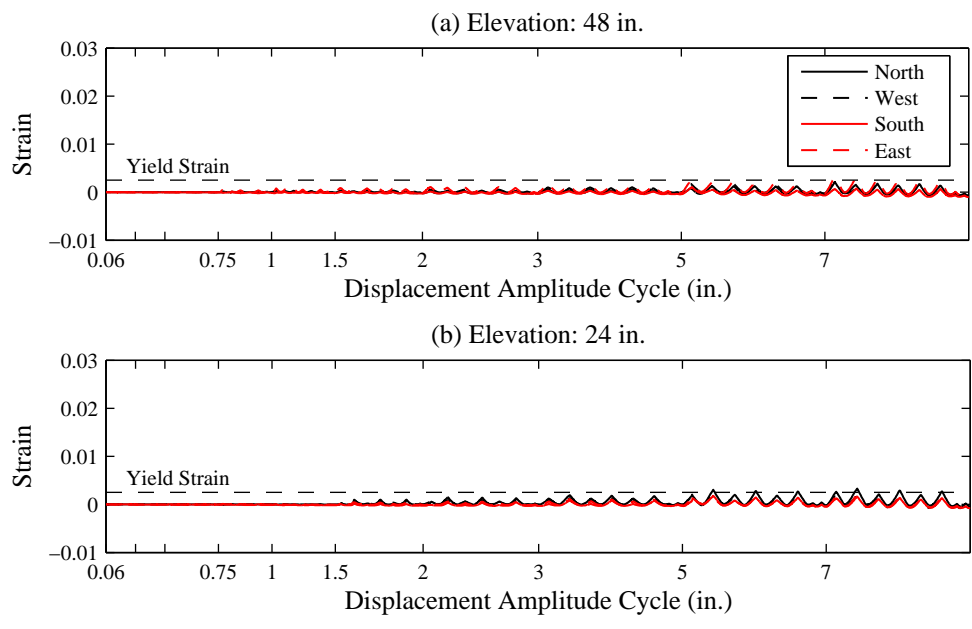


Figure C.58: Column C4 Longitudinal Strain History

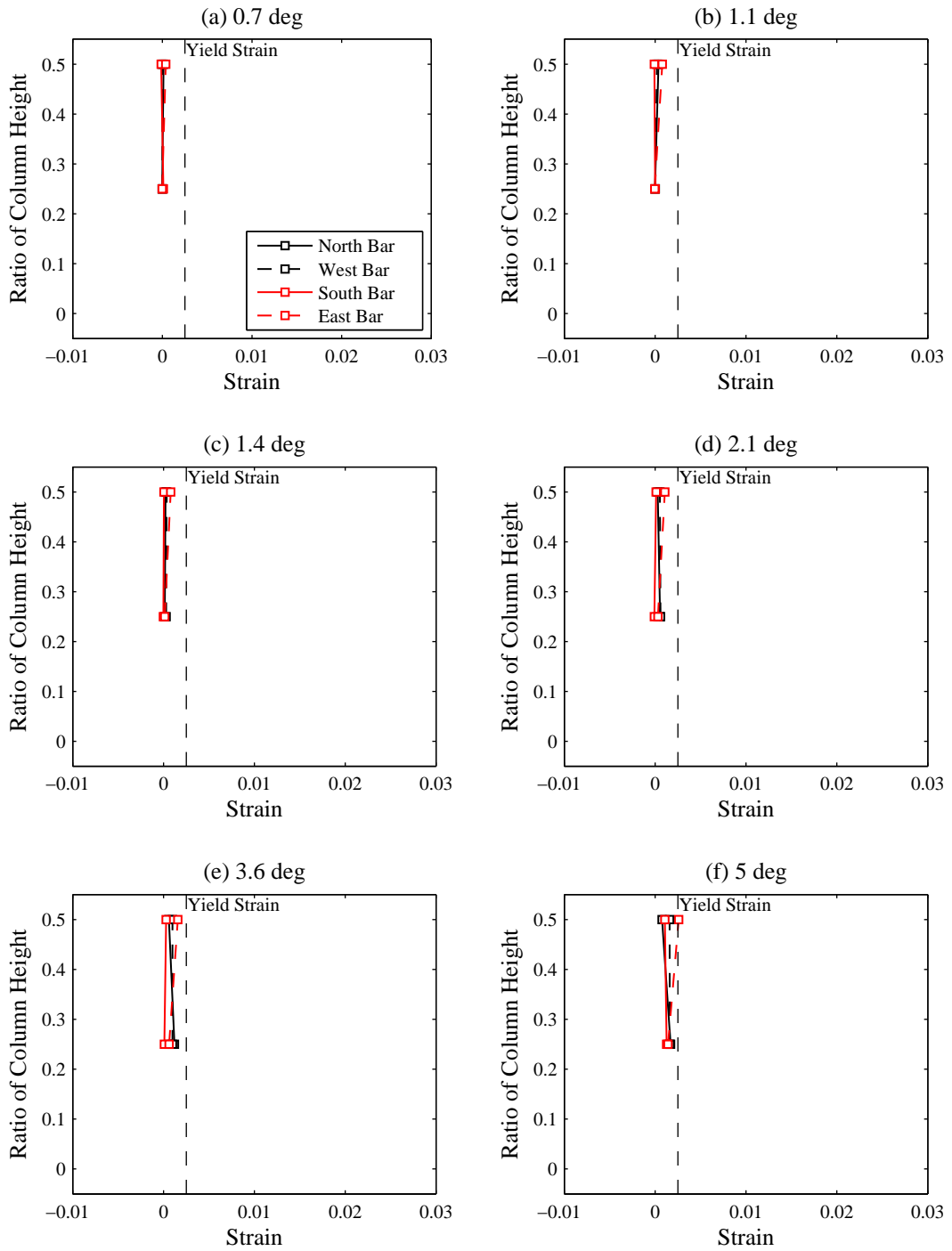


Figure C.59: Column C4 Longitudinal Strain Profile

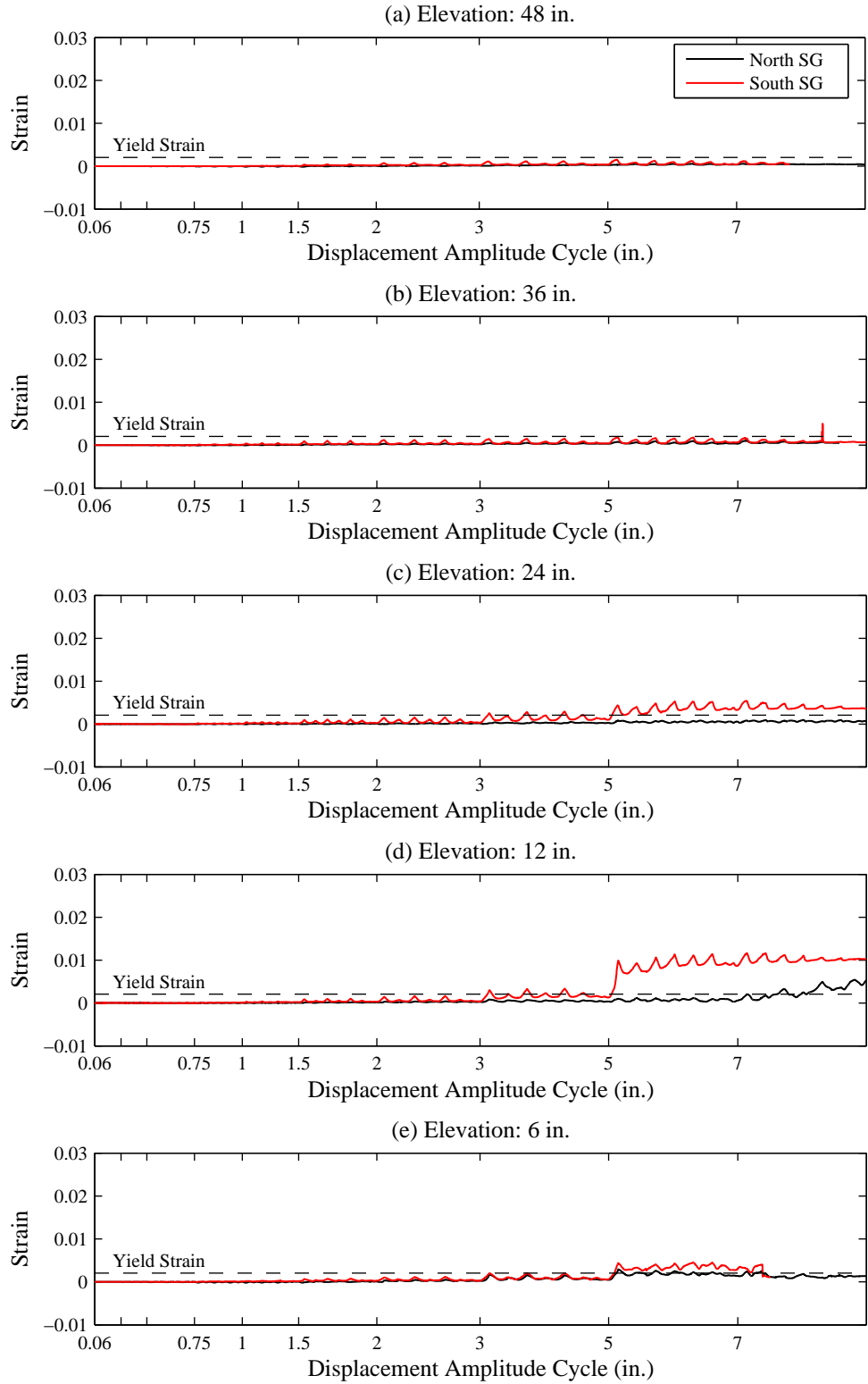


Figure C.60: Column C1 Hoop Strain History – North and South Gauges

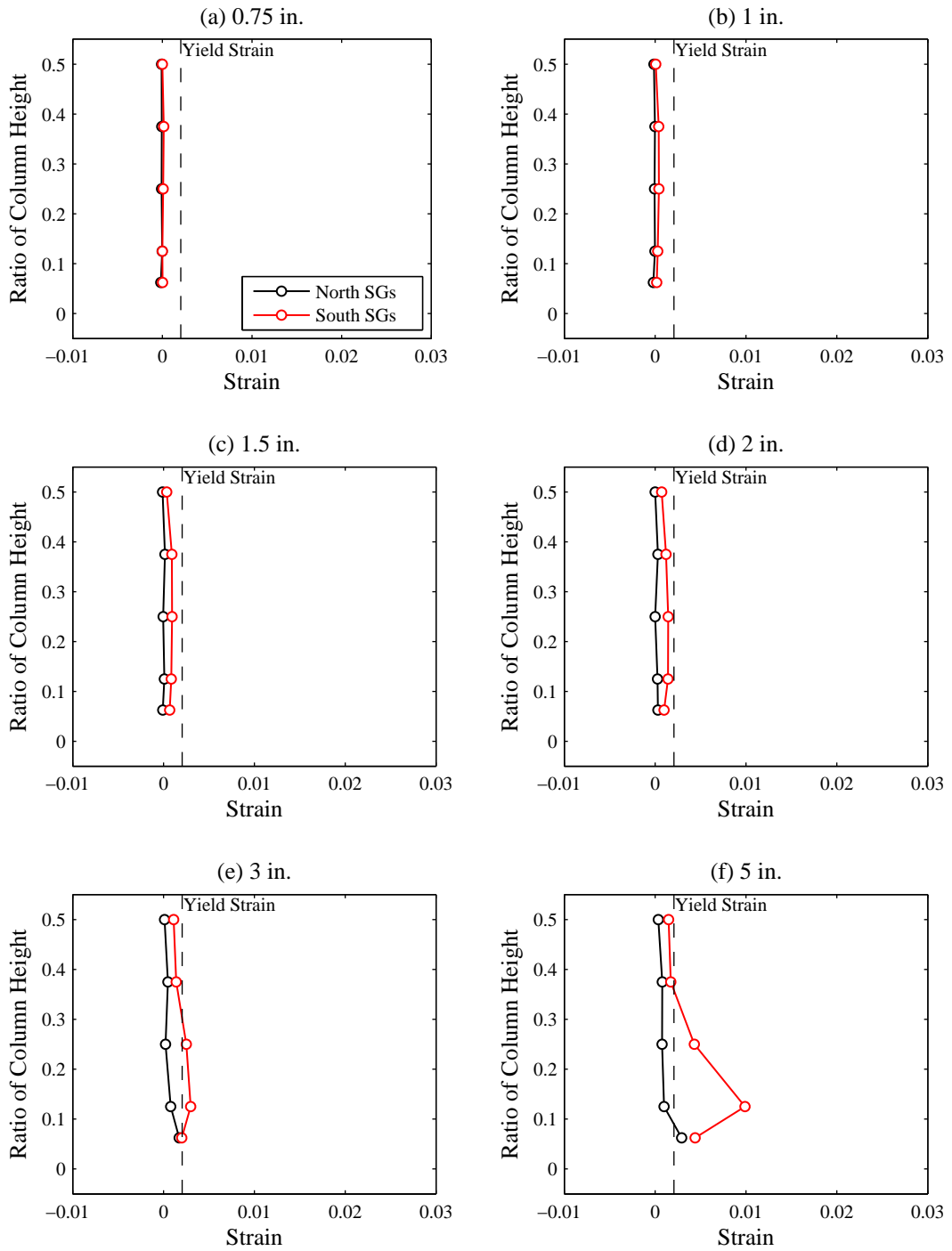


Figure C.61: Column C1 Hoop Strain Profile – North and South Gauges

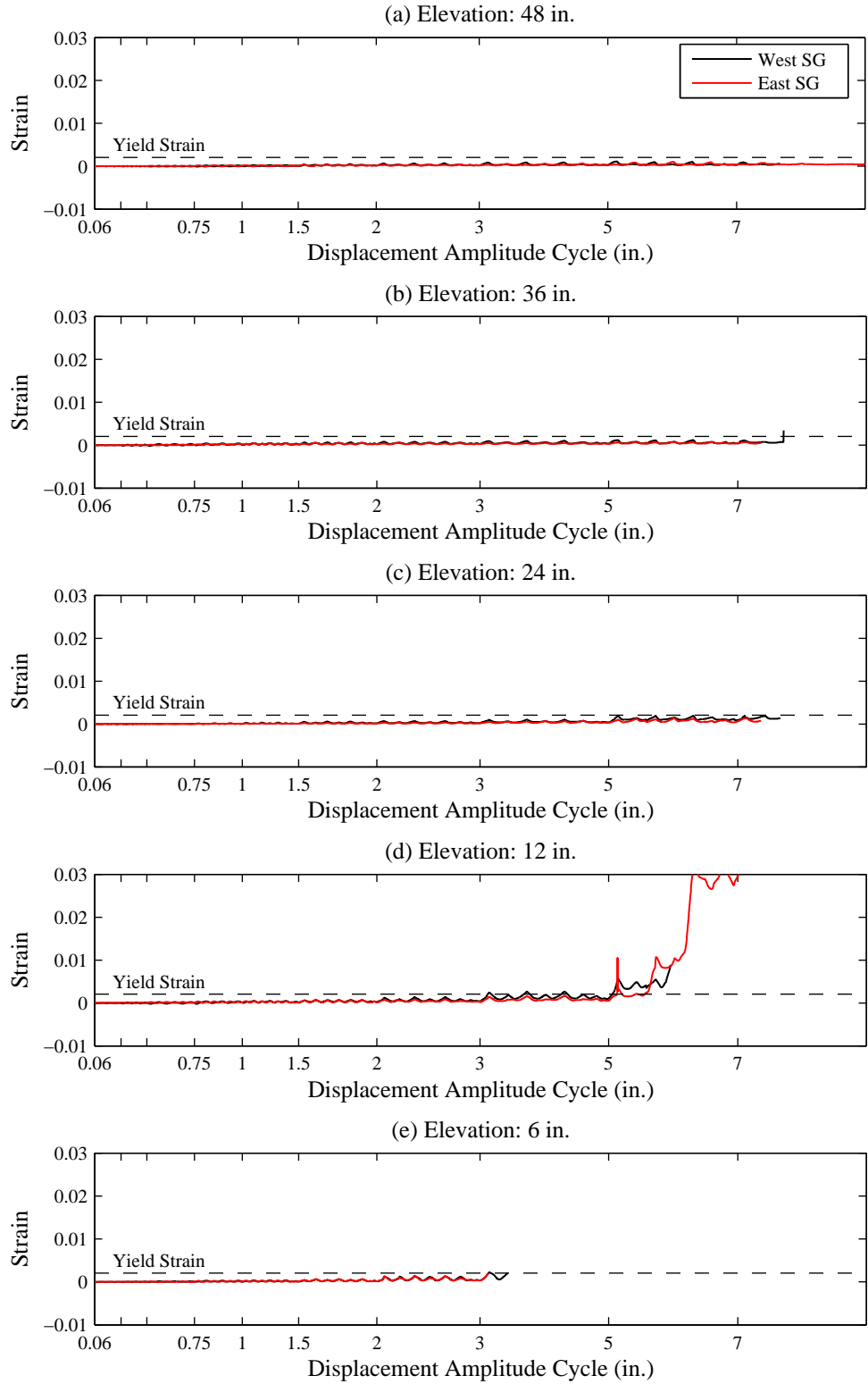


Figure C.62: Column C1 Hoop Strain History – West and East Gauges

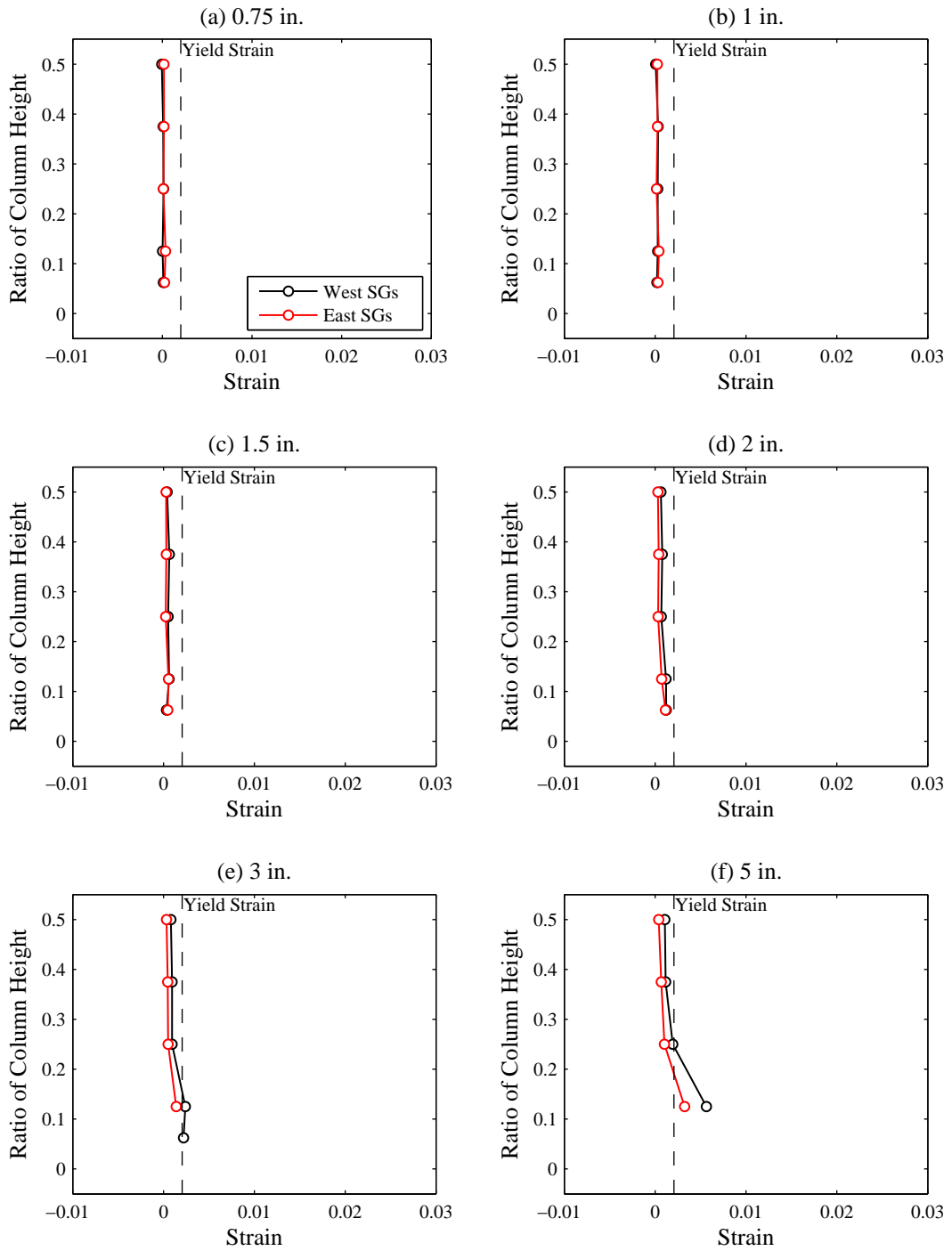


Figure C.63: Column C1 Hoop Strain Profile – West and East Gauges

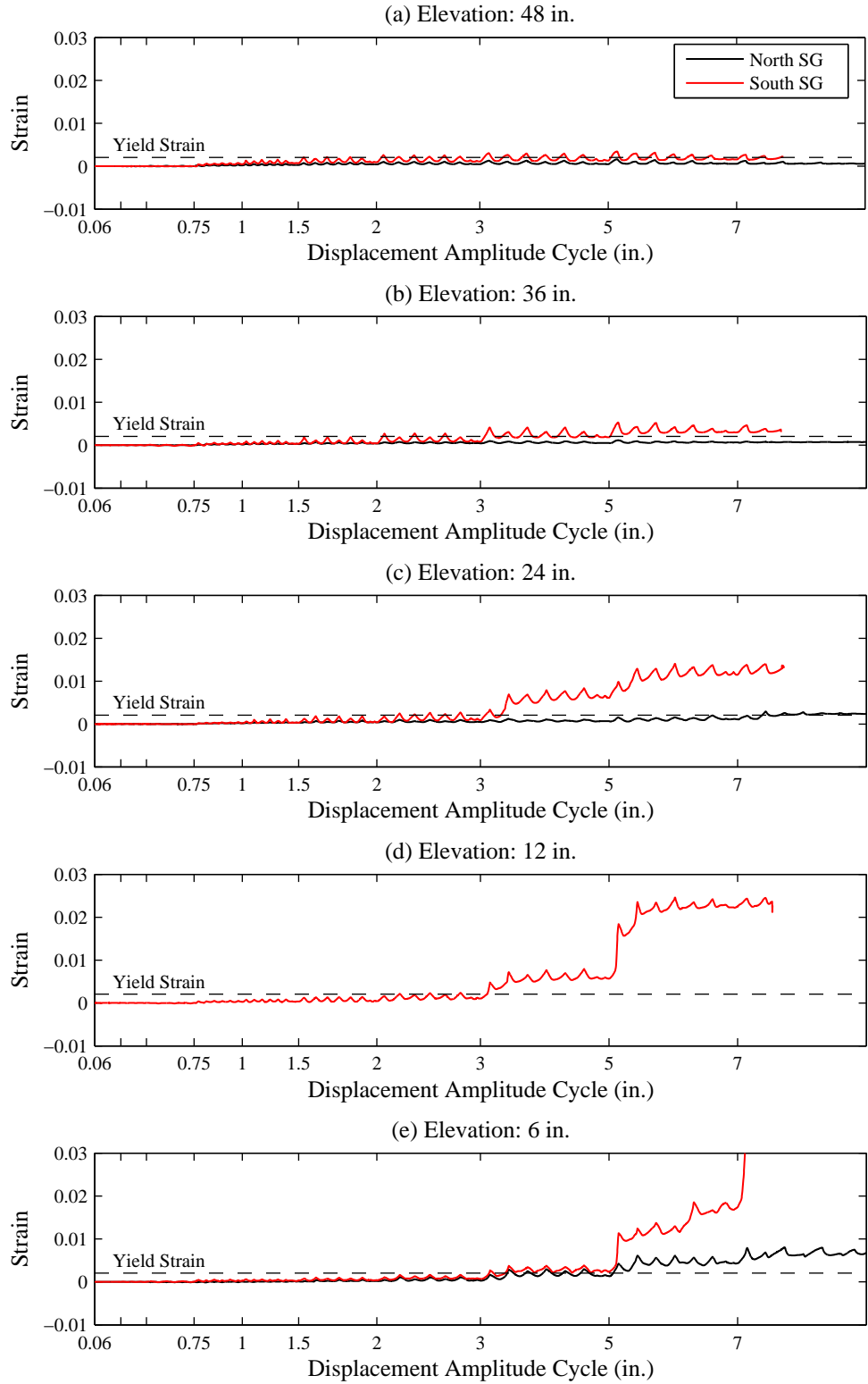


Figure C.64: Column C2 Hoop Strain History – North and South Gauges

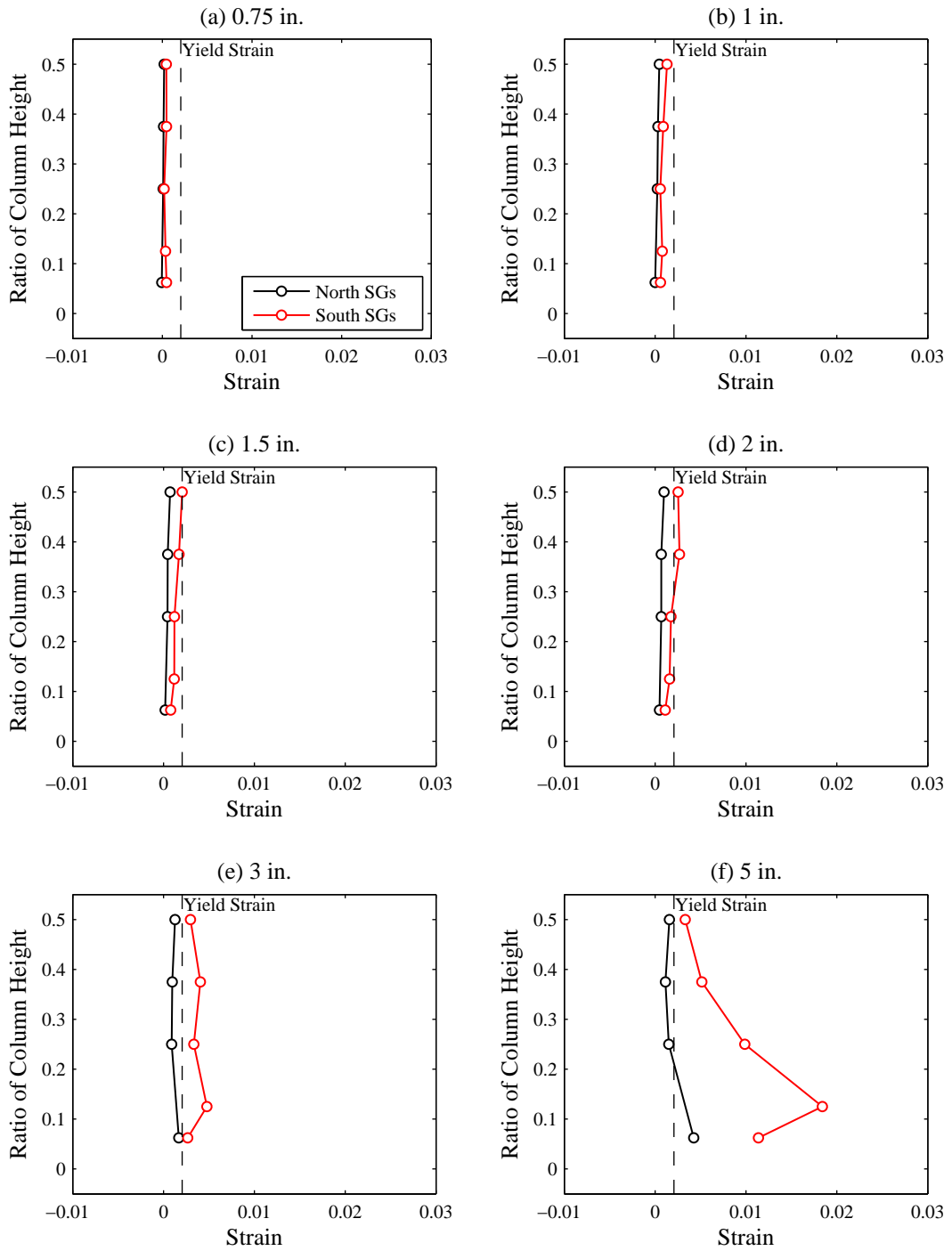


Figure C.65: Column C2 Hoop Strain Profile – North and South Gauges

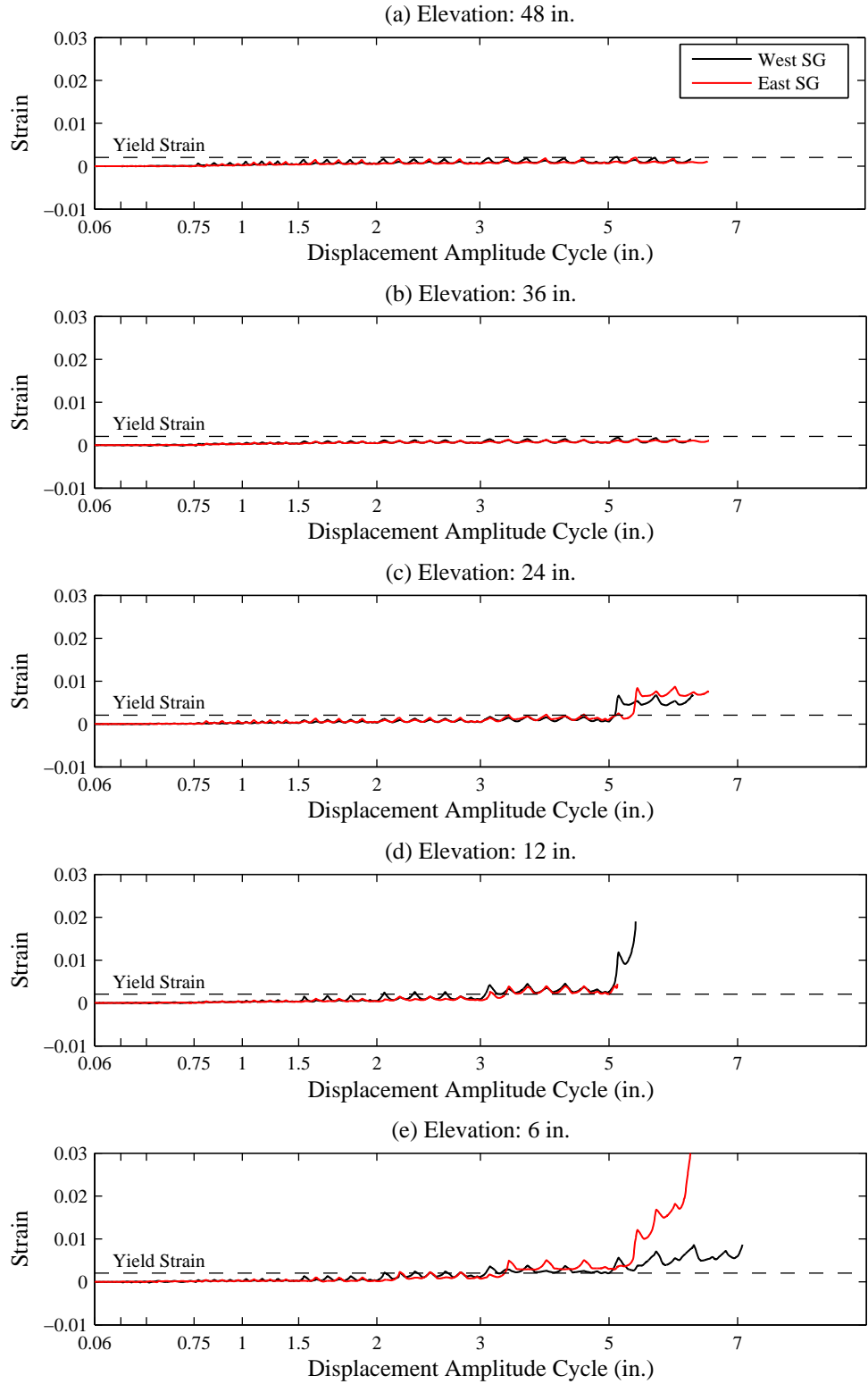


Figure C.66: Column C2 Hoop Strain History – West and East Gauges

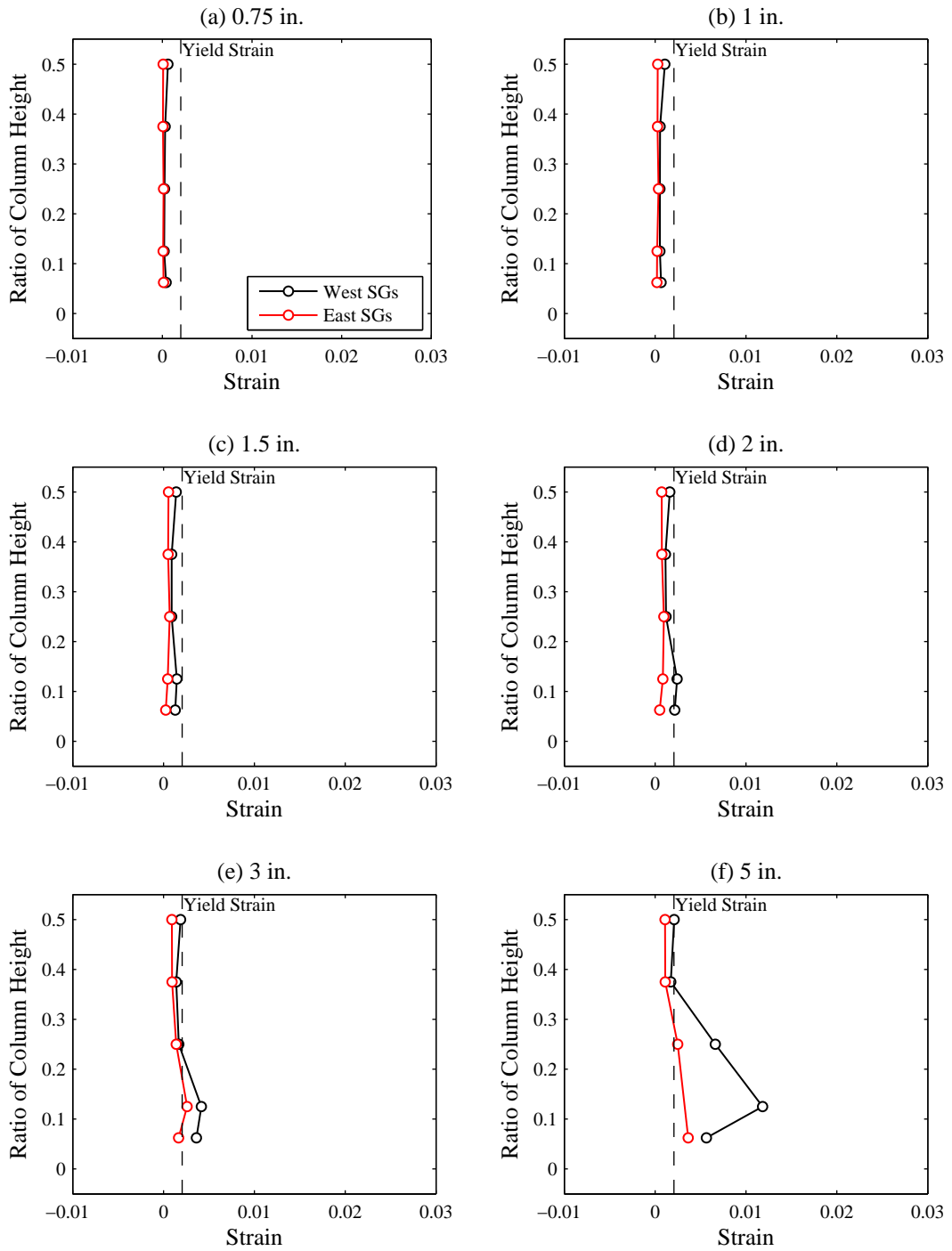


Figure C.67: Column C2 Hoop Strain Profile – West and East Gauges

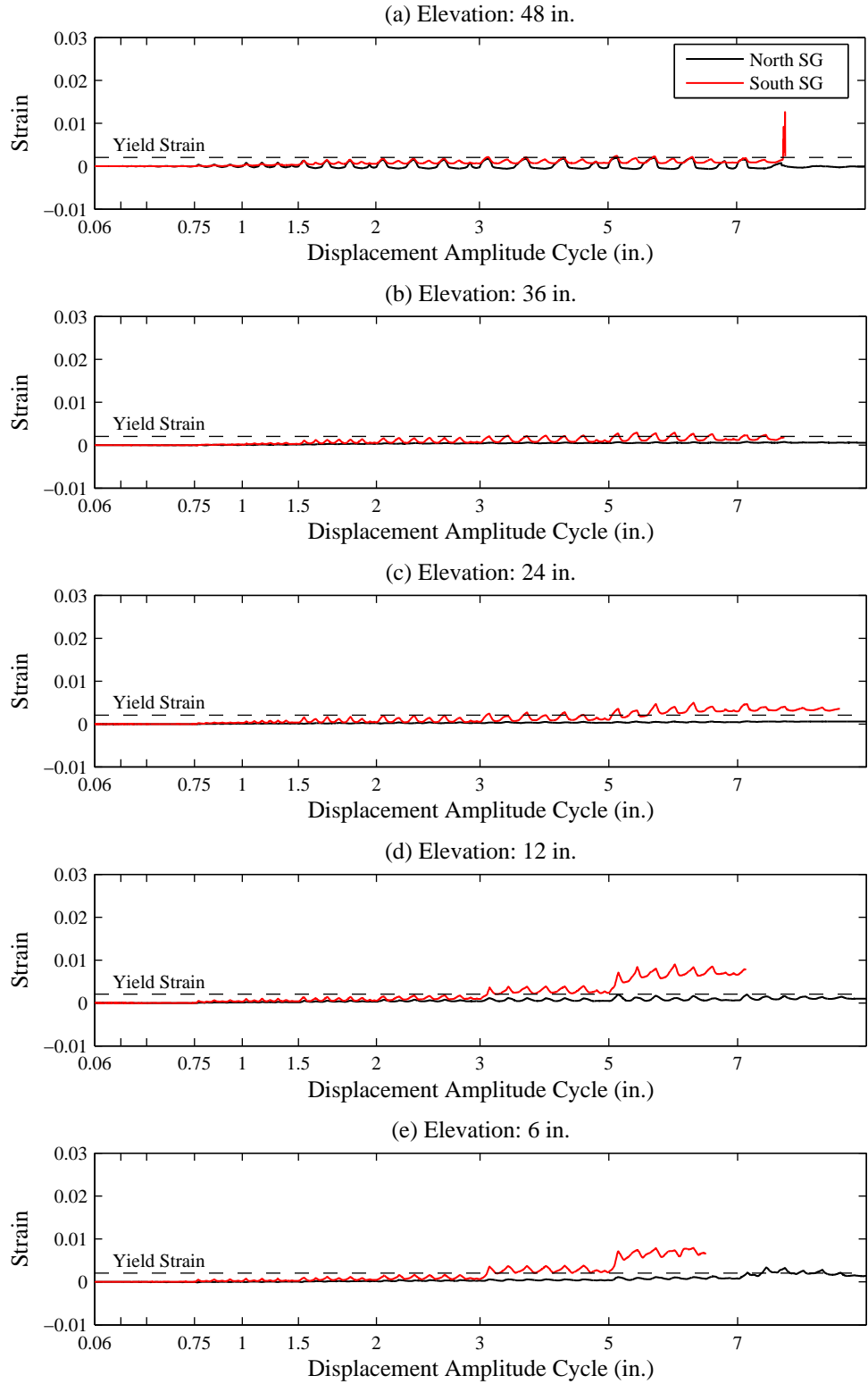


Figure C.68: Column C3 Hoop Strain History – North and South Gauges

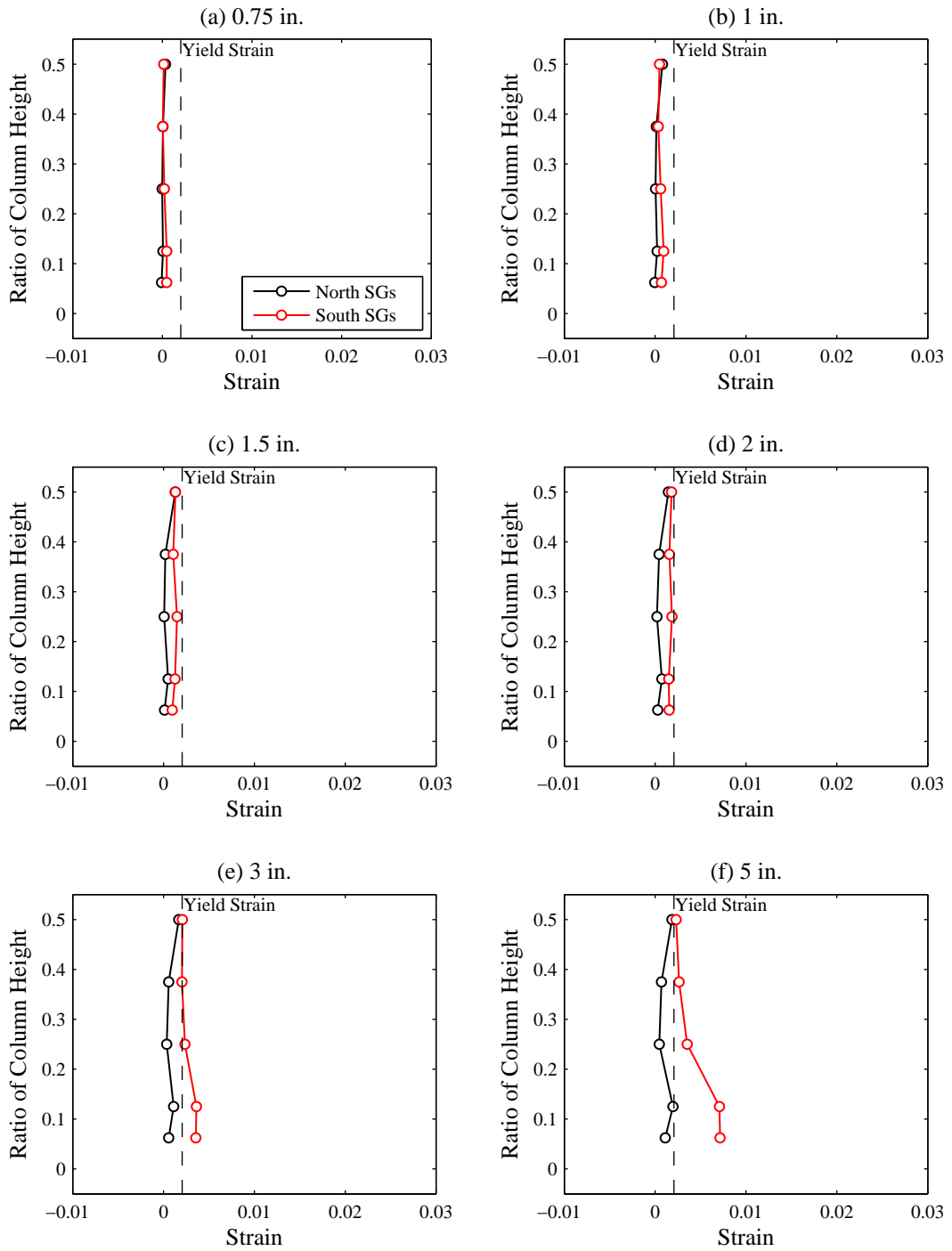


Figure C.69: Column C3 Hoop Strain Profile – North and South Gauges

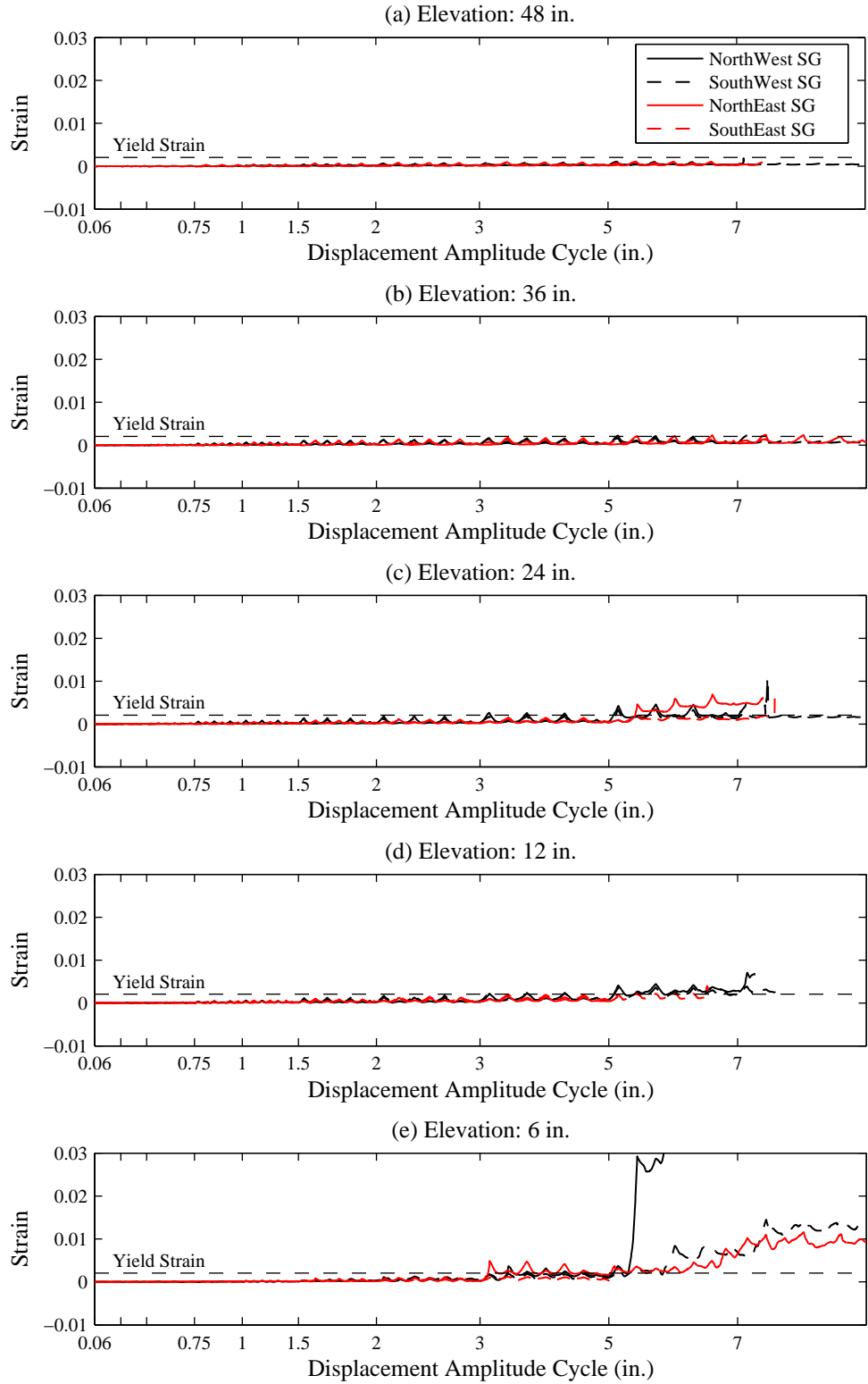


Figure C.70: Column C3 Hoop Strain History – West and East Gauges

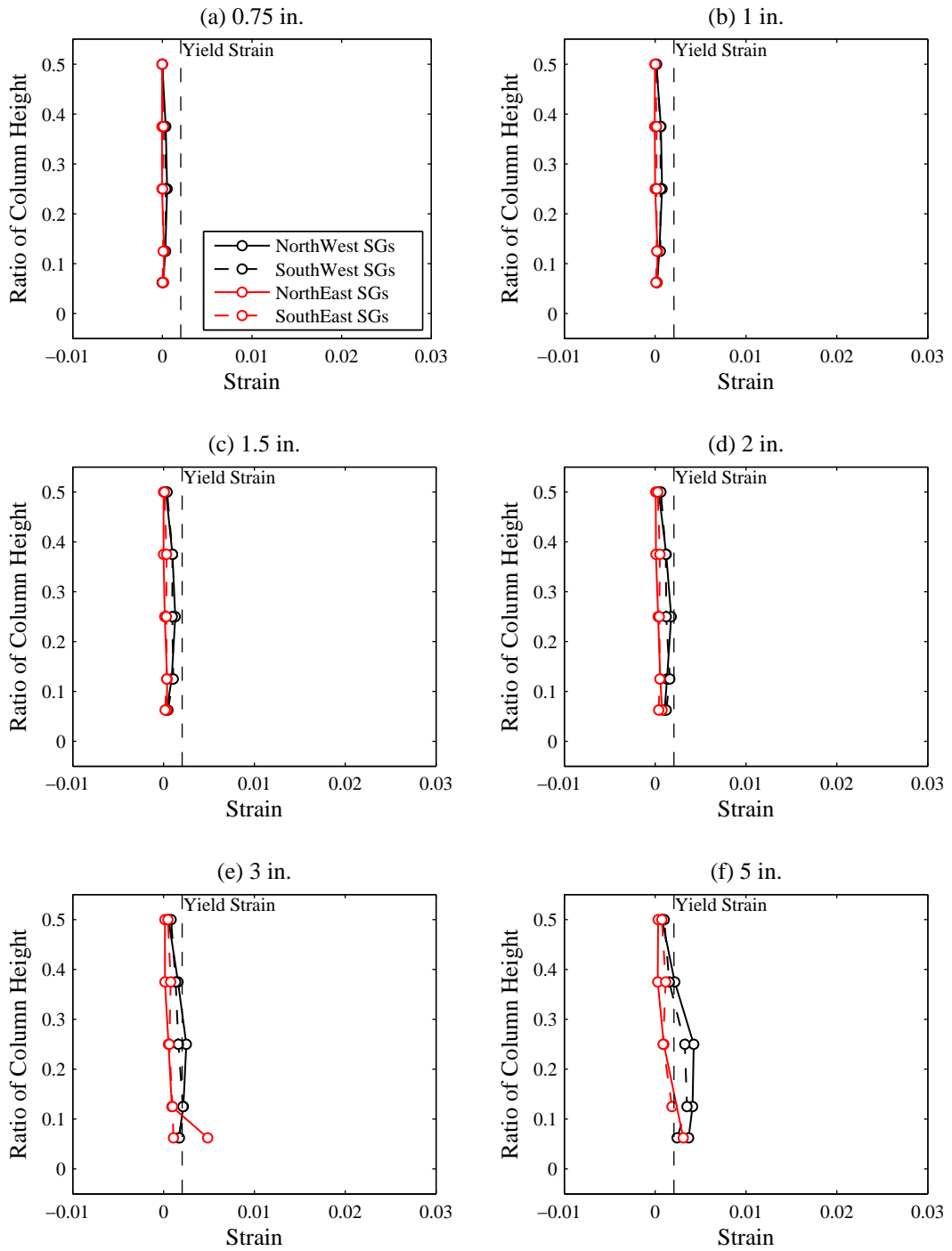


Figure C.71: Column C3 Hoop Strain Profile – West and East Gauges

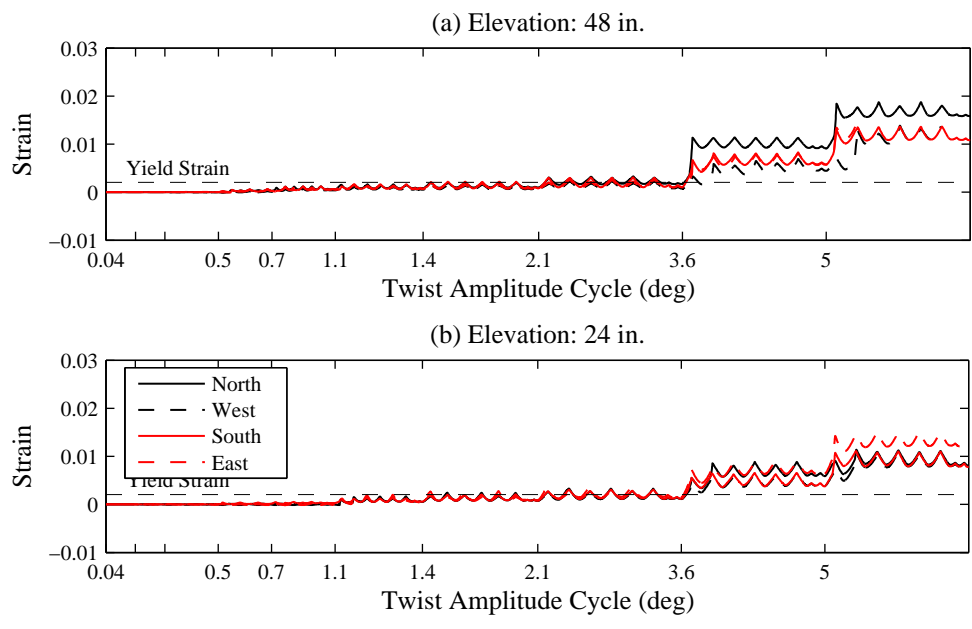


Figure C.72: Column C4 Hoop Strain History

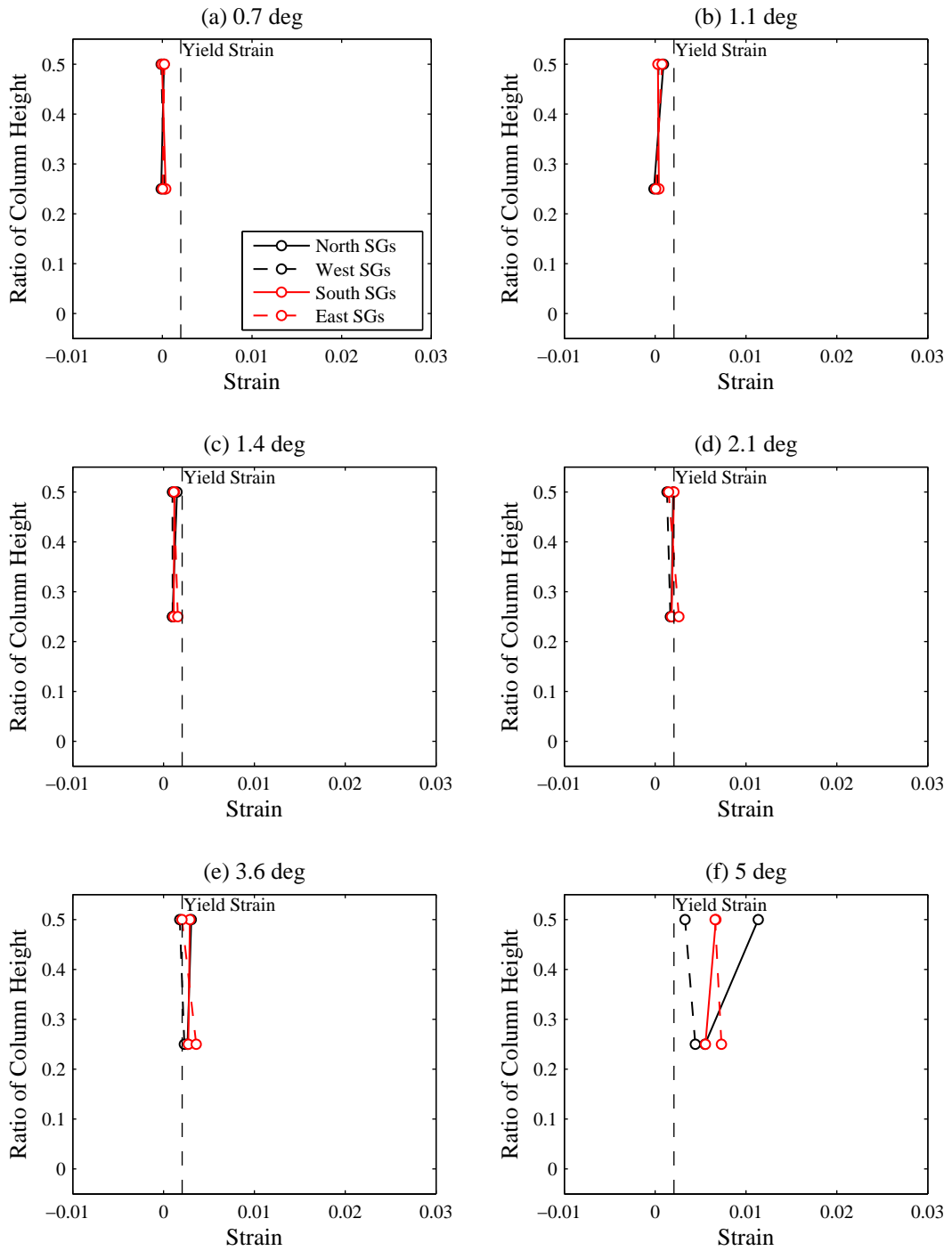


Figure C.73: Column C4 Hoop Strain Profile

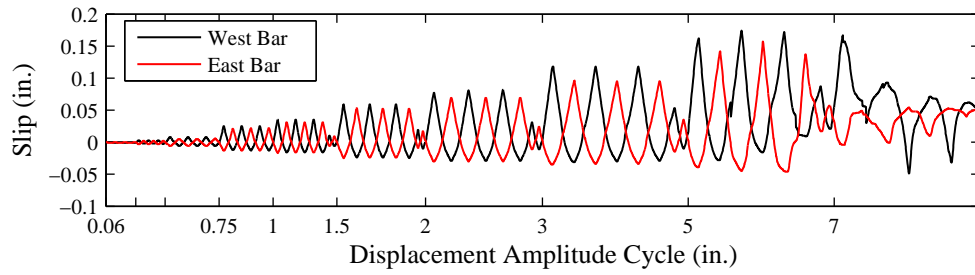


Figure C.74: Column C1 Bar Slip History

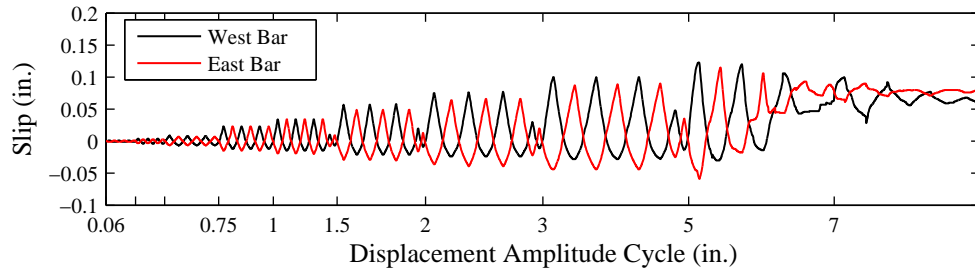


Figure C.75: Column C2 Bar Slip History

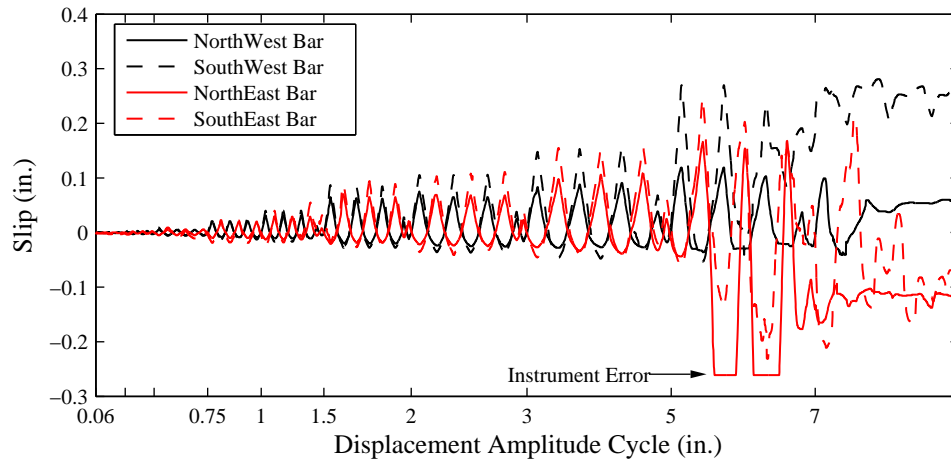


Figure C.76: Column C3 Bar Slip History

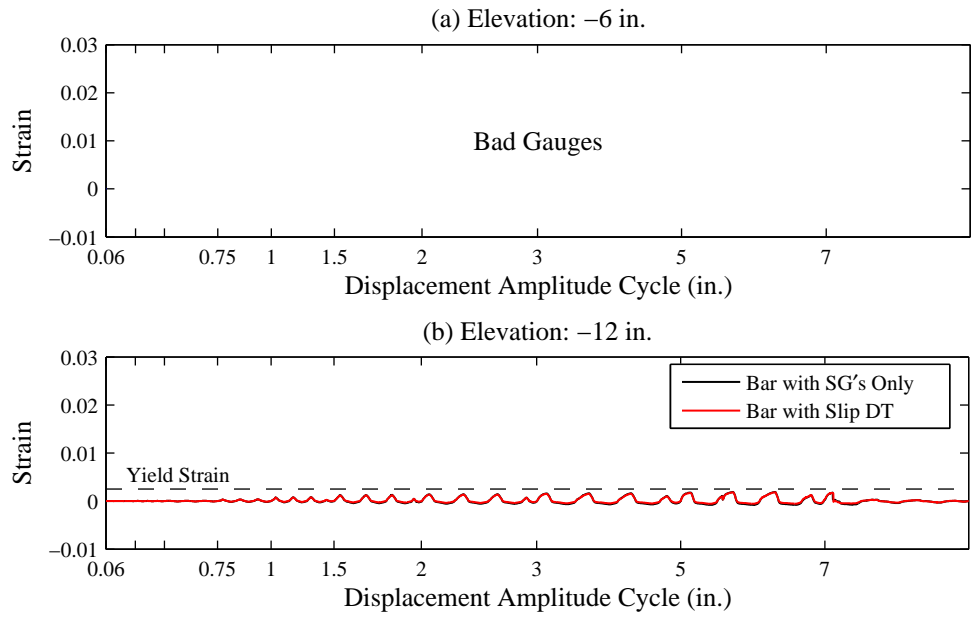


Figure C.77: Column C1 Joint Strain History – West Gauges

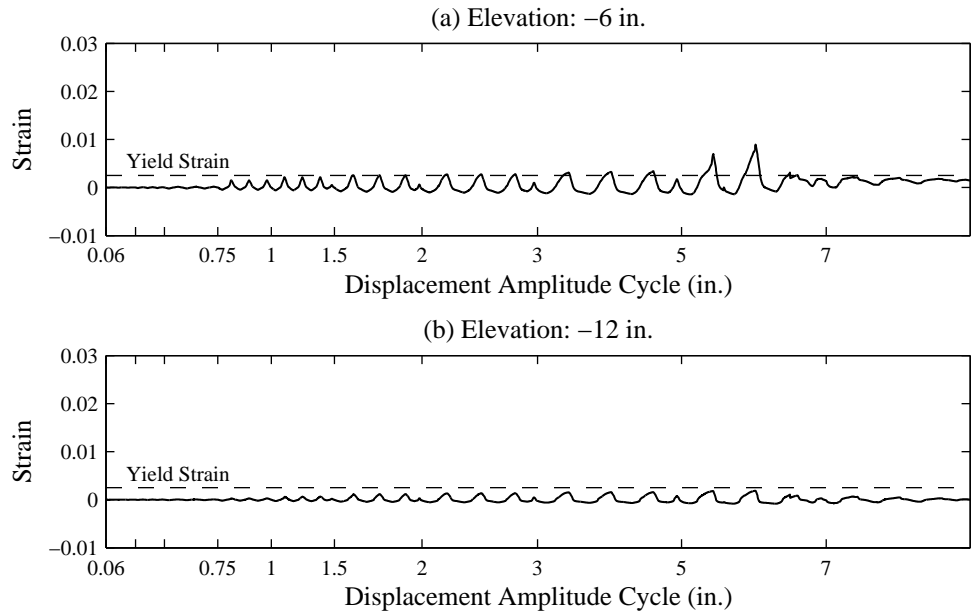


Figure C.78: Column C1 Joint Strain History – East Gauges

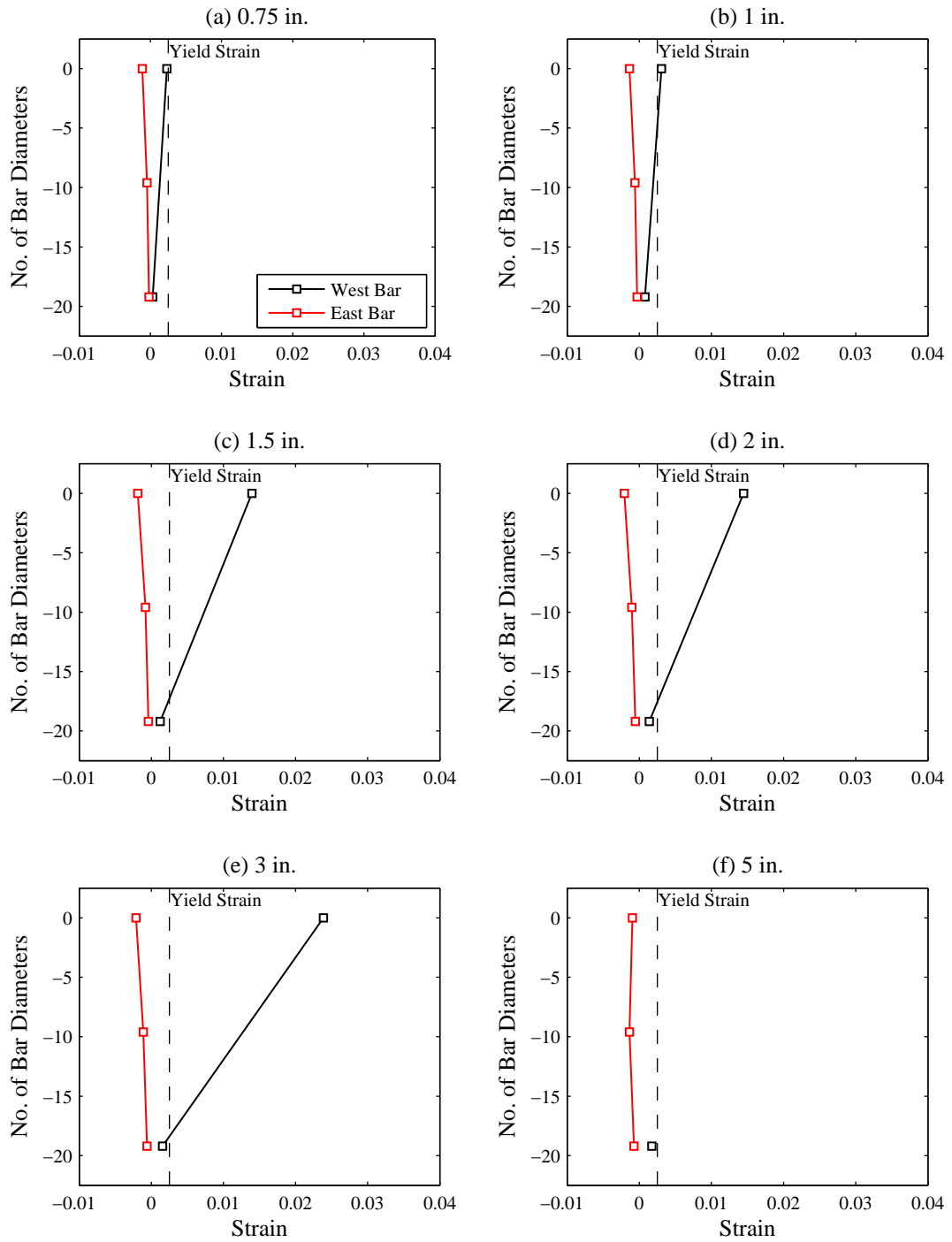


Figure C.79: Column C1 Joint Strain Profile

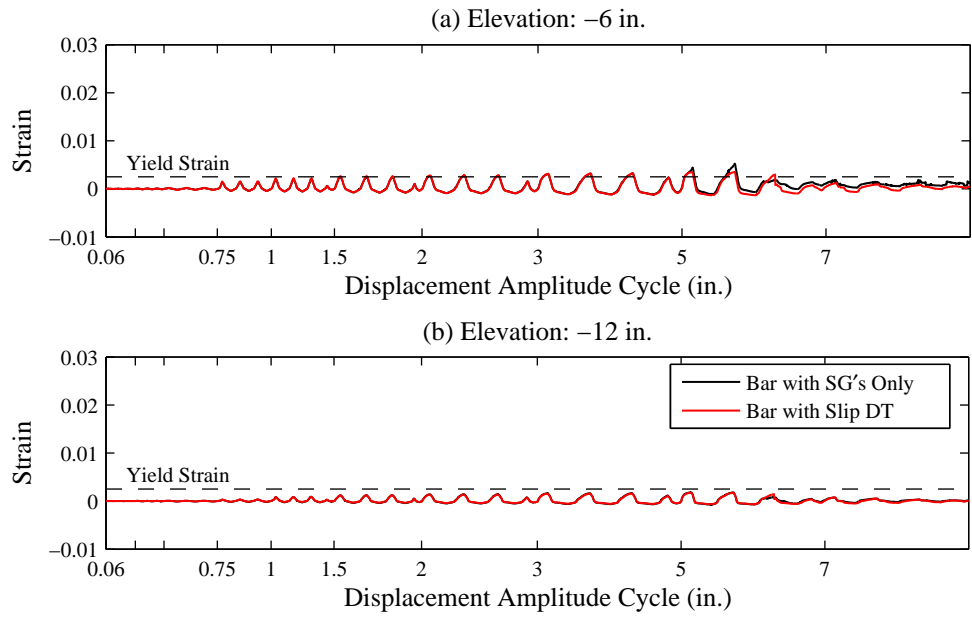


Figure C.80: Column C2 Joint Strain History – West Gauges

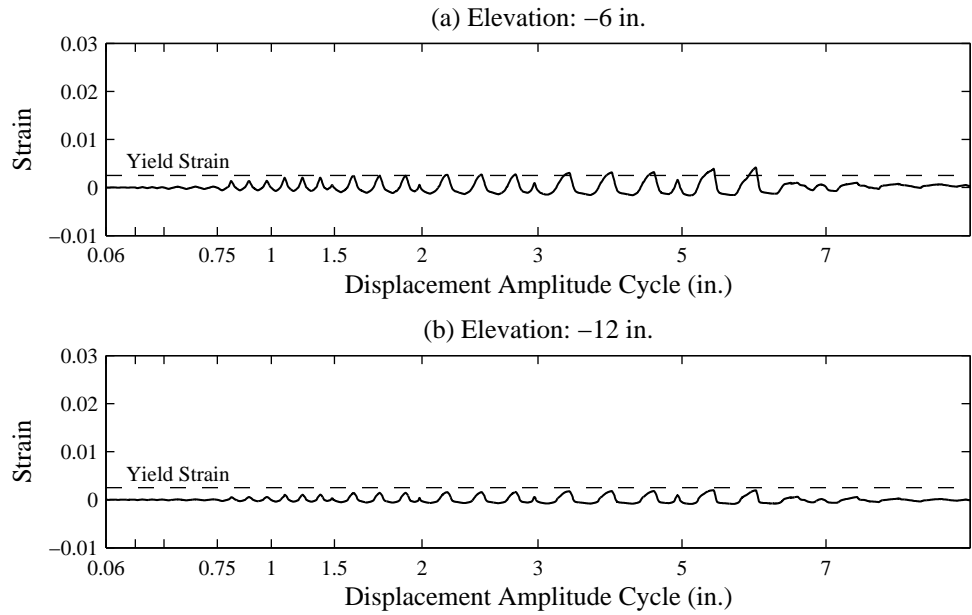


Figure C.81: Column C2 Joint Strain History – East Gauges

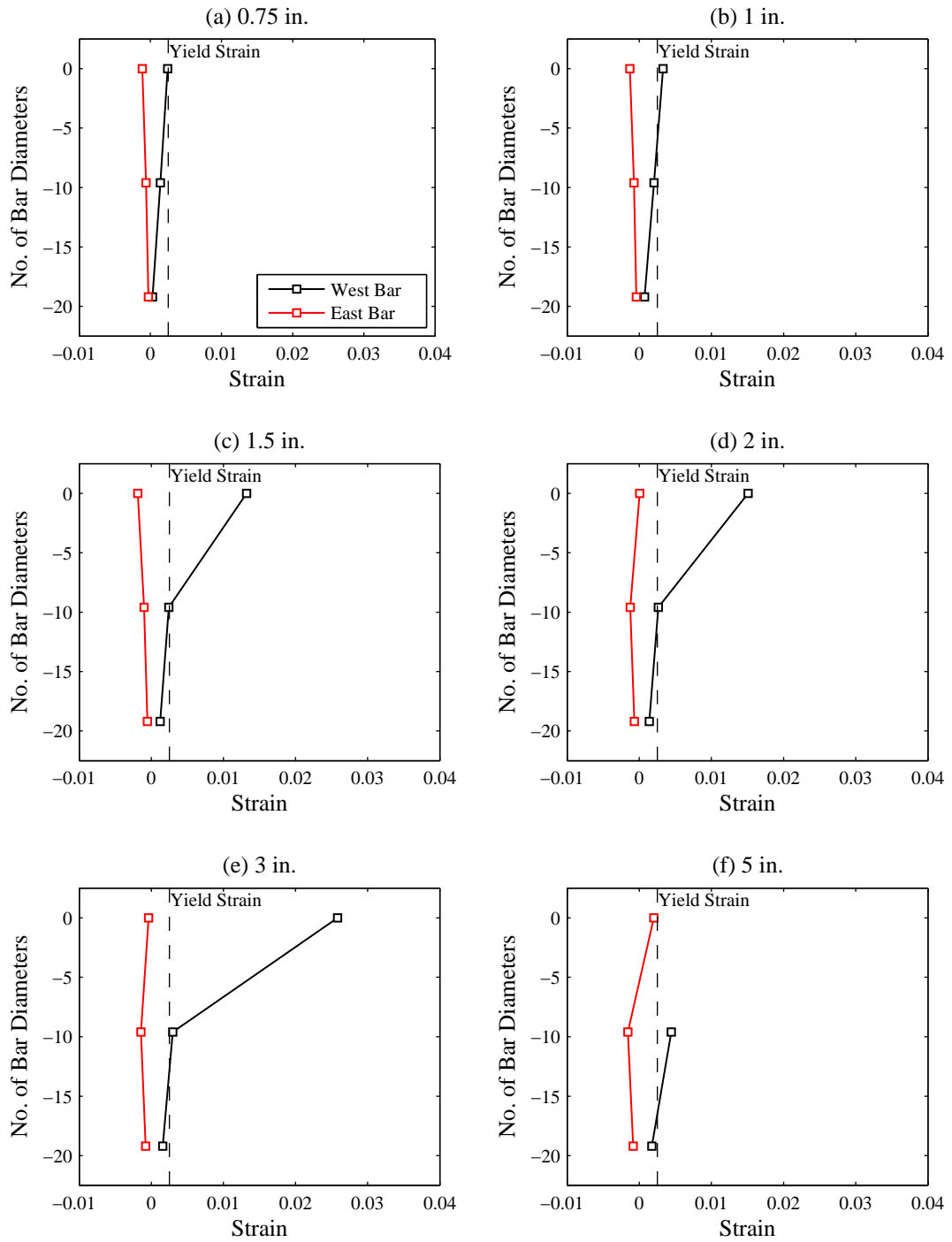


Figure C.82: Column C2 Joint Strain Profile

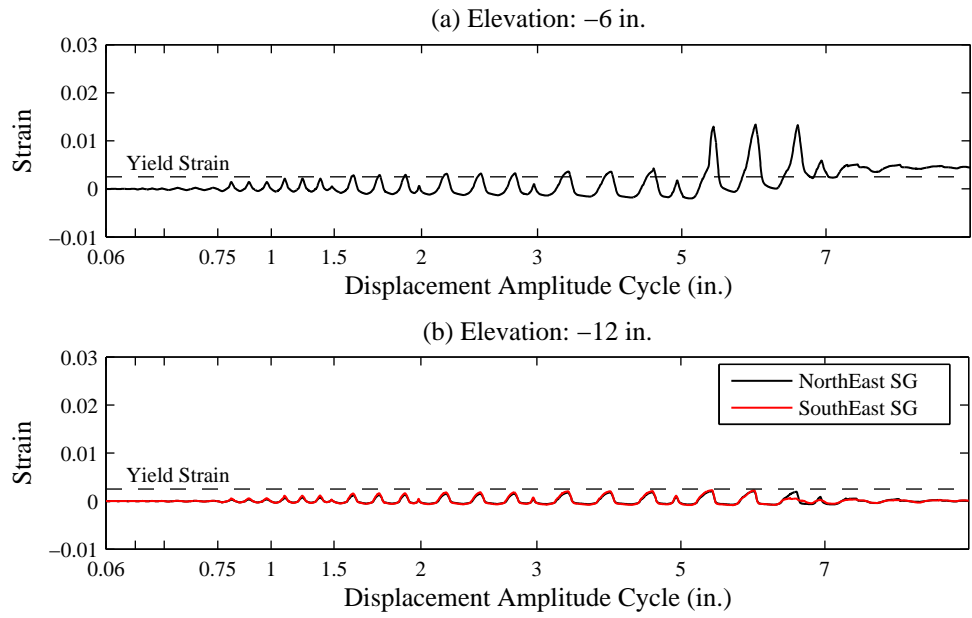


Figure C.83: Column C3 Joint Strain History – West Gauges

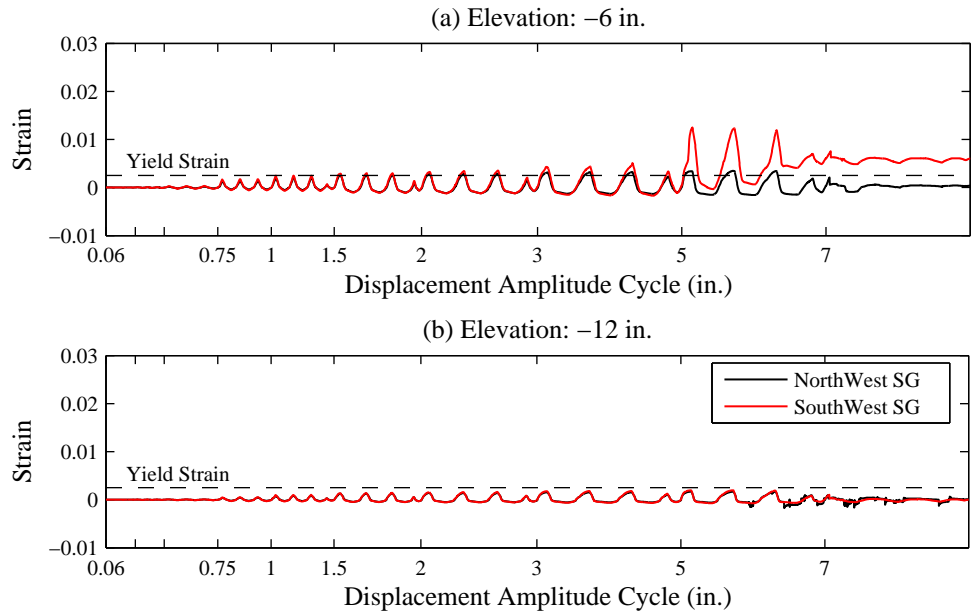


Figure C.84: Column C3 Joint Strain History – East Gauges

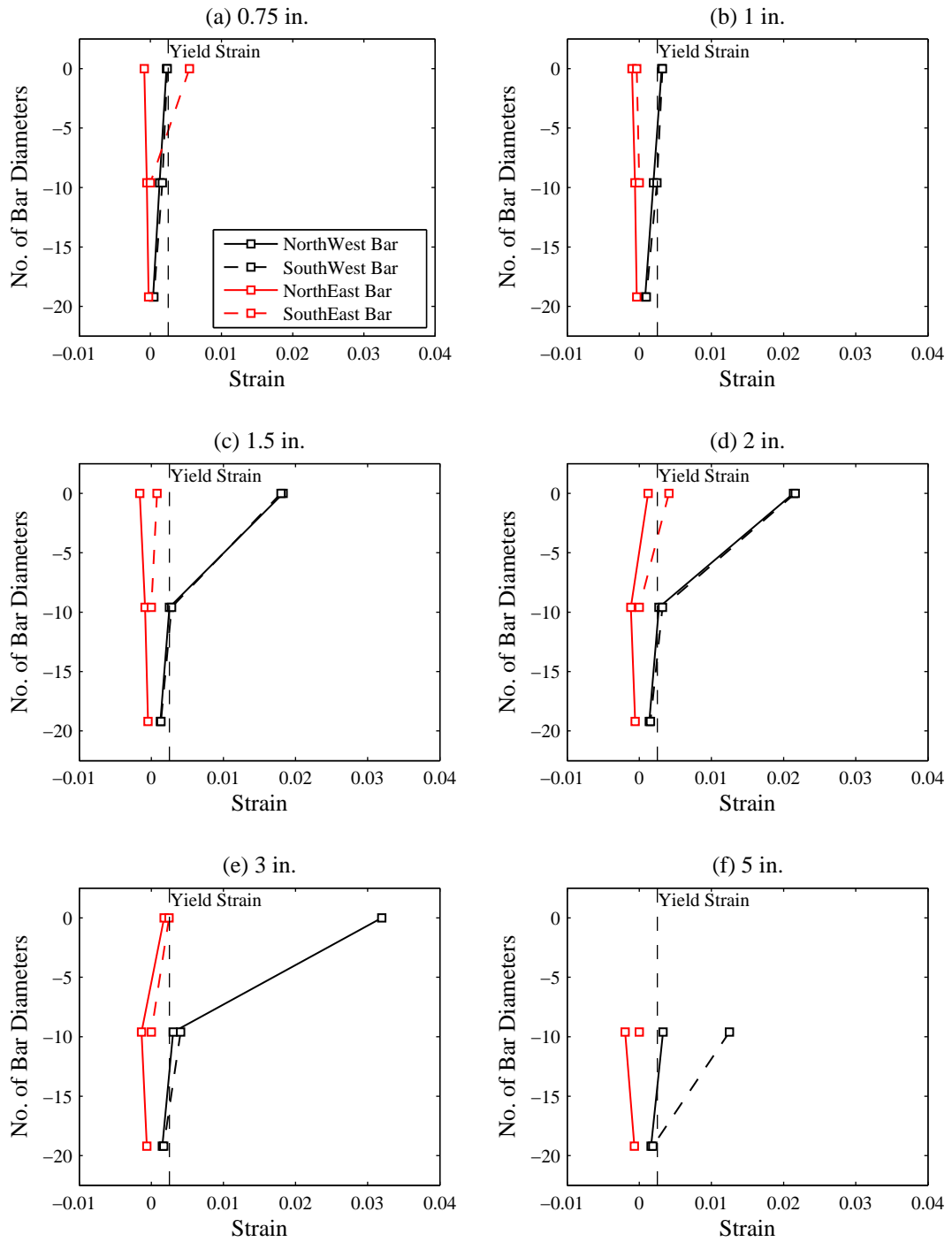


Figure C.85: Column C3 Joint Strain Profile

## Appendix D

# Damage Progression

The progression of damage was documented using photographs taken at the first peak East, first peak West, and at the end of each displacement amplitude cycle. Firewire cameras, which were setup to take images at four to five second intervals, were also positioned on tripods around each test specimen to record column damage.

### D.1 Crack Patterns

Crack patterns were marked at the first peak East, first peak West, and at the end of each displacement amplitude cycle. Figure D.1 illustrates the flattened surface of the circular column, with sides marked N, W, S, and E representing North, West, South, and East, respectively. A similar convention was used for the oblong column (not shown). The crack patterns after completion of the 0.75, 1, 1.5, 2, 3, 5, and 7 in. displacement amplitude cycles for Columns C1, C2, and C3 are shown in Figures D.2, D.3, and D.4, respectively. The crack patterns after completion of the 0.5, 0.7, 1.1, 1.4, 2.1, 3.6, 5 deg twist amplitude cycles for Column C4 are shown in Figure D.5.

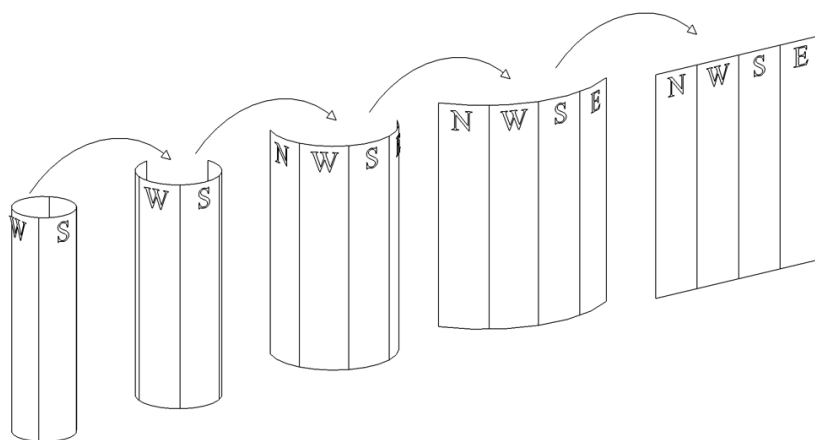
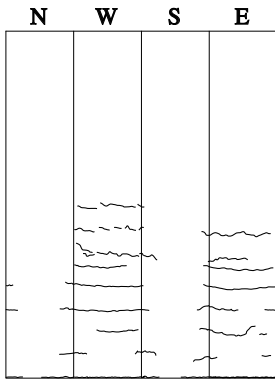
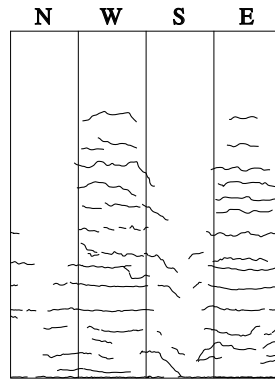


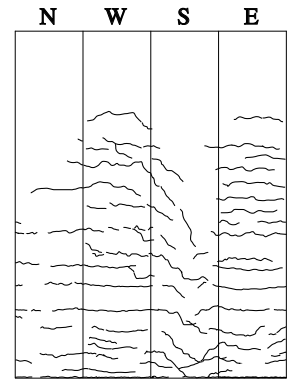
Figure D.1: Illustration of Convention



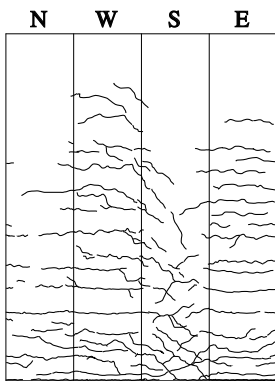
(a) 0.75 in.



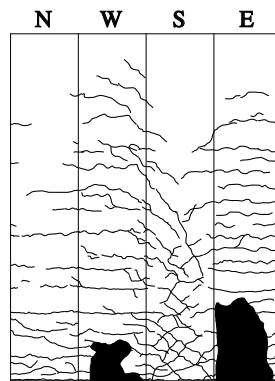
(b) 1 in.



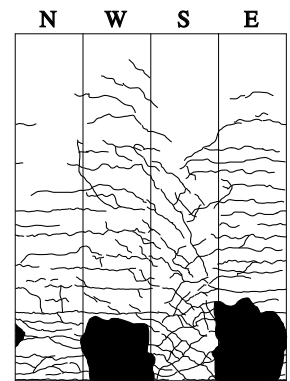
(c) 1.5 in.



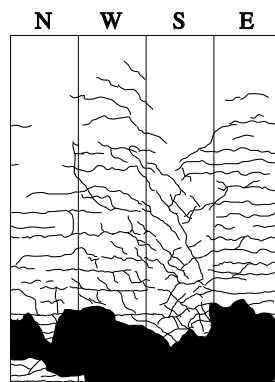
(d) 2 in.



(e) 3 in.

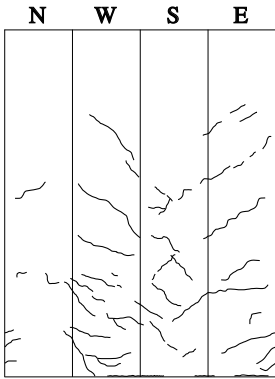


(f) 5 in.

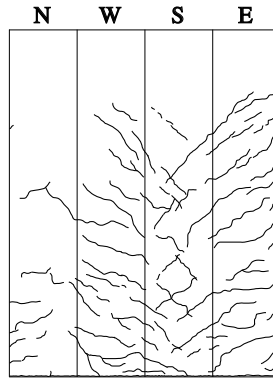


(g) 7 in.

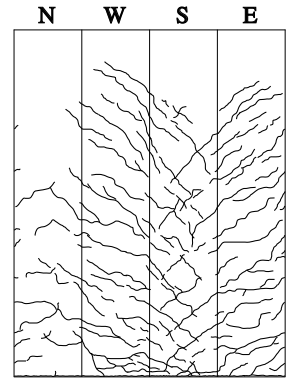
Figure D.2: Column C1 Crack Patterns



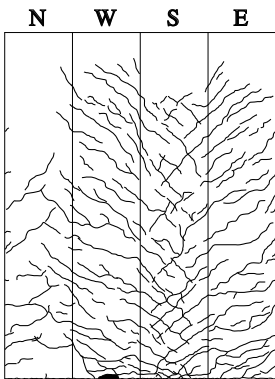
(a) 0.75 in.



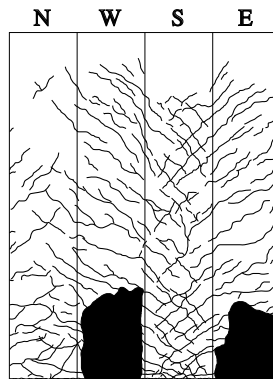
(b) 1 in.



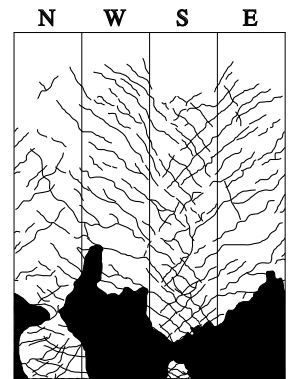
(c) 1.5 in.



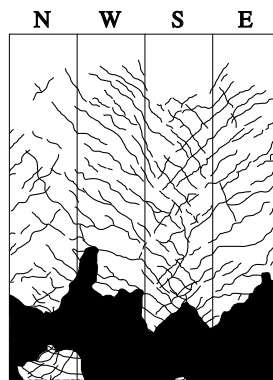
(d) 2 in.



(e) 3 in.

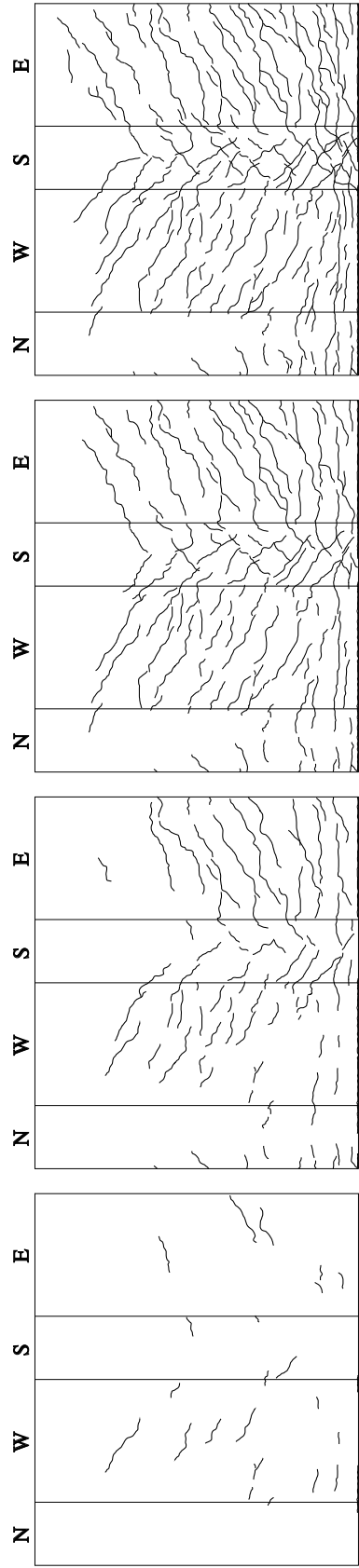


(f) 5 in.



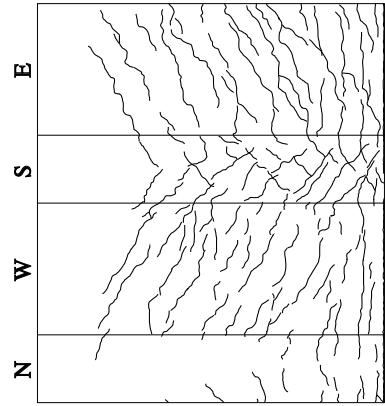
(g) 7 in.

Figure D.3: Column C2 Crack Patterns

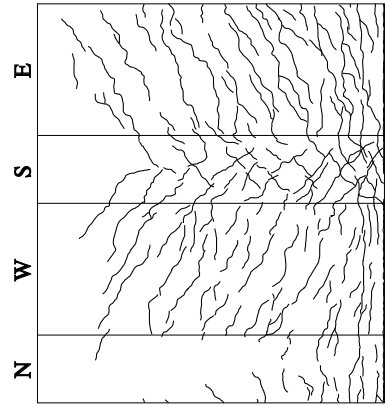


(a) 0.75 in.

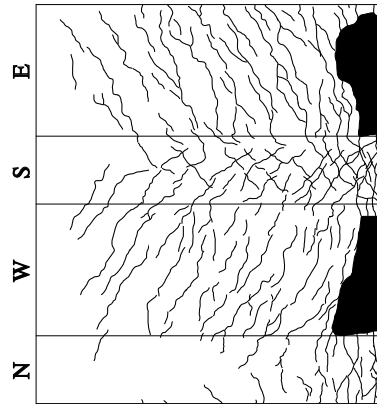
(b) 1 in.



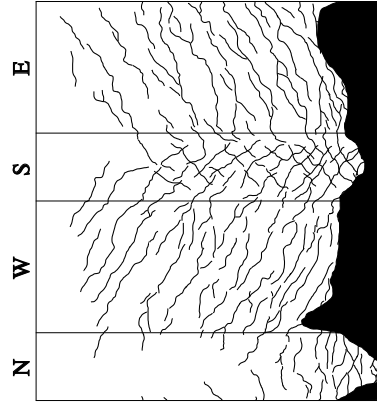
(c) 1.5 in.



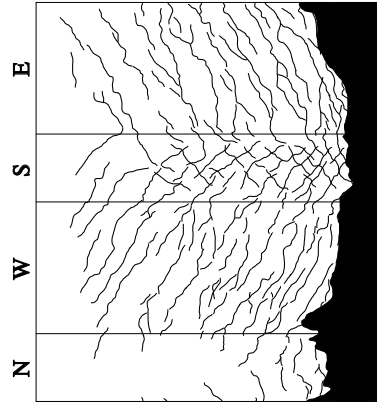
(d) 2 in.



(e) 3 in.

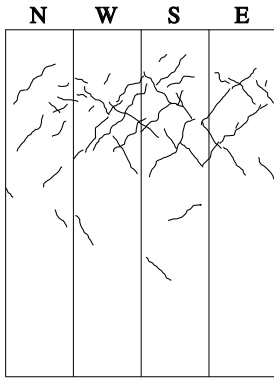


(f) 5 in.

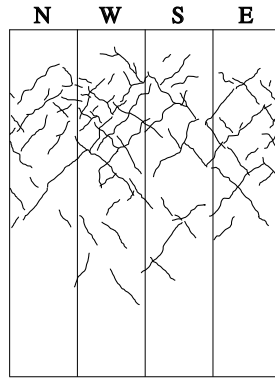


(g) 7 in.

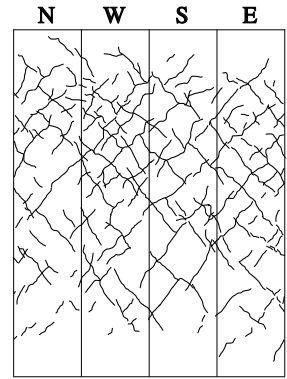
Figure D.4: Column C3 Crack Patterns



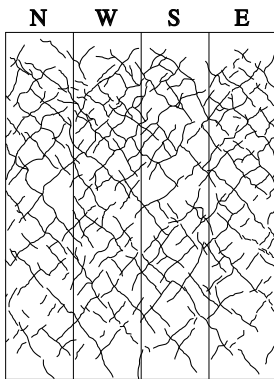
(a) 0.5 deg



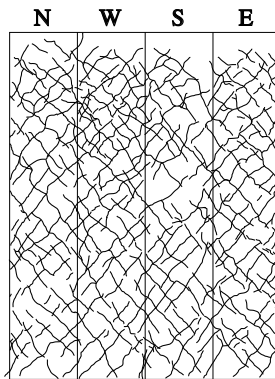
(b) 0.7 deg



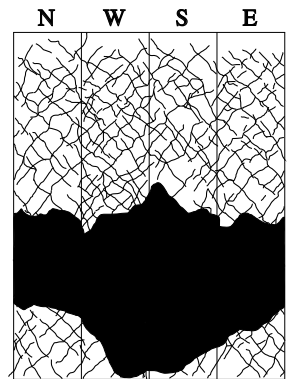
(c) 1.1 deg



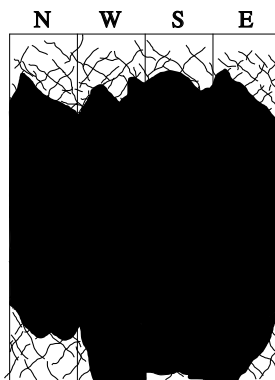
(d) 1.4 deg



(e) 2.1 deg



(f) 3.6 deg



(g) 5 deg

Figure D.5: Column C4 Crack Patterns

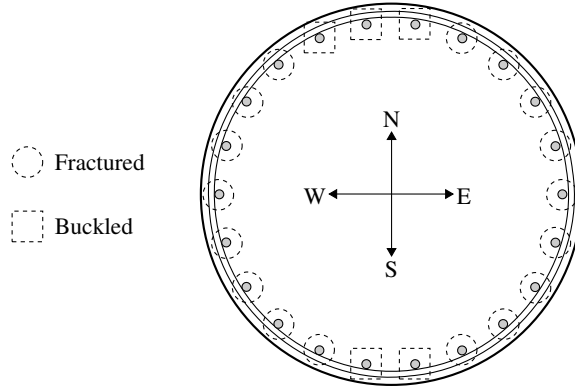


Figure D.6: Column C1 Location of Buckled and Fractured Bars

## D.2 Measured Crack Widths

Crack widths were marked and measured on all sides of the column along the entire height at the first peak East, first peak West, and at the end of each displacement amplitude cycle. The largest of the first peak East or first peak West measured crack widths are summarized for Columns C1, C2, and C3 in Tables D.1, D.3, and D.5, respectively. The residual crack widths measured at the end of the 0.75, 1, 1.5, 2, 3, 5, and 7 in. displacement amplitude cycles for Columns C1, C2, and C3 are summarized in Tables D.2, D.4, and D.6, respectively. The peak and residual cracks widths at the end of the 0.5, 0.7, 1.1, 1.4, 2.1, 3.6, 5 deg twist amplitude cycles for Column C4 are shown in Figures D.7 and D.8, respectively.

## D.3 Location of Fractured and Buckled Bars

The location of fractured and buckled longitudinal reinforcing bars upon completion of testing for Columns C1, C2, and C3 are shown in Figures D.6, D.7, and D.8, respectively.

Table D.1: Column C1 Peak Crack Widths

Location		Displacement Amplitude (in.)						
Face	Elevation	0.75	1	1.5	2	3	5	7
North	Interface	0.010	0.013	0.013	0.016	0.030	0.063	0.050
	0–12 in.	*	*	*	0.016	0.030	0.040	0.060
	12–24 in.	*	*	0.010	0.013	0.013	0.040	0.080
	24–36 in.	*	*	*	*	*	0.010	0.016
	36–48 in.	*	*	*	*	*	*	0.013
	48–96 in.	*	*	*	*	*	*	*
South	Interface	*	0.010	0.016	0.016	0.030	0.060	†
	0–12 in.	*	*	0.013	0.013	0.040	0.060	0.070
	12–24 in.	*	*	0.013	0.013	0.030	0.040	0.080
	24–36 in.	*	*	0.013	0.013	0.016	0.020	0.030
	36–48 in.	*	*	0.010	0.010	0.013	0.013	0.016
	48–96 in.	*	*	0.010	0.010	0.010	0.010	0.010
East	Interface	0.013	0.030	0.040	0.070	0.050	†	†
	0–12 in.	*	*	0.016	0.060	0.050	†	†
	12–24 in.	0.013	0.016	0.030	0.020	0.020	0.050	0.020
	24–36 in.	0.010	0.013	0.016	0.013	0.020	0.020	0.013
	36–48 in.	*	*	0.013	0.013	0.013	0.010	0.010
	48–96 in.	*	*	0.010	*	0.010	0.010	*
West	Interface	0.013	0.020	0.030	0.040	†	†	†
	0–12 in.	0.010	0.013	0.030	0.030	0.040	†	†
	12–24 in.	0.010	0.016	0.016	0.050	0.060	0.188	0.080
	24–36 in.	0.010	0.013	0.013	0.016	0.020	0.030	0.020
	36–48 in.	*	0.010	0.013	0.016	0.020	0.020	0.016
	48–96 in.	*	*	0.013	0.016	0.016	0.016	0.010

\* Less than 0.010 in.

† Not measured

Table D.2: Column C1 Residual Crack Widths

Location		Displacement Amplitude (in.)						
Face	Elevation	0.75	1	1.5	2	3	5	7
North	Interface	*	*	*	*	*	0.010	†
	0–12 in.	*	*	*	*	0.010	0.013	†
	12–24 in.	*	*	*	*	*	0.013	0.030
	24–36 in.	*	*	*	*	*	*	0.013
	36–48 in.	*	*	*	*	*	*	0.010
	48–96 in.	*	*	*	*	*	*	*
South	Interface	*	*	*	*	*	0.010	†
	0–12 in.	*	*	*	*	*	0.016	†
	12–24 in.	*	*	*	*	*	0.013	0.016
	24–36 in.	*	*	*	*	*	0.010	0.013
	36–48 in.	*	*	*	*	*	*	0.010
	48–96 in.	*	*	*	*	*	*	*
East	Interface	*	*	*	*	†	†	†
	0–12 in.	*	*	*	*	0.016	†	†
	12–24 in.	*	*	*	*	0.010	0.016	0.016
	24–36 in.	*	*	*	*	*	0.010	0.010
	36–48 in.	*	*	*	*	*	*	0.010
	48–96 in.	*	*	*	*	*	*	*
West	Interface	*	*	*	*	†	†	†
	0–12 in.	*	*	*	*	0.010	†	†
	12–24 in.	*	*	*	*	0.010	0.016	0.040
	24–36 in.	*	*	*	*	0.010	0.010	0.020
	36–48 in.	*	*	*	*	*	0.010	0.013
	48–96 in.	*	*	*	*	*	0.010	*

\* Less than 0.010 in.

† Not measured

Table D.3: Column C2 Peak Crack Widths

Location		Displacement Amplitude (in.)						
Face	Elevation	0.75	1	1.5	2	3	5	7
North	Interface	*	*	0.010	0.016	0.016	0.020	†
	0–12 in.	*	*	0.013	0.020	0.060	0.070	†
	12–24 in.	*	*	0.010	0.016	0.020	0.040	†
	24–36 in.	*	*	0.010	0.010	0.013	0.016	0.013
	36–48 in.	*	0.010	0.010	0.016	0.013	0.013	0.013
	48–96 in.	*	*	*	*	0.010	0.010	0.010
South	Interface	*	*	*	*	*	0.020	†
	0–12 in.	*	0.010	0.013	0.020	0.070	0.188	†
	12–24 in.	*	0.013	0.013	0.016	0.040	0.125	†
	24–36 in.	0.010	0.010	0.013	0.016	0.016	0.016	0.013
	36–48 in.	*	0.010	0.013	0.013	0.016	0.016	0.010
	48–96 in.	*	0.010	0.013	0.013	0.016	0.016	0.013
East	Interface	0.013	0.016	0.020	0.060	0.125	†	†
	0–12 in.	0.010	0.013	0.030	0.030	†	†	†
	12–24 in.	0.013	0.016	0.020	0.030	0.030	†	†
	24–36 in.	0.013	0.013	0.016	0.020	0.030	0.020	†
	36–48 in.	0.010	0.013	0.016	0.013	0.016	0.020	0.013
	48–96 in.	0.010	0.010	0.013	0.013	0.016	0.013	0.010
West	Interface	0.010	0.016	0.030	0.060	0.125	†	†
	0–12 in.	*	0.013	0.020	0.050	†	†	†
	12–24 in.	0.010	0.016	0.020	0.030	†	†	†
	24–36 in.	0.010	0.016	0.016	0.020	0.030	0.040	†
	36–48 in.	0.010	0.013	0.013	0.016	0.016	0.020	0.013
	48–96 in.	*	0.010	0.010	0.013	0.016	0.016	0.013

\* Less than 0.010 in.

† Not measured

Table D.4: Column C2 Residual Crack Widths

Location		Displacement Amplitude (in.)						
Face	Elevation	0.75	1	1.5	2	3	5	7
North	Interface	*	*	*	*	*	*	†
	0–12 in.	*	*	*	*	*	*	†
	12–24 in.	*	*	*	*	*	†	†
	24–36 in.	*	*	*	*	*	*	0.016
	36–48 in.	*	*	*	*	*	*	*
	48–96 in.	*	*	*	*	*	*	*
South	Interface	*	*	*	*	*	†	†
	0–12 in.	*	*	*	*	*	†	†
	12–24 in.	*	*	*	*	0.013	†	†
	24–36 in.	*	*	*	*	*	*	0.010
	36–48 in.	*	*	*	*	*	*	*
	48–96 in.	*	*	*	*	*	*	*
East	Interface	*	*	*	*	*	†	†
	0–12 in.	*	*	*	*	*	†	†
	12–24 in.	*	*	*	*	*	†	†
	24–36 in.	*	*	*	*	*	†	†
	36–48 in.	*	*	*	*	*	*	*
	48–96 in.	*	*	*	*	*	*	*
West	Interface	*	*	*	0.030	†	†	†
	0–12 in.	*	*	*	0.013	†	†	†
	12–24 in.	*	*	*	*	†	†	†
	24–36 in.	*	*	*	*	*	†	†
	36–48 in.	*	*	*	*	*	*	*
	48–96 in.	*	*	*	*	*	*	*

\* Less than 0.010 in.

† Not measured

Table D.5: Column C3 Peak Crack Widths

Location		Displacement Amplitude (in.)						
Face	Elevation	0.75	1	1.5	2	3	5	7
North	Interface	*	*	0.013	0.030	0.060	0.070	†
	0–12 in.	*	*	0.010	0.010	0.030	0.125	†
	12–24 in.	*	*	0.010	0.010	0.020	0.030	0.125
	24–36 in.	*	*	*	*	0.010	0.020	0.016
	36–48 in.	*	*	*	*	*	*	*
	48–96 in.	*	*	*	*	*	*	*
South	Interface	*	*	0.020	0.020	0.020	†	†
	0–12 in.	*	*	0.020	0.020	0.050	†	†
	12–24 in.	*	*	0.013	0.016	0.020	0.080	0.030
	24–36 in.	*	*	0.016	0.016	0.016	0.020	0.016
	36–48 in.	*	*	0.010	0.013	0.016	0.016	0.013
	48–96 in.	*	*	0.010	0.013	0.013	0.016	0.013
East	Interface	0.013	0.016	0.050	0.050	0.060	†	†
	0–12 in.	*	0.016	0.060	0.060	0.050	†	†
	12–24 in.	*	0.020	0.040	0.040	0.040	†	†
	24–36 in.	0.010	0.016	0.016	0.016	0.020	0.020	0.020
	36–48 in.	0.013	0.013	0.016	0.016	0.020	0.020	0.020
	48–96 in.	0.013	0.013	0.013	0.013	0.030	0.020	0.020
West	Interface	0.016	0.016	0.040	0.070	0.250	†	†
	0–12 in.	*	0.016	0.030	0.060	0.125	†	†
	12–24 in.	0.013	0.016	0.020	0.030	0.050	†	†
	24–36 in.	0.010	0.013	0.020	0.020	0.030	0.016	0.016
	36–48 in.	*	0.013	0.016	0.020	0.016	0.020	0.016
	48–96 in.	*	0.010	0.016	0.016	0.020	0.030	0.016

\* Less than 0.010 in.

† Not measured

Table D.6: Column C3 Residual Crack Widths

Location		Displacement Amplitude (in.)						
Face	Elevation	0.75	1	1.5	2	3	5	7
North	Interface	*	*	*	*	*	†	†
	0–12 in.	*	*	*	*	*	†	†
	12–24 in.	*	*	*	*	*	0.010	†
	24–36 in.	*	*	*	*	*	*	*
	36–48 in.	*	*	*	*	*	*	*
	48–96 in.	*	*	*	*	*	*	*
South	Interface	*	*	*	*	0.010	†	†
	0–12 in.	*	*	*	*	0.010	†	†
	12–24 in.	*	*	*	*	*	0.013	0.030
	24–36 in.	*	*	*	*	*	*	*
	36–48 in.	*	*	*	*	*	*	*
	48–96 in.	*	*	*	*	*	*	*
East	Interface	*	*	*	*	†	†	†
	0–12 in.	*	*	*	*	†	†	†
	12–24 in.	*	*	*	*	0.010	†	†
	24–36 in.	*	*	*	*	*	0.010	0.010
	36–48 in.	*	*	*	*	*	*	0.013
	48–96 in.	*	*	*	*	*	*	0.010
West	Interface	*	*	*	*	†	†	†
	0–12 in.	*	*	*	*	†	†	†
	12–24 in.	*	*	*	*	0.010	†	†
	24–36 in.	*	*	*	*	*	*	*
	36–48 in.	*	*	*	*	*	*	*
	48–96 in.	*	*	*	*	*	*	*

\* Less than 0.010 in.

† Not measured

Table D.7: Column C4 Peak Crack Widths

Location		Twist Amplitude (deg)						
Face	Elevation	0.5	0.7	1.1	1.4	2.1	3.6	5
North	Interface	*	*	†	†	†	†	†
	0–24 in.	*	*	†	†	†	†	†
	24–48 in.	*	*	†	†	†	†	†
	48–96 in.	0.010	*	†	†	†	†	†
South	Interface	*	*	†	†	†	†	†
	0–24 in.	*	*	†	†	†	†	†
	24–48 in.	*	*	†	†	†	†	†
	48–96 in.	0.010	0.015	†	†	†	†	†
East	Interface	*	*	*	†	†	†	†
	0–24 in.	*	*	0.013	†	†	†	†
	24–48 in.	*	*	0.016	†	†	†	†
	48–96 in.	0.015	0.015	0.020	†	†	†	†
West	Interface	*	*	*	*	*	*	†
	0–24 in.	*	*	0.013	0.013	0.016	0.020	†
	24–48 in.	*	*	0.013	0.013	0.016	0.034	†
	48–96 in.	0.010	0.015	0.016	0.016	0.020	0.030	†

\* Less than 0.010 in.

† Not measured

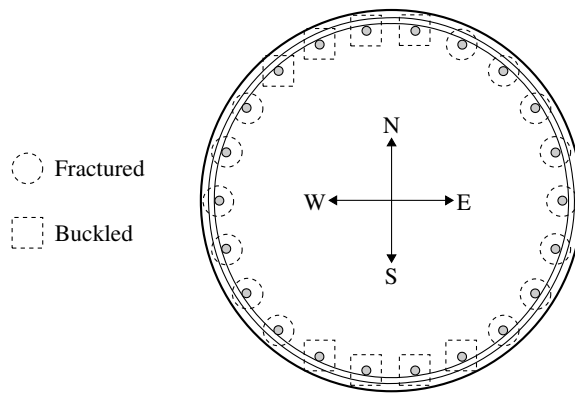


Figure D.7: Column C2 Location of Buckled and Fractured Bars

Table D.8: Column C4 Residual Crack Widths (Adapted from Le, 2008)

Location		Twist Amplitude (deg)						
Face	Elevation	0.5	0.7	1.1	1.4	2.1	3.6	5
North	Interface	*	†	†	†	†	†	†
	0–24 in.	*	†	†	†	†	†	†
	24–48 in.	*	†	†	†	†	†	†
	48–96 in.	*	†	†	†	†	†	†
South	Interface	*	†	†	†	†	†	†
	0–24 in.	*	†	†	†	†	†	†
	24–48 in.	*	†	†	†	†	†	†
	48–96 in.	*	†	†	†	†	†	†
East	Interface	*	†	†	†	†	†	†
	0–24 in.	*	†	†	†	†	†	†
	24–48 in.	*	†	†	†	†	†	†
	48–96 in.	0.010	†	†	†	†	†	†
West	Interface	*	*	*	*	*	*	†
	0–24 in.	*	*	*	*	*	*	*
	24–48 in.	*	*	*	*	*	†	†
	48–96 in.	0.010	0.010	0.010	0.010	0.010	0.010	†

\* Less than 0.010 in.

† Not measured

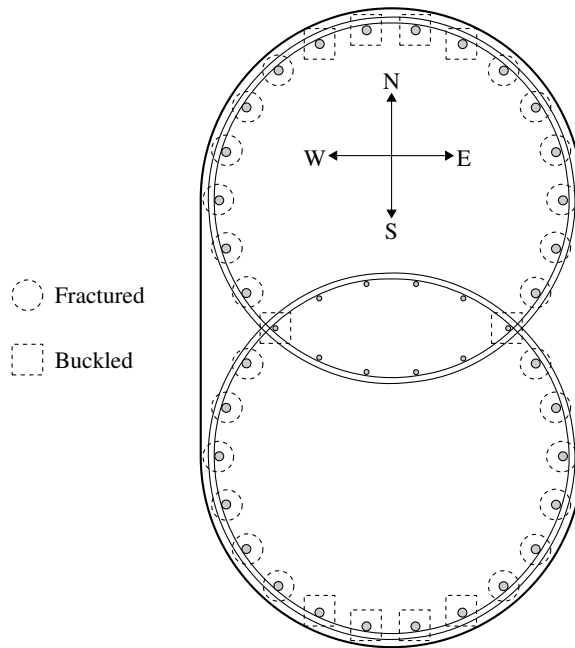
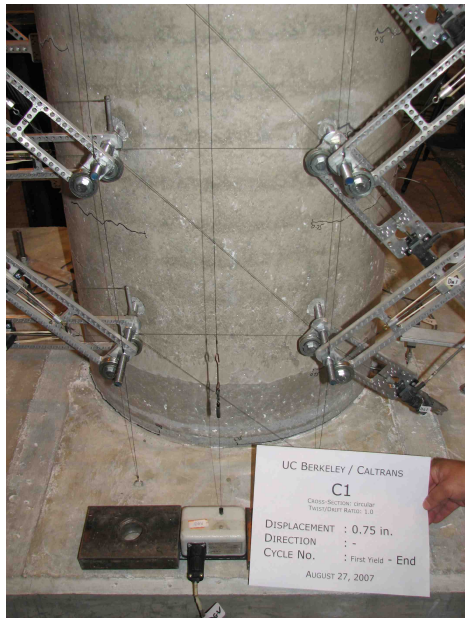


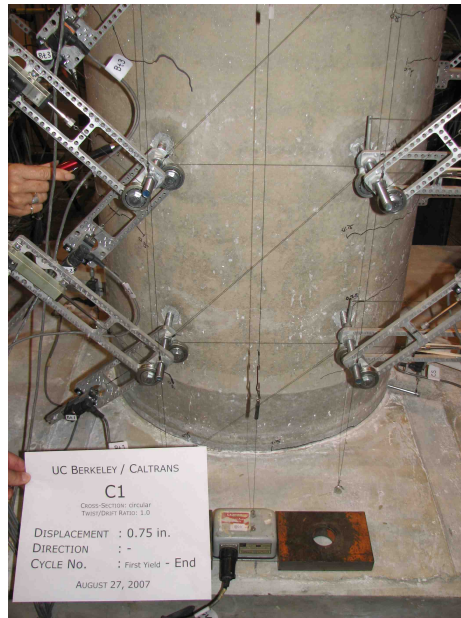
Figure D.8: Column C3 Location of Buckled and Fractured Bars

## D.4 Photographs

The damage states after completion of the 0.75, 1, 1.5, 2, 3, 5, and 7 in. displacement amplitude cycle are shown in Figures D.9 to D.15 for Column C1; Figures D.16 to D.22 for Column C2; and Figures D.23 to D.29 for Column C3. The damage states of Column C4 after completion of the 0.5, 0.7, 1.1, 1.4, 2.1, 3.6, 5 deg twist amplitude cycles are shown in Figures D.30 to D.36.



(a) North Face



(b) South Face

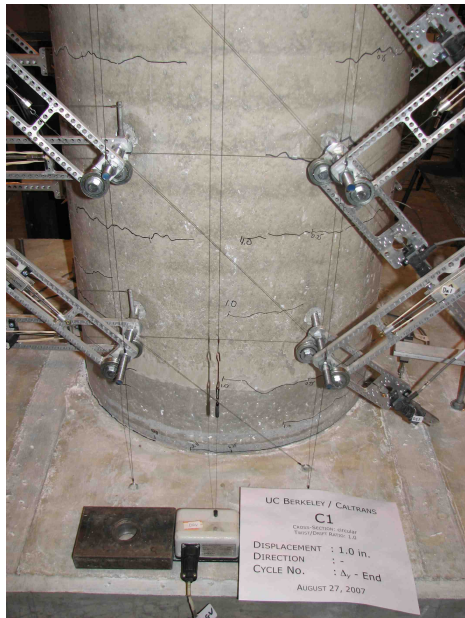


(c) East Face

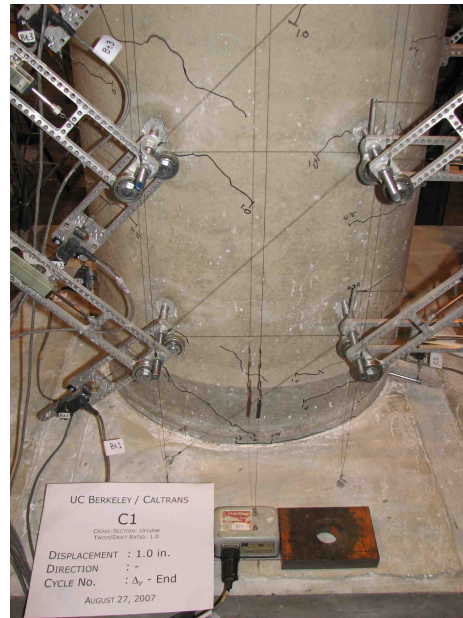


(d) West Face

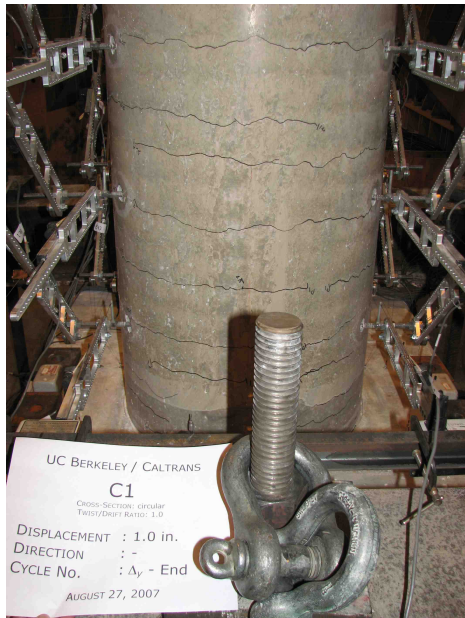
Figure D.9: Column C1 after 0.75 in. Displacement Amplitude Cycle



(a) North Face



(b) South Face

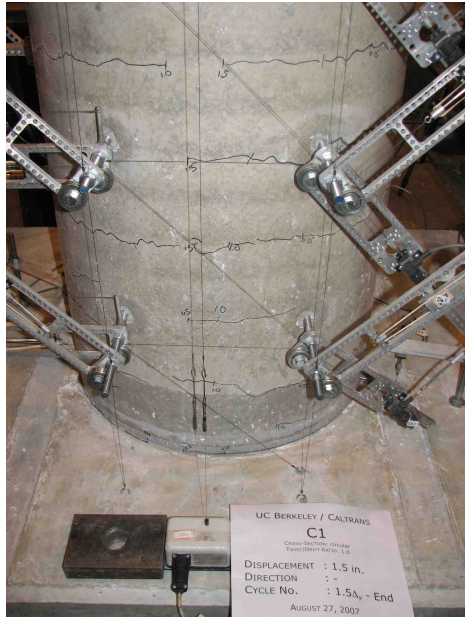


(c) East Face

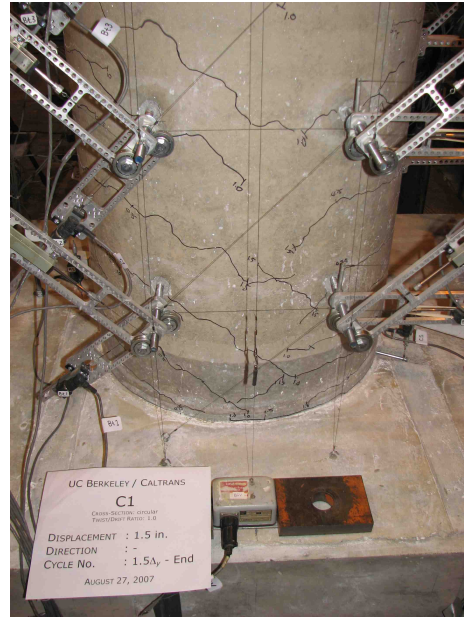


(d) West Face

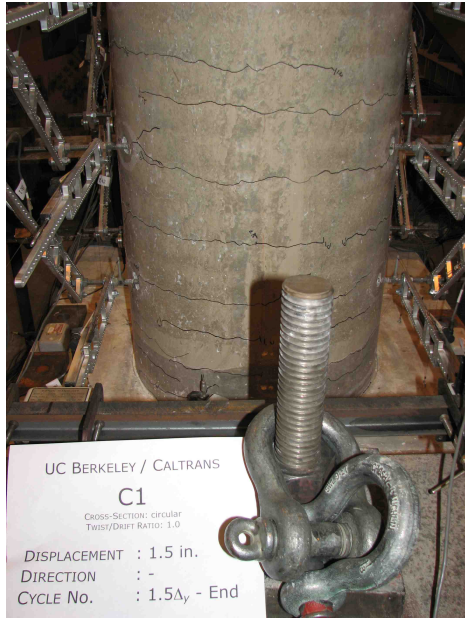
Figure D.10: Column C1 after 1 in. Displacement Amplitude Cycle



(a) North Face



(b) South Face

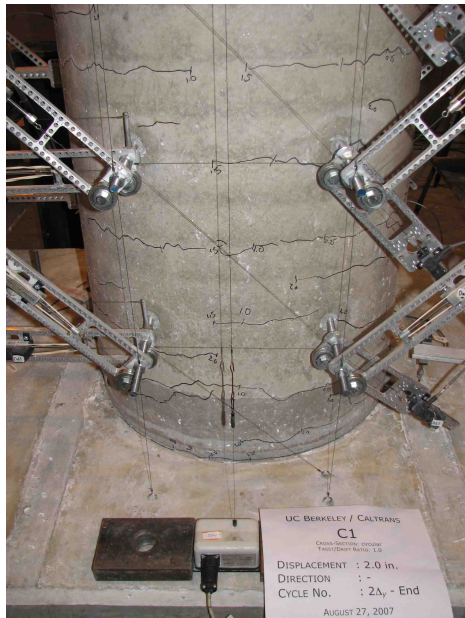


(c) East Face

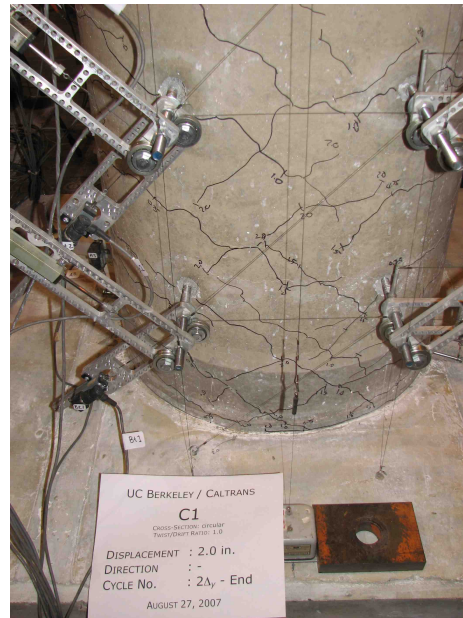


(d) West Face

Figure D.11: Column C1 after 1.5 in. Displacement Amplitude Cycle



(a) North Face



(b) South Face

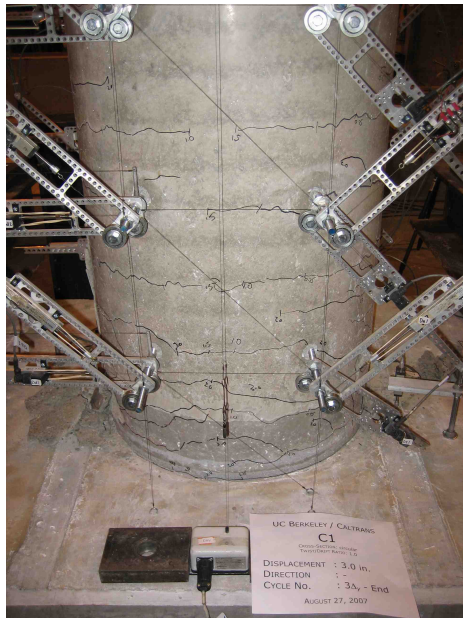


(c) East Face

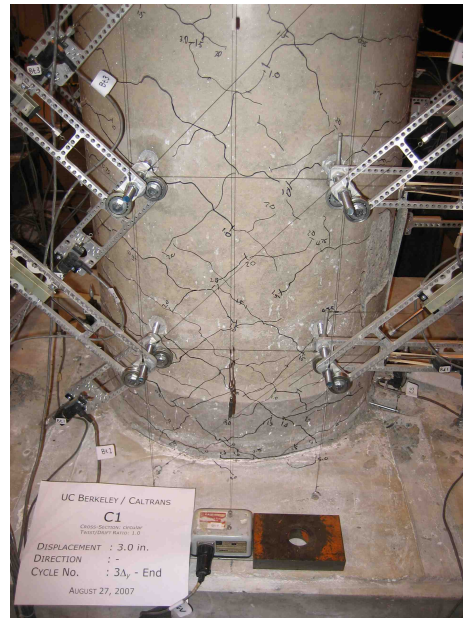


(d) West Face

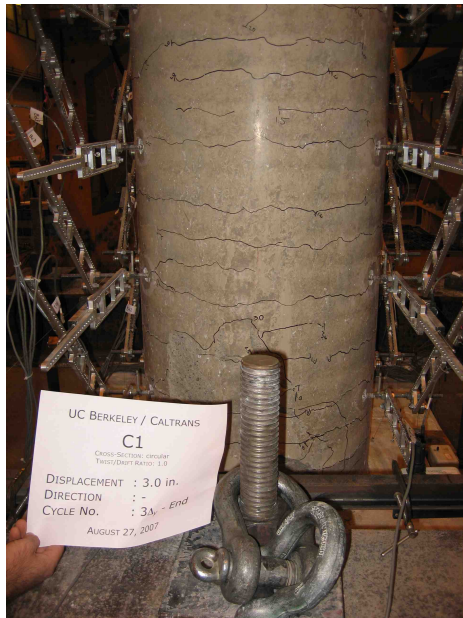
Figure D.12: Column C1 after 2 in. Displacement Amplitude Cycle



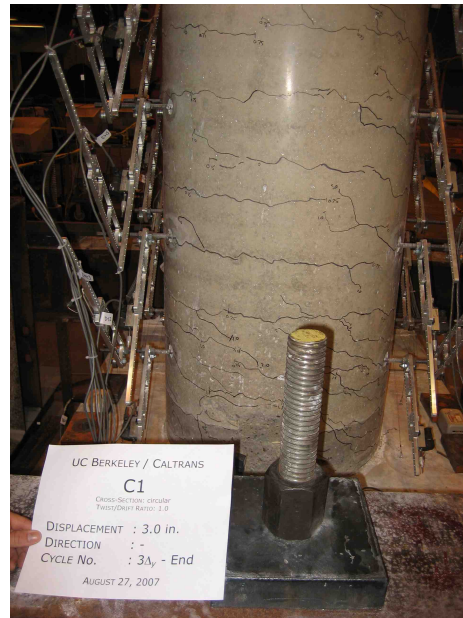
(a) North Face



(b) South Face



(c) East Face

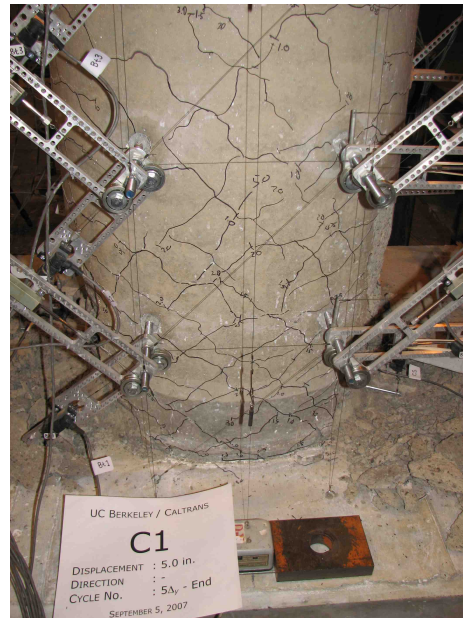


(d) West Face

Figure D.13: Column C1 after 3 in. Displacement Amplitude Cycle



(a) North Face



(b) South Face



(c) East Face



(d) West Face

Figure D.14: Column C1 after 5 in. Displacement Amplitude Cycle



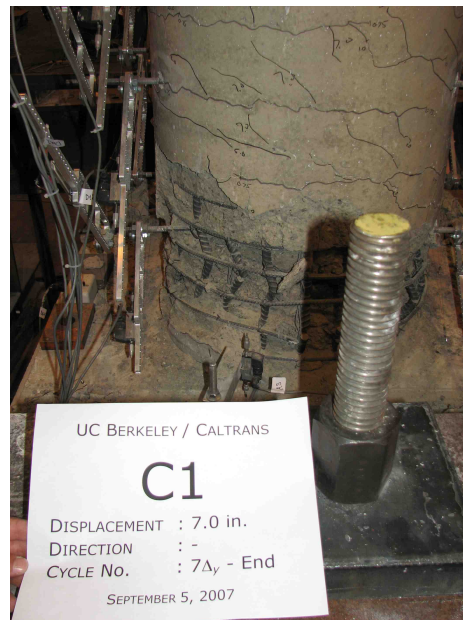
(a) North Face



(b) South Face

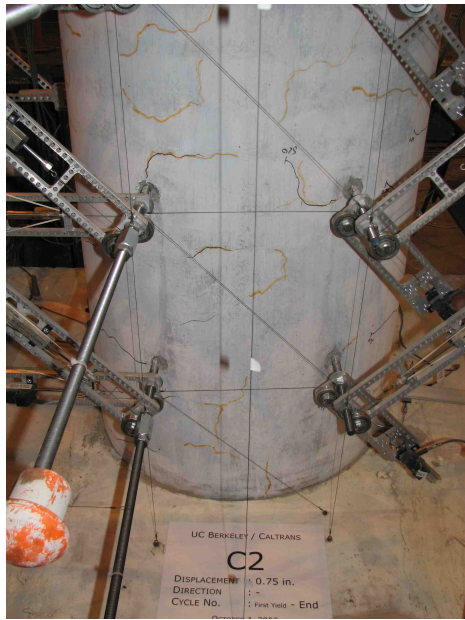


(c) East Face

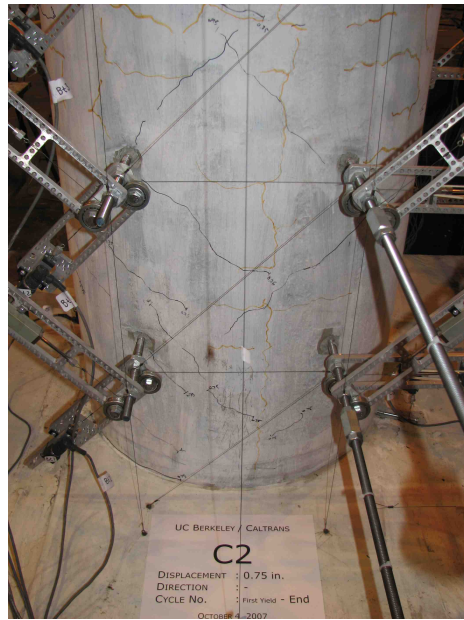


(d) West Face

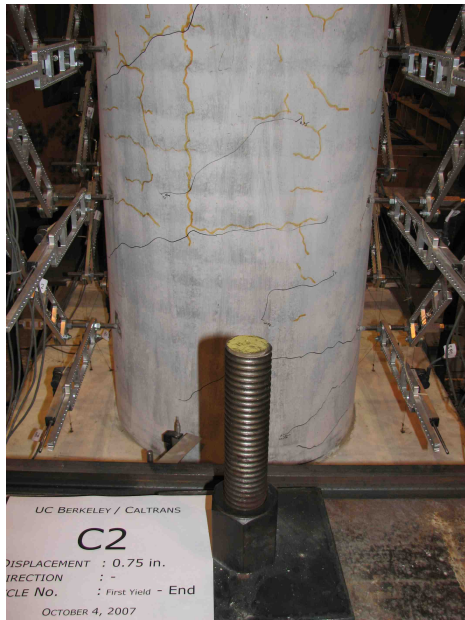
Figure D.15: Column C1 Final Damage State



(a) North Face



(b) South Face

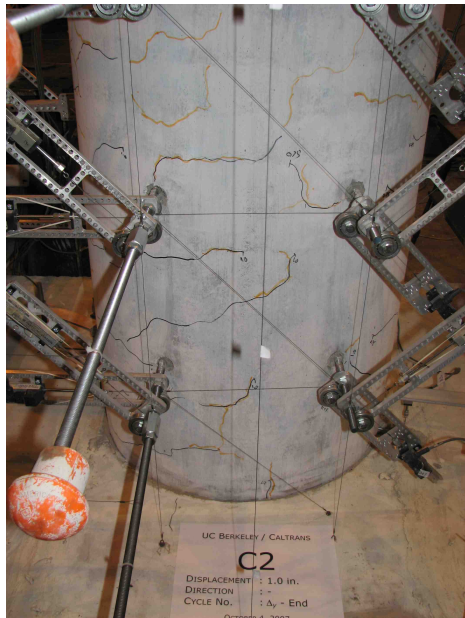


(c) East Face

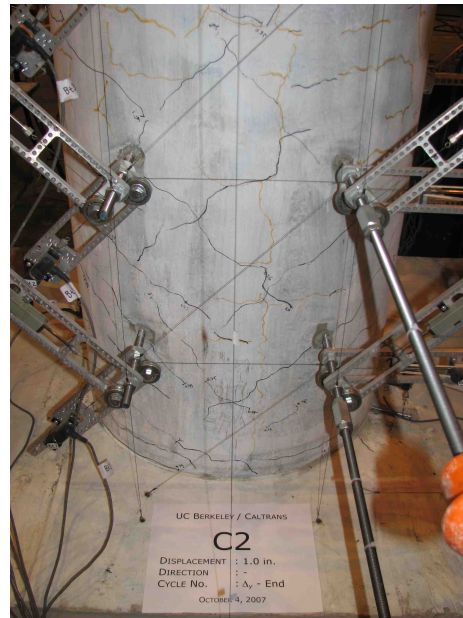


(d) West Face

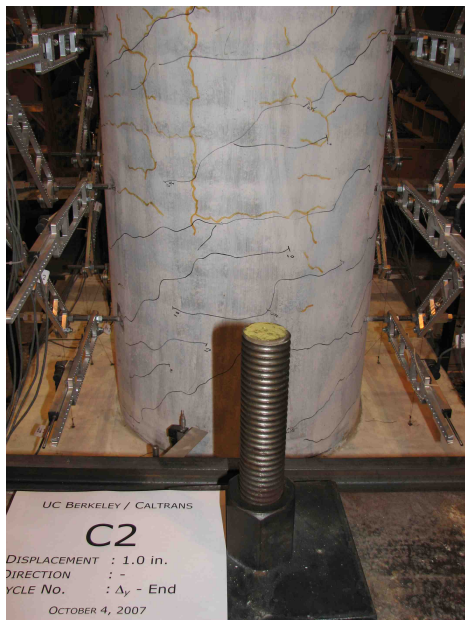
Figure D.16: Column C2 after 0.75 in. Displacement Amplitude Cycle



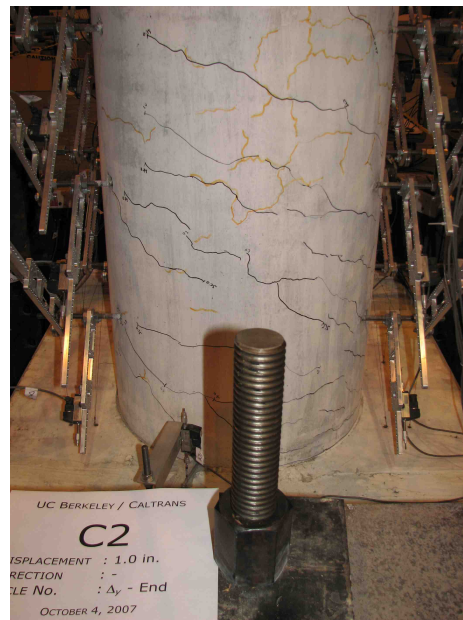
(a) North Face



(b) South Face

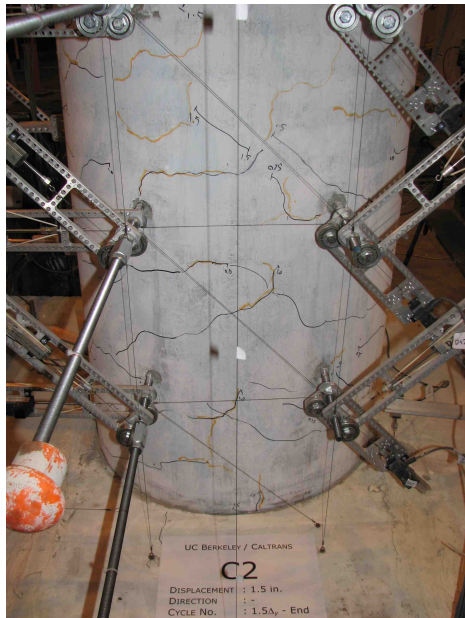


(c) East Face

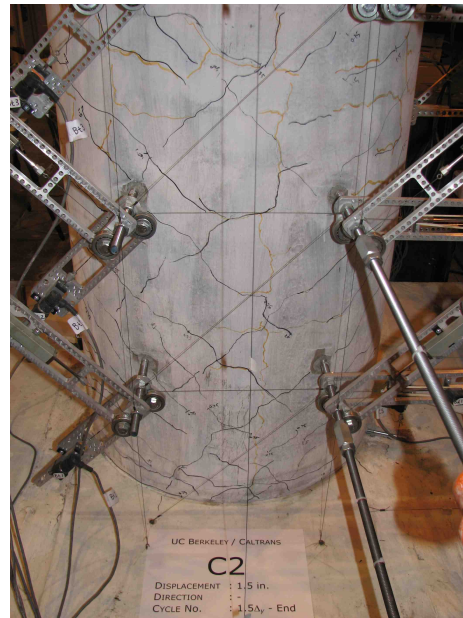


(d) West Face

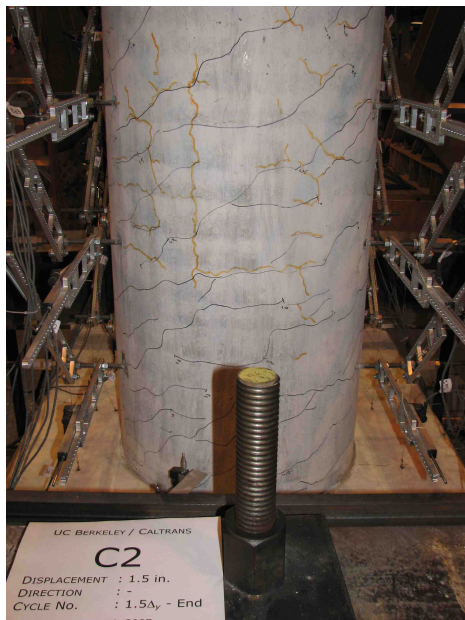
Figure D.17: Column C2 after 1 in. Displacement Amplitude Cycle



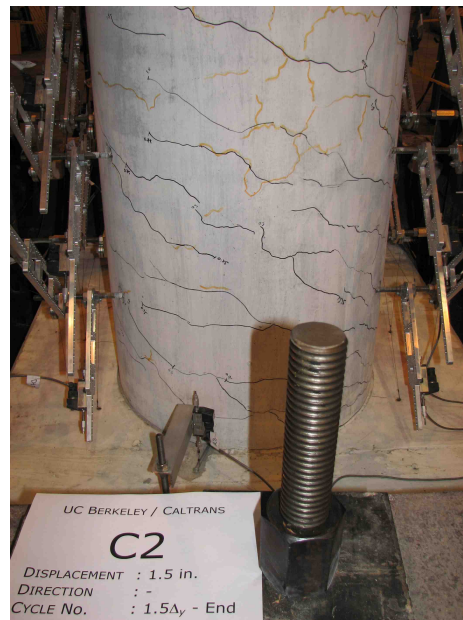
(a) North Face



(b) South Face

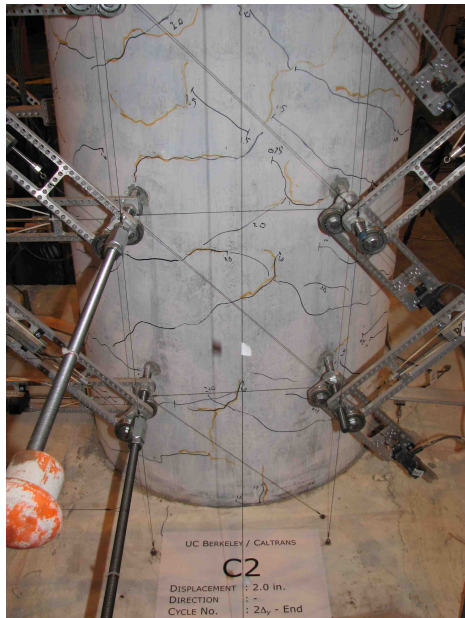


(c) East Face

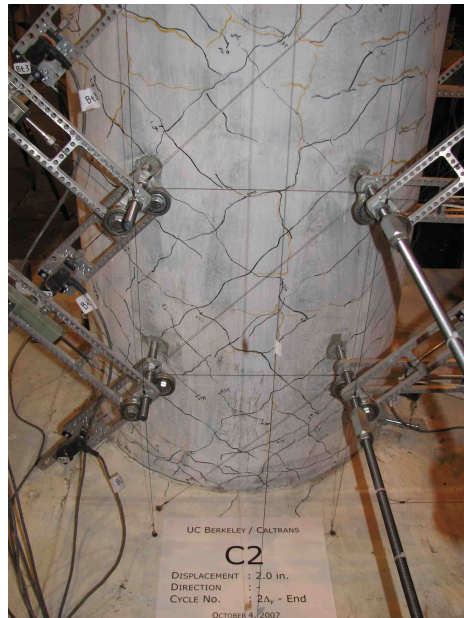


(d) West Face

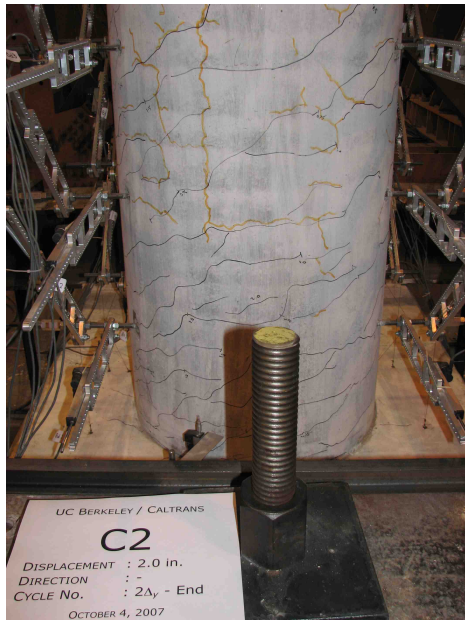
Figure D.18: Column C2 after 1.5 in. Displacement Amplitude Cycle



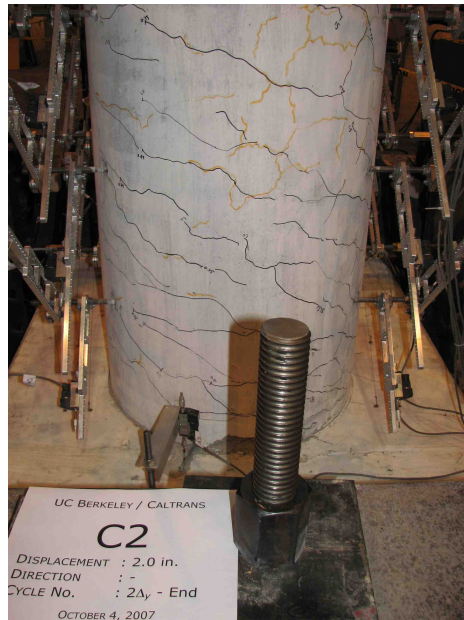
(a) North Face



(b) South Face

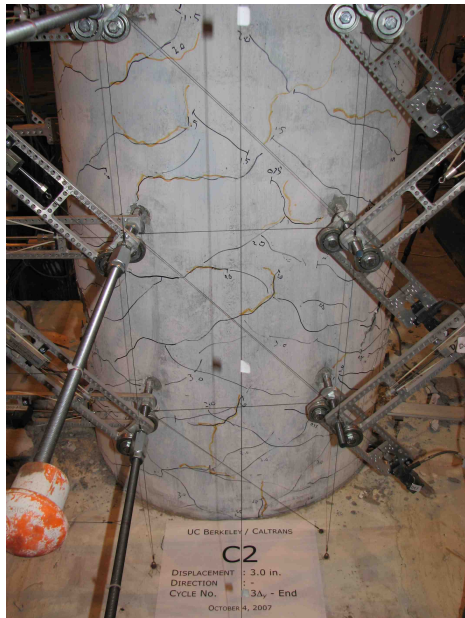


(c) East Face



(d) West Face

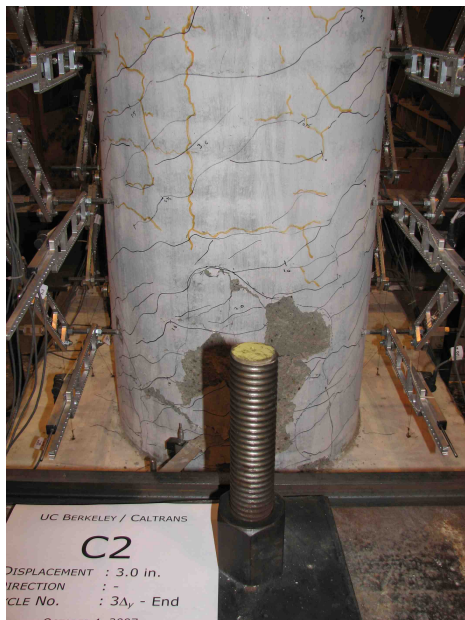
Figure D.19: Column C2 after 2 in. Displacement Amplitude Cycle



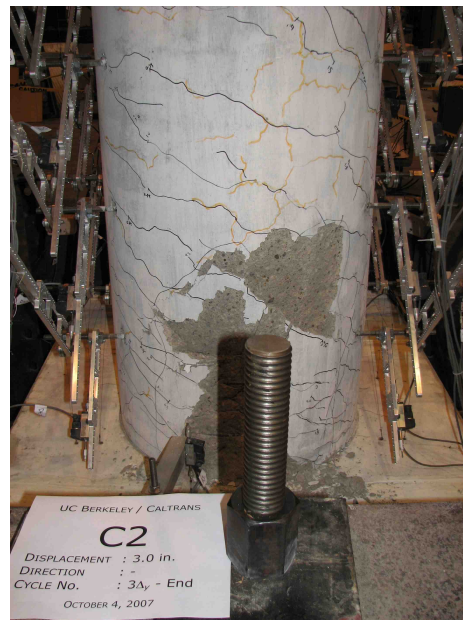
(a) North Face



(b) South Face



(c) East Face



(d) West Face

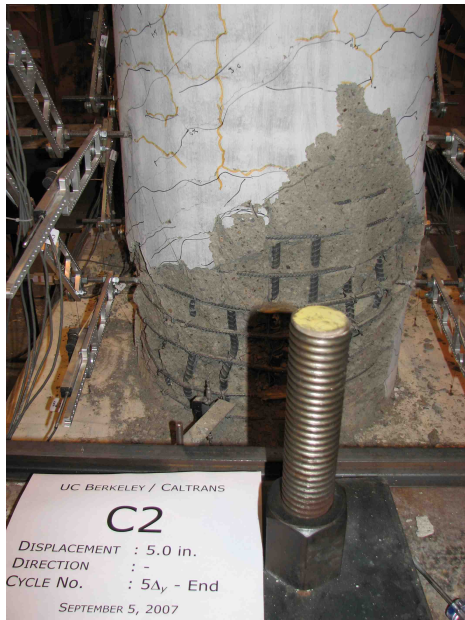
Figure D.20: Column C2 after 3.0 in. Displacement Amplitude Cycle



(a) North Face



(b) South Face

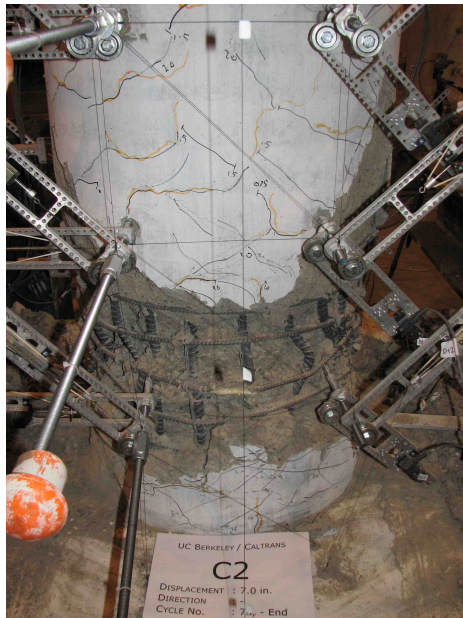


(c) East Face



(d) West Face

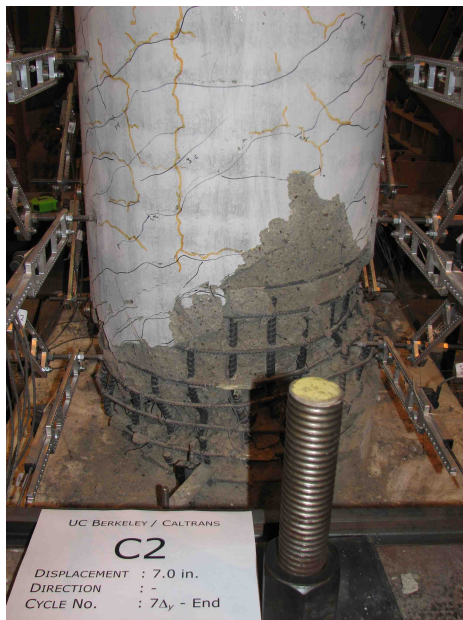
Figure D.21: Column C2 after 5 in. Displacement Amplitude Cycle



(a) North Face



(b) South Face

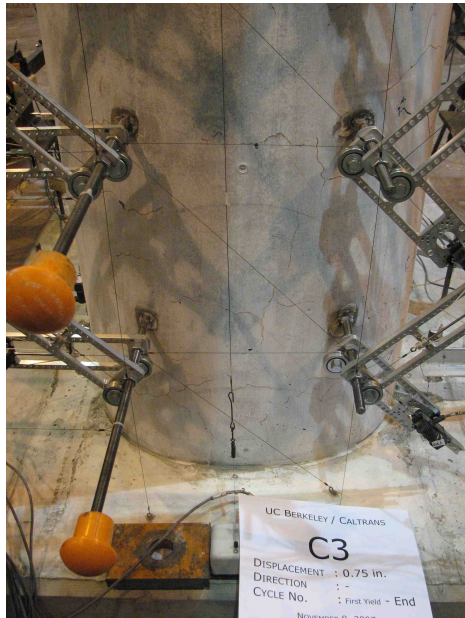


(c) East Face

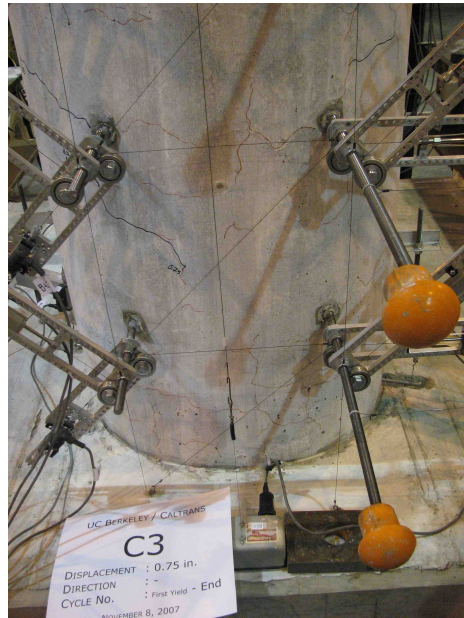


(d) West Face

Figure D.22: Column C2 Final Damage State



(a) North Face



(b) South Face

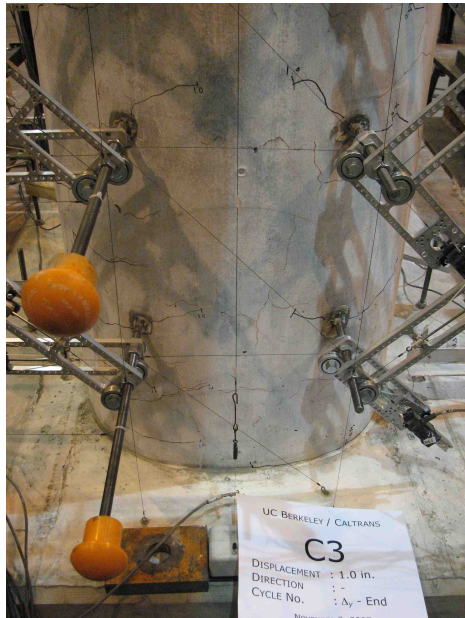


(c) East Face

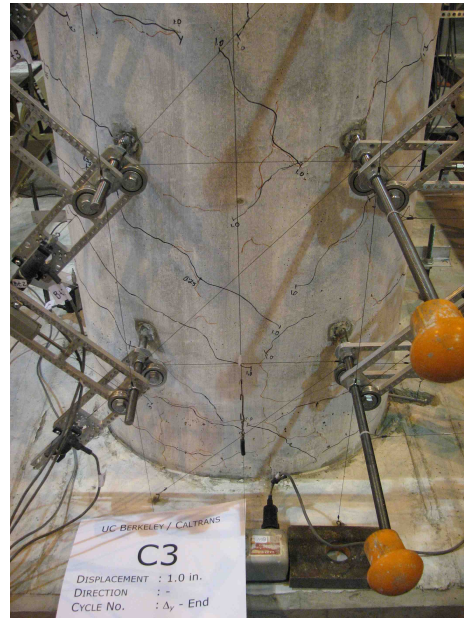


(d) West Face

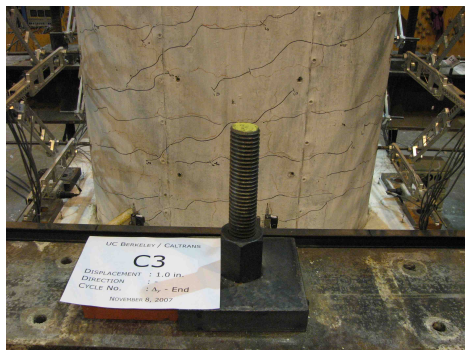
Figure D.23: Column C3 after 0.75 in. Displacement Amplitude Cycle



(a) North Face



(b) South Face

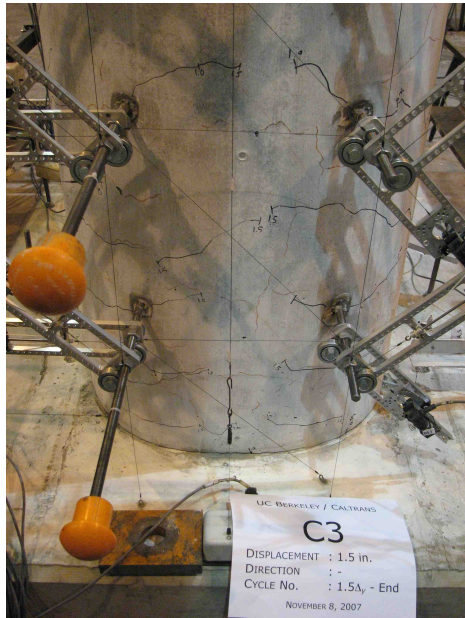


(c) East Face

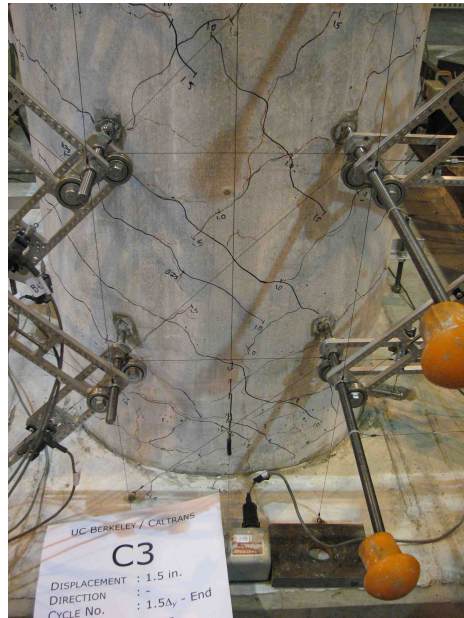


(d) West Face

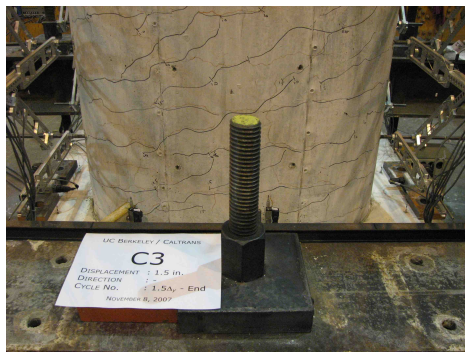
Figure D.24: Column C3 after 1 in. Displacement Amplitude Cycle



(a) North Face



(b) South Face

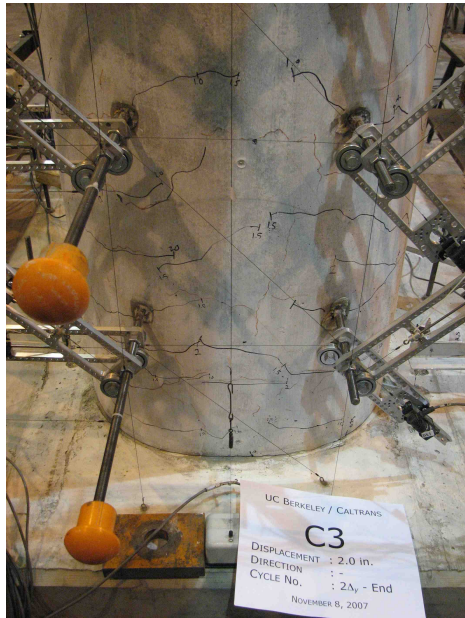


(c) East Face



(d) West Face

Figure D.25: Column C3 after 1.5 in. Displacement Amplitude Cycle



(a) North Face



(b) South Face

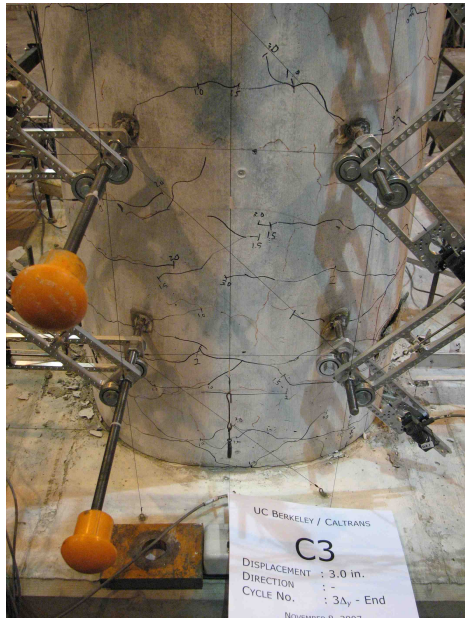


(c) East Face

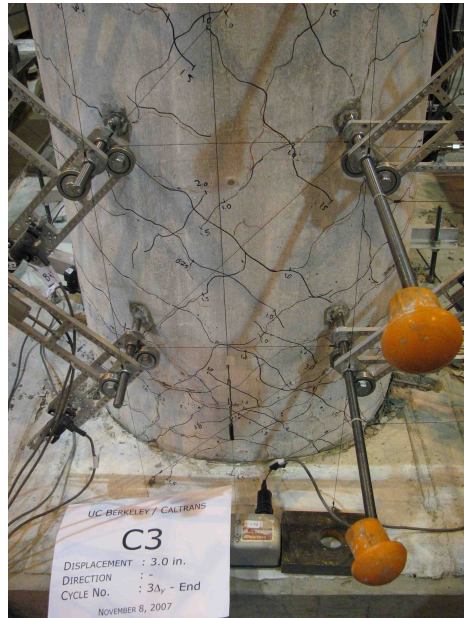


(d) West Face

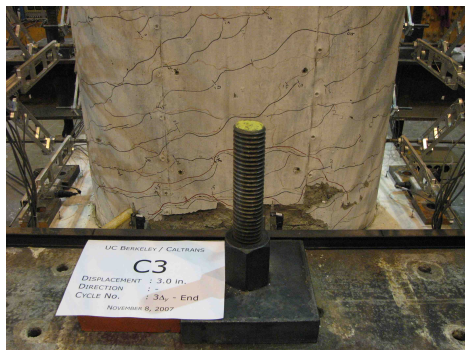
Figure D.26: Column C3 after 2 in. Displacement Amplitude Cycle



(a) North Face



(b) South Face

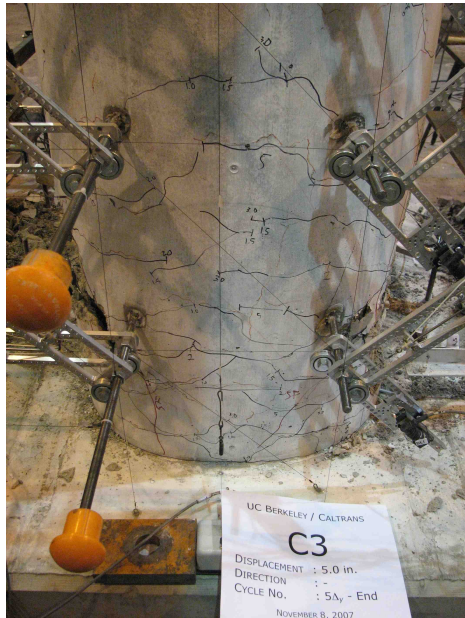


(c) East Face

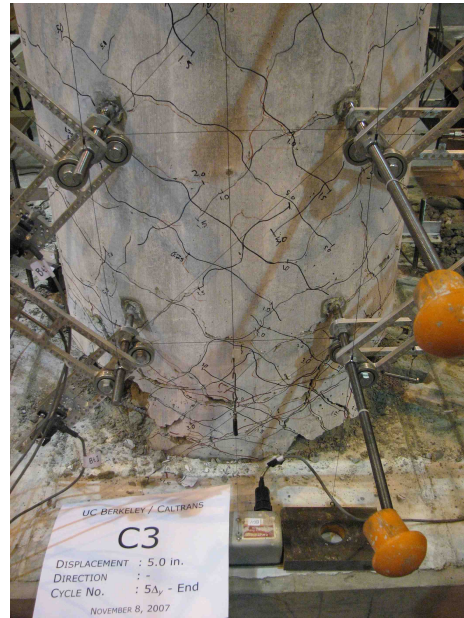


(d) West Face

Figure D.27: Column C3 after 3 in. Displacement Amplitude Cycle



(a) North Face



(b) South Face

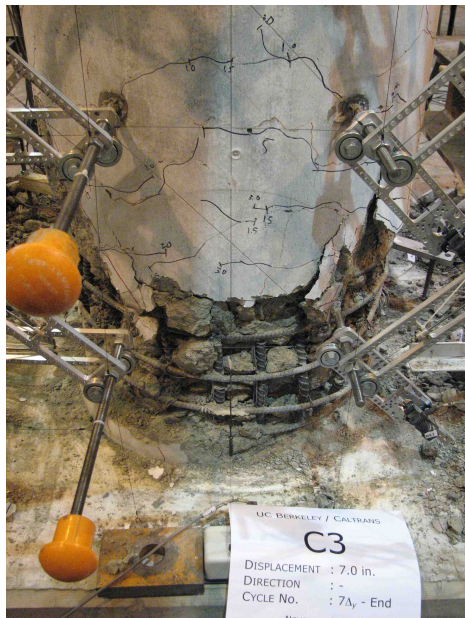


(c) East Face



(d) West Face

Figure D.28: Column C3 after 5 in. Displacement Amplitude Cycle



(a) North Face



(b) South Face

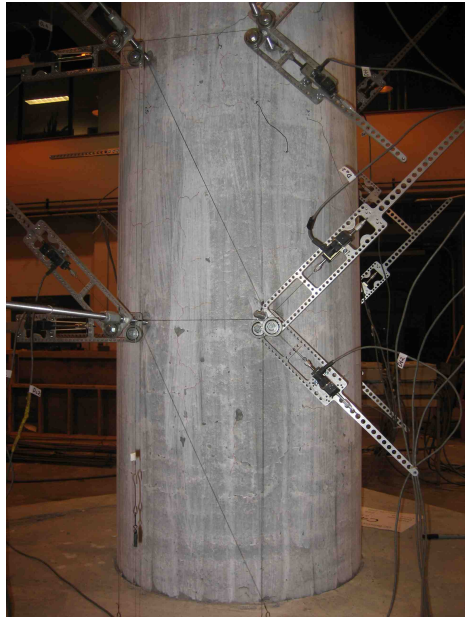


(c) East Face

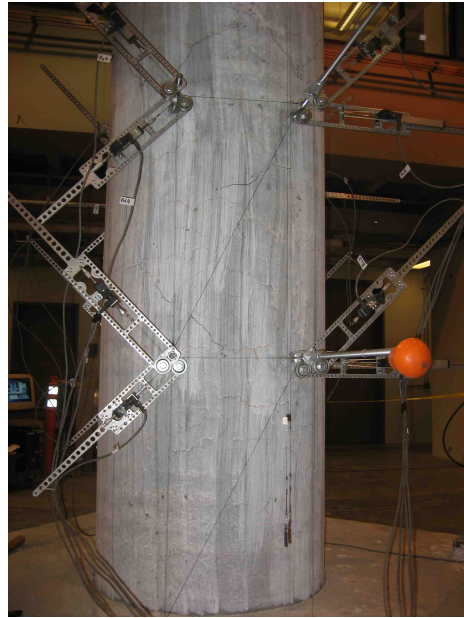


(d) West Face

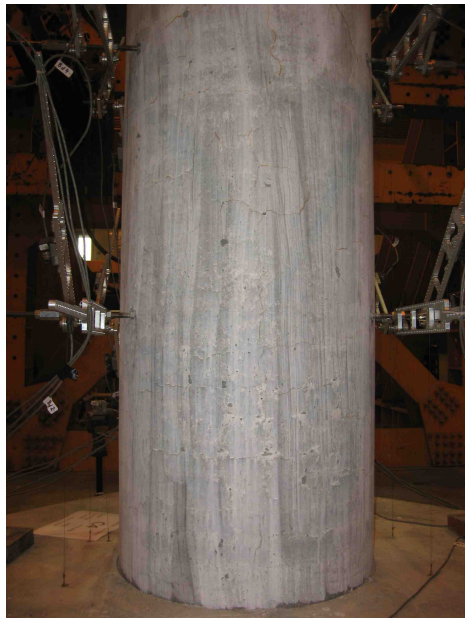
Figure D.29: Column C3 Final Damage State



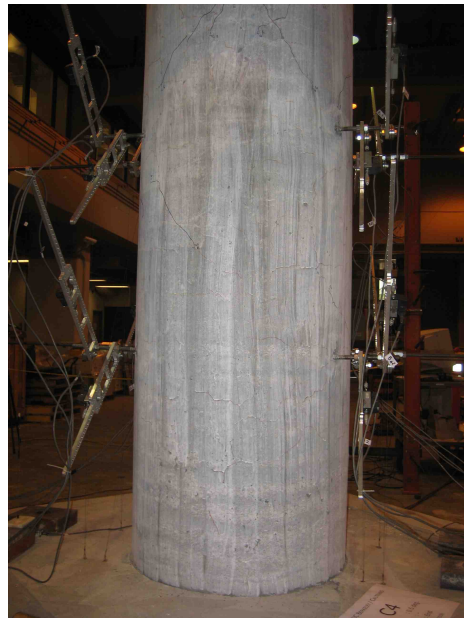
(a) North Face



(b) South Face



(c) East Face



(d) West Face

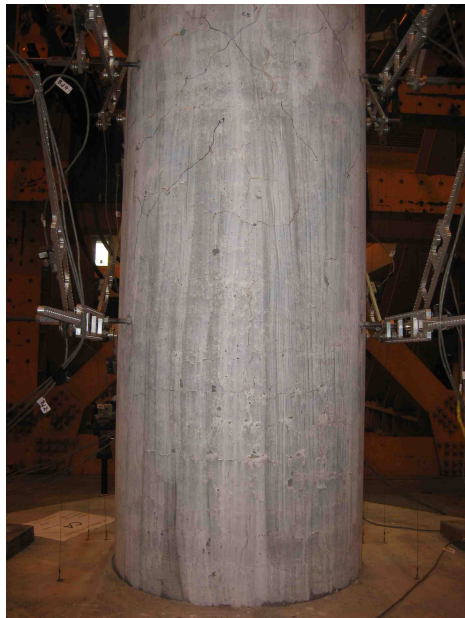
Figure D.30: Column C4 after 0.5 deg Twist Amplitude Cycle



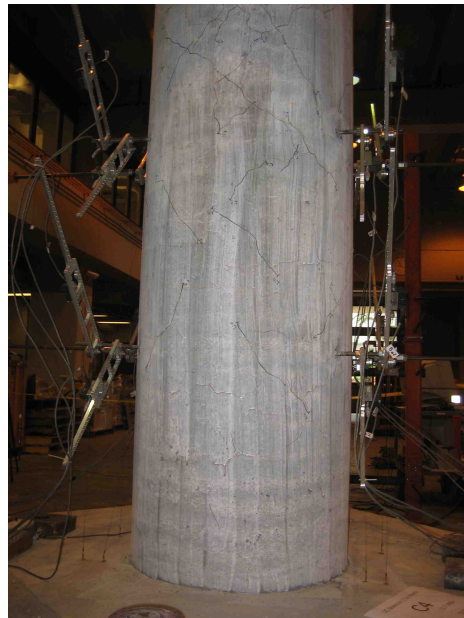
(a) North Face



(b) South Face

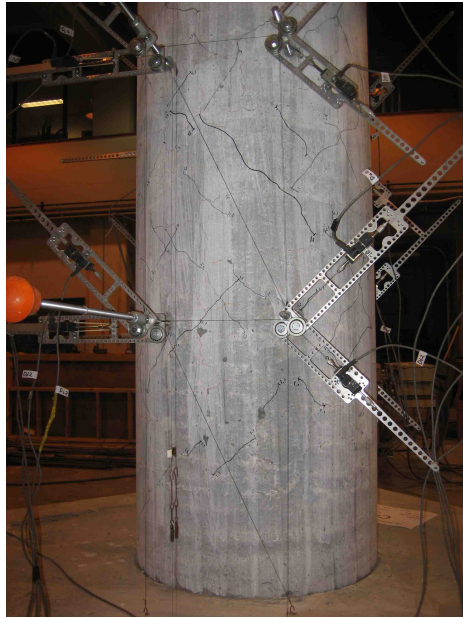


(c) East Face

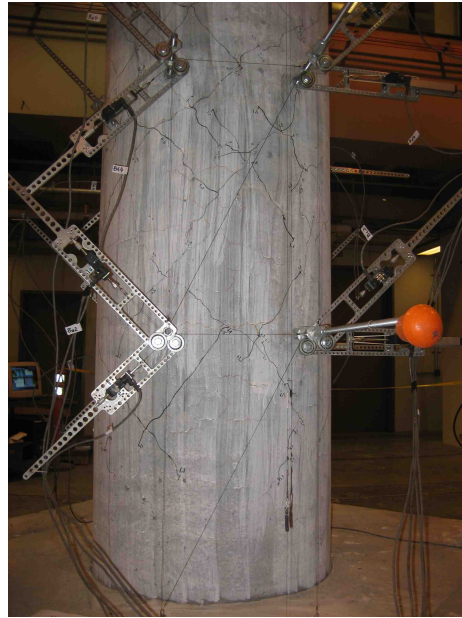


(d) West Face

Figure D.31: Column C4 after 0.7 deg Twist Amplitude Cycle



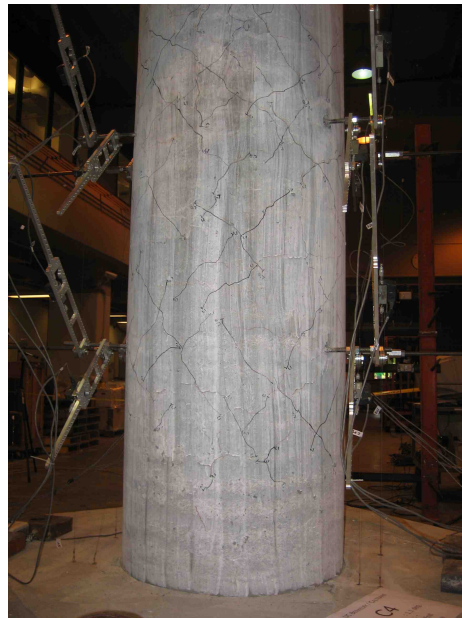
(a) North Face



(b) South Face

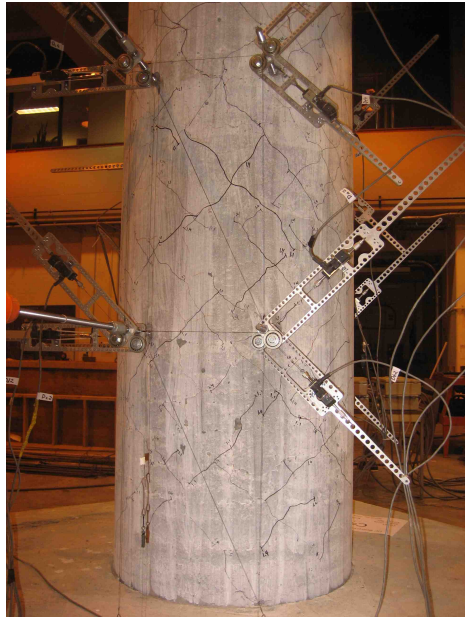


(c) East Face

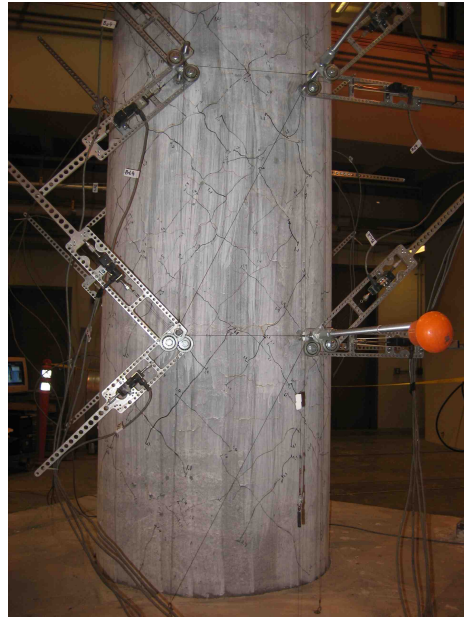


(d) West Face

Figure D.32: Column C4 after 1.1 deg Twist Amplitude Cycle



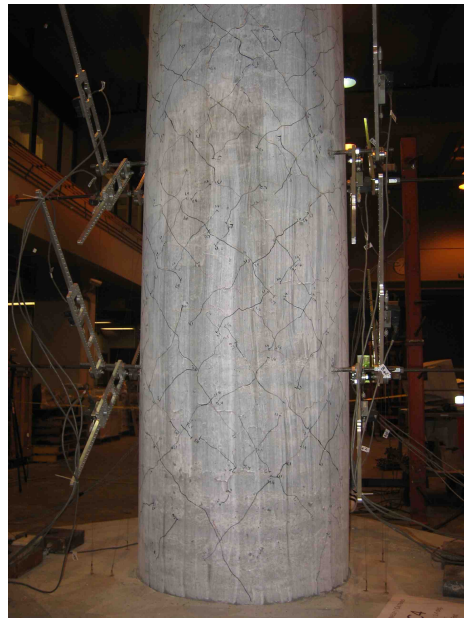
(a) North Face



(b) South Face

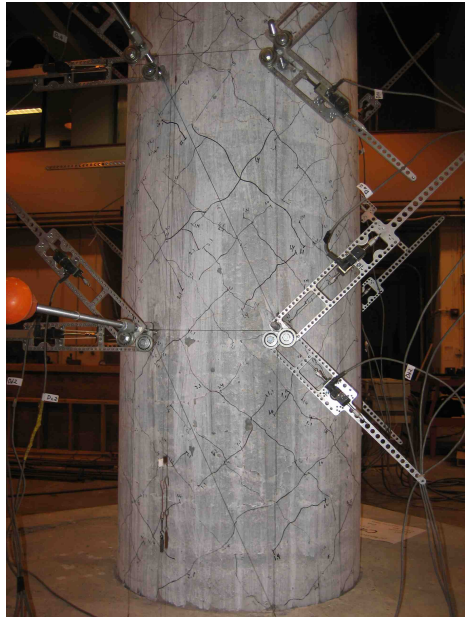


(c) East Face



(d) West Face

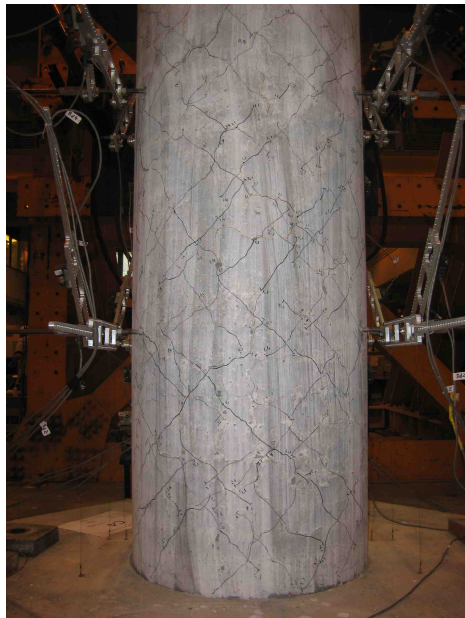
Figure D.33: Column C4 after 1.4 deg Twist Amplitude Cycle



(a) North Face



(b) South Face



(c) East Face



(d) West Face

Figure D.34: Column C4 after 2.1 deg Twist Amplitude Cycle



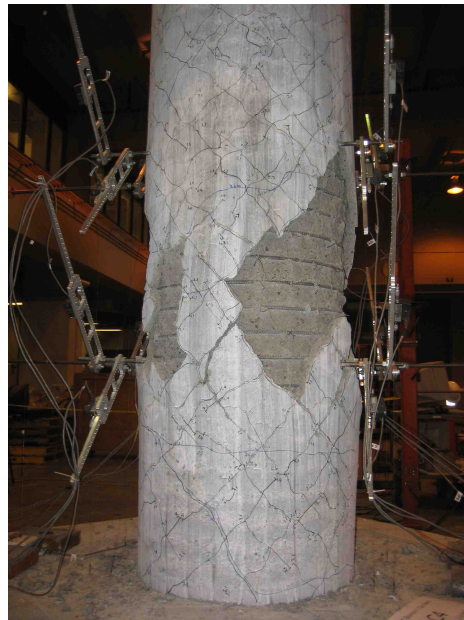
(a) North Face



(b) South Face



(c) East Face



(d) West Face

Figure D.35: Column C4 after 3.6 deg Twist Amplitude Cycle



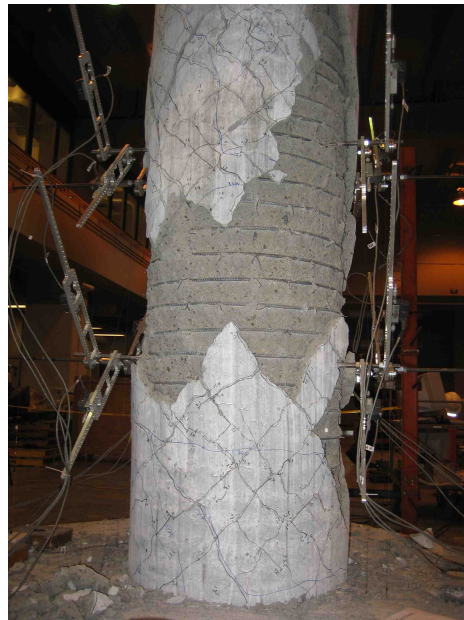
(a) North Face



(b) South Face



(c) East Face



(d) West Face

Figure D.36: Column C4 after 5 deg Twist Amplitude Cycle

## PEER REPORTS

PEER reports are available as a free PDF download from <https://peer.berkeley.edu/peer-reports>. In addition, printed hard copies of PEER reports can be ordered directly from our printer by following the instructions at <https://peer.berkeley.edu/peer-reports>. For other related questions about the PEER Report Series, contact the Pacific Earthquake Engineering Research Center, 325 Davis Hall, Mail Code 1792, Berkeley, CA 94720. Tel.: (510) 642-3437; and Email: [peer\\_center@berkeley.edu](mailto:peer_center@berkeley.edu).

- PEER 2016/08** *Resilience of Critical Structures, Infrastructure, and Communities*. Gian Paolo Cimellaro, Ali Zamani-Noori, Omar Kamouh, Vesna Terzic, and Stephen A. Mahin. December 2016.
- PEER 2016/07** *Hybrid Simulation Theory for a Classical Nonlinear Dynamical System*. Paul L. Drazin and Sanjay Govindjee. September 2016.
- PEER 2016/06** *California Earthquake Early Warning System Benefit Study*. Laurie A. Johnson, Sharyl Rabinovici, Grace S. Kang, and Stephen A. Mahin. July 2006.
- PEER 2016/05** *Ground-Motion Prediction Equations for Arias Intensity Consistent with the NGA-West2 Ground-Motion Models*. Charlotte Abrahamson, Hao-Jun Michael Shi, and Brian Yang. July 2016.
- PEER 2016/04** *The  $M_w$  6.0 South Napa Earthquake of August 24, 2014: A Wake-Up Call for Renewed Investment in Seismic Resilience Across California*. Prepared for the California Seismic Safety Commission, Laurie A. Johnson and Stephen A. Mahin. May 2016.
- PEER 2016/03** *Simulation Confidence in Tsunami-Driven Overland Flow*. Patrick Lynett. May 2016.
- PEER 2016/02** *Semi-Automated Procedure for Windowing time Series and Computing Fourier Amplitude Spectra for the NGA-West2 Database*. Tadahiro Kishida, Olga-Joan Ktenidou, Robert B. Darragh, and Walter J. Silva. May 2016.
- PEER 2016/01** *A Methodology for the Estimation of Kappa ( $\kappa$ ) from Large Datasets: Example Application to Rock Sites in the NGA-East Database and Implications on Design Motions*. Olga-Joan Ktenidou, Norman A. Abrahamson, Robert B. Darragh, and Walter J. Silva. April 2016.
- PEER 2015/13** *Self-Centering Precast Concrete Dual-Steel-Shell Columns for Accelerated Bridge Construction: Seismic Performance, Analysis, and Design*. Gabriele Guerrini, José I. Restrepo, Athanassios Vervelidis, and Milena Massari. December 2015.
- PEER 2015/12** *Shear-Flexure Interaction Modeling for Reinforced Concrete Structural Walls and Columns under Reversed Cyclic Loading*. Kristijan Kolozvari, Kutay Orakcal, and John Wallace. December 2015.
- PEER 2015/11** *Selection and Scaling of Ground Motions for Nonlinear Response History Analysis of Buildings in Performance-Based Earthquake Engineering*. N. Simon Kwong and Anil K. Chopra. December 2015.
- PEER 2015/10** *Structural Behavior of Column-Bent Cap Beam-Box Girder Systems in Reinforced Concrete Bridges Subjected to Gravity and Seismic Loads. Part II: Hybrid Simulation and Post-Test Analysis*. Mohamed A. Moustafa and Khalid M. Mosalam. November 2015.
- PEER 2015/09** *Structural Behavior of Column-Bent Cap Beam-Box Girder Systems in Reinforced Concrete Bridges Subjected to Gravity and Seismic Loads. Part I: Pre-Test Analysis and Quasi-Static Experiments*. Mohamed A. Moustafa and Khalid M. Mosalam. September 2015.
- PEER 2015/08** *NGA-East: Adjustments to Median Ground-Motion Models for Center and Eastern North America*. August 2015.
- PEER 2015/07** *NGA-East: Ground-Motion Standard-Deviation Models for Central and Eastern North America*. Linda Al Atik. June 2015.
- PEER 2015/06** *Adjusting Ground-Motion Intensity Measures to a Reference Site for which  $V_{s30} = 3000$  m/sec*. David M. Boore. May 2015.
- PEER 2015/05** *Hybrid Simulation of Seismic Isolation Systems Applied to an APR-1400 Nuclear Power Plant*. Andreas H. Schellenberg, Alireza Sarebanha, Matthew J. Schoettler, Gilberto Mosqueda, Gianmario Benzoni, and Stephen A. Mahin. April 2015.
- PEER 2015/04** *NGA-East: Median Ground-Motion Models for the Central and Eastern North America Region*. April 2015.
- PEER 2015/03** *Single Series Solution for the Rectangular Fiber-Reinforced Elastomeric Isolator Compression Modulus*. James M. Kelly and Niel C. Van Engelen. March 2015.
- PEER 2015/02** *A Full-Scale, Single-Column Bridge Bent Tested by Shake-Table Excitation*. Matthew J. Schoettler, José I. Restrepo, Gabriele Guerrini, David E. Duck, and Francesco Carrea. March 2015.

- PEER 2015/01** *Concrete Column Blind Prediction Contest 2010: Outcomes and Observations.* Vesna Terzic, Matthew J. Schoettler, José I. Restrepo, and Stephen A Mahin. March 2015.
- PEER 2014/20** *Stochastic Modeling and Simulation of Near-Fault Ground Motions for Performance-Based Earthquake Engineering.* Mayssa Dabaghi and Armen Der Kiureghian. December 2014.
- PEER 2014/19** *Seismic Response of a Hybrid Fiber-Reinforced Concrete Bridge Column Detailed for Accelerated Bridge Construction.* Wilson Nguyen, William Trono, Marios Panagiotou, and Claudia P. Ostertag. December 2014.
- PEER 2014/18** *Three-Dimensional Beam-Truss Model for Reinforced Concrete Walls and Slabs Subjected to Cyclic Static or Dynamic Loading.* Yuan Lu, Marios Panagiotou, and Ioannis Koutromanos. December 2014.
- PEER 2014/17** *PEER NGA-East Database.* Christine A. Goulet, Tadahiro Kishida, Timothy D. Ancheta, Chris H. Cramer, Robert B. Darragh, Walter J. Silva, Youssef M.A. Hashash, Joseph Harmon, Jonathan P. Stewart, Katie E. Wooddell, and Robert R. Youngs. October 2014.
- PEER 2014/16** *Guidelines for Performing Hazard-Consistent One-Dimensional Ground Response Analysis for Ground Motion Prediction.* Jonathan P. Stewart, Kioumars Afshari, and Youssef M.A. Hashash. October 2014.
- PEER 2014/15** *NGA-East Regionalization Report: Comparison of Four Crustal Regions within Central and Eastern North America using Waveform Modeling and 5%-Damped Pseudo-Spectral Acceleration Response.* Jennifer Dreiling, Marius P. Isken, Walter D. Mooney, Martin C. Chapman, and Richard W. Godbee. October 2014.
- PEER 2014/14** *Scaling Relations between Seismic Moment and Rupture Area of Earthquakes in Stable Continental Regions.* Paul Somerville. August 2014.
- PEER 2014/13** *PEER Preliminary Notes and Observations on the August 24, 2014, South Napa Earthquake.* Grace S. Kang and Stephen A. Mahin, Editors. September 2014.
- PEER 2014/12** *Reference-Rock Site Conditions for Central and Eastern North America: Part II – Attenuation (Kappa) Definition.* Kenneth W. Campbell, Youssef M.A. Hashash, Byungmin Kim, Albert R. Kottke, Ellen M. Rathje, Walter J. Silva, and Jonathan P. Stewart. August 2014.
- PEER 2014/11** *Reference-Rock Site Conditions for Central and Eastern North America: Part I - Velocity Definition.* Youssef M.A. Hashash, Albert R. Kottke, Jonathan P. Stewart, Kenneth W. Campbell, Byungmin Kim, Ellen M. Rathje, Walter J. Silva, Sissy Nikolaou, and Cheryl Moss. August 2014.
- PEER 2014/10** *Evaluation of Collapse and Non-Collapse of Parallel Bridges Affected by Liquefaction and Lateral Spreading.* Benjamin Turner, Scott J. Brandenberg, and Jonathan P. Stewart. August 2014.
- PEER 2014/09** *PEER Arizona Strong-Motion Database and GMPEs Evaluation.* Tadahiro Kishida, Robert E. Kayen, Olga-Joan Ktenidou, Walter J. Silva, Robert B. Darragh, and Jennie Watson-Lamprey. June 2014.
- PEER 2014/08** *Unbonded Pretensioned Bridge Columns with Rocking Detail.* Jeffrey A. Schaefer, Bryan Kennedy, Marc O. Eberhard, and John F. Stanton. June 2014.
- PEER 2014/07** *Northridge 20 Symposium Summary Report: Impacts, Outcomes, and Next Steps.* May 2014.
- PEER 2014/06** *Report of the Tenth Planning Meeting of NEES/E-Defense Collaborative Research on Earthquake Engineering.* December 2013.
- PEER 2014/05** *Seismic Velocity Site Characterization of Thirty-One Chilean Seismometer Stations by Spectral Analysis of Surface Wave Dispersion.* Robert Kayen, Brad D. Carkin, Skye Corbet, Camilo Pinilla, Allan Ng, Edward Gorbis, and Christine Truong. April 2014.
- PEER 2014/04** *Effect of Vertical Acceleration on Shear Strength of Reinforced Concrete Columns.* Hyerin Lee and Khalid M. Mosalam. April 2014.
- PEER 2014/03** *Retest of Thirty-Year-Old Neoprene Isolation Bearings.* James M. Kelly and Niel C. Van Engelen. March 2014.
- PEER 2014/02** *Theoretical Development of Hybrid Simulation Applied to Plate Structures.* Ahmed A. Bakhaty, Khalid M. Mosalam, and Sanjay Govindjee. January 2014.
- PEER 2014/01** *Performance-Based Seismic Assessment of Skewed Bridges.* Peyman Kaviani, Farzin Zareian, and Ertugrul Taciroglu. January 2014.
- PEER 2013/26** *Urban Earthquake Engineering.* Proceedings of the U.S.-Iran Seismic Workshop. December 2013.
- PEER 2013/25** *Earthquake Engineering for Resilient Communities: 2013 PEER Internship Program Research Report Collection.* Heidi Tremayne (Editor), Stephen A. Mahin (Editor), Jorge Archbold Monterossa, Matt Brosman, Shelly Dean, Katherine deLaveaga, Curtis Fong, Donovan Holder, Rakeeb Khan, Elizabeth Jachens, David Lam, Daniela Martinez Lopez, Mara Minner, Geffen Oren, Julia Pavicic, Melissa Quinonez, Lorena Rodriguez, Sean Salazar, Kelli Slaven, Vivian Steyert, Jenny Taing, and Salvador Tena. December 2013.

- PEER 2013/24** *NGA-West2 Ground Motion Prediction Equations for Vertical Ground Motions.* September 2013.
- PEER 2013/23** *Coordinated Planning and Preparedness for Fire Following Major Earthquakes.* Charles Scawthorn. November 2013.
- PEER 2013/22** *GEM-PEER Task 3 Project: Selection of a Global Set of Ground Motion Prediction Equations.* Jonathan P. Stewart, John Douglas, Mohammad B. Javanbarg, Carola Di Alessandro, Yousef Bozorgnia, Norman A. Abrahamson, David M. Boore, Kenneth W. Campbell, Elise Delavaud, Mustafa Erdik, and Peter J. Stafford. December 2013.
- PEER 2013/21** *Seismic Design and Performance of Bridges with Columns on Rocking Foundations.* Grigorios Antonellis and Marios Panagiotou. September 2013.
- PEER 2013/20** *Experimental and Analytical Studies on the Seismic Behavior of Conventional and Hybrid Braced Frames.* Jiun-Wei Lai and Stephen A. Mahin. September 2013.
- PEER 2013/19** *Toward Resilient Communities: A Performance-Based Engineering Framework for Design and Evaluation of the Built Environment.* Michael William Mieler, Bozidar Stojadinovic, Robert J. Budnitz, Stephen A. Mahin, and Mary C. Comerio. September 2013.
- PEER 2013/18** *Identification of Site Parameters that Improve Predictions of Site Amplification.* Ellen M. Rathje and Sara Navidi. July 2013.
- PEER 2013/17** *Response Spectrum Analysis of Concrete Gravity Dams Including Dam-Water-Foundation Interaction.* Arnkjell Løkke and Anil K. Chopra. July 2013.
- PEER 2013/16** *Effect of Hoop Reinforcement Spacing on the Cyclic Response of Large Reinforced Concrete Special Moment Frame Beams.* Marios Panagiotou, Tea Visnjic, Grigorios Antonellis, Panagiotis Galanis, and Jack P. Moehle. June 2013.
- PEER 2013/15** *A Probabilistic Framework to Include the Effects of Near-Fault Directivity in Seismic Hazard Assessment.* Shrey Kumar Shahi, Jack W. Baker. October 2013.
- PEER 2013/14** *Hanging-Wall Scaling using Finite-Fault Simulations.* Jennifer L. Donahue and Norman A. Abrahamson. September 2013.
- PEER 2013/13** *Semi-Empirical Nonlinear Site Amplification and its Application in NEHRP Site Factors.* Jonathan P. Stewart and Emel Seyhan. November 2013.
- PEER 2013/12** *Nonlinear Horizontal Site Response for the NGA-West2 Project.* Ronnie Kamai, Norman A. Abramson, Walter J. Silva. May 2013.
- PEER 2013/11** *Epistemic Uncertainty for NGA-West2 Models.* Linda Al Atik and Robert R. Youngs. May 2013.
- PEER 2013/10** *NGA-West 2 Models for Ground-Motion Directionality.* Shrey K. Shahi and Jack W. Baker. May 2013.
- PEER 2013/09** *Final Report of the NGA-West2 Directivity Working Group.* Paul Spudich, Jeffrey R. Bayless, Jack W. Baker, Brian S.J. Chiou, Badie Rowshandel, Shrey Shahi, and Paul Somerville. May 2013.
- PEER 2013/08** *NGA-West2 Model for Estimating Average Horizontal Values of Pseudo-Absolute Spectral Accelerations Generated by Crustal Earthquakes.* I. M. Idriss. May 2013.
- PEER 2013/07** *Update of the Chiou and Youngs NGA Ground Motion Model for Average Horizontal Component of Peak Ground Motion and Response Spectra.* Brian Chiou and Robert Youngs. May 2013.
- PEER 2013/06** *NGA-West2 Campbell-Bozorgnia Ground Motion Model for the Horizontal Components of PGA, PGV, and 5%-Damped Elastic Pseudo-Acceleration Response Spectra for Periods Ranging from 0.01 to 10 sec.* Kenneth W. Campbell and Yousef Bozorgnia. May 2013.
- PEER 2013/05** *NGA-West 2 Equations for Predicting Response Spectral Accelerations for Shallow Crustal Earthquakes.* David M. Boore, Jonathan P. Stewart, Emel Seyhan, and Gail M. Atkinson. May 2013.
- PEER 2013/04** *Update of the AS08 Ground-Motion Prediction Equations Based on the NGA-West2 Data Set.* Norman Abrahamson, Walter Silva, and Ronnie Kamai. May 2013.
- PEER 2013/03** *PEER NGA-West2 Database.* Timothy D. Ancheta, Robert B. Darragh, Jonathan P. Stewart, Emel Seyhan, Walter J. Silva, Brian S.J. Chiou, Katie E. Wooddell, Robert W. Graves, Albert R. Kottke, David M. Boore, Tadahiro Kishida, and Jennifer L. Donahue. May 2013.
- PEER 2013/02** *Hybrid Simulation of the Seismic Response of Squat Reinforced Concrete Shear Walls.* Catherine A. Whyte and Bozidar Stojadinovic. May 2013.
- PEER 2013/01** *Housing Recovery in Chile: A Qualitative Mid-program Review.* Mary C. Comerio. February 2013.

- PEER 2012/08** *Guidelines for Estimation of Shear Wave Velocity*. Bernard R. Wair, Jason T. DeJong, and Thomas Shantz. December 2012.
- PEER 2012/07** *Earthquake Engineering for Resilient Communities: 2012 PEER Internship Program Research Report Collection*. Heidi Tremayne (Editor), Stephen A. Mahin (Editor), Collin Anderson, Dustin Cook, Michael Erceg, Carlos Esparza, Jose Jimenez, Dorian Krausz, Andrew Lo, Stephanie Lopez, Nicole McCurdy, Paul Shipman, Alexander Strum, Eduardo Vega. December 2012.
- PEER 2012/06** *Fragilities for Precarious Rocks at Yucca Mountain*. Matthew D. Purvance, Rasool Anooshehpour, and James N. Brune. December 2012.
- PEER 2012/05** *Development of Simplified Analysis Procedure for Piles in Laterally Spreading Layered Soils*. Christopher R. McGann, Pedro Arduino, and Peter Mackenzie-Helnwein. December 2012.
- PEER 2012/04** *Unbonded Pre-Tensioned Columns for Bridges in Seismic Regions*. Phillip M. Davis, Todd M. Janes, Marc O. Eberhard, and John F. Stanton. December 2012.
- PEER 2012/03** *Experimental and Analytical Studies on Reinforced Concrete Buildings with Seismically Vulnerable Beam-Column Joints*. Sangjoon Park and Khalid M. Mosalam. October 2012.
- PEER 2012/02** *Seismic Performance of Reinforced Concrete Bridges Allowed to Uplift during Multi-Directional Excitation*. Andres Oscar Espinoza and Stephen A. Mahin. July 2012.
- PEER 2012/01** *Spectral Damping Scaling Factors for Shallow Crustal Earthquakes in Active Tectonic Regions*. Sanaz Rezaeian, Yousef Bozorgnia, I. M. Idriss, Kenneth Campbell, Norman Abrahamson, and Walter Silva. July 2012.
- PEER 2011/10** *Earthquake Engineering for Resilient Communities: 2011 PEER Internship Program Research Report Collection*. Heidi Faison and Stephen A. Mahin, Editors. December 2011.
- PEER 2011/09** *Calibration of Semi-Stochastic Procedure for Simulating High-Frequency Ground Motions*. Jonathan P. Stewart, Emel Seyhan, and Robert W. Graves. December 2011.
- PEER 2011/08** *Water Supply in regard to Fire Following Earthquake*. Charles Scawthorn. November 2011.
- PEER 2011/07** *Seismic Risk Management in Urban Areas*. Proceedings of a U.S.-Iran-Turkey Seismic Workshop. September 2011.
- PEER 2011/06** *The Use of Base Isolation Systems to Achieve Complex Seismic Performance Objectives*. Troy A. Morgan and Stephen A. Mahin. July 2011.
- PEER 2011/05** *Case Studies of the Seismic Performance of Tall Buildings Designed by Alternative Means*. Task 12 Report for the Tall Buildings Initiative. Jack Moehle, Yousef Bozorgnia, Nirmal Jayaram, Pierson Jones, Mohsen Rahnama, Nilesh Shome, Zeynep Tuna, John Wallace, Tony Yang, and Farzin Zareian. July 2011.
- PEER 2011/04** *Recommended Design Practice for Pile Foundations in Laterally Spreading Ground*. Scott A. Ashford, Ross W. Boulanger, and Scott J. Brandenburg. June 2011.
- PEER 2011/03** *New Ground Motion Selection Procedures and Selected Motions for the PEER Transportation Research Program*. Jack W. Baker, Ting Lin, Shrey K. Shahi, and Nirmal Jayaram. March 2011.
- PEER 2011/02** *A Bayesian Network Methodology for Infrastructure Seismic Risk Assessment and Decision Support*. Michelle T. Bensi, Armen Der Kiureghian, and Daniel Straub. March 2011.
- PEER 2011/01** *Demand Fragility Surfaces for Bridges in Liquefied and Laterally Spreading Ground*. Scott J. Brandenburg, Jian Zhang, Pirooz Kashighandi, Yili Huo, and Minxing Zhao. March 2011.
- PEER 2010/05** *Guidelines for Performance-Based Seismic Design of Tall Buildings*. Developed by the Tall Buildings Initiative. November 2010.
- PEER 2010/04** *Application Guide for the Design of Flexible and Rigid Bus Connections between Substation Equipment Subjected to Earthquakes*. Jean-Bernard Dastous and Armen Der Kiureghian. September 2010.
- PEER 2010/03** *Shear Wave Velocity as a Statistical Function of Standard Penetration Test Resistance and Vertical Effective Stress at Caltrans Bridge Sites*. Scott J. Brandenburg, Naresh Bellana, and Thomas Shantz. June 2010.
- PEER 2010/02** *Stochastic Modeling and Simulation of Ground Motions for Performance-Based Earthquake Engineering*. Sanaz Rezaeian and Armen Der Kiureghian. June 2010.
- PEER 2010/01** *Structural Response and Cost Characterization of Bridge Construction Using Seismic Performance Enhancement Strategies*. Ady Aviram, Božidar Stojadinović, Gustavo J. Parra-Montesinos, and Kevin R. Mackie. March 2010.
- PEER 2009/03** *The Integration of Experimental and Simulation Data in the Study of Reinforced Concrete Bridge Systems Including Soil-Foundation-Structure Interaction*. Matthew Dryden and Gregory L. Fenves. November 2009.

- PEER 2009/02** *Improving Earthquake Mitigation through Innovations and Applications in Seismic Science, Engineering, Communication, and Response.* Proceedings of a U.S.-Iran Seismic Workshop. October 2009.
- PEER 2009/01** *Evaluation of Ground Motion Selection and Modification Methods: Predicting Median Interstory Drift Response of Buildings.* Curt B. Haselton, Editor. June 2009.
- PEER 2008/10** *Technical Manual for Strata.* Albert R. Kottke and Ellen M. Rathje. February 2009.
- PEER 2008/09** *NGA Model for Average Horizontal Component of Peak Ground Motion and Response Spectra.* Brian S.-J. Chiou and Robert R. Youngs. November 2008.
- PEER 2008/08** *Toward Earthquake-Resistant Design of Concentrically Braced Steel Structures.* Patxi Uriz and Stephen A. Mahin. November 2008.
- PEER 2008/07** *Using OpenSees for Performance-Based Evaluation of Bridges on Liquefiable Soils.* Stephen L. Kramer, Pedro Arduino, and HyungSuk Shin. November 2008.
- PEER 2008/06** *Shaking Table Tests and Numerical Investigation of Self-Centering Reinforced Concrete Bridge Columns.* Hyung IL Jeong, Junichi Sakai, and Stephen A. Mahin. September 2008.
- PEER 2008/05** *Performance-Based Earthquake Engineering Design Evaluation Procedure for Bridge Foundations Undergoing Liquefaction-Induced Lateral Ground Displacement.* Christian A. Ledezma and Jonathan D. Bray. August 2008.
- PEER 2008/04** *Benchmarking of Nonlinear Geotechnical Ground Response Analysis Procedures.* Jonathan P. Stewart, Annie On-Lei Kwok, Youssef M. A. Hashash, Neven Matasovic, Robert Pyke, Zhiliang Wang, and Zhaohui Yang. August 2008.
- PEER 2008/03** *Guidelines for Nonlinear Analysis of Bridge Structures in California.* Ady Aviram, Kevin R. Mackie, and Božidar Stojadinović. August 2008.
- PEER 2008/02** *Treatment of Uncertainties in Seismic-Risk Analysis of Transportation Systems.* Evangelos Stergiou and Anne S. Kiremidjian. July 2008.
- PEER 2008/01** *Seismic Performance Objectives for Tall Buildings.* William T. Holmes, Charles Kircher, William Petak, and Nabih Youssef. August 2008.
- PEER 2007/12** *An Assessment to Benchmark the Seismic Performance of a Code-Conforming Reinforced Concrete Moment-Frame Building.* Curt Haselton, Christine A. Goulet, Judith Mitrani-Reiser, James L. Beck, Gregory G. Deierlein, Keith A. Porter, Jonathan P. Stewart, and Ertugrul Taciroglu. August 2008.
- PEER 2007/11** *Bar Buckling in Reinforced Concrete Bridge Columns.* Wayne A. Brown, Dawn E. Lehman, and John F. Stanton. February 2008.
- PEER 2007/10** *Computational Modeling of Progressive Collapse in Reinforced Concrete Frame Structures.* Mohamed M. Talaat and Khalid M. Mosalam. May 2008.
- PEER 2007/09** *Integrated Probabilistic Performance-Based Evaluation of Benchmark Reinforced Concrete Bridges.* Kevin R. Mackie, John-Michael Wong, and Božidar Stojadinović. January 2008.
- PEER 2007/08** *Assessing Seismic Collapse Safety of Modern Reinforced Concrete Moment-Frame Buildings.* Curt B. Haselton and Gregory G. Deierlein. February 2008.
- PEER 2007/07** *Performance Modeling Strategies for Modern Reinforced Concrete Bridge Columns.* Michael P. Berry and Marc O. Eberhard. April 2008.
- PEER 2007/06** *Development of Improved Procedures for Seismic Design of Buried and Partially Buried Structures.* Linda Al Atik and Nicholas Sitar. June 2007.
- PEER 2007/05** *Uncertainty and Correlation in Seismic Risk Assessment of Transportation Systems.* Renee G. Lee and Anne S. Kiremidjian. July 2007.
- PEER 2007/04** *Numerical Models for Analysis and Performance-Based Design of Shallow Foundations Subjected to Seismic Loading.* Sivapalan Gajan, Tara C. Hutchinson, Bruce L. Kutter, Prishati Raychowdhury, José A. Ugalde, and Jonathan P. Stewart. May 2008.
- PEER 2007/03** *Beam-Column Element Model Calibrated for Predicting Flexural Response Leading to Global Collapse of RC Frame Buildings.* Curt B. Haselton, Abbie B. Liel, Sarah Taylor Lange, and Gregory G. Deierlein. May 2008.
- PEER 2007/02** *Campbell-Bozorgnia NGA Ground Motion Relations for the Geometric Mean Horizontal Component of Peak and Spectral Ground Motion Parameters.* Kenneth W. Campbell and Yousef Bozorgnia. May 2007.
- PEER 2007/01** *Boore-Atkinson NGA Ground Motion Relations for the Geometric Mean Horizontal Component of Peak and Spectral Ground Motion Parameters.* David M. Boore and Gail M. Atkinson. May 2007.

- PEER 2006/12** Societal Implications of Performance-Based Earthquake Engineering. Peter J. May. May 2007.
- PEER 2006/11** *Probabilistic Seismic Demand Analysis Using Advanced Ground Motion Intensity Measures, Attenuation Relationships, and Near-Fault Effects*. Polsak Tothong and C. Allin Cornell. March 2007.
- PEER 2006/10** *Application of the PEER PBEE Methodology to the I-880 Viaduct*. Sashi Kunnath. February 2007.
- PEER 2006/09** *Quantifying Economic Losses from Travel Forgone Following a Large Metropolitan Earthquake*. James Moore, Sungbin Cho, Yue Yue Fan, and Stuart Werner. November 2006.
- PEER 2006/08** *Vector-Valued Ground Motion Intensity Measures for Probabilistic Seismic Demand Analysis*. Jack W. Baker and C. Allin Cornell. October 2006.
- PEER 2006/07** *Analytical Modeling of Reinforced Concrete Walls for Predicting Flexural and Coupled–Shear-Flexural Responses*. Kutay Orakcal, Leonardo M. Massone, and John W. Wallace. October 2006.
- PEER 2006/06** *Nonlinear Analysis of a Soil-Drilled Pier System under Static and Dynamic Axial Loading*. Gang Wang and Nicholas Sitar. November 2006.
- PEER 2006/05** *Advanced Seismic Assessment Guidelines*. Paolo Bazzurro, C. Allin Cornell, Charles Menun, Maziar Motahari, and Nicolas Luco. September 2006.
- PEER 2006/04** *Probabilistic Seismic Evaluation of Reinforced Concrete Structural Components and Systems*. Tae Hyung Lee and Khalid M. Mosalam. August 2006.
- PEER 2006/03** *Performance of Lifelines Subjected to Lateral Spreading*. Scott A. Ashford and Teerawut Juirnarongrit. July 2006.
- PEER 2006/02** *Pacific Earthquake Engineering Research Center Highway Demonstration Project*. Anne Kiremidjian, James Moore, Yue Yue Fan, Nesrin Basoz, Ozgur Yazali, and Meredith Williams. April 2006.
- PEER 2006/01** *Bracing Berkeley. A Guide to Seismic Safety on the UC Berkeley Campus*. Mary C. Comerio, Stephen Tobriner, and Ariane Fehrenkamp. January 2006.
- PEER 2005/17** *Earthquake Simulation Tests on Reducing Residual Displacements of Reinforced Concrete Bridges*. Junichi Sakai, Stephen A Mahin, and Andres Espinoza. December 2005.
- PEER 2005/16** *Seismic Response and Reliability of Electrical Substation Equipment and Systems*. Junho Song, Armen Der Kiureghian, and Jerome L. Sackman. April 2006.
- PEER 2005/15** *CPT-Based Probabilistic Assessment of Seismic Soil Liquefaction Initiation*. R. E. S. Moss, R. B. Seed, R. E. Kayen, J. P. Stewart, and A. Der Kiureghian. April 2006.
- PEER 2005/14** *Workshop on Modeling of Nonlinear Cyclic Load-Deformation Behavior of Shallow Foundations*. Bruce L. Kutter, Geoffrey Martin, Tara Hutchinson, Chad Harden, Sivapalan Gajan, and Justin Phalen. March 2006.
- PEER 2005/13** *Stochastic Characterization and Decision Bases under Time-Dependent Aftershock Risk in Performance-Based Earthquake Engineering*. Gee Liek Yeo and C. Allin Cornell. July 2005.
- PEER 2005/12** *PEER Testbed Study on a Laboratory Building: Exercising Seismic Performance Assessment*. Mary C. Comerio, Editor. November 2005.
- PEER 2005/11** *Van Nuys Hotel Building Testbed Report: Exercising Seismic Performance Assessment*. Helmut Krawinkler, Editor. October 2005.
- PEER 2005/10** *First NEES/E-Defense Workshop on Collapse Simulation of Reinforced Concrete Building Structures*. September 2005.
- PEER 2005/09** *Test Applications of Advanced Seismic Assessment Guidelines*. Joe Maffei, Karl Telleen, Danya Mohr, William Holmes, and Yuki Nakayama. August 2006.
- PEER 2005/08** *Damage Accumulation in Lightly Confined Reinforced Concrete Bridge Columns*. R. Tyler Ranf, Jared M. Nelson, Zach Price, Marc O. Eberhard, and John F. Stanton. April 2006.
- PEER 2005/07** *Experimental and Analytical Studies on the Seismic Response of Freestanding and Anchored Laboratory Equipment*. Dimitrios Konstantinidis and Nicos Makris. January 2005.
- PEER 2005/06** *Global Collapse of Frame Structures under Seismic Excitations*. Luis F. Ibarra and Helmut Krawinkler. September 2005.
- PEER 2005/05** *Performance Characterization of Bench- and Shelf-Mounted Equipment*. Samit Ray Chaudhuri and Tara C. Hutchinson. May 2006.
- PEER 2005/04** *Numerical Modeling of the Nonlinear Cyclic Response of Shallow Foundations*. Chad Harden, Tara Hutchinson, Geoffrey R. Martin, and Bruce L. Kutter. August 2005.

- PEER 2005/03** *A Taxonomy of Building Components for Performance-Based Earthquake Engineering.* Keith A. Porter. September 2005.
- PEER 2005/02** *Fragility Basis for California Highway Overpass Bridge Seismic Decision Making.* Kevin R. Mackie and Božidar Stojadinović. June 2005.
- PEER 2005/01** *Empirical Characterization of Site Conditions on Strong Ground Motion.* Jonathan P. Stewart, Yoojoong Choi, and Robert W. Graves. June 2005.
- PEER 2004/09** *Electrical Substation Equipment Interaction: Experimental Rigid Conductor Studies.* Christopher Stearns and André Filiatrault. February 2005.
- PEER 2004/08** *Seismic Qualification and Fragility Testing of Line Break 550-kV Disconnect Switches.* Shakhzod M. Takhirov, Gregory L. Fenves, and Eric Fujisaki. January 2005.
- PEER 2004/07** *Ground Motions for Earthquake Simulator Qualification of Electrical Substation Equipment.* Shakhzod M. Takhirov, Gregory L. Fenves, Eric Fujisaki, and Don Clyde. January 2005.
- PEER 2004/06** *Performance-Based Regulation and Regulatory Regimes.* Peter J. May and Chris Koski. September 2004.
- PEER 2004/05** *Performance-Based Seismic Design Concepts and Implementation: Proceedings of an International Workshop.* Peter Fajfar and Helmut Krawinkler, Editors. September 2004.
- PEER 2004/04** *Seismic Performance of an Instrumented Tilt-up Wall Building.* James C. Anderson and Vitelmo V. Bertero. July 2004.
- PEER 2004/03** *Evaluation and Application of Concrete Tilt-up Assessment Methodologies.* Timothy Graf and James O. Malley. October 2004.
- PEER 2004/02** *Analytical Investigations of New Methods for Reducing Residual Displacements of Reinforced Concrete Bridge Columns.* Junichi Sakai and Stephen A. Mahin. August 2004.
- PEER 2004/01** *Seismic Performance of Masonry Buildings and Design Implications.* Kerri Anne Taeko Tokoro, James C. Anderson, and Vitelmo V. Bertero. February 2004.
- PEER 2003/18** *Performance Models for Flexural Damage in Reinforced Concrete Columns.* Michael Berry and Marc Eberhard. August 2003.
- PEER 2003/17** *Predicting Earthquake Damage in Older Reinforced Concrete Beam-Column Joints.* Catherine Pagni and Laura Lowes. October 2004.
- PEER 2003/16** *Seismic Demands for Performance-Based Design of Bridges.* Kevin Mackie and Božidar Stojadinović. August 2003.
- PEER 2003/15** *Seismic Demands for Nondeteriorating Frame Structures and Their Dependence on Ground Motions.* Ricardo Antonio Medina and Helmut Krawinkler. May 2004.
- PEER 2003/14** *Finite Element Reliability and Sensitivity Methods for Performance-Based Earthquake Engineering.* Terje Haukaas and Armen Der Kiureghian. April 2004.
- PEER 2003/13** *Effects of Connection Hysteretic Degradation on the Seismic Behavior of Steel Moment-Resisting Frames.* Janise E. Rodgers and Stephen A. Mahin. March 2004.
- PEER 2003/12** *Implementation Manual for the Seismic Protection of Laboratory Contents: Format and Case Studies.* William T. Holmes and Mary C. Comerio. October 2003.
- PEER 2003/11** *Fifth U.S.-Japan Workshop on Performance-Based Earthquake Engineering Methodology for Reinforced Concrete Building Structures.* February 2004.
- PEER 2003/10** *A Beam-Column Joint Model for Simulating the Earthquake Response of Reinforced Concrete Frames.* Laura N. Lowes, Nilanjan Mitra, and Arash Altoontash. February 2004.
- PEER 2003/09** *Sequencing Repairs after an Earthquake: An Economic Approach.* Marco Casari and Simon J. Wilkie. April 2004.
- PEER 2003/08** *A Technical Framework for Probability-Based Demand and Capacity Factor Design (DCFD) Seismic Formats.* Fatemeh Jalayer and C. Allin Cornell. November 2003.
- PEER 2003/07** *Uncertainty Specification and Propagation for Loss Estimation Using FOSM Methods.* Jack W. Baker and C. Allin Cornell. September 2003.
- PEER 2003/06** *Performance of Circular Reinforced Concrete Bridge Columns under Bidirectional Earthquake Loading.* Mahmoud M. Hachem, Stephen A. Mahin, and Jack P. Moehle. February 2003.

- PEER 2003/05** *Response Assessment for Building-Specific Loss Estimation.* Eduardo Miranda and Shahram Taghavi. September 2003.
- PEER 2003/04** *Experimental Assessment of Columns with Short Lap Splices Subjected to Cyclic Loads.* Murat Melek, John W. Wallace, and Joel Conte. April 2003.
- PEER 2003/03** *Probabilistic Response Assessment for Building-Specific Loss Estimation.* Eduardo Miranda and Hesameddin Aslani. September 2003.
- PEER 2003/02** *Software Framework for Collaborative Development of Nonlinear Dynamic Analysis Program.* Jun Peng and Kincho H. Law. September 2003.
- PEER 2003/01** *Shake Table Tests and Analytical Studies on the Gravity Load Collapse of Reinforced Concrete Frames.* Kenneth John Elwood and Jack P. Moehle. November 2003.
- PEER 2002/24** *Performance of Beam to Column Bridge Joints Subjected to a Large Velocity Pulse.* Natalie Gibson, André Filiatrault, and Scott A. Ashford. April 2002.
- PEER 2002/23** *Effects of Large Velocity Pulses on Reinforced Concrete Bridge Columns.* Greg L. Orozco and Scott A. Ashford. April 2002.
- PEER 2002/22** *Characterization of Large Velocity Pulses for Laboratory Testing.* Kenneth E. Cox and Scott A. Ashford. April 2002.
- PEER 2002/21** *Fourth U.S.-Japan Workshop on Performance-Based Earthquake Engineering Methodology for Reinforced Concrete Building Structures.* December 2002.
- PEER 2002/20** *Barriers to Adoption and Implementation of PBEE Innovations.* Peter J. May. August 2002.
- PEER 2002/19** *Economic-Engineered Integrated Models for Earthquakes: Socioeconomic Impacts.* Peter Gordon, James E. Moore II, and Harry W. Richardson. July 2002.
- PEER 2002/18** *Assessment of Reinforced Concrete Building Exterior Joints with Substandard Details.* Chris P. Pantelides, Jon Hansen, Justin Nadauld, and Lawrence D. Reaveley. May 2002.
- PEER 2002/17** *Structural Characterization and Seismic Response Analysis of a Highway Overcrossing Equipped with Elastomeric Bearings and Fluid Dampers: A Case Study.* Nicos Makris and Jian Zhang. November 2002.
- PEER 2002/16** *Estimation of Uncertainty in Geotechnical Properties for Performance-Based Earthquake Engineering.* Allen L. Jones, Steven L. Kramer, and Pedro Arduino. December 2002.
- PEER 2002/15** *Seismic Behavior of Bridge Columns Subjected to Various Loading Patterns.* Asadollah Esmaeily-Gh. and Yan Xiao. December 2002.
- PEER 2002/14** *Inelastic Seismic Response of Extended Pile Shaft Supported Bridge Structures.* T.C. Hutchinson, R.W. Boulanger, Y.H. Chai, and I.M. Idriss. December 2002.
- PEER 2002/13** *Probabilistic Models and Fragility Estimates for Bridge Components and Systems.* Paolo Gardoni, Armen Der Kiureghian, and Khalid M. Mosalam. June 2002.
- PEER 2002/12** *Effects of Fault Dip and Slip Rake on Near-Source Ground Motions: Why Chi-Chi Was a Relatively Mild M7.6 Earthquake.* Brad T. Aagaard, John F. Hall, and Thomas H. Heaton. December 2002.
- PEER 2002/11** *Analytical and Experimental Study of Fiber-Reinforced Strip Isolators.* James M. Kelly and Shakhzod M. Takhirov. September 2002.
- PEER 2002/10** *Centrifuge Modeling of Settlement and Lateral Spreading with Comparisons to Numerical Analyses.* Sivapalan Gajan and Bruce L. Kutter. January 2003.
- PEER 2002/09** *Documentation and Analysis of Field Case Histories of Seismic Compression during the 1994 Northridge, California, Earthquake.* Jonathan P. Stewart, Patrick M. Smith, Daniel H. Whang, and Jonathan D. Bray. October 2002.
- PEER 2002/08** *Component Testing, Stability Analysis and Characterization of Buckling-Restrained Unbonded Braces™.* Cameron Black, Nicos Makris, and Ian Aiken. September 2002.
- PEER 2002/07** *Seismic Performance of Pile-Wharf Connections.* Charles W. Roeder, Robert Graff, Jennifer Soderstrom, and Jun Han Yoo. December 2001.
- PEER 2002/06** *The Use of Benefit-Cost Analysis for Evaluation of Performance-Based Earthquake Engineering Decisions.* Richard O. Zerbe and Anthony Falit-Baiamonte. September 2001.
- PEER 2002/05** *Guidelines, Specifications, and Seismic Performance Characterization of Nonstructural Building Components and Equipment.* André Filiatrault, Constantin Christopoulos, and Christopher Stearns. September 2001.

- PEER 2002/04** *Consortium of Organizations for Strong-Motion Observation Systems and the Pacific Earthquake Engineering Research Center Lifelines Program: Invited Workshop on Archiving and Web Dissemination of Geotechnical Data, 4–5 October 2001.* September 2002.
- PEER 2002/03** *Investigation of Sensitivity of Building Loss Estimates to Major Uncertain Variables for the Van Nuys Testbed.* Keith A. Porter, James L. Beck, and Rustem V. Shaikhutdinov. August 2002.
- PEER 2002/02** *The Third U.S.-Japan Workshop on Performance-Based Earthquake Engineering Methodology for Reinforced Concrete Building Structures.* July 2002.
- PEER 2002/01** *Nonstructural Loss Estimation: The UC Berkeley Case Study.* Mary C. Comerio and John C. Stallmeyer. December 2001.
- PEER 2001/16** *Statistics of SDF-System Estimate of Roof Displacement for Pushover Analysis of Buildings.* Anil K. Chopra, Rakesh K. Goel, and Chatpan Chintanapakdee. December 2001.
- PEER 2001/15** *Damage to Bridges during the 2001 Nisqually Earthquake.* R. Tyler Ranf, Marc O. Eberhard, and Michael P. Berry. November 2001.
- PEER 2001/14** *Rocking Response of Equipment Anchored to a Base Foundation.* Nicos Makris and Cameron J. Black. September 2001.
- PEER 2001/13** *Modeling Soil Liquefaction Hazards for Performance-Based Earthquake Engineering.* Steven L. Kramer and Ahmed-W. Elgamal. February 2001.
- PEER 2001/12** *Development of Geotechnical Capabilities in OpenSees.* Boris Jeremić. September 2001.
- PEER 2001/11** *Analytical and Experimental Study of Fiber-Reinforced Elastomeric Isolators.* James M. Kelly and Shakhzod M. Takhirov. September 2001.
- PEER 2001/10** *Amplification Factors for Spectral Acceleration in Active Regions.* Jonathan P. Stewart, Andrew H. Liu, Yoojoong Choi, and Mehmet B. Baturay. December 2001.
- PEER 2001/09** *Ground Motion Evaluation Procedures for Performance-Based Design.* Jonathan P. Stewart, Shyh-Jeng Chiou, Jonathan D. Bray, Robert W. Graves, Paul G. Somerville, and Norman A. Abrahamson. September 2001.
- PEER 2001/08** *Experimental and Computational Evaluation of Reinforced Concrete Bridge Beam-Column Connections for Seismic Performance.* Clay J. Naito, Jack P. Moehle, and Khalid M. Mosalam. November 2001.
- PEER 2001/07** *The Rocking Spectrum and the Shortcomings of Design Guidelines.* Nicos Makris and Dimitrios Konstantinidis. August 2001.
- PEER 2001/06** *Development of an Electrical Substation Equipment Performance Database for Evaluation of Equipment Fragilities.* Thalia Agnanos. April 1999.
- PEER 2001/05** *Stiffness Analysis of Fiber-Reinforced Elastomeric Isolators.* Hsiang-Chuan Tsai and James M. Kelly. May 2001.
- PEER 2001/04** *Organizational and Societal Considerations for Performance-Based Earthquake Engineering.* Peter J. May. April 2001.
- PEER 2001/03** *A Modal Pushover Analysis Procedure to Estimate Seismic Demands for Buildings: Theory and Preliminary Evaluation.* Anil K. Chopra and Rakesh K. Goel. January 2001.
- PEER 2001/02** *Seismic Response Analysis of Highway Overcrossings Including Soil-Structure Interaction.* Jian Zhang and Nicos Makris. March 2001.
- PEER 2001/01** *Experimental Study of Large Seismic Steel Beam-to-Column Connections.* Egor P. Popov and Shakhzod M. Takhirov. November 2000.
- PEER 2000/10** *The Second U.S.-Japan Workshop on Performance-Based Earthquake Engineering Methodology for Reinforced Concrete Building Structures.* March 2000.
- PEER 2000/09** *Structural Engineering Reconnaissance of the August 17, 1999 Earthquake: Kocaeli (Izmit), Turkey.* Halil Sezen, Kenneth J. Elwood, Andrew S. Whittaker, Khalid Mosalam, John J. Wallace, and John F. Stanton. December 2000.
- PEER 2000/08** *Behavior of Reinforced Concrete Bridge Columns Having Varying Aspect Ratios and Varying Lengths of Confinement.* Anthony J. Calderone, Dawn E. Lehman, and Jack P. Moehle. January 2001.
- PEER 2000/07** *Cover-Plate and Flange-Plate Reinforced Steel Moment-Resisting Connections.* Taejin Kim, Andrew S. Whittaker, Amir S. Gilani, Vitelmo V. Bertero, and Shakhzod M. Takhirov. September 2000.
- PEER 2000/06** *Seismic Evaluation and Analysis of 230-kV Disconnect Switches.* Amir S. J. Gilani, Andrew S. Whittaker, Gregory L. Fenves, Chun-Hao Chen, Henry Ho, and Eric Fujisaki. July 2000.

- PEER 2000/05** *Performance-Based Evaluation of Exterior Reinforced Concrete Building Joints for Seismic Excitation.* Chandra Clyde, Chris P. Pantelides, and Lawrence D. Reaveley. July 2000.
- PEER 2000/04** *An Evaluation of Seismic Energy Demand: An Attenuation Approach.* Chung-Che Chou and Chia-Ming Uang. July 1999.
- PEER 2000/03** *Framing Earthquake Retrofitting Decisions: The Case of Hillside Homes in Los Angeles.* Detlof von Winterfeldt, Nels Roselund, and Alicia Kitsuse. March 2000.
- PEER 2000/02** *U.S.-Japan Workshop on the Effects of Near-Field Earthquake Shaking.* Andrew Whittaker, Editor. July 2000.
- PEER 2000/01** *Further Studies on Seismic Interaction in Interconnected Electrical Substation Equipment.* Armen Der Kiureghian, Kee-Jeung Hong, and Jerome L. Sackman. November 1999.
- PEER 1999/14** *Seismic Evaluation and Retrofit of 230-kV Porcelain Transformer Bushings.* Amir S. Gilani, Andrew S. Whittaker, Gregory L. Fenves, and Eric Fujisaki. December 1999.
- PEER 1999/13** *Building Vulnerability Studies: Modeling and Evaluation of Tilt-up and Steel Reinforced Concrete Buildings.* John W. Wallace, Jonathan P. Stewart, and Andrew S. Whittaker, Editors. December 1999.
- PEER 1999/12** *Rehabilitation of Nonductile RC Frame Building Using Encasement Plates and Energy-Dissipating Devices.* Mehrdad Sasani, Vitelmo V. Bertero, James C. Anderson. December 1999.
- PEER 1999/11** *Performance Evaluation Database for Concrete Bridge Components and Systems under Simulated Seismic Loads.* Yael D. Hose and Frieder Seible. November 1999.
- PEER 1999/10** *U.S.-Japan Workshop on Performance-Based Earthquake Engineering Methodology for Reinforced Concrete Building Structures.* December 1999.
- PEER 1999/09** *Performance Improvement of Long Period Building Structures Subjected to Severe Pulse-Type Ground Motions.* James C. Anderson, Vitelmo V. Bertero, and Raul Bertero. October 1999.
- PEER 1999/08** *Envelopes for Seismic Response Vectors.* Charles Menun and Armen Der Kiureghian. July 1999.
- PEER 1999/07** *Documentation of Strengths and Weaknesses of Current Computer Analysis Methods for Seismic Performance of Reinforced Concrete Members.* William F. Cofer. November 1999.
- PEER 1999/06** *Rocking Response and Overturning of Anchored Equipment under Seismic Excitations.* Nicos Makris and Jian Zhang. November 1999.
- PEER 1999/05** *Seismic Evaluation of 550 kV Porcelain Transformer Bushings.* Amir S. Gilani, Andrew S. Whittaker, Gregory L. Fenves, and Eric Fujisaki. October 1999.
- PEER 1999/04** *Adoption and Enforcement of Earthquake Risk-Reduction Measures.* Peter J. May, Raymond J. Burby, T. Jens Feeley, and Robert Wood. August 1999.
- PEER 1999/03** *Task 3 Characterization of Site Response General Site Categories.* Adrian Rodriguez-Marek, Jonathan D. Bray and Norman Abrahamson. February 1999.
- PEER 1999/02** *Capacity-Demand-Diagram Methods for Estimating Seismic Deformation of Inelastic Structures: SDF Systems.* Anil K. Chopra and Rakesh Goel. April 1999.
- PEER 1999/01** *Interaction in Interconnected Electrical Substation Equipment Subjected to Earthquake Ground Motions.* Armen Der Kiureghian, Jerome L. Sackman, and Kee-Jeung Hong. February 1999.
- PEER 1998/08** *Behavior and Failure Analysis of a Multiple-Frame Highway Bridge in the 1994 Northridge Earthquake.* Gregory L. Fenves and Michael Ellery. December 1998.
- PEER 1998/07** *Empirical Evaluation of Inertial Soil-Structure Interaction Effects.* Jonathan P. Stewart, Raymond B. Seed, and Gregory L. Fenves. November 1998.
- PEER 1998/06** *Effect of Damping Mechanisms on the Response of Seismic Isolated Structures.* Nicos Makris and Shih-Po Chang. November 1998.
- PEER 1998/05** *Rocking Response and Overturning of Equipment under Horizontal Pulse-Type Motions.* Nicos Makris and Yiannis Roussos. October 1998.
- PEER 1998/04** *Pacific Earthquake Engineering Research Invitational Workshop Proceedings, May 14-15, 1998: Defining the Links between Planning, Policy Analysis, Economics and Earthquake Engineering.* Mary Comerio and Peter Gordon. September 1998.
- PEER 1998/03** *Repair/Upgrade Procedures for Welded Beam to Column Connections.* James C. Anderson and Xiaojing Duan. May 1998.

- PEER 1998/02** *Seismic Evaluation of 196 kV Porcelain Transformer Bushings.* Amir S. Gilani, Juan W. Chavez, Gregory L. Fennes, and Andrew S. Whittaker. May 1998.
- PEER 1998/01** *Seismic Performance of Well-Confined Concrete Bridge Columns.* Dawn E. Lehman and Jack P. Moehle. December 2000.

## PEER REPORTS: ONE HUNDRED SERIES

The following PEER reports are available by Internet only at [http://peer.berkeley.edu/publications/peer\\_reports\\_complete.html](http://peer.berkeley.edu/publications/peer_reports_complete.html).

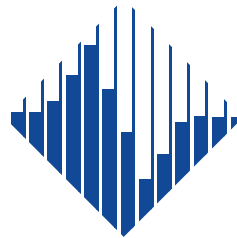
- PEER 2012/103** *Performance-Based Seismic Demand Assessment of Concentrically Braced Steel Frame Buildings*. Chui-Hsin Chen and Stephen A. Mahin. December 2012.
- PEER 2012/102** *Procedure to Restart an Interrupted Hybrid Simulation: Addendum to PEER Report 2010/103*. Vesna Terzic and Božidar Stojadinovic. October 2012.
- PEER 2012/101** *Mechanics of Fiber Reinforced Bearings*. James M. Kelly and Andrea Calabrese. February 2012.
- PEER 2011/107** *Nonlinear Site Response and Seismic Compression at Vertical Array Strongly Shaken by 2007 Niigata-ken Chuetsu-oki Earthquake*. Eric Yee, Jonathan P. Stewart, and Kohji Tokimatsu. December 2011.
- PEER 2011/106** *Self Compacting Hybrid Fiber Reinforced Concrete Composites for Bridge Columns*. Pardeep Kumar, Gabriel Jen, William Trono, Marios Panagiotou, and Claudia Ostertag. September 2011.
- PEER 2011/105** *Stochastic Dynamic Analysis of Bridges Subjected to Spatially Varying Ground Motions*. Katerina Konakli and Armen Der Kiureghian. August 2011.
- PEER 2011/104** *Design and Instrumentation of the 2010 E-Defense Four-Story Reinforced Concrete and Post-Tensioned Concrete Buildings*. Takuya Nagae, Kenichi Tahara, Taizo Matsumori, Hitoshi Shiohara, Toshimi Kabeyasawa, Susumu Kono, Minehiro Nishiyama (Japanese Research Team) and John Wallace, Wassim Ghannoum, Jack Moehle, Richard Sause, Wesley Keller, Zeynep Tuna (U.S. Research Team). June 2011.
- PEER 2011/103** *In-Situ Monitoring of the Force Output of Fluid Dampers: Experimental Investigation*. Dimitrios Konstantinidis, James M. Kelly, and Nicos Makris. April 2011.
- PEER 2011/102** *Ground-Motion Prediction Equations 1964–2010*. John Douglas. April 2011.
- PEER 2011/101** *Report of the Eighth Planning Meeting of NEES/E-Defense Collaborative Research on Earthquake Engineering*. Convened by the Hyogo Earthquake Engineering Research Center (NIED), NEES Consortium, Inc. February 2011.
- PEER 2010/111** *Modeling and Acceptance Criteria for Seismic Design and Analysis of Tall Buildings*. Task 7 Report for the Tall Buildings Initiative - Published jointly by the Applied Technology Council. October 2010.
- PEER 2010/110** *Seismic Performance Assessment and Probabilistic Repair Cost Analysis of Precast Concrete Cladding Systems for Multistory Buildings*. Jeffrey P. Hunt and Božidar Stojadinovic. November 2010.
- PEER 2010/109** *Report of the Seventh Joint Planning Meeting of NEES/E-Defense Collaboration on Earthquake Engineering. Held at the E-Defense, Miki, and Shin-Kobe, Japan, September 18–19, 2009*. August 2010.
- PEER 2010/108** *Probabilistic Tsunami Hazard in California*. Hong Kie Thio, Paul Somerville, and Jascha Polet, preparers. October 2010.
- PEER 2010/107** *Performance and Reliability of Exposed Column Base Plate Connections for Steel Moment-Resisting Frames*. Ady Aviram, Božidar Stojadinovic, and Armen Der Kiureghian. August 2010.
- PEER 2010/106** *Verification of Probabilistic Seismic Hazard Analysis Computer Programs*. Patricia Thomas, Ivan Wong, and Norman Abrahamson. May 2010.
- PEER 2010/105** *Structural Engineering Reconnaissance of the April 6, 2009, Abruzzo, Italy, Earthquake, and Lessons Learned*. M. Selim Günay and Khalid M. Mosalam. April 2010.
- PEER 2010/104** *Simulating the Inelastic Seismic Behavior of Steel Braced Frames, Including the Effects of Low-Cycle Fatigue*. Yuli Huang and Stephen A. Mahin. April 2010.
- PEER 2010/103** *Post-Earthquake Traffic Capacity of Modern Bridges in California*. Vesna Terzic and Božidar Stojadinović. March 2010.
- PEER 2010/102** *Analysis of Cumulative Absolute Velocity (CAV) and JMA Instrumental Seismic Intensity ( $I_{JMA}$ ) Using the PEER–NGA Strong Motion Database*. Kenneth W. Campbell and Yousef Bozorgnia. February 2010.
- PEER 2010/101** *Rocking Response of Bridges on Shallow Foundations*. Jose A. Ugalde, Bruce L. Kutter, and Boris Jeremic. April 2010.
- PEER 2009/109** *Simulation and Performance-Based Earthquake Engineering Assessment of Self-Centering Post-Tensioned Concrete Bridge Systems*. Won K. Lee and Sarah L. Billington. December 2009.

- PEER 2009/108** *PEER Lifelines Geotechnical Virtual Data Center.* J. Carl Stepp, Daniel J. Ponti, Loren L. Turner, Jennifer N. Swift, Sean Devlin, Yang Zhu, Jean Benoit, and John Bobbitt. September 2009.
- PEER 2009/107** *Experimental and Computational Evaluation of Current and Innovative In-Span Hinge Details in Reinforced Concrete Box-Girder Bridges: Part 2: Post-Test Analysis and Design Recommendations.* Matias A. Hube and Khalid M. Mosalam. December 2009.
- PEER 2009/106** *Shear Strength Models of Exterior Beam-Column Joints without Transverse Reinforcement.* Sangjoon Park and Khalid M. Mosalam. November 2009.
- PEER 2009/105** *Reduced Uncertainty of Ground Motion Prediction Equations through Bayesian Variance Analysis.* Robb Eric S. Moss. November 2009.
- PEER 2009/104** *Advanced Implementation of Hybrid Simulation.* Andreas H. Schellenberg, Stephen A. Mahin, Gregory L. Fenves. November 2009.
- PEER 2009/103** *Performance Evaluation of Innovative Steel Braced Frames.* T. Y. Yang, Jack P. Moehle, and Božidar Stojadinovic. August 2009.
- PEER 2009/102** *Reinvestigation of Liquefaction and Nonliquefaction Case Histories from the 1976 Tangshan Earthquake.* Robb Eric Moss, Robert E. Kayen, Liyuan Tong, Songyu Liu, Guojun Cai, and Jiaer Wu. August 2009.
- PEER 2009/101** *Report of the First Joint Planning Meeting for the Second Phase of NEES/E-Defense Collaborative Research on Earthquake Engineering.* Stephen A. Mahin et al. July 2009.
- PEER 2008/104** *Experimental and Analytical Study of the Seismic Performance of Retaining Structures.* Linda Al Atik and Nicholas Sitar. January 2009.
- PEER 2008/103** *Experimental and Computational Evaluation of Current and Innovative In-Span Hinge Details in Reinforced Concrete Box-Girder Bridges. Part 1: Experimental Findings and Pre-Test Analysis.* Matias A. Hube and Khalid M. Mosalam. January 2009.
- PEER 2008/102** *Modeling of Unreinforced Masonry Infill Walls Considering In-Plane and Out-of-Plane Interaction.* Stephen Kadysiewski and Khalid M. Mosalam. January 2009.
- PEER 2008/101** *Seismic Performance Objectives for Tall Buildings.* William T. Holmes, Charles Kircher, William Petak, and Nabih Youssef. August 2008.
- PEER 2007/101** *Generalized Hybrid Simulation Framework for Structural Systems Subjected to Seismic Loading.* Tarek Elkhoraibi and Khalid M. Mosalam. July 2007.
- PEER 2007/100** *Seismic Evaluation of Reinforced Concrete Buildings Including Effects of Masonry Infill Walls.* Alidad Hashemi and Khalid M. Mosalam. July 2007.

The Pacific Earthquake Engineering Research Center (PEER) is a multi-institutional research and education center with headquarters at the University of California, Berkeley. Investigators from over 20 universities, several consulting companies, and researchers at various state and federal government agencies contribute to research programs focused on performance-based earthquake engineering.

These research programs aim to identify and reduce the risks from major earthquakes to life safety and to the economy by including research in a wide variety of disciplines including structural and geotechnical engineering, geology/seismology, lifelines, transportation, architecture, economics, risk management, and public policy.

PEER is supported by federal, state, local, and regional agencies, together with industry partners.



#### **PEER Core Institutions**

University of California, Berkeley (Lead Institution)  
California Institute of Technology  
Oregon State University  
Stanford University  
University of California, Davis  
University of California, Irvine  
University of California, Los Angeles  
University of California, San Diego  
University of Nevada, Reno  
University of Southern California  
University of Washington

PEER reports can be ordered at <https://peer.berkeley.edu/peer-reports> or by contacting

Pacific Earthquake Engineering Research Center  
University of California, Berkeley  
325 Davis Hall, Mail Code 1792  
Berkeley, CA 94720-1792  
Tel: 510-642-3437  
Email: [peer\\_center@berkeley.edu](mailto:peer_center@berkeley.edu)

ISSN 1547-0587X